frontiers | Research Topics

# New advancement in tumor microenvironment remodeling and cancer therapy

**Edited by**
Xiangsheng Zuo, Ying Shen and Yi Yao

**Coordinated by**
Jiayan Chen

**Published in**
Frontiers in Cell and Developmental Biology
Frontiers in Oncology

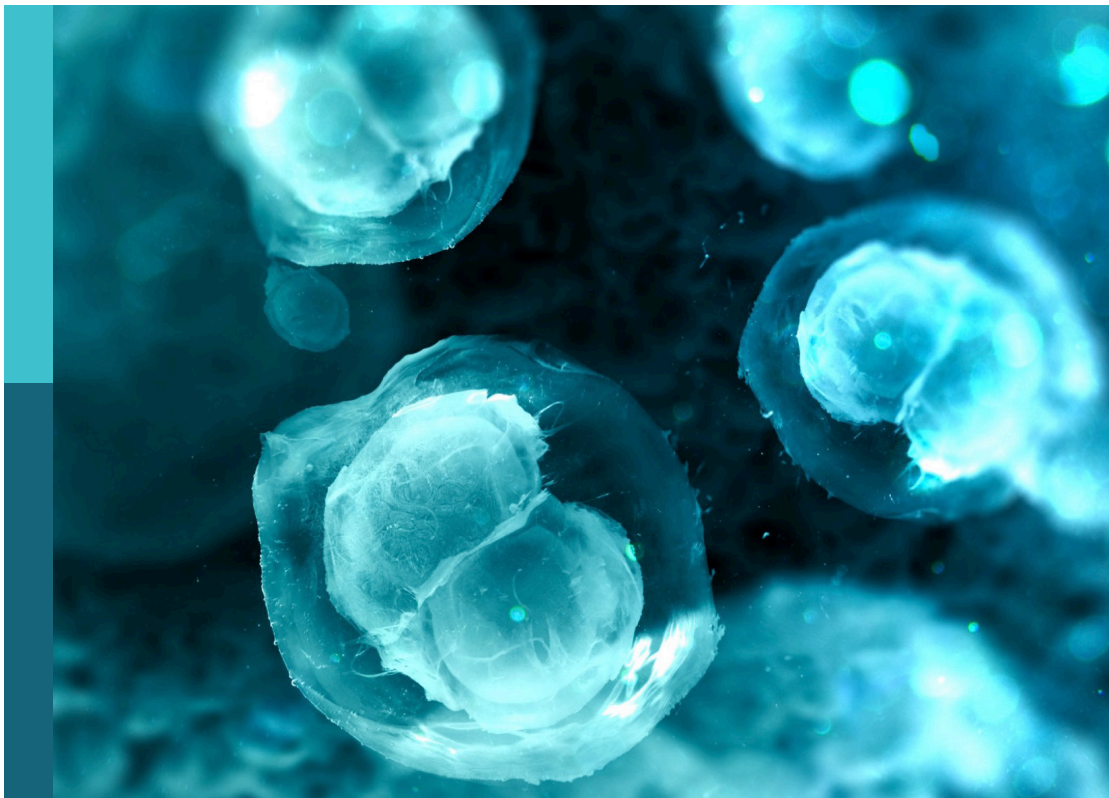

ISSN 1664-8714
ISBN 978-2-8325-4628-4
DOI 10.3389/978-2-8325-4628-4

## About Frontiers

Frontiers is more than just an open access publisher of scholarly articles: it is a pioneering approach to the world of academia, radically improving the way scholarly research is managed. The grand vision of Frontiers is a world where all people have an equal opportunity to seek, share and generate knowledge. Frontiers provides immediate and permanent online open access to all its publications, but this alone is not enough to realize our grand goals.

## Frontiers journal series

The Frontiers journal series is a multi-tier and interdisciplinary set of open-access, online journals, promising a paradigm shift from the current review, selection and dissemination processes in academic publishing. All Frontiers journals are driven by researchers for researchers; therefore, they constitute a service to the scholarly community. At the same time, the *Frontiers journal series* operates on a revolutionary invention, the tiered publishing system, initially addressing specific communities of scholars, and gradually climbing up to broader public understanding, thus serving the interests of the lay society, too.

## Dedication to quality

Each Frontiers article is a landmark of the highest quality, thanks to genuinely collaborative interactions between authors and review editors, who include some of the world's best academicians. Research must be certified by peers before entering a stream of knowledge that may eventually reach the public - and shape society; therefore, Frontiers only applies the most rigorous and unbiased reviews. Frontiers revolutionizes research publishing by freely delivering the most outstanding research, evaluated with no bias from both the academic and social point of view. By applying the most advanced information technologies, Frontiers is catapulting scholarly publishing into a new generation.

## What are Frontiers Research Topics?

Frontiers Research Topics are very popular trademarks of the *Frontiers journals series*: they are collections of at least ten articles, all centered on a particular subject. With their unique mix of varied contributions from Original Research to Review Articles, Frontiers Research Topics unify the most influential researchers, the latest key findings and historical advances in a hot research area.

Find out more on how to host your own Frontiers Research Topic or contribute to one as an author by contacting the Frontiers editorial office: frontiersin.org/about/contact

# New advancement in tumor microenvironment remodeling and cancer therapy

**Topic editors**

Xiangsheng Zuo — University of Texas MD Anderson Cancer Center, United States

Ying Shen — Sun Yat-sen University Cancer Center (SYSUCC), China

Yi Yao — Renmin Hospital of Wuhan University, China

**Topic coordinator**

Jiayan Chen — Fudan University, China

**Citation**

Zuo, X., Shen, Y., Yao, Y., Chen, J., eds. (2024). *New advancement in tumor microenvironment remodeling and cancer therapy*. Lausanne: Frontiers Media SA. doi: 10.3389/978-2-8325-4628-4

# Table of contents

frontiers | Frontiers in Cell and Developmental Biology

TYPE Editorial
PUBLISHED 07 March 2024
DOI 10.3389/fcell.2024.1384567



OPEN ACCESS

EDITED AND REVIEWED BY
Shyamala Maheswaran,
Massachusetts General Hospital and Harvard Medical School, United States

*CORRESPONDENCE
Xiangsheng Zuo,
xzuo@mdanderson.org

RECEIVED 09 February 2024
ACCEPTED 19 February 2024
PUBLISHED 07 March 2024

CITATION
Yao Y, Shen Y, Yao JC and Zuo X (2024), Editorial: New advancement in tumor microenvironment remodeling and cancer therapy.
*Front. Cell Dev. Biol.* 12:1384567.
doi: 10.3389/fcell.2024.1384567



# Editorial: New advancement in tumor microenvironment remodeling and cancer therapy

Yi Yao[1,2], Ying Shen[3,4,5], James C. Yao[6] and Xiangsheng Zuo[6]*

[1]Cancer Center, Renmin Hospital of Wuhan University, Wuhan, China, [2]Hubei Provincial Research Center for Precision Medicine of Cancer, Wuhan, China, [3]State Key Laboratory of Oncology in South China, Guangzhou, China, [4]Guangdong Provincial Clinical Research Center for Cancer, Guangzhou, China, [5]Sun Yat-sen University Cancer Center, Guangzhou, China, [6]Department of Gastrointestinal Medical Oncology, University of Texas MD Anderson Cancer Center, Houston, TX, United States

KEYWORDS

**TME, cancer therapeutics, immune check inhibitor, PD-L1, tumor mutational burden**

Editorial on the Research Topic
New advancement in tumor microenvironment remodeling and cancer therapy

Tumor progression and treatment processes have the potential to remodel tumor microenvironment (TME) (Benavente et al., 2020; Winkler et al., 2020; Arora and Pal, 2021). Conversely, the TME plays a substantial role in altering tumor growth, metastasis, therapeutic response, and development of therapeutic resistance (Sahai et al., 2020; Winkler et al., 2020; Wu et al., 2021; Mantovani et al., 2022). This Research Topic is dedicated to publishing original research and review articles exploring critical factors reshaping TME and the interplays between the TME remodeling and tumor progression, immune therapeutic response, and resistance.

Cancer cells evade immune surveillance through PD-1/PD-L1 axis that inhibits activation and functions of tumor-infiltrating lymphocytes (TILs) in TME. Blocking the PD-1/PD-L1 signaling has shown remarkable effectiveness in restoring T cells from exhaustion and normalizing the dysregulated TME, leading to cancer cell eradication (Cha et al., 2019). Immune checkpoint therapies (ICTs) such as the antibodies against this axis exhibit potent antitumor activities in various cancers, including lung adenocarcinoma (LUAD) (Han et al., 2020; Sun et al., 2023). Determination of PD-L1 expression is crucial for selecting patients benefiting from this therapeutic approach, as PD-L1 expression level in cancer cells is positively associated with a favorable response (Ribas and Hu-Lieskovan, 2016). The regulation of PD-L1 involves intrinsic (cancer cell-associated) and extrinsic (TME-originating) factors, including dysregulation of oncogenic signaling pathways and dependence on inflammatory signals, cytokines, and metabolites. The TME, a complex ecosystem supporting tumor growth, undergoes dynamic communication and metabolic symbiosis between tumor and non-tumor cell populations. Iron, a multifunctional micronutrient, plays a key role in signaling pathways within tumor cells and the TME, influencing cancer progression (Sacco et al., 2021). The iron addiction phenotype, driven by reprogramming intracellular iron metabolism and interactions with immune cells, has dual effects, promoting cancer growth and suppressing antitumor immune functions (Cassim and Pouyssegur, 2019). The study by Battaglia et al. revealed a significant correlation between iron density and PD-L1 expression in LUAD tissues. *In vitro* analyses of H460 and

A549 LUAD cells showed increased PD-L1 mRNA and protein levels in an iron-enriched microenvironment, mediated by reactive oxygen species (ROS)/c-Myc signaling pathway; iron-induced PD-L1 overexpression inhibited T cell activity, demonstrated by reduced IFN-γ release in a co-culture system of tumor and T cells, emphasizing the impact of iron on immune modulation in LUAD. In TCGA LUAD datasets, the levels of transferrin receptor CD71, indicative of an iron-addicted phenotype, correlate with elevated PD-L1 mRNA. This study explores a novel association between high iron density and elevated PD-L1 expression in LUAD and the findings open a door for combinatorial strategies that consider TME iron levels to enhance the efficacy of anti-PD-1/PD-L1-based immune therapies for LUAD patients.

ICTs have significantly transformed clinical outcomes for cancer patients, providing enduring clinical benefits, and even leading to a cure in a subset of individuals (Sharma et al., 2023). Cancer patient response to ICTs (e.g., pembrolizumab) varies across the tumor subtypes, necessitating robust biomarkers for patient selection (Sharma et al., 2023). While PD-L1 expression and microsatellite instability-high (MSI-H) are FDA-approved indicators, tumor mutational burden (TMB), the number of somatic mutations per mega base of interrogated genomic sequence, is emerging as a promising biomarker in solid tumors (Singal et al., 2019; Sha et al., 2020). TMB varies across malignancies. The data from KEYNOTE-158 study showing TMB-high (≥10 mut/Mb) correlates with better pembrolizumab therapy outcomes in multiple cancer types, lead to FDA approval of pembrolizumab for TMB-high tumor subgroup (Marabelle et al., 2020). However, concerns arise regarding the TMB cutoff of 10 mut/Mb and its applicability beyond the KEYNOTE-158 study. The study by Mo et al. aimed to statistically determine the optimal universal cutoff for defining TMB-high in the published clinical trials, predicting anti-PD-L1 therapy efficacy in diverse advanced solid tumors. By integrating MSK-IMPACT TMB data and objective response rate (ORR) across various solid cancer types, the authors identified 10 mut/Mb as the optimal cutoff, strongly correlated with PD-L1 blockade ORR. This study provides a new universal TMB-high cutoff evidence in support of the KEYNOTE-158 study for guiding clinical decisions and addressing challenges associated with tumor-agnostic pembrolizumab approval in TMB-high cases.

Oral squamous cell carcinoma (OSCC) is a highly malignant disease with increasing incidence and lacks effective treatments, urging the exploration of new therapeutic targets. The B7 family, a group of 10 structurally related, cell-surface protein ligands, including PD-L1 (B7-H1), encoded by CD274 gene, and inducible T cell costimulatory ligand (ICOSLG, B7-H2), encoded by CD275 gene, bind to receptors on lymphocytes that regulate adaptive immune responses in cancers (Ni and Dong, 2017). PD-L1 (B7-H1) plays a crucial role in immune escape in OSCC (Zhao et al., 2023). The association of ICOSLG expression levels with immunosuppression, tumor progression and prognosis of different solid cancer types such as gastric cancer (Chen et al., 2003), colorectal cancer (Cao et al., 2018) and glioblastoma (Iwata et al., 2020) has been studied. However, the specific role of ICOSLG in OSCC remains largely unexplored. In a retrospective study, Dong et al. observed that ICOSLG was ubiquitously expressed in OSCC cancer cells, cancer-associated fibroblasts, and TILs. Elevated ICOSLG levels were found to be correlated with advanced TNM stage and lymph node metastasis, serving as a predictive factor for decreased overall or metastasis-free survival in OSCC patients. These findings underscore the potential of ICOSLG as a promising target for precision immunotherapy in the context of OSCC.

B cell malignancies, encompassing B-cell non-Hodgkin's lymphomas (B-NHL) and B-cell chronic lymphocytic leukemias (B-CLL), are prevalent in cancers that arise in B lymphocytes. B-NHL ranks as the seventh most common cancer in the United States, with 74,000 new cases annually. Obinutuzumab, the first humanized type II glycoengineered anti-CD20 monoclonal antibody, displayed superior outcomes in clinical trials for B-NHL and B-CLL (Goede et al., 2014; Gabellier and Cartron, 2016). Despite these advancements, relapse remains common, highlighting the need to further understand the mechanisms to improve the patient therapy. Chemotherapy resistance often stems from malignant B-cell migration to the bone marrow and interaction with the stromal layer. The study by Fagnano et al. explored whether stromal cells impeded this type II anti-CD20 antibody mechanisms, contributing to therapeutic resistance by employing co-cultures of Raji or Daudi human B lymphoblastoid cells and M210B4 bone marrow stromal cells. The results showed direct contact with stromal cell inhibited obinutuzumab-induced programmed cell death, cellular phagocytosis, and cytotoxicity; stromal interference with B-cell adhesion and actin remodeling, was possibly linked to CD20 downregulation. Understanding the significance of direct interactions between stromal and tumor cells may provide great insights for developing better strategies to enhance Obinutuzumab efficacy by targeting both stromal and tumor cells and ultimately improve outcomes in B-cell malignancies.

Heterotypic 3D human tumor cell models, combining tumor cells and fibroblasts, strike a balance by mimicking solid tumor phenomena effectively (Franchi-Mendes et al., 2021). The anthracycline chemotherapy drug Doxorubicin (DOX) is used for the treatment of various cancers, including colon cancer, by disrupting tumor cell DNA to inhibit replication. However, DOX resistance hinders its effectiveness (Chen et al., 2018). Valente et al. study explored the interplay between fibroblasts, DOX resistance, and spheroid characteristics. With establishing DOX-sensitive and -resistant spheroids from HCT116 colon cancer cells with or without fibroblasts, the study unveiled that fibroblasts stabilized spheroids and altered hypoxia- and inflammation-related gene expression. DOX resistance impacted drug internalization. These findings underscore the significance of models resembling *in vivo* tumor cell interactions with TME, offering valuable insights for testing drug treatments, and understanding resistance mechanisms.

Moreover, Yang et al. identified that SH3 domain-binding glutamate-rich protein 3 (SH3BGRL3) was upregulated in acute myeloid leukemia (AML) and was negatively correlated with survival of AML patients. Furthermore, *in-vitro* studies showed that circSH3BGRL3/circRNA_0010984 promoted AML cell proliferation by inhibiting miR-375 activity and increasing YAP1 expression. The study by Jiang et al. revealed that miRNA-146a-5p expression was downregulated in gastric cancer (GC) tissues, and *in-vitro* study showed that miRNA-146a-5p inhibited GC cell growth and promoted GC cell

apoptosis by directly suppressing CDC14A expression. Zhang et al. identified a set of neurotransmitter receptor-related colorectal cancer prognostic gene signature (CHRNA3, GABRD, GRIK3, GRIK5), which were enriched in cellular metabolic pathways. High expression of these genes was positively correlated with immunosuppressive cell infiltration, and their expression levels in cancer cells significantly affected the response of cancer cells to chemotherapy.

There are also 4 review articles published under this Research Topic. Yang et al. emphasized the cGAS/STING's crucial role in mediating innate immunity, enhancing interferon release, and influencing TME. STING modulates diverse pathways, including non-innate immune processes like autophagy-dependent ferroptosis, ROS-induced cell death, endoplasmic reticulum stress-mTOR signaling, apoptosis, senescence-associated secretory phenotypes, and cellular metabolism. These effects collectively shape tumor cell progression, highlighting the multifaceted role of cGAS/STING signaling in cancer biology. 2) Zhang et al. discussed content alterations of tumor-educated platelets, including their coding and noncoding RNA, and protein and their role as potential cancer biomarkers in diverse cancer diagnostics. 3) Chen et al. delved into the role of mechanobiology including genetic, biochemical, and mechanical factors and their interplays in cancer progression. Mechanical alterations, such as changes in stiffness and morphology, significantly impact cancer initiation and dissemination. Exploring cancer mechanobiology offers insights for personalized medicine and innovative treatments. Targeting tumor and microenvironment physical properties provides intervention opportunities, aided by advanced imaging and lab-on-a-chip systems for personalized investigations and drug screening. 4) Saxena et al. discussed the crucial role of complement factor H (CFH) as an innate immune checkpoint in cancer control. They also explored molecular functions, interaction with immune cells, clinical implications, therapeutic potential of CFH, and discussed the challenge for CFH as a target in cancer immunotherapy.

In summary, all publications within this Research Topic have improved our understanding of TME remodeling and cancer therapy interplay. Furthermore, these papers may make valuable contributions towards advancing the treatment options available for diverse cancers.

## Author contributions

YY: Writing–review and editing. YS: Writing–review and editing. JCY: Writing–review and editing. XZ: Conceptualization, Writing–original draft, Writing–review and editing.

## Funding

The author(s) declare that financial support was received for the research, authorship, and/or publication of this article. YY was supported by Natural Science Foundation of Hubei Province of China (2022CFB114). YS was supported by the Natural Science Foundation of China (NSFC) grant (82273314).

## Acknowledgments

We thank all the contributors to this special Research Topic entitled New Advancement in Tumor Microenvironment Remodeling and Cancer Therapy.

## Conflict of interest

The authors declare that the research was conducted in the absence of any commercial or financial relationships that could be construed as a potential conflict of interest.

The author(s) declared that they were an editorial board member of Frontiers, at the time of submission. This had no impact on the peer review process and the final decision.

## Publisher's note



## References

Arora, L., and Pal, D. (2021). Remodeling of stromal cells and immune landscape in microenvironment during tumor progression. *Front. Oncol.* 11, 596798. doi:10.3389/fonc.2021.596798

Benavente, S., Sánchez-García, A., Naches, S., Me, L. L., and Lorente, J. (2020). Therapy-induced modulation of the tumor microenvironment: new opportunities for cancer therapies. *Front. Oncol.* 10, 582884. doi:10.3389/fonc.2020.582884

Cao, Y., Cao, T., Zhao, W., He, F., Lu, Y., Zhang, G., et al. (2018). Expression of B7-H2 on CD8(+) T cells in colorectal cancer microenvironment and its clinical significance. *Int. Immunopharmacol.* 56, 128–134. doi:10.1016/j.intimp.2018.01.018

Cassim, S., and Pouyssegur, J. (2019). Tumor microenvironment: a metabolic player that shapes the immune response. *Int. J. Mol. Sci.* 21, 157. doi:10.3390/ijms21010157

Cha, J. H., Chan, L. C., Li, C. W., Hsu, J. L., and Hung, M. C. (2019). Mechanisms controlling PD-L1 expression in cancer. *Mol. Cell.* 76, 359–370. doi:10.1016/j.molcel.2019.09.030

Chen, C., Lu, L., Yan, S., Yi, H., Yao, H., Wu, D., et al. (2018). Autophagy and doxorubicin resistance in cancer. *Anticancer Drugs* 29, 1–9. doi:10.1097/CAD.0000000000000572

Chen, X. L., Cao, X. D., Kang, A. J., Wang, K. M., Su, B. S., and Wang, Y. L. (2003). *In situ* expression and significance of B7 costimulatory molecules within tissues of human gastric carcinoma. *World J. Gastroenterol.* 9, 1370–1373. doi:10.3748/wjg.v9.i6.1370

Franchi-Mendes, T., Eduardo, R., Domenici, G., and Brito, C. (2021). 3D cancer models: depicting cellular crosstalk within the tumour microenvironment. *Cancers (Basel)* 13, 4610. doi:10.3390/cancers13184610

Gabellier, L., and Cartron, G. (2016). Obinutuzumab for relapsed or refractory indolent non-Hodgkin's lymphomas. *Ther. Adv. Hematol.* 7, 85–93. doi:10.1177/2040620715622613

Goede, V., Fischer, K., Busch, R., Engelke, A., Eichhorst, B., Wendtner, C. M., et al. (2014). Obinutuzumab plus chlorambucil in patients with CLL and coexisting conditions. *N. Engl. J. Med.* 370, 1101–1110. doi:10.1056/NEJMoa1313984

Han, Y., Liu, D., and Li, L. (2020). PD-1/PD-L1 pathway: current researches in cancer. *Am. J. Cancer Res.* 10, 727–742.

Iwata, R., Hyoung Lee, J., Hayashi, M., Dianzani, U., Ofune, K., Maruyama, M., et al. (2020). ICOSLG-mediated regulatory T-cell expansion and IL-10 production promote progression of glioblastoma. *Neuro Oncol.* 22, 333–344. doi:10.1093/neuonc/noz204

Mantovani, A., Allavena, P., Marchesi, F., and Garlanda, C. (2022). Macrophages as tools and targets in cancer therapy. *Nat. Rev. Drug Discov.* 21, 799–820. doi:10.1038/s41573-022-00520-5

Marabelle, A., Fakih, M., Lopez, J., Shah, M., Shapira-Frommer, R., Nakagawa, K., et al. (2020). Association of tumour mutational burden with outcomes in patients with advanced solid tumours treated with pembrolizumab: prospective biomarker analysis of the multicohort, open-label, phase 2 KEYNOTE-158 study. *Lancet Oncol.* 21, 1353–1365. doi:10.1016/S1470-2045(20)30445-9

Ni, L., and Dong, C. (2017). New B7 family checkpoints in human cancers. *Mol. Cancer Ther.* 16, 1203–1211. doi:10.1158/1535-7163.MCT-16-0761

Ribas, A., and Hu-Lieskovan, S. (2016). What does PD-L1 positive or negative mean? *J. Exp. Med.* 213, 2835–2840. doi:10.1084/jem.20161462

Sacco, A., Battaglia, A. M., Botta, C., Aversa, I., Mancuso, S., Costanzo, F., et al. (2021). Iron metabolism in the tumor microenvironment-implications for anti-cancer immune response. Cells *10*.

Sahai, E., Astsaturov, I., Cukierman, E., DeNardo, D. G., Egeblad, M., Evans, R. M., et al. (2020). A framework for advancing our understanding of cancer-associated fibroblasts. *Nat. Rev. Cancer* 20, 174–186. doi:10.1038/s41568-019-0238-1

Sha, D., Jin, Z., Budczies, J., Kluck, K., Stenzinger, A., and Sinicrope, F. A. (2020). Tumor mutational burden as a predictive biomarker in solid tumors. *Cancer Discov.* 10, 1808–1825. doi:10.1158/2159-8290.CD-20-0522

Sharma, P., Goswami, S., Raychaudhuri, D., Siddiqui, B. A., Singh, P., Nagarajan, A., et al. (2023). Immune checkpoint therapy-current perspectives and future directions. *Cell.* 186, 1652–1669. doi:10.1016/j.cell.2023.03.006

Singal, G., Miller, P. G., Agarwala, V., Li, G., Kaushik, G., Backenroth, D., et al. (2019). Association of patient characteristics and tumor genomics with clinical outcomes among patients with non-small cell lung cancer using a clinicogenomic database. *Jama* 321, 1391–1399. doi:10.1001/jama.2019.3241

Sun, Q., Hong, Z., Zhang, C., Wang, L., Han, Z., and Ma, D. (2023). Immune checkpoint therapy for solid tumours: clinical dilemmas and future trends. *Signal Transduct. Target Ther.* 8, 320. doi:10.1038/s41392-023-01522-4

Winkler, J., Abisoye-Ogunniyan, A., Metcalf, K. J., and Werb, Z. (2020). Concepts of extracellular matrix remodelling in tumour progression and metastasis. *Nat. Commun.* 11, 5120. doi:10.1038/s41467-020-18794-x

Wu, F., Yang, J., Liu, J., Wang, Y., Mu, J., Zeng, Q., et al. (2021). Signaling pathways in cancer-associated fibroblasts and targeted therapy for cancer. *Signal Transduct. Target Ther.* 6, 218. doi:10.1038/s41392-021-00641-0

Zhao, M., He, Y., Zhu, N., Song, Y., Hu, Q., Wang, Z., et al. (2023). IL-33/ST2 signaling promotes constitutive and inductive PD-L1 expression and immune escape in oral squamous cell carcinoma. *Br. J. Cancer* 128, 833–843. doi:10.1038/s41416-022-02090-0

frontiers | Frontiers in Oncology

TYPE Review
PUBLISHED 17 April 2023
DOI 10.3389/fonc.2023.1165600



OPEN ACCESS

EDITED BY
Yi Yao,
Renmin Hospital of Wuhan University, China

REVIEWED BY
Zheming Liu,
Renmin Hospital of Wuhan University, China
Orazio Fortunato,
National Cancer Institute Foundation (IRCCS), Italy

*CORRESPONDENCE
Xingguo Song
xgsong@sdfmu.edu.cn

SPECIALTY SECTION
This article was submitted to Cancer Epidemiology and Prevention, a section of the journal Frontiers in Oncology

RECEIVED 23 February 2023
ACCEPTED 30 March 2023
PUBLISHED 17 April 2023

CITATION
Zhang Q, Song X and Song X (2023) Contents in tumor-educated platelets as the novel biosource for cancer diagnostics. *Front. Oncol.* 13:1165600. doi: 10.3389/fonc.2023.1165600



# Contents in tumor-educated platelets as the novel biosource for cancer diagnostics

Qianru Zhang[1], Xianrang Song[1,2] and Xingguo Song[1]*

[1]Department of Clinical Laboratory, Shandong Cancer Hospital and Institute, Shandong First Medical University and Shandong Academy of Medical Sciences, Jinan, Shandong, China, [2]Shandong Provincial Key Laboratory of Radiation Oncology, Shandong Cancer Hospital and Institute, Shandong First Medical University and Shandong Academy of Medical Sciences, Jinan, Shandong, China

Liquid biopsy, a powerful non-invasive test, has been widely used in cancer diagnosis and treatment. Platelets, the second most abundant cells in peripheral blood, are becoming one of the richest sources of liquid biopsy with the capacity to systematically and locally respond to the presence of cancer and absorb and store circulating proteins and different types of nucleic acids, thus called "tumor-educated platelets (TEPs)". The contents of TEPs are significantly and specifically altered, empowering them with the potential as cancer biomarkers. The current review focuses on the alternation of TEP content, including coding and non-coding RNA and proteins, and their role in cancer diagnostics.

KEYWORDS

**tumor-educated platelets (TEPs), cancer diagnostics, mRNA, non-coding RNA, proteome**

## 1 Introduction

There has been remarkable progress in the field of cancer diagnostics; however, tissue biopsy remains the most important and only method of making a definitive diagnosis. Because tissue biopsy is traumatic and infeasible for serial collection, liquid biopsy has become a hot research direction with remarkable advances including non-invasive, easy-to-obtain, and real-time monitoring (1). At present, liquid biopsy mainly focuses on cell-free DNA (cfDNA) (2), circulating tumor cells (CTCs) (3), extracellular vesicles (EVs) (4), circulating tumor RNA (5), and, more recently, tumor-educated platelets (TEPs) (6, 7). All of these biological sources present are considered to be powerful reservoirs of cancer biomarkers, contributing to early diagnosis and treatment, as well as to precision cancer medicine.

Platelets, circulating fragments of anucleate cells originating from mature megakaryocytes (MKs), are the second most abundant cell type in peripheral blood with relatively short lifespans ranging from 8 to 11 days (8) and play a crucial role in hemostasis, thrombosis, and inflammatory processes (9–11). Over the past decades, multiple pieces of evidence indicate that platelets serve much more comprehensive

functions in all steps of tumorigenesis, including tumor growth, tumor cell extravasation, angiogenesis, and metastasis (12). The interaction between platelets and tumor is the prerequisite for hematogenous metastasis (Figure 1). Platelets release many anti-angiogenic or pro-angiogenic factors when activated, which display the regulatory effect on vascular remodeling and vessel integrity, thus helping tumor cells adhere to and penetrate the endothelium (13). Upon arrival in the blood, tumor cells are covered and shielded by platelets from shear forces by lodging in the vessel wall (14), and they evade NK cells attack by impeding the immunologic recognition (15–17). Subsequently, platelets along with platelet-derived particles influence circulating tumor cells, leading to the transmission of mesenchymal-like phenotype, as well as capillary endothelium, to expedite extravasation in distant organs (18–20).

From another point of view, bidirectional tumor–platelet interactions are reciprocal and complicated on those platelets that enhance malignancies while tumors educate platelets (21–23). The education of platelets by tumor cells can be achieved in direct and indirect manners. In the bloodstream, straightforward contact occurs between molecules on platelets and tumor cells, including P-selectin (24–26), integrins (27, 28), and glycoproteins (29, 30), leading to platelet activation, so-called direct manner. Moreover, tumor cells can release metabolites extracellularly, including cytokines, chemokines, and, importantly, the extracellular vesicles, all of which serve as the indirect way to educate not only circulation platelets (31, 32) but also megakaryocytes in the bone marrow to subsequently alter platelet generation (33, 34) (Figure 1). Overall, platelets systematically and locally respond to cancer, absorbing and storing circulating proteins and different types of nucleic acids from

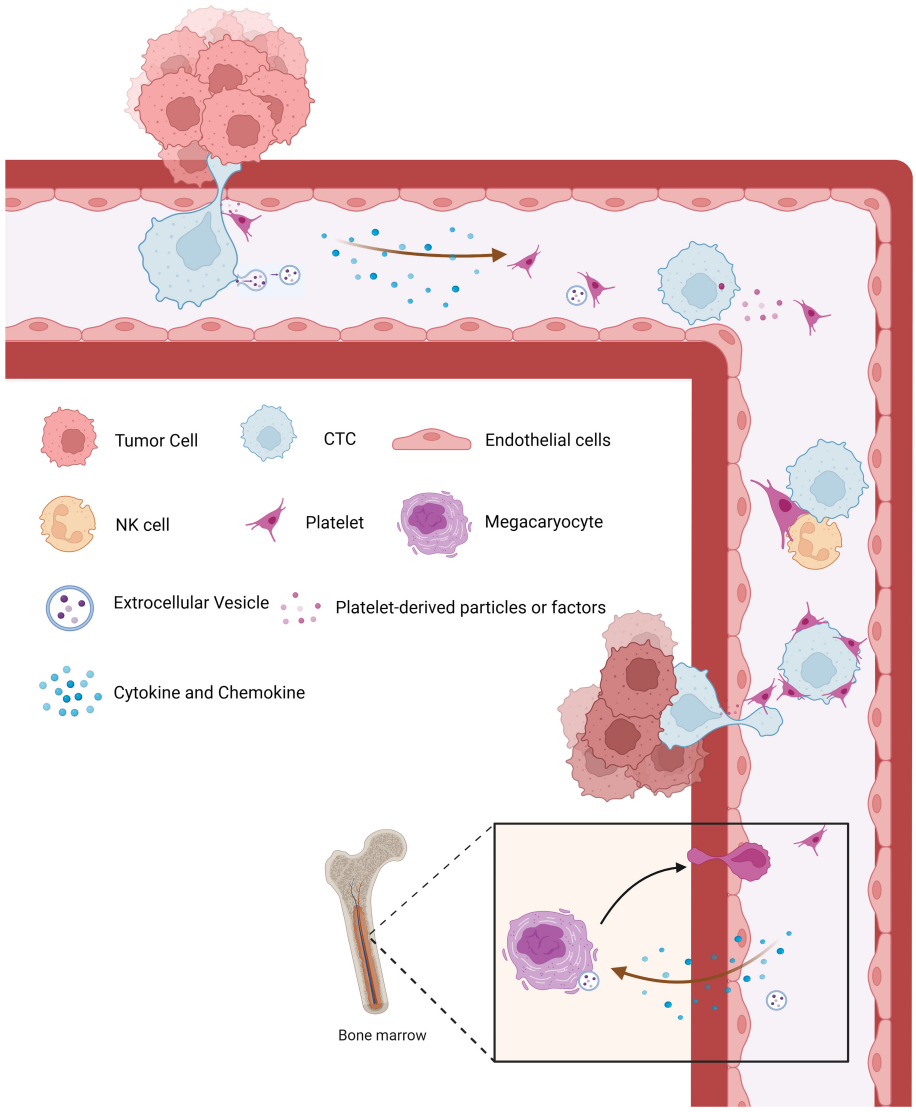


FIGURE 1
The crosstalk between cancer and platelets. Platelets are released into circulation by megakaryocytes and produce tumor-educated platelets through direct or indirect communication with tumor cells or tumor-derived biomolecules. Tumor cells can induce the activation and aggregation of platelets, which in turn secrete various factors that promote the growth and metastasis of the primary tumor. During metastasis, aggregated platelets protect CTCs from shear forces and evade immune surveillance. At the same time, platelets can recruit stromal cells to facilitate the establishment of metastatic niches and promote the metastasis of tumor cells. CTCs, circulating tumor cells.

the peripheral blood and tumor microenvironment (32), consequently sequestering tumor-specified biomolecules including RNA transcripts and proteins, which are called TEPs (7).

As high-throughput sequencing technology (35, 36) and computer identification algorithms (37, 38) have been developed in the past few years, the contents of platelets have been identified and well demonstrated. Platelets lack the nucleus and thus possess no genomic but mitochondrial DNA (39). They contain RNA molecules including coding and non-coding (40), and proteins (41), which can be not only inherited from megakaryocytes but also generated in platelets since platelets exploit functional spliceosome, ribosome, and other non-coding RNA processing mechanisms (42–44) (Figure 2). During tumor education of platelets, the contents in platelets are altered significantly and specifically in response to the presence of cancer, empowering them to serve as an important repository of potential RNA and protein biomarkers for early cancer detection (45), disease progression monitoring (7, 38), and response to treatment (46, 47).

A typical workflow for studying TEPs as biomarkers in cancer, as shown in Figure 3, consists of multiple steps. Platelet separation is the key step in the whole workflow because platelets are fragile and easily activated in the environment. Currently, the most commonly used method of platelet separation is low-speed centrifugation. Anticoagulated whole blood is centrifuged at low speed to obtain platelet-rich plasma (PRP), followed by another centrifugation to precipitate platelets at room temperature (48). D'ambrosi et al. (49) used two methods to isolate platelets, one was conventional centrifugation and the other was adding Iloprost (50 nM) to PRP, both of which obtained the lowest activation and highest purity of platelets without significant differences. The standard for high-purity platelet preparation is less than 5 nucleated cells per 10 million platelets (37) and, more importantly, to avoid platelet activation. Detection of platelet activation markers contributes significantly to the quantitative control of platelet separation. After separation, platelets are lysed for nucleic acids and protein extraction, which are then subjected to high-throughput sequencing or mass spectrometry to screen out the potential biomarkers and verified in a large-scale cohort. In the current review, attention is paid to the alternation of contents in TEPs, including coding and non-coding RNA and proteins, and their role in cancer diagnostics (Table 1).

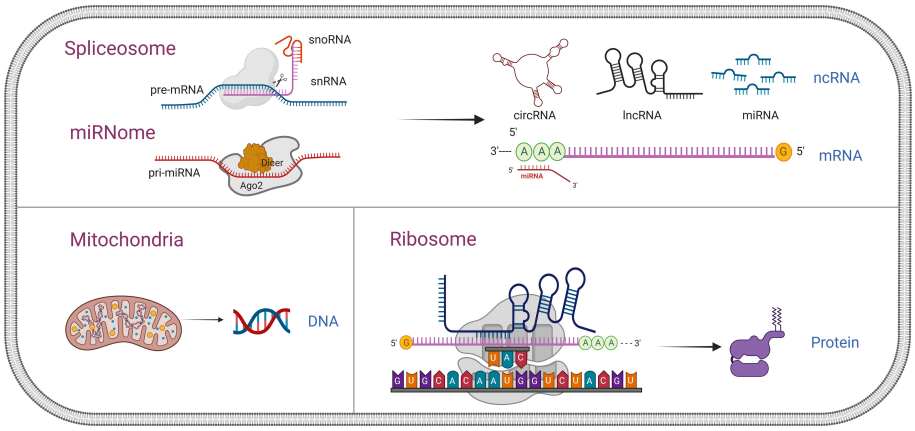


FIGURE 2
Comprehensive overview of nucleic acid and protein in platelets. Platelets lack the nucleus and thus possess no genomic but only mitochondrial DNA. They contain RNA molecules, including coding and non-coding, and proteins, which can be not only inherited from megakaryocytes but also generated in the platelets since platelets exploit functional spliceosome, ribosome, and other non-coding RNA (snRNA, snoRNA, miRNA, circRNA, and lncRNA) processing mechanisms. snRNA, small nuclear RNA; snoRNA, small nucleolar RNA; miRNA, microRNA; circRNA, circular RNA; lncRNA, non-coding RNA.

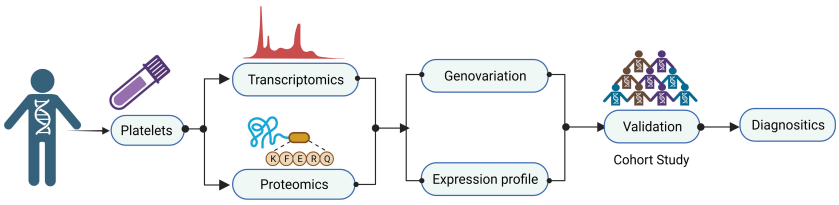


FIGURE 3
Workflow of tumor-educated platelet research for clinical applications. A typical workflow for studying TEPs as biomarkers in cancer consist of multiple steps. Platelet separation is the key step for the whole workflow because the platelets are fragile and easily activated in the environment. After separation, platelets are lysed for nucleic acids and protein extraction, which then are subjected to high-throughput sequencing or mass spectrometry to screen out the potential biomarkers and verified in a large-scale cohort. TEPs, tumor-educated platelets.

TABLE 1 Role of RNA molecules and proteins in cancer diagnosis in TEPs.

| Marker type | TEP biomarkers | Tumor type | Expression | Test | Techniques | References |
|---|---|---|---|---|---|---|
| mRNA | | Pan-cancer: NSCLC, CRC, GBM, PAAD, HBC, BRCA | | Accuracy = 96% | RNA-seq, multiclass support vector machine (SVM)-based classification | (48) |
| | ITGA2B | NSCLC | Up | Test cohort: AUC = 0.922, validation cohort: AUC = 0.888 | RNA-seq, q-PCR, ddPCR | (50) |
| | MAX, MTURN, HLA-B | Lung cancer | Up | AUC = 0.734, AUC = 0.787 (early lung cancer), AUC = 0.825 (MTURN mRNA as diagnostics biomarker for female lung cancer) | Microarray, q-PCR | (51) |
| | TIMP1 | CRC | Up | AUC = 0.9583, TIPM1 mRNA carried into cancer cells by TEPs promotes cancer cell growth | RNA-seq, q-PCR | (52) |
| | TPM3 | Breast cancer | Up | AUC = 0.9705 (diagnosis), AUC = 0.8404 (metastasis), platelet microvesicles from cancer patients promote cancer cell migration by delivering TPM3 mRNA | RNA-seq, q-PCR | (53) |
| | ACIN1 | Lung cancer | Up | AUC = 0.608 | q-PCR | (54) |
| MiRNA | MiR-34c-3p3p, miR-18a-5p | NPC | Up | AUC = 0.952 (miR-34c-3p3p), AUC = 0.884 (miR-18a-5p), AUC = 0.954 (combination) | q-PCR | (55) |
| | MiR-223 | NSCLC | Up | Platelet miR-223 targeted EPB41L3 to promote A549 cell invasion | | (56) |
| CircRNA | CircNRIP1 | NSCLC | Down | p = 0.0302 (NSCLC), p = 0.0263 (late stage NSCLC), p = 0.098 (early-stage NSCLC) | RNA-seq, q-PCR | (49) |
| LncRNA | linc-GTF2H2-1, RP3-466P17.2, LCC-ST8SIA4-12 | NSCLC | | AUC = 0.781 (linc-GTF2H2-1), AUC = 0.788 (RP3-466P17.2), AUC = 0.725 (LCC-ST8SIA4-12), AUC = 0.921 (three lncRNA), early stage AUC = 0.704 (linc-GTF2H2-1), AUC = 0.771 (RP3-466P17.2), AUC = 0.768 (LCC-ST8SIA4-12), AUC = 0.895 (three lncRNA) | Microarray, q-PCR | (57) |
| | MAGI2-AS3, ZFAS1 | NSCLC | Down | MAGI2-AS3 (AUC = 0.853, AD; AUC = 0.892, SCC); ZFAS1 (AUC = 0.780, AD; AUC = 0.744, SCC) | q-PCR | (58) |
| | LncRNA ROR | NPC | Down | Accuracy = 63.9%, AUC = 0.70 | q-PCR | (59) |
| | LNCAROD, SNHG20, LINC00534, TSPOAP-AS1 | CRC | Up | | | (60) |
| SnRNA | U1, U2, U5 | Lung cancer | Down | AUC = 0.769 (U1), AUC = 0.840 (U2), AUC = 0.809 (U5), AUC = 0.840 (three snRNA); early stage AUC = 0.669 (U1), AUC = 0.805 (U2), AUC = 0.752 (U5), AUC = 0.826 (three snRNA) | q-PCR | (61) |
| SnoRNA | SNORD55 | NSCLC | Down | AUC = 0.803 (NSCLC), AUC = 0.784 (early-stage NSCLC), AUC = 0.791 (LUAD), AUC = 0.759 (early-stage LUAD), AUC = 0.826 (LUSC), AUC = 0.854 (early-stage LUSC) | q-PCR | (62) |
| Protein | VEGF, PDGF, PF4 | CRC | Up | AUC = 0.893 | ELISA | (63) |
| | Platelet protein | OC | | Late stage (III–IV): sensitivity = 96%, specificity = 88% Early stage (I–II): sensitivity = 83%, specificity = 76%, AUC = 0.831 | Partial least squares discriminant analysis (PLS-DA) | (64 |
| | Platelet count, MPV, and concentrations of VEGF, PDGF, PF4, CTAPIII, and TSP-1 in platelets and PFP | Lung cancer | | AUC = 0.868 | Multivariate modeling | (65) |

*(Continued)*

TABLE 1 Continued

| Marker type | TEP biomarkers | Tumor type | Expression | Test | Techniques | References |
|---|---|---|---|---|---|---|
| | Platelet count, MPV, and VEGF concentration in platelets | Head of pancreas cancer | | AUC = 0.827 | Multivariate modeling | (65) |

AUC, area under the receiver operating characteristic curve; NSCLC, non-small cell lung carcinoma; LUAD, lung adenocarcinoma; LUSC, lung squamous cell carcinoma; CRC, colorectal cancer; GBM, glioblastoma; PAAD, pancreatic cancer; HBC, hepatobiliary cancer; BRCA, breast cancer; ddPCR, droplet digital PCR; NPC, nasopharyngeal carcinoma; AD, adenocarcinoma; SCC, squamous cell carcinoma; OC, ovarian cancer; MPV, mean platelet volume; PFP, platelet-free plasma.

## 2 The coding platelet transcriptome

Platelets are anucleate and possess no available genomic DNA for the transcription of new RNA molecules but contain mitochondrial DNA with the capacity for RNA transcription activity (39). Therefore, most platelet RNAs are either inherited from the transcription of nuclear DNA in the megakaryocyte or acquired by platelets while in circulation (48). Platelets have functional spliceosomes; therefore, they can splice pre-mRNAs into mature mRNA (66). For example, Lindemann et al. (67) reported that interleukin-1β (IL-1β) pre-mRNA was spliced into intronically translatable mRNA in platelets, indicating a broad post-transcriptional regulatory mechanism for platelet mRNA expression. mRNA is the most studied type of RNA in platelets. With the development of high-throughput characterization methods, about one-third of all human genes (~5,000–9,000 genes) transcripts have been identified within platelets (68, 69). Gene ontology (GO) analysis revealed that detectable mRNAs in platelets were enriched in degranulation, coagulation, cytoskeletal dynamics, receptor binding, secretion, etc., which are biological processes closely related to well-known phenotypic activities (70, 71).

Previous studies have illuminated the diagnostic value of platelet mRNA signatures. Nilsson et al. (32) demonstrated that tumor-derived mRNAs were transferred (mutant EGFRvIII) from tumor cells to circulating platelets *in vitro* and *in vivo*. Platelets isolated from glioma and prostate cancer patients contained cancer-related RNA biomarkers EGFRvIII and PCA3, respectively, paving the way for the new potential for cancer diagnostics. Xing et al. (50) described that ITGA2B levels in TEPs were significantly higher in non-small cell lung cancer (NSCLC) patients than in controls, which could be a promising marker to improve the identification of stage I NSCLC patients and distinguish the benign and malignant pulmonary nodules. Interestingly, TIMP1 mRNA was increased in colorectal cancer (CRC) platelets, could be transferred into CRC cells by platelets, and could promote tumor growth *in vivo* and *in vitro* (52). TEP TPM3 mRNA was significantly increased in breast cancer patients, with its transfer into cancer cells mediated by platelet-derived particles to promote cancer cell migration (53). Our lab had identified a higher platelet mRNA expression of apoptotic chromatin coagulation inducing factor 1 (ACIN1) in lung cancer patients than in healthy controls (54), along with a three-platelet mRNA set—MAX, MTURN, and HLA-B—which was significantly upregulated in lung cancer patients processing a dramatically high diagnostic efficiency in female patients; the area under the curve (AUC) was 0.825 (51).

High-throughput RNA sequencing technologies have been employed in platelet RNA profile characterization. For example, the diagnostic potential of TEPs was determined by mRNA sequencing, which could distinguish tumor patients from healthy individuals with 96% accuracy, correctly identified across six different tumor types with 71% accuracy, and also ascertain MET- or HER2-positive and mutant KRAS, EGFR, or PIK3CA tumors (48). Moreover, to select robust biomarker panels for disease classification, the use of "swarm intelligence" was proposed, especially particle swarm optimization (PSO)-enhanced algorithms to analyze differences in RNA splicing isoforms of platelets from patients with NSCLC and healthy volunteers, which could achieve the accurate TEP-based detection of early and advanced NSCLC (37). More recent research has highlighted the potential properties of TEP-derived RNA panels, which correctly detected the presence of cancer in two-thirds of 1,096 blood samples from stage I–IV cancer patients and one-half of 352 stage I–III tumors, with 99% specificity in asymptomatic and 78% specificity in symptomatic controls (72).

## 3 The non-coding platelet transcriptome

Platelets exploit functional spliceosomes, consisting of RNA-binding protein (RBP) and small nuclear RNAs (snRNAs), including U1, U2, U4, U5, and U6. SnRNAs can bind to pre-mRNA to facilitate splicing (43). Interestingly, small nucleolar RNAs (snoRNAs) have also been described as detectable in anucleate platelets (71). SnoRNAs participate in alternative splicing of pre-mRNA in platelets other than regulation of translation in nucleated cells. Some non-coding RNA generations in the platelet also depend on post-transcriptional splicing such as circular RNAs (circRNAs). CircRNAs are generated from mature mRNAs by exonic back-splicing mediated in the spliceosome (73).

Beyond splicing, non-coding RNAs are the second post-transcriptional regulatory mechanism for platelet gene expression, including microRNAs (miRNAs), circRNAs, and long non-coding RNAs (lncRNAs). They can originate from megakaryocytes and also generate in platelets like coding RNA (40). For example, the

maturation process of miRNAs in platelets is different from that in nucleated cells. In platelets, miRNA maturation begins with unspliced pre-miRNA, and platelets contain related regulatory proteins Dicer and Argonaute 2 (Ago2), which process pre-miRNA into mature miRNA (74). Non-coding RNAs function in platelets similar to those in nucleated cells; miRNAs destabilize mRNAs and repress translation by harboring 3′-UTR but are sponged by circRNAs. Owing to diverse high-throughput techniques, such as microarrays and RNA-seq, dysregulation of non-coding RNA in TEPs can be easily observed.

## 3.1 MicroRNAs

MiRNAs, a class of small non-coding single-stranded RNAs with approximately 22 nucleotides in length, have highly evolutionarily conserved and tissue-specific expression patterns (75). Decades of research have demonstrated that miRNAs play a crucial role in multiple processes of cancer development. In 2009, Landry et al. (74) confirmed that human platelets contain and release miRNAs, and more than 500 different miRNAs have been identified in human platelets. In addition, human platelet miRNA profiles have extremely high stability (76), which makes platelet miRNA advantageous as diagnostic markers for tumors.

Alteration of platelet miRNA in cancer patients seems to be tumor-specific (77). Wang et al. (55) demonstrated that the expression levels of TEPs miR-34c-3p and miR-18a-5p were significantly higher in patients with nasopharyngeal carcinoma (NPC) compared to healthy subjects. The AUC value of the combined diagnosis of NPC was 0.954. However, this altered expression pattern was not found in plasma miR-34c-3p and miR-18a-5p, suggesting that the aberrances of TEP miR-34c-3p and miR-18a-5p might be the result of the "education" from NPC to platelets. The differential expression of miRNAs in platelets was also observed in a small cohort between pancreatic cancer patients and healthy subjects due to horizontal miRNA transfer between tumors and platelets. Interestingly, this differential miRNA expression was also detected between the blood and pancreatic juice-derived platelets (78). In addition, Diehl et al. (79) reported that miRNAs, including miR-19, miR-21, miR-126, miR-133, miR-146, and miR-223, could be detected in platelet-derived particles, suggesting that platelets could secrete their miRNAs through particles with potential cancer biomarkers. Similarly, the level of miR-223 in platelets of NSCLC patients was higher than in healthy subjects, and platelet-derived particles could effectively deliver miR-223 into human lung cancer cells A549, in which platelet miR-223 targeted EPB41L3 and thus promoted A549 invasion (56).

## 3.2 Circular RNAs

CircRNAs, the class of non-coding RNAs with a structure featuring covalently linked 3′ to 5′ ends, are highly abundant in the human genome (80). Recent studies have shown that circRNAs are differentially expressed in different types of cancer and play a crucial role in several steps of cancer initiation, tumor progression, and drug resistance (81–84). CircRNAs are significantly enriched in platelets 17- to 188-fold relative to nucleated tissues (73, 85), serving as a surrogate marker for mRNA stability in the absence of transcription relative to linear RNAs. Alhasan et al. (73) explained this phenomenon through the degradation/decay of cellular platelet RNA. CircRNAs would be more resistant to degradation by exonucleases. The abundance of circRNAs in platelets relative to megakaryocytes might attribute to circRNA generation in platelets rather than inherit from megakaryocytes (40). Thus, platelet-derived circRNAs may serve as potential novel and promising biomarkers for cancer diagnosis, treatment, and prognosis.

Ambrosi and his colleagues examined the differential circRNA profiles in platelets between NSCLC patients and asymptomatic individuals using high-throughput RNA-seq (49). A total of 4,732 circRNAs were identified, 84 of which were significantly upregulated and 327 were significantly downregulated, suggesting that the platelet circular RNA transcriptome was altered in the presence of cancer. RT-qPCR experiments confirmed that circNRIP1 was downregulated in platelet samples from advanced NSCLC, serving as an indicator of cancer progression. Moreover, a machine learning-based model algorithm was constructed for early-stage lung cancer detection based on combinatorial analysis of blood platelet-derived circRNA and mRNA signature. Combinatorial analysis, including both types of RNAs, resulted in an eight-target signature (six mRNAs and two circRNAs), enhancing the differentiation of lung cancer from controls (AUC of 0.92) (86).

## 3.3 Long non-coding RNA

LncRNA refers to transcripts longer than 200 nucleotides without the protein-coding ability (87). LncRNAs can act as decoys, guides, signals, or scaffolds to combine with DNA, RNA, or proteins to exert various biological functions (40). A large number of studies have shown that abnormal expression of lncRNAs in various types of cancer is associated with cancer recurrence, metastasis, and poor prognosis (88). Sun et al. (89) performed large-scale deep sequencing of human platelets, and a large number of lncRNAs were detected; the lncRNAs in TEPs are rarely reported.

Luo et al. (58) found that the levels of MAGI2-AS3 and ZFAS1 in plasma and platelets of NSCLC patients were significantly downregulated compared to those in healthy controls. Wei et al. (59) found that the TEP lncRNA-ROR of NPC patients was significantly lower than that of healthy subjects, while there was no significant difference in plasma lncRNA-ROR. Ye et al. (60) found that four lncRNA (LNCAROD, SNHG20, LINC00534, and TSPOAP-AS1) were dysregulated in TEPs of CRC patients and

could be used as potential diagnostic and discriminative biomarkers for CRC. Our group also identified TEP linc-GTF2H2-1, RP3-466P17.2, and LCC-ST8SIA4-12 as promising biomarkers for NSCLC based on lncRNA microarray and PCR validation (57), suggesting that lncRNAs derived from TEPs can be used in the diagnosis and prediction of cancer progression.

### 3.4 SnRNA and snoRNA

SnRNAs in the spliceosome are not merely the basal factors, ubiquitously expressed in all cells since they are required for post-transcriptional splicing, whereas snRNA levels are extremely variable across a wide range of biological conditions (90). Our lab demonstrated that TEP U1, U2, and U5 were significantly downregulated in lung cancer, which was associated with lung cancer progression, possessing favorable diagnostic efficiencies (61).

The primary function of snoRNAs is not only to guide the epigenetic modification of ribosomal RNAs (rRNAs) (91) but also to mediate pre-mRNA alternative splicing (92). For example, SNORD115 (M/HBII-52) regulated the post-transcriptional processing of serotonin 2C receptor (5-HT2CR) through alternative splicing and control of target mRNA editing (93). The presence of HTR2C pre-mRNA and splicing factors in platelets might indicate that platelet snoRNAs were involved in the mediation of alternative splicing (94). Our group reported that SNORD55 was significantly decreased in TEPs of NSCLC patients, especially of early-stage patients; it exerted a promising diagnostic value for NSCLC with an AUC of 0.803 and also improved the diagnostic accuracy of carcinoembryonic antigen (CEA) for tumor progression (62).

## 4 Platelet proteome

The protein content of platelets can include proteins derived from megakaryocytes, internalized from the extracellular environment, or synthesized within platelets (95). Mature and spliced RNAs can be translated into proteins in the ribosome of platelets.

Tumor cells stimulate platelet activation to release various angiogenic regulatory proteins to promote tumor angiogenesis. Peterson et al. (63) found that vascular endothelial growth factor (VEGF), platelet-derived growth factor (PDGF), and platelet factor 4 (PF4) in platelets of 35 patients with CRC were significantly increased compared to those in 84 healthy controls. Nevertheless, this significant difference was not observed in plasma. Multivariate logistic regression analysis showed that the combined prediction of these three factors for CRC AUC was 0.893. Other studies have found elevated levels of VEGF in platelets in patients with liver cancer (96), lung cancer (97), breast cancer (98), and pancreatic cancer (65).

In recent years, advances in mass spectroscopy-based methods have greatly promoted proteomics research (41). Analysis of platelet protein expression profiles distinguished benign adnexal lesions from International Federation of Gynecology and Obstetrics (FIGO) stage III–IV ovarian cancer, and the multivariate prediction model correctly predicted seven out of eight FIGO stage I–II ovarian cancer cases (64). An analysis of proteomics in patients with early-stage lung cancer (n = 8) and pancreatic cancer (n = 4) found that 85 proteins were significantly altered in platelets in patients with early-stage lung cancer and pancreatic cancer compared to gender- and age-matched controls. After tumor removal, the expression of 81 of the 85 proteins returned to normal levels (99). Multivariate modeling was also performed using six parameters (platelet count, mean platelet volume (MPV), and concentrations of VEGF, PDGF, PF4, CTAPIII, and TSP-1 in platelets and platelet-free plasma (PFP)), and AUC was 0.868 for the diagnosis of lung cancer. The discriminatory ability of the head diagnostic model of pancreatic cancer consisting of three parameters (platelet count, MPV, and VEGF concentration in platelets) to analyze the AUC was 0.827 (65). Taken together, these studies support that platelet-derived proteins can also be used as biomarkers for cancer.

## 5 Conclusion

Early detection of cancer can greatly reduce the probability of distant metastasis, contributing to better treatment outcomes and the quality of life for cancer patients. In recent studies, TEPs appear to be promising candidates as biomarkers for cancer based on liquid biopsies due to the alteration of their transcripts and proteins in response to external signals (100). Platelets are the second most abundant cell in circulation after red blood cells (RBCs) and are easily isolated and counted in blood tests, making them more attractive for clinical applications (8). In recent years, more sensitive new technologies have been developed, such as high-throughput sequencing and mass spectrometry, improving the accuracy and sensitivity of TEP-based liquid biopsies (50).

The unique advantages of platelet RNA and protein in early tumor detection are exciting; however, several challenges still remain to be addressed before they can be applied in clinical trials and practice. All of the studies had small sample sizes that needed to be expanded in further studies. Platelets are easily activated during sample preparation, and the establishment of standardized procedures for TEP research, including pre-analysis processing and specific analysis steps, is far from being implemented so far but is essential and imperative. Moreover, although TEPs are widely recognized as a novel biosource for cancer diagnostics, the mechanisms that tumor educates platelets still remain unclear. Such potential confounding factors should be further addressed in a prospective clinical trial and should be standardized during the blood collection process. Taken together, further characterization of standardized procedures and mechanisms will provide new insights into the diagnostic potential of TEPs and even pave the way for personalized medicine in the future.

## Author contributions

XGS designed and revised the manuscript. QZ wrote the first draft. XGS and XRS reviewed and revised the manuscript. All authors contributed to the article and approved the submitted version.

## Funding

This work was supported by the National Natural Science Foundation of China (81972014).

## Acknowledgments

We really appreciate Dr. Zhaoyun Liu for her kind help in the figure preparation. The figures in the current study were created with BioRender.com.

## Conflict of interest

The authors declare that the research was conducted in the absence of any commercial or financial relationships that could be construed as a potential conflict of interest.

## Publisher's note



## References

1. Fernandez-Lazaro D, Garcia Hernandez JL, Garcia AC, Cordova Martinez A, Mielgo-Ayuso J, Cruz-Hernandez JJ. Liquid biopsy as novel tool in precision medicine: Origins, properties, identification and clinical perspective of cancer's biomarkers. *Diagnostics (Basel).* (2020) 10(4):215. doi: 10.3390/diagnostics10040215

2. Gorgannezhad L, Umer M, Islam MN, Nguyen NT, Shiddiky MJA. Circulating tumor DNA and liquid biopsy: opportunities, challenges, and recent advances in detection technologies. *Lab Chip.* (2018) 18(8):1174–96. doi: 10.1039/C8LC00100F

3. Economopoulou P, Kotsantis I, Kyrodimos E, Lianidou ES, Psyrri A. Liquid biopsy: An emerging prognostic and predictive tool in head and neck squamous cell carcinoma (HNSCC). *Focus Circulating Tumor Cells (CTCs). Oral Oncol* (2017) 74:83–9. doi: 10.1016/j.oraloncology.2017.09.012

4. Di Meo A, Bartlett J, Cheng Y, Pasic MD, Yousef GM. Liquid biopsy: a step forward towards precision medicine in urologic malignancies. *Mol Cancer.* (2017) 16 (1):80. doi: 10.1186/s12943-017-0644-5

5. Hassan S, Blick T, Williams ED, Thompson EW. Applications of RNA from circulating tumor cells. *Front Biosci (Landmark Ed).* (2020) 25(5):874–92. doi: 10.2741/4838

6. In 't Veld S, Wurdinger T. Tumor-educated platelets. *Blood* (2019) 133(22):2359–64. doi: 10.1182/blood-2018-12-852830

7. Best MG, Wesseling P, Wurdinger T. Tumor-educated platelets as a noninvasive biomarker source for cancer detection and progression monitoring. *Cancer Res* (2018) 78(13):3407–12. doi: 10.1158/0008-5472.CAN-18-0887

8. Haemmerle M, Stone RL, Menter DG, Afshar-Kharghan V, Sood AK. The platelet lifeline to cancer: Challenges and opportunities. *Cancer Cell* (2018) 33(6):965–83. doi: 10.1016/j.ccell.2018.03.002

9. Koupenova M, Clancy L, Corkrey HA, Freedman JE. Circulating platelets as mediators of immunity, inflammation, and thrombosis. *Circ Res* (2018) 122(2):337–51. doi: 10.1161/CIRCRESAHA.117.310795

10. Schlesinger M. Role of platelets and platelet receptors in cancer metastasis. *J Hematol Oncol* (2018) 11(1):125. doi: 10.1186/s13045-018-0669-2

11. Morris K, Schnoor B, Papa AL. Platelet cancer cell interplay as a new therapeutic target. *Biochim Biophys Acta Rev Cancer.* (2022) 1877(5):188770. doi: 10.1016/j.bbcan.2022.188770

12. Repsold L, Pool R, Karodia M, Tintinger G, Joubert AM. An overview of the role of platelets in angiogenesis, apoptosis and autophagy in chronic myeloid leukaemia. *Cancer Cell Int* (2017) 17:89. doi: 10.1186/s12935-017-0460-4

13. Liu Y, Zhang Y, Ding Y, Zhuang R. Platelet-mediated tumor metastasis mechanism and the role of cell adhesion molecules. *Crit Rev Oncol Hematol* (2021) 167:103502. doi: 10.1016/j.critrevonc.2021.103502

14. Lowe KL, Navarro-Nunez L, Watson SP. Platelet CLEC-2 and podoplanin in cancer metastasis. *Thromb Res* (2012) 129 Suppl 1:S30–7. doi: 10.1016/S0049-3848(12)70013-0

15. Liu X, Song J, Zhang H, Liu X, Zuo F, Zhao Y, et al. Immune checkpoint HLA-E: CD94-NKG2A mediates evasion of circulating tumor cells from NK cell surveillance. *Cancer Cell* (2023) 41(2):272–87e9. doi: 10.1016/j.ccell.2023.01.001

16. Maurer S, Ferrari de Andrade L. NK cell interaction with platelets and myeloid cells in the tumor milieu. *Front Immunol* (2020) 11:608849. doi: 10.3389/fimmu.2020.608849

17. Amo L, Tamayo-Orbegozo E, Maruri N, Eguizabal C, Zenarruzabeitia O, Rinon M, et al. Involvement of platelet-tumor cell interaction in immune evasion. potential role of podocalyxin-like protein 1. *Front Oncol* (2014) 4:245. doi: 10.3389/fonc.2014.00245

18. Coupland LA, Hindmarsh EJ, Gardiner EE, Parish CR. The influence of platelet membranes on tumour cell behaviour. *Cancer Metastasis Rev* (2017) 36(2):215–24. doi: 10.1007/s10555-017-9671-3

19. Xiong G, Chen J, Zhang G, Wang S, Kawasaki K, Zhu J, et al. Hsp47 promotes cancer metastasis by enhancing collagen-dependent cancer cell-platelet interaction. *Proc Natl Acad Sci U S A.* (2020) 117(7):3748–58. doi: 10.1073/pnas.1911951117

20. Wang X, Zhao S, Wang Z, Gao T. Platelets involved tumor cell EMT during circulation: communications and interventions. *Cell Commun Signal* (2022) 20(1):82. doi: 10.1186/s12964-022-00887-3

21. Lazar S, Goldfinger LE. Platelets and extracellular vesicles and their cross talk with cancer. *Blood* (2021) 137(23):3192–200. doi: 10.1182/blood.2019004119

22. Labelle M, Begum S, Hynes RO. Direct signaling between platelets and cancer cells induces an epithelial-mesenchymal-like transition and promotes metastasis. *Cancer Cell* (2011) 20(5):576–90. doi: 10.1016/j.ccr.2011.09.009

23. Razavi AS, Mohtashami M, Razi S, Rezaei N. TGF-beta signaling and the interaction between platelets and T-cells in tumor microenvironment: Foes or friends? *Cytokine* (2022) 150:155772. doi: 10.1016/j.cyto.2021.155772

24. Haschemi R, Gockel LM, Bendas G, Schlesinger M. A combined activity of thrombin and p-selectin is essential for platelet activation by pancreatic cancer cells. *Int J Mol Sci* (2021) 22(7):3323. doi: 10.3390/ijms22073323

25. Mezouar S, Darbousset R, Dignat-George F, Panicot-Dubois L, Dubois C. Inhibition of platelet activation prevents the p-selectin and integrin-dependent accumulation of cancer cell microparticles and reduces tumor growth and metastasis in vivo. *Int J Cancer* (2015) 136(2):462–75. doi: 10.1002/ijc.28997

26. Fabricius HA, Starzonek S, Lange T. The role of platelet cell surface p-selectin for the direct platelet-tumor cell contact during metastasis formation in human tumors. *Front Oncol* (2021) 11:642761. doi: 10.3389/fonc.2021.642761

27. Qian W, Tao L, Wang Y, Zhang F, Li M, Huang S, et al. Downregulation of integrins in cancer cells and anti-platelet properties are involved in holothurian glycosaminoglycan-mediated disruption of the interaction of cancer cells and platelets in hematogenous metastasis. *J Vasc Res* (2015) 52(3):197–209. doi: 10.1159/000439220

28. Zara M, Canobbio I, Visconte C, Canino J, Torti M, Guidetti GF. Molecular mechanisms of platelet activation and aggregation induced by breast cancer cells. *Cell Signal* (2018) 48:45–53. doi: 10.1016/j.cellsig.2018.04.008

29. Grossi IM, Fitzgerald LA, Kendall A, Taylor JD, Sloane BF, Honn KV. Inhibition of human tumor cell induced platelet aggregation by antibodies to platelet glycoproteins ib and IIb/IIIa. *Proc Soc Exp Biol Med* (1987) 186(3):378–83. doi: 10.3181/00379727-186-3-RC1

30. Clezardin P, Drouin J, Morel-Kopp MC, Hanss M, Kehrel B, Serre CM, et al. Role of platelet membrane glycoproteins Ib/IX and IIb/IIIa, and of platelet alpha-granule proteins in platelet aggregation induced by human osteosarcoma cells. *Cancer Res* (1993) 53(19):4695–700.

31. Sabrkhany S, Kuijpers MJE, Griffioen AW, Oude Egbrink MGA. Platelets: the holy grail in cancer blood biomarker research? *Angiogenesis* (2019) 22(1):1–2. doi: 10.1007/s10456-018-9651-4

32. Nilsson RJ, Balaj L, Hulleman E, van Rijn S, Pegtel DM, Walraven M, et al. Blood platelets contain tumor-derived RNA biomarkers. *Blood* (2011) 118(13):3680–3. doi: 10.1182/blood-2011-03-344408

33. Lemancewicz D, Bolkun L, Mantur M, Semeniuk J, Kloczko J, Dzieciol J. Bone marrow megakaryocytes, soluble p-selectin and thrombopoietic cytokines in multiple myeloma patients. *Platelets* (2014) 25(3):181–7. doi: 10.3109/09537104.2013.805405

34. Leblanc R, Peyruchaud O. The role of platelets and megakaryocytes in bone metastasis. *J Bone Oncol* (2016) 5(3):109–11. doi: 10.1016/j.jbo.2016.02.007

35. Downes K, Megy K, Duarte D, Vries M, Gebhart J, Hofer S, et al. Diagnostic high-throughput sequencing of 2396 patients with bleeding, thrombotic, and platelet disorders. *Blood* (2019) 134(23):2082–91. doi: 10.1182/blood.2018891192

36. Freson K, Turro E. High-throughput sequencing approaches for diagnosing hereditary bleeding and platelet disorders. *J Thromb Haemost.* (2017) 15(7):1262–72. doi: 10.1111/jth.13681

37. Best MG, Sol N, In 't Veld S, Vancura A, Muller M, Niemeijer AN, et al. Swarm intelligence-enhanced detection of non-Small-Cell lung cancer using tumor-educated platelets. *Cancer Cell* (2017) 32(2):238–52 e9. doi: 10.1016/j.ccell.2017.07.004

38. Sol N, In 't Veld S, Vancura A, Tjerkstra M, Leurs C, Rustenburg F, et al. Tumor-educated platelet RNA for the detection and (Pseudo)progression monitoring of glioblastoma. *Cell Rep Med* (2020) 1(7):100101. doi: 10.1016/j.xcrm.2020.100101

39. Melchinger H, Jain K, Tyagi T, Hwa J. Role of platelet mitochondria: Life in a nucleus-free zone. *Front Cardiovasc Med* (2019) 6:153. doi: 10.3389/fcvm.2019.00153

40. Gutmann C, Joshi A, Zampetaki A, Mayr M. The landscape of coding and noncoding RNAs in platelets. *Antioxid Redox Signal* (2021) 34(15):1200–16. doi: 10.1089/ars.2020.8139

41. Loosse C, Swieringa F, Heemskerk JWM, Sickmann A, Lorenz C. Platelet proteomics: from discovery to diagnosis. *Expert Rev Proteomics.* (2018) 15(6):467–76. doi: 10.1080/14789450.2018.1480111

42. Weyrich AS, Lindemann S, Tolley ND, Kraiss LW, Dixon DA, Mahoney TM, et al. Change in protein phenotype without a nucleus: translational control in platelets. *Semin Thromb Hemost.* (2004) 30(4):491–8. doi: 10.1055/s-2004-833484

43. Denis MM, Tolley ND, Bunting M, Schwertz H, Jiang H, Lindemann S, et al. Escaping the nuclear confines: signal-dependent pre-mRNA splicing in anucleate platelets. *Cell* (2005) 122(3):379–91. doi: 10.1016/j.cell.2005.06.015

44. Neu CT, Gutschner T, Haemmerle M. Post-transcriptional expression control in platelet biogenesis and function. *Int J Mol Sci* (2020) 21(20):7614. doi: 10.3390/ijms21207614

45. Sabrkhany S, Kuijpers MJE, Oude Egbrink MGA, Griffioen AW. Platelets as messengers of early-stage cancer. *Cancer Metastasis Rev* (2021) 40(2):563–73. doi: 10.1007/s10555-021-09956-4

46. Hinterleitner C, Strahle J, Malenke E, Hinterleitner M, Henning M, Seehawer M, et al. Platelet PD-L1 reflects collective intratumoral PD-L1 expression and predicts immunotherapy response in non-small cell lung cancer. *Nat Commun* (2021) 12 (1):7005. doi: 10.1038/s41467-021-27303-7

47. Wang Z, Fang M, Li J, Yang R, Du J, Luo Y. High platelet levels attenuate the efficacy of platinum-based treatment in non-small cell lung cancer. *Cell Physiol Biochem* (2018) 48(6):2456–69. doi: 10.1159/000492683

48. Best MG, Sol N, Kooi I, Tannous J, Westerman BA, Rustenburg F, et al. RNA-Seq of tumor-educated platelets enables blood-based pan-cancer, multiclass, and molecular pathway cancer diagnostics. *Cancer Cell* (2015) 28(5):666–76. doi: 10.1016/j.ccell.2015.09.018

49. D'Ambrosi S, Visser A, Antunes-Ferreira M, Poutsma A, Giannoukakos S, Sol N, et al. The analysis of platelet-derived circRNA repertoire as potential diagnostic biomarker for non-small cell lung cancer. *Cancers* (2021) 13(18):4644. doi: 10.3390/cancers13184644

50. Xing S, Zeng T, Xue N, He Y, Lai YZ, Li HL, et al. Development and validation of tumor-educated blood platelets integrin alpha 2b (ITGA2B) RNA for diagnosis and prognosis of non-small-cell lung cancer through RNA-seq. *Int J Biol Sci* (2019) 15 (9):1977–92. doi: 10.7150/ijbs.36284

51. Liu L, Song X, Li X, Xue L, Ding S, Niu L, et al. A three-platelet mRNA set: MAX, MTURN and HLA-b as biomarker for lung cancer. *J Cancer Res Clin Oncol* (2019) 145 (11):2713–23. doi: 10.1007/s00432-019-03032-9

52. Yang L, Jiang Q, Li DZ, Zhou X, Yu DS, Zhong J. TIMP1 mRNA in tumor-educated platelets is diagnostic biomarker for colorectal cancer. *Aging (Albany NY).* (2019) 11(20):8998–9012. doi: 10.18632/aging.102366

53. Yao B, Qu S, Hu R, Gao W, Jin S, Ju J, et al. Delivery of platelet TPM3 mRNA into breast cancer cells *via* microvesicles enhances metastasis. *FEBS Open Bio.* (2019) 9 (12):2159–69. doi: 10.1002/2211-5463.12759

54. Xue L, Xie L, Song X, Song X. [Expression and significance of ACIN1 mRNA in platelets of lung cancer]. *Zhongguo Fei Ai Za Zhi.* (2018) 21(9):677–81. doi: 10.3779/j.issn.1009-3419.2018.09.05

55. Wang H, Wei X, Wu B, Su J, Tan W, Yang K. Tumor-educated platelet miR-34c-3p and miR-18a-5p as potential liquid biopsy biomarkers for nasopharyngeal carcinoma diagnosis. *Cancer Manag Res* (2019) 11:3351–60. doi: 10.2147/CMAR.S195654

56. Liang H, Yan X, Pan Y, Wang Y, Wang N, Li L, et al. MicroRNA-223 delivered by platelet-derived microvesicles promotes lung cancer cell invasion *via* targeting tumor suppressor EPB41L3. *Mol Cancer.* (2015) 14:58. doi: 10.1186/s12943-015-0327-z

57. Li X, Liu L, Song X, Wang K, Niu L, Xie L, et al. TEP linc-GTF2H2-1, RP3-466P17.2, and lnc-ST8SIA4-12 as novel biomarkers for lung cancer diagnosis and progression prediction. *J Cancer Res Clin Oncol* (2021) 147(6):1609–22. doi: 10.1007/s00432-020-03502-5

58. Luo CL, Xu ZG, Chen H, Ji J, Wang YH, Hu W, et al. LncRNAs and EGFRvIII sequestered in TEPs enable blood-based NSCLC diagnosis. *Cancer Manag Res* (2018) 10:1449–59. doi: 10.2147/CMAR.S164227

59. Wei J, Meng X, Wei X, Zhu K, Du L, Wang H. Down-regulated lncRNA ROR in tumor-educated platelets as a liquid-biopsy biomarker for nasopharyngeal carcinoma. *J Cancer Res Clin Oncol* (2022). doi: 10.1007/s00432-022-04350-1

60. Ye B, Li F, Chen M, Weng Y, Qi C, Xie Y, et al. A panel of platelet-associated circulating long non-coding RNAs as potential biomarkers for colorectal cancer. *Genomics* (2022) 114(1):31–7. doi: 10.1016/j.ygeno.2021.11.026

61. Dong X, Ding S, Yu M, Niu L, Xue L, Zhao Y, et al. Small nuclear RNAs (U1, U2, U5) in tumor-educated platelets are downregulated and act as promising biomarkers in lung cancer. *Front Oncol* (2020) 10:1627. doi: 10.3389/fonc.2020.01627

62. Dong X, Song X, Ding S, Yu M, Shang X, Wang K, et al. Tumor-educated platelet SNORD55 as a potential biomarker for the early diagnosis of non-small cell lung cancer. *Thorac Cancer.* (2021) 12(5):659–66. doi: 10.1111/1759-7714.13823

63. Peterson JE, Zurakowski D, Italiano JEJr., Michel LV, Connors S, Oenick M, et al. VEGF, PF4 and PDGF are elevated in platelets of colorectal cancer patients. *Angiogenesis* (2012) 15(2):265–73. doi: 10.1007/s10456-012-9259-z

64. Lomnytska M, Pinto R, Becker S, Engstrom U, Gustafsson S, Bjorklund C, et al. Platelet protein biomarker panel for ovarian cancer diagnosis. *biomark Res* (2018) 6:2. doi: 10.1186/s40364-018-0118-y

65. Sabrkhany S, Kuijpers MJE, van Kuijk SMJ, Sanders L, Pineda S, Olde Damink SWM, et al. A combination of platelet features allows detection of early-stage cancer. *Eur J Cancer.* (2017) 80:5–13. doi: 10.1016/j.ejca.2017.04.010

66. Papasaikas P, Valcarcel J. The spliceosome: The ultimate RNA chaperone and sculptor. *Trends Biochem Sci* (2016) 41(1):33–45. doi: 10.1016/j.tibs.2015.11.003

67. Lindemann S, Tolley ND, Dixon DA, McIntyre TM, Prescott SM, Zimmerman GA, et al. Activated platelets mediate inflammatory signaling by regulated interleukin 1beta synthesis. *J Cell Biol* (2001) 154(3):485–90. doi: 10.1083/jcb.200105058

68. Gnatenko DV, Dunn JJ, Schwedes J, Bahou WF. Transcript profiling of human platelets using microarray and serial analysis of gene expression (SAGE). *Methods Mol Biol* (2009) 496:245–72. doi: 10.1007/978-1-59745-553-4_16

69. Bugert P, Dugrillon A, Gunaydin A, Eichler H, Kluter H. Messenger RNA profiling of human platelets by microarray hybridization. *Thromb Haemost.* (2003) 90 (4):738–48. doi: 10.1055/s-0037-1613622

70. Mills EW, Green R, Ingolia NT. Slowed decay of mRNAs enhances platelet specific translation. *Blood* (2017) 129(17):e38–48. doi: 10.1182/blood-2016-08-736108

71. Bray PF, McKenzie SE, Edelstein LC, Nagalla S, Delgrosso K, Ertel A, et al. The complex transcriptional landscape of the anucleate human platelet. *BMC Genomics* (2013) 14:1. doi: 10.1186/1471-2164-14-1

72. In 't Veld S, Arkani M, Post E, Antunes-Ferreira M, D'Ambrosi S, Vessies DCL, et al. Detection and localization of early- and late-stage cancers using platelet RNA. *Cancer Cell* (2022) 40(9):999–1009 e6. doi: 10.1016/j.ccell.2022.08.006

73. Alhasan AA, Izuogu OG, Al-Balool HH, Steyn JS, Evans A, Colzani M, et al. Circular RNA enrichment in platelets is a signature of transcriptome degradation. *Blood* (2016) 127(9):e1–e11. doi: 10.1182/blood-2015-06-649434

74. Landry P, Plante I, Ouellet DL, Perron MP, Rousseau G, Provost P. Existence of a microRNA pathway in anucleate platelets. *Nat Struct Mol Biol* (2009) 16(9):961–6. doi: 10.1038/nsmb.1651

75. Saliminejad K, Khorram Khorshid HR, Soleymani Fard S, Ghaffari SH. An overview of microRNAs: Biology, functions, therapeutics, and analysis methods. *J Cell Physiol* (2019) 234(5):5451–65. doi: 10.1002/jcp.27486

76. Stratz C, Nuhrenberg TG, Binder H, Valina CM, Trenk D, Hochholzer W, et al. Micro-array profiling exhibits remarkable intra-individual stability of human platelet micro-RNA. *Thromb Haemost.* (2012) 107(4):634–41. doi: 10.1160/TH11-10-0742

77. Sol N, Wurdinger T. Platelet RNA signatures for the detection of cancer. *Cancer Metastasis Rev* (2017) 36(2):263–72. doi: 10.1007/s10555-017-9674-0

78. Diaz-Blancas JY, Dominguez-Rosado I, Chan-Nunez C, Melendez-Zajgla J, Maldonado V. Pancreatic cancer cells induce MicroRNA deregulation in platelets. *Int J Mol Sci* (2022) 23(19):11438. doi: 10.3390/ijms231911438

79. Diehl P, Fricke A, Sander L, Stamm J, Bassler N, Htun N, et al. Microparticles: major transport vehicles for distinct microRNAs in circulation. *Cardiovasc Res* (2012) 93(4):633–44. doi: 10.1093/cvr/cvs007

80. Patop IL, Wust S, Kadener S. Past, present, and future of circRNAs. *EMBO J* (2019) 38(16):e100836. doi: 10.15252/embj.2018100836

81. Yin Y, Long J, He Q, Li Y, Liao Y, He P, et al. Emerging roles of circRNA in formation and progression of cancer. *J Cancer.* (2019) 10(21):5015–21. doi: 10.7150/jca.30828

82. Sarkar D, Diermeier SD. Circular RNAs: Potential applications as therapeutic targets and biomarkers in breast cancer. *Noncoding RNA*. (2021) 7(1):2. doi: 10.3390/ncrna7010002

83. Micallef I, Baron B. The mechanistic roles of ncRNAs in promoting and supporting chemoresistance of colorectal cancer. *Noncoding RNA*. (2021) 7(2):24. doi: 10.3390/ncrna7020024

84. Bach DH, Lee SK, Sood AK. Circular RNAs in cancer. *Mol Ther Nucleic Acids* (2019) 16:118–29. doi: 10.1016/j.omtn.2019.02.005

85. Preusser C, Hung LH, Schneider T, Schreiner S, Hardt M, Moebus A, et al. Selective release of circRNAs in platelet-derived extracellular vesicles. *J Extracell Vesicles*. (2018) 7(1):1424473. doi: 10.1080/20013078.2018.1424473

86. D'Ambrosi S, Giannoukakos S, Antunes-Ferreira M, Pedraz-Valdunciel C, Bracht JWP, Potie N, et al. Combinatorial blood platelets-derived circRNA and mRNA signature for early-stage lung cancer detection. *Int J Mol Sci* (2023) 24 (5):4881. doi: 10.3390/ijms24054881

87. Spizzo R, Almeida MI, Colombatti A, Calin GA. Long non-coding RNAs and cancer: a new frontier of translational research? *Oncogene* (2012) 31(43):4577–87. doi: 10.1038/onc.2011.621

88. Chi Y, Wang D, Wang J, Yu W, Yang J. Long non-coding RNA in the pathogenesis of cancers. *Cells* (2019) 8(9):1015. doi: 10.3390/cells8091015

89. Sun Y, Liu R, Xia X, Xing L, Jiang J, Bian W, et al. Large-Scale profiling on lncRNAs in human platelets: Correlation with platelet reactivity. *Cells* (2022) 11 (14):2256. doi: 10.3390/cells11142256

90. Dvinge H, Guenthoer J, Porter PL, Bradley RK. RNA Components of the spliceosome regulate tissue- and cancer-specific alternative splicing. *Genome Res* (2019) 29(10):1591–604. doi: 10.1101/gr.246678.118

91. Jorjani H, Kehr S, Jedlinski DJ, Gumienny R, Hertel J, Stadler PF, et al. An updated human snoRNAome. *Nucleic Acids Res* (2016) 44(11):5068–82. doi: 10.1093/nar/gkw386

92. Falaleeva M, Pages A, Matuszek Z, Hidmi S, Agranat-Tamir L, Korotkov K, et al. Dual function of C/D box small nucleolar RNAs in rRNA modification and alternative pre-mRNA splicing. *Proc Natl Acad Sci U S A*. (2016) 113(12):E1625–34. doi: 10.1073/pnas.1519292113

93. Kishore S, Khanna A, Zhang Z, Hui J, Balwierz PJ, Stefan M, et al. The snoRNA MBII-52 (SNORD 115) is processed into smaller RNAs and regulates alternative splicing. *Hum Mol Genet* (2010) 19(7):1153–64. doi: 10.1093/hmg/ddp585

94. Best MG, Vancura A, Wurdinger T. Platelet RNA as a circulating biomarker trove for cancer diagnostics. *J Thromb Haemost*. (2017) 15(7):1295–306. doi: 10.1111/jth.13720

95. Zufferey A, Schvartz D, Nolli S, Reny JL, Sanchez JC, Fontana P. Characterization of the platelet granule proteome: evidence of the presence of MHC1 in alpha-granules. *J Proteomics*. (2014) 101:130–40. doi: 10.1016/j.jprot.2014.02.008

96. Kim SJ, Choi IK, Park KH, Yoon SY, Oh SC, Seo JH, et al. Serum vascular endothelial growth factor per platelet count in hepatocellular carcinoma: correlations with clinical parameters and survival. *Jpn J Clin Oncol* (2004) 34(4):184–90. doi: 10.1093/jjco/hyh039

97. Wiesner T, Bugl S, Mayer F, Hartmann JT, Kopp HG. Differential changes in platelet VEGF, tsp, CXCL12, and CXCL4 in patients with metastatic cancer. *Clin Exp Metastasis*. (2010) 27(3):141–9. doi: 10.1007/s10585-010-9311-6

98. Holmes CE, Levis JE, Schneider DJ, Bambace NM, Sharma D, Lal I, et al. Platelet phenotype changes associated with breast cancer and its treatment. *Platelets* (2016) 27 (7):703–11. doi: 10.3109/09537104.2016.1171302

99. Sabrkhany S, Kuijpers MJE, Knol JC, Olde Damink SWM, Dingemans AC, Verheul HM, et al. Exploration of the platelet proteome in patients with early-stage cancer. *J Proteomics*. (2018) 177:65–74. doi: 10.1016/j.jprot.2018.02.011

100. Antunes-Ferreira M, Koppers-Lalic D, Wurdinger T. Circulating platelets as liquid biopsy sources for cancer detection. *Mol Oncol* (2021) 15(6):1727–43. doi: 10.1002/1878-0261.12859

frontiers | Frontiers in Cell and Developmental Biology

TYPE Original Research
PUBLISHED 18 May 2023
DOI 10.3389/fcell.2023.1181628



OPEN ACCESS

EDITED BY
Yi Yao,
Renmin Hospital of Wuhan University, China

REVIEWED BY
Pietro Carotenuto,
Telethon Institute of Genetics and Medicine (TIGEM), Italy
Hexiao Tang,
Wuhan University, China

*CORRESPONDENCE
Qinglin Shen,
qinglinshen@whu.edu.cn
Weirong Yao,
495574116@qq.com

†These authors have contributed equally to this work

RECEIVED 07 March 2023
ACCEPTED 02 May 2023
PUBLISHED 18 May 2023

CITATION
Jiang P, Liang B, Zhang Z, Fan B, Zeng L, Zhou Z, Mao Z, Lin Q, Yao W and Shen Q (2023), MicroRNA-146a-5p induces cell cycle arrest and enhances apoptosis in gastric cancer via targeting CDC14A. *Front. Cell Dev. Biol.* 11:1181628. doi: 10.3389/fcell.2023.1181628



# MicroRNA-146a-5p induces cell cycle arrest and enhances apoptosis in gastric cancer via targeting CDC14A

Piao Jiang[1,2†], Bin Liang[1†], Zhen Zhang[3], Bing Fan[4], Lin Zeng[1], Zhiyong Zhou[1], Zhifang Mao[1], Qing Lin[5], Weirong Yao[1*] and Qinglin Shen[1,3*]

[1]Department of Oncology, Jiangxi Provincial People's Hospital, The First Affiliated Hospital of Nanchang Medical College, Nanchang, China, [2]The First Clinical Medical College, Nanchang University, Nanchang, China, [3]The First Affiliated Hospital of Nanchang Medical College, Institute of Clinical Medicine, Jiangxi Provincial People's Hospital, Nanchang, China, [4]Department of Radiology, Jiangxi Provincial People's Hospital, The First Affiliated Hospital of Nanchang Medical College, Nanchang, China, [5]Department of Thoracic Surgery, Jiangxi Provincial People's Hospital, The First Affiliated Hospital of Nanchang Medical College, Nanchang, China

**Objective**: The present study was designed to investigate the expression of miRNA-146a-5p in gastric cancer (GC) tissues and the paired nonmalignant counterparts, to explore the influences of miRNA-146a-5p on the cell biological behavior of MKN-28 cells (highly metastatic human gastric cancer cells), and to identify the function of abnormal expression of its target gene *cell division cycle 14 homolog A (CDC14A)* in GC.

**Methods:** We detected the expression of miRNA-146a-5p in formalin-fixed and paraffin-embedded (FFPE) GC tissues through microarray and quantitative real-time polymerase chain reaction (qRT-PCR). Then, we employed cell counting kit-8 (CCK-8) assays, cell cycle assays, and apoptosis analysis to uncover the latent function of miRNA-146a-5p in MKN-28 human GC cells. We also validated the target of miRNA-146a-5p via luciferase reporter assays.

**Results:** miRNA-146a-5p levels were examined in the majority of primary GC tissues and several GC cell lines. As a result, miRNA-146a-5p levels were significantly declined in the GC tissues and cells. In addition, miRNA-146a-5p demonstrated a straight act on its 3′-untranslated region (3′-UTR) of CDC14A mRNA, accordingly decreasing the contents of CDC14A mRNA as well as its protein expression. An inverse correlation between CDC14A and miRNA-146a-5p was observed.

**Conclusion:** The data suggest miRNA-146a-5p may contribute to inducing cell cycle arrest as well as prompting GC cell apoptosis via directly targeting CDC14A. Therefore, miRNA-146a-5p may be a potential indicator of the occurrence and development of GC.

KEYWORDS

**microRNA-146a-5p, gastric cancer, CDC14A, cell cycle, apoptosis**

# Introduction

Gastric cancer (GC) is the fifth most frequent malignancy in the world and the third leading cause of cancer-related death. Approximately 768,000 GC patients die annually worldwide (Smyth et al., 2020; Thrift and El-Serag, 2020; Ajani et al., 2022). Despite tremendous improvement in the study concerning oncogenesis and the development of GC, its intrinsic mechanisms are not well understood, thereby desperately compelling us to further investigate the prospective intrinsic mechanism unveiling GC.

MicroRNAs (miRNAs) are a class of short non-coding RNAs that regulate gene expression and manipulate stability as well as translation of mRNAs (Riahi Rad et al., 2021). miRNAs exert a vital part in numerous biological activities, including proliferation, differentiation, apoptosis, and motility (Saliminejad et al., 2019; Hussen et al., 2021; Liu et al., 2022). Dysregulated miRNAs have been observed in various tumors, such as, GC (Liu et al., 2021; Shi et al., 2021). miRNAs fulfill a role through binding to their miRNA recognition sequences which are common in the 3′-UTRs of target mRNAs, resulting in decreased translation and increased cleavage of target mRNAs, hence downregulating the protein expression downstream (Correia de Sousa et al., 2019; Pu et al., 2019). In addition, miRNAs are capable of serving as oncomiRs or oncosuppressor miRs (Ali Syeda et al., 2020; Miliotis and Slack, 2021; Smolarz et al., 2022). Typical instances in GC include miRNA-760, a kind of tumor repressor that targets G-protein-coupled receptor kinase interacting protein-1 (GIT1) (Ge et al., 2019), and miRNA-18, whose effects on gastric carcinogenesis are mediated by downregulating HMGB3 through targeting Meis2 (Zhang et al., 2022).

Cell division cycle 14 homolog A (CDC14A), a member of the dual specificity protein tyrosine phosphatase family, relates to the exit of cell mitosis and initiation of DNA replication, demonstrating its action on cell cycle control. Recent studies have reported that CDC14A might play an important role in cell adhesion (Chen et al., 2017) and apoptosis (Hu et al., 2019). However, the function of CDC14A in the cell cycle and apoptosis of GC remains unknown.

In our present study, we carried out miRNA microarray analysis and discovered that miRNA-146a-5p levels were significantly declined in GC tissues. Furthermore, we demonstrated that miRNA-146a-5p caused a reduction in CDC14A levels, leading to suppressed cell cycle and enhanced apoptosis. Altogether, the results suggest that miRNA-146a-5p may be conducive to cell cycle arrest and promotion of GC cell apoptosis, probably through targeting CDC14A.

# Materials and methods

## Tissue samples

The study was conducted in accordance with the principles of the Declaration of Helsinki. The approval for the study was granted by the Ethics Committee of Jiangxi Provincial People's Hospital, The First Affiliated Hospital of Nanchang Medical College.

The formalin-fixed paraffin-embedded (FFPE) samples from 132 gastric cancer tissues and 66 matched noncancerous samples were obtained during surgery from January 2013 to May 2015 and then utilized after acquiring informed consent. The clinicopathological characteristics of the patients are summarized in Table 1. None of these patients accepted preoperative treatments like radiotherapy or chemotherapy. All patients underwent a definite histologic diagnosis of gastric cancer based on the clinicopathologic criteria according to the Eighth Edition of AJCC/UICC (2017). Invasive ductal carcinoma tissues, accounting for over 80% of the region of malignant epithelial cells, were identified using a microscope. Paired noncancerous samples were confined within 2 cm of tumor tissues and were not allowed to contain any tumor cells. Four pieces of 20-μm-thick segments were cut from each FFPE tissue block and harvested into a 2-mL RNA enzyme-free tube.

## RNA preparation and qRT-PCR

We extracted total RNA from GC FFPE samples utilizing miRNeasy FFPE Kit (QIAGEN, Germany) following manufacturer's instruction. Then, we used the NanoDrop 2000 spectrophotometer (Thermo Scientific, Germany) to determine the concentration and purity of all RNA extracts.

miRNA-146a-5p levels were determined utilizing stem–loop reverse transcription and qRT-PCR according to the previous literature (Jung et al., 2020). All reagents and consumables were purchased from Thermo Scientific (Germany). We carried out qRT-PCR three times and calculated by using the $2^{-\Delta CT}$ method (Calin and Croce, 2006; Damanti et al., 2021), where $\Delta Ct = Ct_{miRNA\text{-}146a\text{-}5p}\text{-}Ct_{U6}$. CDC14A mRNA levels were tested three times, and the results were processed utilizing the $2^{-\Delta\Delta CT}$ method, where $\Delta\Delta Ct = \Delta Ct_{miRNA\text{-}146a\text{-}5p}\text{-}\Delta Ct_{NC}$ and $\Delta Ct = Ct_{CDC14A}\text{-}Ct_{\beta\text{-}actin}$. All primers employed in stem–loop reverse transcription together with qRT-PCR are summarized in Table 2.

## miRNA microarray analysis

Microarrays were operated in four GC samples as well as four paired paracarcinomatous samples. Affymetrix miRNA 3.0 technology platforms, incorporating 1,733 mature human miRNAs, were adopted. Then, total RNA was spiked utilizing MicroRNA Spike-In Kit (Agilent Technologies), labeled using miRNA Complete Labeling and Hyb Kit (Agilent Technologies), hybridized to human miRNA microarrays, washed, and stained, followed by fluorescent signal intensities detection through the Affymetrix Scanner 3000. All of the aforementioned concrete steps were conducted in line with their manufacturer's protocols.

Expression Console 1.3.1 (Affymetrix) was used for dissecting images to gain primitive information, followed by RMA normalization. Then, GeneSpring 12.5 (Agilent Technologies) was used as our analytical and visualization tool for microarrays. Furthermore, we adopted probes that possess flags in "P" in at least one group of the whole samples for a thorough study. Divergently expressed miRNAs were subsequently detected via fold change, where ≥ 2-fold differential expression implies upregulation of miRNA, along with a $p$-value ≤0.05 that implies downregulation of miRNA. In addition, we applied unsupervised hierarchical clustering to display the differences in the miRNA expression profiles amid the specimens.

**TABLE 1 Relationship of expression of miRNA-146a-5p in GC and clinicopathological characteristics.**

| Characteristic | Number (n = 132) | miRNA-146a-5p expression | | *p-value* |
|---|---|---|---|---|
| | | High (n = 40) | Low (n = 92) | |
| Age (years) | | | | |
| <60 | 87 | 29 | 58 | 0.228 |
| ≥60 | 45 | 11 | 34 | |
| Gender | | | | |
| Male | 81 | 24 | 57 | 0.721 |
| Female | 51 | 16 | 35 | |
| Tumor size (cm) | | | | |
| <5 | 89 | 29 | 60 | 0.367 |
| ≥5 | 43 | 11 | 32 | |
| Tumor site | | | | |
| Upper | 30 | 3 | 27 | 0.001 |
| Middle/lower | 102 | 37 | 65 | |
| Lauren's classification | | | | |
| Intestinal | 72 | 8 | 64 | <0.001 |
| Mixed/diffuse | 60 | 32 | 28 | |
| Histologic differentiation | | | | |
| Well/moderate | 48 | 20 | 28 | 0.014 |
| Poor and unknown | 84 | 20 | 64 | |
| Depth of invasion | | | | |
| T1/T2 | 59 | 32 | 27 | <0.001 |
| T3/T4 | 73 | 8 | 65 | |
| TNM stage | | | | |
| I/II | 52 | 22 | 30 | 0.003 |
| III/IV | 80 | 18 | 62 | |
| Lymph node metastasis | | | | |
| N0 | 42 | 19 | 23 | 0.002 |
| N (+) | 90 | 21 | 69 | |

**TABLE 2 Primers utilized for stem–loop RT as well as qRT-PCR.**

| Primer | Sequence |
|---|---|
| U6-F | 5′-CTCGCTTCGGCAGCACA-3′ |
| U6-R | 5′-AACGCTTCACGAATTTGCGT-3′ |
| miRNA-146a-5p-RT | 5′-GTCGTATCCAGTGCAGGGTCCGAGGTATTCGCA CTGGATACG ACCACAAACC-3′ |
| miRNA-146a-5p-F | 5′-GCTAGCAGCACATAATGGTTTGTG-3′ |
| miRNA-146a-5p-R | 5′-GTGCAGGGTCCGAGGTATTC-3′ |
| CDC14A-F | 5′-TACAAAAGGACATCCAAGAGCAG-3′ |
| CDC14A-R | 5′-TGGCACCCGAAGACAAAGA-3′ |

F, forward; R, reverse; RT, reverse transcription.

## miRNA mimics and cell transfection

MKN-28, MGC803, SGC-7901, and GES-1 cell lines were purchased from ATCC (Rockville, MD) and cultured in complete media (Dulbecco's modified Eagle media (DMEM) (Gibco BRL, Grand Island, New York)) supplemented with 15% fetal bovine serum (FBS), and then they were incubated at 37°C in 5% $CO_2$. Negative control (NC) and miRNA-146a-5p mimics were generated and purchased from GenePharma (Shanghai, China). Utilizing Lipofectamine™ 2000 (Invitrogen), transfection of NC or miRNA-146a-5p mimics was performed separately on MKN-28 cells at a concentration of 100 nM, following the manufacturer's guidance.

### Cell cycle as well as apoptosis assays

Post-transfection 48 h, cells were washed twice with phosphate buffered saline (PBS) and then resuspended in ×1 binding buffer,

followed by mixing with 500 μL propidium iodide (PI) [20 μg/mL PI, 50 μL/mL RNaseA, and 0.02% NP40 in PBS] with roughly 0.5 x $10^6$ cells at 4°C for 30 min. DNA quantification was implemented using the FACS Calibur instrument (Becton Dickinson, Mountain View, CA) and CellQuest software (Becton Dickinson). Through 12-h serum starvation and ~18-h 2 mM hydroxyurea (HU) treatment, cells synchronized in G1/S transition. We identified cell apoptosis through fluorescein isothiocyanate (FITC) Annexin V Apoptosis Detection Kit (BD Pharmingen), following manufacturer's suggested procedure. The whole experiment was conducted in triplicate.

### Cell proliferation assay

Cells were loaded into a 96-well plate with a density of $3 \times 10^5$ cells/mL by 0.1 mL/well, followed by miRNA-146a-5p mimics or NC transfection. We chose cell counting kit-8 (CCK-8) to test the absorbance values ($OD_{450nm}$) using a microplate reader (BioTek) every 24 h for 5–7 consecutive days. All experiments were conducted in triplicate.

## Effects of miRNA-146a-5p on CDC14A levels

MiRNAorg, TargetScan, and PITA database were utilized for seeking the joint targets of miRNA-146a-5p in humans, with the pictures plotted using a Venn diagram as well as Cytoscape (version 3.7.0).

MKN-28 cells cultured normally *in vitro* were equally inoculated in six-well plates with $3 \times 10^5$ cells in a volume of 1,000 μL media per well. The miRNA-146a-5p mimics and NC were transfected based on the suggested protocol utilizing Lipofectamine™ 2000. Then, we employed Western blotting (WB) to detect the CDC14A protein expression levels in the cells 48 h after transfection. Concrete steps of experiments demonstrating the effects of miRNA-146a-5p mimics and NC on CDC14A were performed as described in previous studies (Li et al., 2014; Kang et al., 2021).

### CDC14A-3′-UTR luciferase reporter assay

We augmented the 3′-UTR elements of *CDC14A* gene from noncancerous tissues, accompanied by a straight sub-cloning stop codon of Renilla luciferase of psiCHECK2. Primers employed for amplification were as follows: CDC14A 3′-UTR-F: 5′-TACAAA AGGACATCCAAGAGCAG-3′ as well as CDC14A 3′-UTR-R: 5′-TGGCACCCGAAGACAAAGA-3'. β-actin was used as an internal control. β-actin-F: 5′GATCATTGCTCCTCCTGAGC-3′, β-actin-R: 5′-ACTCCTGCTTGCTGATCCAC3'; the wild-type and mutant *CDC14A* 3′-UTRs were determined through sequencing. To perform luciferase screening, MKN-28 cells were inoculated into 96-well plates with approximately 5 x $10^3$ cells/well. After 24 h, MKN-28 cells were cotransfected by 25 pmol/well miRNA-146a-5p mimics or NC, together with 500 ng/well psiCHECK2-3′-UTR-CDC14A construct or psiCHECK2-3′-UTR-CDC14A mutation utilizing Lipofectamine™ 2000, according to their manufacturer's guidelines. After 48-h cell incubation, firefly and Renilla luciferase activities were detected through dual-luciferase reporter assay (Promega). Then, we normalized Renilla luciferase activity to firefly luciferase activity. Similar to every experiment, we utilized the empty vector as the control, accordingly averaging out adjusted luciferase values. We discretionarily presume a value as "1," considering it an antithesis to compare fold-differences of experimental values.

## Statistical analysis

Statistical difference was calculated utilizing Student's t-test and analyzed using SPSS 26.0 (SPSS, Chicago, IL, United States). The chi-squared test was applied to assess the relationship between miRNA-146a-5p expression and clinicopathological parameters. Average outcomes were shown as mean ± standard deviation (SD). $p$-values < 0.05 (utilizing a two-tailed paired $t$-test) were regarded as suggestions of remarkable differences between the two groups of data.

# Results

## miRNA profiling in GC FFPE samples as well as qRT-PCR

To find out the miRNA which probably inhibits GC proliferation in terms of epigenetic regulation, miRNA microarray assay was conducted in four GC FFPE samples and four paracarcinomatous samples. Among the 40 variously expressed miRNAs, miRNA-146a-5p, miRNA-126, miRNA-212, and miRNA-145 were found to be decreased (Figure 1A). Nevertheless, the functions of miRNA-146a-5p in malignant tumors remain poorly understood. Therefore, our attention was predominantly concentrated on the miRNA-146a-5p.

To test and verify the alterations of the miRNA levels on the miRNA microarray, qRT-PCR was implemented to detect miRNA-146a-5p levels in 132 GC FFPE samples and 66 paracarcinomatous samples. In line with the outcomes demonstrated through miRNA microarray, the decline of miRNA-146a-5p was verified in GC FFPE samples ($p < 0.05$) (Figure 1B). In addition, the expression of miRNA-146a-5p was similarly remarkably decreased in GC cell lines, MGC803, SGC-7901, and MKN-28, in contrast to the noncancerous gastric epithelial cells, GES-1 (Figure 1C).

## Association between miRNA-146a-5p expression and clinicopathological characteristics

Comparing the miRNA-146a-5p expression with clinicopathological variables, we observed remarkable positive correlations between miRNA-146a-5p expression and tumor sites ($p = 0.001$), Lauren's classification ($p < 0.001$), histologic differentiation ($p = 0.014$), invasion depth ($p < 0.001$), TNM stage ($p = 0.003$), and lymph node metastasis ($p = 0.002$) (Table 1).

## Cell apoptosis, cell cycle, and cell proliferation assays

MKN-28 cells were transfected by miRNA-146a-5p mimics or NC at the concentration of 100 nM. After 48 hours, MKN-28

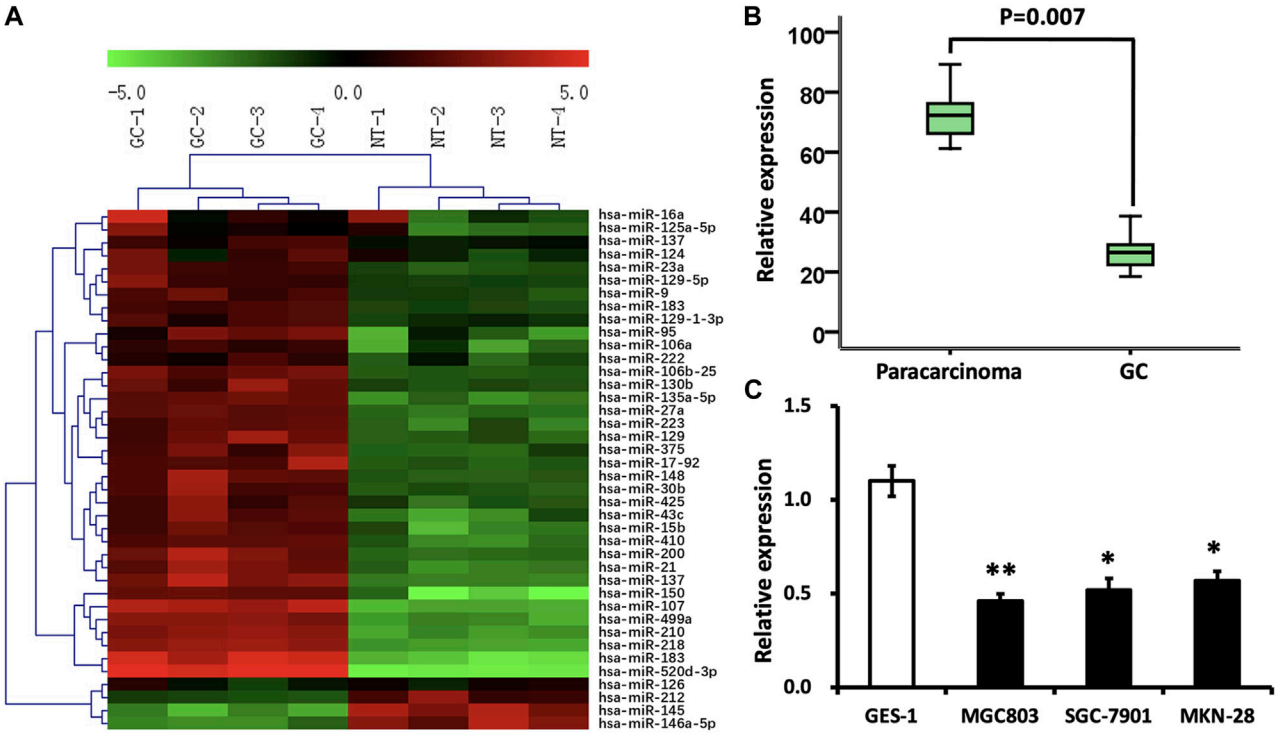


FIGURE 1
Differentially expressed miRNAs in GC. **(A)** Color scale demonstrates the comparative levels of miRNAs. "Red" implies high relative expression, and "green" implies low relative expression. **(B)** miRNA-146a-5p levels were reduced in GC samples ($n$ = 132) in contrast to those in paracarcinomatous samples ($n$ = 66) via stem–loop RT-PCR ($p < 0.05$). **(C)** Expression of miRNA-146a was analyzed in GC cell lines, MGC803, SGC-7901, and MKN-28, as well as normal gastric epithelial cells, GES-1. *$p < 0.05$, **$p < 0.01$ versus control.

cells were stained using Annexin V-FITC and PI, followed by flow cytometry detecting cell apoptosis. Our study exhibited that MKN-28 cells transfected by miRNA-146a-5p mimics led to dramatic alterations in the frequency of apoptosis, which is in contrast with the NC group ($p < 0.05$) (Figures 2A, B).

To validate that miRNA-146a-5p resulted in G1 arrest, MKN-28 cells transfected by miRNA-146a-5p mimics synchronized in the G1/S transition via serum deprivation as well as HU treatment. DNA quantification analysis was conducted upon releasing HU. These outcomes exhibited that all miRNA-146a-5p mimic-transfected cells started arresting at the G1 phase, suppressing their G1-to-S phase transition ($p < 0.05$) (Figures 3A, B).

Utilizing CCK-8 assay, our study demonstrated that the cell proliferation of the miRNA-146a-5p mimic-transfected group descended in contrast to the results of the NC group ($p < 0.05$), indicating that upregulated miRNA-146a-5p decreased MKN-28 cell proliferation (Figure 4).

## CDC14A acts as a target of miRNA-146a-5p

As is known, miRNAs generally exert a crucial influence on cellular behaviors by targeting pivotal downstream genes. To probe the latent intrinsic mechanisms elaborating why miRNA-146a-5p restrained GC cells, two calculation means were applied to assist in determining miRNA-146a-5p targets (Betel et al., 2008). Bioinformatics analysis suggested that 3′-UTR of the *CDC14A* gene incorporates a target site of miRNA-146a-5p, which was purely complementary to the 2–8 nt of miRNA-146a-5p.

In contrast to the NC group, mRNA levels of CDC14A identified by qRT-PCR declined in the miRNA-146a-5p mimic-transfected group ($p < 0.05$) (Figure 5C). Consistently, WB experiments on CDC14A protein levels exhibited remarkably reduced CDC14A levels in the miRNA-146a-5p mimic group compared with those in the NC group ($p < 0.05$) (Figures 5A, B).

A luciferase reporter vector with the speculative CDC14A-3′-UTR target spot for miRNA-146a-5p downstream of psiCHECK2-CDC14A 3′-UTR was fabricated. Likewise, we prepared a 10-bp mutant "psiCHECK2-CDC14A 3'-UTR" whose mutation sites were restricted in the seed region (psiCHECK2-CDC14A 3′-UTR mutating) (Figure 6A). Luciferase reporter vector, accompanied by miRNA-146a-5p mimics or NC, was co-transfected into MKN-28 cells. It turned out that a considerable decline of relative luciferase activity was observed in the experimental group, of which psiCHECK2-CDC14A 3′-UTR was co-transfected by miRNA-146a-5p mimics rather than NC (Figure 6B). Nevertheless, the inhibition was abrogated via mutating the 3′-UTR where miRNA-146a-5p binds to (psiCHECK2-CDC14A 3′-UTR mutating), hence disturbing the interaction between miRNA-146a-5p and *CDC14A*-3′-UTR (Figure 6C).

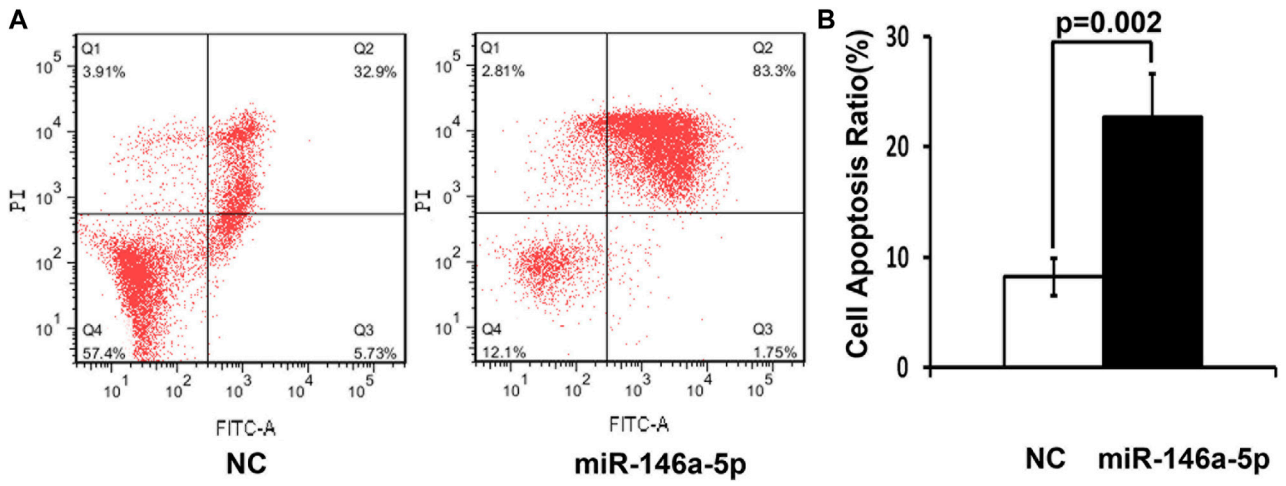


FIGURE 2
High miRNA-146a-5p levels enhance cell apoptosis. **(A)** 48 h after transfection by 100 nM miRNA-146a-5p mimics or NC, MKN-28 cells were stained utilizing Annexin V-FITC along with PI, followed by flow cytometry detecting apoptosis. **(B)** Semiquantitative analysis is shown. Transfection of MKN-28 cells by miRNA-146a-5p mimics led to remarkable alterations of increased apoptosis in contrast to NC ($n$ = 3, mean ± SD) ($p < 0.05$).

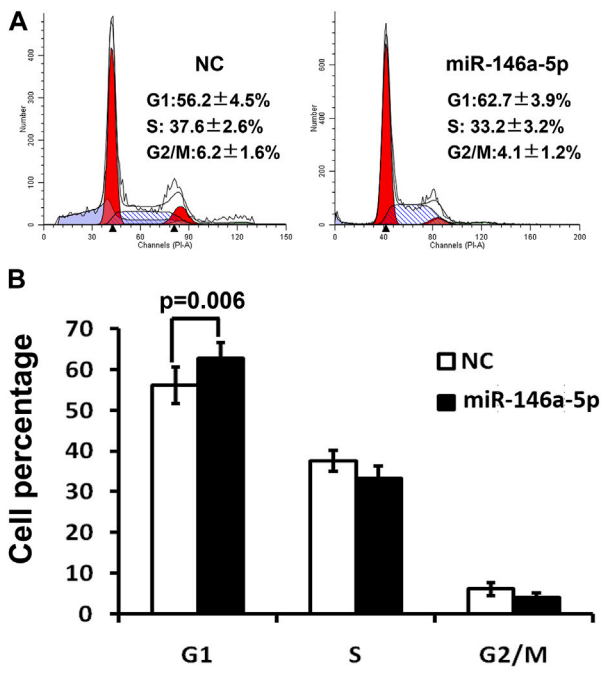


FIGURE 3
Cell cycle was detected via flow cytometry 48 h after transfection of MKN-28 cells by miRNA-146a-5p mimics or NC. **(A)** Flow cytometry demonstrates MKN-28 cell G1 phase arrest, as well as suppression of G1/S transition caused by increased miRNA-146a-5p in contrast to NC. **(B)** Semiquantitative analysis exhibited the relative proportion of cells at G1, S, and G2/M phases ($n$ = 3, mean ± SD).

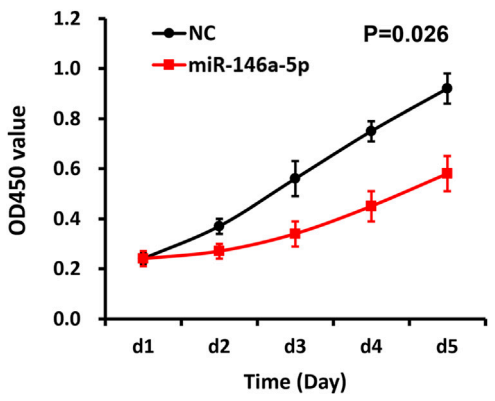


FIGURE 4
miRNA-146a-5p inhibits MKN-28 cell proliferation. Subsequent to transfection of MKN-28 cells by miRNA-146a-5p mimics or NC, absorbance values ($OD_{450nm}$) were determined using CCK-8 assay every 24 h for 5 consecutive days ($n$ = 3, mean ± SD) ($p < 0.05$).

## Discussion

miRNAs have been proven by abundant studies to exert a significant effect on the progression of the malignant phenotype of GC, featuring increased cell survival, proliferation, tumor angiogenesis, dedifferentiation, and generation of cell stemness (Dragomir et al., 2022; Smolarz et al., 2022). Identification of the biological importance of disordered miRNAs in GC cells fills a few dissociated gaps formerly reported and offers a model system by which the effects of miRNA on tumorigenesis as well as tumor progression may be further apprehended. Furthermore, it has been validated that alterations in the expression level of specific miRNAs may stand for a novel type of an indicator of the existence and deterioration of GC, hence possessing diagnostic or therapeutic merits (Condrat et al., 2020; Wu et al., 2020; Ho et al., 2022).

As we all know, dysregulated miRNAs exert a crucial influence on carcinogenesis and cancer progression (Matsuyama and Suzuki, 2019). We demonstrated that miRNA-146a-5p was downregulated in GC tissues according

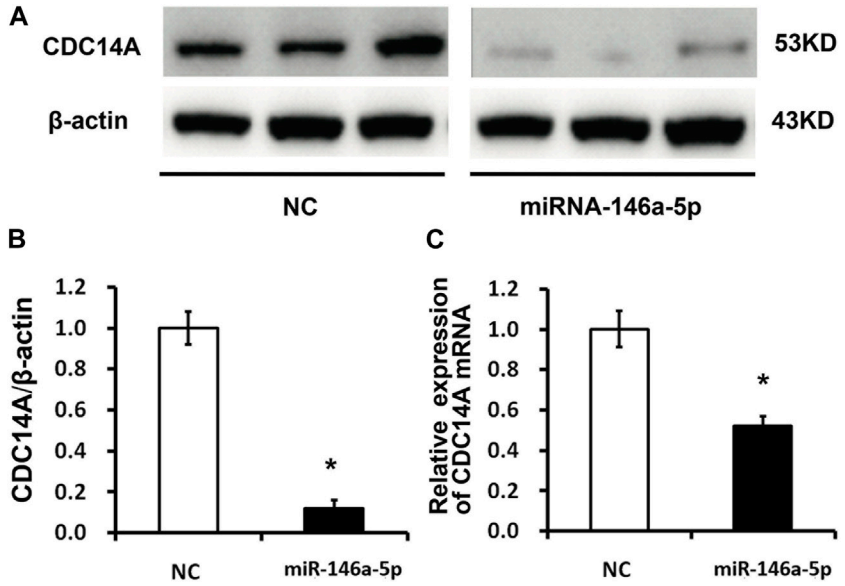


FIGURE 5
CDC14A targeted miRNA-146a-5p via binding to its 3′- UTR. **(A, B)** CDC14A protein levels were detected through WB experiments subsequent to transfection of miRNA-146a-5p mimics or NC into MKN-28 cells ($n$ = 3, mean ± SD). **(C)** mRNA levels of CDC14A were detected via qRT-PCR subsequent to transfection of miRNA-146a-5p mimics or NC into MKN-28 cells. *$p$ < 0.05, **$p$ < 0.01 versus control.

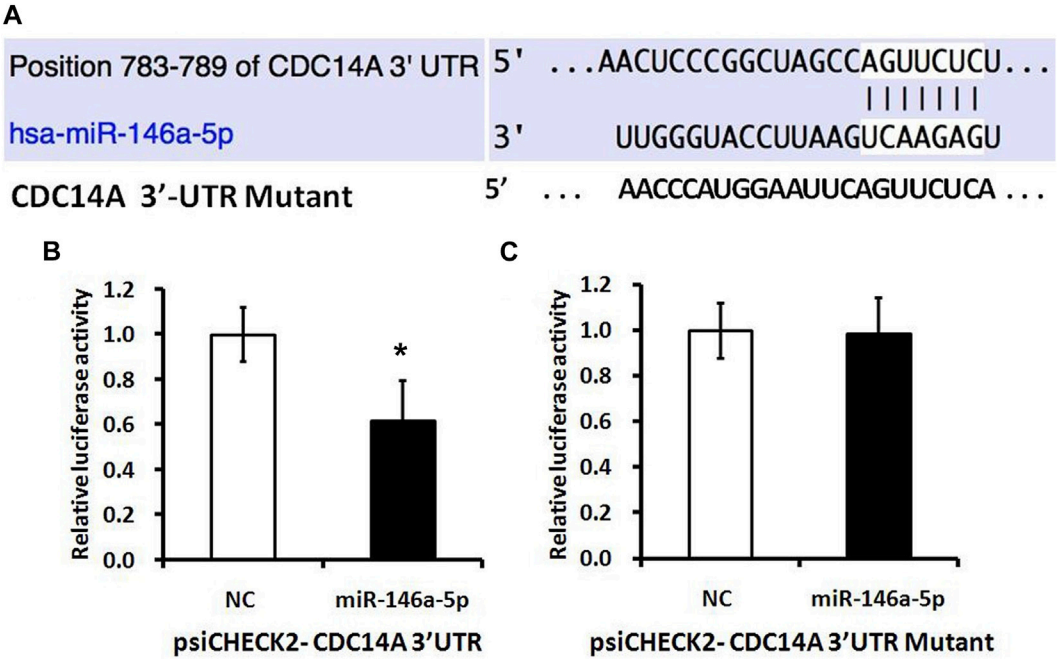


FIGURE 6
miRNA-146a-5p targets *CDC14A* gene. **(A)** Presumptive miRNA-146a-5p binding site in the *CDC14A* gene 3′-UTR. **(B, C)** Luciferase activity assays of luciferase reporters with wild-type or mutant *CDC14A* 3′-UTR were carried out subsequent to the Renilla luciferase activity ($n$ = 3, mean ± SD). *$p$ < 0.05 versus control.

to our results. Furthermore, we also observed that miRNA-146a-5p may function as an oncosuppressor miR to suppress cell proliferation through intercepting the G1/S transition of GC cells. That is to say, decreased miRNA-146a-5p levels in GC cells and tissues probably function to facilitate cell multiplication via attenuating the cell cycle.

Previous reports indicated that miRNA-146a-5p affects the apoptosis and proliferation of cells by regulating the signaling

pathways (Zhang et al., 2015; Noorolyai et al., 2020; Noorolyai et al., 2021). Substantial studies suggested that upregulation of miRNA-146a-5p restricted cell growth, confined migration, arrested cells at the G1 phase, and promoted cellular apoptosis (Huang et al., 2019; Zhu et al., 2020; Ding et al., 2021). Therefore, our results are consistent with previous reports. CCK-8 assays and flow cytometry analysis were employed in our research to identify the roles of miRNA-146a-5p in MKN-28 cells. These outcomes of our research coincide with preceding studies concerning the actions of miRNA-146a-5p in other kinds of cancers.

CDC14A aberrant expression can lead to spindle structural damage, the separation of chromosomes, and cytoplasmic abnormal segregation (Mailand et al., 2002; Villarroya-Beltri et al., 2022). Previous research studies showed that CDC14A overexpression leads to chromosome structural damage and inhibits the regeneration of chromosomal microtubules, thus influencing the spindle shape and resulting in its dysfunction (Vázquez-Novelle et al., 2010; Hu et al., 2019). Therefore, CDC14A may play an important role in every step of mitosis (Ji et al., 2012; Ovejero et al., 2018; Huang et al., 2020). As a result, CDC14A can serve as one of the most significant molecules involved in regulating the cell cycle through the mechanism of regulating the expression of multiple related genes. We discovered that miRNA-146a-5p induced the decline of CDC14A expression, thus causing suppressed cell cycle progression and enhanced cell apoptosis. To sum up, we extrapolate that miRNA-146a-5p affects MKN-28 cell proliferation and apoptosis through manipulating the expression of CDC14A.

Collectively, miRNA-146a-5p levels were decreased in GC cells and tissues, and a converse influence on CDC14A protein levels was confirmed. miRNA-146a-5p may be involved in manipulating cell cycle arrest as well as prompting cell apoptosis of GC cells, probably through directly targeting CDC14A. As a result, miRNA-146a-5p may be implicated in the occurrence and development of GC and may be conducive as a novel prognostic marker and therapeutic tool.

## Data availability statement

The original contributions presented in the study are included in the article/Supplementary Material; further inquiries can be directed to the corresponding authors.

## Ethics statement

The studies involving human participants were reviewed and approved by Jiangxi Provincial People's Hospital, The First Affiliated Hospital of Nanchang Medical College. Written informed consent for participation was not required for this study in accordance with national legislation and institutional requirements.

## Author contributions

Conception: QS. Interpretation or analysis of data: PJ, BL, ZZ, and BF. Preparation of the manuscript: PJ and BL. Revision for important intellectual content: LZ, ZZ, ZM, and QL. Supervision: WY and QS. All authors contributed to the article and approved the submitted version.

## Funding

This work was financially supported by the Scientific Research Projects of Jiangxi Provincial Health Commission (202130003), the Scientific Research Projects of Jiangxi Administration of Traditional Chinese Medicine (2021A370), and the Scientific Research Projects of Department of Education of Jiangxi Province (GJJ218909).

## Conflict of interest

The authors declare that the research was conducted in the absence of any commercial or financial relationships that could be construed as a potential conflict of interest.

## Publisher's note

All claims expressed in this article are solely those of the authors and do not necessarily represent those of their affiliated organizations, or those of the publisher, the editors, and the reviewers. Any product that may be evaluated in this article, or claim that may be made by its manufacturer, is not guaranteed or endorsed by the publisher.

## References

Ajani, J. A., D'Amico, T. A., Bentrem, D. J., Chao, J., Cooke, D., Corvera, C., et al. (2022). Gastric cancer, version 2.2022, NCCN clinical practice guidelines in oncology. *J. Natl. Compr. Canc Netw.* 20 (2), 167–192. doi:10.6004/jnccn.2022.0008

Ali Syeda, Z., Langden, S. S. S., Munkhzul, C., Lee, M., and Song, S. J. (2020). Regulatory mechanism of MicroRNA expression in cancer. *Int. J. Mol. Sci.* 21 (5), 1723. doi:10.3390/ijms21051723

Betel, D., Wilson, M., Gabow, A., Marks, D. S., and Sander, C. (2008). The microRNA.org resource: Targets and expression. *Nucleic Acids Res.* 36, D149–D153. Database issue). doi:10.1093/nar/gkm995

Calin, G. A., and Croce, C. M. (2006). MicroRNA signatures in human cancers. *Nat. Rev. Cancer* 6 (11), 857–866. doi:10.1038/nrc1997

Chen, N. P., Uddin, B., Hardt, R., Ding, W., Panic, M., Lucibello, I., et al. (2017). Human phosphatase CDC14A regulates actin organization through dephosphorylation of epithelial protein lost in neoplasm. *Proc. Natl. Acad. Sci. U. S. A.* 114 (20), 5201–5206. doi:10.1073/pnas.1619356114

Condrat, C. E., Thompson, D. C., Barbu, M. G., Bugnar, O. L., Boboc, A., Cretoiu, D., et al. (2020). miRNAs as biomarkers in disease: Latest findings regarding their role in diagnosis and prognosis. *Cells* 9 (2), 276. doi:10.3390/cells9020276

Correia de Sousa, M., Gjorgjieva, M., Dolicka, D., Sobolewski, C., and Foti, M. (2019). Deciphering miRNAs' action through miRNA editing. *Int. J. Mol. Sci.* 20 (24), 6249. doi:10.3390/ijms20246249

Damanti, C. C., Gaffo, E., Lovisa, F., Garbin, A., Di Battista, P., Gallingani, I., et al. (2021). MiR-26a-5p as a reference to normalize MicroRNA qRT-PCR levels in plasma exosomes of pediatric hematological malignancies. *Cells* 10 (1), 101. doi:10.3390/cells10010101

Ding, J., Zhang, Y., Cai, X., Zhang, Y., Yan, S., Wang, J., et al. (2021). Extracellular vesicles derived from M1 macrophages deliver miR-146a-5p and miR-146b-5p to suppress trophoblast migration and invasion by targeting TRAF6 in recurrent spontaneous abortion. *Theranostics* 11 (12), 5813–5830. doi:10.7150/thno.58731

Dragomir, M. P., Knutsen, E., and Calin, G. A. (2022). Classical and noncanonical functions of miRNAs in cancers. *Trends Genet.* 38 (4), 379–394. doi:10.1016/j.tig.2021.10.002

Ge, L., Wang, Y., Duan, Q. H., Liu, S. S., and Liu, G. J. (2019). MicroRNA-760 acts as a tumor suppressor in gastric cancer development via inhibiting G-protein-coupled receptor kinase interacting protein-1 transcription. *World J. Gastroenterol.* 25 (45), 6619–6633. doi:10.3748/wjg.v25.i45.6619

Ho, P. T. B., Clark, I. M., and Le, L. T. T. (2022). MicroRNA-based diagnosis and therapy. *Int. J. Mol. Sci.* 23 (13), 7167. doi:10.3390/ijms23137167

Hu, H., Shao, D., Wang, L., He, F., Huang, X., Lu, Y., et al. (2019). Phospho-regulation of Cdc14A by polo-like kinase 1 is involved in β-cell function and cell cycle regulation. *Mol. Med. Rep.* 20 (5), 4277–4284. doi:10.3892/mmr.2019.10653

Huang, W. T., He, R. Q., Li, X. J., Ma, J., Peng, Z. G., Zhong, J. C., et al. (2019). miR-146a-5p targets TCSF and influences cell growth and apoptosis to repress NSCLC progression. *Oncol. Rep.* 41 (4), 2226–2240. doi:10.3892/or.2019.7030

Huang, Y., Zhu, Y., Zhang, Z., Li, Z., and Kong, C. (2020). UNC5B mediates G2/M phase arrest of bladder cancer cells by binding to CDC14A and P53. *Cancer Gene Ther.* 27 (12), 934–947. doi:10.1038/s41417-020-0175-x

Hussen, B. M., Hidayat, H. J., Salihi, A., Sabir, D. K., Taheri, M., and Ghafouri-Fard, S. (2021). MicroRNA: A signature for cancer progression. *Biomed. Pharmacother.* 138, 111528. doi:10.1016/j.biopha.2021.111528

Ji, M., Yang, S., Chen, Y., Xiao, L., Zhang, L., and Dong, J. (2012). Phospho-regulation of KIBRA by CDK1 and CDC14 phosphatase controls cell-cycle progression. *Biochem. J.* 447 (1), 93–102. doi:10.1042/bj20120751

Jung, S., Kim, W. J., Kim, B. K., Kim, J., Kim, M. J., Kim, K. P., et al. (2020). In-particle stem-loop RT-qPCR for specific and multiplex microRNA profiling. *Biosens. Bioelectron.* 163, 112301. doi:10.1016/j.bios.2020.112301

Kang, J., Huang, X., Dong, W., Zhu, X., Li, M., and Cui, N. (2021). MicroRNA-1269b inhibits gastric cancer development through regulating methyltransferase-like 3 (METTL3). *Bioengineered* 12 (1), 1150–1160. doi:10.1080/21655979.2021.1909951

Li, P., Xie, X. B., Chen, Q., Pang, G. L., Luo, W., Tu, J. C., et al. (2014). MiRNA-15a mediates cell cycle arrest and potentiates apoptosis in breast cancer cells by targeting synuclein-γ. *Asian Pac J. Cancer Prev.* 15 (16), 6949–6954. doi:10.7314/apjcp.2014.15.16.6949

Liu, J., Yang, T., Huang, Z., Chen, H., and Bai, Y. (2022). Transcriptional regulation of nuclear miRNAs in tumorigenesis (Review). *Int. J. Mol. Med.* 50 (1), 92. doi:10.3892/ijmm.2022.5148

Liu, X., Ma, R., Yi, B., Riker, A. I., and Xi, Y. (2021). MicroRNAs are involved in the development and progression of gastric cancer. *Acta Pharmacol. Sin.* 42 (7), 1018–1026. doi:10.1038/s41401-020-00540-0

Mailand, N., Lukas, C., Kaiser, B. K., Jackson, P. K., Bartek, J., and Lukas, J. (2002). Deregulated human Cdc14A phosphatase disrupts centrosome separation and chromosome segregation. *Nat. Cell Biol.* 4 (4), 317–322. doi:10.1038/ncb777

Matsuyama, H., and Suzuki, H. I. (2019). Systems and synthetic microRNA Biology: From biogenesis to disease pathogenesis. *Int. J. Mol. Sci.* 21 (1), 132. doi:10.3390/ijms21010132

Miliotis, C., and Slack, F. J. (2021). miR-105-5p regulates PD-L1 expression and tumor immunogenicity in gastric cancer. *Cancer Lett.* 518, 115–126. doi:10.1016/j.canlet.2021.05.037

Noorolyai, S., Baghbani, E., Aghebati Maleki, L., Baghbanzadeh Kojabad, A., Shanehbansdi, D., Khaze Shahgoli, V., et al. (2020). Restoration of miR-193a-5p and miR-146 a-5p expression induces G1 arrest in colorectal cancer through targeting of MDM2/p53. *Adv. Pharm. Bull.* 10 (1), 130–134. doi:10.15171/apb.2020.017

Noorolyai, S., Baghbani, E., Shanehbandi, D., Khaze Shahgoli, V., Baghbanzadeh Kojabad, A., Mansoori, B., et al. (2021). miR-146a-5p and miR-193a-5p synergistically inhibited the proliferation of human colorectal cancer cells (HT-29 cell line) through ERK signaling pathway. *Adv. Pharm. Bull.* 11 (4), 755–764. doi:10.34172/apb.2021.085

Ovejero, S., Ayala, P., Malumbres, M., Pimentel-Muiños, F. X., Bueno, A., and Sacristán, M. P. (2018). Biochemical analyses reveal amino acid residues critical for cell cycle-dependent phosphorylation of human Cdc14A phosphatase by cyclin-dependent kinase 1. *Sci. Rep.* 8 (1), 11871. doi:10.1038/s41598-018-30253-8

Pu, M., Chen, J., Tao, Z., Miao, L., Qi, X., Wang, Y., et al. (2019). Regulatory network of miRNA on its target: Coordination between transcriptional and post-transcriptional regulation of gene expression. *Cell Mol. Life Sci.* 76 (3), 441–451. doi:10.1007/s00018-018-2940-7

Riahi Rad, Z., Riahi Rad, Z., Goudarzi, H., Goudarzi, M., Mahmoudi, M., Yasbolaghi Sharahi, J., et al. (2021). MicroRNAs in the interaction between host-bacterial pathogens: A new perspective. *J. Cell Physiol.* 236 (9), 6249–6270. doi:10.1002/jcp.30333

Saliminejad, K., Khorram Khorshid, H. R., Soleymani Fard, S., and Ghaffari, S. H. (2019). An overview of microRNAs: Biology, functions, therapeutics, and analysis methods. *J. Cell Physiol.* 234 (5), 5451–5465. doi:10.1002/jcp.27486

Shi, Y., Liu, Z., Lin, Q., Luo, Q., Cen, Y., Li, J., et al. (2021). MiRNAs and cancer: Key link in diagnosis and therapy. *Genes (Basel)* 12 (8), 1289. doi:10.3390/genes12081289

Smolarz, B., Durczyński, A., Romanowicz, H., Szyłło, K., and Hogendorf, P. (2022). miRNAs in cancer (review of literature). *Int. J. Mol. Sci.* 23 (5), 2805. doi:10.3390/ijms23052805

Smyth, E. C., Nilsson, M., Grabsch, H. I., van Grieken, N. C., and Lordick, F. (2020). Gastric cancer. *Lancet* 396 (10251), 635–648. doi:10.1016/s0140-6736(20)31288-5

Thrift, A. P., and El-Serag, H. B. (2020). Burden of gastric cancer. *Clin. Gastroenterol. Hepatol.* 18 (3), 534–542. doi:10.1016/j.cgh.2019.07.045

Vázquez-Novelle, M. D., Mailand, N., Ovejero, S., Bueno, A., and Sacristán, M. P. (2010). Human Cdc14A phosphatase modulates the G2/M transition through Cdc25A and Cdc25B. *J. Biol. Chem.* 285 (52), 40544–40553. doi:10.1074/jbc.M110.133009

Villarroya-Beltri, C., Martins, A. F. B., García, A., Giménez, D., Zarzuela, E., Novo, M., et al. (2022). Mammalian CDC14 phosphatases control exit from stemness in pluripotent cells. *Embo J.* 42, e111251. doi:10.15252/embj.2022111251

Wu, S. R., Wu, Q., and Shi, Y. Q. (2020). Recent advances of miRNAs in the development and clinical application of gastric cancer. *Chin. Med. J. Engl.* 133 (15), 1856–1867. doi:10.1097/cm9.0000000000000921

Zhang, Y., Lin, W., Jiang, W., and Wang, Z. (2022). MicroRNA-18 facilitates the stemness of gastric cancer by downregulating HMGB3 though targeting Meis2. *Bioengineered* 13 (4), 9959–9972. doi:10.1080/21655979.2022.2062529

Zhang, Z., Zhang, Y., Sun, X. X., Ma, X., and Chen, Z. N. (2015). microRNA-146a inhibits cancer metastasis by downregulating VEGF through dual pathways in hepatocellular carcinoma. *Mol. Cancer* 14, 5. doi:10.1186/1476-4598-14-5

Zhu, F. Y., Gan, C. W., Wang, M. X., Sun, B. C., Li, F. J., Qiu, Y. H., et al. (2020). MiR-146a-5p inhibits proliferation and promotes apoptosis of oral squamous cell carcinoma cells by regulating NF-κB signaling pathway. *Eur. Rev. Med. Pharmacol. Sci.* 24 (7), 3717–3723. doi:10.26355/eurrev_202004_20835

frontiers | Frontiers in Cell and Developmental Biology

TYPE Original Research
PUBLISHED 25 May 2023
DOI 10.3389/fcell.2023.1209243



OPEN ACCESS

EDITED BY
Ying Shen,
Sun Yat-sen University Cancer Center (SYSUCC), China

REVIEWED BY
Yi-Qian Pan,
Sun Yat-sen University Cancer Center (SYSUCC), China
Fei Liu,
Chinese Academy of Medical Sciences and Peking Union Medical College, China

*CORRESPONDENCE
Yu-Tong Chen,
amber04@126.com

†These authors share senior authorship

‡These authors share first authorship

RECEIVED 20 April 2023
ACCEPTED 12 May 2023
PUBLISHED 25 May 2023

CITATION
Mo S-F, Cai Z-Z, Kuai W-H, Li X and Chen Y-T (2023), Universal cutoff for tumor mutational burden in predicting the efficacy of anti-PD-(L)1 therapy for advanced cancers.
*Front. Cell Dev. Biol.* 11:1209243.
doi: 10.3389/fcell.2023.1209243



# Universal cutoff for tumor mutational burden in predicting the efficacy of anti-PD-(L)1 therapy for advanced cancers

Shu-Fen Mo[1‡], Zeng-Zhi Cai[1‡], Wen-Hao Kuai[2‡], Xuexin Li[3†] and Yu-Tong Chen[2,4†*]

[1]Department of Medical Oncology, Guangdong Agriculture Reclamation Central Hospital, Zhanjiang, China, [2]Department of Dermatology, Changhai Hospital of Shanghai, Second Military Medical University (Naval Medical University), Shanghai, China, [3]Department of Medical Biochemistry and Biophysics, Karolinska Institute, Stockholm, Sweden, [4]Faculty of Medical Science, Jinan University, Guangzhou, China

**Background:** The US Food and Drug Administration (FDA)'s tumor-agnostic approval of pembrolizumab in high tumor mutational burden (TMB-high, i.e., TMB≥10 mut/Mb) cases, based on the data from KEYNOTE-158, has raised considerable concerns among the immuno-oncology community. This study aims to statistically infer the optimal universal cutoff in defining TMB-high that is predictive of the efficacy of anti-PD-(L) 1 therapy in advanced solid tumors.

**Methods:** We integrated MSK-IMPACT TMB data from a public cohort and the objective response rate (ORR) for anti-PD-(L) 1 monotherapy across diverse cancer types in published trials. The optimal TMB cutoff was determined by varying the universal cutoff to define TMB-high across cancer types and examining the cancer-level correlation between objective response rate and the proportion of TMB-high cases. The utility of this cutoff in predicting overall survival (OS) benefits from anti-PD-(L) 1 therapy was then evaluated in a validation cohort of advanced cancers with coupled MSK-IMPACT TMB and OS data. In silico analysis of whole-exome sequencing data from The Cancer Genome Atlas was further employed to assess the generalizability of the identified cutoff among panels comprising several hundred genes.

**Results:** The cancer type-level analysis identified 10 mut/Mb as the optimal cutoff for MSK-IMPACT in defining TMB-high, with the corresponding TMB-high (TMB≥10 mut/Mb) percentage strongly correlated with ORR for PD-(L) 1 blockade across cancer types [correlation coefficient, 0.72 (95% CI, 0.45–0.88)]. This cutoff was also the optimum in defining TMB-high (via MSK-IMPACT) when predicting OS benefits from anti-PD-(L) 1 therapy in the validation cohort. In this cohort, TMB≥10 mut/Mb was associated with significantly improved OS (hazard ratio, 0.58 [95% CI, 0.48–0.71]; $p < 0.001$). Moreover, *in silico* analyses revealed excellent agreement of TMB≥10 mut/Mb cases between MSK-IMPACT and the FDA-approved panels and between MSK-IMPACT and various randomly sampled panels.

**Conclusion:** Our study demonstrates that 10 mut/Mb is the optimal, universal cutoff for TMB-high that guides the clinical application of anti-PD-(L) 1 therapy for advanced solid tumors. It also provides rigorous evidence beyond KEYNOTE-158 for the utility of TMB≥10 mut/Mb in predicting the efficacy of PD-(L) 1 blockade in

broader settings, which could help to mitigate the challenges in embracing the tumor-agnostic approval of pembrolizumab in TMB-high cases.

KEYWORDS

**tumor mutational burden (TMB), anti-PD-(L)1 therapy, advanced solid tumors, universal cutoff, biomarker**

# Introduction

Anti-PD-(L) 1 therapy has achieved great success in more than 15 cancer types, given its prolonged duration of response and favorable tolerability profile (Wang et al., 2021; Sharma et al., 2023). However, only a minor subset of patients benefit from this treatment and clinical responses vary greatly across cancer types (Wang et al., 2023). As such, there is a crucial need of robust biomarkers in predicting the efficacy of PD-(L)1 inhibitors to guide patient selection for such treatment (Hegde and Chen, 2020; Wang and Xu, 2023).

Tumor and/or immune cell PD-L1 expression by immunohistochemical assays was first approved by the US Food and Drug Administration (FDA) as a companion diagnostic to pembrolizumab for advanced non-small-cell lung cancer, upper gastrointestinal cancers, cervical cancer, and urothelial cancer, based on convincing evidence for these malignancies (Herbst et al., 2016; Muro et al., 2016; Reck et al., 2016; Bellmunt et al., 2017; Chung et al., 2018; Fuchs et al., 2018). However, this marker alone is insufficient for the precise prediction of anti-PD-(L) 1 response, and there is a lack of standardization across platforms, scoring systems and cutoff values for PD-L1 expression (Wang and Xu, 2023). In addition, high microsatellite instability (MSI-H), an indicator of defects in DNA repair that gives rise to a large quantity of neoantigens, was approved by the FDA in a tumor-agnostic manner, but it was largely aggregated in several malignancies (e.g., colorectal cancer, gastric cancer, and endometrial cancer), with an overall low prevalence (Le et al., 2015; Hause et al., 2016; Diaz et al., 2017; Overman et al., 2017).

Tumor mutational burden (TMB), generally referred to as the total number of mutational events in the genome of a tumor and reflective of tumor immunogenicity, is emerging as a promising biomarker for PD-(L) 1 blockade (Chan et al., 2019). Although whole-exome sequencing (WES) is the standard approach for measuring TMB, targeted next-generation sequencing (NGS) panels appear to be more pragmatic for TMB estimation, given that routine implementation of WES in clinical practice is limited by its substantial costs and long turnaround times (Wu et al., 2019; Merino et al., 2020). Since 2015, mounting evidence has shown that high TMB is associated with greater clinical benefits from anti-PD-(L) 1 therapy among various malignancies (Rizvi et al., 2015; Samstein et al., 2019; Singal et al., 2019; Wang et al., 2023). Most recently, the KEYNOTE-158 study revealed an objective response rate (ORR) of 29% with pembrolizumab for treating refractory advanced solid tumors with high TMB, i.e., TMB≥10 mutations per megabase (mut/Mb) as determined by FoundationOne CDx (F1CDx) (Marabelle et al., 2019; Marabelle et al., 2020); thereby, TMB-high was recently approved by the FDA as another tumor-agnostic companion diagnostic to pembrolizumab in patients refractory to standard treatments (FDA approves, 2020).

Nevertheless, this tumor-agnostic approval based on KEYNOTE-158 has raised considerable concerns and doubts among the immuno-oncology community (Bersanelli, 2020; Prasad and Addeo, 2020). Firstly, the cutoff of 10 mut/Mb in defining TMB-high was not statistically inferred based on anti-PD-(L) 1 efficacy data. Secondly, significant overall survival (OS) benefits in TMB-high cases were not demonstrated with this cutoff. Last but not least, it remains unknown whether this cutoff can be extrapolated to other tumor types, NGS panels, and PD-(L) 1 inhibitors that were not involved in KEYNOTE-158.

Despite these limitations, KEYNOTE-158 has provided promising evidence for the utility of a universal TMB cutoff across cancer types for prediction of anti-PD-(L) 1 response, which is of particular value as it would be challenging and labor-intensive to establish tumor-specific TMB thresholds. In this study, we integrated large-scale genomic and clinical data and performed cancer type-level and patient-level analyses to statistically infer the optimal, universal cutoff in defining TMB-high and predicting the efficacy of anti-PD-(L) 1 therapy in advanced solid tumors.

# Materials and methods

## Study cohort and study design

This study was performed from 27 July 2020, to 15 September 2020. Three steps were included: 1) Cancer type-level analysis to identify the optimal TMB cutoff in predicting responses to PD-(L) 1 inhibitors (Figure 1); 2) patient-level analysis to verify the utility of TMB-high defined by the identified cutoff in predicting the efficacy of PD-(L) 1 inhibitors; and 3) *in silico* analysis to assess the generalizability of the identified TMB cutoff among existing targeted sequencing panels and randomly sampled panels comprising several hundred genes.

At Step 1, we included cancer types with available MSK-IMPACT TMB data as well as anti-PD-(L) 1 monotherapy ORR data consolidated by Yarchoan et al. (Wang et al., 2023) The MSK-IMPACT TMB data were obtained from a public cohort involving over 10,000 advanced cancer patients (Cohort 1) (Zehir et al., 2017). Only cancer types with at least 30 cases in Cohort 1 and at least 10 participants in trials investigating anti-PD-(L) 1 monotherapy were included. The optimal TMB cutoff was determined by varying the universal cutoff to define TMB-high across cancer types and examining the corresponding cancer-level association between ORR and the proportion of TMB-high cases (Figure 1).

At Step 2, we analyzed a public cohort involving over 1,000 advanced cancer patients receiving anti-PD-(L) 1 monotherapy with coupled MSK-IMPACT TMB data and overall survival (OS) data (Cohort 2) (Samstein et al., 2019). We noticed some overlapped patients in Cohorts 1 and 2, but they were

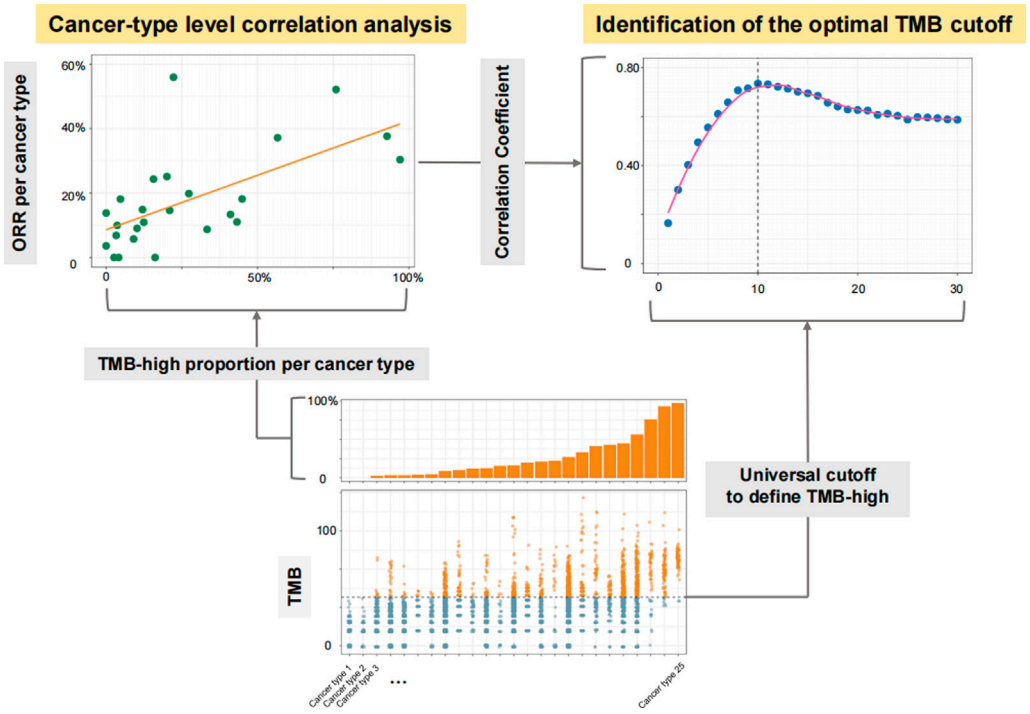


FIGURE 1
Diagram for the process of identifying the optimal universal cutoff for tumor mutational burden (TMB) in predicting responses to PD-(L) 1 inhibitors. For each given universal TMB cutoff, the proportion of TMB-high cases defined by this cutoff was calculated for each cancer type. The cancer type-level correlation between objective response rate (ORR) and the proportion of TMB-high cases was then evaluated. By varying the universal cutoff to define TMB-high, the curve for the association between such cancer type-level correlation and the universal TMB cutoff was depicted, and the Chow test was then applied to determine the structural breakpoint, hence the optimal TMB cutoff.

not excluded from the analyses at Step 2 as the TMB and ORR data at Step 1 were disconnected, i.e., from different populations. TMB-high was defined by the cutoff identified in Step 1, and the association between TMB status (high vs. low) and OS was evaluated.

At Step 3, we analyzed WES data from The Cancer Genome Atlas (TCGA) across 32 solid tumors. The MC3 somatic mutation data were downloaded from the UCSC Xena browser (http://xena.ucsc.edu/). When data on more than one tumor sample were available, the primary tumor sample was the favored choice, and in remaining cases "metastatic" was selected over "additional metastatic". We first generated *in silico* gene panels that comprised genes from the three NGS panels that have thus far received FDA approval or authorization (i.e., MSK-IMPACT, F1CDx, and PGDx elio tissue complete [PGDx]) (Chalmers et al., 2017; Zehir et al., 2017; Wood et al., 2018). TMB for each *in silico* panel was calculated using its own unique bioinformatics pipeline. We also generated *in silico* panels with various sizes and percentages of shared genes with MSK-IMPACT, with 1,000 resampling for each given panel size and percentage of shared genes. We performed three cycles of analyses of randomly sampled panels; in each cycle, we applied one of the bioinformatics pipelines of the three FDA-approved or authorized panels to calculate TMB for the randomly sampled panels. We then used the cutoff identified in Step 1 to define TMB-high across all these panels, and evaluated their concordance with MSK-IMPACT in defining TMB-high cases.

Detailed patient/sample inclusion and exclusion procedures are shown in Supplementary Figure S1

## Statistical analysis

At Step 1, linear regression models were fitted by use of ordinary least-squares regression to examine the cancer-level associations between ORR and the proportion of TMB-high cases. The linear models were weighted by the geometric means of the sample size of trials and that of Cohort 1 per cancer type. The strength of association was indicated by the square root ($R_{TMB\text{-}ORR}$) of the coefficient of determination from the linear models. We then depicted the curve for the association between $R_{TMB\text{-}ORR}$ and the universal cutoff to define TMB-high across cancer types, and applied the Chow test to determine the structural breakpoint (Zeileis et al., 2010). The structural breakpoint was considered as the threshold of clinico-biological impact, hence the optimal TMB cutoff for further investigation.

At Step 2, hazard ratios (HRs) and corresponding 95% confidence intervals (CIs) for the association between TMB status (high vs. low) and OS was evaluated using Cox proportional hazards models adjusted for age, sex, MSK-IMPACT version, and cancer type. We depicted the curve for the association between the Wald test Z score (i.e., β coefficient of TMB divided by its standard error in the multivariable Cox proportional hazards model) and the universal cutoff to define TMB-high across cancer types, and applied the Chow test to

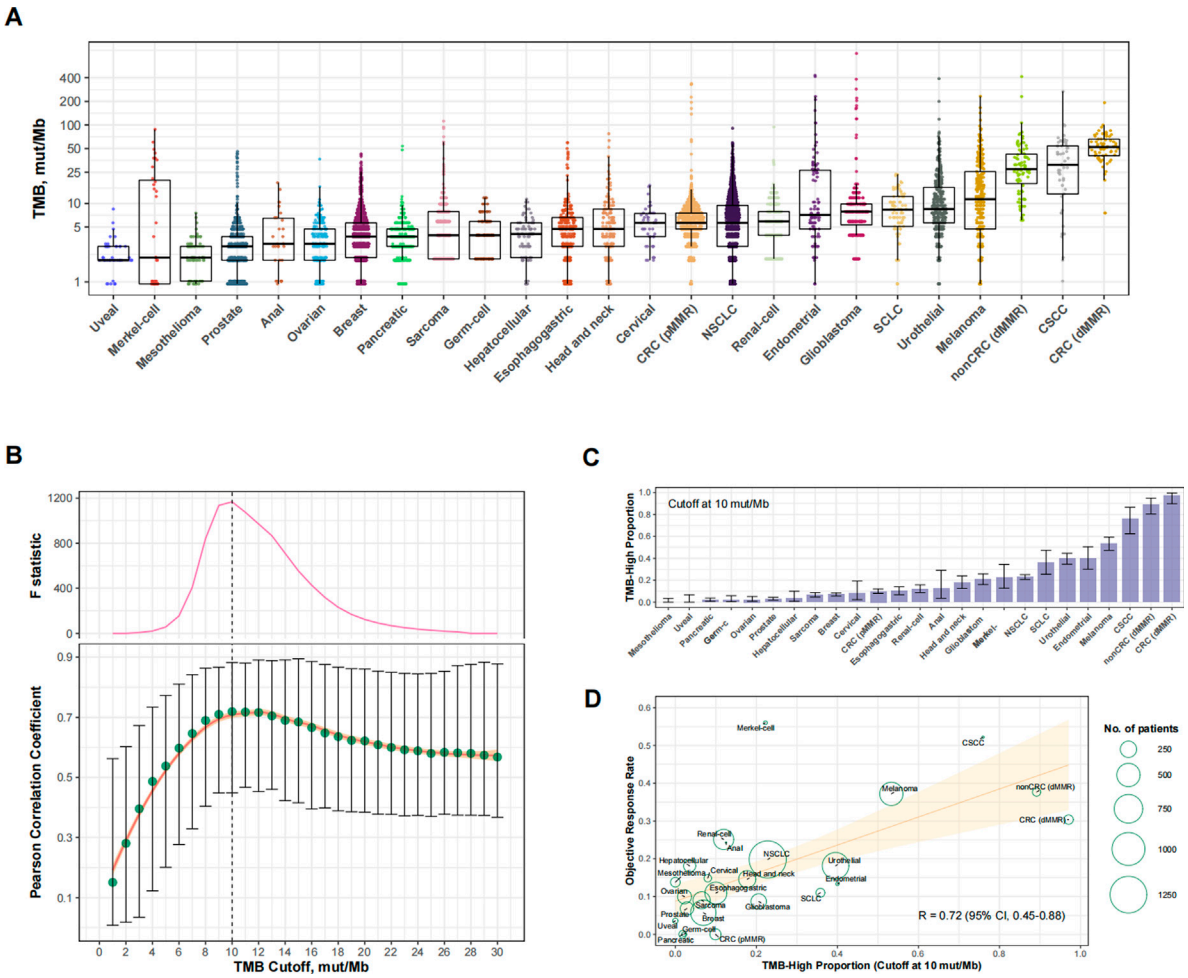


FIGURE 2
Cancer type-level analysis to identify the optimal universal cutoff for tumor mutational burden (TMB) in predicting responses to PD-(L)1 blockade. **(A)** The landscape of TMB across the 25 eligible cancer types in Cohort 1. Abbreviations: NSCLC, non-small-cell lung cancer; CRC (dMMR), microsatellite-instable colorectal cancer; CRC (pMMR), microsatellite-stable colorectal cancer; nonCRC (dMMR), microsatellite-instable non-colorectal cancer; CSCC, cutaneous squamous-cell carcinoma. **(B)** Cancer type-level correlation between anti-PD-(L)1 response rate and the proportion of TMB-high cases, as well as the Chow F statistic, are plotted against varying cutoff for TMB. The yellow curve denotes the LOESS smoother. A structural breakpoint at 10 that maximized the Chow F statistic (i.e., minimizing the ordinary least squares estimator) was identified by Chow test. **(C)** The proportion of TMB-high (i.e., TMB≥10 mut/Mb). cases across cancer types in Cohort 1. **(D)** Cancer type-level correlation between anti-PD-(L) 1 response rate and the proportion of TMB-high when the cutoff was 10 mut/Mb.

determine the structural breakpoint. Concordance indices (C-indices) were used to assess the discriminatory capacity of models (Pencina and D'Agostino, 2004). In this step, the 80th percentile was used as the tumor-specific TMB cutoff to be compared with the universal cutoff of 10 mut/Mb; the 80th percentile was chosen because it was identified as the optimal percentile cutoff to predict the efficacy of PD-(L) 1 blockade in Samstein's study (Samstein et al., 2019).

At Step 3, the Cohen's Kappa coefficient, a statistic measuring inter-rater reliability, was used to evaluate the agreement between TMB-high cases based on MSK-IMPACT and *in silico* panels using the same cutoff. A Kappa of 1 indicates perfect agreement and a Kappa above 0.80 indicates an almost perfect agreement (McHugh, 2012).

The significance level was set at a two-sided $p < 0.05$. All statistical analyses were performed using R software version 3.6.1 (http://www.r-project.org).

## Role of the funding source

The funder of this study had no role in its design, data collection, data analysis, data interpretation, and writing of the report. The corresponding author had full access to all the data in the study and had final responsibility for the decision to submit for publication.

# Results

## Optimal TMB cutoff in predicting responses to PD-(L)1 blockade at the cancer type level

We analyzed a total of 25 eligible cancer types with at least 30 cases in Cohort 1 (totaling 8,201 cases) and at least 10 participants

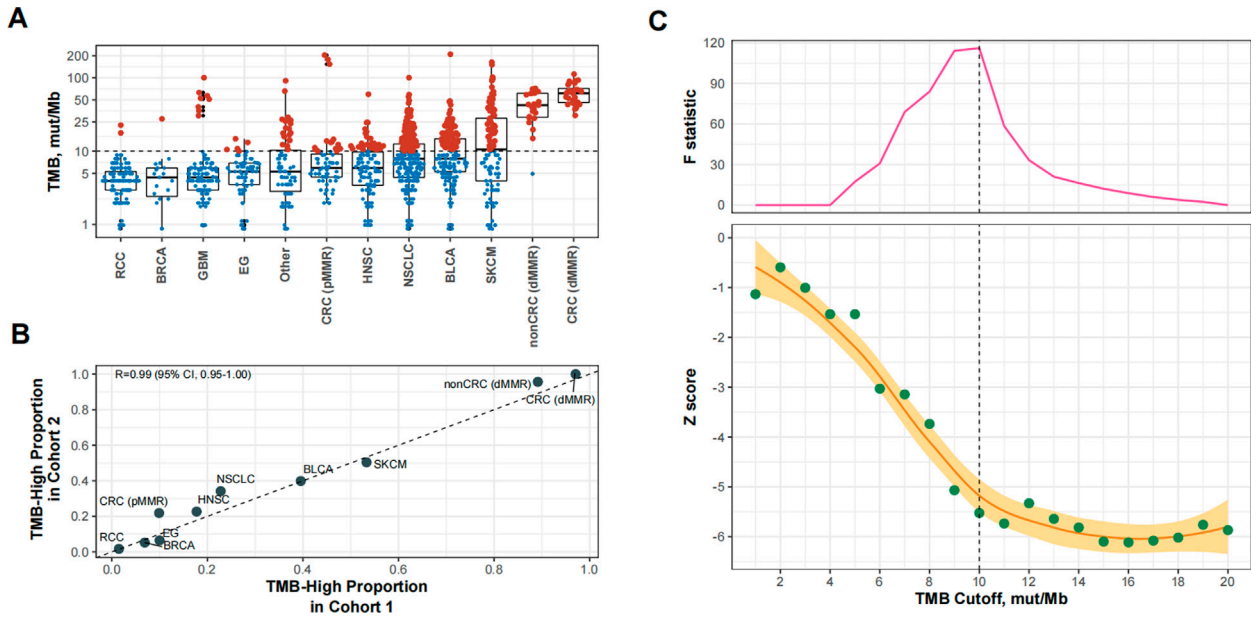


FIGURE 3
Patient-level analysis to verify the identified tumor mutational burden (TMB) cutoff for defining TMB-high in predicting overall survival benefits of PD-(L) 1 inhibitors. **(A)** TMB-high (i.e., TMB≥10 mut/Mb). cases across cancer types in Cohort 2. Abbreviations: RCC, renal-cell carcinoma; BRCA, breast cancer; GBM, glioma; EG, esophagogastric cancer; HNSC, head and neck cancer; NSCLC, non-small-cell lung cancer; BLCA, bladder cancer; SKCM, melanoma; CRC (dMMR), microsatellite-instable colorectal cancer; CRC (pMMR), microsatellite-stable colorectal cancer; nonCRC (dMMR), microsatellite-instable non-colorectal cancer. **(B)** The proportional agreement between TMB-high cases in Cohorts 1 and 2 when the cutoff was 10 mut/Mb. **(C)** The standardized prognostic impact of TMB (measured by the Wald test Z score, i.e., β coefficient of TMB divided by its standard error in Cox proportional hazards model adjusted for age, sex, panel version, and cancer type), as well as the Chow F statistic, are plotted against the varying cutoffs for TMB. The yellow curve denotes the LOESS smoother. A structural breakpoint at 10 that maximized the Chow F statistic (i.e., minimizing the ordinary least squares estimator) was identified by Chow test.

in trials investigating anti-PD-(L) 1 monotherapy (totaling 6,348 cases; Supplementary Table S1). The ORR ranged from 0% to 56.0% across cancer types. The level of TMB varied greatly across cancer types (Figure 2A). Figure 2B shows the relationship between the TMB cutoff and the corresponding $R_{TMB\text{-}ORR}$. With a higher cutoff for TMB, the $R_{TMB\text{-}ORR}$ increased and then plateaued, and a structural breakpoint of 10 mut/Mb was identified by the Chow test (Figure 2B). When this cutoff was used to define TMB-high (TMB≥10 mut/Mb), the proportion of TMB-high cases ranged from 0% to 97.1% across cancer types (totaling 16.2% for the entire cohort; Figure 2C), with $R_{TMB\text{-}ORR}$ reaching 0.72 (95% CI, 0.45–0.88; $p < 0.001$) (Figure 2D).

## Verification of the reliability of the identified TMB cutoff

We then used 10 mut/Mb as the universal cutoff to define TMB-high in Cohort 2 (Supplementary Table S2 and Figure 3A). The proportion of TMB-high cases in this cohort exhibited excellent consistency with Cohort 1 (Figure 3B). Figure 3C shows the relationship between the TMB cutoff and corresponding impact of TMB-high on OS. With a higher cutoff for TMB, the improvement in OS with TMB-high increased and then plateaued, with the structural breakpoint also at 10 mut/Mb (Figure 3C).

Next, we sought to evaluate the performance of 10 mut/Mb compared with the 80th percentile per cancer type as the cutoff for defining TMB-high. The proportion of TMB-high cases was significantly higher when the cutoff was at 10 mut/Mb than at the 80th percentile per cancer type (28.5% vs. 21.3%, $p < 0.001$). As shown in Figure 4A, the impact of TMB-high on OS was comparable when the cutoff was at 10 mut/Mb (HR = 0.58 [95% CI, 0.48–0.71], $p < 0.001$) or the 80th percentile per cancer type (HR = 0.56 [95% CI, 0.63–0.70], $p < 0.001$). The C-index for TMB-high defined by 10 mut/Mb was similar with that by the 80th percentile per cancer type ($p = 0.433$). Notably, consistent findings were obtained when only microsatellite stable (MSS) cases were analyzed (Supplementary Figure S2).

As shown in Figure 4B, OS was consistently in favor of TMB-high across cancer types when the cutoff was at 10 mut/Mb (test of interaction between TMB status and cancer type, $p = 0.756$). In contrast, TMB-high defined by the 80th percentile per cancer type failed to demonstrate improved OS in patients with glioma and renal-cell carcinoma (test of interaction between TMB status and cancer type, $p < 0.001$). For renal-cell carcinoma, using the 80th percentile as the cutoff provided a markedly higher percentage of TMB-high cases than when using 10 mut/Mb as the cutoff (23.0% vs. 1.6%, $p < 0.001$); however, TMB-high defined by the 80th percentile was not associated with improved OS in this cancer type (HR = 0.88 [95% CI, 0.43–1.80], $p = 0.730$). The two TMB-high renal-cell carcinoma cases defined by the cutoff at 10 mut/Mb both remained

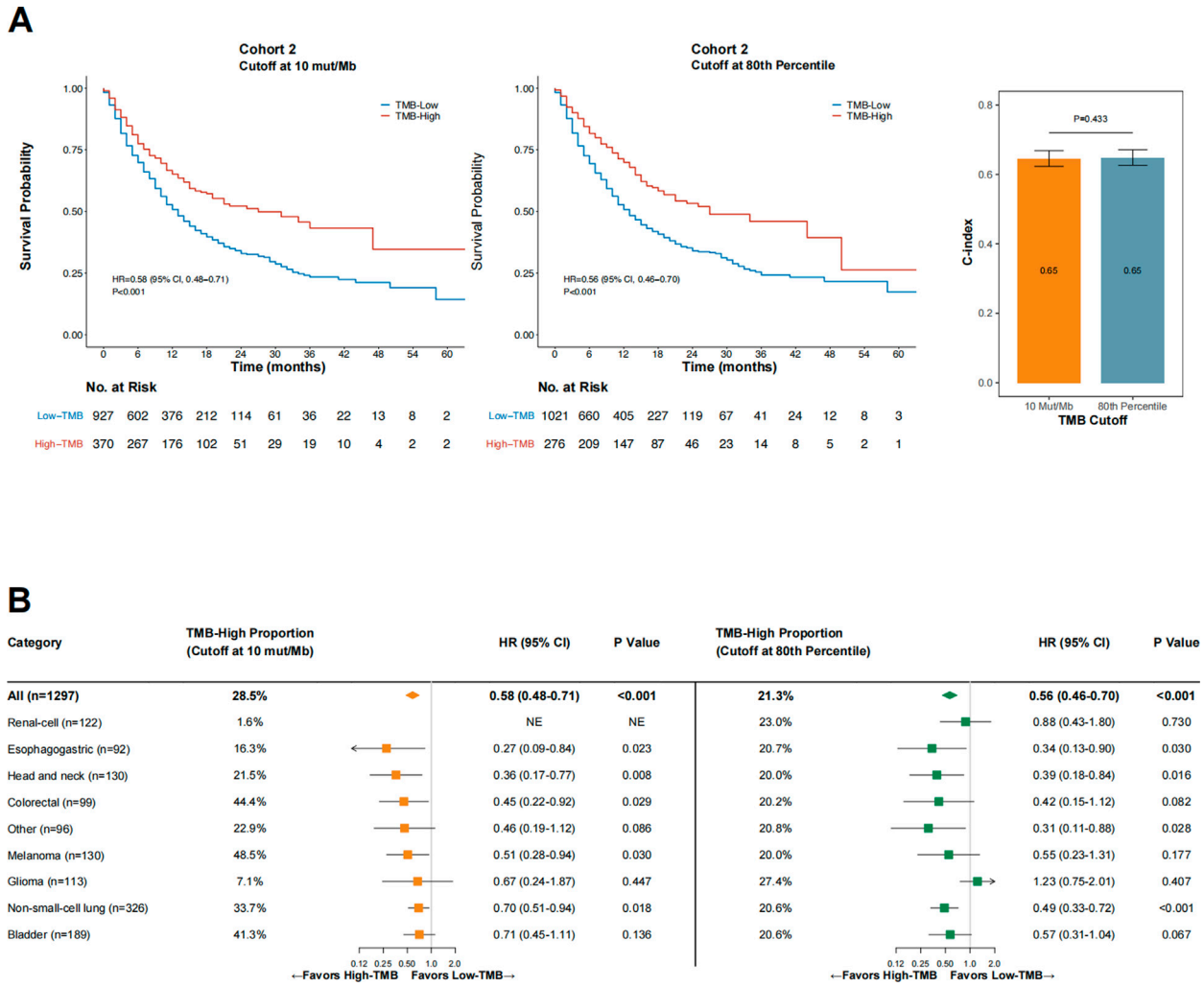


FIGURE 4
The impact of TMB status (high vs. low) on overall survival in Cohort 2 when the cutoff was 10 mut/Mb **(A)**, left panel) or the 80th percentile per cancer type **(A)**, middle panel), and the comparative concordance indices **(A)**, right panel), as well as subgroup analysis findings across cancer types **(B)**. Abbreviations: HR, hazard ratio; CI, confidence interval; C-index, concordance index.

alive at the last follow-up (OS duration, 43 and 26 months, respectively). Similar findings were observed in patients with glioma. For melanoma, using 10 mut/Mb as the cutoff identified a higher percentage of TMB-high cases than using the 80th percentile (48.5% vs. 20.0%, $p < 0.001$); TMB-high was associated with significantly improved OS at the former cutoff but not the latter, although the OS HRs were comparable at both cutoff values.

## The reliability of the identified cutoff in defining TMB-high across panels

Based on WES data from 9,821 samples across 32 solid tumors from the TCGA project, we generated *in silico* gene panels that comprised the genes included in the 468-gene MSK-IMPACT, 324-gene F1CDx, or 507-gene PGDx. The percentage of shared genes with MSK-IMPACT was above 70% for both F1CDx and PGDx (80.0% and 74.1%, respectively). When 10 mut/Mb was used as the universal cutoff in defining TMB-high across these panels, the concordance between F1CDx and MSK-IMPACT and between PGDx and MSK-IMPACT were both excellent (Kappa = 0.808 and 0.803, respectively). The concordance between WES and MSK-IMPACT in defining TMB-high was less prominent (Kappa = 0.767) compared with that between F1CDx and MSK-IMPACT and that between PGDx and MSK-IMPACT. One possible explanation is that frequently mutated genes are enriched in gene panels, and hence the average TMB level for WES was significantly lower than that for MSK-IMPACT (mean difference in TMB: −1.71 mut/Mb [95% CI, 1.63–1.78], paired t-test $p < 0.001$). Based on this finding, we further used a lower universal cutoff of 8 mut/Mb for WES and observed an improved concordance (Kappa = 0.814) between the WES-based TMB-high cases (i.e., TMB≥8 mut/Mb) and MSK-IMPACT-based TMB-high cases (i.e., TMB≥10 mut/Mb).

As shown in Figure 5 and Supplementary Figure S3, the agreement of TMB≥10 mut/Mb cases between MSK-IMPACT

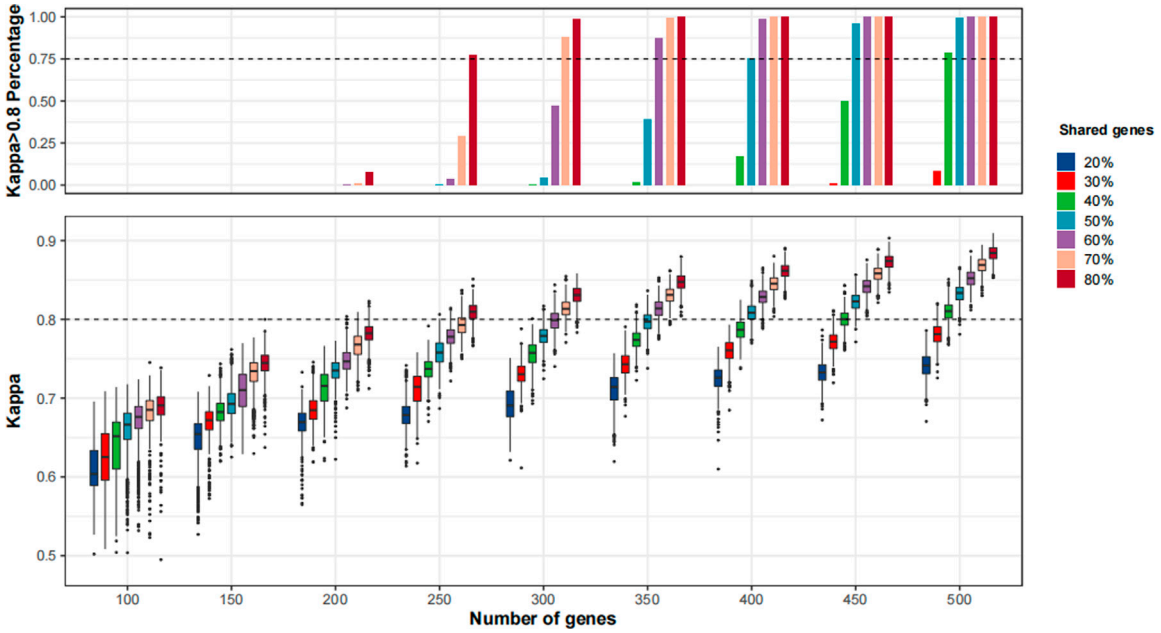


FIGURE 5
The agreement of tumor mutational burden (TMB)≥10 mut/Mb cases between *in silico* panels comprising genes in MSK-IMPACT and *in silico* panels with various sizes and percentages of shared genes with MSK-IMPACT. 1,000 resampling was performed for each given panel size and percentage of genes shared with MSK-IMPACT. The bioinformatics pipeline for MSK-IMPACT was applied to the randomly sampled panels.

and the randomly sampled panels was continuously improved with the increase in panel size and percentages of shared genes with MSK-IMPACT. When we applied the MSK-IMPACT pipeline to calculate TMB for the randomly sampled panels, a Kappa>0.80 was achieved in the vast majority (>75%) of the panels when the panel size was at least 250 with at least 80% of genes shared with MSK-IMPACT (Figure 5). When the F1CDx pipeline was applied, a Kappa>0.80 was achieved among the vast majority of the panels when the panel size was at least 350 with at least 80% of genes shared with MSK-IMPACT (Supplementary Figure S3A); when the PGDx pipeline was applied, a Kappa>0.80 was achieved in the vast majority when the panel size was at least 450 with at least 70% of genes shared with MSK-IMPACT (Supplementary Figure S3B).

## Discussion

In this study, we first identified 10 mut/Mb as the optimal universal cutoff for MSK-IMPACT in defining TMB-high across 25 malignancies, on the basis of cancer type-level correlation analysis. We further verified this cutoff as the optimum when defining TMB-high (via MSK-IMPACT) in predicting OS benefits from anti-PD-(L) 1 therapy in a large cohort of patients with advanced cancers. Moreover, *in silico* analyses of large-scale TCGA WES data revealed excellent agreement of the TMB≥10 mut/Mb cases between MSK-IMPACT and F1CDx, between MSK-IMPACT and PGDx, and between MSK-IMPACT and various randomly sampled panels. As such, our findings firmly support the prespecified TMB cutoff in KEYNOTE-158 (Marabelle et al., 2019; Marabelle et al., 2020) and provide rigorous evidence beyond KEYNOTE-158 for the utility of TMB≥10 mut/Mb as a positive indicator of clinical responses and OS benefits from PD-(L) 1 blockade for a broader range of tumors and panels.

Tumor-specific TMB thresholds for prediction of anti-PD-(L) 1 efficacy have not yet been well established; and it would be challenging and labor-intensive to achieve this goal for each cancer type. As the TMB level varies greatly among cancer types (Chalmers et al., 2017; Zehir et al., 2017), it is intuitive to consider that the cutoff to define TMB-high varies by cancer type as well. Likewise, Samstein et al. applied the 80th percentile per cancer type (ranging between 4.4 mut/Mb and 52.2 mut/Mb) as the cutoff in defining TMB-high, which was shown to be predictive of OS benefits from anti-PD-(L) 1 or anti-CTLA4 therapies among various advanced cancers (Samstein et al., 2019). However, using a fixed percentile as the TMB cutoff is clearly contradictory to the fact that ORR for PD-(L) 1 blockade ranges widely from 0% to above 50% across cancer types (Wang et al., 2023). A universal TMB cutoff could therefore be biologically reasonable as the proportion of TMB-high cases defined by this cutoff would vary by cancer type, thus informing the between-cancer variation in tumor immunogenicity and hence the response to anti-PD-(L) 1 therapy (Goodman et al., 2020). As a representative example in Cohort 2, for melanoma, which is among the tumor types with highest ORRs for PD-(L) 1 blockade, the proportion of TMB-high was substantially higher when the cutoff was 10 mut/Mb rather than the 80th percentile (49% vs. 20%), and TMB-high was associated with significantly improved OS at the former cutoff rather than the latter. For the entire Cohort 2, we also demonstrate that using the optimal universal cutoff of 10 mut/Mb showed comparable predictive capacity with the tissue-specific TMB cutoff (80th percentile), but identified a higher

proportion of TMB-high cases (29% vs. 21%), which may bring survival prolongation to a larger population with the use of anti-PD-(L) 1 therapy. Moreover, when using the universal 10 mut/Mb cutoff across cancer types, the efficacy of anti-PD-(L) 1 therapy did not significantly differ across cancer types with all the HRs less than 1, further supporting that 10 mut/Mb is a broadly practical TMB cutoff.

MSI-H and TMB-high (i.e., TMB≥10 mut/Mb) are currently the two FDA-approved tumor-agnostic indications for pembrolizumab. Although MSI-H is strongly predictive of anti-PD-(L) 1 response and can be readily utilized in clinical practice due to its dichotomized nature, its clinical impact is limited by a rather low prevalence (<5%) among advanced solid tumors (Hause et al., 2016). Additionally, prior evidence suggests that anti-PD-(L) 1 efficacy in patients with MSI-H tumors was largely attributed to high TMB (Schrock et al., 2019). Notably, our study showed a clinically relevant prevalence of TMB-high (TMB≥10 mut/Mb) based on MSI-IMPACT (16% in Cohorts 1% and 29% in Cohort 2), among whom the clinical benefits from PD-(L) 1 blockade were evident. Together with the findings from KEYNOTE-158, these current data indicate that TMB≥10 mut/Mb could effectively complement MSI-H in identifying candidates for anti-PD-(L) 1 therapy, thereby bringing survival benefits to a larger population (Subbiah et al., 2020).

TMB≥10 mut/Mb may also serve the design of future biomarker-guided clinical trials on anti-PD-(L) 1 therapy. Specifically, it will be of great interest to conduct a biomarker-enrichment basket trial to investigate the efficacy of PD-(L) 1 inhibitors in TMB-high (TMB≥10 mut/Mb) cases of cancer types with minimal or no response to these agents. A recent study reported an ORR of 11% in patients with metastatic colorectal cancer (25/27 MSS, 2/27 undetermined) with TMB≥9 mut/Mb via F1CDx (Meiri et al., 2020), suggesting that it could still be feasible to use TMB-high to identify and enrich patients that benefit from PD-(L) 1 inhibitors even in cancer types with generally poor response to these agents. Furthermore, TMB≥10 mut/Mb may be applied as a stratification factor in future randomized studies of anti-PD-(L)1 therapy, which could in turn verify its utility as a predictive marker for such treatment.

The limitations of this study are as follows. Firstly, this universal TMB cutoff of 10 mut/Mb was identified and verified based on data from patients treated with anti-PD-(L) 1 monotherapy; it may not be extrapolated directly to anti-PD-(L) 1-based combinations and regimens involving other immune checkpoint inhibitors, e.g., anti-CTLA-4 antibodies. As shown in CheckMate-227 for advanced non-small-cell lung cancer, dual blockade of PD-1 and CTLA-4 significantly improved OS compared with chemotherapy in both patients with TMB≥10 mut/Mb and those with TMB<10 mut/Mb via F1CDx (Hellmann et al., 2019). Secondly, this study relied on retrospective analysis of publicly available data and published trials; therefore, inherent biases might exist and the TMB cutoff of 10 mut/Mb should be further testified in future prospective trials. Thirdly, our *in silico* panel analysis did not fully account for the various bioinformatics pipelines for TMB estimation in existing panels; hopefully, this issue will be adequately addressed by efforts from the Friends of Cancer Research TMB Harmonization Project, which seeks to establish a uniform approach in measuring TMB across different panels (Merino et al., 2020). Finally, as it was previously reported that a higher tissue TMB was associated with a higher risk of immune-related adverse events (Bomze et al., 2019), further studies are warranted to investigate the TMB cutoff that optimizes the risk-benefit ratio for anti-PD-(L) 1 therapy.

In summary, our study provides compelling evidence for using 10 mut/Mb as the optimal, universal cutoff for TMB-high that guides the clinical application of anti-PD-(L) 1 therapy in patients with advanced solid tumors. Our findings substantially extend the evidence from KEYNOTE-158 to a broader coverage of settings, which could help to mitigate the challenges faced by the immuno-oncology community in embracing the agnostic approval of TMB-high as a companion diagnostic to pembrolizumab, and more importantly, bring survival prolongation to a larger population.

## Data availability statement

The datasets used and analyzed in the study are publicly available. These data can be found in the cBioPortal for Cancer Genomics (http://cbioportal.org/msk-impact), Figure 1 and Supplementary Table S1 of Yarchoan's study (DOI: 10.1056/NEJMc1713444), Supplemental Data S1 of Samstein's study (DOI: 10.1038/s41588-018-0312-8), and the UCSC Xena browser (http://xena.ucsc.edu/).

## Ethics statement

Because the analytic data are publicly available, this study was deemed exempt from the ethical approval process and patient informed consent was waived.

## Author contributions

Y-TC and XL designed this study. S-FM and W-HK collected the data and performed statistical analysis. All authors listed have made a substantial, direct, and intellectual contribution to the work and approved it for publication.

## Funding

This study was supported by the Yangfan Special Project of Shanghai Qimingxing Program (22YF1459200).

## Conflict of interest

The authors declare that the research was conducted in the absence of any commercial or financial relationships that could be construed as a potential conflict of interest.

## Publisher's note

All claims expressed in this article are solely those of the authors and do not necessarily represent those of their

affiliated organizations, or those of the publisher, the editors and the reviewers. Any product that may be evaluated in this article, or claim that may be made by its manufacturer, is not guaranteed or endorsed by the publisher.

## Supplementary material

The Supplementary Material for this article can be found online at: https://www.frontiersin.org/articles/10.3389/fcell.2023.1209243/full#supplementary-material

## References

Bellmunt, J., de Wit, R., Vaughn, D. J., Fradet, Y., Lee, J. L., Fong, L., et al. (2017). Pembrolizumab as second-line therapy for advanced urothelial carcinoma. *N. Engl. J. Med.* 376 (11), 1015–1026. doi:10.1056/NEJMoa1613683

Bersanelli, M. (2020). Tumour mutational burden as a driver for treatment choice in resistant tumours (and beyond). *Lancet Oncol.* 21, 1255–1257. doi:10.1016/S1470-2045(20)30433-2

Bomze, D., Hasan Ali, O., Bate, A., and Flatz, L. (2019). Association between immune-related adverse events during anti-PD-1 therapy and tumor mutational burden. *JAMA Oncol.* 5 (11), 1633–1635. doi:10.1001/jamaoncol.2019.3221

Chalmers, Z. R., Connelly, C. F., Fabrizio, D., Gay, L., Ali, S. M., Ennis, R., et al. (2017). Analysis of 100,000 human cancer genomes reveals the landscape of tumor mutational burden. *Genome Med.* 9 (1), 34. doi:10.1186/s13073-017-0424-2

Chan, T. A., Yarchoan, M., Jaffee, E., Swanton, C., Quezada, S. A., Stenzinger, A., et al. (2019). Development of tumor mutation burden as an immunotherapy biomarker: Utility for the oncology clinic. *Ann. Oncol.* 30 (1), 44–56. doi:10.1093/annonc/mdy495

Chung, H. C., Schellens, J. H. M., Delord, J.-P., Perets, R., Italiano, A., Shapira-Frommer, R., et al. (2018). Pembrolizumab treatment of advanced cervical cancer: Updated results from the phase 2 KEYNOTE-158 study. *J. Clin. Oncol.* 36 (15), 5522. doi:10.1200/jco.2018.36.15_suppl.5522

Diaz, L., Marabelle, A., Kim, T. W., Geva, R., Van Cutsem, E., André, T., et al. (2017). Efficacy of pembrolizumab in phase 2 KEYNOTE-164 and KEYNOTE-158 studies of microsatellite instability high cancers. *Ann. Oncol.* 28, v128–v129. doi:10.1093/annonc/mdx367.020

FDA approves (2020). FDA approves pembrolizumab for adults and children with TMB-H solid tumors. Available at https://www.fda.gov/drugs/drug-approvals-and-databases/fda-approves-pembrolizumab-adults-and-children-tmb-h-solid-tumors; (Accessed July 25, 2020).

Fuchs, C. S., Doi, T., Jang, R. W., Muro, K., Satoh, T., Machado, M., et al. (2018). Safety and efficacy of pembrolizumab monotherapy in patients with previously treated advanced gastric and gastroesophageal junction cancer: Phase 2 clinical KEYNOTE-059 trial. *JAMA Oncol.* 4 (5), e180013. doi:10.1001/jamaoncol.2018.0013

Goodman, A. M., Castro, A., Pyke, R. M., Okamura, R., Kato, S., Riviere, P., et al. (2020). MHC-I genotype and tumor mutational burden predict response to immunotherapy. *Genome Med.* 12 (1), 45. doi:10.1186/s13073-020-00743-4

Hause, R. J., Pritchard, C. C., Shendure, J., and Salipante, S. J. (2016). Classification and characterization of microsatellite instability across 18 cancer types. *Nat. Med.* 22 (11), 1342–1350. doi:10.1038/nm.4191

Hegde, P. S., and Chen, D. S. (2020). Top 10 challenges in cancer immunotherapy. *Immunity* 52 (1), 17–35. doi:10.1016/j.immuni.2019.12.011

Hellmann, M. D., Paz-Ares, L., Bernabe Caro, R., Zurawski, B., Kim, S. W., Carcereny Costa, E., et al. (2019). Nivolumab plus ipilimumab in advanced non-small-cell lung cancer. *N. Engl. J. Med.* 381 (21), 2020–2031. doi:10.1056/NEJMoa1910231

Herbst, R. S., Baas, P., Kim, D. W., Felip, E., Pérez-Gracia, J. L., Han, J. Y., et al. (2016). Pembrolizumab versus docetaxel for previously treated, PD-L1-positive, advanced non-small-cell lung cancer (KEYNOTE-010): A randomised controlled trial. *Lancet* 387 (10027), 1540–1550. doi:10.1016/S0140-6736(15)01281-7

Le, D. T., Uram, J. N., Wang, H., Bartlett, B. R., Kemberling, H., Eyring, A. D., et al. (2015). PD-1 blockade in tumors with mismatch-repair deficiency. *N. Engl. J. Med.* 372 (26), 2509–2520. doi:10.1056/NEJMoa1500596

Marabelle, A., Fakih, M., Lopez, J., Shah, M., Shapira-Frommer, R., Nakagawa, K., et al. (2020). Association of tumour mutational burden with outcomes in patients with advanced solid tumours treated with pembrolizumab: Prospective biomarker analysis of the multicohort, open-label, phase 2 KEYNOTE-158 study. *Lancet Oncol.* 21, 1353–1365. doi:10.1016/S1470-2045(20)30445-9

Marabelle, A., Fakih, M. G., Lopez, J., Shah, M., Shapira-Frommer, R., Nakagawa, K., et al. (2019). Association of tumour mutational burden with outcomes in patients with select advanced solid tumours treated with pembrolizumab in KEYNOTE-158. *Ann. Oncol.* 30, v477–v478. doi:10.1093/annonc/mdz253.018

McHugh, M. L. (2012). Interrater reliability: The kappa statistic. *Biochem. Med. Zagreb.* 22 (3), 276–282. doi:10.11613/bm.2012.031

Meiri, E., Garrett-Mayer, E., Halabi, S., Mangat, P. K., Shrestha, S., Ahn, E. R., et al. (2020). Pembrolizumab (P) in patients (pts) with colorectal cancer (CRC) with high tumor mutational burden (HTMB): Results from the targeted agent and profiling utilization registry (TAPUR) study. *J. Clin. Oncol.* 38 (4), 133. doi:10.1200/jco.2020.38.4_suppl.133

Merino, D. M., McShane, L. M., Fabrizio, D., Funari, V., Chen, S. J., White, J. R., et al. (2020). Establishing guidelines to harmonize tumor mutational burden (TMB): In silico assessment of variation in TMB quantification across diagnostic platforms: phase I of the Friends of cancer research TMB harmonization project. *J. Immunother. Cancer* 8 (1), e000147. doi:10.1136/jitc-2019-000147

Muro, K., Chung, H. C., Shankaran, V., Geva, R., Catenacci, D., Gupta, S., et al. (2016). Pembrolizumab for patients with PD-L1-positive advanced gastric cancer (KEYNOTE-012): A multicentre, open-label, phase 1b trial. *Lancet Oncol.* 17 (6), 717–726. doi:10.1016/S1470-2045(16)00175-3

Overman, M. J., McDermott, R., Leach, J. L., Lonardi, S., Lenz, H. J., Morse, M. A., et al. (2017). Nivolumab in patients with metastatic DNA mismatch repair-deficient or microsatellite instability-high colorectal cancer (CheckMate 142): An open-label, multicentre, phase 2 study. *Lancet Oncol.* 18 (9), 1182–1191. doi:10.1016/S1470-2045(17)30422-9

Pencina, M. J., and D'Agostino, R. B. (2004). Overall C as a measure of discrimination in survival analysis: Model specific population value and confidence interval estimation. *Stat. Med.* 23 (13), 2109–2123. doi:10.1002/sim.1802

Prasad, V., and Addeo, A. (2020). The FDA approval of pembrolizumab for patients with TMB >10 mut/mb: Was it a wise decision? No. *Ann. Oncol.* 31, 1112–1114. doi:10.1016/j.annonc.2020.07.001

Reck, M., Rodríguez-Abreu, D., Robinson, A. G., Hui, R., Csőszi, T., Fülöp, A., et al. (2016). Pembrolizumab versus chemotherapy for PD-L1-positive non-small-cell lung cancer. *N. Engl. J. Med.* 375 (19), 1823–1833. doi:10.1056/NEJMoa1606774

Rizvi, N. A., Hellmann, M. D., Snyder, A., Kvistborg, P., Makarov, V., Havel, J. J., et al. (2015). Cancer immunology. Mutational landscape determines sensitivity to PD-1 blockade in non-small cell lung cancer. *Science* 348 (6230), 124–128. doi:10.1126/science.aaa1348

Samstein, R. M., Lee, C. H., Shoushtari, A. N., Hellmann, M. D., Shen, R., Janjigian, Y. Y., et al. (2019). Tumor mutational load predicts survival after immunotherapy across multiple cancer types. *Nat. Genet.* 51 (2), 202–206. doi:10.1038/s41588-018-0312-8

Schrock, A. B., Ouyang, C., Sandhu, J., Sokol, E., Jin, D., Ross, J. S., et al. (2019). Tumor mutational burden is predictive of response to immune checkpoint inhibitors in MSI-high metastatic colorectal cancer. *Ann. Oncol.* 30 (7), 1096–1103. doi:10.1093/annonc/mdz134

Sharma, P., Goswami, S., Raychaudhuri, D., Siddiqui, B. A., Singh, P., Nagarajan, A., et al. (2023). Immune checkpoint therapy-current perspectives and future directions. *Cell* 186 (8), 1652–1669. doi:10.1016/j.cell.2023.03.006

Singal, G., Miller, P. G., Agarwala, V., Kaushik, G., Backenroth, D., et al. (2019). Association of patient characteristics and tumor genomics with clinical outcomes among patients with non-small cell lung cancer using a clinicogenomic database. *JAMA* 321 (14), 1391–1399. doi:10.1001/jama.2019.3241

Subbiah, V., Solit, D. B., Chan, T. A., and Kurzrock, R. (2020). The FDA approval of pembrolizumab for adult and pediatric patients with tumor mutational burden (TMB) ≥10: A decision centered on empowering patients and their physicians. *Ann. Oncol.* 31, 1115–1118. doi:10.1016/j.annonc.2020.07.002

Wang, Y., Wang, M., Wu, H. X., Qi, X., Fan, Y. Q., He, J. S., et al. (2021). Predicted 10-year cardiovascular disease risk and its association with sleep duration among adults in beijing-tianjin-hebei region, China. *Cancer Commun. (Lond)* 41 (9), 803–813. doi:10.3967/bes2021.109

Wang, Z. X., Pan, Y. Q., Li, X., Tsubata, T., and Xu, R. H., Immunotherapy in gastrointestinal cancers: Advances, challenges, and countermeasures. *Sci. Bull.* 2023; 763–766. doi:10.1016/j.scib.2023.03.036

Wang, Z. X., and Xu, R. H. (2023). Chemo-immunotherapy in advanced esophageal squamous cell carcinoma: Present and future. *Holist. Integ Oncol.* 2, 5. doi:10.1007/s44178-023-00028-x

Wood, D. E., White, J. R., Georgiadis, A., Van Emburgh, B., Parpart-Li, S., Mitchell, J., et al. (2018). A machine learning approach for somatic mutation discovery. *Sci. Transl. Med.* 10 (457), eaar7939. doi:10.1126/scitranslmed.aar7939

Wu, H. X., Wang, Z. X., Zhao, Q., Wang, F., and Xu, R. H. (2019). Designing gene panels for tumor mutational burden estimation: The need to shift from 'correlation' to 'accuracy. *J. Immunother. Cancer* 7 (1), 206. doi:10.1186/s40425-019-0681-2

Zehir, A., Benayed, R., Shah, R. H., Syed, A., Middha, S., Kim, H. R., et al. (2017). Mutational landscape of metastatic cancer revealed from prospective clinical sequencing of 10,000 patients. *Nat. Med.* 23 (6), 703–713. doi:10.1038/nm.4333

Zeileis, A., Shah, A., and Patnaik, I. (2010). Testing, monitoring, and dating structural changes in exchange rate regimes. *Comput. Statistics Data Analysis* 54 (6), 1696–1706. doi:10.1016/j.csda.2009.12.005

frontiers | Frontiers in Cell and Developmental Biology

TYPE Original Research
PUBLISHED 12 June 2023
DOI 10.3389/fcell.2023.1208485



OPEN ACCESS

EDITED BY
Xiangsheng Zuo,
University of Texas MD Anderson Cancer Center, United States

REVIEWED BY
Shamir Cassim,
Addmedica, France
Daoyan Wei,
University of Texas MD Anderson Cancer Center, United States

*CORRESPONDENCE
Flavia Biamonte,
flavia.biamonte@unicz.it

†These authors have contributed equally to this work and share first authorship

RECEIVED 19 April 2023
ACCEPTED 31 May 2023
PUBLISHED 12 June 2023

CITATION
Battaglia AM, Sacco A, Aversa I, Santamaria G, Palmieri C, Botta C, De Stefano R, Bitetto M, Petriaggi L, Giorgio E, Faniello CM, Costanzo F and Biamonte F (2023), Iron-mediated oxidative stress induces PD-L1 expression via activation of c-Myc in lung adenocarcinoma.
*Front. Cell Dev. Biol.* 11:1208485.
doi: 10.3389/fcell.2023.1208485



# Iron-mediated oxidative stress induces PD-L1 expression via activation of c-Myc in lung adenocarcinoma

Anna Martina Battaglia[1†], Alessandro Sacco[1†], Ilenia Aversa[2], Gianluca Santamaria[3], Camillo Palmieri[2], Cirino Botta[4], Roberto De Stefano[5], Maurizio Bitetto[6], Lavinia Petriaggi[1], Emanuele Giorgio[1], Concetta Maria Faniello[1], Francesco Costanzo[1,7] and Flavia Biamonte[1,7]*

[1]Laboratory of Biochemistry and Cellular Biology, Department of Experimental and Clinical Medicine, Magna Graecia University of Catanzaro, Catanzaro, Italy, [2]Laboratory of Immunology, Department of Experimental and Clinical Medicine, Magna Graecia University of Catanzaro, Catanzaro, Italy, [3]Laboratory of Molecular Oncology, Department of Experimental and Clinical Medicine, Magna Graecia University of Catanzaro, Catanzaro, Italy, [4]Department of Health Promotion, Mother, and Child Care, Internal Medicine and Medical Specialties, University of Palermo, Palermo, Italy, [5]Operational Unit of Anatomic Pathology, Annunziata Hospital, Cosenza, Italy, [6]Operational Unit of Thoracic Surgery, Annunziata Hospital, Cosenza, Italy, [7]Department of Experimental and Clinical Medicine, Center of Interdepartmental Services (CIS), Magna Graecia University of Catanzaro, Catanzaro, Italy

**Introduction:** The PD-1/PD-L1 axis is hijacked by lung adenocarcinoma (LUAD) cells to escape immune surveillance. PD-L1 expression in LUAD is affected, among others, by the metabolic trafficking between tumor cells and the tumor microenvironment (TME).

**Methods:** Correlation between PD-L1 expression and iron content within the TME was established on FFPE LUAD tissue samples. The effects of an iron rich microenvironment on PD-L1 mRNA and protein levels were assessed *in vitro* in H460 and A549 LUAD by using qPCR, western blot and flow citometry. c-Myc knockdown was performed to validate the role of this transcription factor on PD-L1 expression. The effects of iron-induced PD-L1 on T cell immune function was assessed by quantifying IFN-γ release in a co-colture system. TCGA dataset was used to analyse the correlation between PD-L1 and CD71 mRNA expression in LUAD patients.

**Results:** In this study, we highlight a significant correlation between iron density within the TME and PD-L1 expression in 16 LUAD tissue specimens. In agreement, we show that a more pronounced innate iron-addicted phenotype, indicated by a higher transferrin receptor CD71 levels, significantly correlates with higher PD-L1 mRNA expression levels in LUAD dataset obtained from TCGA database. *In vitro*, we demonstrate that the addition of $Fe^{3+}$ within the culture media promotes the significant overexpression of PD-L1 in A549 and H460 LUAD cells, through the modulation of its gene transcription mediated by c-Myc. The effects of iron lean on its redox activity since PD-L1 up-regulation is counteracted by treatment with the antioxidant compound trolox. When LUAD cells are co-cultured with CD3/CD28-stimulated T cells in an iron-rich culture condition, PD-L1 up-regulation causes the inhibition of T-lymphocytes activity, as demonstrated by the significant reduction of IFN-γ release.

**Discussion:** Overall, in this study we demonstrate that iron abundance within the TME may enhance PD-L1 expression in LUAD and, thus, open the way for the identification of possible combinatorial strategies that take into account the iron levels within the TME to improve the outcomes of LUAD patients treated with anti-PD-1/PD-L1-based therapies.

KEYWORDS

**iron, PD-L1, TME, lung adenocarcinoma, oxidative stress, c-Myc**

## 1 Introduction

In the tumor microenvironment (TME), the programmed cell death protein 1 (PD-1) and its ligand (PD-L1) axis is hijacked by cancer cells to escape immune surveillance. Indeed, PD-L1 on cancer cells binds to tumor-infiltrating lymphocytes (TILs) and impairs their activation, through the inhibition of their proliferation, survival, and effector functions (Zitvogel and Kroemer, 2012; Yi et al., 2021). Blocking PD-1/PD-L1 signaling has shown remarkable effectiveness in restoring T cells from an exhausted status, and normalizing the dysregulated TME, ultimately leading to cancer cell eradication (Cha et al., 2019). So far, the use of antibodies against the PD-1/PD-L1 axis has shown potent antitumor activities in several cancer types, including lung adenocarcinoma (LUAD), gastric cancer, melanoma, and liver cancer (Sui et al., 2015; Han et al., 2020). Determination of PD-L1 expression is one of the main parameters used to select patients who might benefit from this therapeutic approach and the PD-L1 positivity, resulting from an immune response-mediated PD-L1 expression, is often associated with a good response to anti-PD-1/PD-L1-based therapies. PD-L1 negative tumors, instead, are generally unresponsive to anti-PD-1/PD-L1-based treatments and only the combination with therapies promoting T-cell infiltration might be useful to improve the responsiveness to this therapeutic approach (Ribas and Hu-Lieskovan, 2016).

The understanding of the biological mechanisms underlying PD-L1 regulation is still a very hot topic in cancer biology and new insights are ever-growing. PD-L1 can be modulated by both intrinsic (i.e., cancer cell-associated) and extrinsic (i.e., originating from the TME) factors (Wu et al., 2019; Hudson et al., 2020). The intrinsic factors include dysregulation of oncogenic signaling pathways (i.e., JAK/STAT, ERK/RAS, PI3K/AKT/mTOR) which leads to the abnormal activation of specific transcription factors such as c-Myc, HIF-1α, STAT3, NF-κB, and Nrf2 (Zerdes et al., 2018). Alternatively, the expression of PD-L1 may depend on inflammatory signals, cytokines, and metabolites (i.e., IFN-α, TNF-α, IL-6) arising from the tumor cells themselves or from the TILs, the antigen-presenting cells (APC), and the tumor-associated macrophages (TAMs) (Zhang et al., 2017). To make it more puzzling, intrinsic, and extrinsic factors may regulate PD-L1 expression in multiple ways including genomic alterations, epigenetic modification, transcriptional regulation, post-transcriptional modification, and post-translational modification (Ju et al., 2020).

TME is a complex and continuously evolving entity (Anderson and Simon, 2020). Its features vary between tumor types as a consequence of a complex interplay between tumor cells, non-tumor cells and non-cellular components such as nutrients and extracellular matrix proteins. Recent evidence highlights that tumor and non-tumor cell populations within the TME dynamically communicate with each other through metabolic connections, causing a reciprocal metabolic interplay. Such metabolic symbiosis not only reprograms both anabolic and catabolic processes in the recipient subpopulations but also rewrites cancer mass evolution (Comito et al., 2020). As such, TME is now considered of a complex ecosystem that supports tumor growth, progression, and metastatic dissemination and therefore a promising target for therapy (Pitt et al., 2016; Xiao and Yu, 2021).

Iron is a multifunctional micronutrient involved in different signaling pathways within tumor cells as well as between tumor cells and the surrounding TME (Sacco et al., 2021). Iron can favor cancer progression by acting as a cofactor for enzymes involved in ATP production, DNA replication, and repair (Brown et al., 2020). For these reasons, tumor cells tend to exhibit an "iron-addicted" phenotype. To satisfy the pronounced iron demand, cancer cells adopt two different strategies. The first one is the reprogramming of the intracellular iron metabolism, through the overexpression of proteins involved in iron uptake (i.e., transferrin receptor, CD71) and storage (i.e., ferritin heavy subunit, FtH) and the parallel downregulation of proteins involved in iron export (i.e., ferroportin, FPN) (Zolea et al., 2016; 2017; Pfeifhofer-Obermair et al., 2018; Chirillo et al., 2020). The other one is the diversion of tumor-infiltrating immune cells, in particular tumor-associated macrophages (TAMs) and neutrophils residing in the TME, which can either serve as sources of iron and iron-related proteins or release factors that activate signaling pathways involved in the control of iron metabolism in cancer cells (Sacco et al., 2021). In parallel, functional, metabolic, and immunological features of the TME rely on major shifts in iron metabolism. Indeed, M2-polarized TAMs, showing an "iron-releasing" phenotype, appear to sustain cancer growth through the capacity to repress anti-tumor immune functions. (Cassim and Pouyssegur, 2019). From their side, cancer cells with a pronounced iron demand may deprive the TME of iron, thus producing and releasing ROS, which in turn may suppress the antitumor activities of immune cells (Ying et al., 2021).

The iron addiction phenotype is, however, a double-edged sword as the accumulation of the labile and redox-active iron pool (LIP) within the cytoplasm may lead to the generation of reactive oxygen species (ROS), which in turn cause oxidative damage and eventually ferroptosis (Battaglia et al., 2020; 2022). In this regard, it has been recently reported that "iron-retaining" M1 TAMs, showing a pro-inflammatory M1-like phenotype, induce tumor cell death and through the generation of ROS and pro-inflammatory cytokines (TNFα and IL-6) (Sacco et al., 2021). Costa da Silva M et al. have demonstrated that, when exposed to distinct iron sources such as hemolytic red blood cells, TAMs

polarize towards the M1 pro-inflammatory phenotype and exert a marked anti-tumor activity in LUAD. Notably, this effect is also elicited by the intra-tumoral injection of iron oxide nanoparticles, which significantly reduce tumor size *in vivo* (da Silva et al., 2017). In hyper-inflamed tumors, the TME is over-enriched in iron, which, in turn, promotes T cell dysfunction in a ferroptosis-dependent manner (DeRosa and Leftin, 2021; Sacco et al., 2021). Data supporting the possible implication of iron and/or ROS within the TME in the regulation of immune checkpoints in cancer are still very poor. In breast cancer, treatment with ROS inducers (i.e., paclitaxel or buthionine sulphoximine) promotes the transcription of PD-L1 via NF-κB in TAMs, which in turn acquire an immunosuppressive phenotype and improve the efficacy of anti-PD-L1 antibody-based immunotherapy (Roux et al., 2019). A very recent study conducted on C57Bl/6N female mice with implanted E0771 mammary carcinoma cells, highlights that *in vivo* iron supplementation increases the availability of this metal in the TME and that this is accompanied by suppression of T cells activation as well as by the reduction of anti-PD-L1-based therapy efficacy (Tymoszuk et al., 2020). Recently, Choi EJ et al. demonstrated that ferric ammonium citrate (FAC) induces PD-L1 in bone marrow-derived macrophages (BMDMs macrophages) and that this is mediated by its redox activity (Choi et al., 2022).

In this study, we show for the first time that a high iron density within the TME is associated with high PD-L1 expression levels in LUAD tissue specimens. Furthermore, we demonstrate that *in vitro* supplementation of iron within culture media induces PD-L1 overexpression through the generation of ROS which, in turn, activates the PD-L1 transcription factor c-Myc. The iron-mediated PD-L1 overexpression in LUAD cells inhibits T-cell activation in co-culture conditions.

# 2 Materials and methods

## 2.1 Patients and tissue samples

Sixteen archived LUAD samples (formalin-fixed, paraffin-embedded (FFPE) blocks) were kindly provided by the Annunziata Hospital (Cosenza, Italy). Samples were collected during the surgical tumor resection between 9 January 2020, and 10 November 2020. Informed consent was obtained from all subjects. The main clinical information associated with each sample were not correlated with any clinical studies or immune checkpoint inhibitor therapy.

## 2.2 PD-L1 immunohistochemical staining

The immunohistochemical (IHC) staining for PD-L1 was performed by using the FDA-approved Dako Agilent PD-L1 IHC 22C3 pharmDx kit on the Dako Autostainer Link 48 platform. PD-L1 positive control material for protocol establishment included FFPE specimens from normal tonsil. The analysis was limited to cell blocks with >100 tumor cell. The analysis of stained tissue samples was performed by 2 expert pathologists involved in the routine evaluation of clinical samples for diagnostic purposes. The estimation of PD-L1 expression below or beyond the 2 cut-off points (1% or 50%) were done according to current clinical practice for the determination of patients eligible for anti-PD-1 treatments. According to the Tumor Proportion Score (TPS) patients were classified as low TPS (1%–49%) and high (TPS ≥50%) expressors, respectively (De Marchi et al., 2021).

## 2.3 Perls Van-Gieson iron staining

To determine the iron content in both intra-tumoral and peritumoral TAMs, each tumor sample was stained by using Perls Van-Gieson Kit (Bio-Optica). Briefly, paraffin-embedded tissue samples were rehydrated, stained with Perls solution for 20 min and then rinsed in distilled water. Sections were then counterstained with Van-Gieson solution for 10 min and, rinsed in water. Finally, sections were dehydrated in 70%, 95%, 100% ethanol and embedded using xylene-based mounting media. Producer guidelines have been used to quantify the positivity or negativity to Perls staining. Patients were defined as iron positive or negative according to the positivity (despite of the threshold) or negativity to Perls staining.

## 2.4 Cell lines and cell culture

LUAD cell lines A549 and H460 were purchased from the American Type Culture Collection (ATCC, Rockville, MD, United States) and grown in RPMI-1640 (Sigma-Aldrich, St. Louis, MO, United States) supplemented with (v/v) fetal bovine serum (FBS) (Invitrogen, San Diego, CA), 100 U/mL of penicillin, and 0.1 mg/mL of streptomycin (Sigma-Aldrich, St. Louis, MO, United States). Cells were maintained in a 5% $CO_2$ humidified atmosphere at 37°C and periodically tested for the presence of *mycoplasma*. For each experiment, cells were seeded to obtain 70%–80% confluence.

## 2.5 Reagents

Ferlixit (62.5 mg/5 mL, SANOFI) was obtained from the outpatient pharmacy at Unit of Cardiology, Magna Graecia University, Germaneto, while the antioxidant (±)-6-hydroxy- 2,5,7,8-tetra-methylchromane-2-carboxylic acid (trolox) was ordered from Cayman Chemical (Cayman Chemical Company, Ann Arbor, United States). Cells were seeded in a 6-well plate in serum-free medium. Ferlixit was added into the medium at the final concentration of 250 μM for 24 h while trolox was used at 200 μM for 6 h.

## 2.6 Western blot

To obtain total protein extracts, protein extraction was performed using RIPA buffer as previously described (Biamonte et al., 2015; Zolea et al., 2015; 2016; Di Sanzo et al., 2022), supplemented with cOmplete™ Protease Inhibitor Cocktail provided in EASYpacks (Roche Diagnostics, Mannheim, Germany). Otherwise, nuclear, and cytoplasmic protein extracts were obtained as previously described (Chirillo et al., 2020; Scaramuzzino et al., 2021). Equal amounts of protein (50 μg) from each sample were separated by 8%–12% SDS-PAGE. The migration was

performed at 200 V for 1 h and 30'. Then, proteins were transferred to nitrocellulose membranes (Sigma-Aldrich, St. Louis, MO, United States) at 50 V for 2 h. The membranes were blocked in 5% milk or 5% BSA for 1 h at room temperature and incubated overnight at 4°C with primary antibodies against PD-L1 (1:1,000, PA5-28115, ThermoFisher Scientific), c-Myc (1:500, sc-42, Santa Cruz Biotechnology), Nrf2 (1:200, sc-365949, Santa Cruz Biotechnology), NF-κB (1:500, sc-8008, Santa Cruz Biotechnology), HIF-1α (1:500, sc-10790, Santa Cruz Biotechnology) p-STAT3 (1:500, 4,113s, Cell Signaling Technology), STAT3 (1:500, 9,139s, Cell Signaling Technology), p-mTOR (1:500, 5,536s, Cell Signaling Technology), mTOR (1:500, 2,972s, Cell Signaling Technology), p-ERK (1:500, 9,106s, Cell Signaling Technology), ERK (1:500, 9,107s, Cell Signaling Technology), c-JUN (1:500, sc-1694, Santa Cruz Biotechnology), p70 S6 Kinase (S6, 1:500, 2,708, Cell Signaling Technology) and Phospho-p70 S6 Kinase (p-S6, 1:500, 9,206, Cell Signaling Technology). The membranes were washed for 30 min and then incubated for 1 h at room temperature with peroxidase-conjugated secondary antibodies (Peroxidase AffiniPure Sheep Anti-Mouse IgG, 1:10,000; Peroxidase AffiniPure Donkey Anti-Rabbit IgG, 1:10,000; Peroxidase AffiniPure Donkey Anti-Goat IgG, 1:10,000; Jackson ImmunoResearch Europe Ltd). Signals were detected using chemiluminescence reagents (ECL Western blotting detection system, Santa Cruz Biotechnology, Dallas, Texas) and acquired by Uvitec Alliance Mini HD9 (Uvitec Cambridge, United Kingdom). To calculate the relative expression of specific protein, a goat polyclonal anti-γ-Tubulin antibody (γ-TUB, 1:3,000; sc-17787; Santa Cruz Biotechnology) serves as a reference for citosolic sample loading, while Lamin A (LAMIN, 1:2000, sc-20680, Santa Cruz Biotechnology) was used as loading control for nuclear samples. The protein band intensity on western blots was quantified and normalized to that of γ-TUB or LAMIN by using ImageJ software (http://rsb.info.nih.gov/ij/).

## 2.7 Measurement of the labile iron pool (LIP)

Intracellular labile iron concentration was determined by flow cytometry using the fluorescent iron sensor calcein acetoxymethyl ester (CA-AM). Briefly, cells were incubated with 0.25 μM CA-AM (Aldrich, Missouri, United States) for 30 min at 37°C in the dark. Then, cells were washed twice with PBS (1X) to remove the excess of CA-AM, and thus treated with 200 μM L1 (3-Hydroxy-1,2-dimethyl-4(1H)-pyridone, Sigma-Aldrich, Missouri, United States) or left untreated. The analysis was performed by FACS BD LSRFortessaTM X-20 cytofluorometer (BD Biosciences). The difference in cellular fluorescence after and before incubation with L1 reflected the labile iron pool:

$$\Delta Mean\ Fluorescence\ Intensity, \Delta MFI = \Delta MFI^{after} - \Delta MFI^{before}$$

## 2.8 Mitochondrial ROS analysis

Generation of mitochondrial ROS was measured by flow cytometry with the use of MitoSOX Red Mitochondrial Superoxide Indicator (Thermo Fisher Scientific Inc.). After treatments, cells were incubated with 5 μM MitoSOX Red for 10 min at 37°C, washed in PBS (1X), and then analyzed by flow cytometry using a FACS BD LSRFortessaTM X-20 cytofluorometer (BD Biosciences). A minimum of 20.000 cells was analyzed per condition. Fluorescence was measured using FlowJo software program (Tree Star, Inc.). Each experiment was performed in triplicate.

## 2.9 Flow cytometry analysis of cell surface PD-L1

For the flow cytometry analysis of surface PD-L1, cells were incubated with PD-L1 antibody (anti-human CD274, APC, BioLegend, San Diego, California, United States) for 30 min in the dark. After washing twice with PBS (1X), cells were acquired in a FACS BD LSRFortessaTM X-20 cytofluorometer (BD Biosciences). Data were analyzed using FlowJo software (Tree Star, Inc.). Three independent experiments were conducted.

## 2.10 Apoptosis analysis

For identifying cells actively undergoing apoptosis, a double staining with Annexin V and PI was performed using Alexa Fluor®488 Annexin V/Dead Cell Apoptosis Kit (Thermo Fisher Scientific, Waltham, Massachusetts, United States) as previously described (Scicchitano et al., 2023). After staining, cells were incubated at room temperature for 15 min in the dark. Each tube was diluted with 400 μL of Annexin Binding Buffer and then cells were analyzed by flow cytometry using the FACS BD LSRFortessaTM X-20 cytofluorometer (BD Biosciences). Data were analyzed using FlowJo software (Tree Star, Inc.). Three independent experiments were conducted.

## 2.11 Real-time quantitative reverse transcription (qRT)-PCR

Total RNA was extracted using the Trizol method (Life Technologies, Carlsbad, CA, United States) as previously described (Biamonte et al., 2017; De Vitis et al., 2023). Then, 1 μg of total RNA were retrotranscribed using High-Capacity cDNA Reverse Transcription Kit (Thermo Fisher Scientific, Waltham, Massachusetts, United States). qRT-PCR was performed using the SYBR Green qPCR Master Mix (Thermo Fisher Scientific, Waltham, Massachusetts, United States) (Guglielmelli et al., 2010; Biamonte et al., 2021). Analysis was performed on QuantStudio 3 Applied Biosystems by Thermo Fisher Scientific. The relative mRNA expression level was calculated by the $2^{-\Delta\Delta CT}$ method and glyceraldehyde 3-phosphate dehydrogenase (GAPDH) and actin beta (ACTB) were used as the housekeeping genes (Di Sanzo et al., 2016; 2018).

## 2.12 c-Myc transient knock-down

A549 and H460 cells were transfected using Lipofectamine 3,000 transfection reagent (Thermo Fisher Scientific, Waltham, Massachusetts, United States) according to the manufacturers'

protocol. c-Myc transient knockdown was performed by using a specific c-Myc siRNA (s912, Thermo Fisher Scientific, Waltham, Massachusetts, United States). To ensure an optimal control, the two cell lines were further transfected with Silencer™ Select Negative Control siRNA (Thermo Fisher Scientific, Waltham, Massachusetts, United States). The transfection efficiency was evaluated by Western blot at 48 h.

## 2.13 IFN-γ ELISpot assay

Human Peripheral blood mononuclear cells (PBMCs) were isolated from sodium heparin anticoagulated whole blood drawn from healthy donors. PBMCs isolation was performed through a density gradient centrifugation method using Ficoll Histopaque (Sigma-Aldrich, St. Louis, MO, United States). Then, PBMCs were cultured in RPMI 1640 medium and stimulated with Dynabeads Human T-Activator CD3/CD28 (11131D, Thermo Fisher Scientific) for 1 h at 37°C. Stimulated and not-stimulated PBMCs were co-colture for 3 h with H460 and A549 cells, previously treated with 250 μM ferlixit (24 h). T cell responses were assessed by ELISPOT assay using the Human IFN-ɣ ELISpot Kit (856.051.005S, Diaclone) according to the manufacturer's protocol. Briefly, the assay plate was re-hydrated by washing with 1X PBS and blocked with capture antibody overnight at 37°C. The day after, culture medium collected from the above-mentioned co-cultures was added to each well and incubated for 2 h at room temperature followed by 1 h-incubation after adding both the detection antibody and the streptavidin conjugated with alkaline phosphatase. Finally, BCIP/NBT substrate solution was added, kept for 15–25 min until a color change was noted. Plate development was stopped with a water wash and the plate was air-dried at room temperature, avoiding exposure to light. Spots were enumerated using an automated spot counter (BIOSYS Bioreader 3,000 Auto Macroscope ELIspot Plate Reader) and data were expressed as mean values of triplicate determinations (Garofalo et al., 2023).

## 2.14 Analysis of the databases

Statistical analysis was performed using R environment (R: a language and environment for statistical computing, n.d.). The expression data and relative clinical information under the project TCGA Lung Adenocarcinoma (LUAD) were downloaded from the GDC Data Portal using R package TCGAbiolinks (Mounir et al., 2019). TIMER2.0 (Li et al., 2020), a comprehensive resource platform tool, was used for the systematic analysis of immune infiltrates in TCGA-LUAD dataset. Non-parametric test was used for statistical analyses, as PDL1 and CD71 expression values did not follow a normal distribution (Shapiro-Wilk test).

## 2.15 Statistical analyses

Correlation of PD-L1 expression with iron positivity in tissue samples was tested by Fisher's exact test analysis. For all the analyses, the unpaired, two-tailed Student's t-test was used to test for significant differences between two experimental groups. A $p$-value <0.05 was considered statistically significant. Each experiment was performed at least three times; results are, then, presented as mean ± SD.

# 3 Results

## 3.1 Iron density within the TME correlates with PD-L1 levels in LUAD tissue samples

First, we assessed whether and how PD-L1 expression in tumor cells correlates with iron content within the TME on FFPE tissue samples derived from 16 LUAD patients, whose clinicopathological features are reported in Table 1. Upon staining with the 22C3 clone anti-PD-L1 antibody, according to the TPS, 5 out of 16 samples (31%) were classified as "high PD-L1 expressors" (TPS ≥50%) while 11 out of 16 (69%) were classified as "low PD-L1 expressors" (TPS = 1–49%). By using the Perls Van-Gieson staining method, samples were also classified as "low iron" when the presence of iron inclusions within the TME were not detectable (see representative image in Figure 1A, top left) while samples with clearly recognizable iron inclusions were considered as "high iron" (Figure 1A, bottom left). Notably, 7 out of the 11 patients (64%) with low PD-L1 expression presented a low iron density within the TME, while 4 out of the 5 patients (80%) expressing high levels of PD-L1 presented a high iron density (Figure 1B, Fisher Exact Test: $p < 0.001$). These results suggest that a higher iron density within the TME might correlate with higher PD-L1 expression levels in LUAD cells.

## 3.2 Iron addition within culture media causes oxidative stress and PD-L1 overexpression in LUAD cells

In light of the direct correlation between intratumoral iron density and PD-L1 levels, we hypothesized that iron levels could causally regulate PD-L1 expression. To this end, we investigated the effects of iron addition within culture media on PD-L1 expression in LUAD cell lines. To this, we cultured A549 and H460 for 24 h in their relative culture media with or without 250 μM ferlixit, a $Fe^{3+}$ compound normally used to treat patients with anemia. As shown in Figure 2A, when growth in the iron-rich culture condition, H460 and A549 cells show an intracellular accumulation of free-iron ($A549^{untreated}$ ΔMFI: 1948; $A549^{ferlixit}$ ΔMFI: 6,944; $H460^{untreated}$ ΔMFI: 10,559; $H460^{ferlixit}$ ΔMFI: 17,067), and an overproduction of mitochondrial ROS ($A549^{untreated}$ MFI: 103; $A549^{ferlixit}$ MFI: 324; $H460^{untreated}$ MFI: 267; $H460^{ferlixit}$ MFI: 474, Figure 2B). This is accompanied by a significant upregulation of PD-L1 surface levels in both th cell lines (Figure 2C). The strength of the upregulation inversely correlates with PD-L1 steady state amounts of the two LUAD cell lines: in H460 cells, showing very high levels of baseline PD-L1, iron causes a 2-fold increase, while in A549, with very low baseline PD-L1 expression, iron determines more than 20-fold increase. Notably, in both cell lines, PD-L1 overexpression is consistently counteracted by treatment with the antioxidant and ROS quencher trolox (200 μM for 6 h) ($A549^{untreated}$ MFI: 148; $A549^{ferlixit}$ MFI: 4,672; $A549^{ferlixit+trolox}$ MFI: 2,639; $H460^{untreated}$ MFI: 6,762; $H460^{ferlixit}$ MFI: 10,723, $H460^{ferlixit+ferlixit}$ MFI:8,893, Figure 2C), thus strongly suggesting that iron promotes

**TABLE 1 Clinicopathological features of 16 LUAD patients.**

| | Low PD-L1 expression (1%–50%) | High PD-L1 expression (>50%) | |
|---|---|---|---|
| Variables | n (%) | n (%) | *p*-value |
| *Sex* | | | n.s |
| Male | 5 (45.5) | 4 (80) | |
| Female | 6 (54.5) | 1 (20) | |
| *Age* | | | $p < 0.001$ |
| <65 years | 3 (27.3) | 1 (20) | |
| ≥65 years | 8 (72.7) | 4 (80) | |
| *Pleural invasion* | | | $p < 0.001$ |
| Absent | 10 (91) | 4 (80) | |
| Present | 1 (9) | 1 (20) | |
| *Venous and lymphatic invasion* | | | $p < 0.001$ |
| Absent | 11 (100) | 3 (60) | |
| Present | 0 (0) | 2 (40) | |
| *Metastasis* | | | $p < 0.0001$ |
| Absent | 10 (91) | 5 (100) | |
| Present | 1 (9) | 0 (0) | |
| *Iron content* | | | $p < 0.001$ |
| Low | 7 (64) | 1 (20) | |
| High | 4 (36) | 4 (80) | |
| Tot | 11 | 5 | |

PD-L1 overexpression in a ROS-dependent manner. No signs of apoptosis or ferroptosis are detectable by annexin/PI flow cytometry analysis, thus excluding the possibility that PD-L1 overexpression in A549 and H460 is determined by potential cytotoxic effects triggered by the iron-mediated oxidative stress (Supplementary Figure S1).

## 3.3 Iron-mediated PD-L1 upregulation occurs at transcriptional level through c-myc activation

In cancer cells, the expression of PD-L1 is intricately regulated either at transcriptional, post-transcriptional, and post-translational levels (Ribas, 2015; Ju et al., 2020). As shown by qPCR analysis in Figure 3A (see also Supplementary Figure S2A), we demonstrated that iron promotes PD-L1 overexpression essentially at mRNA levels and that this is accompanied by the enhanced nuclear translocation of c-Myc, a well-defined trancription factor of PD-L1 (Figure 3B). Once again, The administration of trolox reduces the translocation of c-Myc, which correlated with the lack of PD-L1 upregulation in both the cell lines (Figure 3B). No significant variations were observed, instead, for other PD-L1 transcription factors c-JUN, p-mTOR, HIF-1α, p-ERK, p-s6, NF-kB, p-STAT3, and Nrf2 (Supplementary Figure S2B). To better dissect the role of c-Myc on iron-mediated PD-L1 regulation, we performed the transient knockdown of c-Myc (48 h) in A549 and H460 cultured either in iron-rich or non iron-rich culture media. As shown in Figures 3C, D (see also Supplementary Figure S2C), c-Myc silencing alone causes a reduction of both cytoplasmic and nuclear c-Myc and a parallel downregulation of PD-L1 mRNA and protein levels. Besides, c-Myc knockdown in A549 and H460 grown in iron-rich culture conditons significantly attenuates its translocation and, as a consequence, the overexpression of PD-L1 induced by iron. The effects of c-Myc on iron-mediated PD-L1 regulation was further confirmed at surface levels (Figure 3E). Together, these results suggest that, in A549 and H460 LUAD cells, the iron-dependent PD-L1 upregulation is mediated by the transcription factor c-Myc.

## 3.4 Enhanced PD-L1 in LUAD cells growth in iron-rich culture media reduces the production of IFN-γ by T cells in a co-culture system

To assess whether the overexpression of PD-L1 induced by iron in LUAD cells can affect the immune function of T cells, we measured the production and the release of IFN-γ by T cells in a co-culture system. PBMCs isolated from peripheral blood donated by healthy volunteers were stimulated with antiCD3/CD28 beads to

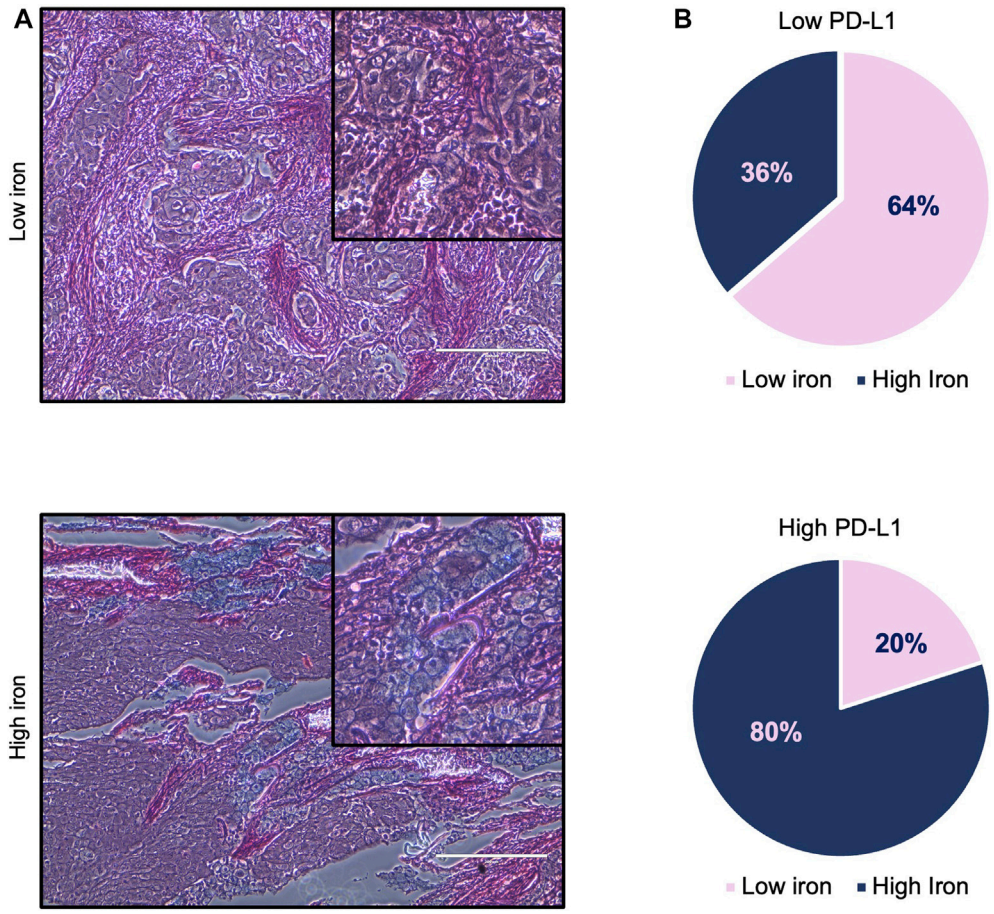


FIGURE 1
High iron density within the TME is associated with higher PD-L1 levels in LUAD tissue samples. **(A)** Representative images of LUAD tissue specimens with low (top) and high (bottom) iron content quantified by Perls Van-Gieson staining. **(B)** Pie charts representing the correlation between iron content within the TME and PD-L1 expression on tumor cells. Scale bars: 200 μm. Fisher Exact Test: $p < 0.001$.

activate T cells. Then, stimulated and not-stimulated (ns) PBMCs were co-cultured for 3 h with H460 and A549 cells in a culture medium supplemented with 250 μM ferlixit. As shown in Figure 4A, iron supplementation strongly enhances the overexpression of PD-L1 in A549 co-cultured with antiCD3/CD28 stimulated PBMCs ($A549^{untreated}$ PD-L1 MFI: 236; $A549^{untreated+PBMCs\ ns}$ PD-L1 MFI: 259; $A549^{untreated+PBMCs\ antiCD3/CD28}$ PD-L1 MFI: 499; $A549^{ferlixit+PBMCs\ ns}$ PD-L1 MFI: 1738; $A549^{ferlixit+PBMCs\ antiCD3/CD28}$ PD-L1 MFI: 4,219). In agreement, the IFN-γ ELISPOT assay shows a remarkable reduction of IFN-γ release from stimulated PBMCs co-cultured with A549 in the iron-rich culture medium compared to those co-cultured with A549 without iron supplementation (Figure 4B). This result is partially replicated when stimulated PBMCs were co-cultured with H460 cells. Indeed, PD-L1 is only slightly overexpressed in H460 co-cultured with stimulated PBMCs in the iron-rich culture condition ($H460^{untreated}$ PD-L1 MFI: 2,712; $H460^{untreated+PBMCs\ ns}$ PD-L1 MFI: 2,563; $H460^{untreated+PBMCs\ antiCD3/CD28}$ PD-L1 MFI: 2,697; $H460^{ferlixit+PBMCs\ ns}$ PD-L1 MFI: 5,018; $H460^{ferlixit+PBMCs\ antiCD3/CD28}$ PD-L1 MFI: 5,787) and IFN-γ release undergoes a small reduction (Figures 4A, B). Overall, these data show that an iron rich-environment promotes the overexpression of a functional PD-L1, which can significantly suppress the immune function of T cells in A549 cells. The less efficient iron-mediated induction of a functional PD-L1 in H460 cells requires further investigation; however, it can be attributed to the already very high levels of PD-L1 at baseline.

## 3.5 The expression of PD-L1 is associated with CD71 in LUAD patients

Cancer cells equipped with hyper functional iron uptake, often exerted by the overexpression of proteins devoted on iron intake (i.e., CD71), deprive the TME of iron to boost their protumoral functions or to suppress the anticancer activities of innate immune cells (Liang and Ferrara, 2021). Here, we finally explored whether an "iron addiction" phenotype, characterized by higher levels of CD71, may correlate with PD-L1 baseline expression in LUAD. To this, we analyzed PD-L1 and CD71 mRNA expression by using The Cancer Genome Atlas (TCGA) for LUAD dataset. We observed that in a cohort of primary LUAD patients ($n = 433$), higher levels of PD-L1 significantly correlates with higher CD71 expression levels ($p =$

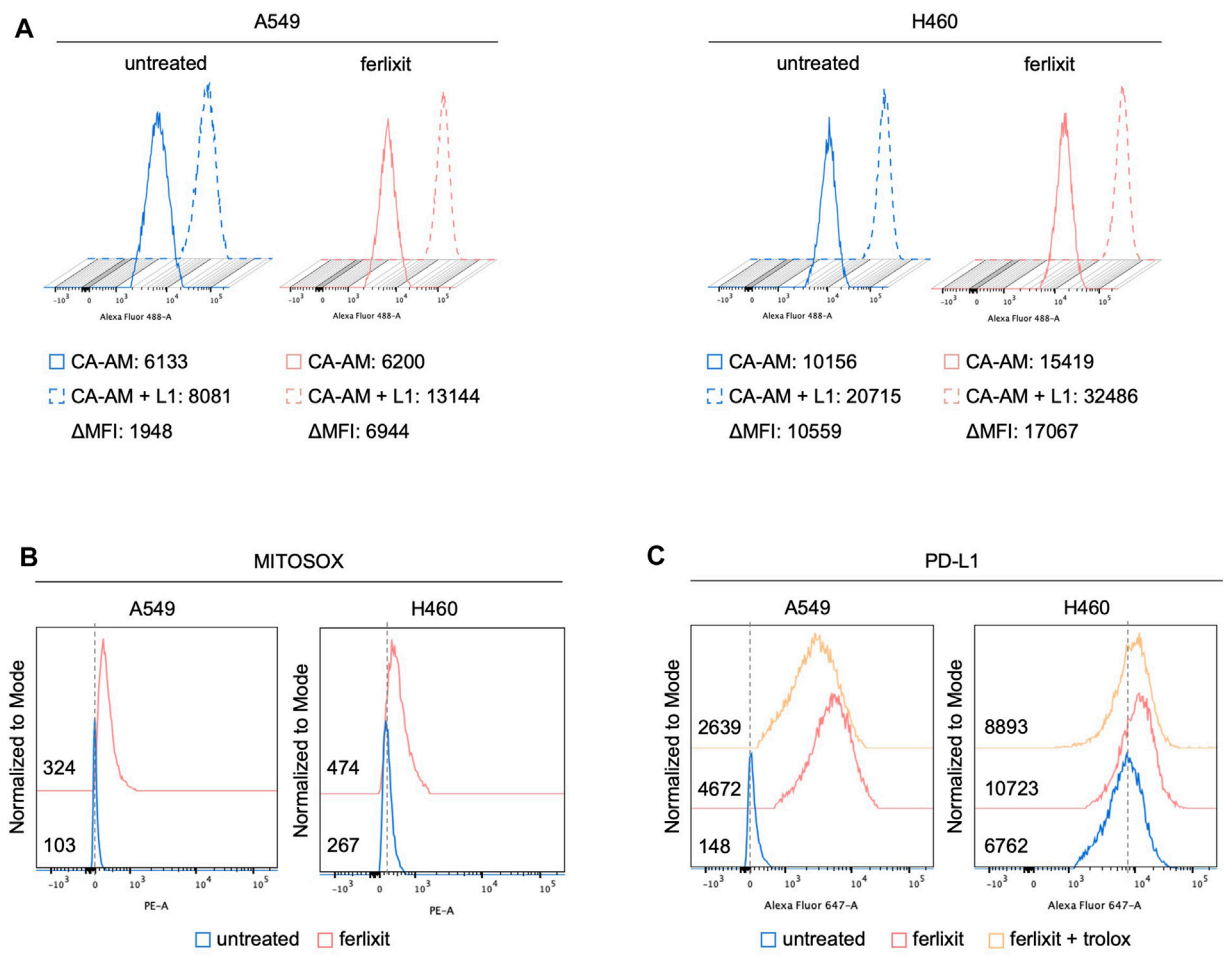


FIGURE 2
Ferlixit administration induces an increase in ROS amounts and PD-L1 overexpression in LUAD cells. Flow cytometry analysis of LIP amounts **(A)** and mitochondrial ROS levels **(B)** quantified by using CA-AM and MitoSOX reagent, respectively, in A549 and H460 cells untreated and treated with 250 μM ferlixit for 24 h. **(C)** Flow cytometry analysis of PD-L1 surface levels in A549 and H460 cells untreated or treated with 250 μM ferlixit for 24 h alone or in combination with 200 μM trolox for 6 h.

2.15e-07, rho = 0.3) (Figure 5A). The correlation becomes more significant in LUAD patients with a higher T cell immune infiltration ($n$ = 24) identified by using TIMER 2.0 ($p$ < 0.004, rho = 0.6; Figure 5B).

## 4 Discussion

Blocking PD-1/PD-L1 axis has shown a great potential to restore TILs from exhausted status and, thus, to eradicate cancer cells (Ilcus et al., 2017). For many cancer types, the PD-1/PD-L1 status is the main speed-limiting factor of the anti-cancer immune response (Yi et al., 2021). However, a growing body of evidence suggests that oncogenic signal-mediated constitutive PD-L1, evaluated alone, could be inaccurate to select patients who might benefit from anti-PD-1/PD-L1-based therapy (Tang et al., 2015; Sui et al., 2018). Rather, understanding the difference between TME-induced PD-L1 and oncogenic signal-mediated constitutive PD-L1 can be a further valuable tool for patient selection; indeed, the environmental factors that regulate PD-L1 expression may display synergistic effects or, alternatively, elevate the sensitivity to α-PD-1/PD-L1 and other immune checkpoint inhibitors (Deng et al., 2018; Yi et al., 2021).

In this study, we aimed to investigate the impact of high iron density within the TME on PD-L1 expression in LUAD. We chose to evaluate the effects of iron on PD-L1 tumor expression in LUAD samples for two primary reasons. Firstly, although antibodies against PD-1/PD-L1 are one of the most effective immunotherapies for treating LUAD, their effects are limited to only a fraction of patients (Jiang et al., 2019). Secondly, the TME of LUAD contains one of the highest densities of TAMs (Jung et al., 2015). Our findings indicate, for the first time, that the iron density within the TME is significantly correlated with PD-L1 expression in a cohort of 16 LUAD patients. Specifically, LUAD tissue samples with higher iron density exhibit higher PD-L1 protein expression on tumor cells than those with low iron content. Based on this observation, we investigated whether iron could act as a regulatory factor for PD-L1 expression in LUAD cell lines. To do this, we treated A549 and H460 cells with ferlixit, an FDA-approved $Fe^{3+}$ compound used to treat iron deficiency. We found that increasing the availability of iron within the culture media leads to intracellular iron overload and pronounced ROS production, resulting

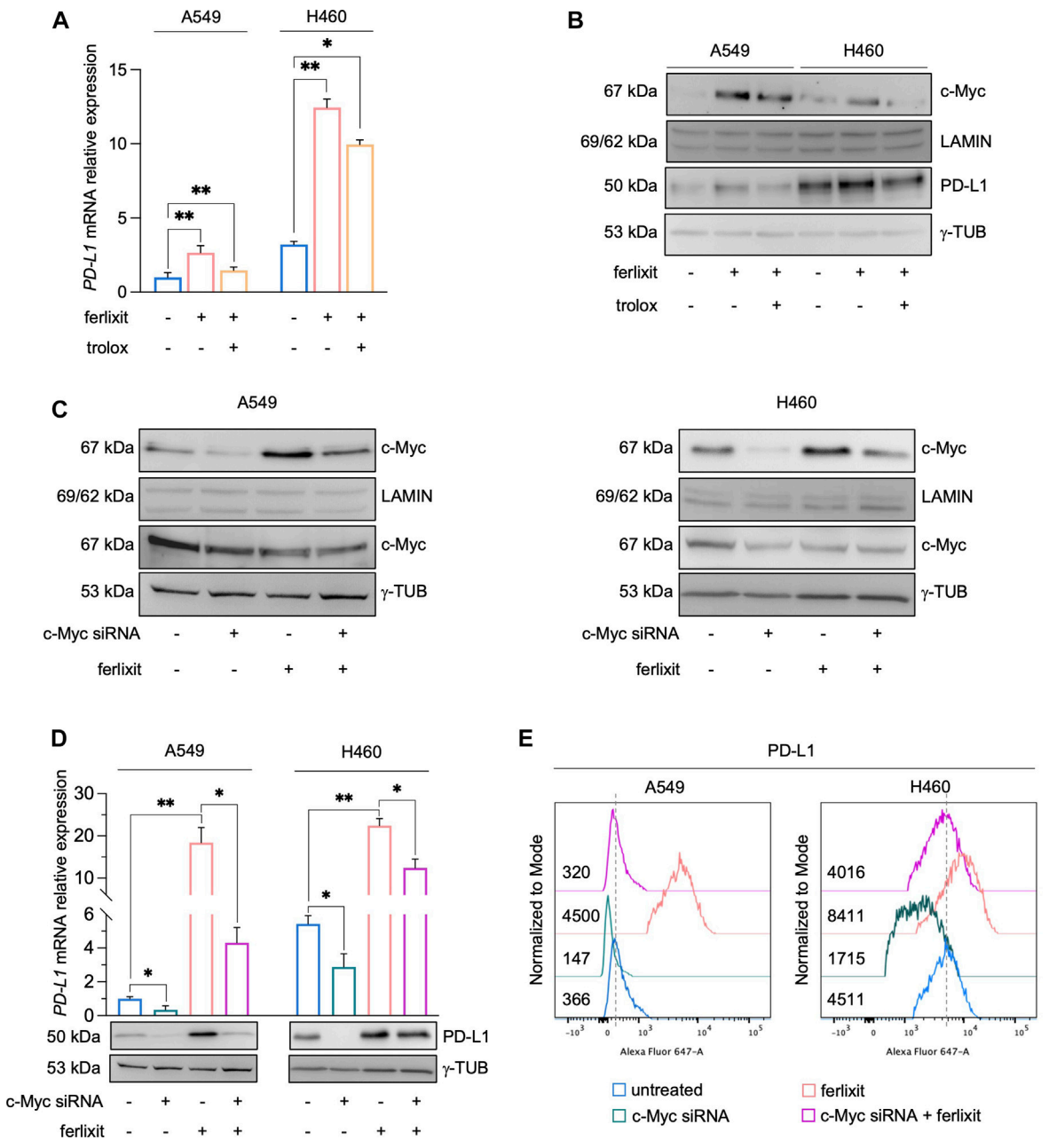


FIGURE 3
Ferlixit-dependent PD-L1 upregulation is mediated by the transcription factor c-Myc in A549 and H460 cells. **(A)** qRT-PCR of PD-L1 mRNA levels in A549 and H460 cells upon administration of 250 μM ferlixit for 24 h or additionally treated with 200 μM trolox for 6 h. **(B)** Western blot of PD-L1 and nuclear c-Myc protein levels in A549 and H460 cells upon administration of 250 μM ferlixit for 24 h or additionally treated with 200 μM trolox for 6 h. LAMIN was used as a normalization control for nuclear protein quantification, while γ-TUB as cytosolic loading control. **(C)** Western blot of PD-L1 and nuclear/cytosolic c-Myc in A549 and H460 cells untreated or treated with ferlixit (250 μM for 24 h) and upon c-Myc knockdown for 48 h. **(D)** Real-time PCR and Western Blot analyses of PD-L1 expression in A549 and H460 cells untreated or treated with ferlixit (250 μM for 24 h) and upon c-Myc silencing (48 h). **(E)** Flow cytometry analysis of PD-L1 surface levels in A549 and H460 cells untreated or treated with ferlixit (250 μM for 24 h) and upon c-Myc silencing (48 h). Results are presented as mean ± SD from three independent experiments. *$p$-value <0.05; **$p$-value <0.01.

in a significant upregulation of PD-L1 expression. This effect is consistently counteracted by the antioxidant compound trolox, strongly suggesting that PD-L1 upregulation in LUAD cells grown in iron-rich culture conditions is ROS-dependent. Previous studies have reported that ferroptotic cancer cells overexpress immune checkpoint ligands to promote immune escape (Dang et al., 2022; Deng et al., 2022). It is important to note that the addition of iron to the culture media does not have any cytotoxic effects on A549 and H460 cells, thus excluding the possibility that PD-L1 expression is due to a phenomenon of ferroptosis.

The correlation between PD-L1 levels and tumor iron availability, which we have demonstrated experimentally, is also supported by querying the TCGA database. This publicly available resource provides gene expression and clinical information of

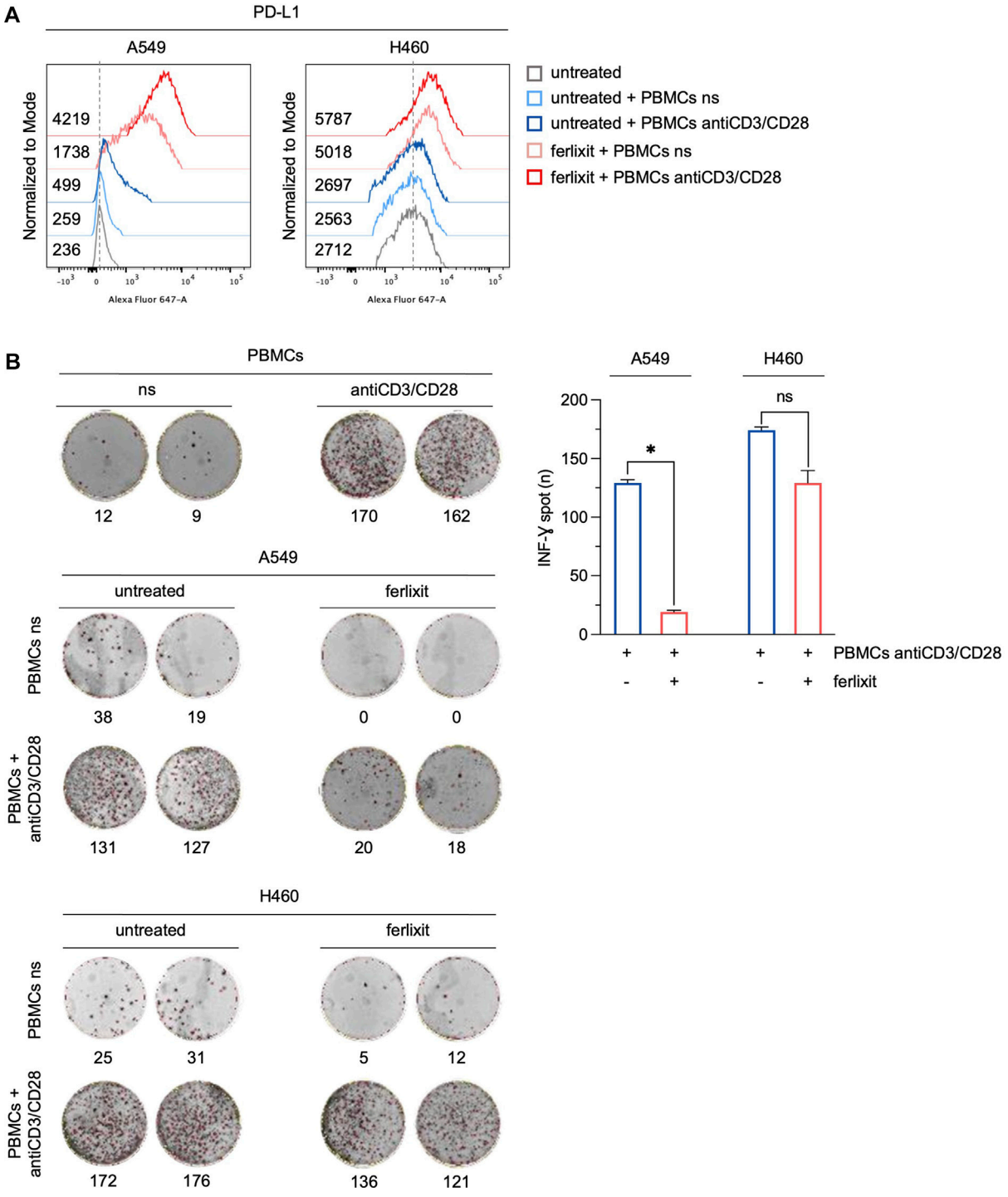


FIGURE 4
Ferlixit-induced PD-L1 overexpression reduces the release of IFN-γ by T cells in a co-culture system. **(A)** Flow cytometry analysis of PD-L1 surface levels in A549 and H460 cells treated with 250 μM ferlixit (24 h) or left untreated, and co-cultured with PBMCs either not stimulated or stimulated with antiCD3/CD28 beads. **(B)** Reactivity of PBMCs either not stimulated or stimulated with antiCD3/CD28 beads against A549 and H460 cells upon treatment with 250 μM ferlixit (24 h) in the IFN-γ ELISPOT assay. All the experiments were carried out in triplicate. The graph and error bar display data as mean ± SD. *$p$-value <0.05; ns: not significant.

thousands of cancer patients (Tomczak et al., 2015). Our observations in a dataset from 433 LUAD patients indicate that higher levels of PD-L1 significantly correlate with higher levels of transferrin receptor CD71, an affordable marker of cellular iron status. These findings led us to hypothesize that the pronounced iron addiction of LUAD cells, indicated by the enhanced expression of CD71, may contribute to an intrinsic propensity to overexpress constitutive PD-L1. This correlation is more significant in LUAD

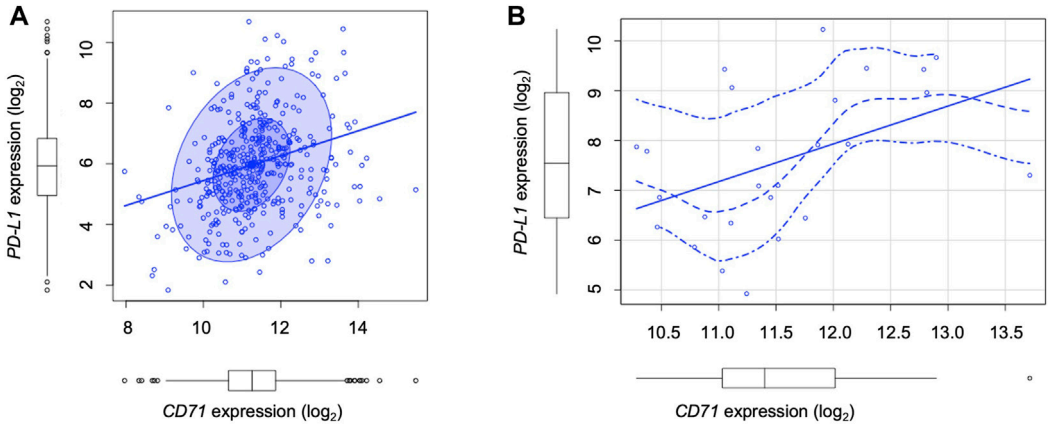


FIGURE 5
TCGA analysis show the correlation between PD-L1 and CD71 levels in LUAD patients. **(A)** Correlation between PD-L1 and CD71 mRNA levels according to the TCGA Lung Adenocarcinoma (LUAD) dataset ($n$ = 433, number of patients) ($p$ = 2.15e-07, rho = 0.3). **(B)** Correlation between PD-L1 and CD71 mRNA levels in LUAD patients with a higher T cell immune infiltration ($n$ = 24) identified by using TIMER 2.0 ($p$ < 0.004, rho = 0.6).

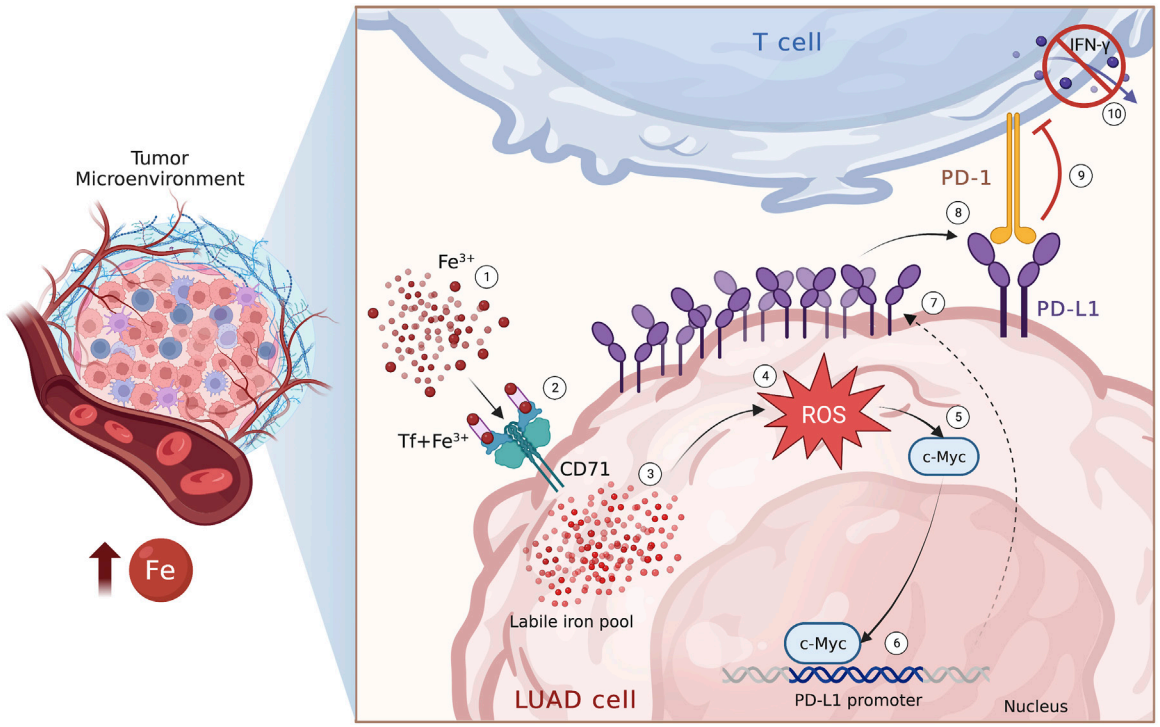


FIGURE 6
Iron within the TME promotes PD-L1 induction via ROS/c-Myc signalling pathway. Schematic representation of the iron-mediated PD-L1 induction via ROS/c-Myc signalling pathway in LUAD cells.

samples with a more pronounced T-cell infiltration, suggesting that cells with a greater ability to intake iron may release signals that foster lymphocyte recruitment within the TME. In line with this hypothesis, recent reports have shown that ferroptotic cells expose or secrete molecules such as calreticulin and HMGB, which induce the prominent activation of the immune system against tumor cells (Kroemer et al., 2013; 2022; Wiernicki et al., 2022). Therefore, ferroptosis can be classified among the "immunogenic cell-death" (Sacco et al., 2021).

The regulation of PD-L1 expression is affected by a wide array of intrinsic and extrinsic factors and is exerted either at transcriptional, post-transcriptional, and post-translational levels (Ju et al., 2020). Our results indicate that, in LUAD cells, the regulatory role of iron on PD-L1 is most likely exerted at the transcriptional level by c-Myc. The addition

of ferlixit to culture media, in fact, causes c-Myc nuclear translocation and PD-L1 overexpression at mRNA levels in both H460 and A549 cells, and this effect is strongly counteracted when c-Myc is knocked down by using a specific siRNA. The role of c-Myc in regulating PD-L1 transcription has been already pointed out in many cancer types (Cha et al., 2019; Liu et al., 2022). In LUAD, Wang et al. (2017) demonstrated that overexpression of bridging integrator-1 (BIN1) reverse PD-L1-mediated immune escape by inhibiting the expression of c-Myc. Cell cycle protein-dependent kinase 7 (CDK7) inhibitor THZ1 downregulates PD-L1 expression by inhibiting c-Myc activation, and when combined with the PD-L1 inhibitor Atezolizumab improves the outcome of LUAD patients (Wang et al., 2020). Data explaining the effects of iron on c-Myc activation are, instead, still unavailable. We hypothesize that the biological mechanisms underlying c-Myc activation upon iron administration rely on the accumulation of ROS. Oxidative stress, indeed, is largely considered one of the main inducers of mitogen-activated protein kinase (MAPK) and PI3K/AKT signalling pathways, which in turn, activate c-Myc transcriptional activity through different mechanisms (Son et al., 2011). RAS signaling and the effector ERK and PI3K/AKT/GSK-3β kinase cascades induce the phosphorylation, the stabilization and thus the activation of c-Myc in melanoma cells (Tsai et al., 2012). The activation of PI3K/Akt and MAPK pathways regulates c-Myc-mediated transcription through the phosphorylation and the degradation of the c-Myc antagonist Mad1 in MCF-7 breast cancer cells (Zhu et al., 2008). At the moment, our results add iron to the list of the environmental factors able to promote PD-L1 expression and put the ground for the in-depth analysis of the biological mechanisms underlying ferlixit-mediated c-Myc activation.

In this study, we show that PD-L1 is overexpressed not only at gene but also at surface levels in A549 and H460 when grown in culture media enriched for iron, thus suggesting that environmental iron can alter tumor immune response. Indeed, we demonstrate that the release of IFN-γ by activated T cells co-cultured with LUAD cells is inhibited in culture media rich in iron, and that the inhibition of T cell activity is correlated with the levels of c-Myc/PD-L1 induced by iron. The immunosuppressive effect is particularly noteworthy in A549 cells, which exhibit a significant increase in PD-L1 expression in iron-rich culture conditions despite having low levels of PD-L1 at baseline. Conversely, H460 cells, which have high constitutive PD-L1 expression, show only a slight increase in PD-L1 expression in response to iron, resulting in little evidence of immunosuppressive activity on T cells. While we do not currently have a biological explanation for this difference, it is possible that H460 cells, like other tumor cells, use alternative strategies in addition to the PD-L1 pathway to evade immune recognition (Vinay et al., 2015). Further investigation is necessary to confirm this hypothesis. It is important to note that, as with other regulatory factors, the effects of iron on PD-L1 expression can be context-dependent, as demonstrated by previous research (Noguchi et al., 2017).

In conclusion, in this study we have reported, for the first time, the existence of a relationship between PD-L1 expression and iron bioavailability within the TME in LUAD samples. Additionally, we have demonstrated that iron can promote the c-Myc/PD-L1 axis in a redox-dependent manner, which may cause T cell inhibition, at least *in vitro* (Figure 6). From a clinical perspective, these findings may provide a basis for identifying and optimizing possible combinatorial strategies that consider the iron levels within the TME to enhance the therapeutic effect of immune checkpoint inhibitors and improve the outcomes of advanced LUAD patients.

## Data availability statement

Publicly available datasets were analyzed in this study. This data can be found here: https://portal.gdc.cancer.gov/projects/TCGA-LUAD.

## Ethics statement

Ethical review and approval was not required for the study on human participants in accordance with the local legislation and institutional requirements. The patients/participants provided their written informed consent to participate in this study.

## Author contributions

FB and FC contributed to conception and design of the study. AMB, AS, IA, LP, EG, and CMF performed the experiments and analyze data. GS performed the statistical analysis. CB, RDS, and MB provide clinical samples and information. FB wrote the first draft of the manuscript. AMB, FB, CP, and FC revised the final version of the manuscript. All authors approved the submitted version.

## Acknowledgments

We thank Caterina Alessi for the editorial assessment of this manuscript.

## Conflict of interest

The authors declare that the research was conducted in the absence of any commercial or financial relationships that could be construed as a potential conflict of interest.

## Publisher's note

All claims expressed in this article are solely those of the authors and do not necessarily represent those of their affiliated organizations, or those of the publisher, the editors and the reviewers. Any product that may be evaluated in this article, or claim that may be made by its manufacturer, is not guaranteed or endorsed by the publisher.

## Supplementary material

The Supplementary Material for this article can be found online at: https://www.frontiersin.org/articles/10.3389/fcell.2023.1208485/full#supplementary-material

# References


Anderson, N. M., and Simon, M. C. (2020). The tumor microenvironment. *Curr. Biol.* 30, R921–R925. doi:10.1016/J.CUB.2020.06.081

Battaglia, A. M., Chirillo, R., Aversa, I., Sacco, A., Costanzo, F., and Biamonte, F. (2020). Ferroptosis and cancer: Mitochondria meet the "iron maiden" cell death. *Cells* 9, 1505. doi:10.3390/cells9061505

Battaglia, A. M., Sacco, A., Perrotta, I. D., Faniello, M. C., Scalise, M., Torella, D., et al. (2022). Iron administration overcomes resistance to erastin-mediated ferroptosis in ovarian cancer cells. *Front. Oncol.* 12, 868351. doi:10.3389/fonc.2022.868351

Biamonte, F., Buffone, C., Santamaria, G., Battaglia, A. M., Mignogna, C., Fortunato, L., et al. (2021). Gene expression analysis of autofluorescence margins in leukoplakia and oral carcinoma: A pilot study. *Oral Dis.* 27, 193–203. doi:10.1111/ODI.13525

Biamonte, F., Zolea, F., Bisognin, A., Di Sanzo, M., Saccoman, C., Scumaci, D., et al. (2015). H-ferritin-regulated microRNAs modulate gene expression in K562 cells. *PLoS One* 10, e0122105. doi:10.1371/JOURNAL.PONE.0122105

Biamonte, F., Zolea, F., Santamaria, G., Battaglia, A. M., Cuda, G., and Costanzo, F. (2017). Human haematological and epithelial tumor-derived cell lines express distinct patterns of onco-microRNAs. *Cell Mol. Biol. (Noisy-le-grand)* 63, 75–85. doi:10.14715/CMB/2017.63.11.14

Brown, R. A. M., Richardson, K. L., Kabir, T. D., Trinder, D., Ganss, R., and Leedman, P. J. (2020). Altered iron metabolism and impact in cancer biology, metastasis, and immunology. *Front. Oncol.* 10, 476. doi:10.3389/FONC.2020.00476

Cassim, S., and Pouyssegur, J. (2019). Tumor microenvironment: A metabolic player that shapes the immune response. *Int. J. Mol. Sci.* 21, 157. doi:10.3390/IJMS21010157

Cha, J. H., Chan, L. C., Li, C. W., Hsu, J. L., and Hung, M. C. (2019). Mechanisms controlling PD-L1 expression in cancer. *Mol. Cell* 76, 359–370. doi:10.1016/J.MOLCEL.2019.09.030

Chirillo, R., Aversa, I., Di Vito, A., Salatino, A., Battaglia, A. M., Sacco, A., et al. (2020). FtH-mediated ROS dysregulation promotes CXCL12/CXCR4 Axis activation and EMT-like trans-differentiation in erythroleukemia K562 cells. *Front. Oncol.* 10, 698. doi:10.3389/fonc.2020.00698

Choi, E. J., Jeon, C. H., and Lee, I. K. (2022). Ferric ammonium citrate upregulates PD-L1 expression through generation of reactive oxygen species. *J. Immunol. Res.* 2022, 6284124. doi:10.1155/2022/6284124

Comito, G., Ippolito, L., Chiarugi, P., and Cirri, P. (2020). Nutritional exchanges within tumor microenvironment: Impact for cancer aggressiveness. *Front. Oncol.* 10, 396. doi:10.3389/FONC.2020.00396

da Silva, M. C., Breckwoldt, M. O., Vinchi, F., Correia, M. P., Stojanovic, A., Thielmann, C. M., et al. (2017). Iron induces anti-tumor activity in tumor-associated macrophages. *Front. Immunol.* 8, 1479. doi:10.3389/fimmu.2017.01479

Dang, Q., Sun, Z., Wang, Y., Wang, L., Liu, Z., and Han, X. (2022). Ferroptosis: A double-edged sword mediating immune tolerance of cancer. *Cell Death Dis.* 13, 925–1016. doi:10.1038/s41419-022-05384-6

De Marchi, P., Leal, L. F., Duval Da Silva, V., Da Silva, E. C. A., Cordeiro De Lima, V. C., and Reis, R. M. (2021). PD-L1 expression by Tumor Proportion Score (TPS) and Combined Positive Score (CPS) are similar in non-small cell lung cancer (NSCLC). *J. Clin. Pathol.* 74, 735–740. doi:10.1136/JCLINPATH-2020-206832

De Vitis, C., Battaglia, A. M., Pallocca, M., Santamaria, G., Mimmi, M. C., Sacco, A., et al. (2023). ALDOC- and ENO2- driven glucose metabolism sustains 3D tumor spheroids growth regardless of nutrient environmental conditions: A multi-omics analysis. *J. Exp. Clin. Cancer Res.* 42, 69. 1–25. doi:10.1186/S13046-023-02641-0

Deng, J., Wang, E. S., Jenkins, R. W., Li, S., Dries, R., Yates, K., et al. (2018). CDK4/6 inhibition augments anti-tumor immunity by enhancing T cell activation. *Cancer Discov.* 8, 216–233. doi:10.1158/2159-8290.CD-17-0915

Deng, J., Zhou, M., Liao, T., Kuang, W., Xia, H., Yin, Z., et al. (2022). Targeting cancer cell ferroptosis to reverse immune checkpoint inhibitor therapy resistance. *Front. Cell Dev. Biol.* 10, 818453. doi:10.3389/FCELL.2022.818453

DeRosa, A., and Leftin, A. (2021). The iron curtain: Macrophages at the interface of systemic and microenvironmental iron metabolism and immune response in cancer. *Front. Immunol.* 12, 614294. doi:10.3389/FIMMU.2021.614294

Di Sanzo, M., Aversa, I., Santamaria, G., Gagliardi, M., Panebianco, M., Biamonte, F., et al. (2016). FTH1P3, a novel H-ferritin pseudogene transcriptionally active, is ubiquitously expressed and regulated during cell differentiation. *PLoS One* 11, e0151359. doi:10.1371/JOURNAL.PONE.0151359

Di Sanzo, M., Chirillo, R., Aversa, I., Biamonte, F., Santamaria, G., Giovannone, E. D., et al. (2018). shRNA targeting of ferritin heavy chain activates H19/miR-675 axis in K562 cells. *Gene* 657, 92–99. doi:10.1016/J.GENE.2018.03.027

Di Sanzo, M., Cozzolino, F., Battaglia, A. M., Aversa, I., Monaco, V., Sacco, A., et al. (2022). Ferritin heavy chain binds peroxiredoxin 6 and inhibits cell proliferation and migration. *Int. J. Mol. Sci.* 23, 12987. doi:10.3390/ijms232112987

Garofalo, E., Biamonte, F., Palmieri, C., Battaglia, A. M., Sacco, A., Biamonte, E., et al. (2023). Severe and mild-moderate SARS-CoV-2 vaccinated patients show different frequencies of IFNγ-releasing cells: An exploratory study. *PLoS One* 18, e0281444. doi:10.1371/JOURNAL.PONE.0281444

GBIF (2022). R: a language and environment for statistical computing. Available at: https://www.gbif.org/en/tool/81287/r-a-language-and-environment-for-statistical-computing (Accessed August 1, 2022).

Guglielmelli, P., Biamonte, F., Spolverini, A., Pieri, L., Isgrò, A., Antonioli, E., et al. (2010). Frequency and clinical correlates of JAK2 46/1 (GGCC) haplotype in primary myelofibrosis. *Leukemia* 24, 1533–1537. doi:10.1038/leu.2010.126

Han, Y., Liu, D., and Li, L. (2020). PD-1/PD-L1 pathway: Current researches in cancer. *Am. J. Cancer Res.* 10, 727–774.

Hudson, K., Cross, N., Jordan-Mahy, N., and Leyland, R. (2020). The extrinsic and intrinsic roles of PD-L1 and its receptor PD-1: Implications for immunotherapy treatment. *Front. Immunol.* 11, 568931. doi:10.3389/FIMMU.2020.568931

Ilcus, C., Bagacean, C., Tempescul, A., Popescu, C., Parvu, A., Cenariu, M., et al. (2017). Immune checkpoint blockade: The role of PD-1-PD-L axis in lymphoid malignancies. *Onco Targets Ther.* 10, 2349–2363. doi:10.2147/OTT.S133385

Jiang, Y., Chen, M., Nie, H., and Yuan, Y. (2019). PD-1 and PD-L1 in cancer immunotherapy: Clinical implications and future considerations. *Hum. Vaccin Immunother.* 15, 1111–1122. doi:10.1080/21645515.2019.1571892

Ju, X., Zhang, H., Zhou, Z., and Wang, Q. (2020). Regulation of PD-L1 expression in cancer and clinical implications in immunotherapy. *Am. J. Cancer Res.* 10, 1–11.

Jung, K. Y., Cho, S. W., Kim, Y. A., Kim, D., Oh, B. C., Park, D. J., et al. (2015). Cancers with higher density of tumor-associated macrophages were associated with poor survival rates. *J. Pathol. Transl. Med.* 49, 318–324. doi:10.4132/JPTM.2015.06.01

Kroemer, G., Galassi, C., Zitvogel, L., and Galluzzi, L. (2022). Immunogenic cell stress and death. *Nat. Immunol.* 23, 487–500. doi:10.1038/S41590-022-01132-2

Kroemer, G., Galluzzi, L., Kepp, O., and Zitvogel, L. (2013). Immunogenic cell death in cancer therapy. *Annu. Rev. Immunol.* 31, 51–72. doi:10.1146/ANNUREV-IMMUNOL-032712-100008

Li, T., Fu, J., Zeng, Z., Cohen, D., Li, J., Chen, Q., et al. (2020). TIMER2.0 for analysis of tumor-infiltrating immune cells. *Nucleic Acids Res.* 48, W509. doi:10.1093/NAR/GKAA407

Liang, W., and Ferrara, N. (2021). Iron metabolism in the tumor microenvironment: Contributions of innate immune cells. *Front. Immunol.* 11, 3919. doi:10.3389/fimmu.2020.626812

Liu, Z., Yu, X., Xu, L., Li, Y., and Zeng, C. (2022). Current insight into the regulation of PD-L1 in cancer. *Exp. Hematol. Oncol.* 11, 44–16. doi:10.1186/S40164-022-00297-8

Mounir, M., Lucchetta, M., Silva, T. C., Olsen, C., Bontempi, G., Chen, X., et al. (2019). New functionalities in the TCGAbiolinks package for the study and integration of cancer data from GDC and GTEx. *PLoS Comput. Biol.* 15, e1006701. doi:10.1371/JOURNAL.PCBI.1006701

Noguchi, T., Ward, J. P., Gubin, M. M., Arthur, C. D., Lee, S. H., Hundal, J., et al. (2017). Temporally distinct PD-L1 expression by tumor and host cells contributes to immune escape. *Cancer Immunol. Res.* 5, 106–117. doi:10.1158/2326-6066.CIR-16-0391

Pfeifhofer-Obermair, C., Tymoszuk, P., Petzer, V., Weiss, G., and Nairz, M. (2018). Iron in the tumor microenvironment-connecting the dots. *Front. Oncol.* 8, 549. doi:10.3389/FONC.2018.00549

Pitt, J. M., Marabelle, A., Eggermont, A., Soria, J. C., Kroemer, G., and Zitvogel, L. (2016). Targeting the tumor microenvironment: Removing obstruction to anticancer immune responses and immunotherapy. *Ann. Oncol.* 27, 1482–1492. doi:10.1093/ANNONC/MDW168

Ribas, A. (2015). Adaptive immune resistance: How cancer protects from immune attack. *Cancer Discov.* 5, 915–919. doi:10.1158/2159-8290.CD-15-0563

Ribas, A., and Hu-Lieskovan, S. (2016). What does PD-L1 positive or negative mean? *J. Exp. Med.* 213, 2835–2840. doi:10.1084/JEM.20161462

Roux, C., Jafari, S. M., Shinde, R., Duncan, G., Cescon, D. W., Silvester, J., et al. (2019). Reactive oxygen species modulate macrophage immunosuppressive phenotype through the up-regulation of PD-L1. *Proc. Natl. Acad. Sci. U. S. A.* 116, 4326–4335. doi:10.1073/PNAS.1819473116

Sacco, A., Battaglia, A. M., Botta, C., Aversa, I., Mancuso, S., Costanzo, F., et al. (2021). Iron metabolism in the tumor microenvironment— Implications for anti-cancer immune response. *Cells* 10, 303. doi:10.3390/cells10020303

Scaramuzzino, L., Lucchino, V., Scalise, S., Lo Conte, M., Zannino, C., Sacco, A., et al. (2021). Uncovering the metabolic and stress responses of human embryonic stem cells to FTH1 gene silencing. *Cells* 10, 2431. doi:10.3390/CELLS10092431

Scicchitano, S., Vecchio, E., Battaglia, A. M., Oliverio, M., Nardi, M., Procopio, A., et al. (2023). The double-edged sword of oleuropein in ovarian cancer cells: From antioxidant functions to cytotoxic effects. *Int. J. Mol. Sci.* 24, 842. doi:10.3390/IJMS24010842

Son, Y., Cheong, Y.-K., Kim, N.-H., Chung, H.-T., Kang, D. G., and Pae, H.-O. (2011). Mitogen-activated protein kinases and reactive oxygen species: How can ROS activate MAPK pathways? *J. Signal Transduct.* 2011, 792639–792646. doi:10.1155/2011/792639

Sui, H., Ma, N., Wang, Y., Li, H., Liu, X., Su, Y., et al. (2018). Anti-PD-1/PD-L1 therapy for non-small-cell lung cancer: Toward personalized medicine and combination strategies. *J. Immunol. Res.* 2018, 6984948. doi:10.1155/2018/6984948

Sui, X., Ma, J., Han, W., Wang, X., Fang, Y., Li, D., et al. (2015). The anticancer immune response of anti-PD-1/PD-L1 and the genetic determinants of response to anti-PD-1/PD-L1 antibodies in cancer patients. *Oncotarget* 6, 19393–19404. doi:10.18632/ONCOTARGET.5107

Tang, Y., Fang, W., Zhang, Y., Hong, S., Kang, S., Yan, Y., et al. (2015). The association between PD-L1 and EGFR status and the prognostic value of PD-L1 in advanced non-small cell lung cancer patients treated with EGFR-TKIs. *Oncotarget* 6, 14209–14219. doi:10.18632/ONCOTARGET.3694

Tomczak, K., Czerwińska, P., and Wiznerowicz, M. (2015). The cancer Genome Atlas (TCGA): An immeasurable source of knowledge. *Contemp. Oncol.* 19, A68–A77. doi:10.5114/WO.2014.47136

Tsai, W. B., Aiba, I., Long, Y., Lin, H. K., Feun, L., Savaraj, N., et al. (2012). Activation of Ras/PI3K/ERK pathway induces c-Myc stabilization to upregulate argininosuccinate synthetase, leading to arginine deiminase resistance in melanoma cells. *Cancer Res.* 72, 2622–2633. doi:10.1158/0008-5472

Tymoszuk, P., Nairz, M., Brigo, N., Petzer, V., Heeke, S., Kircher, B., et al. (2020). Iron supplementation interferes with immune therapy of murine mammary carcinoma by inhibiting anti-tumor T cell function. *Front. Oncol.* 10, 1. doi:10.3389/fonc.2020.584477

Vinay, D. S., Ryan, E. P., Pawelec, G., Talib, W. H., Stagg, J., Elkord, E., et al. (2015). Immune evasion in cancer: Mechanistic basis and therapeutic strategies. *Semin. Cancer Biol.* 35, S185–S198. doi:10.1016/J.SEMCANCER.2015.03.004

Wang, J., Jia, Y., Zhao, S., Zhang, X., Wang, X., Han, X., et al. (2017). BIN1 reverses PD-L1-mediated immune escape by inactivating the c-MYC and EGFR/MAPK signaling pathways in non-small cell lung cancer. *Oncogene* 36, 6235–6243. doi:10.1038/ONC.2017.217

Wang, J., Zhang, R., Lin, Z., Zhang, S., Chen, Y., Tang, J., et al. (2020). CDK7 inhibitor THZ1 enhances antiPD-1 therapy efficacy via the p38α/MYC/PD-L1 signaling in non-small cell lung cancer. *J. Hematol. Oncol.* 13, 99. doi:10.1186/S13045-020-00926-X

Wiernicki, B., Maschalidi, S., Pinney, J., Adjemian, S., Vanden Berghe, T., Ravichandran, K. S., et al. (2022). Cancer cells dying from ferroptosis impede dendritic cell-mediated anti-tumor immunity. *Nat. Commun.* 13, 3676. doi:10.1038/s41467-022-31218-2

Wu, Y., Chen, W., Xu, Z. P., and Gu, W. (2019). PD-L1 distribution and perspective for cancer immunotherapy-blockade, knockdown, or inhibition. *Front. Immunol.* 10, 2022. doi:10.3389/FIMMU.2019.02022

Xiao, Y., and Yu, D. (2021). Tumor microenvironment as a therapeutic target in cancer. *Pharmacol. Ther.* 221, 107753. doi:10.1016/J.PHARMTHERA.2020.107753

Yi, M., Niu, M., Xu, L., Luo, S., and Wu, K. (2021). Regulation of PD-L1 expression in the tumor microenvironment. *J. Hematol. Oncol.* 14, 10. doi:10.1186/S13045-020-01027-5

Ying, J.-F., Lu, Z.-B., Fu, L.-Q., Tong, Y., Wang, Z., Li, W.-F., et al. (2021). The role of iron homeostasis and iron-mediated ROS in cancer. *Am. J. Cancer Res.* 11, 1895–1912.

Zerdes, I., Matikas, A., Bergh, J., Rassidakis, G. Z., and Foukakis, T. (2018). Genetic, transcriptional and post-translational regulation of the programmed death protein ligand 1 in cancer: Biology and clinical correlations. *Oncogene* 37, 4639–4661. doi:10.1038/S41388-018-0303-3

Zhang, X., Zeng, Y., Qu, Q., Zhu, J., Liu, Z., Ning, W., et al. (2017). PD-L1 induced by IFN-γ from tumor-associated macrophages via the JAK/STAT3 and PI3K/AKT signaling pathways promoted progression of lung cancer. *Int. J. Clin. Oncol.* 22, 1026–1033. doi:10.1007/S10147-017-1161-7

Zhu, J., Blenis, J., and Yuan, J. (2008). Activation of PI3K/Akt and MAPK pathways regulates Myc-mediated transcription by phosphorylating and promoting the degradation of Mad1. *Proc. Natl. Acad. Sci. U. S. A.* 105, 6584–6589. doi:10.1073/pnas.0802785105

Zitvogel, L., and Kroemer, G. (2012). Targeting PD-1/PD-L1 interactions for cancer immunotherapy. *Oncoimmunology* 1, 1223–1225. doi:10.4161/ONCI.21335

Zolea, F., Battaglia, A. M., Chiarella, E., Malanga, D., De Marco, C., Bond, H. M., et al. (2017). Ferritin heavy subunit silencing blocks the erythroid commitment of K562 cells via miR-150 up-regulation and GATA-1 repression. *Int. J. Mol. Sci.* 18, 2167. doi:10.3390/IJMS18102167

Zolea, F., Biamonte, F., Battaglia, A. M., Faniello, M. C., Cuda, G., and Costanzo, F. (2016). Caffeine positively modulates ferritin heavy chain expression in H460 cells: Effects on cell proliferation. *PLoS One* 11, e0163078. doi:10.1371/JOURNAL.PONE.0163078

Zolea, F., Biamonte, F., Candeloro, P., Di Sanzo, M., Cozzi, A., Di Vito, A., et al. (2015). H ferritin silencing induces protein misfolding in K562 cells: A Raman analysis. *Free Radic. Biol. Med.* 89, 614–623. doi:10.1016/J.FREERADBIOMED.2015.07.161

frontiers | Frontiers in Cell and Developmental Biology

TYPE Original Research
PUBLISHED 12 June 2023
DOI 10.3389/fcell.2023.1173491



OPEN ACCESS

EDITED BY
Yi Yao,
Renmin Hospital of Wuhan University, China

REVIEWED BY
Chunjie Yu,
University of Florida, United States
Boshi Wang,
Shanghai Cancer Institute, China

*CORRESPONDENCE
Youjie Li,
liyoujie@bzmc.edu.cn
Zhenguo Su,
szg68@126.com
Shuyang Xie,
xieshuyang@bzmc.edu.cn

RECEIVED 24 February 2023
ACCEPTED 22 May 2023
PUBLISHED 12 June 2023

CITATION
Yang X, Wang Y, Rong S, An J, Lan X, Yin B, Sun Y, Wang P, Tan B, Xuan Y, Xie S, Su Z and Li Y (2023), Gene SH3BGRL3 regulates acute myeloid leukemia progression through circRNA_0010984 based on competitive endogenous RNA mechanism. *Front. Cell Dev. Biol.* 11:1173491. doi: 10.3389/fcell.2023.1173491



# Gene SH3BGRL3 regulates acute myeloid leukemia progression through circRNA_0010984 based on competitive endogenous RNA mechanism

Xiancong Yang[1,2], Yaoyao Wang[3], Simin Rong[2], Jiayue An[1,2], Xiaoxu Lan[2], Baohui Yin[3], Yunxiao Sun[3], Pingyu Wang[2], Boyu Tan[2], Ye Xuan[2], Shuyang Xie[2]*, Zhenguo Su[1]* and Youjie Li[2]*

[1]Department of Clinical Laboratory, The Second Medical College of Binzhou Medical University, Yantai, China, [2]Department of Biochemistry and Molecular Biology, Binzhou Medical University, Yantai, China, [3]Department of Pediatrics, Yantai Affiliated Hospital of Binzhou Medical University, Yantai, China

**Introduction:** Acute myeloid leukemia (AML) is a malignant proliferative disease affecting the bone marrow hematopoietic system and has a poor long-term outcome. Exploring genes that affect the malignant proliferation of AML cells can facilitate the accurate diagnosis and treatment of AML. Studies have confirmed that circular RNA (circRNA) is positively correlated with its linear gene expression. Therefore, by exploring the effect of SH3BGRL3 on the malignant proliferation of leukemia, we further studied the role of circRNA produced by its exon cyclization in the occurrence and development of tumors.

**Methods:** Genes with protein-coding function obtained from the TCGA database. we detected the expression of SH3BGRL3 and circRNA_0010984 by real-time quantitative polymerase chain reaction (qRT-PCR). We synthesized plasmid vectors and carried out cell experiments, including cell proliferation, cell cycle and cell differentiation by cell transfection. We also studied the transfection plasmid vector (PLVX-SHRNA2-PURO) combined with a drug (daunorubicin) to observe the therapeutic effect. The miR-375 binding site of circRNA_0010984 was queried using the circinteractome databases, and the relationship was validated by RNA immunoprecipitation and Dual-luciferase reporter assay. Finally, a protein-protein interaction network was constructed with a STRING database. GO and KEGG functional enrichment identified mRNA-related functions and signaling pathways regulated by miR-375.

**Results:** We identified the related gene SH3BGRL3 in AML and explored the circRNA_0010984 produced by its cyclization. It has a certain effect on the disease progression. In addition, we verified the function of circRNA_0010984. We found that circSH3BGRL3 knockdown specifically inhibited the proliferation of AML cell lines and blocked the cell cycle. We then discussed the related molecular biological mechanisms. CircSH3BGRL3 acts as an endogenous sponge for miR-375 to isolate miR-375 and inhibits its activity, increases the expression of its target YAP1, and ultimately activates the Hippo signaling pathway involved in malignant tumor proliferation.

**Discussion:** We found that SH3BGRL3 and circRNA_0010984 are important to AML. circRNA_0010984 was significantly up-regulated in AML and promoted cell proliferation by regulating miR-375 through molecular sponge action.

KEYWORDS
Acute myeloid leukemia, TCGA, SH3BGRL3, Hsa_circ_0010984, qRT-PCR

# Introduction

With high heterogeneity and invasive ability, acute myeloid leukemia (AML) is a malignant proliferative disease affecting the hematopoietic system (Jie and Xiaochun, 2021). Many studies have claimed that circular RNA (circRNA) is an important regulator involved in AML progression. Developments in molecular targeted therapy techniques and cell transplantation have significantly improved the conditions of most patients with AML. However, many patients still relapse and have poor long-term prognosis (Azmi and Balasubramanian, 2021; Xiaodan et al., 2021). Therefore, exploring genes that affect and improve the prognosis of AML is necessary to developing effective monitoring and treatment options.

The post-translational modification of SH3 domain-binding glutamate-rich protein 3 (SH3BGRL3) was identified as tumor necrosis factor-α (TNF-α) inhibitory protein TIP-B1. SH3BGRL3 encodes a highly conserved small protein composed of 93 amino acids. A study showed that the SH3BGRL3 gene expression was upregulated in HL60 cells, which was related to the differentiation induced by phorbol myristate acetate. These results indicated that SH3GRL3 plays a role in the differentiation-related signal transduction pathway network (Shuhong et al., 2005). The expression of some circRNA molecules has a certain degree of coexpression with host linear genes, such as the positive correlation between gene PDK1 and circPDK1 expression levels (Jiewei et al., 2022). Therefore, we decided to study the circRNA produced by the cyclization of SH3BGRL3 exons.

CircRNA is an emerging reference tool for the diagnosis and treatment of various hematological malignancies. It is a product of closed reverse splicing of precursor mRNA. The disorder of a circRNA is significantly correlated with the malignancy and drug resistance of cancer and has reliable detection potential in plasma, saliva, and other samples. In addition, circRNA and host genes have a certain degree of correlation. For example, the interactions of circRNA molecules with sites in host genes can repair DNA damage and increase cell sensitivity to drug toxicity (Gao et al., 2020; Junhong et al., 2022; Kjems, 2022; Zhang, 2022). Most circRNA molecules consist of different numbers of exons, are covalently closed RNA molecules produced by the reverse splicing of pre-mRNA molecules, have no 5′ caps and 3′ tails, are extremely stable, and have cell- or tissue-specific expression patterns (Ming et al., 2022). circRNA is involved in tumorigenesis due to its biological characteristics and through a variety of mechanisms, such as microRNA (miRNA) sponge, RNP binding, and translation template, and plays a potential regulatory role in a variety of cancer diseases (cardiovascular diseases, lung cancer, and leukemia) (Jie et al., 2022; Qidong et al., 2022; Zhang et al., 2022). In addition, circRNA affects tumor progression by regulating autophagy (Miao et al., 2022). circRNA has been reported in many human malignancies, including liver, lung, and bladder cancer. circRNA_0079593 can promote the proliferation, metastasis, and glucose metabolism of melanoma by regulating the miR-516b/GRM3 axis (Jiajing and Lu, 2020). circ_POLA2 can promote the proliferation of AML cells by regulating miR-34a (Wang and Zhu, 2021). circRNA_0010984 has not been reported in the literature.

# Materials and methods

## Patients and samples

Diagnostic peripheral blood samples were collected from 13 patients with AML (16–63 years) and 13 healthy controls at Binzhou Medical University Hospital between October 2021 and November 2022. Normal and tumor blood samples were stored at −80°C until RNA extraction. Detailed information about these patients has been added to the Notes form. The study was approved by the ethics committee of Binzhou Medical University according to the principles of the Helsinki Declaration.

## Data download and identification

Sample information of the TCGA database included 136 patients with leukemia and 15 sample controls. The DESeq2 package of R software was used in screening differentially expressed mRNA (DEmRNA) in AML and selecting DEmRNA ($|\log2FC| > 1$, padj <0.05). The GEOquery package of R software was used in obtaining the GSE193094 microarray data set of the GEO database, and the grouping was designated as parental HL-60, Ara-C resistant (HRA) and DNR-resistant (HRD). The limma package of R software was used for data correction and gene expression analysis. Construction and Functional Enrichment of Competitive Endogenous Regulatory RNA Network CircRNA–miRNA regulatory sites were queried using circinteractome (http://circinteractome.nia.nih.gov), and miRNA–mRNA regulatory sites were queried using Targetscan (www.targetscan.org), microT (www.biostars.org). Commonly recognized mRNA molecules in these miRNA-related databases were obtained. A visual regulatory network was constructed using cytoscape (version v3.9.0). Commonly identified hub genes were used for GO and KEGG functional enrichment analyses, and the clusterprofiler plug-in of R software was used in obtaining biological pathways.

## Weighted gene coexpression network analysis

Gene modules can be detected, and the correlation between each module and patient survival characteristics can be evaluated using a constructed a weighted gene coexpression network (Lin, 2022). We performed data processing on the information of 136 patients leukemia from the TCGA database for WGCNA analysis. The soft threshold (β value) was set at 9, and then the adjacency matrix of the sample was transformed into a topological overlap matrix. After merging and clustering similar modules, we sorted the module feature matrix, and the correlation between the model

feature and sample information matrices was calculated. The above correlation matrix and *p* values were visualized using a labeled heatmap plug-in.

## Cell culture and processing

AML cell lines THP-1, HL-60, and U937 and human embryonic kidney cell line HEK-293T were provided by Cell Bank of Chinese Academy of Sciences (Shanghai, China). Daunorubicin (DAU; Aladdin Industries) was added to HL-60 cells at the logarithmic growth phase and U937 cell suspension at different final concentrations. Drug dose was gradually increased during the drug action period, and the optimal drug concentration (IC50) that affected the inhibition of cells at 50% survival in the drug culture system after 24 h was finally screened. The cells were cultured in 10% fetal bovine serum (all from Gibco; Thermo Fisher Scientific) and 1% penicillin–streptomycin (Beyotime Institute of Biotechnology) in RPMI 1640 medium or DMEM in a humidified incubator (37°C, 5% CO2).

## Real-time polymerase chain reaction

Blood cells and serum were separated from peripheral blood samples, and a threefold volume of red blood cell lysate (Biosharp Biotechnology) was added to the extracted blood cells. The mixture was gently mixed, allowed to stand for 15 min, and centrifuged at 2,000 rpm for 5 min. Total RNA was extracted from leukocyte precipitation with TRIzol reagent (Thermo Fisher Scientific). We first used a PrimeScript RT kit (Takara Bio) to reverse-transcribed RNA to produce cDNA, which was then determined by real-time quantitative polymerase chain reaction (qRT-PCR) with a real-time fluorescent quantitative PCR system. The qPCR conditions were as follows: initial denaturation at 95°C for 3 min; 40 cycles, 95°C for 20 s, annealing at 60°C for 20 s, extension at 72°C for 20 s. Then, 2−ΔΔ Cq was calculated using relative expression and fold change. Primers were purchased from Guangzhou Ruibo Biological Co., Ltd. The sequences of the primers were as follows: SH3BGRL3, forward 5′-ACATCTCCCAGGACAACG-3′ and reverse 5′-TCCACAGCC TCCACGAA-3′; circSH3BGRL3, forward 5′-TCCATTGGCAAT CAAGTCC-3′ and reverse 5′-AAGGCTCGCATCTCATCC-3′; GAPDH forward 5′-GCTGAACGGGAAGCTCACTG-3′ and reverse 5′-GTGCTCAGTGTAGCCCAGGA-3′; miR-375-3p, forward 5′-TTTGTTCGTTCGGCTCGCGTGA-3′ and reverse 5′-CGAACATGTACAGTCCATGGATAG-3′; U6, forward 5′-CTC GCTTCGGCAGCACA-3′ and reverse 5′-AACGCTTCACGA ATTTGCGT-3′. GAPDH and U6 were used as reference genes. Sanger sequencing was performed to validate the sequence of hsa_ circ_0010984.

## RNA R assay and actinomycin D

Total RNA (5 μg) was exposed to 1–3 U/μg RNA RNase R (20 U/μL) at 37°C for 30 min, and water without RNase was used as the control (Mock). The total volume of the reaction system was 20 μL, and the internal reference in the RNase R-group was used as the calculation standard. After RNase R digestion, RT-PCR was performed directly, and the enzyme was inactivated at 70°C for 10 min. For actinomycin D experiment, AML cells were exposed to 2 μg/mL actinomycin D for 4, 8, 12, and 24 h. The cells were then harvested, and the stability of circSH3BGRL3 and SH3BGRL3 was analyzed using qRT-PCR.

## Small interfering RNAs (siRNAs), vector construction

Small interfering RNAs (siRNAs) against circ_0010984 and the negative control RNA duplex (siRNA-NC) were purchased from RiboBio, Guangzhou, China. For the overexpression vector, Front circular Frame (2,278–2,510 bp) and Back circular Frame (3,149–3,400 bp) were added to the circRNA fragment sequence. We used PCR amplification, cloned into plasmid vector (plv-circRNA). The PCR conditions were as follows: initial denaturation at 95°C for 1 min; 30 cycles of 95°C for 20 s, 60°C annealing for 20 s and extension at 72°C for 20 s. The amplification was completed with a final step of 72°C for 5 min. PCR products were separated by electrophoresis on a 1% agarose gel followed by visualization under the Tanon 2,500 gel imaging system (Tanon Science and Technology Co., Ltd.). Circbase ()was" title = "http://www.circbase.org/)was">http://www.circbase.org/)was used to analyze the sequence of circular RNA.

## Lentivirus packaging and cell infection

The 293T cells were prepared, and the cell density reached 80%–90% 24 h before transfection, and the cells were starved for 1 h. The objective plasmid:PSPAX2 plasmid:MD2G plasmid (7.5:5.5:2 μg; v = m/c) was diluted with normal saline to a volume of 500 μL and placed at room temperature for 5 min. PEI (45 μL) was prepared, diluted with normal saline to a volume of 500 μL, mixed, and transfected into a 293T cell culture. The virus supernatant was collected and filtered with a 0.45 μm filter. The supernatant was centrifuged at 8,000 g for 30 min at 4 °C for the removal of cell debris. HL-60 and U937 cells were seeded in six-well plates and cultured in a 5% CO2 incubator at 37 °C until the cell density was 50%–60%. Lentivirus infection was performed, and the liquid was replaced after 6–8 h for subsequent experiments. After 24 h, changes in GFP expression were detected by fluorescence microscopy and flow cytometry, and the images were captured. For conventional cell transfection, we used a Lipofectamine 2000 transfection reagent (liposome 2000: siRNA = 1:1, liposome 2000: plasmid = 1:1, mimic final concentration = 20 nM).

## Cell viability assay

Cell viability was measured by a cell counting kit-8 (CCK-8). HL-60 and U937 cells were seeded in 96-well plates (4 × 103 cells/well) and cultured at 37°C in an incubator. CCK-8 (10 μL; Beyotime Institute of Biotechnology) was added to the well at 0, 24, 48, and 72 h for 2 h. Absorbance at 450 nm was measured by a microplate reader.

## Cell cycle analysis

The cells were washed with PBS, centrifuged at 1,500 rpm for 3 min, collected, and adjusted to a cell concentration of 1 × 106/mL. Then, 1 mL of single cell suspension was collected. After centrifugation, the supernatant was removed, and 1 mL of 70% precooled ethanol was added to the cells for 2 h of fixation overnight. The samples were stored in a refrigerator at 4°C. The fixative was washed before staining, and 100 μL of LRNaseA solution was added to the cell precipitate and placed in a 37°C water bath for 1 h. Approximately 400 μL of PI staining solution was mixed, subjected to ta temperature of 4°C away from light incubation for 1 h. Flow cytometry detection was performed at a wavelength of 488 nm (red fluorescence).

## Cell differentiation

THP-1 cells were treated with 50 ng/mL phorbol myristate 13-acetate for 24 h, and the morphology of cells was observed. LPS (100 ng/mL) was added and incubated for 48 h. Wright–Giemsa staining was performed after 48 h. Finally, monocyte differentiation was assessed by observing cell morphology on the slides and detecting macrophage surface molecular marker CD86(FACS analysis). Cells were stained with anti-human CD86-PE (eBioscience, Carlsbad, CA, United States) monoclonal antibodies. The data were analyzed using FlowJo software.

## RNA-binding protein immunoprecipitation

The interaction between circRNA_0010984 and miR-375 was determined with an RIP assay kit (Guangzhou Geneseed Biotech Co., Ltd.). After sample pretreatment according to this protocol, leukemia cells THP-1, HL-60, and U937 were lysed. After pretreatment with magnetic beads, they were ligated with antibodies for 2 h, and IP (capture antigen) was reacted at 4°C for 2 h overnight. The experimental group used human Argonaute 2 (Ago2) and mouse immunoglobulin G (IgG) as negative controls. After the RNA-binding protein was eluted and purified, the coprecipitated RNA was extracted, and the expression was detected by qRT-PCR.

## Luciferase activity assay

Wild type (WT) and mutant (Mut) fragments of circ_0010984 containing miR-375 binding sites were amplified and inserted into pmiR-GLO vector to generate recombinant plasmids WT-pmiR-GLO-circ_0010984, Mut-pmiR-GLO-circ_0010984. For the dual-luciferase reporter assay, Cancer cells (1 × 105 cells/well) were plated into 6-well plates and were cotransfected with WT-circ_0010984, or Mut-circ_0010984 and miR-375 mimics or scramble control. The luciferase activity was detected according to the manufacturer's instructions using a double luciferase detection kit (Vazyme).

## Protein imprinting analysis

The transfected cells were collected, washed twice with cold PBS, and lysed on ice with 150 μL RIPA lysis buffer (Beyotime Biotechnology Institute) for 30 min. After each lane sample protein, 10% SDS-PAGE was used in separating the protein and transferred to a PVDF membrane. The membrane was blocked in 5% milk powder at 37°C for 2 h, and the primary antibody was incubated at 4°C overnight. The next day, the membrane was washed three times with TBST and incubated with goat anti-rabbit IgG (H + L) HRP at 4°C for 2 h for the capturing of the bands. ImageJ software was used in analyzing the density of the strip and measuring the gray value.

## Statistical analysis

R software (version 4.1.3) was used for single factor cox regression and Lasso regression analyses, and GraphPad Prism (version 8.0) software was used for processing receiver operating characteristic curve (ROC) analysis (Francis, 2022). The Kaplan-Meier method was used in evaluating the correlation between survival status and gene expression, and the survival curve was drawn. Log-rank test was used in evaluating significance. The control and experimental groups were compared using *t*-test. For unpaired samples, unpaired *t*-test was used. For paired samples, paired *t*-test was used. All calculations were performed using GraphPad Prism 8.0 and R software. In addition, Fisher exact test was performed using SPSS software. $p < 0.05$ was considered statistically significant.

# Results

## Characteristics of patients

The workflow chart of this study is shown in Figure 1. Patients without survival data or histopathological information were excluded.

## Screening of prognostic genes affecting acute myeloid leukemia

A comprehensive analysis of RNA sequencing data of 151 TCGA gene-related expression from the UCSC Xena database, including 136 patients with leukemia and 15 related controls (Figure 2A). For the counts data, after log conversion (fpkm does not require log conversion), the R project DESeq2 package was used in analyzing the differential analysis of 19,620 protein-coding mRNA molecules (|log2FC| > 1, padj >1) DEGs. Subsequent Lasso regression model was constructed, the correlation coefficient of the prediction model was output, and the risk score was calculated. Ten genes related to prognostic risk (RARRES3, SH3BGRL3, AL365205.1, LAMA3, OTOA, TEX101, IGDCC4, ASTN1, G6PC, and LGALS1) were obtained (Figure 2B), and the risk score was calculated by multiplying the gene expression level by its corresponding regression coefficient

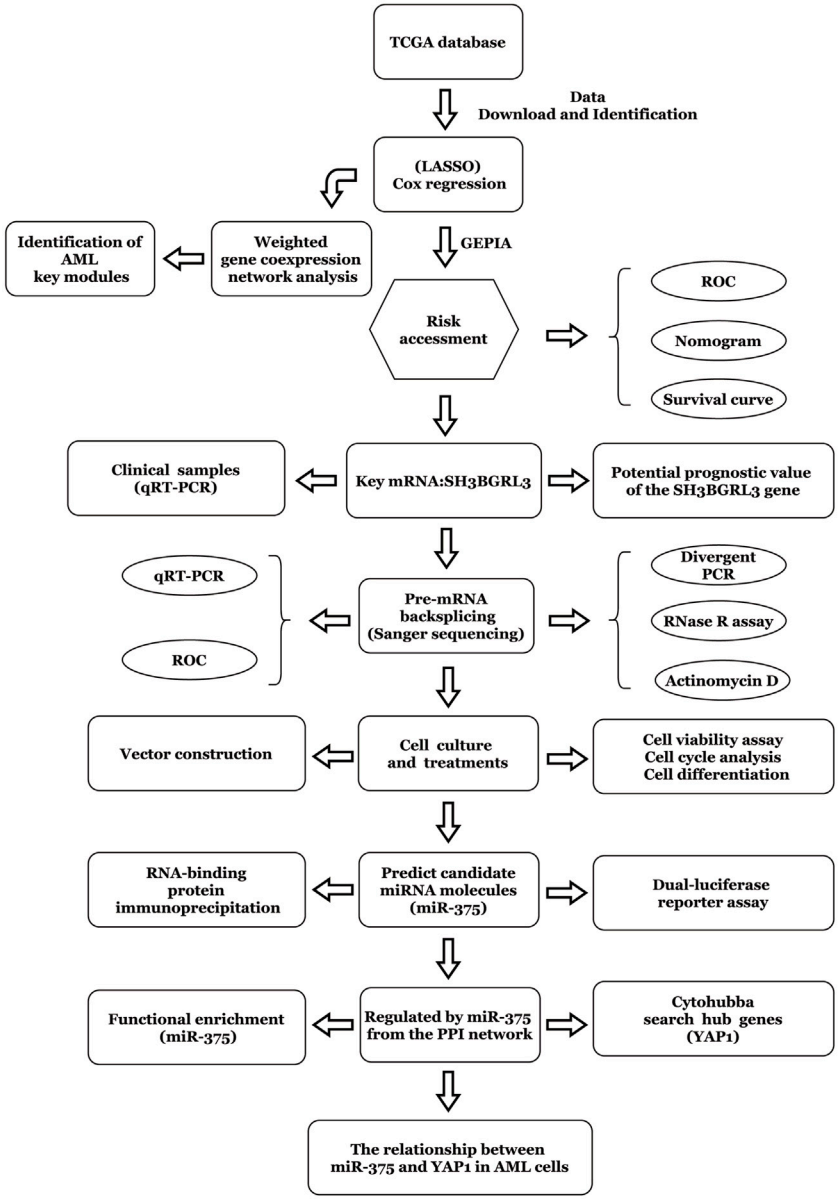


FIGURE 1
Method flow chart based on the construction of prognostic risk model.

(FanHongyi and Zhou, 2022). According to the median risk score, 117 AML samples containing prognostic information were divided into high-risk group (n = 58) and low-risk group (*n* = 59) (Figure 2C). A risk-related ROC curve was plotted using the ROCR package (Figure 2D). An area under the ROC curve (AUC) of 0.73 indicates that the risk score can be used in predicting a model (Zhiyuan et al., 2021). Survival analysis showed that the overall survival rate of patients in the high-risk group was significantly lower than that in the low-risk group (*P* 1, $p < 0.05$) (Figure 2E). The forest plot package was used in plotting the forest. Among the 10 genes shown in this model, SH3BGRL3 had a significant correlation with prognosis prediction (Figure 2F). Through multivariate regression analysis, we integrated multiple predictors. The risk assessment score was used in distinguishing high and low risk samples (Supplementary Figures S1A, B). The core gene SH3BGRL3 was selected for the establishment of a risk model nomogram. The total score of the nomogram showed that the gene SH3BGRL3 is useful in predicting the prognosis of AML. We used the GEO database to verify our conclusion (Supplementary Figure S1C).

## Construction of a weighted coexpression network and identification of disease key modules

To study the relationship between genes and survival characteristics, WGCNA analysis was performed to construct a

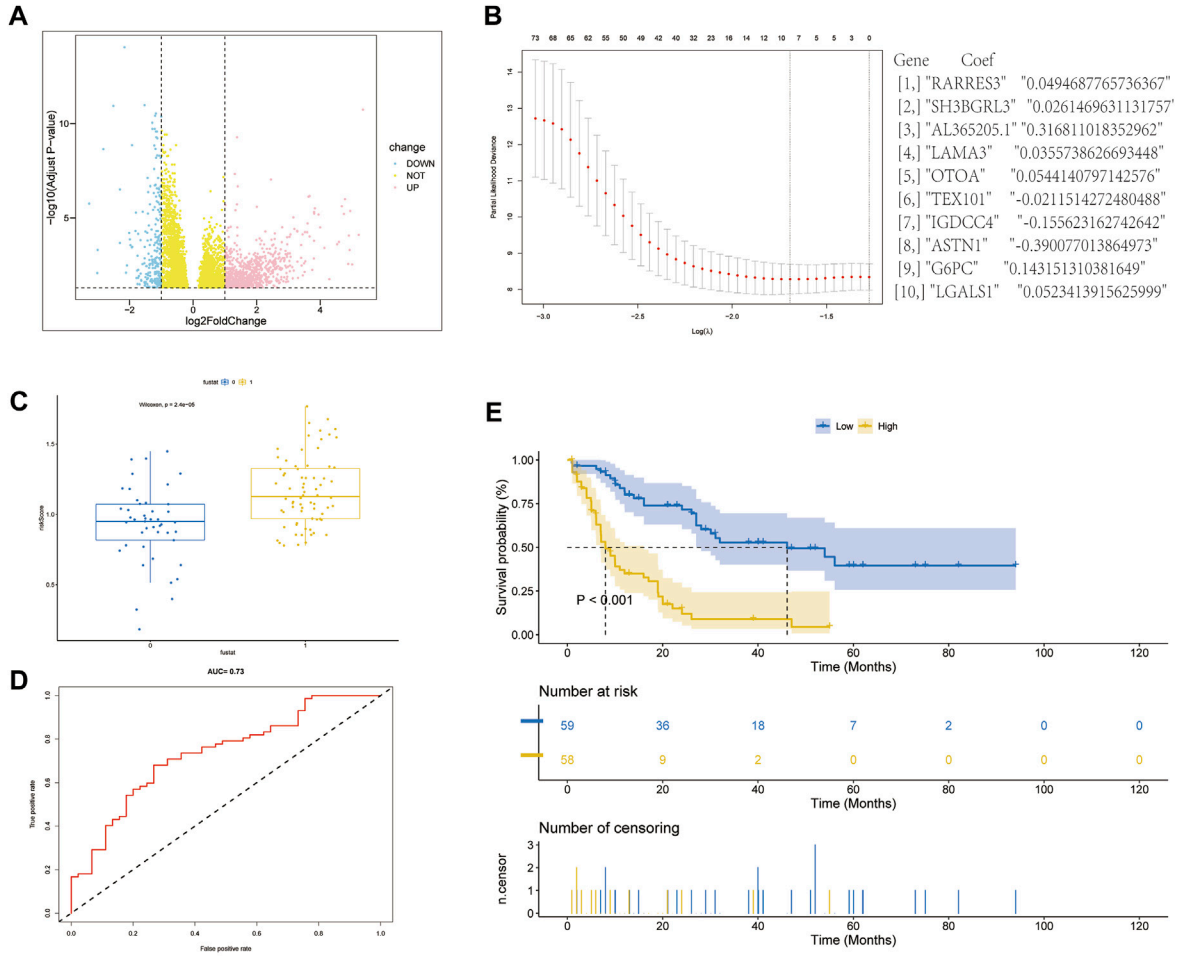


F

| Gene | HR | lower 95%CI | upper 95%CI | pvalue |
|---|---|---|---|---|
| THBS1 | 1.193 | 1.065 | 1.337 | 0.002 |
| SLC44A1 | 1.242 | 1.037 | 1.486 | 0.018 |
| BCL2A1 | 1.255 | 1.080 | 1.458 | 0.003 |
| SCO2 | 1.421 | 1.078 | 1.874 | 0.013 |
| FIGN | 1.424 | 1.104 | 1.836 | 0.006 |
| RARRES3 | 1.434 | 1.090 | 1.886 | 0.010 |
| RELT | 1.475 | 1.156 | 1.881 | 0.002 |
| PRR7 | 1.553 | 1.229 | 1.962 | 0.000 |
| CRIP1 | 1.651 | 1.269 | 2.148 | 0.000 |
| SH3BGRL3 | 1.711 | 1.316 | 2.224 | 0.000 |



FIGURE 2
Screening of genes related to the prognosis of acute myeloid leukemia (AML): **(A)** Volcano map of differentially expressed gene mRNA (DEmRNA) from the TCGA database (*p*-value of differential genes is sorted from small to large). **(B)** Lasso coefficient spectrum of DEmRNA in AML prognosis. **(C,D)** ROC curve and scatter plot based on the risk model. The area under the curve (AUC) is 0.73. **(E)** The survival curve based on the risk model. **(F)** Forest plot to represent the COX regression model for evaluating AML prognosis-related genes.

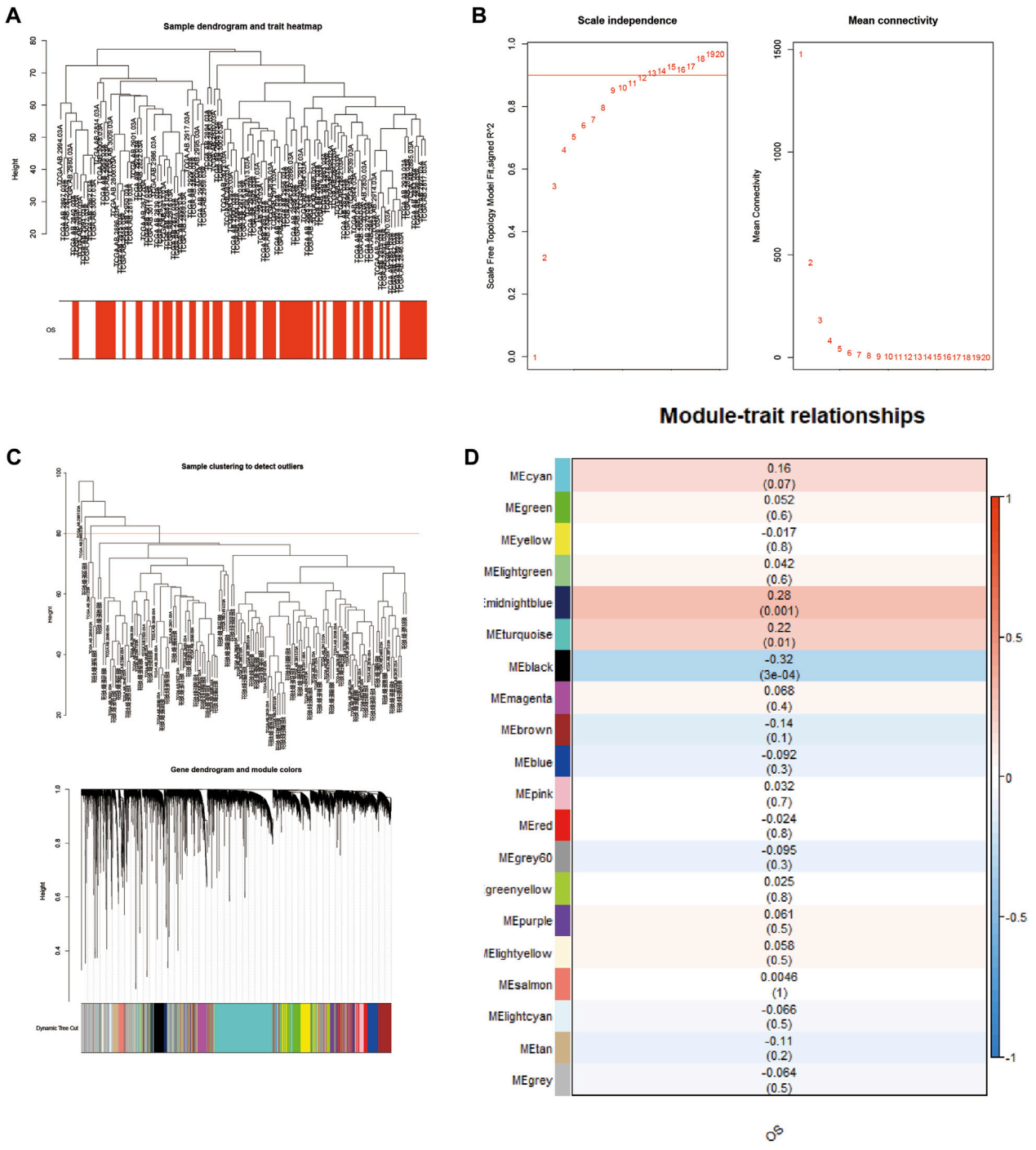


FIGURE 3
Construction of a weighted coexpression network, and identification of AML key modules: **(A)** Sample tree diagram and trait heat map based on TCGA database patient data. **(B)** Fitting index and power value scatter plot and average connectivity and power value scatter plot, view the best power value. **(C)** Based on the mRNA sample clustering tree from the TCGA database (clinical information is converted to color, white indicates low, red indicates high, and gray indicates missing). **(D)** Correlation between different modules and AML (correlation coefficients and *p* values are shown in the heat map).

weighted gene coexpression network, detect gene modules, and correlate gene modules with the survival status of AML patients (Yang, 2020). After clustering 136 patient samples from the TCGA database, the samples below the shear line were deleted and re-clustered, and a dendritic map was produced (Figure 3A). The function "sft $ powerEstimate" was used in estimating the best power value, and soft power of 9 was selected (Figure 3B). Then, using the TOM matrix gene clustering recognition dynamic detection module, we detected 20 modules (Figure 3C). After clustering and merging similar modules, the correlation between

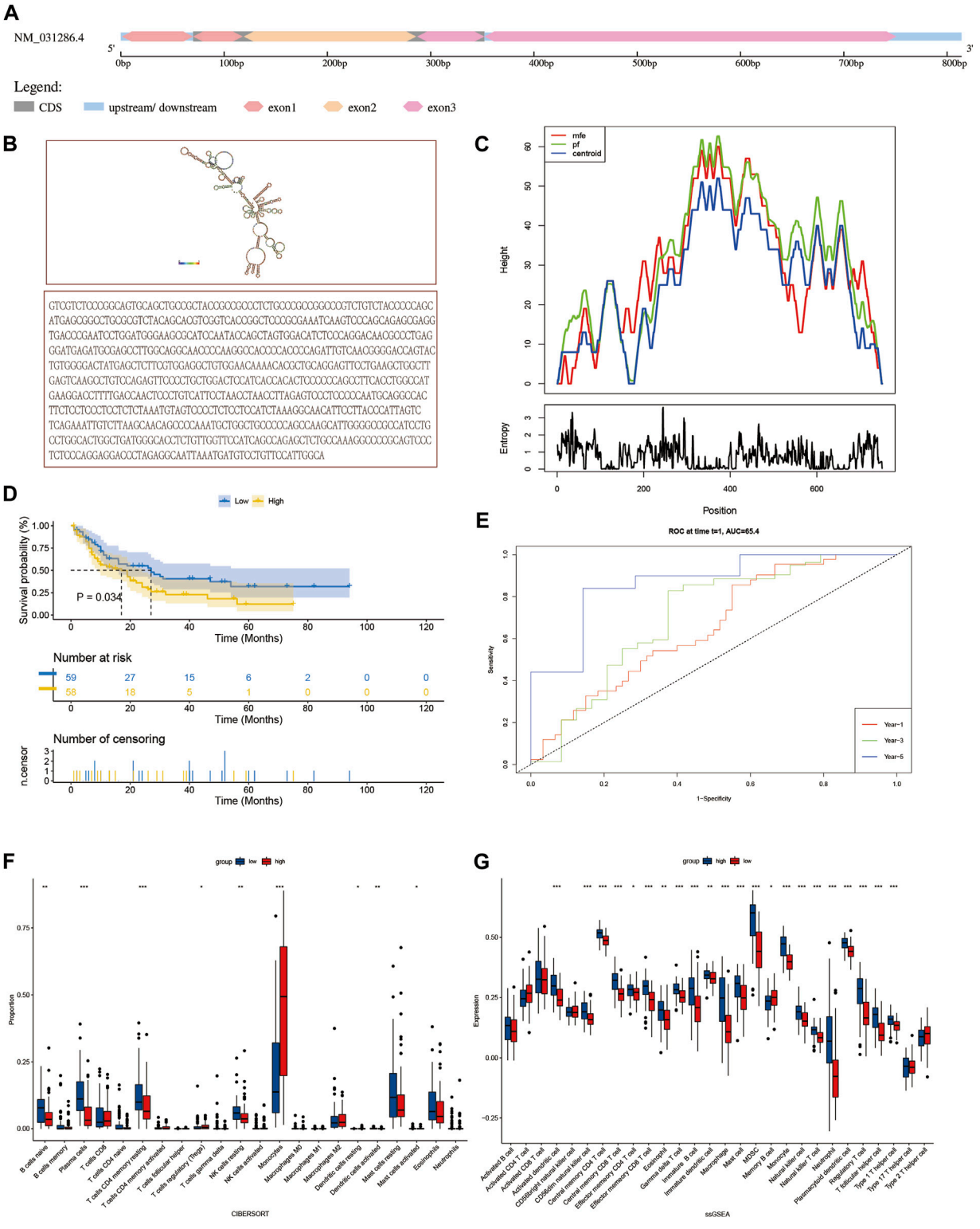


FIGURE 4
Characteristics and related biological functions of SH3BGRL3 gene: **(A)** The schematic diagram of human SH3BGRL3 genome locus. **(B)** SH3BGRL3 sequence and SH3BGRL3 secondary structure obtained from RNA fold web server (http://rna.tbi.univie.ac.at/cgi-bin/RNAWebSuite/RNAfold.cgi). **(C)** Mountain plot of MFE structure of gene SH3BGRL3. **(D)** Survival curve based on the expression of gene SH3BGRL3. **(E)** Time-related ROC curve (select 1, 3, and 5 years survival prediction variable SH3BGRL3 expression). **(F,G)** To explore the correlation between gene SH3BGRL3 expression and ciber, ssGSEA was used in quantifying immune infiltration.

the model feature matrix and the sample information matrix is calculated, and the correlation map between the gene module and the clinical information is generated (Figure 3D). The correlation between gene module and clinical information showed that 11 modules, such as midnightblue module ($p$ = 0.001, correlation coefficient = 0.28) and turquoise module ($p$ = 0.01, correlation coefficient = 0.22), were positively correlated with patient death, and nine modules, such as MEblack module ($P$ = 3e−04, correlation coefficient = −0.32), were negatively correlated with patient death. Notably, the gene SH3BGRL3 belongs to the turquoise module, suggesting that the SH3BGRL3 gene plays a key role in the prognosis of patients with AML.

## Potential prognostic value and related biological functions of the SH3BGRL3 gene

The SH3 domain-binding glutamate-rich (SH3BGR) gene family consists of SH3BGR, SH3BGRL, SH3BGRL2, and SH3BGRL3. In humans, SH3BGRL3 is 751 bp in length, located on 1p36.11, and consists of three exons. The spatial secondary structure of SH3BGRL3 was predicted using RNA fold web server (http://rna.tbi.univie.ac.at/cgi-bin/RNAWebSuite/RNAfold.cg) (Figure 4A–C) (Shi et al., 2016). To further study the role of SH3BGRL3 in acute myeloid leukocytes, we performed gene expression profiling interactive analysis (GEPIA). (Supplementary Figure S1D) (Gao et al., 2017) Verifying the differential expression of SH3BGRL3 in AML patient samples, GEPIA histogram visualization showed that SH3BGRL3 was significantly overexpressed in patients with AML compared with healthy normal subjects. Kaplan–Meier survival curve showed that high SH3BGRL3 gene expression was associated with poor overall survival in patients with AML (Figure 4D). Combined with the results of time-related ROC curve evaluation (Figure 4E), the results indicated that the upregulation of SH3BGRL3 gene is involved in the progression of AML. Gene set enrichment analysis (GSEA) was used in annotating biological function and identifying the potential enrichment pathways of patients with AML and highly expressed SH3BGRL3 gene. Related functional networks were mainly involved in cell activation and cellular immune response, particularly in regulating the activation and immune function of myeloid leukocytes (Supplementary Figure S1E). (Qin et al., 2022). ssGSEA and cibersort were used in quantifying the relative infiltration level of various immune cell subsets and exploring the relationship between predictive features and immune status. The results showed that B, naïve plasma, T, CD4 memory resting, resting NK, and other immune-related cells were significantly downregulated, revealing the biological mechanism in which genes may be involved in tumor immune microenvironment (Figure 4F, G).

## Verification and identification of circSH3BGRL3 in acute myeloid leukemia

To study the differential expression of SH3BGRL3 and circSH3BGRL3 between primary AML patients and normal samples, we collected and used clinical blood samples from 13 AML patients and 13 normal individuals (controls) for qRT-PCR analysis (Figures 5A, B). The clinicopathological features of patients was shown in Table 1. We found sustained and significant increases in SH3BGRL3 and circSH3BGRL3 expression in primary AML patient samples compared to healthy controls. We analyzed the correlation between the expression of SH3BGRL3 and the expression of circSH3BGRL3 (Figure 5C). The correlation coefficient showed that the expression of circSH3BGRL3 and SH3BGRL3 mRNA was positively correlated in the clinical blood samples of patients with AML and normal individuals (controls) (Figure 5D). Next, we verified the existence of circSH3BGRL3 (has-circ-0010984) in the circBase database (Petar and Nikolaus, 2014) and the circBank database (Yang and Ding, 2019). The genome structure showed that circSH3BGRL3 is located in chr1: 26607255–26608013 strand:+ and contain two relatively large second exons (633 bp) (Figure 5E), which were derived from the SH3BGRL3 gene. To further characterize circSH3BGRL3, we designed primers in different directions to amplify transcripts and used convergent and divergent primers to detect linear transcripts in cDNA and gDNA. The PCR results showed that divergent primers did not amplify circular products in gDNA but amplified circular products in cDNA. Convergent primers amplified linear products in cDNA and gDNA (Figure 5F). Then, we studied the stability of circSH3BGRL3 in AML cells. Cells were harvested at different time points after treatment with actinomycin D (a transcription inhibitor), and total RNA was isolated and extracted. The analysis of circSH3BGRL3 and SH3BGRL3 mRNAshowed that the circRNA subtype was highly stable, and the resistance of exonuclease RNase R to digestion confirmed that circSH3BGRL3 was round (Figures 5G, H). In summary, we confirmed that circSH3BGRL3 is a stable circRNA expressed in human AML cells.

## Overexpression of circSH3BGRL3 promotes cell proliferation and accelerates cell cycle in AML

To evaluate whether circSH3BGRL3 affects the progression of leukemia, we constructed a vector (pLV-circRNA0010984) that effectively expresses circSH3BGRL3 in AML cell lines (Supplementary Figure S2A). Three groups of small interfering RNA molecules targeting circSH3BGRL3 were used for circ-SH3BGRL3 silencing, and si-NC was used as a control. To verify the knockdown efficiency, we detected the expression of circSH3BGRL3 in transfected cells. The second group of small interfering RNA (si-hsa-circ-0010984-002) was the most effective in down-regulating the endogenous expression of circSH3BGRL3 and more effective than si-NC (Figure 6A), so we selected the second group to construct the vector (PLVX-SHRNA2-PURO) for lentivirus packaging (Supplementary Figures S2B, C). To determine the efficiency of overexpression and knockdown, we performed qRT-PCR analysis and detected the expression of circSH3BGRL3 in transfected cells (Figures 6B, C). The siRNAs and overexpression plasmid affected the expression of circSH3BGRL3, but not the linear SH3BGRL3 mRNA (Supplementary Figures S2D–F). The overexpression of circSH3BGRL3 significantly accelerated the proliferation of AML

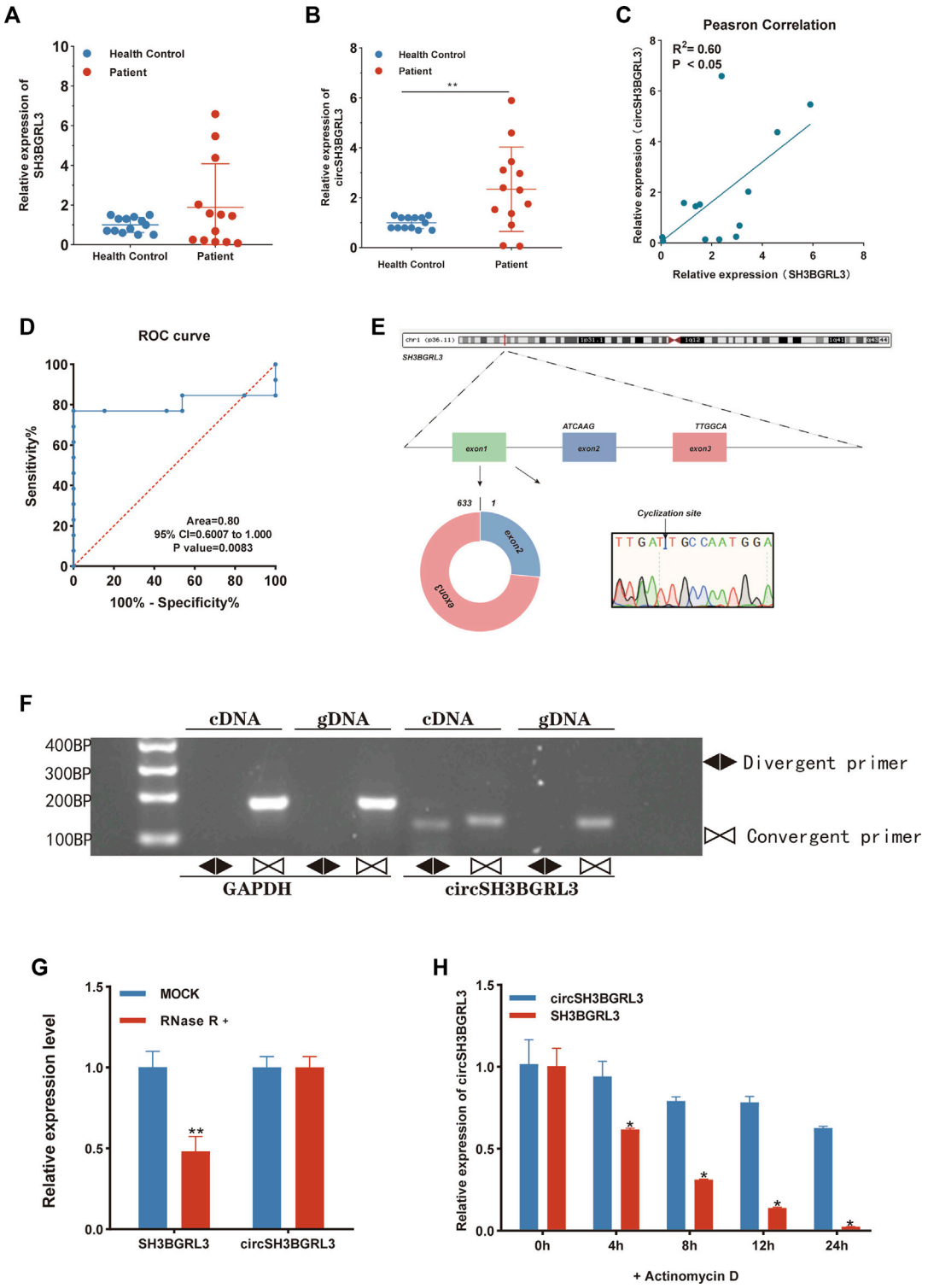


FIGURE 5
Verification and identification of circSH3BGRL3 in acute myeloid leukemia. **(A)** Real-time quantitative polymerase chain reaction (qRT-PCR) was used in determining the expression of SH3BGRL3 in 13 patients with AML and 13 healthy controls. **(B)** The expression level of circSH3BGRL3 between patients with AML ($n$ = 13) and healthy controls ($n$ = 13). **(C)** The expression of SH3BGRL3 was observed in the peripheral blood leukocytes of patients with AML ($n$ = 13). The expression level of circSH3BGRL3 was positively correlated with the expression level of circSH3BGRL3 (R = 0.60, $p < 0.05$). **(D)** ROC analysis of circSH3BGRL3 in the peripheral blood leukocytes of patients with AML. The AUC used in distinguishing patients from normal controls was 0.80, $p$ = 0.008. **(E)** Structure map of circSH3BGRL3, and the splicing junction was verified by Sanger sequencing.**(F)** Different primers were designed using the software "Primer Premier 5.00," and divergent primers were used in amplifying circSH3BGRL3 in cDNA rather than genomic DNA (gDNA). Convergent primers amplified SH3BGRL3 and linear GAPDH RNA. **(G)** qRT-PCR analysis of circSH3BGRL3 and SH3BGRL3 mRNA abundance in AML cells treated with RNase R In cDNA and gDNA. **(H)** AML cells treated with actinomycin D were subjected to qRT-PCR analysis at 4, 8, 12, and 24 h. Measurement of circSH3BGRL3 and SH3BGRL3 mRNA abundance.

**TABLE 1 The relationship between the expression of circSH3BGRL3 and various clinicopathological variables.**

| Characteristics | Total (*N* = 26) | circSH3BGRL3 expression (High = 12,Low = 14) | *p*-value* |
|---|---|---|---|
| Gender | | | |
| Male | 9 | 7 | $p = 0.019$* |
| female | 17 | 5 | |
| Age | | | |
| ≥60 | 5 | 4 | $p = 0.091$ |
| <60 | 21 | 8 | |
| State | | | |
| Patient | 13 | 11 | $p < 0.001$*** |
| health | 13 | 1 | |
| No recurrence | | | |
| Yes | 1 | 1 | $p = 0.657$ |
| No | 12 | 10 | |

*$p < 0.05$, ***$p < 0.001$, ****$p < 0.0001$.

cells (Figures 6D, E). Meanwhile, the overexpression of circSH3BGRL3 affected THP-1 cell differentiation, inducing less-lobulated nuclei to exhibit immature appearance (Figure 6F). Monocyte differentiation was assessed by observing cell morphology on the slides and detecting macrophage surface molecular marker CD86 by FACS analysis (Supplementary Figure S3A). In addition, the upregulation of circSH3BGRL3 significantly reduced the percentage of G0/G1 phase cells and increased the percentage of S phase cells. Compared with pLV-circSH3BGRL3-NC control transfection, the overexpression of circSH3BGRL3 accelerated the cell cycle (Figures 6G, H). As for the knockdown group, the cells transfected with si-circSH3BGRL3 proliferated slowly, and the cell division cycle was slowed down. These data showed the functional relevance of circSH3BGRL3 in AML.

## CircSH3BGRL3 silencing reduces resistance of AML cells to DAU

DA regimen is mainly used to treat AML and composed of DAU and cytarabine. We studied the function of circSH3BGRL3 in DAU-treated AML cells to observe the role of circSH3BGRL3 in combined clinical drug therapy (Supplementary Figure S3B) (Tracy and Murphy, 2017). First, apart from using bioinformatics, we designated nine cell sample groups from GSE193094 as parental HL-60, HRA, and HRD. To screen genes involved in DAU resistance, we analyzed the differentially expressed genes (DEGs) between parental HL-60 and HRD (Figures 7A, B). SH3BGRL3 was identified as one of the dysregulated mRNA molecules between parental HL-60 and HRD. The expression of SH3BGRL3 in DAU-resistant AML cells significantly increased relative to that in normal AML cells (Supplementary Figure S3C), indicating that SH3BGRL3 plays a role in DAU drug tolerance mechanism. Given that the concentration of DAU is unknown, we first screened the IC50 of DAU on different AML cells (Figures 7C, D). The silencing of circSH3BGRL3 affected the resistance of AML cells to DAU. Compared with the knockout of circSH3BGRL3 alone, AML cells treated with DAU after the knockout of circSH3BGRL3 showed more obvious proliferation arrest (Figures 7E, F). circSH3BGRL3 silencing inhibited the activity of AML cells and enhanced the sensitivity of AML cells to DAU.

## CircSH3BGRL3 acts as a sponge for mir-375-3p

CircRNA usually interacts with miRNA. Hence, we used circRNA interactome (https://circinteractome.nia.nih.gov/) to predict candidate miRNA molecules that interact with circSH3BGRL3. The results showed that twenty-three miRNAs might act as targets of circ_0010984 (Supplementary Table S2). We then analyzed the impact of all miRNAs on patient survival status through the Oncolnc database. The results showed that Oncolnc database could only retrieve three miRNAs (miR-375, miR-338-3p, and miR-940) containing prognostic information (Supplementary Figures S4A, B). The expression of only one miRNA (miRNA-375) is beneficial and significantly correlated with the survival status of patients. We analyzed the expression level of miRNA-375 in healthy controls and AML patients (qRT-PCR) (Figure 8A), and the results revealed that miRNA-375 expression was markedly increased in healthy controls relative to AML patients (Figure 8B). We found that circSH3BGRL3 has a binding site that regulates miR-375, which is a conserved noncoding RNA involved in tumor cell proliferation and migration and drug resistance (Xu et al., 2021). The upregulation of miR-375 is related to the poor prognosis of AML in children and is a potential biomarker for alleviating AML in pediatric patients (Feng and Weijing, 2013). We chose miR-375 for further study. We analyzed the correlation between the expression levels of miR-375 and circSH3BGRL3 (Supplementary Figure S4C). The overexpression of circSH3BGRL3 reduced the content of miR-375 in

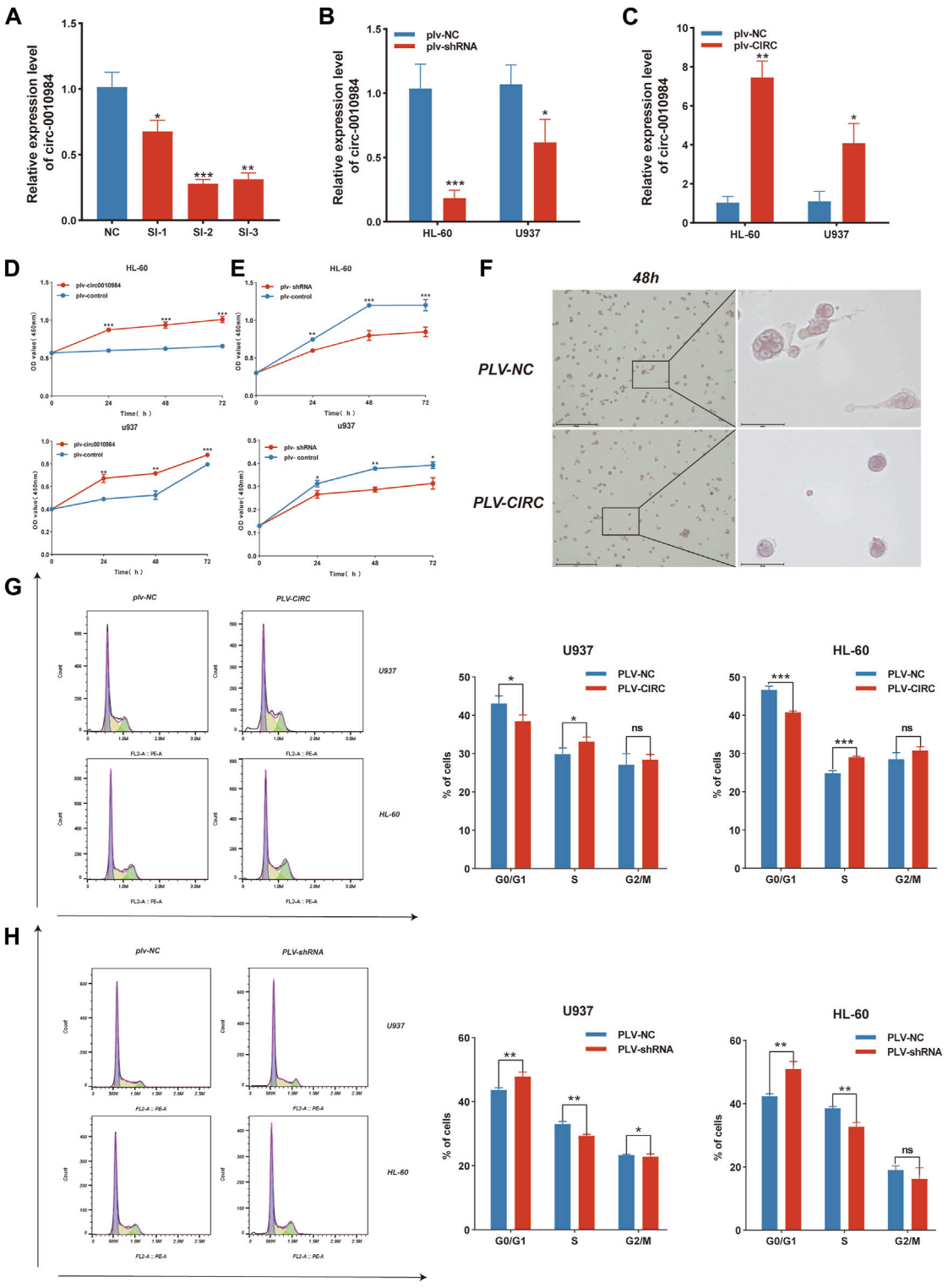


FIGURE 6
CircSH3BGRL3 promotes the proliferation of AML cells and accelerates the cell cycle. **(A)** Three siRNA molecules with different structures were designed for circ-0010984 and transfected into cells to verify the knockdown effect (*$p < 0.05$, **$p < 0.01$, ***$p < 0.001$). **(B)** Construction of siRNA plasmid vector. The expression level of circ_0010984 in U937 and HL-60 cells treated with si-circ_0010984 and si-NC was detected by real-time quantitative polymerase chain reaction (qRT-PCR) after lentivirus packaging infection (*$p < 0.05$, ***$p < 0.001$). **(C)** The overexpression plasmid vector of circ-0010984 was constructed. The expression levels of circ_0010984 in U937 and HL-60 cells were detected by qRT-PCR after lentivirus packaging infection (*$p < 0.05$, **$p < 0.01$). **(D)** CCK-8 assay was used to analyze the effect of circ_0010984 overexpression on the viability of U937 and HL-60 cells. **(E)** The effect of circ_0010984 knockdown on si-circ_0010984-treated U937 and HL-60 cells was evaluated by CCK-8 assay. **(F)** After THP-1 cells were induced to differentiate, Cell morphology was observed under a microscope (scale bar = 50 μm). Use Swiss–Giemsa staining. **(G)** Cell cycle analysis of U937 and HL-60 cells after transfection with overexpression vector and control vector. **(H)** Cell cycle analysis of U937 and HL-60 cells subjected to plv-sh-circ_0010984 and plv-sh-NC transfection.

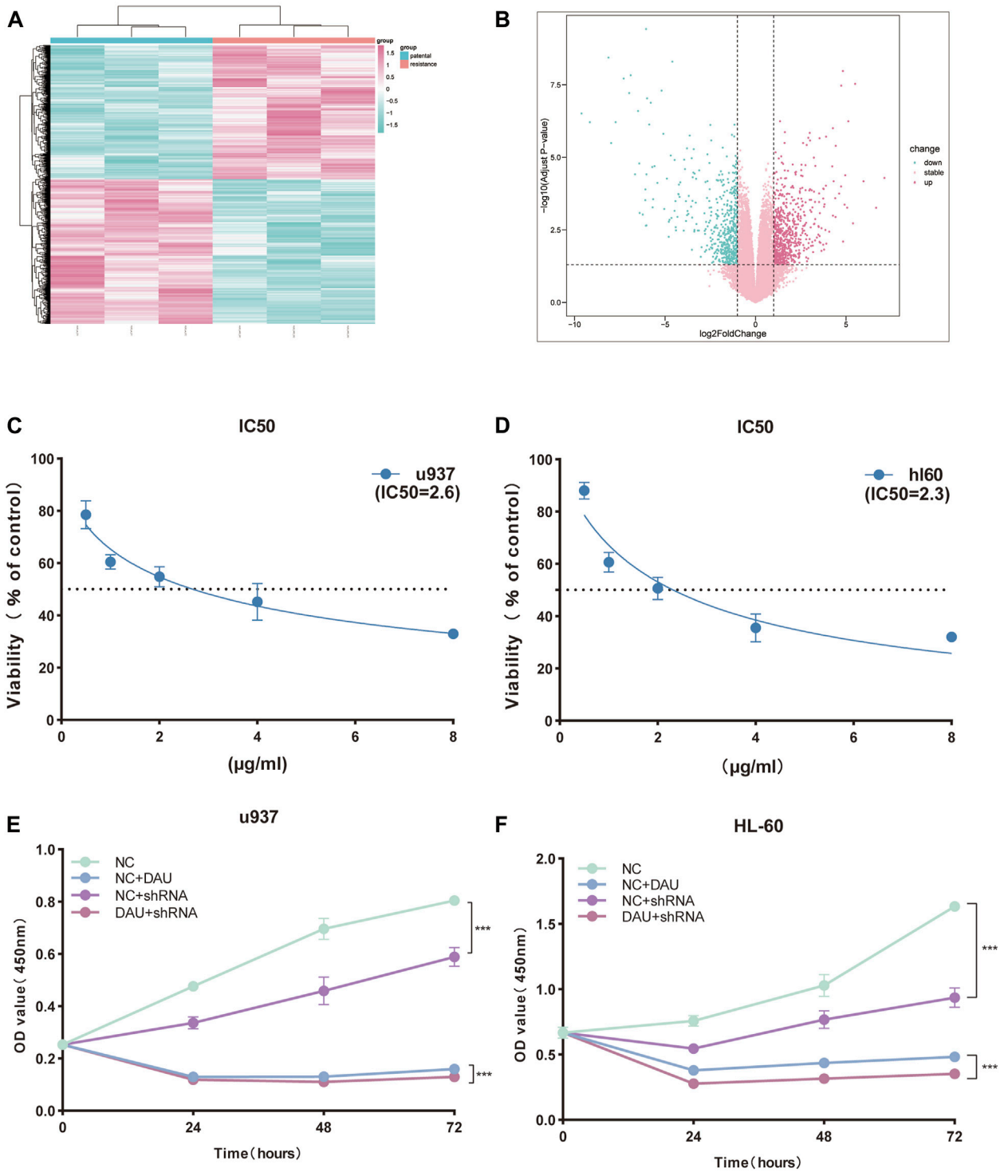


FIGURE 7
CircSH3BGRL3 Silencing Reduces Resistance of AML Cells to DAU. **(A)** For the GSE193094 dataset, the differentially expressed mRNA molecules of daunorubicin-resistant cell lines were presented in the form of a heat map ($p < 0.05$). **(B)** The differentially expressed mRNA molecules were presented in the form of a volcano map (|log2FoldChange| < 1 indicates no expression difference), and the $p$ values of the differentially expressed genes were sorted from small to large. **(C)** CCK-8 was used in determining the half-inhibitory concentration of daunorubicin on U937 cells. **(D)** Determination of half-inhibitory concentration. **(E)** Determination of circ_0010984 knockdown by CCK-8 and the effect of combination drug daunorubicin on U937 cell viability. **(F)** Daunorubicin on HL-60 cells by CCK-8 determination of circ_0010984 knockdown and the effect of combination drug daunorubicin on HL-60 cell viability.

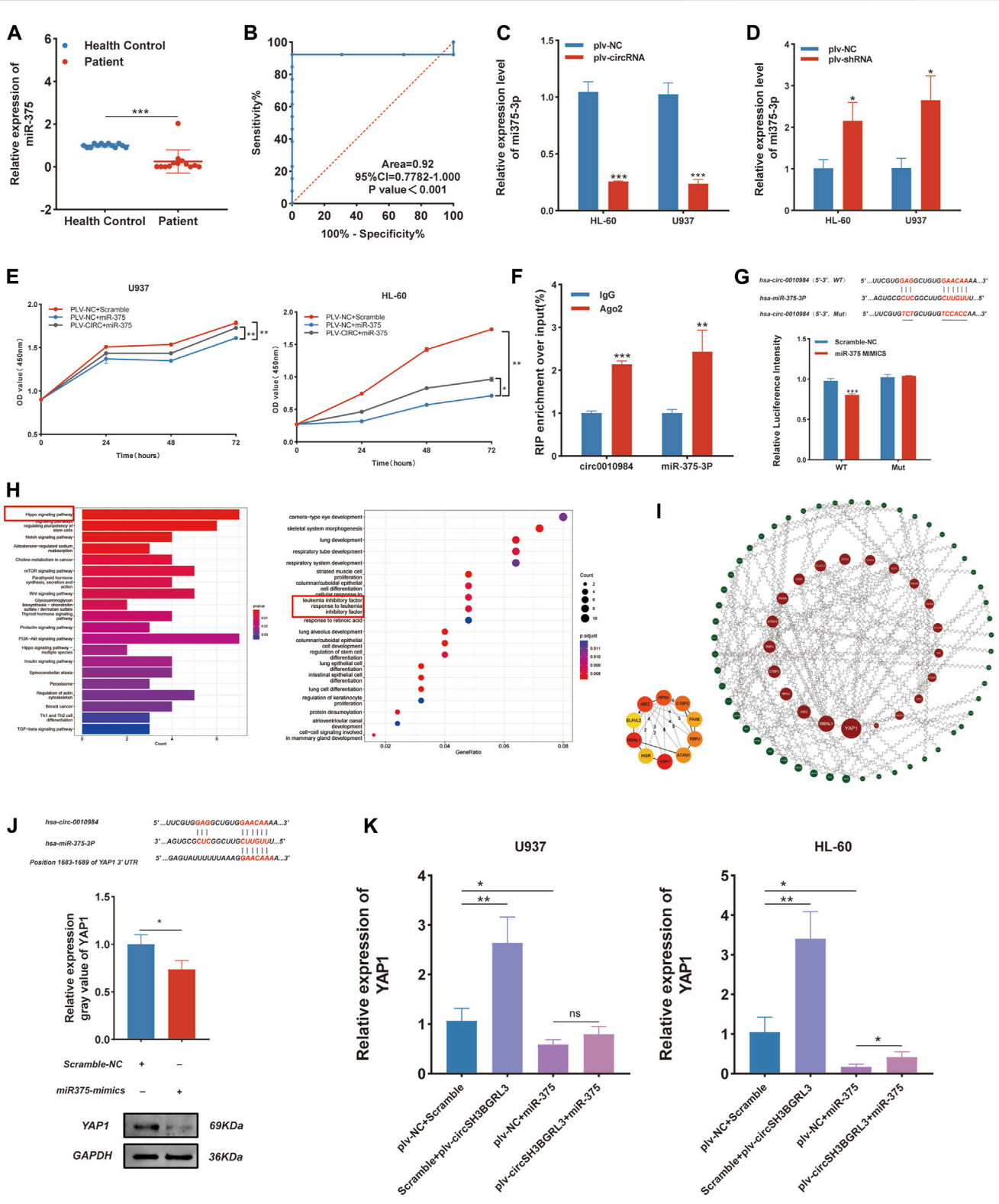


FIGURE 8
CircSH3BGRL3 Acts as a Sponge for miR-375-3P. **(A)** Real-time quantitative polymerase chain reaction (qRT-PCR) was used in determining the expression of miR-375 in 13 patients with AML and 13 healthy controls. **(B)** ROC analysis of miR-375 in the peripheral blood leukocytes of patients with AML. The AUC used in distinguishing patients from normal controls was 0.92, $p < 0.001$. **(C)** The relative levels of miR-375 in HL-60 and U937 cells transfected with plv-NC or plv-circSH3BGRL3 were measured by real-time quantitative polymerase chain reaction (qRT-PCR). **(D)** The relative level of miR-375 in HL-60 and U937 cells transfected with plv-NC or plv-shRNA was measured by qRT-PCR (*$p < 0.05$). **(E)** Cell proliferation decreased upon miR-375 overexpression and was rescued after circRNA_0010984 overexpression in U937 and HL-60 cells.**(F)** RIP experiments were performed using
(*Continued*)

FIGURE 8 (Continued)
anti-Ago2 antibodies in AML cell lysates, and anti-IgG antibodies were selected as negative controls. **(G)** Dual-luciferase reporter assay was utilized to verify the interaction between circ_0010984 and miR-375. **(H)** GO and KEGG functional enrichment analysis of miR-375. **(I)**Regulated by miR-375 from the protein-protein interaction network. **(J)** Inferred binding site sequences between circ_0010984 and miR-375 and between miR-375 and YAP1. Transfection mimics were used in detecting the relative expression of YAP1 in AML cells with Western blot assay (*$p < 0.05$). **(K)**Relative expression of YAP1 was measured by qRT-PCR in circ_0010984 and miR-375 mimics treated U937 cells and HL-60 cells.

AML cells. By contrast, the knockdown of circSH3BGRL3 increased the content of miR-375 in AML cells (Figures 8C, D). Furthermore, the mimics of miR-375 significantly attenuated the proliferation which induced by enhancing circ_0010984 expression in U937 and HL-60 cells (Figure 8E). The results of RNA immunoprecipitation experiments further confirmed that circSH3BGRL3 has the binding site of Ago2 protein, which can be enriched to miR-375. In the dual-luciferase reporter assay, we found that miR-375 mimics could significantly decrease the luciferaseactivity of cancer cells driven by circ_0010984-WT, but not that driven by circ_0010984-Mut, compared with the scramble group (Figures 8F, J). We explored the biological functions and metabolic pathways of miR-375 and performed GO and KEGG functional enrichment (Figure 8H). Subsequently, we analyzed the specific target mRNA of miR-375 and used the STRING (functional protein association networks) database to construct a protein–protein interaction network (Supplementary Table S3), and miRNA–mRNA regulatory sites were queried using Targetscan (www.targetscan.org), microT (www.biostars.org). Then, we used ClueGo to visualize the enrichment pathway (Supplementary Figures S4D, E). The Cytoscape plug-in cytoNCA was used in screening the most reliable core genes of betweenness centrality. The results showed that YAP1 played the most significant role in the regulatory network of protein interactions (Figure 8I). Western blot results showed that YAP1 can be used as a downstream target regulated by miR-375, and miR-375 treatment resulted in the significant downregulation of YAP1 protein in cells (Figure 8J). In addition, we demonstrated that circ_0010984 treatment resulted in a significant upregulation of YAP1, and miR-375 treatment resulted in a remarkable downregulation of YAP1 in U937 cells and HL-60 cells. The miR-375 induced downregulation of YAP1 could be reversed by circ_0010984 (Figure 8K).

## Discussion

Although some breakthroughs have been made in the treatment and diagnosis of AML in recent years, it is still one of the most lethal hematological malignancies due to its complex genetic and molecular mechanisms. AML treatment with DAU and cytarabine is a common method for patients. Although the application of drugs is expected to overcome the disease, a large number of clinical data have shown that the treatment effect worsens with increasing treatment duration. Therefore, fully understanding the molecular mechanisms involved in the occurrence and development of AML and determining novel prognostic treatment options are important. Wang et al. (Yanjun et al., 2021) explored the relationship between genes and AML and demonstrated that ferroptosis-related genes play an important role in the development of AML. Laura et al. (Hueneman et al., 2022) proposed that blocking UBE2N can eliminate the carcinogenic immune signal of AML. However, whether these target genes and their signaling pathways can be successfully applied to clinical practice and exert clinical efficacy requires long-term clinical experiments and exploration. The purpose of this study is to identify genes with diagnostic and prognostic values and to explore novel diagnostic and therapeutic options for AML patients.

In the current study, we found that some genes in patients with AML that can be used in predicting the prognoses of patients by constructing a risk model. We found that the SH3BGRL3 gene, which may produce circRNA by exon cyclization, regulates downstream genes and affects the related functions of diseases through molecular sponge mechanism. To study SH3BGRL3, Yin et al. (Wang et al., 2019) presented evidence that SH3BGRL3 can promote the growth and metastasis of renal clear cell carcinoma. Nie et al. (Wei et al., 2021) demonstrated that the high expression of SH3BGRL3 is related to the poor prognosis of glioblastoma. These results indicate that SH3BGRL3 is closely related to the diagnosis and prognosis of various malignant proliferative diseases. SH3BGRL3 is associated with the malignant proliferation of tumors and is involved in tumor progression in many different types of cancer.

In this study, we found a possible exon-cycling RNA of SH3BGRL3:circRNA_0010984. circRNA is a noncoding RNA with a closed circular single-stranded structure and currently at the forefront of tumor molecular biology research. The expression of circRNA is tissue specific and highly conserved. Many related studies have reported that circRNA is closely related to the occurrence and development of AML. CircNFIX can affect the tumorigenicity of AML by targeting the miR876-3P/TRIM31 axis (Wu et al., 2022). circ_0015278 can regulate AML progression through ferroptosis-related genes (Yang et al., 2022).

In this experiment, we hypothesized that circRNA_0010984 has a certain degree of correlation with the transcriptional expression of the host linear gene SH3BGRL3. To verify our hypothesis, we first examined the coexpression relationship between SH3BGRL3 and circRNA_0010984. The results showed that the expression level of circRNA_0010984 was positively correlated with the expression level of its host linear gene SH3BGRL3. We further verified the function of circRNA_0010984 in AML cell lines. Knocking out circ-0010984 can effectively inhibit the proliferation of AML cells. Therefore, we believe that the abnormal expression level of SH3BGRL3 transcript is closely related to AML, and the upregulation of circ-0010984 can promote the malignant proliferation of AML.

Our study aims to identify the key DEGs associated with AML, establish a prognostic model, and link gene expression with patient prognosis. Bioinformatics data involved in this study come from different bioinformatics platforms (including TCGA database). To eliminate errors as much as possible, we deleted missing data. Lasso regression has advantages over univariate

analysis and can solve the problem of multicollinearity between variables. In this study, we established a nomogram based on the Lasso-Cox regression model, which has certain reference value for analyzing the risk of multiple different variables affecting patients. The prognostic feature model constructed by Kaplan–Meier survival curve and ROC model fully guaranteed the credibility of the results. We then constructed a ceRNA regulatory network to determine the regulatory relationship between the diagnosis and prognosis of AML. It was reliably confirmed in the statistical analysis of the clinical samples.

To better explore the potential mechanism of circRNA_0010984 and determine whether circRNA_0010984 plays its biological function as a miRNA sponge. We speculate that in addition to Ago2 protein, EIF4A3, FUS and SFRS1 can also be used as RNA-binding proteins to match circRNA_0010984. The experimental data proved that miR-375 is a key downstream effector of circRNA_0010984 in our model. Many studies have confirmed that miR-375 interacts with a large number of target genes and participates in regulating many physiological processes related to human diseases (MatveevaBaulina et al., 2022). The downregulation of miR-375 contributes to ERBB2-mediated VEGFA overexpression in esophageal cancer (Ren et al., 2021). Although miR-375 is a key regulator of human cancer progression, studies on the function and mechanism of AML are few. The regulation of the hippo signaling pathway can affect cell proliferation, division, and death. When the pathway is abnormally inhibited, the tissues and organs of animals will proliferate excessively and cause tumors. Through GO and KEGG functional enrichment analysis, we confirmed the key role of miR-375 in regulating target gene YAP1. miRNA regulates the expression of target mRNA through complementary sequences in the 3′-untranslated region. Finally, we studied the relationship between miR-375 and YAP1 in leukemia cells. Western blot results showed that YAP1 expression was negatively correlated with miR-375 expression.

## Conclusion

This study identified the upregulated expression of the hub gene SH3BGRL3 in AML, and we predicted the targeting effect of circ_0010984. The ceRNA network obtained from bioinformatics analysis and its potential function of binding to target genes can be confirmed in future experiments. These data suggest that circRNA_0010984 and its parent gene SH3BGRL3 are potential therapeutic targets for AML.

## Data availability statement

Publicly available datasets were analyzed in this study. This data can be found here, NCBI Gene Expression Omnibus (GSE193094,GSE17054).

## Ethics statement

The studies involving human participants were reviewed and approved by The Medical Ethics Committee of Binzhou Medical University. Written informed consent to participate in this study was provided by the participants' legal guardian/next of kin.

## Author contributions

XY designed and performed the research, analyzed data, and wrote the manuscript. YL reviewed the manuscript. YW, XL, and JA performed experiments such as cell culture. All authors contributed to the article and approved the submitted version.

## Funding

The present study was supported by The Support Plan for Youth Entrepreneurship and Technology of Colleges and Universities in Shandong (grant nos. 2019KJK014 and 2021KJ101), The National Natural Science Foundation of China (grant nos. 81800169 and 82002604), The Shandong Science and Technology Committee (grant nos. ZR2020QH221 and ZR2022LSW002), The Foundation of Binzhou Medical University (grant no. BY2021LCX04), College Students' Innovation and Entrepreneurship Training Program (grant nos. 202210440069 and S202210440097), The Shandong Province Taishan Scholar Project (grant no. ts201712067).

## Acknowledgments

We acknowledge professional editing support from ShineWrite.com (service@shinewrite.com) in editing the English text of a draft of this manuscript.

## Conflict of interest

The authors declare that the research was conducted in the absence of any commercial or financial relationships that could be construed as a potential conflict of interest.

## Publisher's note



## Supplementary material

The Supplementary Material for this article can be found online at: https://www.frontiersin.org/articles/10.3389/fcell.2023.1173491/full#supplementary-material

# References

Azmi, A. S., and Balasubramanian, S. K. (2021). Circular RNAs in acute myeloid leukemia. *Mol. Cancer* 20 (1), 149. doi:10.1186/s12943-021-01446-z

FanHongyi, J., and Zhou, S. (2022). Identification of critical biomarkers and immune infiltration in rheumatoid arthritis based on WGCNA and LASSO algorithm. *Front. Immunol.* 13, 925695. doi:10.3389/fimmu.2022.925695

Feng, G., and Weijing, F. (2013). Upregulation of microRNA-375 is associated with poor prognosis in pediatric acute myeloid leukemia. *Mol. Cell Biochem.* 383 (1-2), 59–65. doi:10.1007/s11010-013-1754-z

Francis, S. N. (2022). Receiver operating characteristic curve: Overview and practical use for clinicians. *Korean J. Anesthesiol.* 75 (1), 25–36. doi:10.4097/kja.21209

Gao, G., Li, C., and Zhang, Z. (2017). Gepia: A web server for cancer and normal gene expression profiling and interactive analyses. *Nucleic Acids Res.* 45 (W1), W98–W102. doi:10.1093/nar/gkx247

Gao, Y., Dong, X., and Chen, W. (2020). CircRNA inhibits DNA damage repair by interacting with host gene. *Mol. Cancer* 19 (1), 128. doi:10.1186/s12943-020-01246-x

Hueneman, K. M., Choi, K., and Pujato, M. A. (2022). Blocking UBE2N abrogates oncogenic immune signaling in acute myeloid leukemia. *Sci. Transl. Med.* 14 (635), eabb7695. doi:10.1126/scitranslmed.abb7695

Jiajing, Y., and Lu, L. (2020). Circ_0079593 facilitates proliferation, metastasis, glucose metabolism and inhibits apoptosis in melanoma by regulating the miR-516b/GRM3 axis. *Mol. Cell Biochem.* 475 (1-2), 227–237. doi:10.1007/s11010-020-03875-8

Jie, D., and Xiaochun, Z. (2021). CircNPM1 strengthens Adriamycin resistance in acute myeloid leukemia by mediating the miR-345-5p/FZD5 pathway. *Cent. Eur. J. Immunol.* 46 (2), 162–182.

Jie, J., Wang, T., Liu, C. Y., and Wang, K. (2022). circRNA is a potential target for cardiovascular diseases treatment. *Mol. Cell Biochem.* 477 (2), 417–430. doi:10.1007/s11010-021-04286-z

Jiewei, L., Xinjing, W., Shuyu, Z., Shi, M., Peng, C., and Deng, X. (2022). Hypoxia-induced exosomal circPDK1 promotes pancreatic cancer glycolysis via c-myc activation by modulating miR-628-3p/BPTF axis and degrading BIN1. *J. Hematol. Oncol.* 15, 128. doi:10.1186/s13045-022-01348-7

Junhong, C., Jie, G., Mengtian, T., Liao, Z., and Zhou, L. (2022). Regulation of cancer progression by circRNA and functional proteins. *J. Cell Physiol.* 237 (1), 373–388. doi:10.1002/jcp.30608

Kjems, J. (2022). The emerging roles of circRNAs in cancer and oncology. *Nat. Rev. Clin. Oncol.* 19 (3), 188–206. doi:10.1038/s41571-021-00585-y

Lin, Z. (2022). Identification of six diagnostic biomarkers for chronic lymphocytic leukemia based on machine learning algorithms. *J. Oncol.* 2022, 3652107. doi:10.1155/2022/3652107

MatveevaBaulina, N. A. M., Kiselev, I. S., Titov, B. V., and Favorova, O. O. (2022). MiRNA miR-375 as a multifunctional regulator of the cardiovascular system. *Mol. Biol. Mosk.* 56 (3), 418–427. doi:10.31857/S0026898422020100

Miao, P., Zhang, S., Gong, Z., and Yan, Q. (2022). The influence of circular RNAs on autophagy and disease progression. *Autophagy* 18 (2), 240–253. doi:10.1080/15548627.2021.1917131

Ming, C., Xu, J., and Zhu, D. (2022). Circular RNA in cancer development and immune regulation. *J. Cell Mol. Med.* 26 (6), 1785–1798. doi:10.1111/jcmm.16102

Petar, P., and Nikolaus, G. (2014). circBase: a database for circular RNAs. *RNA* 20 (11), 1666–1670. doi:10.1261/rna.043687.113

Qidong, Y., Nan, L., and Kai, Z. (2022). Homo sapiens circular RNA 0003602 (Hsa_circ_0003602) accelerates the tumorigenicity of acute myeloid leukemia by modulating miR-502-5p/IGF1R axisMol. *Cell biochem.* 477 (2), 635–644.

Qin, T., Li, S., and Liu, J. (2022). Bioinformatics analysis and identification of hub genes and immune-related molecular mechanisms in chronic myeloid leukemia. *PeerJ* 10, e12616. doi:10.7717/peerj.12616

Ren, S., Wu, X., and Chen, T. (2021). Downregulation of miR-375 contributes to ERBB2-mediated VEGFA overexpression in esophageal cancer. *J. Cancer* 12 (23), 7138–7146. doi:10.7150/jca.63836

Shi, H., Li, L., and Guan, W. (2016). Expression patterns of SH3BGR family members in zebrafish development. *Dev. Genes Evol.* 226 (4), 287–295. doi:10.1007/s00427-016-0552-5

Shuhong, S., Xu, Y., Wei, L., and Gao, H. (2005). NMR structure and regulated expression in APL cell of human SH3BGRL3. *febslet* 579, 2788–2794. doi:10.1016/j.febslet.2005.04.011

Tracy, K., and Murphy, W. L. Y. (2017). Cytarabine and daunorubicin for the treatment of acute myeloid leukemia. *Expert Opin. Pharmacother.* 18 (16), 1765–1780. doi:10.1080/14656566.2017.1391216

Wang, K., Yang, H., and Peng, B. (2019). TIP-B1 promotes kidney clear cell carcinoma growth and metastasis via EGFR/AKT signaling. *Aging (Albany NY)* 11 (18), 7914–7937. doi:10.18632/aging.102298

Wang, Y., and Zhu, C. (2021). CircRNA circ_POLA2 is upregulated in acute myeloid leukemia (AML) and promotes cell proliferation by suppressing the production of mature miR-34a. *Cancer Manag. Res.* 13, 3629–3637. doi:10.2147/CMAR.S281690

Wei, Z., Wang, C., and Wang, C. (2021). SH3BGRL3, transcribed by STAT3, facilitates glioblastoma tumorigenesis by activating STAT3 signaling. *Biochem. Biophys. Res. Commun2021* 556, 114–120. doi:10.1016/j.bbrc.2021.03.165

Wu, J., Liu, W., and Xiao, Y. (2022). CircNFIX knockdown inhibited AML tumorigenicity by the miR-876-3p/TRIM31 axis. *Hematology* 27 (1), 1046–1055. doi:10.1080/16078454.2022.2115699

Xiaodan, L., Xiaoping, L., Mansi, C., Luo, A., He, Y., and Liu, S. (2021). CircRNF220, not its linear cognate gene RNF220, regulates cell growth and is associated with relapse in pediatric acute myeloid leukemia. *Mol. Cancer* 20, 139. doi:10.1186/s12943-021-01395-7

Xu, X., Liu, Q., and He, S. (2021). MicroRNA-375: Potential cancer suppressor and therapeutic drug. *Biosci. Rep.* 41 (9), BSR20211494. doi:10.1042/BSR20211494

Yang, B. B., and Ding, X. (2019). Circbank: A comprehensive database for circRNA with standard nomenclature. *RNA Biol.* 16 (7), 899–905. doi:10.1080/15476286.2019.1600395

Yang, Q. (2020). Identification of DGUOK-AS1 as a prognostic factor in breast cancer by bioinformatics analysis. *Front. Oncol.* 10, 1092. doi:10.3389/fonc.2020.01092

Yang, Q., Zhao, H., and Zhao, R. (2022). Hsa_circ_0015278 regulates FLT3-ITD AML progression via ferroptosis-related genes. *Genes Cancers (Basel)* 15 (1), 71. doi:10.3390/cancers15010071

Yanjun, W., Yang, S., Chen, J., and Wang, Y. (2021). Identification and validation of a prognostic risk-scoring model based on ferroptosis-associated cluster in acute myeloid leukemia. *Front. Cell Dev. Biol2022* 9, 800267. doi:10.3389/fcell.2021.800267

Zhang, J. (2022). Predicting circRNA-drug sensitivity associations via graph attention auto-encoder. *BMC Bioinforma.* 23 (1), 160. doi:10.1186/s12859-022-04694-y

Zhang, P. F., Yang, X., and Zhu, S. Q. (2022). The circular RNA circHMGB2 drives immunosuppression and anti-PD-1 resistance in lung adenocarcinomas and squamous cell carcinomas via the miR-181a-5p/CARM1 axis. *Mol. Cancer* 21 (1), 110. doi:10.1186/s12943-022-01586-w

Zhiyuan, Z., Wei, W., Zehang, L., Liu, S., Chen, Q., and Jiang, X. (2021). Identification of seven novel ferroptosis-related long non-coding RNA signatures as a diagnostic biomarker for acute myeloid leukemia. *BMC Med. Genomics* 14, 236. doi:10.1186/s12920-021-01085-9

frontiers | Frontiers in Cell and Developmental Biology

TYPE Original Research
PUBLISHED 28 September 2023
DOI 10.3389/fcell.2023.1257314



OPEN ACCESS

EDITED BY
Yi Yao,
Renmin Hospital of Wuhan University, China

REVIEWED BY
Eswari Dodagatta-Marri,
University of California, United States
Luis Chávez-Sánchez,
Mexican Social Security Institute (IMSS), Mexico

*CORRESPONDENCE
Liang Ding,
879269339@qq.com
Zhiyong Wang,
wangzhiyong67@163.com
Yanhong Ni,
niyanhong12@163.com

†These authors have contributed equally to this work

RECEIVED 12 July 2023
ACCEPTED 18 September 2023
PUBLISHED 28 September 2023

CITATION
Dong Y, Hu X, Xie S, Song Y, He Y, Jin W, Ni Y, Wang Z and Ding L (2023), ICOSLG-associated immunological landscape and diagnostic value in oral squamous cell carcinoma: a prospective cohort study. *Front. Cell Dev. Biol.* 11:1257314. doi: 10.3389/fcell.2023.1257314



# ICOSLG-associated immunological landscape and diagnostic value in oral squamous cell carcinoma: a prospective cohort study

Yuexin Dong[1†], Xinyang Hu[1†], Shixin Xie[1], Yuxian Song[1], Yijia He[1], Wanyong Jin[1], Yanhong Ni[1*], Zhiyong Wang[2*] and Liang Ding[1*]

[1]Central Laboratory of Stomatology, Affiliated Hospital of Medical School, Nanjing Stomatological Hospital, Nanjing University, Nanjing, China, [2]Department of Oral and Maxillofacial Surgery, Affiliated Hospital of Medical School, Nanjing Stomatological Hospital, Nanjing University, Nanjing, China

**Background:** We previously reported that stroma cells regulate constitutive and inductive PD-L1 (B7-H1) expression and immune escape of oral squamous cell carcinoma. ICOSLG (B7-H2), belongs to the B7 protein family, also participates in regulating T cells activation for tissue homeostasis via binding to ICOS and inducing ICOS$^+$ T cell differentiation as well as stimulate B-cell activation, while it appears to be abnormally expressed during carcinogenesis. Clarifying its heterogeneous clinical expression pattern and its immune landscape is a prerequisite for the maximum response rate of ICOSLG-based immunotherapy in a specific population.

**Methods:** This retrospective study included OSCC tissue samples (n = 105) to analyze the spatial distribution of ICOSLG. Preoperative peripheral blood samples (n = 104) and independent tissue samples (n = 10) of OSCC were collected to analyze the changes of immunocytes (T cells, B cells, NK cells and macrophages) according to ICOSLG level in different cellular contents.

**Results:** ICOSLG is ubiquitous in tumor cells (TCs), cancer-associated fibroblasts (CAFs) and tumor infiltrating lymphocytes (TILs). Patients with high ICOSLGTCs or TILs showed high TNM stage and lymph node metastasis, which predicted a decreased overall or metastasis-free survival. This sub-cohort was featured with diminished CD4$^+$ T cells and increased Foxp3+ cells in invasive Frontier *in situ*, and increased absolute numbers of CD3$^+$CD4$^+$ and CD8$^+$ T cells in peripheral blood. ICOSLG also positively correlated with other immune checkpoint molecules (PD-L1, CSF1R, CTLA4, IDO1, IL10, PD1).

**Conclusion:** Tumor cell-derived ICOSLG could be an efficient marker of OSCC patient stratification for precision immunotherapy.

KEYWORDS

**ICOSLG, oral squamous cell carcinoma, prognosis, lymphocyte subsets, immune checkpoints**

# 1 Introduction

Head and neck squamous cell carcinoma (HNSCC) is one of the most deadly cancers in the world. Oral squamous cell carcinoma (OSCC) is the most common cancer in HNSCC and has the characteristics of high metastasis rate and high recurrence rate (Yang et al., 2021).The treatment of OSCC is still mainly using traditional methods (surgery, chemotherapy, radiotherapy), unfortunately, this treatment mode is sticky to further improve the survival of OSCC patients (Chai et al., 2020).Tumor immunotherapy is a relatively novel treatment method, which has respectable prospects for controlling tumor recurrence and metastasis. Currently, the choice of immunotherapy for OSCC is extremely especially limited, so we urgently need more therapeutic targets to advance the survival and prognosis of OSCC patients (Almangush et al., 2021).

We previously found that stromal IL-33/ST2 signaling directly or indirectly enhanced PD-L1 (B7-H1)-mediated immune escape and OSCC progression (Ding et al., 2018; Zhao et al., 2023). ST2high/PD-L1high OSCC patients might be benefit more from anti-PD-1/L1 therapy. Notably, another immune checkpoint ICOSLG (ICOS ligand, B7-H2) is also a member of the B7 family, encoded by CD275, and is a ligand for the Inducible T cell co-stimulator (ICOS) (Greenwald et al., 2005; Henderson et al., 2011). In addition to the expression of professional antigen presenting cells (APCs, including B cells, macrophages, and dendritic cells), ICOSLG is also found in non-lymphocytes (including mesenchymal cells, vascular endothelial cells, Fibroblasts, tumor cells) in certain environments, such as tumor microenvironment. ICOSLG locates in the cell membrane and cytoplasm (Roussel and Vinh, 2021; Külp et al., 2022) and its interaction with ICOS can induce the production of various cytokines, thereby stimulating the differentiation and proliferation of T cells and promoting the activation of B cells (Zhang et al., 2023). Deletion or overexpression of ICOSLG may be associated with immune system diseases. Deletion may lead to T cell dysfunction-related diseases, such as Combined immunodeficiencies (CIDs) (Robertson et al., 2015; Roussel et al., 2018), and its overexpression may be associated with acute myeloid leukemia (AML) (Han et al., 2018).

As a co-stimulator of T cells, ICOSLG has also received much attention in the tumor microenvironment and its immune escape process (Zhang et al., 2022). It has been reported that high expression of ICOSLG promotes immunosuppression and tumor escape in gastric cancer by down-regulating function of Th1 type cells (Chen et al., 2003). In colorectal cancer, studies have found that increased expression of ICOSLG in $CD8^+$ T cells leads to poor prognosis in patients (Cao et al., 2018). In patients with liver cancer, the high expression of ICOSLG is significantly associated with the recurrence and metastasis of patients, and the prognosis of positive patients is regularly poor (Zheng et al., 2019). In addition, in glioblastoma, high expression of ICOSLG promotes the proliferation of $CD4^+$ T cells by stimulating the secretion of IL-10, but knocking out ICOSLG of tumor cells increases the number of $CD8^+$ T cells (Iwata et al., 2020). However, the expression pattern and prognostic value of ICOSLG in OSCC remain unclear.

In this study, we investigated the expression pattern of ICOSLG in oral squamous cell carcinoma, including tumor cells (TCs), cancer-associated fibroblasts (CAFs) and tumor infiltrating lymphocytes (TILs). Then the clinicopathological features of ICOSLG and its correlation with prognostic value were further analyzed. Considering the important role of ICOSLG in immune cells, we also analyzed the relationship between ICOSLG and lymphocyte subsets in peripheral blood and resident tissue misgovernment. In addition, considering that tumor cells can be used as the main mechanism of immune resistance through the immune checkpoint pathway, we further studied the association between ICOSLG and immune checkpoint molecules. The research concept of this paper is shown in Figure 1.

# 2 Materials and methods

## 2.1 Patients and samples

All the schemes of this study were examined and approved by the Ethics Committee of Nanjing Stomatology Hospital, Medical School of Nanjing University (No.2019NL-009(KS)). Informed consent was provided by the patients for the use of their tissues and data. The study was carried out in accordance with the Declaration of Helsinki. From 2014 to 2017, 105 primary OSCC patients were enrolled. The inclusion and exclusion criteria of patients were the same as those of our previous studies (Zhu et al., 2020). None of the patients received preoperative chemotherapy, radiotherapy, or other cancer-related treatments. Patients with history of systemic illness or missing survival data were excluded. These patients with primary tumor were diagnosed by hematoxylin and eosin staining by two experienced pathologists. These patients were followed up for 2–60 months, and the median was 38 months. Paraffin-embedded OSCC tissue slices were obtained from the pathology department and used for IHC study. 104 blood samples from OSCC patients were obtained for flow cytometry assay before any related treatments.

## 2.2 Immunohistochemistry and quantification

The protocol of IHC of formalin-fixed paraffin-embedded sections and scoring details of IHC was performed as previously described (Zhao et al., 2019). Anti-ICOSLG (ab257321, Abcam, Waltham, MA, USA) were used at a dilution ratio of 1:400, and the serial sections were incubated with primary antibodies such as anti-CD4 (ZSGB-BIO, ZM-0418), anti-CD8 (ZSGB-BIO, ZA-0508), anti-CD19 (ZSGB-BIO, ZM-0038), anti-CD56 (ZSGB-BIO, ZM-0057), anti-CD68 (ZSGB-BIO, ZM-0464), and anti-Foxp3 (ab253297, Abcam). We used PBS to replace the primary antibody as negative control. Due to insufficient tissues and individual differences in OSCC samples, certain regions or cell types, such as CAFs and TILs, could not be detected in the IHC staining.

Protein expression was evaluated according to stain intensity and the percentage of positive cells. The intensity of staining was graded as 1 = weak staining, 2 = moderate staining and 3 = strong staining. The percentage of stained cells was graded as 0 = 0–5%, 1 = 6–25%, 2 = 26–50%, 3 = 51–75% and 4 = 75–100%. The final

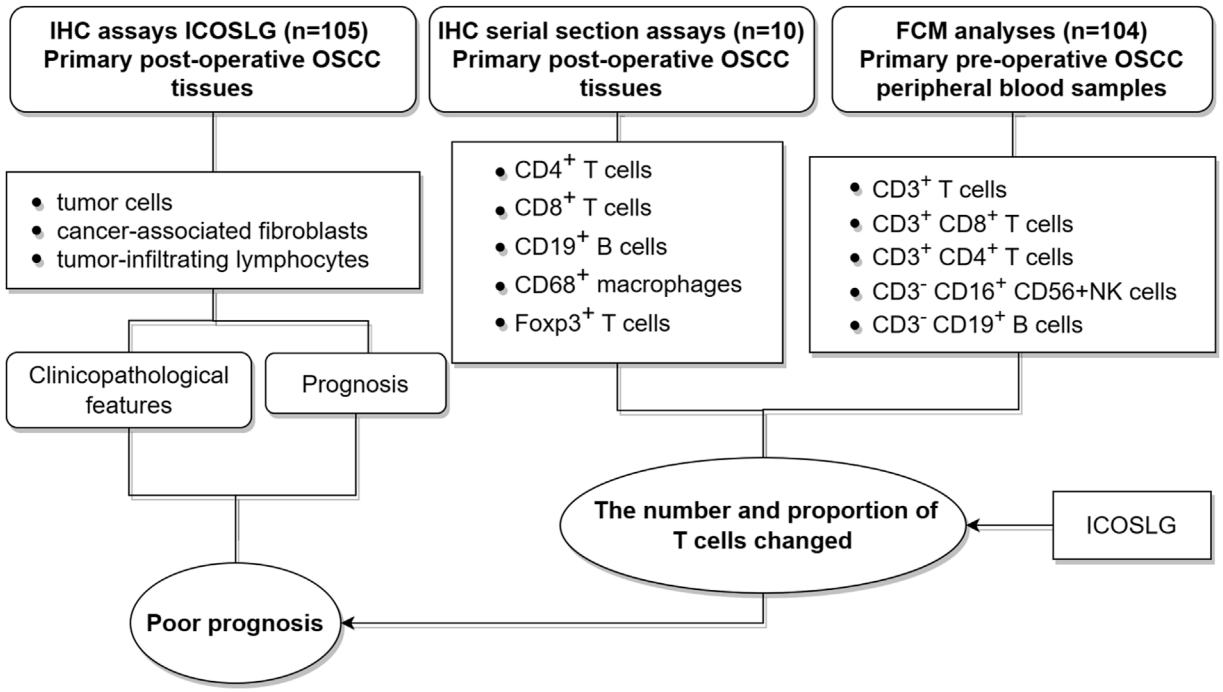


FIGURE 1
Experimental process design diagram.

score was obtained by multiplying the two scores. The expression levels of ICOSLG in TCs and CAFs, TILs were defined as "low" when it is lower than the median value and as "high" when it is equal to or greater than the median. The IHC staining results of ICOSLG were evaluated by two senior pathologists who did not know the patient's data, and the median values were calculated for further analysis.

## 2.3 Preparation of PBMC

Fresh whole blood from patients was collected with EDTA tube (ethylenediamine tetraacetic acid tube, BD Vacutainer). On average, 1.0 × 107 cells were isolated from 5 mL of whole blood. The collected whole blood was 2× diluted with Hanks' Balanced Salt solution (HBSS, Gibco, Rockville, MD, USA) for loading on Ficoll-paque (Pharmacia, Uppsala, Sweden). The blood-loaded sample on Ficoll solution is centrifuged at 2000 rpm for 20 min (Acceleration/Break = lowest/zero), and middle layer was collected as PBMC. The collected cells were enumerated and stored in liquid nitrogen tank until us. All study participants provided informed consent, and was approved by the ethical committee of Nanjing Stomatology Hospital, Medical School of Nanjing University.

## 2.4 Flow cytometry assay

For the cell subtypes of PBMC analysis, cells were collected and washed with PBS twice and then suspended in 200 μL PBS. For enumeration of mature human T ($CD3^+$) cells, helper/inducer T ($CD3^+$ $CD4^+$) cells, cytotoxic T ($CD3^+$ $CD8^+$) cells, B ($CD19^+$) cells, and NK ($CD3^-CD16^+$and/or$CD56^+$) lymphocytes, $CD3^-$FITC/$CD8^-$PE/$CD45^-$PerCP/$CD4^-$APC reagent, BD Multitest $CD3^-$FITC/$CD16^-PE^+$ $CD56^-$PE/$CD45^-$PerCP/$CD19^-$APC reagent were used according to the manufacturer's instructions, respectively (Cat No.340503, BD Multitest™), then quantified by flow cytometry on a FACS Calibur instrument.

## 2.5 Gene correlation analysis in cBioPortal

The cBioPortal for Cancer Genomics (http://cBioPortal.org) is a website for exploration of multi-dimensional cancer genomics data, providing readily understandable gene expression event (Gao et al., 2013). We used cBioPortal to analyze the correlation between ICOSLG and specific lymphocyte subset markers as well as specific immune checkpoint molecules in HNSCC. Co-expression was calculated based on the cBioPortal's online instructions.

## 2.6 Tisch2 analysis

Tumor Immune Single-cell Hub 2 (Tisch2, http://tisch.comp-genomics.org) is a scRNA-seq database focusing on tumor microenvironment (TME). TISCH2 provides detailed cell-type annotation at the single-cell level, enabling the exploration of TME across different cancer types. We used TISCH2 to evaluate the difference in ICOSLG between tumor cells and normal cells in different tumors. In addition, according to the online description of

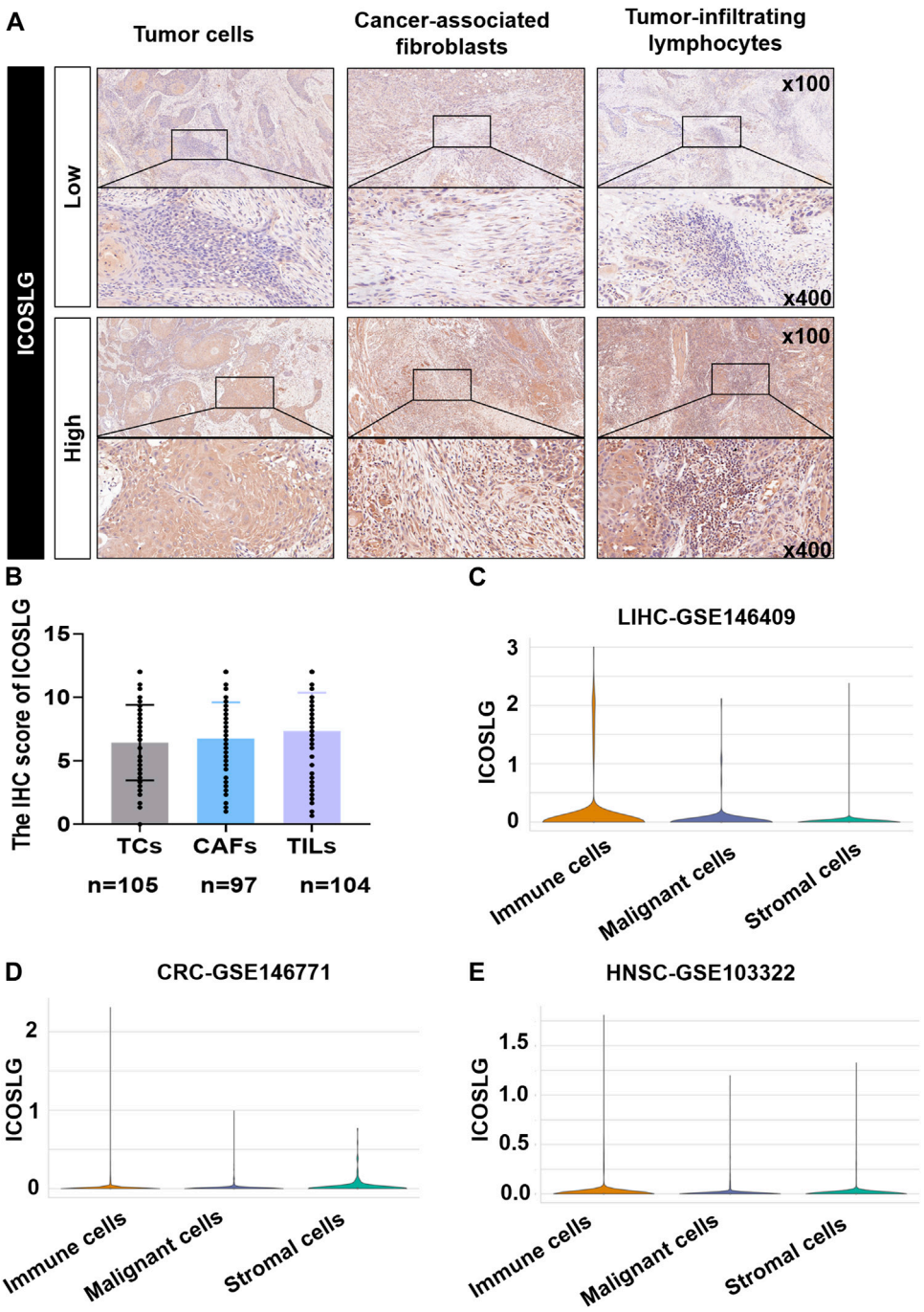


FIGURE 2
The expression of ICOSLG in OSCC and other tumors. **(A)**. Typical IHC staining of ICOSLG on TCs, CAFs and TILs. **(B)**. The IHC score of ICOSLG in TCs, FLCs, and TILs from OSCC patients. The ICOSLG expression in liver hepatocellular carcinoma **(C)**, colorectal cancer **(D)**, and head and neck squamous cell carcinoma **(E)** with Tisch2.

Tisch2, we also evaluated the correlation between ICOSLG and specific immune infiltrating cell subsets at the transcriptional level.

## 2.7 Statistical analysis

SPSS 18.0 and GraphPad Prism 8.0 software packages were used for data analysis and graphic processing. Pearson's chi-square test, Fisher's exact test and Chi-square test were used to compare clinicopathological features. The Mann–Whitney U test was used to compare the two groups. Survival analysis includes overall survival (OS), metastasis-free survival (MFS) and disease-free survival (DFS), which were evaluated by Kaplan–Meier and log-rank test. Further multivariate analysis was carried out by Cox proportional hazards regression model to determine the independent risk factors, adjusted hazard ratio (HR) and 95%

**TABLE 1** Association between ICOSLG expression and clinicopathological characteristics in OSCC patients.

| Characteristics | TCs | | | | | CAFs | | | | | TILs | | | | |
|---|---|---|---|---|---|---|---|---|---|---|---|---|---|---|---|
| | Total | Low | High | χ2 | *P* | Total | Low | High | χ2 | *P* | Total | Low | High | χ2 | *P* |
| **Gender** | | | | | | | | | | | | | | | |
| Female | 43 | 21 (48.8%) | 22 (51.2%) | 0.138 | 0.71 | 38 | 19 (50%) | 19 (50%) | 0.06 | 0.807 | 43 | 22 (51.2%) | 21 (48.8%) | 0.28 | 0.597 |
| Male | 62 | 28 (45.2%) | 34 (54.8%) | | | 59 | 28 (47.5%) | 31 (52.5%) | | | 61 | 28 (45.9%) | 33 (54.1%) | | |
| **Age** | | | | | | | | | | | | | | | |
| <60 | 32 | 17 (53.1%) | 15 (46.9%) | 0.771 | 0.38 | 31 | 16 (51.6%) | 15 (48.4%) | 0.182 | 0.67 | 32 | 17 (53.1%) | 15 (46.9%) | 0.472 | 0.492 |
| ≥60 | 73 | 32 (43.8%) | 41 (56.2%) | | | 66 | 31 (47%) | 35 (53%) | | | 72 | 33 (45.8%) | 39 (54.2%) | | |
| **TNM** | | | | | | | | | | | | | | | |
| I-II | 37 | 23 (62.2%) | 14 (37.8%) | 5.512 | **0.019*** | 32 | 20 (62.5%) | 12 (37.5%) | 3.772 | 0.052 | 37 | 24 (64.9%) | 13 (35.1%) | 6.484 | **0.011*** |
| III-IV | 68 | 26 (38.2%) | 42 (61.8%) | | | 65 | 27 (41.5%) | 38 (58.5%) | | | 67 | 26 (38.8%) | 41 (61.2%) | | |
| **T stage** | | | | | | | | | | | | | | | |
| 1–2 | 69 | 36 (52.2%) | 33 (47.8%) | 2.452 | 0.117 | 62 | 34 (54.8%) | 28 (45.2%) | 2.805 | 0.094 | 69 | 38 (55.1%) | 31 (44.9%) | 4.019 | **0.045*** |
| 3–4 | 36 | 13 (36.1%) | 23 (63.9%) | | | 35 | 13 (37.1%) | 22 (62.9%) | | | 35 | 12 (34.3%) | 23 (65.7%) | | |
| **Lymph node metastasis** | | | | | | | | | | | | | | | |
| No | 53 | 32 (60.4%) | 21 (39.6%) | 8.083 | **0.004*** | 48 | 29 (60.4%) | 19 (39.6%) | 5.445 | **0.020*** | 52 | 31 (59.6%) | 21 (40.4%) | 5.547 | **0.019*** |
| Yes | 52 | 17 (32.7%) | 35 (67.3%) | | | 49 | 19 (38.8%) | 31 (61.2%) | | | 52 | 19 (36.5%) | 33 (63.5%) | | |
| **Differentiation** | | | | | | | | | | | | | | | |
| Well | 21 | 6 (28.6%) | 15 (71.4%) | 3.453 | 0.063 | 20 | 9 (45%) | 11 (55%) | 0.12 | 0.729 | 21 | 7 (33.3%) | 14 (66.7%) | 2.291 | 0.13 |
| Moderate to poor | 84 | 43 (51.2%) | 41 (48.8%) | | | 77 | 38 (49.4%) | 39 (50.6%) | | | 83 | 43 (51.8%) | 40 (48.2%) | | |

TCs, tumor cells; CAFs, cancer-associated fibroblasts; TILs, tumor-infiltrating lymphocytes; χ2, Pearson's chi-squared test.* represented that differences were considered statistically significant with $P < 0.05$.





10.3389/fcell.2023.1257314

10.3389/fcell.2023.1257314

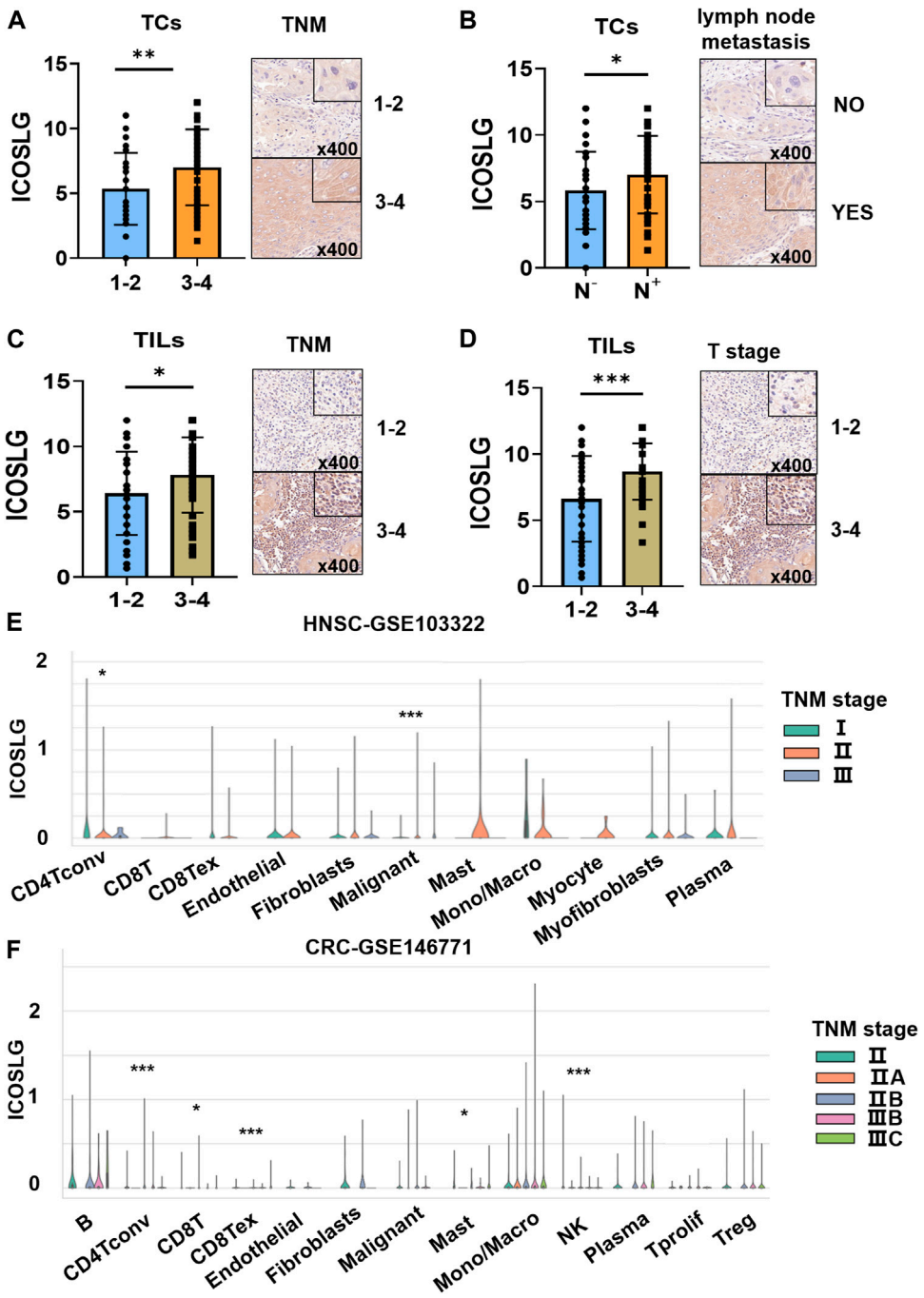


FIGURE 3
The relationship between ICOSLG and clinicopathological parameters. ICOSLG expression with different TNM stages **(A)** and lymph node metastasis **(B)** in TCs, different TNM stages **(C)** and T stages **(D)** in TILs. Tisch2 database was used to detect the relationship between the expression of ICOSLG in different cells and TNM stage in colorectal cancer **(E)** and head and neck squamous cell carcinoma **(F)**. *, **, *** represented that differences were considered statistically significant with $p < 0.05$, $p < 0.01$ and $p < 0.001$ respectively, and ns represented no statistical differences.

confidence interval (CI) of OSCC. Co-expression between ICOSLG and immune cell markers and immune checkpoint molecules was investigated by Pearson correlation analysis. The partial Spearman's correlation analysis was used to analyze the association between ICOSLG and markers of specific immune infiltrating cell subset at transcription level. All statistical tests were two-sided, and $p < 0.05$ was considered to be significant.

# 3 Results

## 3.1 ICOSLG is widely expressed in TC, CAF and TIL in OSCC

ICOSLG was expressed in the cell membrane and cytoplasm of tumor cells (TCs), cancer-associated fibroblasts (CAFs) and tumor

10.3389/fcell.2023.1257314

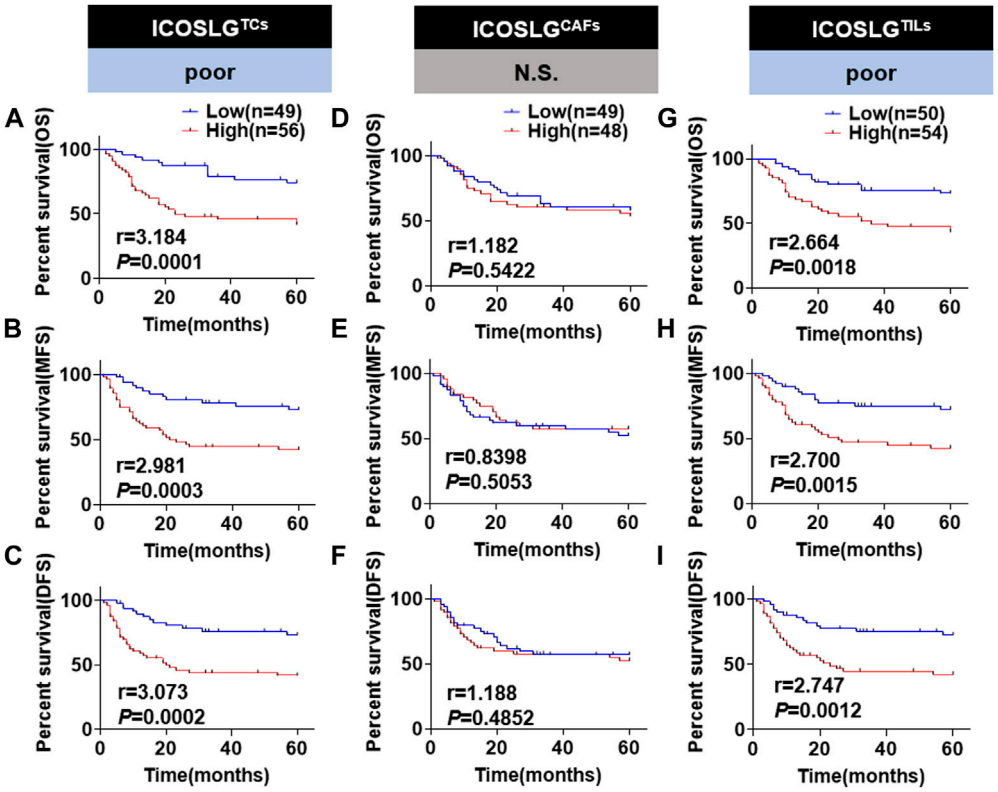


J

| OS Univariate analysis | Hazard ratio (95% CI) | | P value |
|---|---|---|---|
| Gender( Female vs Male) | 1.318 | (0.711-2.443) | 0.380 |
| Age(≥60 vs <60) | 1.066 | (0.552-2.059) | 0.849 |
| TNM Stage(III–IV vs I–II) | 1.763 | (0.864-3.596) | 0.119 |
| T-stage(3–4 vs. 1–2) | 0.794 | (0.411-1.533) | 0.491 |
| Lymph node metastasis(Yes vs. no) | 2.776 | (1.434-5.375) | **0.002*** |
| Differentiation( Moderate to poor vs Well) | 1.822 | (0.766-4.336) | 0.175 |
| ICOSLG in TCs (High vs Low) | 3.136 | (1.568-6.273) | **0.001*** |
| ICOSLG in CAFs (High vs Low) | 1.819 | (0.970-3.412) | 0.062 |
| ICOSLG in TILs (High vs Low) | 2.426 | (1.256-4.685) | **0.008*** |
| **MFS Univariate analysis** | | | |
| Gender( Female vs Male) | 1.363 | (0.735-2.526) | 0.326 |
| Age(≥60 vs <60) | 1.156 | (0.599-2.233) | 0.665 |
| TNM Stage(III–IV vs I–II) | 1.765 | (0.865-3.605) | 0.119 |
| T-stage(3–4 vs. 1–2) | 0.807 | (0.418-1.558) | 0.522 |
| Lymph node metastasis(Yes vs. no) | 2.594 | (1.341-5.021) | **0.005*** |
| Differentiation( Moderate to poor vs Well) | 1.841 | (0.774-4.382) | 0.168 |
| ICOSLG in TCs (High vs Low) | 2.933 | (1.468-5.860) | **0.002*** |
| ICOSLG in CAFs (High vs Low) | 1.746 | (0.932-3.271) | 0.082 |
| ICOSLG in TILs (High vs Low) | 2.458 | (1.272-4.751) | **0.007*** |
| **OS Multivariate analysis** | | | |
| Lymph node metastasis(Yes vs. no) | 2.035 | (1.018-4.066) | **0.044*** |
| ICOSLG in TCs (High vs Low) | 2.059 | (0.952-4.452) | 0.066 |
| ICOSLG in TILs (High vs Low) | 1.621 | (0.797-3.294) | 0.182 |



FIGURE 4
The relationship between ICOSLG and the prognosis of OSCC patients. Kaplan-Meier survival curve of overall survival time (OS), metastasis-free survival time (MFS) and disease-free survival time (DFS) of OSCC patients, according to the expression of ICOSLG in TCs **(A–C)**, CAFs **(D–F)** and TILs **(G–I)**. Cox-regression analysis and forest plot of OS and MFS in OSCC patients **(J)**. CI, confidence interval; ICOSLGTCs, ICOSLG in TCs; ICOSLGCAFs, ICOSLG in CAFs; ICOSLGTILs, ICOSLG in TILs. * represented that differences were considered statistically significant with $p < 0.05$, N.S. represented no significance.

infiltrating lymphocytes (TILs) in 105 patients with OSCC. The typical low expression and high expression of ICOSLG IHC staining were shown in Figure 2A. In OSCC, the IHC score of TILs was generally higher than that of TCs. (Figure 2B). In the TISCH2 database, single-cell sequencing analysis showed that the mRNA expression of ICOSLG was significantly higher in TILs in liver hepatocellular carcinoma (Figure 2C), colorectal cancer (Figure 2D), and head and neck squamous cell carcinoma (Figure 2E).

## 3.2 Patients with high ICOSLG have a higher risk of TNM stage and lymph node metastasis

We then analyzed the relationship between the expression of ICOSLG and clinicopathological features of OSCC patients (Table 1). The results showed that in OSCC patients, the expression of ICOSLG was not significantly correlated with gender, age, and differentiation, but the high expression of ICOSLG in TCs (ICOSLGTCs) and TILs (ICOSLGTILs) was associated with higher risk of lymph node metastasis and advanced TNM stage. IHC results showed that high expression of ICOSLG in TCs (ICOSLGTCs) was associated with higher risk of lymph node metastasis (Figure 3A) and advanced TNM stage (Figure 3B), while ICOSLG in TILs (ICOSLGTILs) was significantly associated with advanced TNM stage (Figure 3C) and T stage (Figure 3D).We analyzed the Tisch2 database and found that in patients with head and neck squamous cell carcinoma, the high expression of ICOSLGTCs was significantly positively correlated with advanced TNM stage, while the high expression of ICOSLGTILs, especially $CD4^+$ T cells, was negatively correlated with advanced TNM stage (Figure 3E). The high expression of ICOSLG on $CD4^+$ T cells is positively correlated with advanced TNM stage in colorectal cancer (CRC) (Figure 3F).

## 3.3 High ICOSLG level in tumor cell and TILs predicts low survival rate of OSCC patients

In order to confirm the prognostic value of ICOSLG for OSCC, we used Kaplan-Meier survival rate to analyze the survival rate of patients with oral squamous cell carcinoma included in this study. The results showed that patients with increased ICOSLG expression in TCs had shorter overall survival (OS r = 3.184), metastasis-free survival (MFS r = 2.981) and disease-free survival (DFS r = 3.073) (Figures 4A–C). In addition, OSCC patients with more ICOSLG in TILs had shorter OS (r = 2.664), MFS (r = 2.700) and DFS (r = 2.747) (Figures 4G–I), which was not observed in ICOSLG in CAFs (ICOSLGCAFs) (Figures 4D–F).

We used univariate and multivariate Cox regression to analyze the prognostic value of clinicopathological features. The results showed that gender, age, TNM stage, T stage, differentiation and ICOSLG in CAFs (ICOSLGCAFs) had no significant predictive value for OS and MFS (all $p > 0.05$). Lymph node metastasis and high expression of ICOSLG in TCs and TILs were significantly different in OS and MFS, but not independent prognostic indicators of oral squamous cell carcinoma (Figure 4J).

## 3.4 Resident tissue $CD4^+$ T cells show an exhausted trend in patients with high $ICOSLG^{TCs\ or\ TILs}$

To explore whether the immune cell subsets of tumor tissues with high expression of ICOSLGTCs in OSCC patients changed, we determined the ICOSLG, CD4, CD8, CD19, CD68 and Foxp3 level of tumor centers and infiltration fronts in serial sections (Figures 5A,B). Next, we compared the proportion of CD4, CD8, CD19, CD68 and Foxp3 positive cells in lymphocytes of patients with high and low expression of ICOSLGTCs, as well as the proportion of CD4, CD8 positive cells and Fopx3+ cells, and divided them into invasive Frontier (Figure 5C) and tumor center (Figure 5D) for analysis. $CD4^+$ cells and $CD19^+$ cells in patients with high expression of ICOSLGTCs at the invasive Frontier showed a decreasing trend, while Foxp3+ cells showed an increasing trend. However, $CD4^+$ cells and $CD8^+$ cells in patients with high expression of ICOSLGTCs at the tumor center showed a decreasing trend.

We also analyzed the ICOSLGTILs-regulated in the intra-group correlation comparison of CD4, CD8, CD19, CD68, Foxp3, CD8/Foxp3, ICOSLGTCs, ICOSLGCAFs and ICOSLGTILs, we found that ICOSLGTILs were negatively correlated with CD4 and CD19 in the invasive Frontier (Figure 5E), while ICOSLGTILs were positively correlated with Foxp3 and ICOSLGTCs. In the tumor center (Figure 5F), ICOSLGTCs and ICOSLGTILs were negatively correlated with CD4 and CD8. Immune checkpoint proteins play a crucial role in the negative regulation of cellular immunity. Therefore, we used cBioPortal to further analyze the correlation between ICOSLG and immune checkpoint molecules, and analyzed the correlation between immune checkpoints (Figure 5G). We found that ICOSLG was positively correlated with inducible T cell co-stimulator (ICOS r = 0.403), TACTILE (CD96 r = 0.444), programmed death-ligand 1 (CD274 r = 0.124), colony-stimulating factor 1 receptor (CSF1R r = 0.409), cytotoxic T lymphocyte antigen 4 (CTLA4 r = 0.356), hepatitis A virus cellular receptor 2 (HAVCR2 r = 0.404), indoleamine 2,3-dioxygenase 1(IDO1 r = 0.224), interleukin 10 (IL10 r = 0.247), programmed cell death 1 (PDCD1 r = 0.400), and these immune checkpoints were also positively correlated.

## 3.5 $CD4^+$ and $CD8^+$ T cells in peripheral blood of patients with high expression of ICOSLGTCs are also significantly reduced

IHC serial sections of OSCC patients showed a correlation between ICOSLG and the number of $CD4^+$, $CD8^+$, $CD19^+$, Foxp3+ cells *in situ*. Therefore, we used flow cytometry to analyze the proportion of peripheral blood T, B and NK cells between the low ICOSLG group and the high ICOSLG group, and the strategy of gating lymphocytes was shown in Figure 6A. We found that the absolute counts of $CD3^+$ T cells, $CD3^+$ $CD4^+$ T cells and $CD3^+$ $CD8^+$ T cells in ICOSLGTCs high expression samples were significantly lower (Figure 6E). However, there was no difference in the percentage of lymphocyte subsets in ICOSLGTCs (Figure 6B) and the frequency and number of lymphocyte subsets in ICOSLGCAFs (Figures 6C, F), ICOSLGTILs (Figures 6D, G) between the low and high subgroups of ICOSLG.

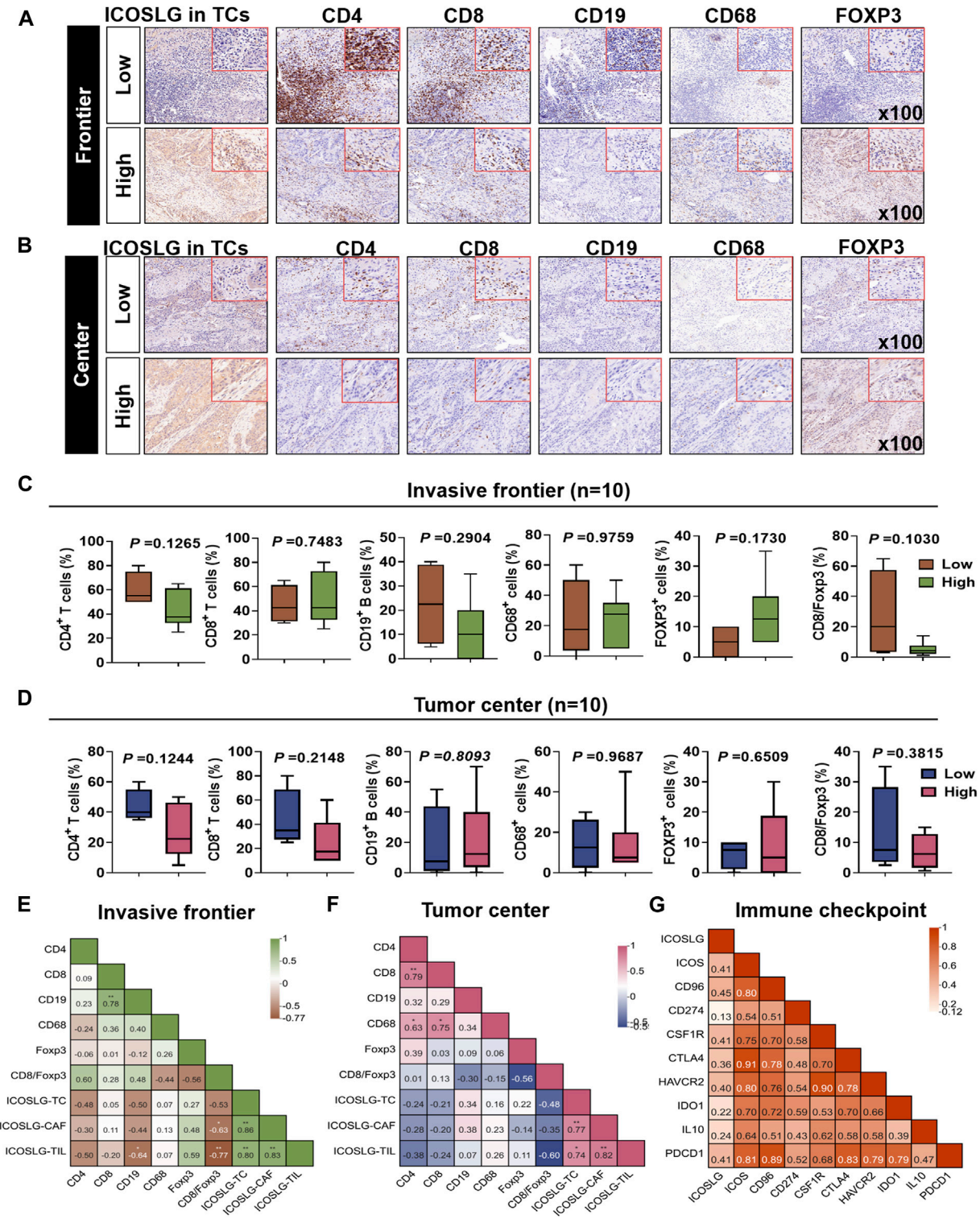


FIGURE 5
The proportion of different immune cells was affected by ICOSLG. The correlation between ICOSLG expression and CD4⁺ T cells, CD8⁺ T cells, CD19⁺ B cells, CD68⁺ TAMs and FOXP3+ Tregs in OSCC tumor invasive Frontier **(A)** and tumor center **(B)** serial sections with immunohistochemistry. The proportion of the above cells in the tumor invasive Frontier **(C)** and tumor center **(D)** was compared between the ICOSLG high expression group and the low expression group, as well as the intra-group correlation analysis with ICOSLGTC, ICOSLGCAF, ICOSLGTILs **(E,F)**. Intra-group correlation analysis between ICOSLG expression and immune checkpoints in HNSCC with cBioPortal database **(G)**.

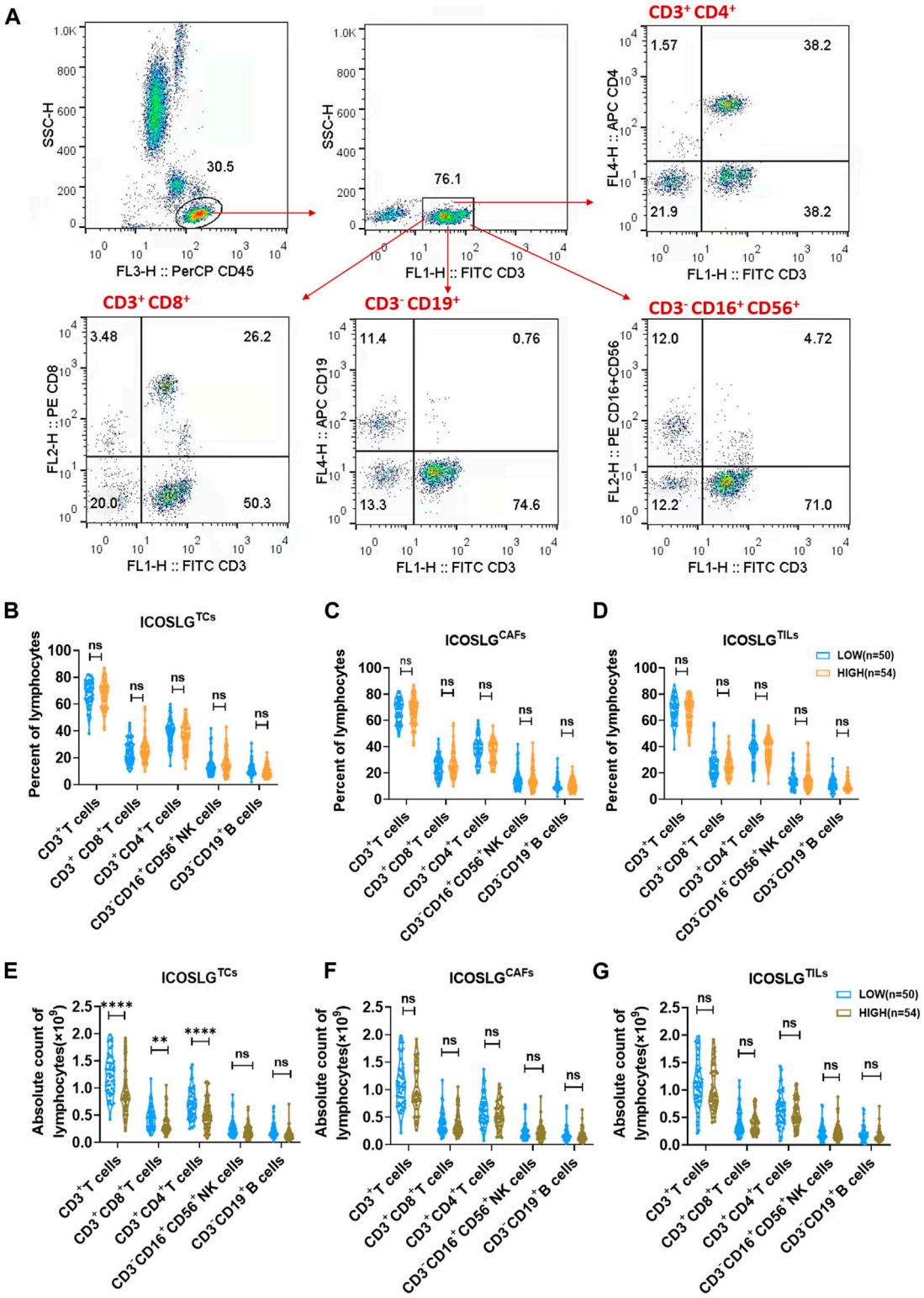


FIGURE 6
The change of lymphocytes subset in PBMC and tissue of OSCC patients according to ICOSLG level. **(A)**: Flow-cytometry dot plots show the strategy for gating lymphocytes, $CD3^+$ T cells, $CD3^+CD4^+$ T cells and $CD3^-CD16^+CD56^+$ NK cells with distinct expression of ICOSLG TILs. The radio of lymphocytes subset of PBMCs in patients with distinct expression of ICOSLGTCs **(B)**, ICOSLGCAFs **(C)**, ICOSLGTILs **(D)**. The absolute count of lymphocytes subset of PBMCs in patients with distinct expression of ICOSLGTCs **(E)**, ICOSLGCAFs **(F)**, ICOSLGTILs **(G)**. **, **** represented that differences were considered statistically significant with $p < 0.01$, $p < 0.0001$ respectively, and ns represented no statistical differences.

# 4 Discussion

ICOSLG was found in monocyte-derived dendritic cells, initial studies of ICOSLG focused on immune cells, its co-expression with ICOS can regulate the activation of $CD4^+$ T cells (Wang et al., 2000; Wallin et al., 2001; Witsch et al., 2002).At present, with the expansion of research, ICOSLG has been confirmed to be associated with a variety of diseases, including immunodeficiency diseases (Dalakas, 2005), hematological diseases (Tamura et al., 2005). In addition, ICOSLG is expressed in a variety of tumors, such as glioblastoma (Schreiner et al., 2003), gastric cancer (Chen et al., 2003), colorectal cancer (Xiao et al., 2005), etc. The results of this study showed that ICOSLG was widely expressed in OSCC samples and was significantly expressed. Therefore, we conclude that ICOSLG is actually involved in the occurrence and development of tumors, and can regulate the behavior of tumor cells and affect the changes of tumor microenvironment.

Current studies have shown that the expression of ICOSLG in a variety of tumors is related to the biological behavior of tumors and the poor prognosis of patients. In melanoma, the high expression of ICOSLG on tumor cells is closely related to the decrease of patient survival. In addition, in gastric cancer, co-stimulation of ICOS and ICOSLG can lead to the activation of Tregs cells and may be associated with poor prognosis of patients (Nagase et al., 2017). According to our analysis, in OSCC, the high expression of ICOSLG in TCs and TILs was related to TNM stage and lymph node metastasis, and the OS, MFS and DFS of patients with high expression of ICOSLG in TCs and TILs were significantly shorter, indicating that the high expression of ICOSLG in OSCC may be a poor prognostic indicator. However, it should be noted that the high expression of ICOSLG in TCs and TILs is not an independent prognostic factor for OSCC.

ICOSLG is closely related to the functional activation of T cells. In the tumor microenvironment, it plays an important role in the development of tumors by participating in the regulation of immune cell function. In breast cancer, the activation of ICOS and ICOSLG is closely related to the accumulation of Tregs cells and DCs, and is also an indispensable key factor in the activation of Tregs cells (Faget et al., 2012). In esophageal squamous cell carcinoma, inhibition of ICOSLG can reduce the number of Tregs cells, thereby improving the effect of tumor immunotherapy (Zhang et al., 2022). In myeloma, tumor cells with high expression of ICOSLG have stronger proliferation ability and can activate ICOS-ICOSLG pathway to inhibit tumor immune response (Yamashita et al., 2009). Our results also found that in OSCC, the high expression of ICOSLG in TCs led to a decrease in $CD4^+$ T cells in the tumor front and center and peripheral blood, while the proportion of Foxp3+ cells in the tumor infiltration front showed an increasing trend, indicating that the high expression of ICOSLG is likely to be involved in the occurrence of immunosuppression in the tumor microenvironment.

In the past few years, with the increasing use of immunotherapy, especially immune checkpoint inhibitors, there have been significant breakthroughs in the survival rate and prognosis of cancer patients (Miller et al., 2016). Immune checkpoint therapy enhances the anti-tumor effect in the tumor microenvironment by regulating the function of T cells (Sharma and Allison, 2015).In a preclinical drug experiment, it was found that the ICOS-ICOSLG pathway has a good clinical application prospect for immunotherapy of various tumors (Solinas et al., 2020). Our study found that the high expression of ICOSLG in HNSCC was positively correlated with multiple immune checkpoints. Including ICOS, CD96, PD-L1 (CD274), CSF1, CTLA, HAVCR2, IDO1, IL10, and PDCD1 were positively correlated.

In summary, we determined that ICOSLG was associated with the survival of OSCC patients and had a significant tumor-promoting effect. In addition, ICOSLG was positively correlated with Foxp3+ cells and negatively correlated with $CD4^+$ T cells, indicating that ICOSLG is closely related to the immunosuppressive process in the tumor microenvironment. However, the specific mechanism and related molecular pathways of ICOSLG in OSCC for immune regulation in tumor microenvironment remain to be further studied. Future studies need to reveal the role of ICOSLG in tumorigenesis and development through immune regulation.

# Data availability statement

The original contributions presented in the study are included in the article/Supplementary Material, further inquiries can be directed to the corresponding authors.

# Ethics statement

The studies involving humans were approved by Ethics Committee of Nanjing Stomatology Hospital, Medical School of Nanjing University. The studies were conducted in accordance with the local legislation and institutional requirements. The participants provided their written informed consent to participate in this study.

# Author contributions

YD: Investigation, Methodology, Software, Writing–original draft. XH: Investigation, Methodology, Software, Writing–original draft. SX: Investigation, Writing–original draft. YS: Data curation, Writing–original draft. YH: Methodology, Software, Writing–original draft. WJ: Software, Writing–original draft. YN: Validation, Writing–review and editing. ZW: Supervision, Writing–review and editing. LD: Formal Analysis, Software, Supervision, Writing–review and editing.

# Funding

The author(s) declare financial support was received for the research, authorship, and of this article. Research was supported by grants by the National Natural Science Foundation of China (Grant No. 82373037); Natural Science Foundation of Jiangsu Province (No. BK20190304, and BE2020628); Nanjing Medical Science and Technology Development Foundation, Nanjing Department of Health (No. YKK21182, and YKK20151).

## Conflict of interest

The authors declare that the research was conducted in the absence of any commercial or financial relationships that could be construed as a potential conflict of interest.

## Publisher's note

All claims expressed in this article are solely those of the authors and do not necessarily represent those of their affiliated organizations, or those of the publisher, the editors and the reviewers. Any product that may be evaluated in this article, or claim that may be made by its manufacturer, is not guaranteed or endorsed by the publisher.

## Supplementary material

The Supplementary Material for this article can be found online at: https://www.frontiersin.org/articles/10.3389/fcell.2023.1257314/full#supplementary-material

## References

Almangush, A., Leivo, I., and Mäkitie, A. A. (2021). Biomarkers for immunotherapy of oral squamous cell carcinoma: current status and challenges. *Front. Oncol.* 11, 616629. doi:10.3389/fonc.2021.616629

Cao, Y., Cao, T., Zhao, W., He, F., Lu, Y., Zhang, G., et al. (2018). Expression of B7-H2 on CD8(+) T cells in colorectal cancer microenvironment and its clinical significance. *Int. Immunopharmacol.* 56, 128–134. doi:10.1016/j.intimp.2018.01.018

Chai, A. W. Y., Lim, K. P., and Cheong, S. C. (2020). Translational genomics and recent advances in oral squamous cell carcinoma. *Semin. Cancer Biol.* 61, 71–83. doi:10.1016/j.semcancer.2019.09.011

Chen, X. L., Cao, X. D., Kang, A. J., Wang, K. M., Su, B. S., and Wang, Y. L. (2003). *In situ* expression and significance of B7 costimulatory molecules within tissues of human gastric carcinoma. *World J. Gastroenterol.* 9 (6), 1370–1373. doi:10.3748/wjg.v9.i6.1370

Dalakas, M. C. (2005). Autoimmune muscular pathologies. *Neurol. Sci.* 26 (1), S7–S8. doi:10.1007/s10072-005-0390-0

Ding, L., Ren, J., Zhang, D., Li, Y., Huang, X., Hu, Q., et al. (2018). A novel stromal lncRNA signature reprograms fibroblasts to promote the growth of oral squamous cell carcinoma via LncRNA-CAF/interleukin-33. *Carcinogenesis* 39 (3), 397–406. doi:10.1093/carcin/bgy006

Faget, J., Bendriss-Vermare, N., Gobert, M., Durand, I., Olive, D., Biota, C., et al. (2012). ICOS-ligand expression on plasmacytoid dendritic cells supports breast cancer progression by promoting the accumulation of immunosuppressive CD4+ T cells. *Cancer Res.* 72 (23), 6130–6141. doi:10.1158/0008-5472.CAN-12-2409

Gao, J., Aksoy, B. A., Dogrusoz, U., Dresdner, G., Gross, B., Sumer, S. O., et al. (2013). Integrative analysis of complex cancer genomics and clinical profiles using the cBioPortal. *Sci. Signal* 6 (269), pl1. doi:10.1126/scisignal.2004088

Greenwald, R. J., Freeman, G. J., and Sharpe, A. H. (2005). The B7 family revisited. *Annu. Rev. Immunol.* 23, 515–548. doi:10.1146/annurev.immunol.23.021704.115611

Han, Y., Dong, Y., Yang, Q., Xu, W., Jiang, S., Yu, Z., et al. (2018). Acute myeloid leukemia cells express ICOS ligand to promote the expansion of regulatory T cells. *Front. Immunol.* 9, 2227. doi:10.3389/fimmu.2018.02227

Henderson, P., van Limbergen, J., Anderson, N. H., Nimmo, E. R., Russell, R. K., Satsangi, J., et al. (2011). Variation in ICOSLG influences Crohn's disease susceptibility. *Gut* 60 (10), 1444. doi:10.1136/gut.2010.235325

Iwata, R., Hyoung Lee, J., Hayashi, M., Dianzani, U., Ofune, K., Maruyama, M., et al. (2020). ICOSLG-mediated regulatory T-cell expansion and IL-10 production promote progression of glioblastoma. *Neuro Oncol.* 22 (3), 333–344. doi:10.1093/neuonc/noz204

Külp, M., Siemund, A. L., Larghero, P., Dietz, A., Alten, J., Cario, G., et al. (2022). The immune checkpoint ICOSLG is a relapse-predicting biomarker and therapeutic target in infant t(4;11) acute lymphoblastic leukemia. *iScience* 25 (7), 104613. doi:10.1016/j.isci.2022.104613

Miller, K. D., Siegel, R. L., Lin, C. C., Mariotto, A. B., Kramer, J. L., Rowland, J. H., et al. (2016). Cancer treatment and survivorship statistics. *CA Cancer J. Clin.* 66 (4), 271–289. doi:10.3322/caac.21349

Nagase, H., Takeoka, T., Urakawa, S., Morimoto-Okazawa, A., Kawashima, A., Iwahori, K., et al. (2017). ICOS(+) Foxp3(+) TILs in gastric cancer are prognostic markers and effector regulatory T cells associated with *Helicobacter pylori*. *Int. J. Cancer* 140 (3), 686–695. doi:10.1002/ijc.30475

Robertson, N., Engelhardt, K. R., Morgan, N. V., Barge, D., Cant, A. J., Hughes, S. M., et al. (2015). Astute clinician report: a novel 10 bp frameshift deletion in exon 2 of ICOS causes a combined immunodeficiency associated with an enteritis and hepatitis. *J. Clin. Immunol.* 35 (7), 598–603. doi:10.1007/s10875-015-0193-x

Roussel, L., Landekic, M., Golizeh, M., Gavino, C., Zhong, M. C., Chen, J., et al. (2018). Loss of human ICOSL results in combined immunodeficiency. *J. Exp. Med.* 215 (12), 3151–3164. doi:10.1084/jem.20180668

Roussel, L., and Vinh, D. C. (2021). ICOSL in host defense at epithelial barriers: lessons from ICOSLG deficiency. *Curr. Opin. Immunol.* 72, 21–26. doi:10.1016/j.coi.2021.03.001

Schreiner, B., Wischhusen, J., Mitsdoerffer, M., Schneider, D., Bornemann, A., Melms, A., et al. (2003). Expression of the B7-related molecule ICOSL by human glioma cells *in vitro* and *in vivo*. *Glia* 44 (3), 296–301. doi:10.1002/glia.10291

Sharma, P., and Allison, J. P. (2015). The future of immune checkpoint therapy. *Science* 348 (6230), 56–61. doi:10.1126/science.aaa8172

Solinas, C., Gu-Trantien, C., and Willard-Gallo, K. (2020). The rationale behind targeting the ICOS-ICOS ligand costimulatory pathway in cancer immunotherapy. *ESMO Open* 5 (1), e000544. doi:10.1136/esmoopen-2019-000544

Tamura, H., Dan, K., Tamada, K., Nakamura, K., Shioi, Y., Hyodo, H., et al. (2005). Expression of functional B7-H2 and B7.2 costimulatory molecules and their prognostic implications in de novo acute myeloid leukemia. *Clin. Cancer Res.* 11 (16), 5708–5717. doi:10.1158/1078-0432.CCR-04-2672

Wallin, J. J., Liang, L., Bakardjiev, A., and Sha, W. C. (2001). Enhancement of CD8+ T cell responses by ICOS/B7h costimulation. *J. Immunol.* 167 (1), 132–139. doi:10.4049/jimmunol.167.1.132

Wang, S., Zhu, G., Chapoval, A. I., Dong, H., Tamada, K., Ni, J., et al. (2000). Costimulation of T cells by B7-H2, a B7-like molecule that binds ICOS. *Blood* 96 (8), 2808–2813. doi:10.1182/blood.v96.8.2808.h8002808_2808_2813

Witsch, E. J., Peiser, M., Hutloff, A., Büchner, K., Dorner, B. G., Jonuleit, H., et al. (2002). ICOS and CD28 reversely regulate IL-10 on re-activation of human effector T cells with mature dendritic cells. *Eur. J. Immunol.* 32 (9), 2680–2686. doi:10.1002/1521-4141(200209)32:9<2680::AID-IMMU2680>3.0.CO;2-6

Xiao, J. X., Bai, P. S., Lai, B. C., Li, L., Zhu, J., and Wang, Y. L. (2005). B7 molecule mRNA expression in colorectal carcinoma. *World J. Gastroenterol.* 11 (36), 5655–5658. doi:10.3748/wjg.v11.i36.5655

Yamashita, T., Tamura, H., Satoh, C., Shinya, E., Takahashi, H., Chen, L., et al. (2009). Functional B7.2 and B7-H2 molecules on myeloma cells are associated with a growth advantage. *Clin. Cancer Res.* 15 (3), 770–777. doi:10.1158/1078-0432.CCR-08-0501

Yang, Z., Yan, G., Zheng, L., Gu, W., Liu, F., Chen, W., et al. (2021). YKT6, as a potential predictor of prognosis and immunotherapy response for oral squamous cell carcinoma, is related to cell invasion, metastasis, and CD8+ T cell infiltration. *Oncoimmunology* 10 (1), 1938890. doi:10.1080/2162402X.2021.1938890

Zhang, C., Wang, F., Sun, N., Zhang, Z., Zhang, G., Zhang, Z., et al. (2022). The combination of novel immune checkpoints HHLA2 and ICOSLG: a new system to predict survival and immune features in esophageal squamous cell carcinoma. *Genes Dis.* 9 (2), 415–428. doi:10.1016/j.gendis.2020.08.003

Zhang, Y., Wang, X. L., Liu, J. J., Qian, Z. Y., Pan, Z. Y., Song, N. P., et al. (2023). ICOS/ICOSLG and PD-1 Co-expression is associated with the progression of colorectal precancerous- carcinoma immune microenvironment. *J. Inflamm. Res.* 16, 977–992. doi:10.2147/JIR.S401123

Zhao, M., Ding, L., Yang, Y., Chen, S., Zhu, N., Fu, Y., et al. (2019). Aberrant expression of PDCD4/eIF4A1 signal predicts postoperative recurrence for early-stage oral squamous cell carcinoma. *Cancer Manag. Res.* 11, 9553–9562. doi:10.2147/CMAR.S223273

Zhao, M., He, Y., Zhu, N., Song, Y., Hu, Q., Wang, Z., et al. (2023). IL-33/ST2 signaling promotes constitutive and inductive PD-L1 expression and immune escape in oral squamous cell carcinoma. *Br. J. Cancer* 128 (5), 833–843. doi:10.1038/s41416-022-02090-0

Zheng, Y., Liao, N., Wu, Y., Gao, J., Li, Z., Liu, W., et al. (2019). High expression of B7-H2 or B7-H3 is associated with poor prognosis in hepatocellular carcinoma. *Mol. Med. Rep.* 19 (5), 4315–4325. doi:10.3892/mmr.2019.10080

Zhu, N., Ding, L., Fu, Y., Yang, Y., Chen, S., Chen, W., et al. (2020). Tumor-infiltrating lymphocyte-derived MLL2 independently predicts disease-free survival for patients with early-stage oral squamous cell carcinoma. *J. Oral Pathol. Med.* 49 (2), 126–136. doi:10.1111/jop.12969

frontiers | Frontiers in Cell and Developmental Biology

TYPE Review
PUBLISHED 25 October 2023
DOI 10.3389/fcell.2023.1278461



OPEN ACCESS

EDITED BY
Xiangsheng Zuo,
University of Texas MD Anderson Cancer Center, United States

REVIEWED BY
Khyati Maulik Kariya,
Massachusetts General Hospital and Harvard Medical School, United States
Milton Roy,
Johns Hopkins Medicine, United States

*CORRESPONDENCE
Baofeng Guo,
gbf@jlu.edu.cn
Ling Zhang,
zhangling3@jlu.edu.cn

RECEIVED 16 August 2023
ACCEPTED 13 October 2023
PUBLISHED 25 October 2023

CITATION
Yang J, Yang M, Wang Y, Sun J, Liu Y, Zhang L and Guo B (2023), STING in tumors: a focus on non-innate immune pathways.
*Front. Cell Dev. Biol.* 11:1278461.
doi: 10.3389/fcell.2023.1278461



# STING in tumors: a focus on non-innate immune pathways

Jiaying Yang[1,2], Mei Yang[2], Yingtong Wang[2], Jicheng Sun[1], Yiran Liu[1], Ling Zhang[2]* and Baofeng Guo[1]*

[1]Department of Plastic Surgery, China-Japan Union Hospital, Jilin University, Changchun, China, [2]Key Laboratory of Pathobiology, Ministry of Education, and Department of Biomedical Science, College of Basic Medical Sciences, Jilin University, Changchun, China

Cyclic GMP-AMP synthase (cGAS) and downstream stimulator of interferon genes (STING) are involved in mediating innate immunity by promoting the release of interferon and other inflammatory factors. Mitochondrial DNA (mtDNA) with a double-stranded structure has greater efficiency and sensitivity in being detected by DNA sensors and thus has an important role in the activation of the cGAS-STING pathway. Many previous findings suggest that the cGAS-STING pathway-mediated innate immune regulation is the most important aspect affecting tumor survival, not only in its anti-tumor role but also in shaping the immunosuppressive tumor microenvironment (TME) through a variety of pathways. However, recent studies have shown that STING regulation of non-immune pathways is equally profound and also involved in tumor cell progression. In this paper, we will focus on the non-innate immune system pathways, in which the cGAS-STING pathway also plays an important role in cancer.

KEYWORDS

**mtDNA, cGAS-STING, PD-L1, TME, extracellular vesicles**

## 1 Introduction

cGAS is highly conserved and is the double-stranded DNA (dsDNA) sensor, which is responsible for monitoring the changes in cytoplasmic DNA content in most mammalian cells (Sun et al., 2013; Ablasser and Chen, 2019). In contrast to Toll-like receptor 9 and NLRP3, whose expression appears to be restricted to immune cells, cGAS and the downstream STING signaling are widely expressed in most cell types (Chen et al., 2016a; Riley and Tait, 2020). It has been shown that cytoplasmic leakage of mtDNA is the major source of cytoplasmic dsDNA in ATM-deficient tumor cells (Hu et al., 2021a), suggesting that mtDNA may play an important role in the innate immunity of tumor cells. The mtDNA is located near the five complexes that transfer electrons across the inner mitochondrial membrane (IMM) to ensure efficient synthesis of the proteins encoded by the mitochondrial genes, but the electron transport chain as a major source of mitochondrial reactive oxygen species (ROS) will result in mtDNA being more susceptible to oxidative damage and leakage into the cytoplasm. The cyclic structure of mtDNA and the presence of unmethylated CpG motifs allow cGAS to recognize mtDNA leakage into the cytoplasm as a "foreign" molecule that triggers an inflammatory response (West and Shadel, 2017; Kausar et al., 2020; De Gaetano et al., 2021), which is then involved in tumorigenesis through subsequent STING signaling. By analyzing The Cancer Genome Atlas of 18 malignancies, several scientists found that the expression of four key molecules in the cGAS-STING pathway, MB21D1 which encodes cGAS, TMEM173 which encodes STING, as well as TANK-binding kinase 1 (TBK1) and interferon-regulating factor 3 (IRF3), are significantly upregulated in almost all detected cancer types compared to normal control tissues,

suggesting that cGAS-STING and the signaling molecules may be activated in all cancer processes (An et al., 2019).

It is now widely accepted that the cGAS-STING signaling cascade may rely primarily on synthetic interferons (IFNs) to exert anti-tumor effects, but recent studies have found that it also has significant regulatory effects on non-immune pathways and influences tumor progression. At the same time, it has been found that there is significant heterogeneity in the outcomes exhibited by tumor cells upon STING activation, and the mechanism of this double-edged role in tumor progression deserves to be explored. Therefore, in this review, we summarize the main mechanisms of mtDNA escaping from mitochondria and the recent advances in the impact on tumor cells after the occurrence of horizontal metastasis, with a focus on the role of the subsequent non-innate immunoregulatory pathways of the cGAS-STING pathway in tumor progression and the potential factors that influence STING bi-directionality.

## 2 Overview of cGAS-STING

cGAS is a member of the nucleotidyltransferase family and is normally present in the cytoplasm as an inactive protein, and current evidence suggests that cGAS also has a diverse cellular distribution (Kuchta et al., 2009; Sun et al., 2013; Wu et al., 2013; Hopfner and Hornung, 2020). Jiang et al. showed that cGAS is also constitutively present in the nucleus. When it is activated, it accelerates genomic instability, the formation of micronuclei (MNi), and cell death under stress conditions by inhibiting homologous recombination pathways (Jiang et al., 2019). This dual function of cGAS as an innate immune sensor in the cytoplasm and a negative regulator of DNA repair in the nucleus highlights the importance of cGAS in cells. Briefly, After the recognition and binding of free cytoplasmic DNA to form the complexes in the cytoplasm, there has been a conformational change in the active site of cGAS, which causes cGAS activation. Then the cyclic guanosine monophosphate-adenosine monophosphate (cGAMP) is synthesized by cGAS with intracytoplasmic ATP and GTP as raw materials. As the secondary messenger, cGAMP or cyclic dinucleotides (CDNs) bind to the adapter protein STING anchored to the endoplasmic reticulum (ER) (Ablasser et al., 2013; Gao et al., 2013a; Diner et al., 2013; Sun et al., 2013; Zhang et al., 2013). Upon binding to cGAMP, STING undergoes extensive conformational rearrangements (Huang et al., 2012; Shang et al., 2012; Shu et al., 2012; Gao et al., 2013b; Ergun et al., 2019; Shang et al., 2019). After conformational rearrangement, STING is translocated from the ER to the Golgi through the ER-Golgi intermediate compartment (Dobbs et al., 2015). Upon arrival at the Golgi compartment, STING is palmitoylated at two cysteine residues (Cys88 and Cys91) and recruits TBK1 (Mukai et al., 2016). TBK1 then phosphorylates itself. STING and IRF3 dimerize and enter the nucleus, triggering type I interferon production (Hopfner and Hornung, 2020). Phosphorylated TBK1 and its cognate IκB kinase (IKK) also mediate activation of the IKK complex, which in turn activates the atypical NF-κB pathway to induce the production of other inflammatory cytokines (Smale, 2010). For detailed mechanisms, see the excellent review by Hopfner and Hornung (2020).

## 3 Regulation and modification of cGAS and STING expression

cGAS is constitutively expressed in most cell types. Thus, unlike other pattern recognition receptor systems, the levels of cGAS and its ability to be activated are not regulated at the transcriptional level. Conversely, many post-translational mechanisms have been shown to play an important role in regulating the activity of this receptor toward its ligand, enzymatic activity, or half-life (Hopfner and Hornung, 2020). cGAS and STING undergo several types of post-translational modifications, including protein hydrolysis (Wang et al., 2017), acetylation (Dai et al., 2019), glutamylation (Xia et al., 2016a), ubiquitination (Zhang et al., 2012), sumoylation (Hu et al., 2016), and phosphorylation (Tanaka and Chen, 2012). These post-translational modifications affect cGAS and STING either by direct modification or by cleavage of active site residues. In particular, STING signaling is defective in a variety of cancers (e.g., colon cancer and melanoma), and its behavior may allow damaged cells to escape immune surveillance (Xia et al., 2016b; Xia et al., 2016c). Konno et al. found that cGAS or STING genes were mutated in a variety of human tumors by searching the cBioPortal database. Among them, cGAS missense mutants R376Q and E383K lost the ability to produce cGAMP upon binding to dsDNA, while STING mutants (R169W and P203S) were unable to promote the production of oncogene-induced pro-inflammatory cytokines. Hypermethylation of cGAS or STING promoter regions is present in several types of tumor samples, resulting in cGAS or STING repression (Konno et al., 2018). It has been shown that this methylation process is reversible, and in STING-deficient melanoma cell lines, demethylation-mediated restoration of STING signaling can increase the antigenicity of MHC-like molecules by upregulating them, thereby enhancing their recognition and killing by cytotoxic T cells (Falahat et al., 2021).

## 4 mtDNA is a potent inducer of the cGAS-STING pathway

One of the characteristics of tumor cells is the massive replication of chromosomes in the nucleus, which can lead to the leakage of genomic DNA into the cytoplasm (Chin et al., 2020). When the mitotic process of cells is damaged endogenously or exogenously, some chromatin segments may be missegregated into the cytoplasm, either passively or actively, forming one or more spatially separated MNi (Guo et al., 2019). Gupta et al. found Cisplatin-induced massive MNi production in cutaneous squamous carcinoma (Gupta et al., 2011). Using high-resolution live-cell imaging, Hatch et al. found that spontaneous rupture of the micronuclear envelope can occur in the majority of MNi (Hatch et al., 2013), and that ruptured MNi are an important source of cytoplasmic self-DNA (mainly dsDNA) (Harding et al., 2017). Approximately 55% of metastatic tumor-derived cells were reported to be cGAS positive (Bakhoum et al., 2018). Similarly, cytoplasmic translocation of mtDNA has been detected in many disease states and has been associated with cancer progression (Liu et al., 2019b; Piantadosi, 2020). In particular, when tumor cells are often subjected to multiple physicochemical insults during treatment, their mitochondrial damage is further aggravated and

more mtDNA is released into the cytoplasm (Cheng et al., 2020; Zhu et al., 2022). Numerous studies have shown that mtDNA is a potent inducer of cGAS-STING signaling (Wu et al., 2021b). Interestingly, Tigano et al. used the inducible restriction endonuclease AsiSi to selectively induce DNA double-strand breaks (DSBs) in the nucleus and ionization radiation (IR) to induce DSBs in both mtDNA and nuclear DNA. The results showed that although AsiSi and IR caused the cells to produce similar levels of cGAS-positive MNi (~15%), the induction of nuclear DNA and mtDNA co-damage showed stronger interferon-stimulated gene activation and significantly increased transcript levels than the induction of nuclear DNA damage alone. This suggests that damaged mtDNA synergizes with MNi to produce a stronger type I IFN response (Tigano et al., 2021). The reason for the strong activation of cGAS by mtDNA may be related to the fact that mtDNA is more susceptible to damage due to its high copy number and inefficient repair system (Wu et al., 2021a). In addition, the structural features of mtDNA, i.e., shorter circular DNA, and no histone hindrance, seem to be the critical factors (Andreeva et al., 2017). However, it has also been shown that cytoplasmic chromatin is equally competent for cGAS-STING activation (Dou et al., 2017). Structurally, the N-terminus of cGAS is required for nuclear chromatin sensing, not mtDNA (Li et al., 2021c). Compared with naked dsDNA, reconstituted nucleosomes *in vitro* have higher affinities for cGAS, but lower capacities to activate it (Wang et al., 2020a). The reason for this may be that nucleosomes interfere to some extent with the formation of this DNA structure, and thus some studies have used nucleosomes as markers to distinguish their DNA from pathogenic DNA (Zierhut et al., 2014; Zierhut and Funabiki, 2015). Given that mtDNA is an important component of dsDNA and plays an important role in cGAS-STING activation, the next section will explore the main mechanisms of mtDNA leakage into the cytosol in the context of the current findings.

## 5 The main mechanism of mtDNA leakage

Mitochondrial outer membrane permeability (MOMP), initiated by endogenous or mitochondrial apoptotic processes, is one of the major forms of mtDNA release. Previous studies have long shown that free Bax and Bak oligomerize in the outer mitochondrial membrane (OMM) during apoptosis to form a proteic pore, which can lead to the release of mitochondrial contents such as cyt C, mtDNA, *etc.*, into the cytosol (Chipuk et al., 2006). However, since the IMM is thought to remain intact during apoptosis (Bernardi et al., 2015), it is particularly mysterious how mtDNA escapes from the mitochondria during this process. McArthur et al. examined mitochondria from mouse embryonic fibroblasts using live-cell lattice light-sheet microscopy and found that BAX/BAK activation and subsequent cyt C release are followed by mitochondrial lattice rupture and the appearance of large BAX/BAK pores on the OMM. These large pores allow IMM-carrying mitochondrial matrix components, including the mitochondrial genome, to protrude into the cytosol, ultimately leading to the release of contents such as mtDNA (McArthur et al., 2018). The study by Riley et al. also confirmed the above and indicated that after the occurrence of BAX-dependent MOMP, mitochondrial inner membrane permeability (MIMP) may also follow (Riley et al., 2018). It is noteworthy that tBID, a member of the BH3-only family, can mediate MOMP in a BAX/BAK-independent manner. The finding defines tBID as an effector of mitochondrial permeability in apoptosis (Flores-Romero et al., 2022) and may influence the process of mtDNA release through MOMP.

Another important pathway for mtDNA escape from mitochondria is the opening of the mitochondrial permeability transition pore (mPTP). The opening of mPTP leads to increased IMM permeability and thus to changes in mitochondrial permeability (Bernardi and Di Lisa, 2015; Bernardi, 2018). It has been shown that mtDNA fragments are released from the brains of irradiated mice by briefly opening the mPTP (Patrushev et al., 2006). Under oxidative stress conditions, DNA from liver mitochondria can also be released by nonspecific mPTP. In the presence of $Ca^{2+}$, the addition of $Fe^{2+}$ and $H_2O_2$ induces the opening of mPTP, and mtDNA is observed to be hydrolyzed after oxidative stress, with partial release of mDNA fragments into the cytoplasm (Garcia et al., 2005). Different studies have shown differences in the amount of mtDNA fragments released. Garcia et al. found that the DNA content in the mitochondrial matrix decreased to 42% ± 6% and the number of MTCO1, MTND3, and MTCYB genes in the mitochondria decreased by approximately 46%, 22%, and 54%, respectively, and mtDNA release could be inhibited in the presence of cyclosporin A, an mPTP inhibitor (Garcia and Chavez, 2007). In summary, mtDNA can be released by mPTP, and incomplete mtDNA fragments are released, which is consistent with the fact that mPTP only allows the transport of molecules<1.5 kDa (Halestrap et al., 2002). Recent studies have revealed the mechanism by which this process occurs. When mitochondrial stress occurs, ROS induces the production of oxidized mtDNA (Ox-mtDNA), which can be repaired by the DNA glycosylase OGG1, and when the repair mechanism is limited, Ox-mtDNA is cleaved within the mitochondria by the nucleic acid endonuclease FEN1 into 500–650 bp fragments, which leave the mPTP- and voltage-dependent anion channel-(VDAC) dependent channels through the mitochondria, thus initiating the activation of inflammation (Xian et al., 2022; Cabral et al., 2023). During this time, VDAC plays a role in helping mtDNA open the door to the cytoplasm. VDAC, also known as mitochondrial porin, is the major protein involved in transporting OMM (Shoshan-Barmatz et al., 2006). One of the VDAC-1 isoforms can form oligomers on the OMM (Keinan et al., 2010). Kim et al. found in the mice model of systemic lupus erythematosus (SLE) that when mitochondria are stressed in multiple ways, the fragmented mtDNA binds to the VDAC on the OMM, which causes multiple VDAC monomers to cluster together and form a mesopore in their middle, allowing mtDNA to be released into the cytoplasm through this mesopore by direct interaction between the three positively charged residues at the N-terminal end of the VDAC and mtDNA (Kim et al., 2019). Researchers applied the oligomerization inhibitor VBIT-4 to block only one of the channel forms, VDAC1, to reduce mtDNA release in the mice model of SLE, demonstrating the potential role of VDAC in mtDNA release (Kim et al., 2019). In conclusion, when oxidative stress damages mitochondria, it triggers the opening of mPTP on IMM while oxidizing mtDNA. Ox-mtDNA undergoes shearing by nucleic acid endonucleases and then enters cytoplasmic

lysis through mPTP and VDAC on OMM in sequence, which in turn triggers subsequent inflammatory responses. It is worth mentioning that the structural opening of the pores may also lead to mitochondrial swelling, resulting in IMM disruption and thus cytosolic release of mtDNA (Riley and Tait, 2020). Whether this effect of mPTP on IMM is related to MIMP needs to be further explored. Li et al. also showed that the inherent tripartite motif 21 of tumor cells promotes VDAC2 degradation through K48-linked ubiquitination, which inhibits the pore-forming capacity of VDAC2 oligomers and reduces mtDNA leakage, which in turn inhibits the type I interferon response following exposure to IR (Li et al., 2023). Notably, the structural opening of the pore can also lead to mitochondrial swelling and IMM disruption, which promotes the release of mtDNA into the cytosol (Riley and Tait, 2020). Whether this effect of mPTP on IMM is related to MIMP deserves further investigation. It has been shown that chitosan, a vaccine adjuvant, activates the cGAS-STING pathway and induces the type I IFN response via mPTP-dependent release of mtDNA (Carroll et al., 2016). These results suggest that mPTP may play a more important role in activating the cGAS-STING pathway, and although the structural integrity of mtDNA is difficult to maintain, this fragmented DNA does not affect the recognition of cGAS.

Gasdermins (GSDMs) play a key role in pyroptosis. Its N-terminal structural domain can form transmembrane pores in the plasma membrane, leading to changes in membrane permeability (Chen et al., 2016b; Ding et al., 2016; Liu et al., 2016). Besides the plasma membrane, there is evidence that the GSDM family can form pores in the mitochondrial membrane. Weindel et al. also found that in macrophages, elevated mitochondrial ROS (mtROS) direct the binding of GSDMD to the mitochondrial membrane, followed by the formation of mitochondrial GSDMD pores and then the release of mtROS (Weindel et al., 2022). Huang et al. showed that lipopolysaccharide (LPS) activates GSDMD and forms a mitochondrial pore that induces the release of mtDNA into the cytoplasm of endothelial cells to be recognized by cGAS (Huang et al., 2020). These findings suggest that GSDM may be involved in the release of mtDNA as a novel pathway.

In addition, changes in mitochondrial dynamics contribute to the release of mtDNA from the mitochondria. Mitochondrial transcription factor A (TFAM) plays an important role in mitochondrial quality control, and imbalances in TFAM and/or mtDNA homeostasis are frequently observed in tumor cells (Wallace, 2012). West et al. showed that TFAM-deficient fibroblasts display elongated and highly fused mitochondria and increased cytosolic mtDNA (West et al., 2015). Similarly, inhibition of ataxia-mutated protein (ATM) leads to downregulation of TFAM, allowing mtDNA to escape to the cytoplasm (Hu et al., 2021b). Mitochondrial division is important to ensure proper nucleoid distribution and removal of damaged mtDNA (Meyer et al., 2017). It has been shown that activation of STING signaling in Kupffer cells after LPS stimulation may be associated with enhanced mitochondrial division and increased mtDNA release caused by upregulation of dynamin-related protein 1 (DRP1) (Zhang et al., 2023c). Furthermore, LPS enhanced DRP1-dependent mtROS production, which further enhanced STING signaling by promoting mtDNA leakage into the cytosol (Li et al., 2022; Zhang et al., 2023c). Similarly, a recent study showed that the knockdown of GTPase—MxB, a member of the membrane-deforming dynamin family located in the IMM, resulted in mitochondrial fragmentation, IMM breakage, and increased cytoplasmic mtDNA levels (Cao et al., 2020). This suggests that homeostatic imbalance is likely another factor in the release of mtDNA into the cytoplasm.

## 6 Presence of intercellular transfer of mtDNA, cGAS, and STING

In recent years, horizontal transfer of mitochondria and mtDNA between tumor cells and surrounding non-tumor cells has been reported. Tumor cells acquire functional mitochondria and mtDNA from healthy host cells to repair or even enhance impaired mitochondrial function, thereby restoring tumorigenic potential. Tumor cells show a significant delay in tumor growth in the absence of mtDNA (Rebbeck et al., 2011). Salaud et al. found that mitochondria can be transferred from tumor-activated stromal cells present in the glioblastoma (GBM) microenvironment to GBM, and this transfer increases the proliferation of GBM and its resistance to radiotherapy and chemotherapy (Salaud et al., 2020). This transfer of intact mitochondria from host cells may be an important way for tumor cells to acquire mtDNA (Tan et al., 2015; Dong et al., 2017) (Figure 1). Interestingly, Kleih et al. found that cisplatin-sensitive high-grade plasmacytoid ovarian cancer cell lines contained higher mitochondrial content than cisplatin-resistant cells (Kleih et al., 2019). This suggests that mtDNA or mitochondria may play different roles depending on the specific context and stage of tumor progression.

The transfer of mtDNA through “tunneling nanotubes” (TnTs) may be an important way of cross-talk between stromal cells and cancer cells (Pasquier et al., 2013). In addition to the TnTs pathway of cellular level translocation of mtDNA, the extracellular vesicle (EV) pathway is another important way of mtDNA level transfer. Circulating EVs from breast cancer patients identify complete mitochondrial genomes (Sansone et al., 2017). Rabas et al. also found that in breast cancer cells, PINK1 drives the production of mtDNA-loaded EVs and transfers invasive properties to “recipient” tumor cells (Rabas et al., 2021). Recent studies have identified mechanisms that regulate the translocation of mitochondrial components, including mtDNA, into EVs. Mitochondria-derived vesicles can transport components of the mitochondrial interior to nearby organelles. This process is dependent on the proteins optic atrophy 1 and categorical connexin 9 (Todkar et al., 2021). Notably, the presence of mitochondrial proteins in EVs has been demonstrated in the absence of pro-inflammatory stimuli (Hurwitz et al., 2016; Kowal et al., 2016). So, is it possible that mitochondria regulate tumor cells survival by actively releasing mtDNA-containing EVs, or is the acquisition of mtDNA by tumor cells a “voluntary act” that occurs when the tumor cells force the normal cells through certain pathways? Besides mitochondria and mtDNA, activated cGAS and STING can be transferred to recipient cells via EVs. Clancy et al. found that a portion of the dsDNA coupled to activated cGAS was encapsulated in tumor microvesicles (TMVs) and that the TMVs transferred both to the recipient cells and influenced the behavior of the recipient cells (Clancy et al., 2022). In addition, RAB22A mediates the

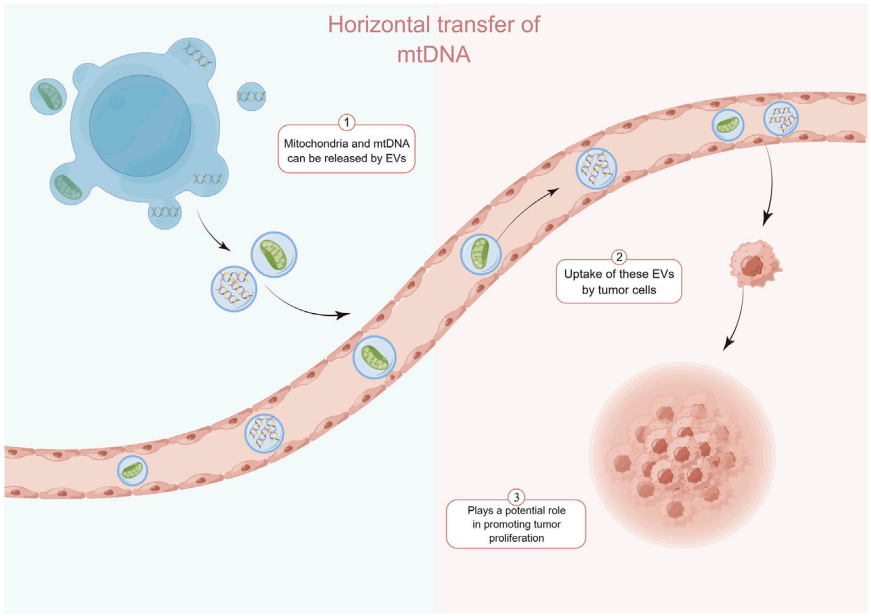


FIGURE 1
Normal cell-derived mtDNA and mitochondria can be transferred to tumor cells via the extracellular vesicle pathway and enhance the recovery of their tumorigenic potential. By Figdraw.

formation of atypical autophagosomes containing STING activated by agonists or radiotherapy, while RAB22A inactivates RAB7 and inhibits the fusion of formed autophagosomes with lysosomes, resulting in the release of endo-vesicular vesicles of autophagosomes with activated STING into the extracellular space (Gao et al., 2022). It is foreseeable that this direct cell-to-cell transfer of activators may have a faster and more direct effect than the transfer of DNA, leading to different consequences.

# 7 STING exerts anti-tumor effects through the innate immune pathway

Given the role of the cGAS-STING pathway in activating immune surveillance, current studies have focused on innate immune function to exert anti-tumor effects (Li et al., 2019; Kwon and Bakhoum, 2020). Due to the inherent genomic instability of cancer cells, they can display constitutive activation of intrinsic immunity and cGAS-STING pathway-mediated IFN signaling, with the production of IFN-a and IFN-b that bind to IFN receptors on themselves, neighboring cells or immune cells, mobilizing immune cells such as dendritic cells (DCs) and TME infiltration of $CD8^+$T cells to eliminate the tumor (Diamond et al., 2011; Fuertes et al., 2011; Reislander et al., 2020). Grabosch et al. activated the cGAS-STING pathway in ovarian cancer mice using the DNA damage inducer cisplatin and increased $CD8^+$T cells infiltration (Grabosch et al., 2019). Chemosuppression of ATM activated the cGAS-STING signaling pathway by downregulating TFAM to promote mtDNA release, which similarly enhanced T lymphocytes infiltration into TME (Hu et al., 2021b). Harabuchi and others used a combination of cisplatin and cGAMP to increase chemokine expression in tumor tissue, transform tumors from "cold" to "hot" via STING, increase $CD8^+$T cells infiltration, and significantly inhibit tumor growth in tumor-bearing mice (Harabuchi et al., 2020). This transformation to "hot" tumors may be associated with the expression of chemokines, such as CXCL9, CXCL10, CCL5, CCL20, *etc.*, which recruit antigen-presenting cells (APCs), T cells, and NK cells to infiltrate the TME and kill tumor cells (Corbera-Bellalta et al., 2016; Hu et al., 2023).

# 8 STING exerts anti-tumor effects through non-innate immune pathways

## 8.1 STING regulated autophagy

Induction of autophagy is one of the important functions of STING and may play a role in the interferon signaling process before STING (Gui et al., 2019; Nassour et al., 2019). Nassour et al. showed that STING-driven macroautophagy, a subtype of autophagy involving autophagic lysosomes, is a critical step in preventing cancer development (Nassour et al., 2019). Liu et al. reported STING-induced atypical autophagy dependent on ATG5 (Liu et al., 2019a). Typical autophagy can also be triggered by the interaction of cGAS and Beclin-1, fluid-phase separation of cGAS-DNA complexes, and STING-triggered ER stress-mTOR signaling (Zhang et al., 2023c). Autophagy-dependent cell death can be triggered when DNA damage-induced STING activation clears cancer cell (Zhang et al., 2021).

## 8.2 STING-regulated cell death pathways

The molecular mechanisms behind STING-associated cell death involve multiple signaling cascades. Ferroptosis is a form of cell death characterized by iron-mediated membrane

lipid peroxidation and dysregulation of anti-oxidant levels (Tang et al., 2021). The nucleoside analog zalcitabine induces mitochondrial damage and mtDNA release, activates the cGAS-STING pathway, which in turn induces autophagy-dependent ferroptosis and inhibits pancreatic tumor growth in mice (Li et al., 2021b). STING also promotes ferroptosis in human pancreatic cancer cell lines by increasing mitofusin 1/2-dependent mitochondrial fusion, which induces massive ROS production and ultimately membrane lipid peroxidation (Li et al., 2021a). Zierhut et al. showed that cGAS activation is inhibited by nucleosomes during normal mitosis, but during prolonged mitotic arrest, cGAS promotes a slow accumulation of IRF3 phosphorylation, which in turn may contribute to apoptosis by inhibiting Bcl-xL. This ability to exert inflammatory signaling in transcriptionally competent interphase cells while inducing apoptosis in transcriptionally attenuated mitotic cells contributes to increased sensitivity to paclitaxel, a chemotherapeutic agent that acts by inhibiting cell mitosis, in patients with lung and ovarian cancer (Zierhut et al., 2019). Since certain types of DNA damage can lead to mitotic blockage and mitotic cell death (Garner et al., 2013), cGAS may also affect other types of anti-tumor responses that use DNA damage as a mechanism of action. For example, Banerjee et al. found that STING affects cell death through the DNA damage response (DDR) system independently of the typical IFN pathway. The STING-TBK1 axis stimulates phosphorylation of the kinase ATM, which activates the CHK2-p53-p21 pathway and induces apoptosis by blocking the cellular G1 phase (Banerjee et al., 2021). In addition, a genome-wide CRISPR-Cas9 screen by Hayman et al. revealed that STING acts as a regulator of ROS homeostasis that deletion of STING leads to enhanced cellular ROS metabolism and therapeutic resistance to DNA damaging agents in head and neck squamous cell carcinoma, and that pharmacological activation of STING enhances the anti-tumor effects of IR *in vivo*. A rationale for the therapeutic combination of STING agonists and DNA-damaging agents is provided (Hayman et al., 2021).

## 8.3 STING in metabolism

In the presence of *Brucella* infection, STING regulates the metabolic reprogramming of macrophages via HIF-1α involving oxidative phosphorylation and glycolysis (Gomes et al., 2021). It is then worth exploring whether the restoration of impaired respiratory function by tumor cells through horizontal transfer of mtDNA to enhance tumor-promoting behavior may also be related to STING, as mentioned above. The current study demonstrated the regulatory role of STING in glucose metabolism. Rong et al. found that in an environment of adequate nutrition and unactivated innate immunity, STING molecules could inhibit the autophagosome-lysosome fusion process involved in STX17 and downregulate autophagic flux by binding to STX17, an important protein for the fusion of autophagic membranes, and allowing it to reside in the ER. In the absence of STING, or upon activation by cGAMP, and ER-GIC translocation, STX17 is released from STING, leading to an upregulation of autophagy levels, which enhances AMPK activity in skeletal muscle cells (Rong et al., 2022). This reveals a novel non-immune function of STING, i.e., spatial modulation of the classical autophagy pathway induced by energy deprivation, suggesting a new link between innate immunity and energy metabolism. Tumor cells promote proliferation through aerobic glycolysis, or the Warburg effect, which is another hallmark of cancer. Tumor aerobic glycolysis produces an unfavorable TME, resulting in impaired anti-tumor immunity. Local nutrient depletion inhibits anti-tumor T-cells proliferation and activation, while accumulation of waste products (e.g., lactate) enhances the immunosuppressive TME (Wang et al., 2020b). Zhang et al. found that STING can target hexokinase II to block its activity, thereby promoting anti-tumor immunity by limiting aerobic glycolysis in tumor cells. In human colorectal cancer samples, lactate, which can be used as a proxy for aerobic glycolysis, was negatively correlated with STING expression levels and anti-tumor immunity (Zhang et al., 2023a). Collectively, these findings reveal a role for STING in the regulation of cellular metabolism and establish a critical link between the glycolytic regulation of STING and tumor suppressor activity.

## 8.4 STING in senescence

STING, through activation of the downstream NF-κB pathway, also mediates the secretion of pro-inflammatory cytokines, chemokines, proteases, and growth factors, collectively referred to as SASPs (senescence-associated secretory phenotypes), which attenuate tumor growth by promoting cell cycle arrest in tumor cells (Dou et al., 2017; Yang et al., 2017). Yang et al. found that cGAS deletion accelerated spontaneous immortalization of mouse embryonic fibroblasts, and cGAS deletion also eliminated SASPs induced by multiple factors, including radiation and etoposide (Yang et al., 2017). These cytokines signaling programs can also induce enhanced inflammatory responses. For example, both IL-1β and IFN-α disrupt mitochondrial homeostasis to induce enhanced immune responses, demonstrating a novel function of IL-1β in initiating or enhancing STING-mediated intrinsic cellular immunity (Aarreberg et al., 2019). In this perspective, STING-mediated IFNs production and inflammatory factors generated by activation of the NF-κB pathway may further amplify the damaging effects of mitochondria, leading to increased mtDNA release and enhanced cGAS recognition, resulting in a cascade of amplified responses to inflammatory signals. Interestingly, it has recently been shown that NF-κB activation enhances STING signaling by modulating microtubule-mediated STING transport and that this synergistic interaction between NF-κB and STING triggers a cascade-amplified interferon response and robust host antiviral defense (Zhang et al., 2023b). In addition, Zhu et al. found that VDAC2 is a novel STING-binding ligand. STING deficiency or inhibition of the STING palmitoyltransferase ZDHHCs by 2-BP enhanced VDAC2/GRP75-mediated mitochondria-ER contact, increased mtROS/calcium levels, impaired mitochondrial function, and inhibited signaling in the mTOR pathway, which ultimately led to growth retardation in renal cell carcinoma (Zhu et al., 2023) (Figure 2). Table 1 summarizes the non-innate immunoregulatory pathways mediated by STING.

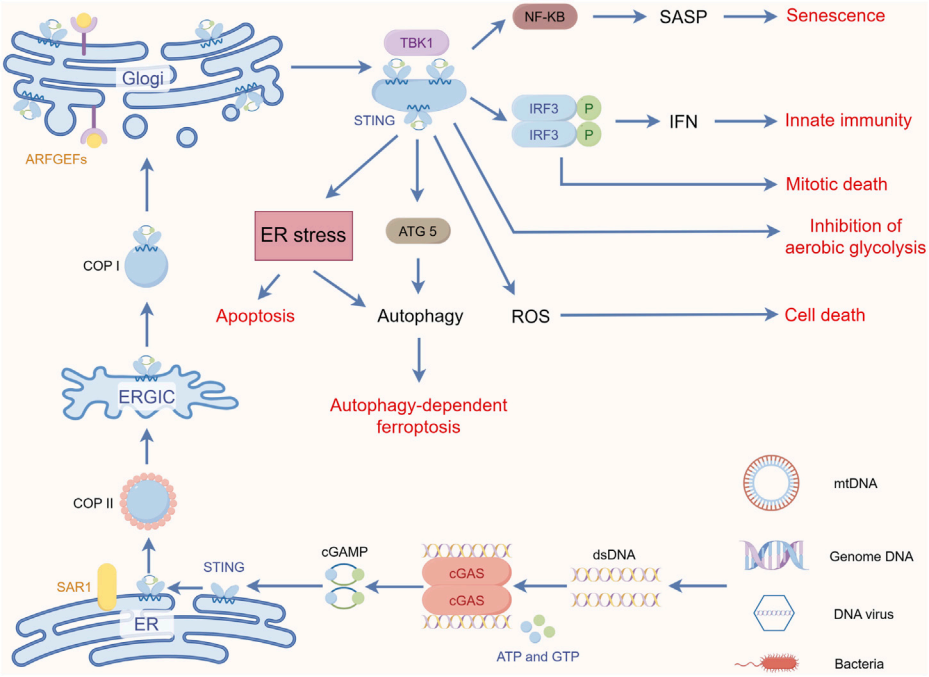


FIGURE 2
STING-mediated key non-innate immune pathways. By Figdraw.

## 9 The intensity of STING activation in tumor cells influences their outcome

Recent evidence suggests that cGAS-STING signaling may also be involved in the promotion of tumor proliferation and metastasis. Cheng et al. showed that in tumor cells, ROS induced by mitochondrial Lon, a chaperone and DNA-binding protein involved in protein quality control and stress response pathways, triggers mtDNA damage, and Ox-mtDNA is released into the cytoplasm to activate IFN signaling, which further upregulates the expression of programmed death ligand-1 (PD-L1) and indoleamine 2,3-dioxygenase (IDO-1) to inhibit T-cells activation. In addition, Lon upregulation induced the secretion of loaded mtDNA and PD-L1 EVs, which further induced the production of IFNs and IL-6 by macrophages, thereby attenuating innate and $CD8^+$T cells immunity in the TME (Cheng et al., 2020). This process may be the mechanism for the formation of immunosuppressive TME in tumors, and mtDNA levels may serve as a potential diagnostic biomarker for anti-PD-L1 immunotherapy (Cheng et al., 2020). Zeng et al. also found that IL-6-induced ROS production in endometrial cancer (EC) cells and high levels of ROS cause cytoplasmic leakage of mtDNA and activate downstream cGAS-STING signaling, which increased PD-L1 levels. In IL-6-induced EC cell-derived EVs, mtDNA and PD-L1 expression levels were similarly significantly elevated (Zeng et al., 2022). Similarly, IR of radiotherapy activates innate immune pathways, leading to the upregulation of PD-L1 in hepatocellular carcinoma (HCC), inhibition of cytotoxic T lymphocytes activity and immune infiltration, and protection of tumor cells from cellular immune-mediated killing (Du et al., 2022).

The emergence of this paradoxical phenomenon of STING may be related to its activation state, and its chronic activation may induce the formation of immunosuppressive TME (Coussens and Werb, 2002; Kwon and Bakhoum, 2020) (Figure 3). It has been shown that STING-deficient mice often develop more and larger tumors in advanced stages of HCC and show reduced levels of phosphorylated STAT1, autophagy, and cleaved caspase-3. Treatment with CDNs, a STING agonist, activates these responses in the liver, and CDNs treatment of advanced HCC in mice effectively reduces the size of most tumors (Thomsen et al., 2020). Application of engineered EVs exogenously loaded with CDNs preferentially activated APCs in the TME, enhanced local Th1 response and $CD8^+$T cells infiltration in tumors as well as systemic anti-tumor immunity (Jang et al., 2021). Wang-Bishop et al. researchers mediated effective cytoplasmic delivery of the endogenous STING ligand cGAMP via intratumoral nanoparticle delivery, which enhanced STING activation relative to free cGAMP and improved response to PD-L1 immune checkpoint blockade, inducing immunogenic death in neuroblastoma (Wang-Bishop et al., 2020). Furthermore, the combination treatment of cGAMP with cisplatin exerted a stronger anti-tumor effect (Harabuchi et al., 2020).

Furthermore, the levels of intracellularly detectable DNA fragments are even more important for the degree of activation of the cGAS-STING pathway. Liu et al. recently found that STING signaling in $CD11c^+$ dendritic cells is required for the anti-tumor effects of CD47 blockade therapy and that tumor cells clearance by CD47 blockade is dependent on the recognition of tumor cells cytoplasmic DNA. Impaired recognition of endogenous DNA, including mtDNA, would result in ineffective tumor cells clearance (Liu et al., 2015).

**TABLE 1 Non-innate immune functions performed by cGAS-STING and their mechanisms.**

| Functionality | Mechanism | Pmcid |
|---|---|---|
| autophagy | Increased Drp1 promotes autophagy and ESCC progression by mtDNA stress mediated cGAS-STING pathway | 35,209,954 |
| | TFAM downregulation promotes autophagy and ESCC survival through mtDNA stress-mediated STING pathway | 35,750,756 |
| | GBP3-STING interaction in glioblastoma coordinates autophagy | 37,204,260 |
| Ferroptosis | Mitochondrial damage releases mtDNA, activates the cGAS-STING pathway, and induces autophagy-dependent ferroptosis | 32,186,434 |
| | STING increases mfn1/2-dependent mitochondrial fusion-induced ROS production causing ferroptosis | 34,195,205 |
| | Binding of cGAS localized on mitochondria to DRP1 promotes its oligomerization thereby inducing mitochondrial ROS accumulation and ferroptosis | 36,864,172 |
| Mitotic Cell Death | Mitotic inhibition activates the cGAS/STING pathway and induces apoptosis in breast cancer | 31,937,780 |
| | Slow accumulation of IRF3 phosphorylation by cGAS during mitotic arrest promotes cellular regulation through inhibition of Bcl-xL | 31,299,200 |
| DNA damage response | STING - TBK1 axis stimulates phosphorylation of kinase ATM, activates CHK2-p53-p21 pathway, and induces apoptosis due to cellular G1 phase blockade | 34,707,113 |
| glycolysis | STING targets hexokinase II and blocks its activity, limiting aerobic glycolysis in tumor cells to promote anti-tumor immunity | 37,443,289 |
| SASP | Cytoplasmic chromatin fragments accumulate in senescent cells and activate cGAS-STING-NF-κB signaling to promote SASP and cellular senescence | 32,047,109 |
| | nuclear porin Tpr activate the cGAS-STING pathway, and promoted the secretion of SASP in cancer cells | 37,543,653 |
| | cGAS-STING activation initiates oncogene-induced senescent TLR2 and A-SAAs expression to regulate SASP | 31,183,403 |

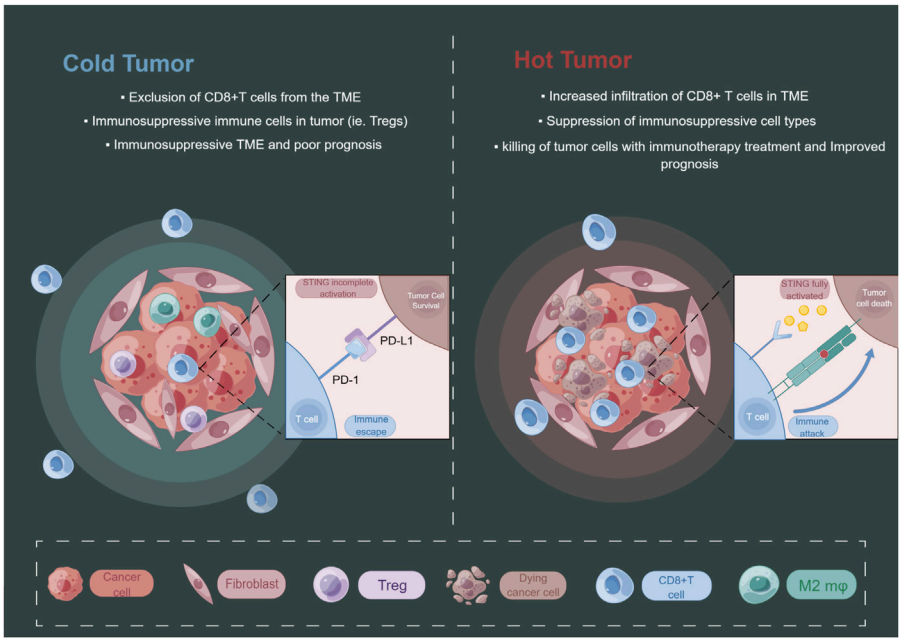


FIGURE 3
The level of STING activation in tumor cells may have an impact on the state of the tumor immune microenvironment. By Figdraw.

Gusho et al. found significantly elevated cGAS levels in human papillomavirus (a dsDNA virus) positive cells that stably maintained viral-free bodies (Gusho and Laimins, 2022). Given the complex regulatory roles of STING and its downstream pathways in immunotherapy targeting tumor cells, the combination of STING agonists with immune checkpoint blockade therapies may be a better approach. This combination application could reduce the use of one drug and provide an economical, beneficial, and safe option for patients. For example, the combination of STING agonists and IDO inhibitors significantly inhibited tumor progression in a mouse colorectal cancer model compared to immune checkpoint therapy alone (Shi et al., 2021). Yi et al. combined the STING agonists and the anti-TGF-β/PD-L1 bispecific antibody successfully enhanced innate and acquired immunity in mice, promoted antigen presentation, improved T-cells migration and chemotaxis, and upregulated the number and activity of tumor-infiltrating lymphocytes, demonstrating new perspectives for overcoming immunotherapy resistance (Yi et al., 2022). Since mtDNA acts as a potent agonist of cGAS, facilitating the release of mtDNA into the cytoplasm may be another promising direction. However, this places greater demands on the understanding of the temporal and spatial mechanisms involved in the tumor-promoting or inhibitory effects of cGAS-STING, as well as on the ability to correctly localize this pathway. Since whether horizontally transferred mtDNA is "friend" or "foe" is determined by the role played by STING at the stage of tumor progression, if the release of mtDNA is not high enough to reach the threshold for full activation of STING, it is more likely that the tumor will choose the path of no return, driving malignant programs and inhibiting their anti-tumor functions, producing counterproductive effects. Therefore, it may be possible to choose to combine with STING agonists and immune checkpoint inhibitors for better therapeutic effects when perhaps necessary.

## 10 Conclusion

Under conditions of oxidative stress or impaired mitochondrial quality control, mtDNA escapes into intra- or extracellular compartments of the cytoplasm. Once shed, mtDNA acts as damage-associated molecular patterns (DAMPs) that bind danger-signaling receptors to trigger an innate immune response (Picca et al., 2020). The consequences of mtDNA also depend on the cellular context and cover a wide range of states, including triggering an innate immune response, inducing cell death, or acting as a tumorigenic agent. mtDNA follows MOMP into the cytoplasm. In the past, MOMP appeared to play a bipolar role in cells, i.e., as long as apoptotic signals are generated, they can be propagated to all mitochondria in cells, leading to apoptotic cell death. However, under sublethal stress conditions, a fraction of mitochondria undergoe MOMP without inducing cell death, the phenomenon known as minority MOMP (miMOMP) (Ichim et al., 2015). The escape of mtDNA from mitochondria under miMOMP conditions is worth exploring because tumor cells are constantly exposed to chronic stress conditions such as hypoxia, and thus mtDNA leakage induced by miMOMP under such sublethal stress conditions may be involved in the maintenance of cytoplasmic dsDNA in tumor cells as well as its delivery to the outside of the cells. This chronic stimulation of the cGAS-STING pathway of appropriate intensity in tumor cells may mediate tumor cells survival and metastasis. In addition, the transfer of mtDNA from tumor cells to surrounding immune cells via EVs or TnTs may trigger an apoptotic cascade in host immune cells, thus creating an "immunoparalyzing" microenvironment for tumor cells, which may partly explain the depletion of $CD8^+$T cells in the immunosuppressive TME. There are still many unanswered questions about the pathway of mtDNA escape, including the lack of conclusive evidence for the increase in MIMP when mtDNA is extruded from MOMP. Further studies are needed on the influence of the GSDM family and mitochondrial dynamics aspects on mtDNA release.

The fact that cGAS-STING has complex consequences during tumor progression suggests that our understanding of the two sides of cGAS-STING in cancer progression is important for advancing cancer therapeutic strategies. As mentioned above, the use of STING agonists to induce tumor immunogenicity for anti-tumor therapy has achieved some efficacy. However, there is still a lack of detailed studies on individual differences in different tumors, stages, genotypes, *etc.*, as well as large sample data. These will determine the therapeutic response of tumor cells to STING agonists or antagonists. Admittedly, these studies have focused on the role of STING in innate immunity, and the exploration of the non-immune direction is currently very limited. Since STING modulation of processes such as tumor glycolysis, autophagy, and cell cycle has also shown anti-tumor effects, attempting to bypass the innate immunity aspect could prevent its potential for immune escape. For example, the atypical pathway autophagy process induced by STING participation is relatively independent and can be generated in the absence of TBK1 and IRF3 activation, and blocking IKK activation does not impair STING-induced autophagy (Gui et al., 2019). The cGAS-STING pathway can exert anti-tumor effects independent of IFNs and autophagy, which mainly depends on the recruitment ability of STING to TBK1. This suggests that the recruitment function of TBK1 to STING may be broader than the activation of IRF3 to promote IFNs synthesis (Yum et al., 2021). Overall, targeting STING will be a promising therapeutic prospect, whether focusing on the traditional innate immune aspects of STING or focusing on the emerging non-innate immune aspects of STING.

## Author contributions

JY: Writing–original draft. MY: Writing–original draft. YW: Visualization, Writing–review and editing. JS: Investigation, Writing–review and editing. YL: Writing–review and editing. LZ: Conceptualization, Writing–review and editing. BG: Supervision, Writing–review and editing.

## Funding

The author(s) declare financial support was received for the research, authorship, and/or publication of this article. This study research was funded by The National Natural Science Foundation of China (Grant No. 82273479 to LZ), The Research Fund of Jilin Provincial Science and Technology Department (Grant No. 20210204072YY to BG), and China-Japan Union Hospital and College of Basic Medical Sciences, Jilin University Union Project (Grant No. KYXZ2022JC05 to LZ).

## Acknowledgments

Thanks to Jian Wang in the lab for his help with this paper and to the institution Home for Researchers (www.home-for-researchers.com).

## Conflict of interest

The authors declare that the research was conducted in the absence of any commercial or financial relationships that could be construed as a potential conflict of interest.

## Publisher's note



## References

Aarreberg, L. D., Esser-Nobis, K., Driscoll, C., Shuvarikov, A., Roby, J. A., and Gale, M., JR. (2019). Interleukin-1β induces mtDNA release to activate innate immune signaling via cGAS-STING. *Mol. Cell.* 74, 801–815. doi:10.1016/j.molcel.2019.02.038

Ablasser, A., and Chen, Z. J. J. (2019). cGAS in action: expanding roles in immunity and inflammation. *Science* 363, eaat8657. doi:10.1126/science.aat8657

Ablasser, A., Goldeck, M., Cavlar, T., Deimling, T., Witte, G., Rohl, I., et al. (2013). cGAS produces a 2 '-5 '-linked cyclic dinucleotide second messenger that activates STING. *Nature* 498, 380–384. doi:10.1038/nature12306

An, X., Zhu, Y. Y., Zheng, T. S., Wang, G. Y., Zhang, M. H., Li, J. D., et al. (2019). An analysis of the expression and association with immune cell infiltration of the cGAS/STING pathway in pan-cancer. *Mol. Therapy-Nucleic Acids* 14, 80–89. doi:10.1016/j.omtn.2018.11.003

Andreeva, L., Hiller, B., Kostrewa, D., Lassig, C., Mann, C. C. D., Drexler, D. J., et al. (2017). cGAS senses long and HMGB/TFAM-bound U-turn DNA by forming protein-DNA ladders. *Nature* 549, 394–398. doi:10.1038/nature23890

Bakhoum, S., Ngo, B., Bakhoum, A., Cavallo-Fleming, J. A., Murphy, C. W., Powell, S. N., et al. (2018). Chromosomal instability drives metastasis through a cytosolic DNA response. *Int. J. Radiat. Oncol. Biol. Phys.* 102, S118. doi:10.1016/j.ijrobp.2018.06.295

Banerjee, D., Langberg, K., Abbas, S., Odermatt, E., Yerramothu, P., Volaric, M., et al. (2021). A non-canonical, interferon-independent signaling activity of cGAMP triggers DNA damage response signaling. *Nat. Commun.* 12, 6207. doi:10.1038/s41467-021-26240-9

Bernardi, P., and Di Lisa, F. (2015). The mitochondrial permeability transition pore: molecular nature and role as a target in cardioprotection. *J. Mol. Cell. Cardiol.* 78, 100–106. doi:10.1016/j.yjmcc.2014.09.023

Bernardi, P., Rasola, A., Forte, M., and Lippe, G. (2015). The mitochondrial permeability transition pore: channel formation by F-atp synthase, integration in signal transduction, and role in pathophysiology. *Physiol. Rev.* 95, 1111–1155. doi:10.1152/physrev.00001.2015

Bernardi, P. (2018). Why F-ATP synthase remains a strong candidate as the mitochondrial permeability transition pore. *Front. Physiology* 9, 1543. doi:10.3389/fphys.2018.01543

Cabral, A., Cabral, J. E., Wang, A. E. L. A., Zhang, Y. Y., Liang, H. L., Nikbakht, D., et al. (2023). Author correction: differential binding of NLRP3 to non-oxidized and ox-mtDNA mediates NLRP3 inflammasome activation. *Commun. Biol.* 6, 632. doi:10.1038/s42003-023-05019-2

Cao, H., Krueger, E. W., Chen, J., Drizyte-Miller, K., Schulz, M. E., and Mcniven, M. A. (2020). The anti-viral dynamin family member MxB participates in mitochondrial integrity. *Nat. Commun.* 11, 1048. doi:10.1038/s41467-020-14727-w

Carroll, E. C., Jin, L., Mori, A., Munoz-Wolf, N., Oleszycka, E., Moran, H. B. T., et al. (2016). The vaccine adjuvant chitosan promotes cellular immunity via DNA sensor cGAS-STING-dependent induction of type I interferons. *Immunity* 44, 597–608. doi:10.1016/j.immuni.2016.02.004

Chen, Q., Sun, L. J., and Chen, Z. J. J. (2016a). Regulation and function of the cGAS-STING pathway of cytosolic DNA sensing. *Nat. Immunol.* 17, 1142–1149. doi:10.1038/ni.3558

Chen, X., He, W. T., Hu, L. C., Li, J. X., Fang, Y., Wang, X., et al. (2016b). Pyroptosis is driven by non-selective gasdermin-D pore and its morphology is different from MLKL channel-mediated necroptosis. *Cell. Res.* 26, 1007–1020. doi:10.1038/cr.2016.100

Cheng, A. N., Cheng, L. C., Kuo, C. L., Lo, Y. K., Chou, H. Y., Chen, C. H., et al. (2020). Mitochondrial Lon-induced mtDNA leakage contributes to PD-L1-mediated immunoescape via STING-IFN signaling and extracellular vesicles. *J. Immunother. Cancer* 8, e001372. doi:10.1136/jitc-2020-001372

Chin, E. N., Yu, C. G., Vartabedian, V. F., Jia, Y., Kumar, M., Gamo, A. M., et al. (2020). Antitumor activity of a systemic STING-activating non-nucleotide cGAMP mimetic. *Science* 369, 993–999. doi:10.1126/science.abb4255

Chipuk, J. E., Bouchier-Hayes, L., and Green, D. R. (2006). Mitochondrial outer membrane permeabilization during apoptosis: the innocent bystander scenario. *Cell. Death Differ.* 13, 1396–1402. doi:10.1038/sj.cdd.4401963

Clancy, J. W., Sheehan, C. S., Boomgarden, A. C., and D'Souza-Schorey, C. (2022). Recruitment of DNA to tumor-derived microvesicles. *Cell. Rep.* 38, 110443. doi:10.1016/j.celrep.2022.110443

Corbera-Bellalta, M., Planas-Rigol, E., Lozano, E., Terrades-Garcia, N., Alba, M. A., Prieto-Gonzalez, S., et al. (2016). Blocking interferon gamma reduces expression of chemokines CXCL9, CXCL10 and CXCL11 and decreases macrophage infiltration in *ex vivo* cultured arteries from patients with giant cell arteritis. *Ann. Rheumatic Dis.* 75, 1177–1186. doi:10.1136/annrheumdis-2015-208371

Coussens, L. M., and Werb, Z. (2002). Inflammation and cancer. *Nature* 420, 860–867. doi:10.1038/nature01322

Dai, J., Huang, Y. J., He, X. H., Zhao, M., Wang, X. Z., Liu, Z. S., et al. (2019). Acetylation blocks cGAS activity and inhibits self-DNA-induced autoimmunity. *Cell.* 176, 1447–1460. doi:10.1016/j.cell.2019.01.016

De Gaetano, A., Solodka, K., Zanini, G., Selleri, V., Mattioli, A. V., Nasi, M., et al. (2021). Molecular mechanisms of mtDNA-mediated inflammation. *Cells* 10, 2898. doi:10.3390/cells10112898

Diamond, M. S., Kinder, M., Matsushita, H., Mashayekhi, M., Dunn, G. P., Archambault, J. M., et al. (2011). Type I interferon is selectively required by dendritic cells for immune rejection of tumors. *J. Exp. Med.* 208, 1989–2003. doi:10.1084/jem.20101158

Diner, E. J., Burdette, D. L., Wilson, S. C., Monroe, K. M., Kellenberger, C. A., Hyodo, M., et al. (2013). The innate immune DNA sensor cGAS produces a noncanonical cyclic dinucleotide that activates human STING. *Cell. Rep.* 3, 1355–1361. doi:10.1016/j.celrep.2013.05.009

Ding, J. J., Wang, K., Liu, W., She, Y., Sun, Q., Shi, J. J., et al. (2016). Pore-forming activity and structural autoinhibition of the gasdermin family. *Nature* 535, 111–116. doi:10.1038/nature18590

Dobbs, N., Burnaevskiy, N., Chen, D. D., Gonugunta, V. K., Alto, N. M., and Yan, N. (2015). STING activation by translocation from the ER is associated with infection and autoinflammatory disease. *Cell. Host Microbe* 18, 157–168. doi:10.1016/j.chom.2015.07.001

Dong, L.-F., Kovarova, J., Bajzikova, M., Bezawork-Geleta, A., Svec, D., Endaya, B., et al. (2017). Horizontal transfer of whole mitochondria restores tumorigenic potential in mitochondrial DNA-deficient cancer cells. *ELife* 6, e22187. doi:10.7554/eLife.22187

Dou, Z. X., Ghosh, K., Vizioli, M. G., Zhu, J. J., Sen, P., Wangensteen, K. J., et al. (2017). Cytoplasmic chromatin triggers inflammation in senescence and cancer. *Nature* 550, 402–406. doi:10.1038/nature24050

Du, S. S., Chen, G. W., Yang, P., Chen, Y. X., Hu, Y., Zhao, Q. Q., et al. (2022). Radiation therapy promotes hepatocellular carcinoma immune cloaking via PD-L1 upregulation induced by cGAS-STING activation. *Int. J. Radiat. Oncol. Biol. Phys.* 112, 1243–1255. doi:10.1016/j.ijrobp.2021.12.162

Ergun, S. L., Fernandez, D., Weiss, T. M., and Li, L. Y. (2019). STING polymer structure reveals mechanisms for activation, hyperactivation, and inhibition. *Cell.* 178, 290–301. doi:10.1016/j.cell.2019.05.036

Falahat, R., Berglund, A., Putney, R. M., Perez-Villarroel, P., Aoyama, S., Pilon-Thomas, S., et al. (2021). Epigenetic reprogramming of tumor cell-intrinsic STING function sculpts antigenicity and T cell recognition of melanoma. *Proc. Natl. Acad. Sci. U. S. A.* 118, e2013598118. doi:10.1073/pnas.2013598118

Flores-Romero, H., Hohorst, L., John, M., Albert, M. C., King, L. E., Beckmann, L., et al. (2022). BCL-2-family protein tBID can act as a BAX-like effector of apoptosis. *Embo J.* 41, e108690. doi:10.15252/embj.2021108690

Fuertes, M. B., Kacha, A. K., Kline, J., Woo, S. R., Kranz, D. M., Murphy, K. M., et al. (2011). Host type I IFN signals are required for antitumor CD8+ T cell responses through CD8{alpha}+ dendritic cells. *J. Exp. Med.* 208, 2005–2016. doi:10.1084/jem.20101159

Gao, P., Ascano, M., Wu, Y., Barchet, W., Gaffney, B. L., Zillinger, T., et al. (2013a). Cyclic [G(2 ',5 ') pA(3 ',5 ')p] is the metazoan second messenger produced by DNA-activated cyclic GMP-AMP synthase. *Cell.* 153, 1094–1107. doi:10.1016/j.cell.2013.04.046

Gao, P., Ascano, M., Zillinger, T., Wang, W. Y., Dai, P. H., Serganov, A. A., et al. (2013b). Structure-function analysis of STING activation by c[G(2 ',5 ') pA(3 ',5 ')p] and targeting by antiviral DMXAA. *Cell.* 154, 748–762. doi:10.1016/j.cell.2013.07.023

Gao, Y., Zheng, X. P., Chang, B. Y., Lin, Y. J., Huang, X. D., Wang, W., et al. (2022). Intercellular transfer of activated STING triggered by RAB22A-mediated non-canonical autophagy promotes antitumor immunity. *Cell. Res.* 32, 1086–1104. doi:10.1038/s41422-022-00731-w

Garcia, N., and Chavez, E. (2007). Mitochondrial DNA fragments released through the permeability transition pore correspond to specific gene size. *Life Sci.* 81, 1160–1166. doi:10.1016/j.lfs.2007.08.019

Garcia, N., Garcia, J. J., Correa, F., and Chavez, E. (2005). The permeability transition pore as a pathway for the release of mitochondrial DNA. *Life Sci.* 76, 2873–2880. doi:10.1016/j.lfs.2004.12.012

Garner, E., Kim, Y., Lach, F. P., Kottemann, M. C., and Smogorzewska, A. (2013). Human GEN1 and the SLX4-associated nucleases MUS81 and SLX1 are essential for the resolution of replication-induced Holliday junctions. *Cell. Rep.* 5, 207–215. doi:10.1016/j.celrep.2013.08.041

Gomes, M. T. R., GuimarãES, E. S., Marinho, F. V., Macedo, I., Aguiar, E. R. G. R., Barber, G. N., et al. (2021). STING regulates metabolic reprogramming in macrophages via HIF-1α during Brucella infection. *PLoS Pathog.* 17, e1009597. doi:10.1371/journal.ppat.1009597

Grabosch, S., Bulatovic, M., Zeng, F. T. Z., Ma, T. Z., Zhang, L. X., Ross, M., et al. (2019). Cisplatin-induced immune modulation in ovarian cancer mouse models with distinct inflammation profiles. *Oncogene* 38, 2380–2393. doi:10.1038/s41388-018-0581-9

Gui, X., Yang, H., Li, T., Tan, X. J., Shi, P. Q., Li, M. H., et al. (2019). Autophagy induction via STING trafficking is a primordial function of the cGAS pathway. *Nature* 567, 262–266. doi:10.1038/s41586-019-1006-9

Guo, X. H., Ni, J., Liang, Z. Q., Xue, J. L., Fenech, M. F., and Wang, X. (2019). The molecular origins and pathophysiological consequences of micronuclei: new insights into an age-old problem. *Mutat. Research-Reviews Mutat. Res.* 779, 1–35. doi:10.1016/j.mrrev.2018.11.001

Gupta, V., Agrawal, R. C., and Trivedi, P. (2011). Reduction in cisplatin genotoxicity (micronucleus formation) in non target cells of mice by protransfersome gel formulation used for management of cutaneous squamous cell carcinoma. *Acta Pharm.* 61, 63–71. doi:10.2478/v10007-011-0004-8

Gusho, E., and Laimins, L. A. (2022). Human papillomaviruses sensitize cells to DNA damage induced apoptosis by targeting the innate immune sensor cGAS. *Plos Pathog.* 18, e1010725. doi:10.1371/journal.ppat.1010725

Halestrap, A. P., Mcstay, G. P., and Clarke, S. J. (2002). The permeability transition pore complex: another view. *Biochimie* 84, 153–166. doi:10.1016/s0300-9084(02)01375-5

Harabuchi, S., Kosaka, A., Yajima, Y., Nagata, M., Hayashi, R., Kumai, T., et al. (2020). Intratumoral STING activations overcome negative impact of cisplatin on antitumor immunity by inflaming tumor microenvironment in squamous cell carcinoma. *Biochem. Biophysical Res. Commun.* 522, 408–414. doi:10.1016/j.bbrc.2019.11.107

Harding, S. M., Benci, J. L., Irianto, J., Discher, D. E., Minn, A. J., and Reenberg, R. A. G. (2017). Mitotic progression following DNA damage enables pattern recognition within micronuclei. *Nature* 548, 466–470. doi:10.1038/nature23470

Hatch, E. M., Fischer, A. H., Deerinck, T. J., and Hetzer, M. W. (2013). Catastrophic nuclear envelope collapse in cancer cell micronuclei. *Cell.* 154, 47–60. doi:10.1016/j.cell.2013.06.007

Hayman, T. J., Baro, M., Macneil, T., Phoomak, C., Aung, T. N., Cui, W., et al. (2021). STING enhances cell death through regulation of reactive oxygen species and DNA damage. *Nat. Commun.* 12, 2327. doi:10.1038/s41467-021-22572-8

Hopfner, K. P., and Hornung, V. (2020). Molecular mechanisms and cellular functions of cGAS-STING signalling. *Nat. Rev. Mol. Cell. Biol.* 21, 501–521. doi:10.1038/s41580-020-0244-x

Hu, M. M., Yang, Q., Xie, X. Q., Liao, C. Y., Lin, H., Liu, T. T., et al. (2016). Sumoylation promotes the stability of the DNA sensor cGAS and the adaptor STING to regulate the kinetics of response to DNA virus. *Immunity* 45, 555–569. doi:10.1016/j.immuni.2016.08.014

Hu, M., Zhou, M., Bao, X., Pan, D., Jiao, M., Liu, X., et al. (2021a). ATM inhibition enhances cancer immunotherapy by promoting mtDNA leakage and cGAS/STING activation. *J. Clin. Invest.* 131, e139333. doi:10.1172/JCI139333

Hu, M. J., Zhou, M., Bao, X. H., Pan, D., Jiao, M., Liu, X. J., et al. (2021b). ATM inhibition enhances cancer immunotherapy by promoting mtDNA leakage and cGAS/STING activation. *J. Clin. Investigation* 131, e139333. doi:10.1172/JCI139333

Hu, J., Sanchez-Rivera, F. J., Wang, Z. H., Johnson, G. N., Ho, Y. J., Ganesh, K., et al. (2023). STING inhibits the reactivation of dormant metastasis in lung adenocarcinoma. *Nature* 616, 806–813. doi:10.1038/s41586-023-05880-5

Huang, Y. H., Liu, X. Y., Du, X. X., Jiang, Z. F., and Su, X. D. (2012). The structural basis for the sensing and binding of cyclic di-GMP by STING. *Nat. Struct. Mol. Biol.* 19, 728–730. doi:10.1038/nsmb.2333

Huang, L. S., Hong, Z. G., Wu, W., Xiong, S. Q., Zhong, M., Gao, X. P., et al. (2020). mtDNA activates cGAS signaling and suppresses the YAP-mediated endothelial cell proliferation program to promote inflammatory injury. *Immunity* 52, 475–486. doi:10.1016/j.immuni.2020.02.002

Hurwitz, S. N., Rider, M. A., Bundy, J. L., Liu, X., Singh, R. K., and Meckes, D. G. (2016). Proteomic profiling of NCI-60 extracellular vesicles uncovers common protein cargo and cancer type-specific biomarkers. *Oncotarget* 7, 86999–87015. doi:10.18632/oncotarget.13569

Ichim, G., Lopez, J., Ahmed, S. U., Muthalagu, N., Giampazolias, E., Delgado, M. E., et al. (2015). Limited mitochondrial permeabilization causes DNA damage and genomic instability in the absence of cell death. *Mol. Cell.* 58, 900. doi:10.1016/j.molcel.2015.05.028

Jang, S. C., Economides, K. D., Moniz, R. J., Sia, C. L., Lewis, N., Mccoy, C., et al. (2021). ExoSTING, an extracellular vesicle loaded with STING agonists, promotes tumor immune surveillance. *Commun. Biol.* 4, 497. doi:10.1038/s42003-021-02004-5

Jiang, H., Xue, X. Y., Panda, S., Kawale, A., Hooy, R. M., Liang, F. S., et al. (2019). Chromatin-bound cGAS is an inhibitor of DNA repair and hence accelerates genome destabilization and cell death. *Embo J.* 38, e102718. doi:10.15252/embj.2019102718

Kausar, S., Yang, L. Q., Abbas, M. N., Hu, X., Zhao, Y. J., Zhu, Y., et al. (2020). Mitochondrial DNA: a key regulator of anti-microbial innate immunity. *Genes* 11, 86. doi:10.3390/genes11010086

Keinan, N., Tyomkin, D., and Shoshan-Barmatz, V. (2010). Oligomerization of the mitochondrial protein voltage-dependent anion channel is coupled to the induction of apoptosis. *Mol. Cell. Biol.* 30, 5698–5709. doi:10.1128/MCB.00165-10

Kim, J., Gupta, R., Blanco, L. P., Yang, S. T., Shteinfer-Kuzmine, A., Wang, K. N., et al. (2019). VDAC oligomers form mitochondrial pores to release mtDNA fragments and promote lupus-like disease. *Science* 366, 1531–1536. doi:10.1126/science.aav4011

Kleih, M., Bopple, K., Dong, M., Gaissler, A., Heine, S., Olayioye, M. A., et al. (2019). Direct impact of cisplatin on mitochondria induces ROS production that dictates cell fate of ovarian cancer cells. *Cell. Death Dis.* 10, 851. doi:10.1038/s41419-019-2081-4

Konno, H., Yamauchi, S., Berglund, A., Putney, R. M., Mule, J. J., and Barber, G. N. (2018). Suppression of STING signaling through epigenetic silencing and missense mutation impedes DNA damage mediated cytokine production. *Oncogene* 37, 2037–2051. doi:10.1038/s41388-017-0120-0

Kowal, J., Arras, G., Colombo, M., Jouve, M., Morath, J. P., Primdal-Bengtson, B., et al. (2016). Proteomic comparison defines novel markers to characterize heterogeneous populations of extracellular vesicle subtypes. *Proc. Natl. Acad. Sci. U. S. A.* 113, E968–E977. doi:10.1073/pnas.1521230113

Kuchta, K., Knizewski, L., Wyrwicz, L. S., Rychlewski, L., and Ginalski, K. (2009). Comprehensive classification of nucleotidyltransferase fold proteins: identification of novel families and their representatives in human. *Nucleic Acids Res.* 37, 7701–7714. doi:10.1093/nar/gkp854

Kwon, J., and Bakhoum, S. F. (2020). The cytosolic DNA-sensing cGAS-STING pathway in cancer. *Cancer Discov.* 10, 26–39. doi:10.1158/2159-8290.CD-19-0761

Li, A. P., Yi, M., Qin, S., Song, Y. P., Chu, Q., and Wu, K. M. (2019). Activating cGAS-STING pathway for the optimal effect of cancer immunotherapy. *J. Hematol. Oncol.* 12, 35. doi:10.1186/s13045-019-0721-x

Li, C. F., Liu, J., Hou, W., Kang, R., and Tang, D. L. (2021a). STING1 promotes ferroptosis through MFN1/2-dependent mitochondrial fusion. *Front. Cell. Dev. Biol.* 9, 698679. doi:10.3389/fcell.2021.698679

Li, C. F., Zhang, Y., Liu, J., Kang, R., Klionsky, D. J., and Tang, D. L. (2021b). Mitochondrial DNA stress triggers autophagy-dependent ferroptotic death. *Autophagy* 17, 948–960. doi:10.1080/15548627.2020.1739447

Li, T., Huang, T. Z., and Chen, Z. J. J. (2021c). Phosphorylation and chromatin tethering prevent cGAS activation during mitosis. *J. Immunol.* 206, 15.17. doi:10.4049/jimmunol.206.supp.15.17

Li, Y. J., Chen, H., Yang, Q., Wan, L. X., Zhao, J., Wu, Y. Y., et al. (2022). Increased Drp1 promotes autophagy and ESCC progression by mtDNA stress mediated cGAS-STING pathway. *J. Exp. Clin. Cancer Res.* 41, 76. doi:10.1186/s13046-022-02262-z

Li, J.-Y., Zhao, Y., Gong, S., Wang, M.-M., Liu, X., He, Q.-M., et al. (2023). TRIM21 inhibits irradiation-induced mitochondrial DNA release and impairs antitumour immunity in nasopharyngeal carcinoma tumour models. *Nat. Commun.* 14, 865. doi:10.1038/s41467-023-36523-y

Liu, X. J., Pu, Y., Cron, K., Deng, L. F., Kline, J., Frazier, W. A., et al. (2015). CD47 blockade triggers T cell-mediated destruction of immunogenic tumors. *Nat. Med.* 21, 1209–1215. doi:10.1038/nm.3931

Liu, X., Zhang, Z. B., Ruan, J. B., Pan, Y. D., Magupalli, V. G., Wu, H., et al. (2016). Inflammasome-activated gasdermin D causes pyroptosis by forming membrane pores. *Nature* 535, 153–158. doi:10.1038/nature18629

Liu, D., Wu, H., Wang, C. G., Li, Y. J., Tian, H. B., Siraj, S., et al. (2019a). STING directly activates autophagy to tune the innate immune response. *Cell. Death Differ.* 26, 1735–1749. doi:10.1038/s41418-018-0251-z

Liu, R. Q., Xu, F., Bi, S. W., Zhao, X. S., Jia, B. S., and Cen, Y. (2019b). Mitochondrial DNA-induced inflammatory responses and lung injury in thermal injury murine model: protective effect of cyclosporine-A. *J. Burn Care & Res.* 40, 355–360. doi:10.1093/jbcr/irz029

Mcarthur, K., Whitehead, L. W., Heddleston, J. M., Li, L., Padman, B. S., Oorschot, V., et al. (2018). BAK/BAX macropores facilitate mitochondrial herniation and mtDNA efflux during apoptosis. *Science* 359, eaao6047. doi:10.1126/science.aao6047

Meyer, J. N., Leuthner, T. C., and Luz, A. L. (2017). Mitochondrial fusion, fission, and mitochondrial toxicity. *Toxicology* 391, 42–53. doi:10.1016/j.tox.2017.07.019

Mukai, K., Konno, H., Akiba, T., Uemura, T., Waguri, S., Kobayashi, T., et al. (2016). Activation of STING requires palmitoylation at the Golgi. *Nat. Commun.* 7, 11932. doi:10.1038/ncomms11932

Nassour, J., Radford, R., Correia, A., Fuste, J. M., Schoell, B., Jauch, A., et al. (2019). Autophagic cell death restricts chromosomal instability during replicative crisis. *Nature* 565, 659–663. doi:10.1038/s41586-019-0885-0

Pasquier, J., Guerrouahen, B. S., al Thawadi, H., Abu Kaoud, N., Maleki, M., Le Foll, F., et al. (2013). Preferential transfer of mitochondria from endothelial to cancer cells through tunneling nanotubes modulates chemoresistance. *Clin. Cancer Res.* 19, 94. doi:10.1186/1479-5876-11-94

Patrushev, M., Kasymov, V., Patrusheva, V., Ushakova, T., Gogvadze, V., and Gaziev, A. I. (2006). Release of mitochondrial DNA fragments from brain mitochondria of irradiated mice. *Mitochondrion* 6, 43–47. doi:10.1016/j.mito.2005.12.001

Piantadosi, C. A. (2020). Mitochondrial DNA, oxidants, and innate immunity. *Free Radic. Biol. Med.* 152, 455–461. doi:10.1016/j.freeradbiomed.2020.01.013

Picca, A., Calvani, R., Coelho, H. J., Landi, F., Bernabei, R., and Marzetti, E. (2020). Mitochondrial dysfunction, oxidative stress, and neuroinflammation: intertwined roads to neurodegeneration. *Antioxidants* 9, 647. doi:10.3390/antiox9080647

Rabas, N., Palmer, S., Mitchell, L., Ismail, S., Gohlke, A., Riley, J. S., et al. (2021). PINK1 drives production of mtDNA-containing extracellular vesicles to promote invasiveness. *J. Cell. Biol.* 220, e202006049. doi:10.1083/jcb.202006049

Rebbeck, C. A., Leroi, A. M., and Burt, A. (2011). Mitochondrial capture by a transmissible cancer. *Science* 331, 303. doi:10.1126/science.1197696

Reislander, T., Groelly, F. J., and Tarsounas, M. (2020). DNA damage and cancer immunotherapy: a STING in the tale. *Mol. Cell.* 80, 21–28. doi:10.1016/j.molcel.2020.07.026

Riley, J. S., and Tait, S. W. G. (2020). Mitochondrial DNA in inflammation and immunity. *Embo Rep.* 21, e49799. doi:10.15252/embr.201949799

Riley, J. S., Quarato, G., Cloix, C., Lopez, J., O'Prey, J., Pearson, M., et al. (2018). Mitochondrial inner membrane permeabilisation enables mtDNA release during apoptosis. *Embo J.* 37, e99238. doi:10.15252/embj.201899238

Rong, Y., Zhang, S., Nandi, N., Wu, Z., Li, L., Liu, Y., et al. (2022). STING controls energy stress-induced autophagy and energy metabolism via STX17. *J. Cell. Biol.* 221, e202202060. doi:10.1083/jcb.202202060

Salaud, C., Alvarez-Arenas, A., Geraldo, F., Belmonte-Beitia, J., Calvo, G. F., Gratas, C., et al. (2020). Mitochondria transfer from tumor-activated stromal cells (TASC) to primary Glioblastoma cells. *Biochem. Biophysical Res. Commun.* 533, 139–147. doi:10.1016/j.bbrc.2020.08.101

Sansone, P., Savini, C., Kurelac, I., Chang, Q., Amato, L. B., Strillacci, A., et al. (2017). Packaging and transfer of mitochondrial DNA via exosomes regulate escape from dormancy in hormonal therapy-resistant breast cancer (vol 114, pg E9066, 2017). *Proc. Natl. Acad. Sci. U. S. A.* 114, E10255. doi:10.1073/pnas.1704862114

Shang, G. J., Zhu, D. Y., Li, N., Zhang, J. B., Zhu, C. Y., Lu, D. F., et al. (2012). Crystal structures of STING protein reveal basis for recognition of cyclic di-GMP. *Nat. Struct. Mol. Biol.* 19, 725–727. doi:10.1038/nsmb.2332

Shang, G. J., Zhang, C. G., Chen, Z. J. J., Bai, X. C., and Zhang, X. W. (2019). Cryo-EM structures of STING reveal its mechanism of activation by cyclic GMP-AMP. *Nature* 567, 389–393. doi:10.1038/s41586-019-0998-5

Shi, J. Q., Liu, C. Q., Luo, S. N., Cao, T. Y., Lin, B. L., Zhou, M., et al. (2021). STING agonist and Ido inhibitor combination therapy inhibits tumor progression in murine models of colorectal cancer. *Cell. Immunol.* 366, 104384. doi:10.1016/j.cellimm.2021.104384

Shoshan-Barmatz, V., Israelson, A., Brdiczka, D., and Sheu, S. S. (2006). The voltage-dependent anion channel (VDAC): function in intracellular signalling, cell life and cell death. *Curr. Pharm. Des.* 12, 2249–2270. doi:10.2174/138161206777585111

Shu, C., Yi, G. H., Watts, T., Kao, C. C., and Li, P. W. (2012). Structure of STING bound to cyclic di-GMP reveals the mechanism of cyclic dinucleotide recognition by the immune system. *Nat. Struct. Mol. Biol.* 19, 722–724. doi:10.1038/nsmb.2331

Smale, S. T. (2010). Selective transcription in response to an inflammatory stimulus. *Cell.* 140, 833–844. doi:10.1016/j.cell.2010.01.037

Sun, L. J., Wu, J. X., Du, F. H., Chen, X., and Chen, Z. J. J. (2013). Cyclic GMP-AMP synthase is a cytosolic DNA sensor that activates the type I interferon pathway. *Science* 339, 786–791. doi:10.1126/science.1232458

Tan, A. S., Baty, J. W., Dong, L. F., Bezawork-Geleta, A., Endaya, B., Goodwin, J., et al. (2015). Mitochondrial genome acquisition restores respiratory function and tumorigenic potential of cancer cells without mitochondrial DNA. *Cell. Metab.* 21, 81–94. doi:10.1016/j.cmet.2014.12.003

Tanaka, Y., and Chen, Z. J. J. (2012). STING specifies IRF3 phosphorylation by TBK1 in the cytosolic DNA signaling pathway. *Sci. Signal.* 5, ra20. doi:10.1126/scisignal.2002521

Tang, D. L., Chen, X., Kang, R., and Kroemer, G. (2021). Ferroptosis: molecular mechanisms and health implications. *Cell. Res.* 31, 107–125. doi:10.1038/s41422-020-00441-1

Thomsen, M. K., Skouboe, M. K., Boularan, C., Vernejoul, F., Lioux, T., Leknes, S. L., et al. (2020). The cGAS-STING pathway is a therapeutic target in a preclinical model of hepatocellular carcinoma. *Oncogene* 39, 1652–1664. doi:10.1038/s41388-019-1108-8

Tigano, M., Vargas, D. C., Tremblay-Belzile, S., Fu, Y., and Sfeir, A. (2021). Nuclear sensing of breaks in mitochondrial DNA enhances immune surveillance. *Nature* 591, 477–481. doi:10.1038/s41586-021-03269-w

Todkar, K., Chikhi, L., Desjardins, V., El-Mortada, F., Pepin, G., and Germain, M. (2021). Selective packaging of mitochondrial proteins into extracellular vesicles prevents the release of mitochondrial DAMPs. *Nat. Commun.* 12, 1971. doi:10.1038/s41467-021-21984-w

Wallace, D. C. (2012). Mitochondria and cancer. *Nat. Rev. Cancer* 12, 685–698. doi:10.1038/nrc3365

Wang, Y. T., Ning, X. H., Gao, P. F., Wu, S. X., Sha, M. Y., Lv, M. Z., et al. (2017). Inflammasome activation triggers caspase-1-mediated cleavage of cGAS to regulate responses to DNA virus infection. *Immunity* 46, 393–404. doi:10.1016/j.immuni.2017.02.011

Wang, H. W., Zang, C. L., Ren, M. T., Shang, M. D., Wang, Z. H., Peng, X. M., et al. (2020a). Cellular uptake of extracellular nucleosomes induces innate immune responses by binding and activating cGMP-AMP synthase (cGAS). *Sci. Rep.* 10, 15385. doi:10.1038/s41598-020-72393-w

Wang, J. X., Choi, S. Y. C., Niu, X. J., Kang, N., Xue, H., Killam, J., et al. (2020b). Lactic acid and an acidic tumor microenvironment suppress anticancer immunity. *Int. J. Mol. Sci.* 21, 8363. doi:10.3390/ijms21218363

Wang-Bishop, L., Wehbe, M., Shae, D., James, J., Hacker, B. C., Garland, K., et al. (2020). Potent STING activation stimulates immunogenic cell death to enhance antitumor immunity in neuroblastoma. *J. Immunother. Cancer* 8, e000282. doi:10.1136/jitc-2019-000282

Weindel, C. G., Martinez, E. L., Zhao, X., Mabry, C. J., Bell, S. L., Vail, K. J., et al. (2022). Mitochondrial ROS promotes susceptibility to infection via gasdermin D-mediated necroptosis. *Cell.* 185, 3214–3231.e23. doi:10.1016/j.cell.2022.06.038

West, A. P., and Shadel, G. S. (2017). Mitochondrial DNA in innate immune responses and inflammatory pathology. *Nat. Rev. Immunol.* 17, 363–375. doi:10.1038/nri.2017.21

West, A. P., Khoury-Hanold, W., Staron, M., Tal, M. C., Pineda, C. M., Lang, S. M., et al. (2015). Mitochondrial DNA stress primes the antiviral innate immune response. *Nature* 520, 553–557. doi:10.1038/nature14156

Wu, J. X., Sun, L. J., Chen, X., Du, F. H., Shi, H. P., Chen, C., et al. (2013). Cyclic GMP-AMP is an endogenous second messenger in innate immune signaling by cytosolic DNA. *Science* 339, 826–830. doi:10.1126/science.1229963

Wu, Z., Sainz, A. G., and Shadel, G. S. (2021a). Mitochondrial DNA: cellular genotoxic stress sentinel. *Trends Biochem. Sci.* 46, 812–821. doi:10.1016/j.tibs.2021.05.004

Wu, Z., Sainz, A. G., and Shadel, G. S. (2021b). Mitochondrial DNA: cellular genotoxic stress sentinel. *Trends Biochem. Sci.* 46, 812–821. doi:10.1016/j.tibs.2021.05.004

Xia, P. Y., Ye, B. Q., Wang, S., Zhu, X. X., Du, Y., Xiong, Z., et al. (2016a). Erratum: glutamylation of the DNA sensor cGAS regulates its binding and synthase activity in antiviral immunity. *Nat. Immunol.* 17, 469. doi:10.1038/ni0416-469e

Xia, T. L., Konno, H., Ahn, J., and Barber, G. N. (2016b). Deregulation of STING signaling in colorectal carcinoma constrains DNA damage responses and correlates with tumorigenesis. *Cell. Rep.* 14, 282–297. doi:10.1016/j.celrep.2015.12.029

Xia, T. L., Konno, H., and Barber, G. N. (2016c). Recurrent loss of STING signaling in melanoma correlates with susceptibility to viral oncolysis. *Cancer Res.* 76, 6747–6759. doi:10.1158/0008-5472.CAN-16-1404

Xian, H. X., Watari, K., Sanchez-Lopez, E., Offenberger, J., Onyuru, J., Sampath, H., et al. (2022). Oxidized DNA fragments exit mitochondria via mPTP- and VDAC-dependent channels to activate NLRP3 inflammasome and interferon signaling. *Immunity* 55, 1370–1385.e8. doi:10.1016/j.immuni.2022.06.007

Yang, H., Wang, H., Ren, J., Chen, Q., and Chen, Z. J. (2017). cGAS is essential for cellular senescence. *Proc. Natl. Acad. Sci. U. S. A.* 114, E4612–e4620. doi:10.1073/pnas.1705499114

Yi, M., Niu, M., Wu, Y., Ge, H., Jiao, D., Zhu, S., et al. (2022). Combination of oral STING agonist MSA-2 and anti-TGF-β/PD-L1 bispecific antibody YM101: a novel immune cocktail therapy for non-inflamed tumors. *J. Hematol. Oncol.* 15, 142. doi:10.1186/s13045-022-01363-8

Yum, S., Li, M., Fang, Y., and Chen, Z. J. (2021). TBK1 recruitment to STING activates both IRF3 and NF-κB that mediate immune defense against tumors and viral infections. *Proc. Natl. Acad. Sci. U. S. A.* 118, e2100225118. doi:10.1073/pnas.2100225118

Zeng, X., Li, X. S., Zhang, Y. D., Cao, C. X., and Zhou, Q. (2022). IL6 induces mtDNA leakage to affect the immune escape of endometrial carcinoma via cGAS-STING. *J. Immunol. Res.* 2022, 3815853. doi:10.1155/2022/3815853

Zhang, J., Hu, M. M., Wang, Y. Y., and Shu, H. B. (2012). TRIM32 protein modulates type I interferon induction and cellular antiviral response by targeting MITA/STING protein for K63-linked ubiquitination. *J. Biol. Chem.* 287, 28646–28655. doi:10.1074/jbc.M112.362608

Zhang, X., Shi, H. P., Wu, J. X., Zhang, X. W., Sun, L. J., Chen, C., et al. (2013). Cyclic GMP-AMP containing mixed phosphodiester linkages is an endogenous high-affinity ligand for STING. *Mol. Cell.* 51, 226–235. doi:10.1016/j.molcel.2013.05.022

Zhang, R. X., Kang, R., and Tang, D. L. (2021). The STING1 network regulates autophagy and cell death. *Signal Transduct. Target. Ther.* 6, 208. doi:10.1038/s41392-021-00613-4

Zhang, L., Jiang, C., Zhong, Y., Sun, K., Jing, H., Song, J., et al. (2023a). STING is a cell-intrinsic metabolic checkpoint restricting aerobic glycolysis by targeting HK2. *Nat. Cell. Biol.* 25, 1208–1222. doi:10.1038/s41556-023-01185-x

Zhang, L., Wei, X., Wang, Z., Liu, P., Hou, Y., Xu, Y., et al. (2023b). NF-κB activation enhances STING signaling by altering microtubule-mediated STING trafficking. *Cell. Rep.* 42, 112185. doi:10.1016/j.celrep.2023.112185

Zhang, Q., Wei, J. Y., Liu, Z. H., Huang, X. X., Sun, M. M., Lai, W. J., et al. (2023c). Corrigendum to "STING signaling sensing of DRP1-dependent mtDNA release in kupffer cells contributes to lipopolysaccharide-induced liver injury in mice" [Redox Biol. 54 (2022) 102367/PMID:35724543]. *Redox Biol.* 62, 102664. doi:10.1016/j.redox.2023.102664

Zhu, X. Q., Luo, L., Xiong, Y. Y., Jiang, N., Wang, Y. R., Lv, Y., et al. (2022). VDAC1 oligomerization may enhance DDP-induced hepatocyte apoptosis by exacerbating oxidative stress and mitochondrial DNA damage. *Febs Open Bio* 12, 516–522. doi:10.1002/2211-5463.13359

Zhu, Z. C., Zhou, X., Du, H. W., Cloer, E. W., Zhang, J. M., Mei, L., et al. (2023). STING suppresses mitochondrial VDAC2 to govern RCC growth independent of innate immunity. *Adv. Sci.* 10, e2203718. doi:10.1002/advs.202203718

Zierhut, C., and Funabiki, H. (2015). Nucleosome functions in spindle assembly and nuclear envelope formation. *Bioessays* 37, 1074–1085. doi:10.1002/bies.201500045

Zierhut, C., Jenness, C., Kimura, H., and Funabiki, H. (2014). Nucleosomal regulation of chromatin composition and nuclear assembly revealed by histone depletion. *Nat. Struct. Mol. Biol.* 21, 617–625. doi:10.1038/nsmb.2845

Zierhut, C., Yamaguchi, N., Paredes, M., Luo, J. D., Carroll, T., and Funabiki, H. (2019). The cytoplasmic DNA sensor cGAS promotes mitotic cell death. *Cell.* 178, 302–315. doi:10.1016/j.cell.2019.05.035

frontiers | Frontiers in Cell and Developmental Biology

TYPE Original Research
PUBLISHED 31 October 2023
DOI 10.3389/fcell.2023.1270398



OPEN ACCESS

EDITED BY
Yi Yao,
Wuhan University, China

REVIEWED BY
Haopeng Yang,
University of Texas MD Anderson Cancer Center, United States
Alexander Deutsch,
Medical University of Graz, Austria

*CORRESPONDENCE
Eleanor J. Cheadle,
eleanor.j.cheadle@manchester.ac.uk
Timothy M. Illidge,
tmi@manchester.ac.uk

†These authors share senior authorship

RECEIVED 31 July 2023
ACCEPTED 12 October 2023
PUBLISHED 31 October 2023

CITATION
Fagnano E, Pendharkar S, Colton M, Jones PN, Sallan MC, Klymenko T, Braun A, Klein C, Honeychurch J, Cheadle EJ and Illidge TM (2023), Stromal cell inhibition of anti-CD20 antibody mediated killing of B-cell malignancies. *Front. Cell Dev. Biol.* 11:1270398. doi: 10.3389/fcell.2023.1270398



# Stromal cell inhibition of anti-CD20 antibody mediated killing of B-cell malignancies

Ester Fagnano[1], Swati Pendharkar[1], Madyson Colton[1], Philip N. Jones[1], Marta Crespi Sallan[2], Tetyana Klymenko[3], Andrejs Braun[2], Christian Klein[4], Jamie Honeychurch[1], Eleanor J. Cheadle[1*†] and Timothy M. Illidge[1*†]

[1]Targeted Therapy Group, Division of Cancer Sciences, The University of Manchester, Manchester, United Kingdom, [2]Centre for Haemato-Oncology, John Vane Science Centre, Barts Cancer Institute, Queen Mary University of London, London, United Kingdom, [3]Department of Biosciences and Chemistry, Sheffield Hallam University, Sheffield, United Kingdom, [4]Roche Innovation Center Zurch, Roche Glycart AG, Schlieren, Switzerland

**Introduction:** The glycoengineered type II anti-CD20 monoclonal antibody obinutuzumab has been licensed for treatment in follicular non-Hodgkin lymphoma and B-CLL following clinical trials demonstrating superior outcomes to standard of care treatment. However, ultimately many patients still relapse, highlighting the need to understand the mechanisms behind treatment failure to improve patient care. Resistance to chemotherapy is often caused by the ability of malignant B-cells to migrate to the bone marrow and home into the stromal layer. Therefore, this study aimed to investigate whether stromal cells were also able to inhibit type II anti-CD20 antibody mechanisms of action, contributing to resistance to therapy.

**Methods:** A stromal-tumor co-culture was established *in vitro* between Raji or Daudi B-cell tumor cells and M210B4 stromal cells in 24 well plates.

**Results:** Contact with stromal cells was able to protect tumor cells from obinutuzumab mediated programmed cell death (PCD), antibody dependent cellular phagocytosis and antibody dependent cellular cytotoxicity. Furthermore, such protection required direct contact between stroma and tumor cells. Stromal cells appeared to interfere with obinutuzumab mediated B-cell homotypic adhesion through inhibiting and reversing actin remodelling, potentially as a result of stromal-tumor cell contact leading to downregulation of CD20 on the surface of tumor cells. Further evidence for the potential role of CD20 downregulation comes through the reduction in surface CD20 expression and inhibition of obinutuzumab mediated PCD when tumor cells are treated with Ibrutinib in the presence of stromal cells. The proteomic analysis of tumor cells after contact with stromal cells led to the identification of a number of altered pathways including those involved in cell adhesion and the actin cytoskeleton and remodeling.

**Discussion:** This work demonstrates that contact between tumor cells and stromal cells leads to inhibition of Obinutuzumab effector functions and has important implications for future therapies to improve outcomes to anti-CD20 antibodies. A deeper understanding of how anti-CD20 antibodies interact with

stromal cells could prove a useful tool to define better strategies to target the micro-environment and ultimately improve patient outcomes in B-cell malignancies.

KEYWORDS

CD20, antibody, lymphoma, tumor microenvironment, stroma

# 1 Introduction

B cell malignancies include those cancers that arise in B lymphocytes, such as B-cell non-Hodgkin's lymphomas (B-NHL) and B-cell chronic lymphocytic leukaemias (B-CLL). B-NHL is the seventh most common cancer in the United States (as per 2018 projections (National Cancer Institute, 2020a; National Cancer Institute, 2020b)), and 74,000 new cases are reported every year (National Cancer Institute, 2020b). Since the introduction of the anti-CD20 monoclonal antibody (mAb) rituximab in combination with standard chemotherapeutic agents, mortality rates for B-NHL have significantly dropped (National Cancer Institute, 2012). Even better outcomes have been observed with the novel anti-CD20 mAb obinutuzumab: its use in a phase III clinical trial in patients with B-cell chronic lymphocytic leukemia (B-CLL) in combination with chlorambucil led to improved overall survival, progression-free survival and higher complete response rates than rituximab plus chlorambucil (Goede et al., 2014). In general, mAb targeting CD20 work through four main mechanisms of action: induction of programmed cell death (PCD), immune effector cell-mediated antibody-dependent cellular phagocytosis (ADCP) and antibody-dependent cellular cytotoxicity (ADCC), and complement-dependent cytotoxicity (CDC). PCD has been recently characterised, and involves the homotypic adhesion (HA) of B cells upon treatment, followed by reorganisation of the actin cytoskeleton and the movement of F-actin towards the cell-cell junction points (Ivanov et al., 2009; Alduaij et al., 2011). This process triggers the release of lysosomal content (lysosomal membrane permeabilisation, LMP), such as cathepsin B, which in turn leads to NAPDH oxidase-dependent generation of reactive oxygen species (ROS) and cell death (Ivanov et al., 2009; Honeychurch et al., 2012). Whilst type I mAbs such as rituximab strongly induce CDC but not PCD, type II mAbs such as obinutuzumab or tositumomab have greater ability at inducing PCD (Herter et al., 2013). Obinutuzumab is also specifically engineered in its Fc region to have an increased binding to Fc receptors on immune effector cells and thus is more effective at triggering ADCP and ADCC compared to rituximab and other mAbs (Mössner et al., 2010; Herter et al., 2014). However, despite the improvements in treatment outcomes obtained with the development of potent anti-CD20 mAbs, relapse is still common. One possible cause of relapse could be the protective tumour microenvironment (TME) in the bone marrow. In fact, leukemic cell (e.g., B-CLL, B-ALL) proliferation was found to be strictly dependent on the presence of TME components *in vitro* (Manabe et al., 1994; Lagneaux et al., 1998) and co-culture of B-CLL cells with stromal cells was also shown to provide resistance to standard chemotherapy (Panayiotidis et al., 1996; de la Fuente et al., 2002; Kurtova et al., 2009a). Similar observations were made in mantle cell lymphoma (MCL), where the presence of stromal components conferred protection from drug-induced apoptosis, possibly via p42/p44 MAPK pathway activation (Kurtova et al., 2009b). In diffuse large B-cell lymphoma (DLBCL), culturing human B cells in the presence of the stromal cell line HS-5 protected malignant cells from treatment with mitoxantrone via NFκB upregulation and subsequent inhibition of apoptosis. This effect, although lessened, was also observed in the absence of direct contact between tumour and stromal cells (Lwin et al., 2007). More recently, a protective effect of the TME on malignant B cells has been observed upon treatment with rituximab, and several therapeutic strategies, such as VLA-4 integrin blockade or inhibition of the CXCR-4/CXCL-12 signalling axis, have been developed to abrogate this protection (Buchner et al., 2010; Mraz et al., 2011; Hu et al., 2012; Beider et al., 2013). However, to date no studies have been performed in order to investigate whether the TME can influence the efficacy of type II mAb such as obinutuzumab-mediated killing of malignant B cells. Therefore, we sought to determine whether a stromal microenvironment protects against obinutuzumab-mediated B-cell killing. Our findings indicate that contact between stromal fibroblasts and B-NHL cell lines protects the latter from obinutuzumab-induced PCD, ADCC and ADCP. Interestingly, such a protective effect does not appear to be mediated by soluble factors, but rather by the direct contact between stromal and B-NHL tumour cells. A potential mechanism of protection from obinutuzumab-induced PCD appears to be related to the ability of stromal cells to downregulate CD20 and inhibit and reverse HA and actin remodelling that are caused by obinutuzumab treatment and are known to trigger the downstream signalling pathways leading to PCD (Honeychurch et al., 2012). Additionally, contact with stromal cells in the presence of the BTK inhibitor Ibrutinib further decreased obinutuzumab mediated PCD. A large-scale proteomic analysis highlighted several pathways which are differentially expressed in B-NHL cells upon culture on stromal cells and could potentially be targeted in order to abrogate resistance to treatment with obinutuzumab in patients with B cell malignancies. This work should aid the development of future therapeutic strategies which will enhance antibody-mediated tumour cell killing in protected niches throughout the body including the bone marrow and reduce the risk of relapse for patients with B cell malignancies.

# 2 Materials and Methods

## 2.1 Cell lines

B-cell lymphoma cell lines Raji and Daudi (Burkitt's lymphoma) were purchased from American Type Culture

Collection (ATCC). Murine bone marrow stromal cell line M2-10B4 was kindly provided by Claire Hart (University of Manchester, United Kingdom). Human bone marrow stromal cell line HS-5 and human embryonic kidney stromal cell line HEK293T were obtained from ATCC. Raji-GFP-actin cells (transfected to express a GFP-actin fusion protein) were generated by Dr Andrejs Ivanov (University of Manchester, United Kingdom) as described in Ivanov et al. (2009). Raji-YFP-CD20 cells (transfected to express a YFP-CD20 fusion protein) were kindly provided by Dr Andrejs Ivanov. All tumour cells and M2-10B4 stromal cells were grown under standard conditions (5% $CO_2$, 37°C) in RPMI 1640 media (Gibco, Life Technology) supplemented with 10% heat-inactivated Foetal Bovine Serum (Invitrogen, Life Technologies, Thermo Fisher Scientific) and 2 mM L-glutamine (Invitrogen). HS-5 stromal cells were grown under standard conditions (5% $CO_2$, 37°C) in DMEM media supplemented with 10% FBS and 2 mM L-glutamine. Cells were routinely screened to confirm negativity to *mycoplasma* infection.

## 2.2 Co-cultures

Murine M2-10B4 or human HS-5 bone marrow stromal cells were labelled with the fluorescence linker for general cell membrane labelling PKH67 (Sigma-Aldrich), following the manufacturer's instructions, and plated in either 24- or 96-well plates ($2.5 \times 10^4$ cells/well or $5 \times 10^3$ cells/well, respectively) until confluency (72 h approx.). Culture media were replaced with fresh media containing tumour cells at either $1.25 \times 10^5$ cells/well or $2.5 \times 10^4$ cells/well (24- and 96-well plates, respectively) and cells were co-cultured for 24 h. For stroma-conditioned media, M2-10B4 bone marrow stromal cells were plated in 24-well plates for 72 h and media were collected and centrifuged. The resulting supernatant was filtered through a 0.45 µm filter (Appleton Woods Ltd.) and used to culture tumour cells for 24 h. For tumour/stroma-conditioned media, M2-10B4 bone marrow stromal cells were plated in 24-well plates for 72 h. Tumour cells were added for additional 24 h, before being harvested and centrifuged. The resulting supernatant was filtered through a 0.45 µm filter and used to culture fresh tumour cells for 24 h. For non-contact transwell assays, 24-well polycarbonate transwell plates containing inserts of 0.4 µm pore size (Appleton Woods) were used. M2-10B4 stromal cells were plated into the bottom compartment ($2.5 \times 10^4$ cells/well) until confluency and tumour cells were added in the upper compartment ($1 \times 10^5$ cells/insert, in 100 µL media) for 24 h. For culture on fibronectin-coated wells, human fibronectin (Thermo Fisher Scientific) was added to 24-well plate wells at 5 µg/cm$^2$ and incubated for 1 h at room temperature. The wells were then rinsed with distilled $H_2O$ and used to plate cells for 24 h.

## 2.3 Antibodies and reagents

Anti-CD20 monoclonal antibody obinutuzumab was provided by Dr Christian Klein (Roche Innovation Centre, Zurich, Switzerland). Anti-Her2 monoclonal antibody Herceptin was purchased from The Christie Hospital NHS Trust (Manchester, United Kingdom). Anti-human CD11b-APC antibody, anti-human CD20 APC, mouse IgG2b APC, anti-human CD56-APC antibody and anti-IFN-γ-PE antibody were obtained from eBioscience, Thermo Fisher Scientific. The Bruton's tyrosine kinase inhibitor PCI-32765 (ibrutinib) was purchased from ApexBio Technology. Clones for each antibody can be found in Supplementary Material.

## 2.4 Generation of mCherry-M2-10B4 cell line

An mCherry lentiviral vector, containing an ampicillin-resistant gene under the Amp-R promoter and an mCherry-encoding gene under the SFFV promoter, was kindly provided by Dr Tiziana Monteverde (Cancer Research UK Manchester Institute, Manchester, United Kingdom). HEK293T cells ($3 \times 10^6$ cells/10 cm dish) were transfected with SFFV-mCherry plasmid (10 µg) plus the packaging plasmids pΔ19.8 (6.5 µg) and pMNG.2 (3.5 µg), provided by Dr Claire Dempsey, University of Manchester, United Kingdom, using 50 µL $CaCl_2$. Lentiviral supernatant was collected 48 and 72 h later from transfected HEK293T cells and used to infect M2-10B4 cells by co-culture for 48 h, in the presence of 4 µg/mL polybrene (Sigma-Aldrich). Transduced cells were purified using FACS sorting.

## 2.5 Isolation of immune effector cells

Buffy coats of blood from healthy donors were purchased from Manchester Plymouth Grove Blood Donor Centre, Manchester, United Kingdom. Blood was obtained with ethical consent from the South Manchester Ethics committee in accordance with the declaration of Helsinki. Peripheral blood mononuclear cells (PBMCs) were extracted from buffy coats as described in Supplementary Material. Human monocytes were isolated from PBMCs by using a pan monocyte isolation kit (Miltenyi Biotec) following the manufacturer's instructions. Human NK cells were isolated by using an NK cell isolation kit (Miltenyi Biotec) following the manufacturer's instructions. Human macrophages were differentiated from monocytes by adding 50 µg/mL recombinant human M-CSF (macrophage colony-stimulating factor, Bio-Rad Laboratories Ltd.) on day 0 and day 4 to the culture media and growing them for 6 days.

## 2.6 Measurement of cell viability and NK cell activation

For programmed cell death, cells were harvested, washed in FACS buffer (PBS +1% FBS) and re-suspended in 0.5 µg/mL 7-Aminoactinomycin D (7-AAD, eBioscience) and 1 µg/mL AnnexinV-Cy5.5 (Becton-Dickinson). Samples were analysed by flow cytometry and percentages of viable tumour cells were calculated by measuring the percentage of cells negative to 7-AAD and AnnexinV, after excluding the PKH67+ population.

For antibody-dependent cellular phagocytosis (ADCP), tumour cells were labelled with the red fluorescence linker for general cell

membrane labelling PKH26 (Sigma-Aldrich), following the manufacturer's instructions. Human monocytes were isolated as described previously and added to the co-culture system at an effector to target ratio of 1 to 1 for 2 h. Cells were then harvested, washed in FACS buffer and labelled with an anti-CD11b-APC antibody. Samples were analysed by flow cytometry and cell viability was measured as percentage of cells positive to PKH26 and negative to CD11b, after excluding the PKH67+ population.

For antibody-dependent cellular cytotoxicity (ADCC), human NK cells were isolated as described previously, treated with an inhibitor of intracellular protein transport (Brefeldin A solution 1000X, eBioscience), and added to the co-culture system at an effector to target ratio of 1 to 1 for 4 h. Cells were then harvested, washed in FACS buffer and labelled with an anti-CD56-APC antibody. Cells were then fixed and permeabilised using a Foxp3/Transcription Factor Staining Buffer Set (eBioscience), following the manufacturer's instructions, and intracellularly labelled with an anti-IFN-γ-PE antibody. Samples were analysed by flow cytometry and activation of NK cells was measured as percentage of cells positive to both IFN-γ and CD56, after excluding the PKH67+ population.

## 2.7 Stable isotope labelling by amino acids in cell culture (SILAC) experiment

SILAC RPMI 1640 media (Gibco, Life Technology) was supplemented with 10% heat-inactivated dialysed Fetal Bovine Serum and 2 mM L-glutamine, and isotopically labelled by adding either 0.3 mM L-Lysine-$^{13}C_6$ and 0.3 mM L-Arginine-$^{13}C_6$ (medium isotope), or 0.3 mM L-Lysine-$^{13}C_6$,$^{15}N_2$ and 0.3 mM L-Arginine-$^{13}C_6$,$^{15}N_4$ (heavy isotope), all kindly provided by Dr Amy McCarthy, Cancer Research UK, Manchester, United Kingdom. Cells were grown in either medium or heavy RPMI media for 5 passages and a labelling efficiency test was performed to verify that cell labelling had been achieved. Medium-labelled Raji cells (Raji-M) and heavy-labelled Raji cells (Raji-H) were cultured for 24 h on plastic and on a layer of M2-10B4 stromal cells, respectively. Cells were separated by FACS sorting, lysed as previously described and protein content was measured by BCA assay. 10 µg Raji-M and 10 µg Raji-H were mixed 1 to 1, resolved by SDS-PAGE and analysed by mass spectrometry (Supplementary Material).

## 2.8 Microscopy and high-content screening

For re-organisation of the actin cytoskeleton in the presence or absence of stromal cells, cells were imaged in 24-well plates under a Zeiss lowlight microscope (×10 air objectives). For time-lapse experiments, cells were kept in an environmental chamber at 37°C, 5% $CO_2$ and imaged every 30 min for 24 h with a Zeiss lowlight microscope (×20 air objective). Videos were developed using the MetaMorph Microscopy Automation and Image Analysis Software (Molecular Devices). For characterisation of the actin cytoskeleton and of the CD20 molecule in the presence or absence of stromal cells, mCherry-M2-10B4 cells were plated in CellCarrier-96 Black, Optically Clear Bottom plates (Perkin Elmer). Raji-GFP-actin cells or Raji-YFP-CD20 cells were added to the culture for 24 h. Cells were then centrifuged, labelled with Hoechst 33,342 (0.1 µg/mL) by incubating the cells for 1 h at 37°C and imaged under an Opera Phenix High-Content Screening System (Perkin Elmer, X40 water immersion objective). Images were taken in confocal mode and analysed by using the software Harmony High-Content Imaging and Analysis Software (Perkin Elmer) and Columbus Image Data Storage and Analysis System (Perkin Elmer).

## 2.9 Data analysis and statistics

Flow cytometric data were analysed by using FlowJo (Tree Star, Inc.). Graphs and statistical analyses were performed by using two-way Anova in GraphPad Prism. Differences were deemed significant when $p < 0.05$. Data are the average ±SEM of three independent experiments each performed in duplicates or triplicates, unless differently stated in figure legends. In IPA $p$-values are calculated using a right-tailed Fisher's Exact Test. In DAVID $p$-values are calculated using a modified Fisher's Exact Test, namely, EASE score. Statistical significance was $p < 0.05$ or ES > 1.3.

# 3 Results

## 3.1 The presence of stromal cells protects B-cell lymphoma cells from obinutuzumab-induced cell death

To determine whether the presence of stroma could influence obinutuzumab-induced killing of B-cell lymphoma tumour cells, Burkitt's lymphoma Raji cells were cultured either on plastic or on a layer of murine bone marrow M2-10B4 stromal cells. Cells were treated with 10 µg/mL obinutuzumab for 24 h and then harvested and cell death quantified using 7-AAD/AnnexinV staining. Whilst Raji cells were efficiently killed by obinutuzumab when cultured on plastic (72% ± 3% dead cells), the presence of stromal cells significantly reduced the killing to 47% ± 3% (Figure 1A, $p = 0.0022$). A similar decrease in cell death was observed when culturing Raji cells on a layer of human bone marrow stromal cells HS-5 (Figure 1B, $p = 0.0006$). To determine whether the presence of stromal cells could also influence obinutuzumab-induced ADCP, Raji cells were cultured either on plastic or on a layer of M2-10B4 cells for 24 h. Human monocytes were added to the co-culture and wells were treated with obinutuzumab for 2 h. The percentage of monocytes that had engulfed Raji cells cultured on plastic was 48% ± 10, however, this was significantly decreased to 17% ± 2 when Raji cells were cultured on stromal cells (Figure 1C, $p = 0.0076$). Similar results were observed using differentiated human macrophages as effector cells (Figure 1D, $p = 0.0092$). Next, the influence of stroma on obinutuzumab-induced ADCC was determined by measuring the production of IFN-γ by NK cells. NK cells were isolated from PBMCs and added to the co-culture system. After a 4-h treatment with obinutuzumab, the

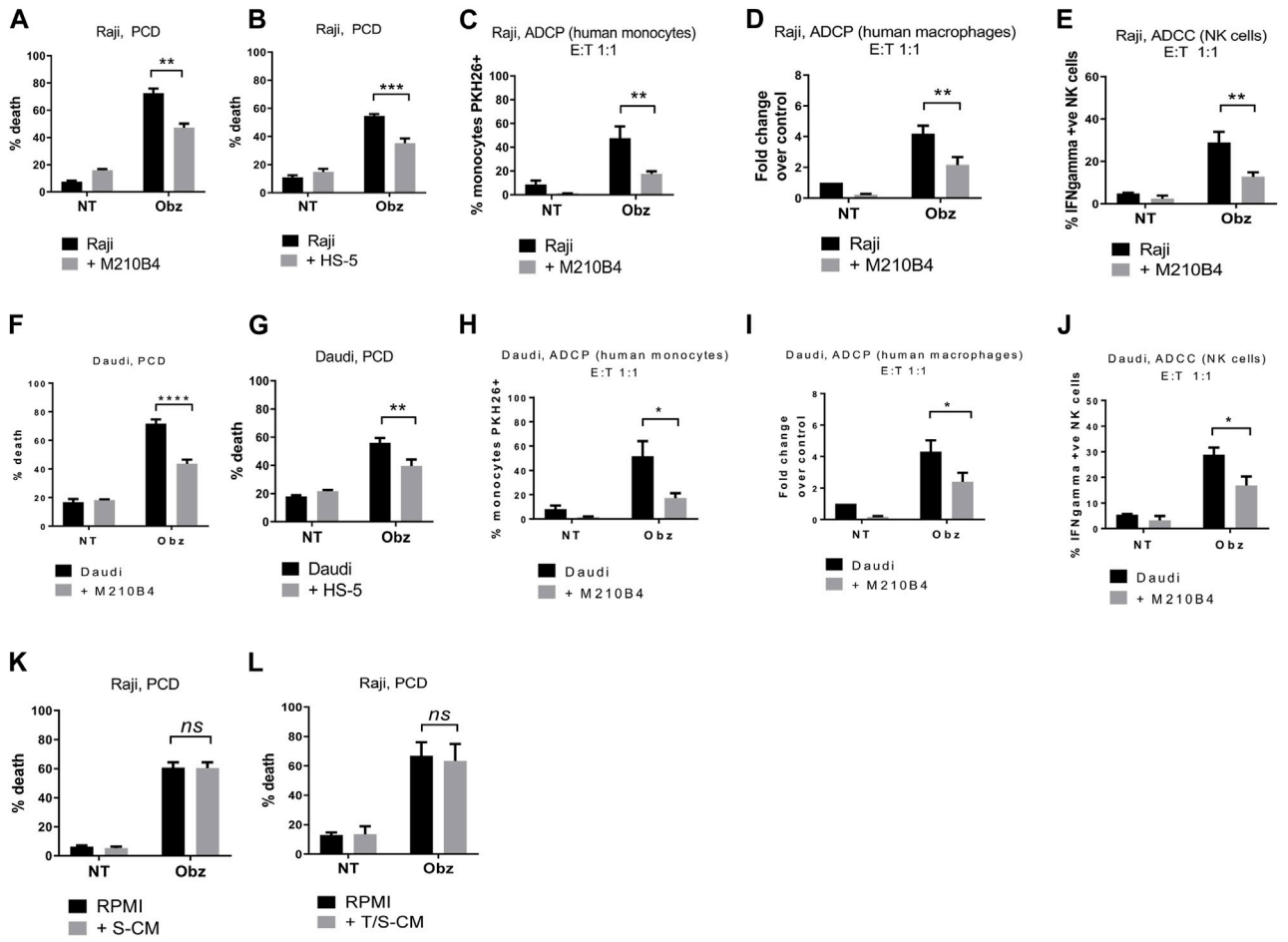


FIGURE 1
**(A)** Raji cells were cultured either on plastic (black bars) or on a layer of M2-10B4 murine stromal cells (grey bars) for 1 h and either treated with obinutuzumab (Obz) at 10 μg/mL, or left untreated (NT) for 23 h. Survival percentages were calculated by labelling cells with 7-AAD and AnnexinV. **(B)** The same experiment was repeated with the human stromal line HS-5. **(C)** Human monocytes were isolated from PBMCs and added to the co-culture (E:T ratio = 1:1) for 24 h. Percentage phagocytosis were measured as percentage of PKH26-labelled tumour cells which were $CD11b^+$. **(D)** Human macrophages were isolated from PBMCs, differentiated by addition of M-CSF and added to the co-culture (E:T ratio = 1:1) for 24 h. Percentages of phagocytosis were measured as percentage of PKH26-labelled tumour cells which were $CD11b^+$. **(E)** Human NK cells were isolated from PBMCs and added to the co-culture (E:T ratio = 1:1) for 24 h. Percentages of NK cell activation were measured as percentage of PKH26-labelled tumour cells which were $IFN\gamma^+$. **(F–J)** The experiments were repeated with the B-cell lymphoma cell line Daudi. **(K)** Raji cells were cultured either in RPMI media (black bars) or M2-10B4-conditioned media (S-CM, grey bars) for 1 h and either treated with obinutuzumab (Obz) at 10 μg/mL or left untreated (NT) for 23 h. Survival percentages were calculated by labelling cells with 7-AAD and AnnexinV. **(L)** Raji cells were cultured either in RPMI media (black bars) or in a Raji/M2-10B4-conditioned media (T/S-CM, grey bars) for 1 h and either treated with obinutuzumab (Obz) at 10 μg/mL or left untreated (NT) for 23 h. Survival percentages were calculated by labelling cells with 7-AAD and AnnexinV. Data is mean ± SEM of at least 3 independent experiments.

levels of activated (IFN-γ-producing) NK cells was 29% ± 5, but this decreased to 13% ± 2 when cells were cultured in the presence of stromal cells (Figure 1E, $p = 0.0078$). These observations were replicated when studies were performed in a second Burkitt's lymphoma line, Daudi (Figures 1F–J) and PCD by the type II anti-CD20 antibody tositumomab and the type I antibody rituximab was also inhibited in the presence of stromal cells (Supplementary Figures S1I, S1J). To understand whether such a protective effect from obinutuzumab could also be mediated by the ECM component fibronectin (FN), tumour cells were treated with obinutuzumab either on plastic, or on stroma, or in FN-coated wells. However, the presence of FN could not recapitulate the effect observed with M2-10B4 (Supplementary Figures S1A, S1B). Finally, we sought to determine whether soluble factors played any roles on the protective effect mediated by stromal cells. Raji cells were cultured with conditioned media released by either stromal cells on their own (S-CM) or by stromal cells after a 24 h culture with tumour cells (T/S-CM) treated with obinutuzumab for 24 h and the percentage of death for Raji cells cultured either in normal RPMI media or in S-CM (Figure 1K) and T/S-CM (Figure 1L) was measured by labelling cells with 7-AAD/AnnexinV. Interestingly, no differences were observed between the efficacy of obinutuzumab at inducing PCD when cells were treated in normal RPMI media vs. S-CM ($p = 0.9993$) or T/S-CM ($p = 0.9472$), suggesting that the protective effect is not dependent on soluble factors produced by M2-10B4 stromal cells. The same results were obtained with Daudi cells (Supplementary Figures S1C, S1D). In addition, ADCP and ADCC were not affected by

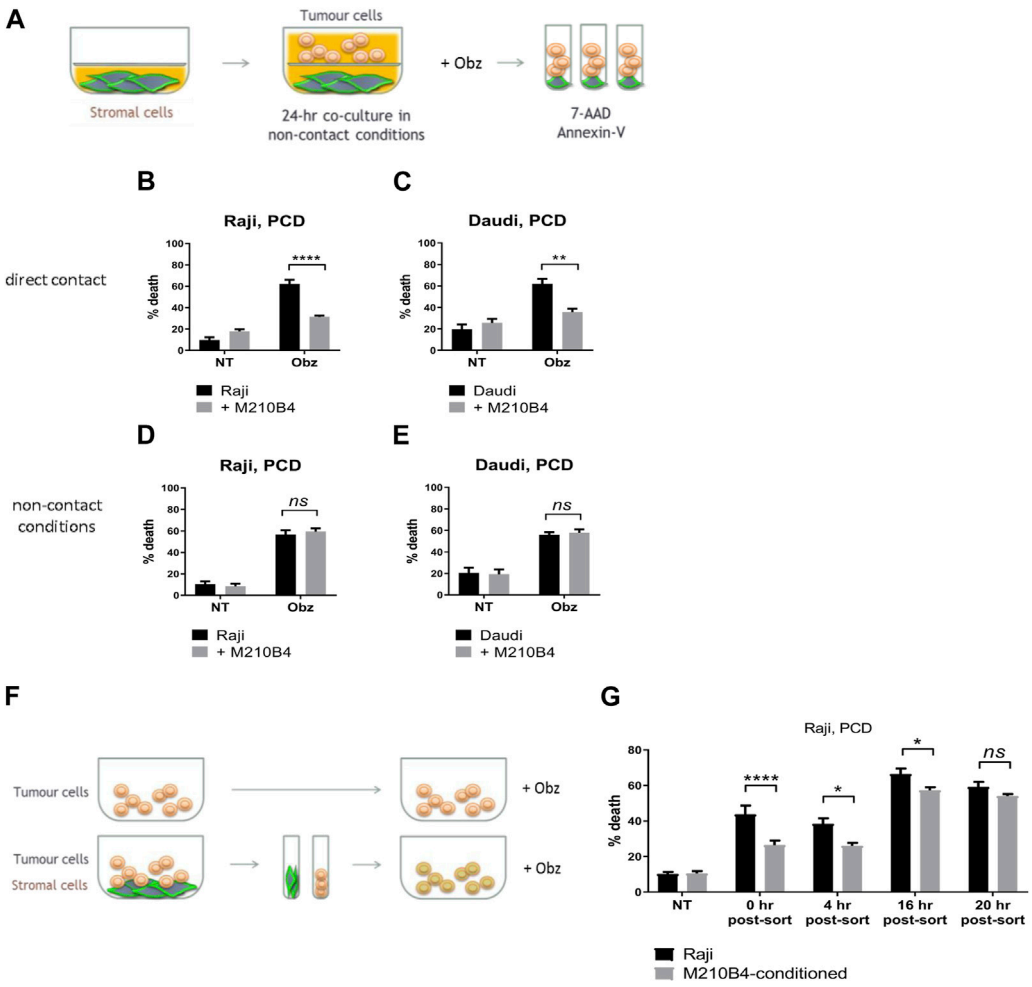


FIGURE 2
**(A)** Stromal cells were cultured on the bottom compartment of a transwell plate. Tumour cells were added to the upper compartment for 1 h and treated with Obz for 23 h. Survival percentages in direct contact conditions [shown in **(B)** for Raji, **(C)** for Daudi] were calculated by labelling cells with 7-AAD and AnnexinV. Survival percentages for a control assay, were cells were plated in non-contact conditions with the stromal layer, are shown in **(D)** for Raji and **(E)** for Daudi. **(F)** Tumour cells were cultured either on plastic or on a layer of PKH67-labelled M2-10B4 cells for 24 h. Cells were separated through the use of a FACS sorter and PKH67$^-$ tumour cells were plated on plastic. Cells were treated with Obz on plastic for further 4 h either immediately after sort (0 h post-sort) or 4, 16 or 20 h post-sort. Survival percentages, shown in **(G)**, were calculated by labelling cells with 7-AAD and AnnexinV. Data is mean ± SEM of two to four independent experiments.

culturing tumour cells in S-CM or T/S-CM (Supplementary Figures S1E–H).

## 3.2 Protection from obinutuzumab-induced cell death is dependent on direct contact between stromal and tumour cells

To investigate whether the protective effect from obinutuzumab-induced cell death was dependent on direct contact between stromal and tumour cells, a transwell assay was performed. As shown in Figure 2A, microporous inserts of 0.4 µm pore size were employed to separate the bottom compartment of wells, where M2-10B4 cells were grown, from the upper compartment, where tumour cells were cultured and treated with obinutuzumab for 24 h. Such a pore size was chosen so that media and soluble factors could cross the barrier, but not cells. Whilst Raji cells cultured in normal wells, and therefore in direct contact with M2-10B4 stromal cells, were protected from obinutuzumab-induced PCD (Figure 2B, $p < 0.0001$), Raji cells cultured in non-contact conditions were efficiently killed by obinutuzumab (Figure 2D, $p = 0.7759$), despite the presence of stromal cells in the bottom compartment of transwell plates. The same results were obtained with Daudi cells (Figures 2C, E), further indicating that direct contact between stroma and tumour cells is necessary to achieve protection from obinutuzumab. To determine whether the protection mediated by contact between stromal and tumour cells could also be observed after removal of direct interaction, Raji cells were cultured either on plastic or on PKH67-labelled M2-10B4 stromal cells for 24 h. Cells were then separated by FACS sorting and purified Raji cells were collected, cultured on plastic and treated with obinutuzumab for 4 h at the following times: immediately after sort (0 h post-sort) or 4 h, 16 h, 20 h post-sort (Figure 2F). Intriguingly, a protection from obinutuzumab-induced PCD was still visible in cells that were previously grown on stroma (M2-

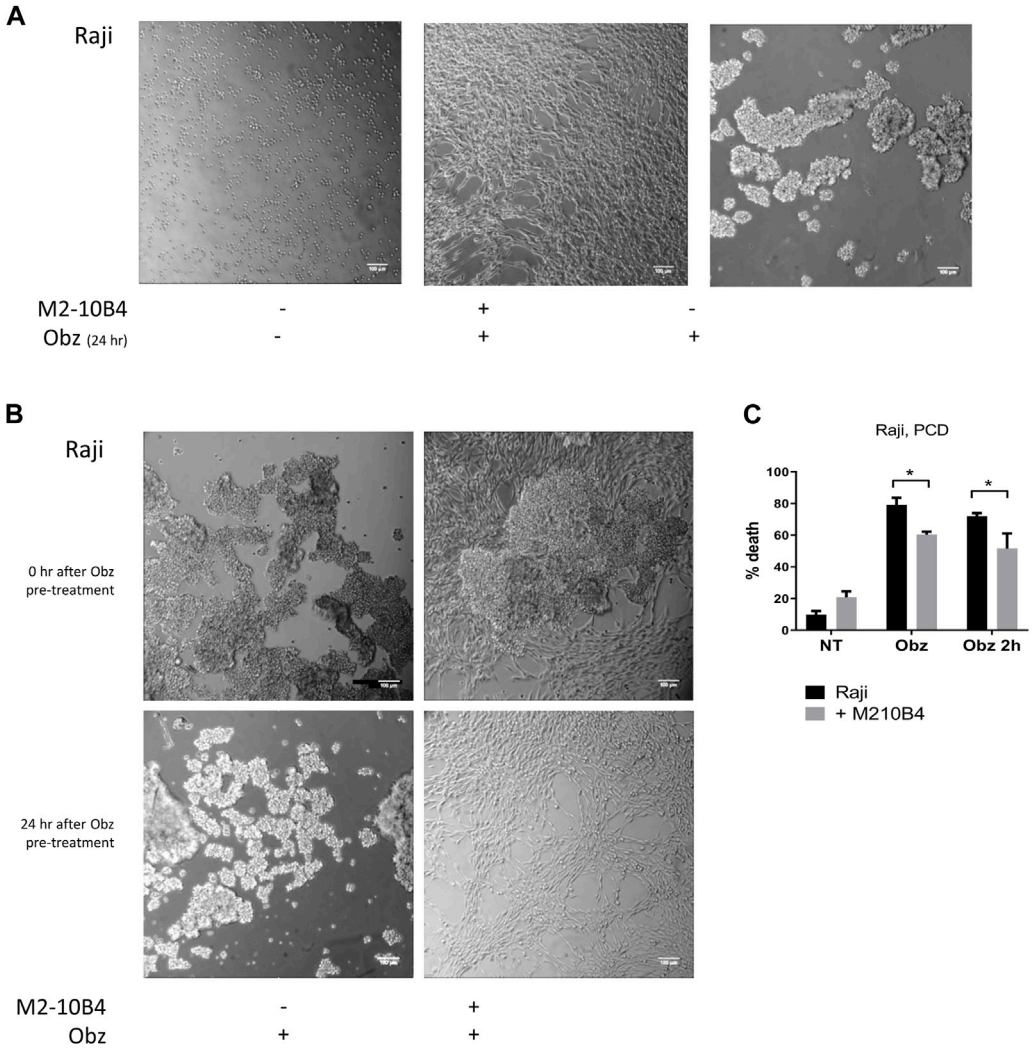


FIGURE 3
**(A)** Raji cells were cultured either on plastic (left panel) or on a layer of M2-10B4 stromal cells (middle panel) and treated with Obinutuzumab (Obz) at 10 μg/mL. Images were taken on a Zeiss lowlight microscope (10X) 24 h later. Non-treated Raji cells cultured on plastic are shown in the right panel. **(B)** Raji cells were pre-treated with Obz in tubes for 2 h and poured onto either plastic (left panels) or onto a layer of M2-10B4 stromal cells (right panels). Images were taken on a Zeiss lowlight microscope (10X) either straight after the pouring (upper panels) or 24 h later (lower panels). **(C)** Raji cells were cultured either on plastic (black bars) or onto a layer of M2-10B4 stromal cells (grey bars) and either left untreated (NT) or treated with Obz at 10 μg/mL (Obz) or pre-treated with Obz at 10 μg/mL for 2 h (Obz 2h) in a tube and then poured onto the wells. Survival percentages were calculated by labelling cells with 7-AAD and AnnexinV. Data is mean ± SEM of at least 3 independent experiments.

10B4-conditioned) and treated on plastic immediately after removal of direct contact (Figure 2G, 0 h post-sort, $p < 0.0001$). Furthermore, this protective effect was observed for up to 16 h post-sort but disappeared within 20 h. These data suggest that the protective effects of signalling pathways which are activated by stromal cell contact persist for at least 16 h after removal of direct interaction.

## 3.3 Interaction with stroma influences obinutuzumab-induced homotypic adhesion of tumour cells

Obinutuzumab-induced PCD involves a process of actin re-organisation and formation of HA between tumour cells (Alduaij et al., 2011; Honeychurch et al., 2012). We sought to understand whether the presence of stromal cells could affect such a process and thus hamper the initiation of PCD. First, tumour cells were cultured either on plastic or on M2-10B4 stromal cells and were either left untreated or treated with obinutuzumab. 24 h later, cells were imaged under a lowlight microscope. As expected, obinutuzumab-treated Raji cells cultured on plastic underwent HA and formed B-cell aggregates (Figure 3A, right panel). However, when cultured on M2-10B4 stromal cells, obinutuzumab-treated Raji cells appeared organised as single cells and attached to the stromal layer (fibroblast-like stellate cells, Figure 3A middle panel) and resembling untreated cells (Figure 3A, left panel). To understand whether HA could also be reversed by stromal cells Raji cells were pre-treated with obinutuzumab for 2 h. The B-cell aggregates were then poured onto a layer of M2-10B4 stromal cells, and images were taken either immediately after addition or 24 h later. After the 2-h pre-

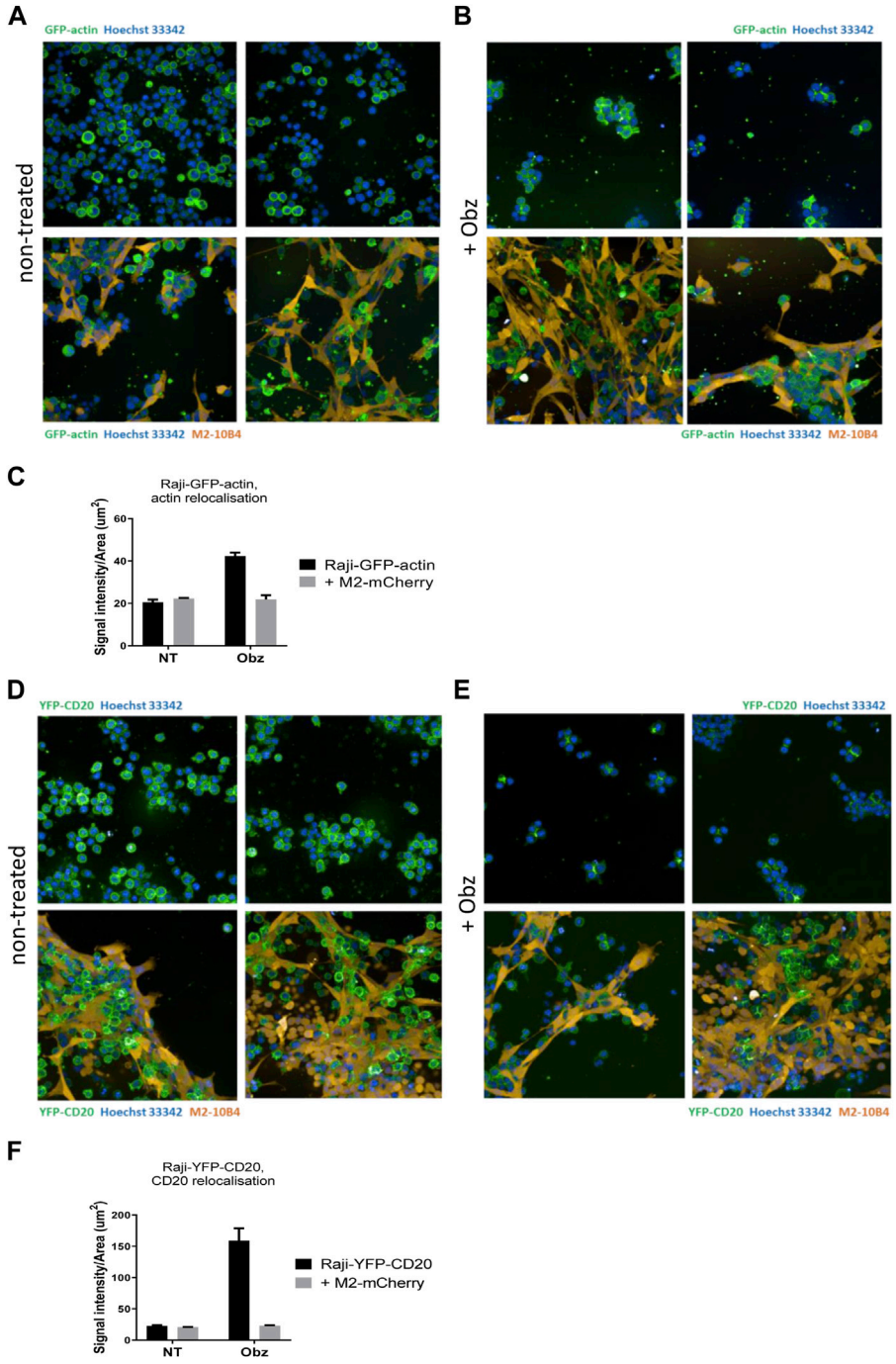


FIGURE 4
**(A,B)** Raji-GFP-actin cells (green) were cultured either on plastic (upper panels) or on a layer of mCherry-M2-10B4 stromal cells (orange, lower panels) and either left untreated **(A)** or treated with Obz at 10 μg/mL **(B)** for 24 h. Nuclei (blue) were labelled with Hoechst 33,342 (0.1 μg/mL) and plates were scanned on a PerkinElmer Opera Phenix (20X) 24 h later. **(C)** The signal intensity to area ratio for Raji-GFP-actin cells was calculated using Columbus software. **(D–E)** Raji-YFP-CD20 cells (green) were cultured either on plastic (upper panels) or on a layer of mCherry-M2-10B4 stromal cells (orange, lower panels) and either left untreated **(D)** or treated with Obz at 10 μg/mL **(E)** for 24 h. Nuclei (blue) were labelled with Hoechst 33,342 (0.1 μg/mL) and plates were scanned on a PerkinElmer Opera Phenix (20X) 24 h later. **(F)** The signal intensity to area ratio for Raji-YFP-CD20 cells was calculated using Columbus software. $^{**}p < 001$ unpaired *t*-test. Data is mean ± SEM of at least 3 independent experiments.

treatment with obinutuzumab, Raji cells poured either onto plastic or onto stroma both displayed HA and formation of cell aggregates (Figure 3B, upper panels). Whilst the aggregates were still present in Raji cell cultured on plastic 24 h later (Figure 3B, lower panel, left), aggregated Raji cells cultured in the presence of stromal cells appeared to have disaggregated and returned to normal morphology (Figure 3B, lower panel, right). These data suggest that the contact with stromal cells can reverse HA and B-cell aggregation initiated upon

10.3389/fcell.2023.1270398

obinutuzumab treatment. This was mirrored by a reduction in the percentage cell death when treatment was started in co-culture conditions ("Obz," $p$ = 0.0464), and when lymphoma cells were pre-treated and then added to the stromal layer ("Obz 2h," Figure 3C, $p$ = 0.0299). A similar reduction in the percentage of death in pre-treated cells when co-cultured with M2-10B4 was also observed with Daudi cells (Supplementary Figure S2A). To further confirm the finding that HA is reversed in the presence of stroma, a time-lapse analysis was performed. Raji cells were pre-treated with obinutuzumab for 2 h and added to a layer of M2-10B4 stromal cells. Pictures of the wells were then taken every 30 min for 24 h. Whilst at time 0 (immediately after addition) aggregated cells are clearly visible (Supplementary Figure S2B, top left), cells re-organise over time, and B lymphoma cells detach from each other by 24 h (Supplementary Figure S2B, bottom right), suggesting that actin reorganisation is able to reverse HA.

## 3.4 Stromal interaction reduces actin cytoskeleton reorganisation and CD20 relocalisation in response to obinutuzumab

To better visualise the actin re-organisation of Raji cells in the presence of stroma, Raji-GFP-actin cells were used. An M2-10B4 stromal line expressing mCherry, (M2-mCherry), was generated and used instead of the parental M2-10B4 line. Raji-GFP-actin cells were cultured either on plastic or on a layer of M2-mCherry for 24 h. Then, nuclei were labelled with Hoechst 33,342 and wells were scanned by high-content screening. Whilst the actin cytoskeleton was evenly distributed around the nuclei in non-treated Raji-GFP-actin cells (Figure 4A, upper panels), HA and movement of the actin signal towards junction points between cells was observed in obinutuzumab-treated cells (Figure 4B, upper panels), as previously shown in Honeychurch et al. (2012). In the presence of M2-mCherry cells, however, Raji-GFP-actin cells appeared attached to the stromal layer and the shape of their actin cytoskeleton did not change following obinutuzumab treatment (Figure 4B, lower panels). This behaviour is reflected by the signal intensity to signal area ratio, which is higher for cells having a similar or higher intensity contained in a smaller area. On plastic (black bars) the ratio increased significantly from 20.5 (untreated cells) to 42.2 (obinutuzumab-treated cells). However, in the presence of stroma (grey bars), there was no statistically significant difference between untreated and obinutuzumab-treated cells (Figure 4C). We sought to determine whether treatment with obinutuzumab could also lead to re-organisation and movement of the CD20 molecule towards the cell-cell junction points. Raji-YFP-CD20 cells were treated as described for Raji-GFP-actin cells and nuclei were labelled with Hoechst 33,342 before scanning wells by high-content screening. In non-treated cells, the CD20 molecules are all evenly disposed on the membrane of tumour cells (Figure 4D, upper panels). When cultured on stroma, Raji-YFP-CD20 cells appear to attach to M2-10B4 stromal cells (Figure 4D, lower panels). Similarly to what was observed with the actin cytoskeleton, treatment with obinutuzumab led to a re-localisation of the CD20 molecules towards the cell-cell junction points, with Raji-YFP-CD20 cells now undergoing HA and aggregating in clumps (Figure 4E, upper panels). When the treatment was performed in the presence of stroma, however, this CD20 re-localisation is reduced, and Raji-YFP-CD20 cells appear attached to the stromal layer instead (Figure 4E, lower panels). Again, this is reflected by the signal intensity to signal area ratio, with an increased ratio only observed in obinutuzumab-treated cells cultured on plastic, but not on stroma (Figure 4F).

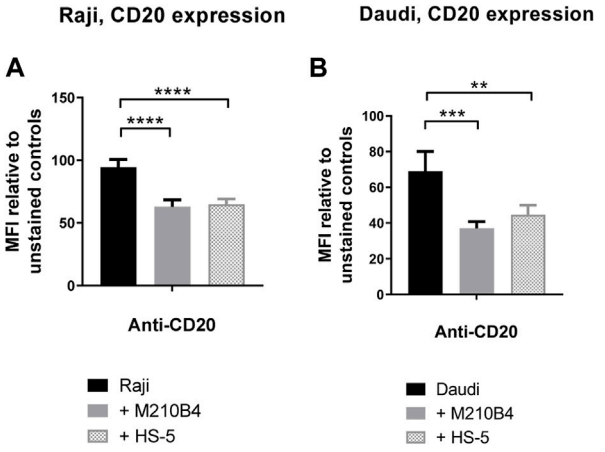


FIGURE 5
**(A,B)** Co-culture of tumour cells with stromal cells significantly decreases surface levels of the CD20 molecule. Raji **(A)** and Daudi **(B)** cells were cultured for 24 h on either plastic (black bars) or M2-10B4 (gray bars) or HS-5 (checked bars). After 24 h, cells were collected and either left unlabelled, or incubated with isotype control (mouse IgG2b-APC), or anti-CD20-APC antibody (0.24 µg/mL). Percentage of positivity to the antibodies was measured as % of PKH67- cells which were APC+. The MFI (geometric mean fluorescence intensity) measured for isotype controls was then subtracted by the MFI of stained samples. Data is mean ± SEM of three independent experiments performed in duplicate.

## 3.5 Direct contact with stroma leads to downregulation of CD20 on the surface of tumour cells

Given the finding that interaction with stromal cells was able to inhibit the obinutuzumab-mediated re-modelling of CD20 on the surface of Raji-YFP-CD20 cells, and that a reduction in surface levels of CD20 was previously observed upon culture of Raji cells with HS-5 stromal cells (Marquez et al., 2015), we sought to determine whether the contact with stroma led to a decrease of CD20 level in our model. To address this question, Raji and Daudi cells were cultured for 24 h in the presence of either M2-10B4 or HS-5 stromal cell lines, and CD20 expression was analysed by flow cytometry at the end of the culture. Surface levels of CD20 were significantly decreased after culture with stromal cells, compared to culture on plastic (Raji: $p < 0.0001$ for both stromal lines; Daudi: $p = 0.0005$ for M2-10B4, $p = 0.0083$ for HS-5) (Figures 5A, B; Supplementary Figure S3), suggesting that the reduced ability of obinutuzumab to induce cell death might be due to a downregulation of the target CD20 molecule.

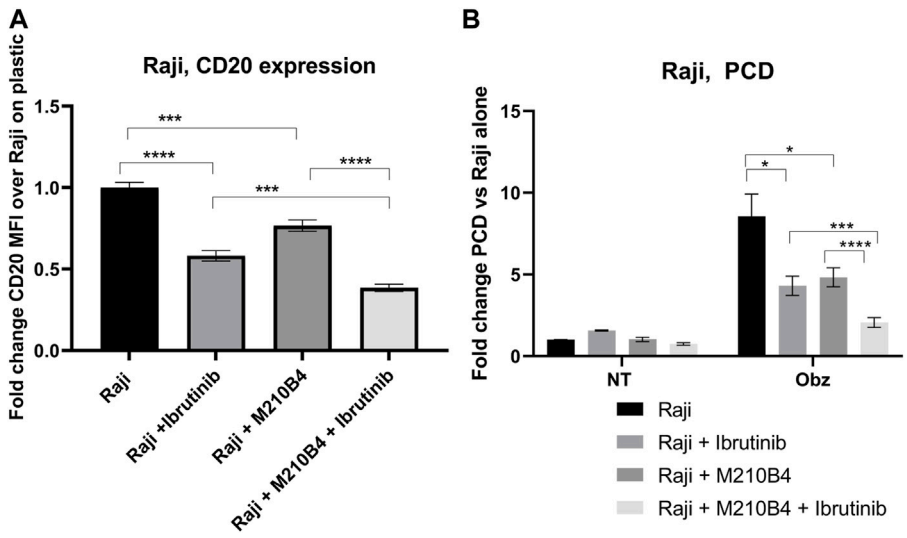


FIGURE 6
**(A,B)** Effect of pre-treatment with ibrutinib on CD20 expression levels and obinutuzumab-induced PCD. Raji cells were either left untreated (circles), or pre-treated with ibrutinib for 1 h (squares), and then cultured in the presence of M2-mCherry (triangles) and 10 μg/mL obinutuzumab [all four conditions **(B)**] for further 24 h. After 24 h, cells were collected and either left unlabelled, or incubated with isotype control (mouse IgG2b-APC), or anti-CD20-APC antibody (0.24 μg/mL) **(A)**, or labelled with 7-AAD and AnnexinV **(B)** Percentage of positivity to the antibodies was measured as % of mCherry-cells which were APC+. The MFI (geometric mean fluorescence intensity) measured for isotype controls was then subtracted by the MFI of stained samples. Survival percentages were calculated by labelling cells with 7-AAD and AnnexinV. The percentage of cells AnnexinV$^{+ve}$/7-AAD$^{+ve}$ were calculated and are expressed as a fold change relative to untreated Raji cells alone. Data is the mean + SEM of three independent experiments performed in triplicate.

## 3.6 Treatment with ibrutinib further decreases CD20 expression level and obinutuzumab-induced PCD

Ibrutinib, a Bruton's tyrosine kinase (BTK) inhibitor, has been recently introduced for treatment of B cell malignancies, showing success in patients with CLL (Moreno et al., 2019). Despite the improved therapeutic outcomes that were observed which led to ibrutinib being granted FDA approval in combination with obinutuzumab in 2019, several studies have shown contrasting results with regards to the effect of ibrutinib on the efficacy of anti-CD20 mAb (Bojarczuk et al., 2014; Da Roit et al., 2015). Interestingly, Bojarczuk and colleagues suggested that the diminished efficacy of anti-CD20 mAb in killing tumour B cells could be due to a decrease in CD20 expression level on the surface of such cells upon treatment with ibrutinib (Bojarczuk et al., 2014). Against this background, we decided to investigate the effect of a pre-treatment with ibrutinib followed by treatment with obinutuzumab in our system, in order to understand whether a reduction in CD20 expression correlated with a lower efficacy of obinutuzumab at inducing PCD. Raji cells were pre-treated in tubes with 10 μM ibrutinib for 1 h before being transferred onto M2-10B4-mCherry stromal cells or onto plastic. Obinutuzumab was then added at 10 μg/mL for 24 h. After 24 h, both PCD and CD20 expression were measured by flow cytometry. As previously published (Bojarczuk et al., 2014) pre-treatment with ibrutinib led to a significant downregulation of CD20 expression compared to untreated Raji cells on plastic (Figure 6A, $p < 0.0001$, Supplementary Figure S3) and this correlated with a significant reduction in obinutuzumab mediated PCD (Figure 6B, $p = 0.011$). When Raji cells were cultured on M2-10B4, PCD was also efficiently abrogated (Figure 6B, $p = 0.022$) despite a reduction in CD20 levels which was less pronounced than with ibrutinib treatment on plastic (Figure 6A, $p = 0.0002$). Ibrutinib treatment in the presence of M2-10B4 stromal cells led to a greater reduction in CD20 expression than either treatment alone ($p < 0.000$) and further reduced the efficacy of obinutuzumab at inducing PCD compared to treatment with obinutuzumab alone in the presence of M2-10B4 ($p = 0.0006$). These results suggest that contact with stromal cells leads to reduced surface expression of CD20 and decreased obinutuzumab mediated PCD, which could potentially be via a similar mechanism to the ibrutinib mediated reduction in CD20 expression and obinutuzumab mediated PCD. Furthermore, combining ibrutinib treatment of Raji cells with contact with M2-10B4 stromal cells leads to a further reduction in CD20 expression ($p = 0.0002$) and significantly reduced PCD ($p = 0.003$), suggesting that combination treatment with obinutuzumab and ibrutinib would be detrimental, especially in stromal rich tumour areas.

## 3.7 The anti-tumour efficacy of obinutuzumab is lower when treatment is delayed until tumour is established in bone marrow niches

In order to see whether stromal cells might impair obinutuzumab efficacy *in vivo*, a murine model was established where mice received a systemic injection of hCD20$^{+ve}$ lymphoma cells, which led to the development of tumour metastases to spleen and bone marrow and development of hind leg paralysis (Sarzotti et al., 1987; Meunier et al., 2003). Mice were treated with obinutuzumab either 1 day or 7 days after tumour injection

**A**

| | Enrichment Score: 28.12 | Count | P-value | Benjamini |
|---|---|---|---|---|
| Annotation cluster 1 | Cadherin binding involved in cell-cell adhesion | 86 | 4.7E-31 | 1.8E-28 |
| | Cell-cell adhesion junction | 86 | 6.2E-29 | 6.9E-27 |
| | Cell-cell adhesion | 77 | 1.5E-26 | 1.3E-23 |
| | **Enrichment Score: 25.32** | **Count** | **P-value** | **Benjamini** |
| Annotation cluster 2 | Translational initiation | 64 | 2.4E-36 | 8.6E-33 |
| | Nuclear-transcribed mRNA catabolic process, nonsense-mediated decay | 57 | 4.3E-33 | 7.5E-30 |
| | Ribonucleoprotein | 83 | 1.1E-32 | 6.0E-31 |
| | SRP-dependent cotranslational protein targeting to membrane | 50 | 8.7E-32 | 1.0E-28 |
| | Ribosomal protein | 59 | 1.6E-26 | 7.1E-25 |
| | Viral transcription | 49 | 2.8E-26 | 2.0E-23 |
| | rRNA processing | 65 | 3.2E-24 | 1.9E-21 |
| | Translation | 69 | 9.8E-23 | 4.9E-20 |
| | Ribosome | 53 | 6.8E-22 | 5.3E-20 |
| | Structural constituent of ribosome | 61 | 2.6E-20 | 6.1E-18 |
| | Cytosolic large ribosomal subunit | 32 | 5.0E-19 | 2.9E-17 |
| | **Enrichment Score: 20.81** | **Count** | **P-value** | **Benjamini** |
| Annotation cluster 3 | Mitochondrion | 164 | 7.2E-27 | 3.6E-25 |
| | Transit peptide | 95 | 2.8E-21 | 9.7E-20 |
| | Mitochondrial matrix | 65 | 4.9E-15 | 2.5E-13 |

**B**


| | -log(P-value) | Ratio | Z-score |
|---|---|---|---|
| eIF2 Signaling | 47.4 | 0.475 | 5.345 |
| Protein Ubiquitination Pathway | 41.7 | 0.411 | N/A |
| Regulation of eIF4 and p70S6K Signaling | 25.2 | 0.414 | 1.5 |
| mTOR Signaling | 21.2 | 0.343 | 1.095 |
| Sirtuin Signaling Pathway | 16.5 | 0.267 | 1.905 |
| Remodeling of Epithelial Adherens Junctions | 14.5 | 0.464 | 0.577 |
| Actin Cytoskeleton Signaling | 13.2 | 0.269 | 1.953 |
| Antigen Presentation Pathway | 11.6 | 0.553 | N/A |
| NRF2-mediated Oxidative Stress Response | 11.4 | 0.269 | 1.953 |
| Signaling by Rho Family GTPases | 11 | 0.242 | 0.944 |
| Integrin Signaling | 10.7 | 0.251 | 2.219 |
| Sumoylation Pathway | 10.5 | 0.344 | 0 |
| Epithelial Adherens Junction Signaling | 9.71 | 0.281 | N/A |
| RhoA Signaling | 9.65 | 0.298 | 0.493 |
| Actin Nucleation by ARP-WASP Complex | 9.28 | 0.411 | 1.342 |
| Germ Cell-Sertoli Cell Junction Signaling | 8.86 | 0.254 | N/A |
| ILK Signaling | 8.43 | 0.239 | 2.111 |
| Fcγ Receptor-mediated Phagocytosis | 8.2 | 0.312 | 1.671 |
| RhoGDI Signaling | 8.02 | 0.243 | 0.469 |
| p70S6K Signaling | 7.68 | 0.265 | 1.671 |

FIGURE 7
Raji cells were grown in RPMI media containing either heavy (Raji-H) or medium (Raji-M) isotopes of Lysine and Arginine. Cells were cultured either on plastic (Raji-M) or on a layer of PKH67-labelled M2-10B4 stromal cells (Raji-H) for 24 h. Tumour cells were separated from stromal cells by FACS sorting and the resulting populations of Raji-M and Raji-H were lysed. Protein content was calculated and lysates from Raji-M and Raji-H were mixed in a 1 to 1 ratio before being resolved in a SDS-PAGE and analysed by mass spectrometry. **(A)** Protein IDs which had *p*-value <0.05 and had expression fold change < -2 or >2 were uploaded in DAVID. The cluster annotation tool was used to identify the mostly enriched clusters of pathways which were differentially expressed in Raji-H. **(B)** Protein IDs which had *p*-value <0.05 and expression fold change < -2 or >2 were uploaded in IPA. Pathways which were altered in Raji-H compared to Raji-M are shown. For each of them, their significance, ratio and Z-score are shown. Data is from one experiment.

(Supplementary Figure S4). Whilst treatment at day 1 led to around 85% long-term survivors, delaying treatment to day 7 (when tumour can be detected by bioluminescent imaging within the mouse femurs, Supplementary Figure S4D) led to only 4 of 14 mice as long-term survivors (28%) suggesting that the close proximity of bone marrow stromal cells to tumour cells might impair obinutuzumab efficacy.

## 3.8 Proteomic analysis of tumour cells in the presence and absence of stroma reveals clusters of pathways which are altered upon co-culture with stromal cells

To understand which pathways in tumour cells were being altered by the interaction with stromal cells that could explain

the observed effect on obinutuzumab efficacy, a SILAC experiment was performed. Raji cells were grown in a media supplemented with either heavy or medium isotopes of Lys and Arg, as described in Materials and Methods. The resulting isotopically-labelled cell lines Raji-M and Raji-H were cultured on plastic or on a layer of PKH67-labelled M2-10B4, respectively (Supplementary Figure S5). 24 h later, tumour cells were separated from M2-10B4 stromal cells by FACS sorting. Raji-M and Raji-H were lysed and a 1 to 1 mix of the two conditions was resolved on SDS-PAGE. The proteins thus obtained were then run on a mass spectrometer and adjusted *p*-values and expression values were retrieved by running the total protein IDs on PEAKS Studio. All the hits that met the cut-offs "adjusted *p*-value < 0.05" and "expression fold change < −2, >2" were analysed using both DAVID and IPA. In DAVID (Figure 7A), the mostly enriched functional annotation cluster included pathways involved in cadherin-mediated adherens junction signalling (ES = 28.12), translational initiation (ES = 25.32) and mitochondrion (ES = 20.81). IPA also displayed as mostly enriched three pathways involved in translational initiation (Figure 7B, highlighted in green) and two cadherin-mediated adhesion-related pathways (orange). Interestingly, pathways related to the actin cytoskeleton and remodelling were also present (blue). The predicted activation status of each pathway (Z-score) revealed that the majority of the 20 most enriched signalling pathways were also predicted to be upregulated in Raji cultured on stroma compared to Raji cultured on plastic (Figure 7B).

# 4 Discussion

In haematological malignancies, the TME plays an important role in supporting the growth and survival of tumour cells. In $CD20^+$ B-cell malignancies, anti-CD20 mAbs have revolutionised therapeutic strategies, however it is currently unclear whether interactions between the TME and anti-CD20 mAb affects treatment outcomes.

Obinutuzumab is a novel glycoengineered type II antibody that only in recent years has been granted FDA approval. Despite the demonstrated superiority of this antibody compared to rituximab in different B-cell malignancies (Goede et al., 2014; Hiddemann et al., 2018), our *in vitro* experiments reveal that the presence of the stromal microenvironment can still significantly reduce killing of tumour cells, affecting the execution of both direct cell death and immune effector-mediated mechanisms of action.

The stromal microenvironment-mediated protection was dependent on direct contact rather than on soluble factors. Although soluble factors have been recognised to play a role in conferring resistance to chemotherapy-induced apoptosis (Kay et al., 2007; Lwin et al., 2007) and the CXCR-4/CXCL-12 signalling axis has been proven instrumental in mediating protection from rituximab (Hu et al., 2012; Beider et al., 2013), other studies have highlighted the importance of direct contact and the relative lack of a role for stroma-conditioned media (Panayiotidis et al., 1996; Edelmann et al., 2008). The discrepancy in these observations could be due to intrinsic differences in the lines and/or samples from different B-cell malignancies tested in those studies. Thus, stroma-mediated drug resistance in different tumour subtypes could be regulated by distinct mechanisms. In addition to this, most published articles protection from either chemotherapeutic drugs or from the type-I antibody rituximab was studied. Obinutuzumab is known to work through distinct mechanisms of action compared to both chemotherapeutic agents and type-I antibodies, suggesting that different mechanisms of protection could be employed by tumour cells against this specific antibody.

As shown by Alduaij et al. (2011), obinutuzumab induces PCD via a non-apoptotic mechanism involving HA between B cells and the reorganisation of the actin cytoskeleton towards the cell-cell junction points. However, in the presence of stromal cells these initial steps leading to PCD were not observed. In fact, stromal cells seem able to interfere with the initiation of PCD by reversing antibody-induced HA of B lymphoma cells. It is not clear how this phenomenon occurs. One hypothesis could be that the interaction between stroma and tumour cells is mediated by the same (set of) receptors involved in obinutuzumab-induced HA between B cell aggregates. Thus, stromal cells could compete for the same adhesion molecules and engage them with a higher affinity, leading to the disruption of B cell aggregates and inhibition of HA. Further investigations into these mechanisms could also help us increase our knowledge of which molecules are involved in the initial steps of obinutuzumab-induced PCD.

Antibody-induced actin cytoskeleton remodelling was also halted by the presence of stromal cells. Tumour cells on plastic adhere to each other forming visible aggregates upon treatment with obinutuzumab, and the actin cytoskeleton relocates towards the cell-cell junction points. However, our high-content screening images reveal that, when cultured on stroma, tumour cells tend to adhere to the stromal layer, and a clear polarisation of the actin signal is absent. Interestingly, a similar pattern of re-localisation–and lack of, when in contact with stroma–was observed for the CD20 molecule. This stroma-dependent alteration in re-localisation of CD20 has not previously been reported, and might suggest that the CD20 molecule could also be involved in stroma-mediated protection from obinutuzumab-induced PCD. Indeed, culture on stromal cells leads to CD20 downregulation and one could hypothesise that reduced surface CD20 might reduce susceptibility to type II anti-CD20 antibodies, as has previously been shown for type I antibodies following CD20 modulation and for ibrutinib treated tumour cells (Beers et al., 2010; Bojarczuk et al., 2014; Tipton et al., 2015; Tomita, 2016). Indeed, killing of $CD19^+$ cells in the blood of CLL patients by obinutuzumab was found to directly correlate with surface levels of CD20 (Patz et al., 2011) and downregulation of CD20 through depletion of the transcriptional coactivator CREB binding protein led to reductions in obinutuzumab mediated killing (Scialdone et al., 2019).

The BTK inhibitor ibrutinib was approved by the FDA in 2019 in combination with obinutuzumab in patients with CLL/SLL (Moreno et al., 2019), representing the first instance that anti-CD20 mAbs were employed in a combination treatment that does not include any standard chemotherapeutic agents. The ability of ibrutinib to block adhesion of CLL cells to the TME appeared to be one mechanism that could explain the success of this treatment approach (Herman et al., 2015). Crucially, several studies have since highlighted a detrimental effect of ibrutinib on CD20 expression levels in B-NHL cells, with a subsequent reduction in the efficacy of anti-CD20 mAbs when used in combination therapies (Bojarczuk

et al., 2014; Da Roit et al., 2015; Pavlasova et al., 2016). Others have observed a negative effect of ibrutinib on anti-CD20 mAb-mediated ADCC, with decreased ability of NK cells to degranulate and lyse tumour cells (Kohrt et al., 2014). Our data confirmed that ibrutinib mediates downregulation of CD20 expression on the surface of Raji cells with a concomitant decrease in obinutuzumab mediated PCD. Similarly, contact with stromal cells downregulates CD20 expression, and leads to a significant reduction in PCD, suggesting that the level of CD20 on the cell surface might play an important role in the efficacy of anti-CD20 mAbs. Pre-treatment of Raji cells with ibrutinib followed by culture with stromal cells further reduced surface CD20 and obinutuzumab mediated PCD. However, whilst the combination of ibrutinib and obinutuzumab has been shown to be effective in the clinic (Moreno et al., 2019) and *in vivo* models show no loss of obinutuzumab efficacy when ibrutinib is given as a co-treatment (Duong et al., 2015), consideration should be given to whether anti-CD20mAbs and ibrutinib should be given concurrently in the clinic or whether careful scheduling might improve outcomes further.

Proteomic analysis suggested that the presence of stroma could lead to the differential expression of several clusters of pathways. Among these, the cadherin-mediated adherens junction signalling seemed to be the most relevant, as our previous results strongly suggested that interactions between stromal and tumour cells are mediated by direct contact. The expression level of cadherin molecules has previously been reported to be altered in B-cell malignancies (Sharma and Lichtenstein, 2009; Takata et al., 2014), and there is some evidence suggesting that cadherins might play a role in mediating interactions with stromal components in blood malignancies: in T-cell lymphoma, for instance, the expression of N-cadherin enabled interactions of malignant cells with fibroblasts (Kawamura-Kodama et al., 1999). Furthermore, N-cadherin was also shown to be responsible for the protective effect upon contact between $CD34^+$ CML cells and mesenchymal stromal cells (Zhang et al., 2013). Therefore, we looked at the expression levels of cadherin molecules in tumour cells cultured on plastic or with stroma, revealing that indeed the presence of stroma caused an upregulation of the R-cadherin molecule (data not shown). However, a CRISPR-Cas9 knock-out of R-cadherin molecule in Raji cells failed to abrogate the stroma-mediated protection from obinutuzumab (data not shown), indicating that the R-cadherin signalling pathway (and its upregulation) was not involved with the observed phenotype.

Our results indicate that the interaction of Burkitt's lymphoma B cells with the stromal microenvironment negatively influences the efficacy of the anti-CD20 mAb obinutuzumab and suggest that blockade of these interactions could restore obinutuzumab efficacy. Whilst bone marrow derived stromal cells were used in this study it would be important to expand these observations to other types of stromal cells found to interact with B-cell tumours including nodal stromal cells. Several signalling pathways that appeared upregulated in tumour cells upon direct contact with stromal cells were identified, and further studies into which of such candidate pathways is responsible for the stroma-mediated protection from obinutuzumab, and possibly for the additional effect achieved by pre-treatment with ibrutinib in the presence of stroma, are warranted. Pharmaceutical targeting of these pathways could constitute a novel therapeutic strategy that could potentially improve treatment outcomes in patients with B cell malignancies. In the clinical setting, impeding the interactions between stromal and tumour cells might lead to the release into the circulation of those malignant cells which had homed into the protective bone marrow environment. This in turn might be translated into a greater ability of the anti-CD20 mAb obinutuzumab, in combination with standard chemotherapeutic agents, to clear the body of malignant B cells.

## Data availability statement

The original contributions presented in the study are included in the article/Supplementary Material, further inquiries can be directed to the corresponding authors.

## Ethics statement

The studies involving humans were approved by the South Manchester Ethics Committee. The studies were conducted in accordance with the local legislation and institutional requirements. The human samples used in this study were acquired from a by-product of routine care or industry. Written informed consent for participation was not required from the participants or the participants' legal guardians/next of kin in accordance with the national legislation and institutional requirements.

## Author contributions

EF: Data curation, Formal Analysis, Investigation, Methodology, Writing–original draft, Writing–review and editing. SP: Data curation, Investigation, Methodology, Writing–review and editing. MC: Data curation, Investigation, Methodology, Writing–review and editing. PJ: Data curation, Investigation, Methodology, Writing–review and editing. MS: Investigation, Writing–review and editing. TK: Conceptualization, Writing–review and editing. AB: Conceptualization, Writing–review and editing. CK: Conceptualization, Funding acquisition, Resources, Supervision, Writing–review and editing. JH: Conceptualization, Writing–original draft, Writing–review and editing. EC: Conceptualization, Data curation, Formal Analysis, Funding acquisition, Investigation, Methodology, Supervision, Writing–original draft, Writing–review and editing. TI: Conceptualization, Funding acquisition, Resources, Supervision, Visualization, Writing–original draft, Writing–review and editing.

## Funding

The authors declare financial support was received for the research, authorship, and/or publication of this article. Work was funded by Roche Glycart and Cancer Research UK (C431/A28280). EC is funded by the NIHR Manchester Biomedical Research Centre (NIHR203308) and TI is the recipient of an NIHR Senior

Investigator Award and supported by the NIHR Manchester Biomedical Research Centre (NIHR203308) as theme lead.

## Acknowledgments

The authors would like to thank AB for provision of Raji-GFP actin and Raji YFP-CD20 cells, Claire Hart for provision of M2-10B4 stromal cells (University of Manchester) and Tiziana Monteverde for the mcherry lentiviral vector (Cancer Research UK Manchester Institute). The authors would like to thank members of the CRUK Manchester Institute Flow and Mass cytometry and Visualization and imaging analysis core facilities for their assistance with flow cytometry and microscopy experiments.

## Conflict of interest

CK declares employment, stock ownership and patients with Roche.

The authors declare that this study received funding from Roche. The funder had the following involvement in the study: provision of materials, funding for consumables and EF, approval of manuscript for publication.

The remaining authors declare that the research was conducted in the absence of any commercial or financial relationships that could be construed as a potential conflict of interest.

## Publisher's note



## Supplementary material

The Supplementary Material for this article can be found online at: https://www.frontiersin.org/articles/10.3389/fcell.2023.1270398/full#supplementary-material

## References

Alduaij, W., Ivanov, A., Honeychurch, J., Cheadle, E. J., Potluri, S., Lim, S. H., et al. (2011). Novel type II anti-CD20 monoclonal antibody (GA101) evokes homotypic adhesion and actin-dependent, lysosome-mediated cell death in B-cell malignancies. *Blood* 117 (17), 4519–4529. doi:10.1182/blood-2010-07-296913

Beers, S. A., French, R. R., Chan, H. T., Lim, S. H., Jarrett, T. C., Vidal, R. M., et al. (2010). Antigenic modulation limits the efficacy of anti-CD20 antibodies: implications for antibody selection. *Blood* 115 (25), 5191–5201. doi:10.1182/blood-2010-01-263533

Beider, K., Ribakovsky, E., Abraham, M., Wald, H., Weiss, L., Rosenberg, E., et al. (2013). Targeting the CD20 and CXCR4 pathways in non-hodgkin lymphoma with rituximab and high-affinity CXCR4 antagonist BKT140. *Clin. Cancer Res.* 19 (13), 3495–3507. doi:10.1158/1078-0432.CCR-12-3015

Bojarczuk, K., Siernicka, M., Dwojak, M., Bobrowicz, M., Pyrzynska, B., Gaj, P., et al. (2014). B-cell receptor pathway inhibitors affect CD20 levels and impair antitumor activity of anti-CD20 monoclonal antibodies. *Leukemia* 28 (5), 1163–1167. doi:10.1038/leu.2014.12

Buchner, M., Brantner, P., Stickel, N., Prinz, G., Burger, M., Bär, C., et al. (2010). The microenvironment differentially impairs passive and active immunotherapy in chronic lymphocytic leukaemia - CXCR4 antagonists as potential adjuvants for monoclonal antibodies. *Br. J. Haematol.* 151 (2), 167–178. doi:10.1111/j.1365-2141.2010.08316.x

Da Roit, F., Engelberts, P. J., Taylor, R. P., Breij, E. C., Gritti, G., Rambaldi, A., et al. (2015). Ibrutinib interferes with the cell-mediated anti-tumor activities of therapeutic CD20 antibodies: implications for combination therapy. *Haematologica* 100 (1), 77–86. doi:10.3324/haematol.2014.107011

de la Fuente, M. T., Casanova, B., Moyano, J. V., Garcia-Gila, M., Sanz, L., Garcia-Marco, J., et al. (2002). Engagement of α4β1 integrin by fibronectin induces *in vitro* resistance of B chronic lymphocytic leukemia cells to fludarabine. *J. Leukoc. Biol.* 71 (3), 495–502. doi:10.1189/jlb.71.3.495

Duong, M. N., Matera, E. L., Mathe, D., Evesque, A., Valsesia-Wittmann, S., Clemenceau, B., et al. (2015). Effect of kinase inhibitors on the therapeutic properties of monoclonal antibodies. *MAbs* 7 (1), 192–198. doi:10.4161/19420862.2015.989020

Edelmann, J., Klein-Hitpass, L., Carpinteiro, A., Führer, A., Sellmann, L., Stilgenbauer, S., et al. (2008). Bone marrow fibroblasts induce expression of PI3K/NF-kappaB pathway genes and a pro-angiogenic phenotype in CLL cells. *Leuk. Res.* 32 (10), 1565–1572. doi:10.1016/j.leukres.2008.03.003

Goede, V., Fischer, K., Busch, R., Engelke, A., Eichhorst, B., Wendtner, C. M., et al. (2014). Obinutuzumab plus chlorambucil in patients with CLL and coexisting conditions. *N. Engl. J. Med.* 370 (12), 1101–1110. doi:10.1056/NEJMoa1313984

Herman, S. E., Mustafa, R. Z., Jones, J., Wong, D. H., Farooqui, M., and Wiestner, A. (2015). Treatment with ibrutinib inhibits BTK- and VLA-4-dependent adhesion of chronic lymphocytic leukemia cells *in vivo*. *Clin. Cancer Res.* 21 (20), 4642–4651. doi:10.1158/1078-0432.CCR-15-0781

Herter, S., Birk, M. C., Klein, C., Gerdes, C., Umana, P., and Bacac, M. (2014). Glycoengineering of therapeutic antibodies enhances monocyte/macrophage-mediated phagocytosis and cytotoxicity. *J. Immunol.* 192 (5), 2252–2260. doi:10.4049/jimmunol.1301249

Herter, S., Herting, F., Mundigl, O., Waldhauer, I., Weinzierl, T., Fauti, T., et al. (2013). Preclinical activity of the type II CD20 antibody GA101 (obinutuzumab) compared with rituximab and ofatumumab *in vitro* and in xenograft models. *Mol. Cancer Ther.* 12 (10), 2031–2042. doi:10.1158/1535-7163.MCT-12-1182

Hiddemann, W., Barbui, A. M., Canales, M. A., Cannell, P. K., Collins, G. P., Dürig, J., et al. (2018). Immunochemotherapy with obinutuzumab or rituximab for previously untreated follicular lymphoma in the GALLIUM study: influence of chemotherapy on efficacy and safety. *J. Clin. Oncol.* 36 (23), 2395–2404. doi:10.1200/JCO.2017.76.8960

Honeychurch, J., Alduaij, W., Azizyan, M., Cheadle, E. J., Pelicano, H., Ivanov, A., et al. (2012). Antibody-induced nonapoptotic cell death in human lymphoma and leukemia cells is mediated through a novel reactive oxygen species-dependent pathway. *Blood* 119 (15), 3523–3533. doi:10.1182/blood-2011-12-395541

Hu, Y., Gale, M., Shields, J., Garron, C., Swistak, M., Nguyen, T. H., et al. (2012). Enhancement of the anti-tumor activity of therapeutic monoclonal antibodies by CXCR4 antagonists. *Leuk. Lymphoma* 53 (1), 130–138. doi:10.3109/10428194.2011.601698

Ivanov, A., Beers, S. A., Walshe, C. A., Honeychurch, J., Alduaij, W., Cox, K. L., et al. (2009). Monoclonal antibodies directed to CD20 and HLA-DR can elicit homotypic adhesion followed by lysosome-mediated cell death in human lymphoma and leukemia cells. *J. Clin. Invest.* 119 (8), 2143–2159. doi:10.1172/JCI37884

Kawamura-Kodama, K., Tsutsui, J., Suzuki, S. T., Kanzaki, T., and Ozawa, M. (1999). N-cadherin expressed on malignant T cell lymphoma cells is functional, and promotes heterotypic adhesion between the lymphoma cells and mesenchymal cells expressing N-cadherin. *J. Invest. Dermatol* 112 (1), 62–66. doi:10.1046/j.1523-1747.1999.00479.x

Kay, N. E., Shanafelt, T. D., Strege, A. K., Lee, Y. K., Bone, N. D., and Raza, A. (2007). Bone biopsy derived marrow stromal elements rescue chronic lymphocytic leukemia B-cells from spontaneous and drug induced cell death and facilitates an "angiogenic switch. *Leuk. Res.* 31 (7), 899–906. doi:10.1016/j.leukres.2006.11.024

Kohrt, H. E., Sagiv-Barfi, I., Rafiq, S., Herman, S. E., Butchar, J. P., Cheney, C., et al. (2014). Ibrutinib antagonizes rituximab-dependent NK cell-mediated cytotoxicity. *Blood* 123 (12), 1957–1960. doi:10.1182/blood-2014-01-547869

Kurtova, A. V., Balakrishnan, K., Chen, R., Ding, W., Schnabl, S., Quiroga, M. P., et al. (2009a). Diverse marrow stromal cells protect CLL cells from spontaneous and drug-induced apoptosis: development of a reliable and reproducible system to assess stromal cell adhesion-mediated drug resistance. *Blood* 114 (20), 4441–4450. doi:10.1182/blood-2009-07-233718

Kurtova, A. V., Tamayo, A. T., Ford, R. J., and Burger, J. A. (2009b). Mantle cell lymphoma cells express high levels of CXCR4, CXCR5, and VLA-4 (CD49d): importance for interactions with the stromal microenvironment and specific targeting. *Blood* 113 (19), 4604–4613. doi:10.1182/blood-2008-10-185827

Lagneaux, L., Delforge, A., Bron, D., De Bruyn, C., and Stryckmans, P. (1998). Chronic lymphocytic leukemic B cells but not normal B cells are rescued from apoptosis by contact with normal bone marrow stromal cells. *Blood* 91 (7), 2387–2396. doi:10.1182/blood.v91.7.2387

Lwin, T., Hazlehurst, L. A., Li, Z., Dessureault, S., Sotomayor, E., Moscinski, L. C., et al. (2007). Bone marrow stromal cells prevent apoptosis of lymphoma cells by upregulation of anti-apoptotic proteins associated with activation of NF-kappaB (RelB/p52) in non-Hodgkin's lymphoma cells. *Leukemia* 21 (7), 1521–1531. doi:10.1038/sj.leu.2404723

Manabe, A., Murti, K. G., Coustan-Smith, E., Kumagai, M., Behm, F. G., Raimondi, S. C., et al. (1994). Adhesion-dependent survival of normal and leukemic human B lymphoblasts on bone marrow stromal cells. *Blood* 83 (3), 758–766. doi:10.1182/blood.v83.3.758.758

Marquez, M. E., Hernández-Uzcátegui, O., Cornejo, A., Vargas, P., and Da Costa, O. (2015). Bone marrow stromal mesenchymal cells induce down regulation of CD20 expression on B-CLL: implications for rituximab resistance in CLL. *Br. J. Haematol.* 169 (2), 211–218. doi:10.1111/bjh.13286

Meunier, M. C., Roy-Proulx, G., Labrecque, N., and Perreault, C. (2003). Tissue distribution of target antigen has a decisive influence on the outcome of adoptive cancer immunotherapy. *Blood* 101 (2), 766–770. doi:10.1182/blood-2002-04-1032

Moreno, C., Greil, R., Demirkan, F., Tedeschi, A., Anz, B., Larratt, L., et al. (2019). Ibrutinib plus obinutuzumab versus chlorambucil plus obinutuzumab in first-line treatment of chronic lymphocytic leukaemia (iLLUMINATE): a multicentre, randomised, open-label, phase 3 trial. *Lancet Oncol.* 20 (1), 43–56. doi:10.1016/S1470-2045(18)30788-5

Mössner, E., Brünker, P., Moser, S., Püntener, U., Schmidt, C., Herter, S., et al. (2010). Increasing the efficacy of CD20 antibody therapy through the engineering of a new type II anti-CD20 antibody with enhanced direct and immune effector cell-mediated B-cell cytotoxicity. *Blood* 115 (22), 4393–4402. doi:10.1182/blood-2009-06-225979

Mraz, M., Zent, C. S., Church, A. K., Jelinek, D. F., Wu, X., Pospisilova, S., et al. (2011). Bone marrow stromal cells protect lymphoma B-cells from rituximab-induced apoptosis and targeting integrin α-4-β-1 (VLA-4) with natalizumab can overcome this resistance. *Br. J. Haematol.* 155 (1), 53–64. doi:10.1111/j.1365-2141.2011.08794.x

National Cancer Institute (2020b). Cancer statistics. Available from: https://www.cancer.gov/about-cancer/understanding/statistics.

National Cancer Institute (2020a). Non-Hodgkin lymphoma — cancer stat facts. Available from: https://seer.cancer.gov/statfacts/html/nhl.html.

National Cancer Institute (2012). Using the immune system in the fight against cancer: discovery of rituximab. Available from: https://www.cancer.gov/research/progress/discovery/blood-cancer.

Panayiotidis, P., Jones, D., Ganeshaguru, K., Foroni, L., and Hoffbrand, A. V. (1996). Human bone marrow stromal cells prevent apoptosis and support the survival of chronic lymphocytic leukaemia cells *in vitro*. *Br. J. Haematol.* 92 (1), 97–103. doi:10.1046/j.1365-2141.1996.00305.x

Patz, M., Isaeva, P., Forcob, N., Muller, B., Frenzel, L. P., Wendtner, C. M., et al. (2011). Comparison of the *in vitro* effects of the anti-CD20 antibodies rituximab and GA101 on chronic lymphocytic leukaemia cells. *Br. J. Haematol.* 152 (3), 295–306. doi:10.1111/j.1365-2141.2010.08428.x

Pavlasova, G., Borsky, M., Seda, V., Cerna, K., Osickova, J., Doubek, M., et al. (2016). Ibrutinib inhibits CD20 upregulation on CLL B cells mediated by the CXCR4/SDF-1 axis. *Blood* 128 (12), 1609–1613. doi:10.1182/blood-2016-04-709519

Sarzotti, M., Baron, S., and Klimpel, G. R. (1987). EL-4 metastases in spleen and bone marrow suppress the NK activity generated in these organs. *Int. J. Cancer* 39 (1), 118–125. doi:10.1002/ijc.2910390121

Scialdone, A., Khazaei, S., Hasni, M. S., Lennartsson, A., Gullberg, U., and Drott, K. (2019). Depletion of the transcriptional coactivators CREB-binding protein or EP300 downregulates CD20 in diffuse large B-cell lymphoma cells and impairs the cytotoxic effects of anti-CD20 antibodies. *Exp. Hematol.* 79, 35–46. doi:10.1016/j.exphem.2019.10.004

Sharma, S., and Lichtenstein, A. (2009). Aberrant splicing of the E-cadherin transcript is a novel mechanism of gene silencing in chronic lymphocytic leukemia cells. *Blood* 114 (19), 4179–4185. doi:10.1182/blood-2009-03-206482

Takata, K., Tanino, M., Ennishi, D., Tari, A., Sato, Y., Okada, H., et al. (2014). Duodenal follicular lymphoma: comprehensive gene expression analysis with insights into pathogenesis. *Cancer Sci.* 105 (5), 608–615. doi:10.1111/cas.12392

Tipton, T. R., Roghanian, A., Oldham, R. J., Carter, M. J., Cox, K. L., Mockridge, C. I., et al. (2015). Antigenic modulation limits the effector cell mechanisms employed by type I anti-CD20 monoclonal antibodies. *Blood* 125 (12), 1901–1909. doi:10.1182/blood-2014-07-588376

Tomita, A. (2016). Genetic and epigenetic modulation of CD20 expression in B-cell malignancies: molecular mechanisms and significance to rituximab resistance. *J. Clin. Exp. Hematop* 56 (2), 89–99. doi:10.3960/jslrt.56.89

Zhang, B., Li, M., McDonald, T., Holyoake, T. L., Moon, R. T., Campana, D., et al. (2013). Microenvironmental protection of CML stem and progenitor cells from tyrosine kinase inhibitors through N-cadherin and Wnt-β-catenin signaling. *Blood* 121 (10), 1824–1838. doi:10.1182/blood-2012-02-412890

frontiers | Frontiers in Cell and Developmental Biology

TYPE Mini Review
PUBLISHED 31 October 2023
DOI 10.3389/fcell.2023.1239749



OPEN ACCESS

EDITED BY
Namrata Gundiah,
Indian Institute of Science (IISc), India

REVIEWED BY
Susan E. Leggett,
University of Illinois at Urbana-Champaign, United States

*CORRESPONDENCE
Emad Moeendarbary,
e.moeendarbary@ucl.ac.uk

†These authors have contributed equally to this work

RECEIVED 14 June 2023
ACCEPTED 10 October 2023
PUBLISHED 31 October 2023

CITATION
Chen MB, Javanmardi Y, Shahreza S, Serwinski B, Aref A, Djordjevic B and Moeendarbary E (2023), Mechanobiology in oncology: basic concepts and clinical prospects.
*Front. Cell Dev. Biol.* 11:1239749.
doi: 10.3389/fcell.2023.1239749



# Mechanobiology in oncology: basic concepts and clinical prospects

Michelle B. Chen[1†], Yousef Javanmardi[2†], Somayeh Shahreza[2], Bianca Serwinski[2,3,4], Amir Aref[5], Boris Djordjevic[2,3] and Emad Moeendarbary[1,2*]

[1]Department of Biological Engineering, Massachusetts Institute of Technology, Cambridge, MA, United States, [2]Department of Mechanical Engineering, University College London, London, United Kingdom, [3]199 Biotechnologies Ltd., London, United Kingdom, [4]Northeastern University London, London, United Kingdom, [5]Belfer Center for Applied Cancer Science, Dana-Farber Cancer Institute, Harvard Medical School, Boston, MA, United States

The interplay between genetic transformations, biochemical communications, and physical interactions is crucial in cancer progression. Metastasis, a leading cause of cancer-related deaths, involves a series of steps, including invasion, intravasation, circulation survival, and extravasation. Mechanical alterations, such as changes in stiffness and morphology, play a significant role in all stages of cancer initiation and dissemination. Accordingly, a better understanding of cancer mechanobiology can help in the development of novel therapeutic strategies. Targeting the physical properties of tumours and their microenvironment presents opportunities for intervention. Advancements in imaging techniques and lab-on-a-chip systems enable personalized investigations of tumor biomechanics and drug screening. Investigation of the interplay between genetic, biochemical, and mechanical factors, which is of crucial importance in cancer progression, offers insights for personalized medicine and innovative treatment strategies.

KEYWORDS

**cancer, mechanobiolgy, extracellular matrix (ECM), metastasis (cancer metastasis), invasion, mechanotherapeutics**

## Introduction: mechanobiology and cancer

Genetic transformations, biochemical communications and physical interactions are interconnected processes involved from the initial steps of tumor formation until the latter phases of cancer metastasis, a major cause of cancer related deaths. Metastatic cascade begins when the primary tumor cells gain aggressive and migratory phenotypes resulting in leaving the primary tumor (Figure 1A), invading the local tissue (Figure 1B) (Craene and Berx, 2013) and transmigrating through the endothelial barrier into the blood or lymphatic microvasculature (a process known as intravasation, Figure 1C) (Van Zijl et al., 2011). The latter steps of disease involve survival of cancer cells in blood circulation (Figure 1D) (Aceto et al., 2015; Reymond et al., 2013) and exit from the vessels at distal tissues (a process known as extravasation) to ultimately invade and colonize in the secondary sites (Figure 1E) (Nguyen et al., 2009). In addition to a number of unique genetic and biochemical factors associated with metastasis (Suresh, 2007; Kumar and Weaver, 2009; Wirtz et al., 2011), irregular mechanical alterations such as structural, morphological and stiffness changes, in both cells and the extracellular environment, play a significant role during all stages of cancer initiation and

dissemination. For example, the primary tumor is characterized by biochemically and mechanically altered environment that results from oncogenic mutations and epigenetic changes disrupting key physiological cellular processes such as cell cycle (Spill et al., 2016). Taking advantage of the abnormal mechanical properties of most tumors, palpation has been a conventional diagnostic method to assess the stiffness of tumor within the surrounding soft tissue. The disease stage is linked with tumor stiffness as monitored by *in vivo* MRI elastography or through *ex vivo* atomic force microscopy (Lopez et al., 2011). On the other hand, during tumor growth, the mechanical alterations in tumor environments trigger complex bio-mechanical signalling pathways, which may ultimately enhance the ability of tumor cells to acquire a malignant phenotype. The malignant evolution of cancer cells de-regulates cell-cell and cell-extracellular matrix (ECM) adhesions and cytoskeletal remodeling leading to abnormal tumor cell morphology, enhancement of metabolism (Torrino et al., 2021), and migratory behavior which facilitate invasion at the primary site and ultimately leads to intravasation. Following intravasation, circulating tumor cells (CTCs) must resist the mechanical forces in the bloodstream to survive and reach the secondary organ. Once at the secondary site, tumor cells must exert forces and undergo morphological changes to escape from the vasculature and invade the ECM of the distal organ.

These mechanical interactions during the metastatic journey of tumor cells highlight the importance of biomechanics in cancer dissemination (Kumar and Weaver, 2009; Moeendarbary and Harris, 2014; Malandrino et al., 2018a). Here we describe the crucial interplay between mechanics and biology during cancer initiation and progression together with recent conceptual and technological advances in mechanobiology which have led to a remarkable progress in leveraging cancer biomechanics to develop novel therapeutic strategies.

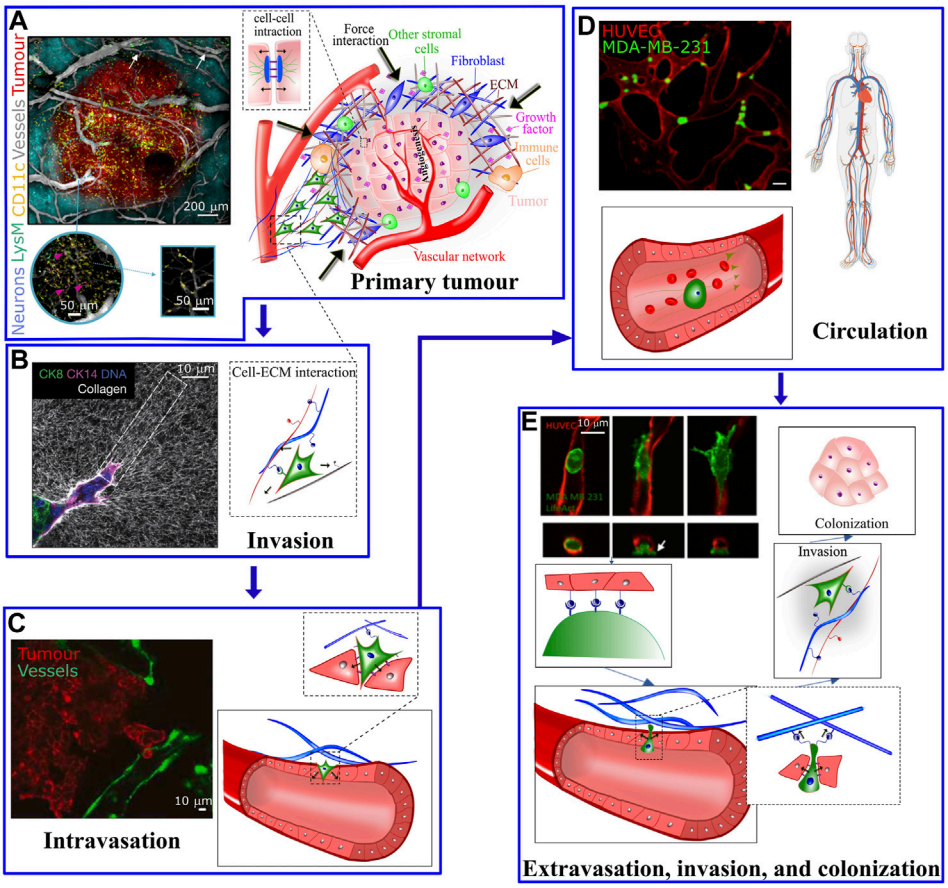


FIGURE 1
**(A)** The tumour microenvironment at the primary site is very complex; Hypoxic pathways and signaling with other supporting cells, including immune cells, mesenchymal stromal cells and fibroblasts activates endothelial cells to form vascular network in the tumor and surrounding areas. The left panel shows a five-color intravital two-photon image acquired from a bevacizumab-treated triple transgenic mouse. Arrows show the LysM-EGFP$^{+}$ cells present in the vessels. The cells colored in pink refer to double-labelled cells (pink arrows) (CD11c-EYFP+/LysM-EGFP+) inside the tumor [taken from Soubéran et al. (2019)]. **(B)** At the primary tumor site, factors including matrix pore size, density, stiffness, and fiber orientation play a role in modulating the migratory and invasive capabilities of tumor cells. Left panel: Confocal reflection microscopy reveals that invasive organoids align the collagen network to facilitate tumor invasion (taken from Koorman et al. (2022)]. **(C)** Tumor cells cross the endothelial barrier to enter the circulation. **(D)** During circulation tumor cells are exposed to shear stress from the blood flow (left panel in C and D are taken from Agrawal et al. (2022) and Beyer et al. (2021), respectively). **(E)** To exit the circulation, tumor cells pass through the endothelial barrier. The process of transendothelial migration involves significant tumor cell deformations and generation of cellular forces that may activate downstream mechanosensitive pathways. Upper left image is taken from Chen et al. (2017). White arrow depicts actin-rich tumor cell protrusion passing through the endothelium.

## Mechanical forces during tumor initiation and growth

Even in a seemingly static tissue, the extracellular microenvironment exerts forces to the cells. Such forces are originated from adjacent cells, the interstitial fluid, or interaction with the ECM, and are sensed via cellular mechanosensitive receptors that regulate major cellular functions such as the cell cycle, morphogenesis, and migration (Wang et al., 1993). Indeed, the bio-mechanical interactions between intracellular biological machinery and the surrounding microenvironment, through mechanosensitive receptors, create a normal physiological condition. However, in the setting of cancer, genetic and epigenetic (Burdziak et al., 2023), including biochemical and physical, perturbations in intracellular or extracellular environments, disrupt the cellular homeostasis leading to dysplasia and in most cases to the formation of a solid tumor. During tumor growth, the aforementioned normal forces are disrupted as a result of mechanical stresses originated from aberrant homeostasis, excessive growth and tissue dysplasia (Jain et al., 2014). Tumor growth is known to generate compressional forces that perturb the interstitial space, the ECM and the flow in the vasculature. In turn, perturbations in the interstitial space may cause accumulation of growth factors and cytokines that facilitate tumor growth; whereas disruption in the mechanical properties of ECM and flow may alter cellular behaviour (Malandrino et al., 2018b).

It is now evident that the mechanical aspects such as ECM stiffness are critical in regulating a wide range of cellular behaviour. For example, in the context of stem cell differentiation, human mesenchymal stem cells preferentially differentiate into neurons or osteocytes when cultured on substrates with stiffnesses matching brain or bone tissues respectively (Saha et al., 2008). In the setting of cancer transformation, when epithelial cells are cultured on a compliant substrate, normal cells show a decrease in the rate of DNA synthesis and an increase in the rate of apoptosis while transformed cancer cells maintain their growth and apoptotic characteristics (Wang et al., 2000). Furthermore, transformed cells exert higher traction forces compared to non-transformed cells. Consequently, the increase in ECM stiffness and the extent of compression can lead to activation and increased expression of Rho GTPase and downstream effectors as well as high levels of extracellular signal-regulated kinases (ERK) activity that facilitate the process of epithelial-mesenchymal transformation (EMT) (Klein et al., 2009).

## The impact of physical interactions in malignancy and invasion

Biochemical and biophysical characteristics of the ECM influences cell migration (Barenholz-Cohen et al., 2020) through variations in growth factors or chemokines (chemotaxis), stiffness (durotaxis), ligand density (haptotaxis), and topographical organization (contact guidance) to direct cells to target destinations (Wang et al., 2019). Recent advances in intravital imaging have revealed that cells can adopt a diverse set of migration strategies involving migration as single cells or collective strands, transitions between mesenchymal, epithelial, and amoeboid migration modes, deformation of the cell body and nucleus to squeeze through matrix pores, and remodeling of matrix structure to bypass the physical barriers presented by the ECM (Wang et al., 2019) (Figure 1B). Furthermore, heterogeneity of stiffness in tumor microenvironment, triggered by matrix remodeling can mechanically guide the tumor cells directional migration (Zhang et al., 2020).

EMT is a critical process in metastasis and involves loss of epithelial characteristics (Bocci et al., 2019), resulting from downregulation of cell-cell adhesion strength (for example, through loss of E-cadherin and cytokeratin) and acquisition of a mesenchymal phenotype via activation of migratory processes (for example, through upregulation of vimentin and N-cadherin). Taken together, the EMT process disrupts cellular force balances and polarity leading to morphological changes and detachment of tumor cells from the tumor epithelium (Thiery and Sleeman, 2006; Kalluri and Weinberg, 2009; Chaffer and Weinberg, 2011). By developing a high-throughput screening assay to track displacements generated by 3D cultured multicellular clusters, Leggett et al. (2020) showed a successive reduction in protrusive and circumferential tractions during EMT. Subsequently, the modulation of cellular shape and forces in combination with mechanisms favouring migration including proteolytic (matrix metalloproteinase), adhesive, protrusive (invadopodia) and contractile processes, promote invasion of cancer cells (Wolf and Friedl, 2009). Therefore, to facilitate their three-dimensional motility, cancer cells navigate through the ECM via invadopodial protrusions, balance cell-ECM adhesion, and apply contractile forces to squeeze through ECM pores and ultimately digest and remodel the ECM via force application and matrix metalloproteinase secretion.

The generation of a new tumor-specific vasculature that aids tumor growth, is concomitant with tumor development and transformation to malignancy and facilitates the escape of tumor cells into the circulation. In addition to biochemical signals (Chen et al., 2021), physical factors such as mechanical, hydrodynamical, and collective processes (Rieger and Welter, 2015) influence the generation and architecture of tumor-specific vasculature. Indeed, the growth of an avascular tumor is limited to a critical size (<1 mm) because of the inability of diffusion mechanisms to supply oxygen and soluble factors into the tumor core. This phenomenon results in the development of a necrotic/hypoxic region at the tumor core, which is surrounded by a highly proliferative outer rim. Therefore, robust vascularization mechanisms are recruited to boost tumor growth in order to enhance delivery of different factors, such as oxygen. Vascularization of the tumor and surrounding areas is initiated and maintained through the recruitment and activation of endothelial cells, mainly triggered by hypoxic pathways (Madsen et al., 2015), and signaling with other supporting cells in the tumor microenvironment. These include, immune cells, mesenchymal stromal cells and fibroblasts (Figure 1A) (Weis and Cheresh, 2011). The newly developed vessels perturb the normal architecture of blood and lymphatic networks and induce an aberrant interaction between the fluid and solid phases within the tumor leading to high levels of the interstitial fluid pressure and the lack of gas and nutrients (Figure 1A) (Koumoutsakos et al., 2013). Due to such a chemically and mechanically disordered tumor environment, direct drug delivery to solid tumors is often inefficient (Minchinton and Tannock, 2006). Following tumor vascularization, the combination of protracted tumor cell proliferation, continuous genetic transformations,

angiogenesis and activation of bio-mechanical signaling pathways promote malignancy, invasion, and metastasis (Polyak and Weinberg, 2009; Wirtz et al., 2011; Mierke, 2019; Yang et al., 2020; Dou et al., 2022).

# Biomechanics of cancer cell during intravasation, circulation and extravasation

## Intravasation and extravasation

Intravasation describes the process by which individual or multiple tumor cells migrate away from the primary tumor site, cross the endothelial barrier to gain entry into the circulation (Figure 1C). Similarly, extravasation is the sequences of events where CTCs exit the bloodstream and invade the parenchyma of a secondary metastatic site. The efficiency of these events may be modulated by the external physical microenvironment that drives intracellular signaling, as well as the cell's ability to perturb its inherent mechanical properties.

## External environment

To enter or leave the circulation, tumor cells must migrate across dense parenchymal tissue, which is composed of a network of highly cross-linked extracellular matrix and stromal cells. On average, pore sizes are on the scale of nanometers (<1 micron) (Laudani et al., 2020) while tumor cell size ranges 5–30 microns in diameter, suggesting that both matrix alterations and extreme cell deformation are required. One of the rate limiting steps of migration is the deformation of the tumor cell nucleus, which is approximately 5–10 times stiffer than the cytoplasm (Lammerding, 2011). As such, the matrix pore size and the deformability of the interstitial spaces are the factors that might dictate migration. Tumor cells are known to secrete matrix metalloproteinase (MMPs) like MMP2 to enable collagen proteolysis (Leong et al., 2014; Deryugina and Quigley, 2015; Micalet et al., 2022) and are shown to localize MT1-MMP at the leading edge of protrusion during migration, indicating an active role of degradation. Notably, the majority of vasculature is surrounded by a dense network of basement membrane (BM) proteins such as collagen IV and laminin, requiring further degradation processes like the secretion of gelatinases (e.g., MMP-9) prior to entering circulation (Maity et al., 2011; Sounni et al., 2011). Sikic et al. (2022) by tracking force-induced displacements and measuring local viscoelastic properties of Matrigel via magnetic micro-rheology, quantified tumor cell generated forces during invasion towards basement membrane in a 3D culture environment. They showed that protrusions extension involves stepwise increases in forces ranging from piconewtons to nanonewtons being exerted every few minutes. While matrix degradation could decrease the burden for the cell to undergo severe deformation, recent work has also shown the ability of tumor cells to exhibit substantial morphological changes in the absence of matrix loss (Wolf et al., 2003; Voura et al., 2013). This may involve large deformations of the tumor cell nucleus, which depends on mechanical properties of the nuclear lamina and organization of chromatin (Cao et al., 2016). In this regard, it is known that linker proteins (such as SUN domain-containing proteins) between nuclear and cytoplasmic (LINC) complexes can facilitate the proper positioning of the nucleus relative to the cell body to allow motility through narrow constrictions (Kraning-Rush et al., 2012; Denais et al., 2016).

The endothelium presents yet another barrier for tumor cell migration. Microvessels are lined with a single layer of endothelial cells connected to each other through junctional proteins such as VE-cadherin and CD31 (PECAM 1) that are responsible for the tight regulation of soluble factor transport between the blood and the surrounding tissue. The open gaps between endothelial cells are typically less than a few microns (McEvoy et al., 2022), suggesting that the transmigration of tumor cells may involve deformation of both tumor and endothelial cells. It has been shown that tumor cells can secrete inflammatory factors such as TNF-α which mediate endothelial junctional permeability and create discontinuities in the barrier to facilitate transmigration (Zervantonakis et al., 2012). Furthermore, the ability of tumor cells to anchor onto the endothelium through tumor-EC adhesion proteins such as integrins is critical for the generation of forces that allow translocation. Since integrins provide a connection between the ECM and the actin cytoskeleton, this mechanosensitive protein coupling and activation may lead to downstream intracellular signaling, thus determining the extent of intracellular forces required to maintain or obtain a certain cellular morphology. Also, BM mechanics at the primary and secondary tumour site plays a critical role in cancer progression, independent of tumour-mediated alterations; Reuten et al. showed that the BM stiffness is regulated through Netrin-4 in a laminin-binding-dependent manner by diluting laminin ternary node complexes. The more Netrin-4 molecules are present, the softer the laminin network and the more resistant it is to metastases formation (Reuten et al., 2021).

## Influence of extracellular physical signals on intracellular environment

Interestingly, it has been found that cancer cells are consistently softer than their non-cancerous counterparts (Rianna et al., 2020), and that the softening correlates positively with metastatic potential (Xu et al., 2012). The softer cytoplasm of more aggressive tumor cell lines is often correlated with a loss of cytoskeletal organization. Since the ability to migrate through dense matrix and endothelial barriers likely depends on the intrinsic mechanical properties of the cells, an increase in tumor cell compliance may act in its favor. Additionally, external stimuli including the presence of interstitial flow, ECM stiffness, 2D or 3D dimensionality (Galarza et al., 2020), and availability of binding sites for cell surface receptors (Wei et al., 2015) may influence the nature and deformability of the cell membrane and cytoskeleton. For instance, features that appear to be important for 2D motility—focal adhesion, stress fibres, broad lamellipodia—are largely absent for models of 3D invasion, particularly in invasive cancer cells (Shibue and Weinberg, 2009; Mierke, 2013). On the other hand, several mechanosensory proteins, such as vinculin, play an important role in tumor cell migration within reconstituted 3D matrices, but not in 2D motility (e.g., on plastic culture dishes coated with the same ECM proteins).

## Circulating tumor cells and shear stress

After entering the circulation, tumor cells are exposed to a variety of hemodynamic forces of flowing blood and collision with other cell types (Marrella et al., 2021). For example, shear flow can influence the motility of tumor cells and determine the likelihood that intercellular adhesions with the endothelium or circulating immune cells can occur. The average shear stresses a CTC experiences is estimated to be around 1–4 dyn/cm$^2$ in the venous circulation, and 4–30 dyn/cm$^2$ in arterial circulation. This is comparable to the levels of shear stress that cartilage and bone cells are subjected to on a daily basis from normal interstitial fluid movement (~30 dyn/cm$^2$), and to the level of renal epithelial cells undergo during hypertension (~1 dyne/cm$^2$) (Nagrath et al., 2007; Aceto et al., 2015; Au et al., 2016). Thus, it is highly possible that shear stress levels experienced by CTCs are significant enough to induce mechanotransductive cellular responses.

Additionally, shear flow can induce the deformation of tumor cells and influence their viability. For instance, CTCs migration in groups exhibit higher survival rates due to protection from deleterious shear stresses (Au et al., 2016). Thus, only tumor cells that overcome the effects of fluid shear stress and escape immunosurveillance can adhere to the vasculature and enter the tissues of the secondary site.

Tumor cell extravasation is thought to first require the firm adhesion and arrest of tumor cells on the endothelium. There are two mechanisms of tumor cell arrest (Craene and Berx, 2013): physical occlusion in capillaries narrower than the diameters of the CTC, and (Van Zijl et al., 2011) active adhesion between endothelial-tumor cell ligands/receptors. *In vivo*, tumor cells have mostly been observed to arrest in small capillaries of the brain and lung, suggesting the possibility of physical occlusion. Integrins and selectins are critical to determine tumor cell retention in several organs such as the lung and the liver, indicating that active cell adhesion may be involved in addition to pure physical occlusion. The increased ability of tumor cells to arrest on the endothelium may offer higher probability of exiting the bloodstream.

Adhesion to blood vessels is followed by cancer cell transendothelial migration (TEM). Depending on the vascular bed and tumor cell types, two mechanistically different routes are possible *in vivo*: transcellular (migration of CTCs through the EC body) and paracellular (moving between ECs junctions) (Herman et al., 2019). The latter is the most frequent accessed way for cancer cells to penetrate the vascular wall *in vitro*. This process involves many chemokines, receptors and intracellular signaling molecules leading to significant cytoskeletal changes of endothelial and cancer cells (Reymond et al., 2013). Additionally, Javanmardi et al. showed that mechanical properties of ECM, such as stiffness and porosity, regulate cell generated forces through mediating RhoA activity (Javanmardi et al., 2023). Furthermore, complex push–pull forces generated by cancer cell actin-rich protrusions are essential to initiate and drive transendothelial migration (Javanmardi et al., 2023).

Interactions with other cells in the blood have also been shown to be critical. For example, adhesion to platelets through tumor integrin αvβ3 can promote tumor-platelet aggregation, which leads to the protection of tumor cells from shear flow. Additionally, platelets can secrete pro-extravasation factors such as platelet-derived nucleotides, which act to increase endothelial permeability and facilitate the transmigration of tumor cells (Labelle et al., 2011; Schumacher et al., 2013). Interactions with circulating neutrophils can increase tumor cell retention and extravasation via neutrophil CD11b, endothelial ICAM-1; and the success of these interactions decline with increasing shear rates resulting from blood flow (Peng et al., 2007; Huh et al., 2010).

# Probing cancer biomechanics and emerging technologies

Recent technological advances provide a better insight on the biomechanical phenomena during cancer cell dissemination by probing morphological changes, mechanical properties and force interactions between cells and the extracellular environment. While advanced light microscopy techniques such as optical super-resolution imaging offer unprecedented information about the nano-scale molecular organisation of the cell (Colin-York et al., 2019a) and its link to cellular morphology and function, they are mostly limited to isolated two-dimensional (2D) cultures in which a monolayer of cells are grown on flat plastic or glass substrates. To access high resolution tumor pathophysiology *in vivo*, intravital imaging has revealed some fascinating morphological changes and cell migration processes associated with invasion and intravasation (Jain et al., 2002). Three dimensional (3D) interactions among cells and the extracellular environment are unique at all stages of metastasis and cannot be recapitulated in conventional 2D cultures. On the other hand, under *in vivo* conditions, it is extremely difficult to fully follow the temporal evolution of 3D interactions and run parametric studies to dissect the role of different factors. Therefore, advanced 3D engineered models such as microfluidic based approaches, have been used in recapitulating key biomechanical features that are specific to each step of metastasis (Chen et al., 2017; Agrawal et al., 2022; Straehla et al., 2022; Watson et al., 2022) and to quantify tumor cell secretions at the single cell resolution over a long period of culture (Hassanzadeh-Barforoushi et al., 2020). Together, they have allowed the investigation of a variety of cellular events with high spatiotemporal resolution and under tunable environments (Malandrino et al., 2018a).

The measurement of mechanical properties is critically important in cancer biomechanics. Mechanical changes and alternations in the composition, architecture and stiffness of tumor microenvironment regulate tumor growth, transformation to malignancy, and invasion (Pickup et al., 2014) being therefore critical aspects in cancer progression (Cox and Erler, 2011; Lu et al., 2012; Popova and Jücker, 2022). For instance, tumor-associated collagen exhibits specific features due to variation in fiber orientation and collagen deposition. Notably, three distinct tumor-associated collagen signatures (TACS) have been identified in relation to human breast cancers: the accumulation of collagen fibers around small tumors (TACS-1), the straighten fibers in the vicinity of non-invasive tumors (TACS-2) and the perpendicular alignment of collagen fibers at the tumor periphery (TACS-3) (Warli et al., 2023). Such irregularities have been visualized through microscopy techniques, such as second harmonic generation, which highlights the structural transformations in collagen fibers (Figure 2A). Furthermore, aberrant mechanical properties of the

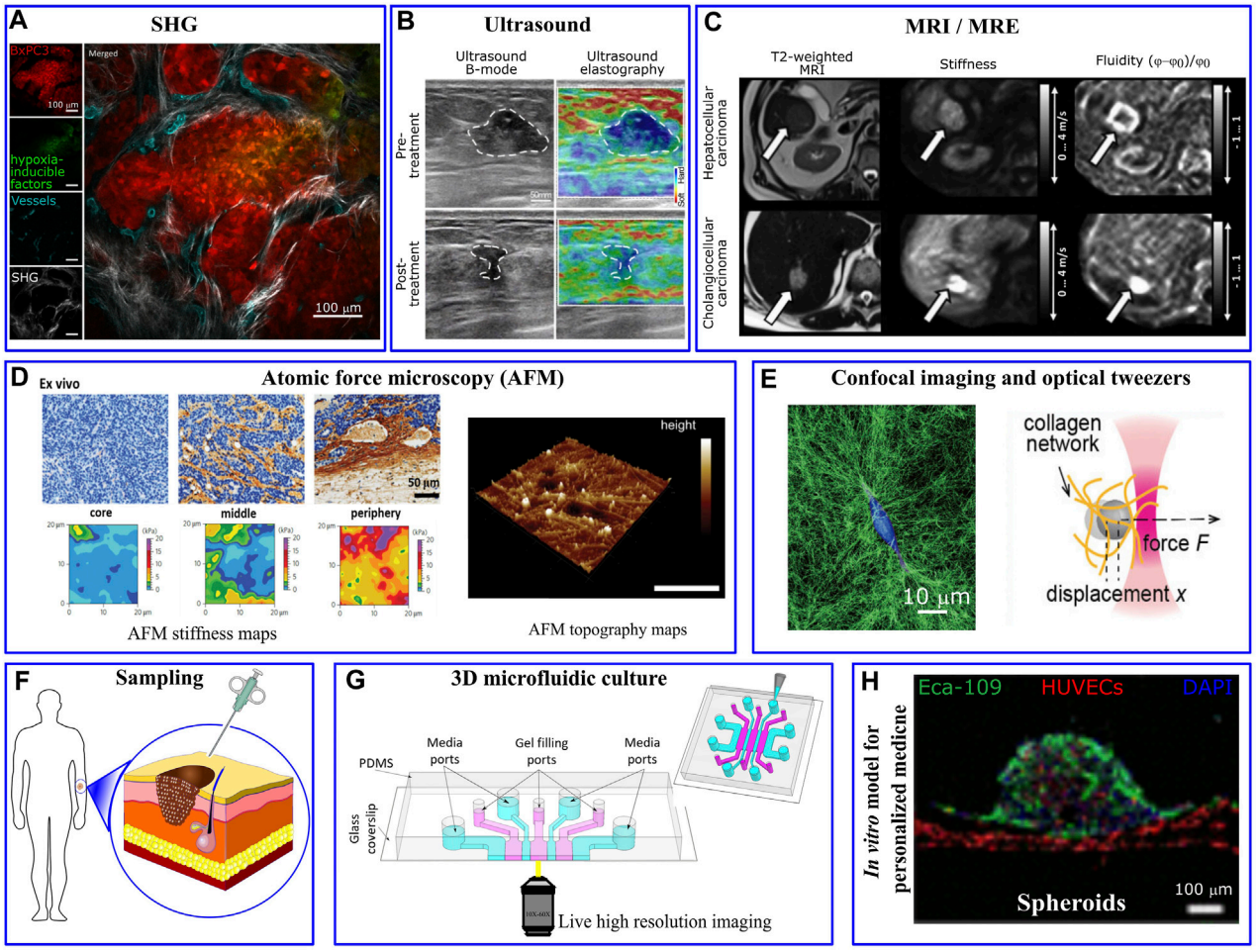


FIGURE 2
Mechanical/structural properties of the tumor microenvironment and microfluidic platform in personalized medicine. **(A)** Different tumor associated collagen signatures have been captured via *in vivo* second harmonic generation (SHG) imaging of mouse pancreatic tumor. Irregularly shaped and newly formed vessels are observed in the inner regions of the tumor, taken from Samuel et al. (2023). **(B)** Ultrasound and **(C)** Magnetic resonance elastography show various levels of tumor stiffness that can inform the planning of resection procedures, taken from Liu et al. (2023) and Sauer et al. (2023), respectively. **(D)** High resolution AFM stiffness maps of mouse mammary tumor shows highly heterogeneous tumor mechanical properties with a soft signature at the tumor core and significantly stiffer periphery. Taken from Plodinec et al. (2012). AFM topographic maps provides helpful information about matrix architecture (taken from Budden et al. (2021)). **(E)** Single MDA-MB-231 cancer cell embedded within collagen-I gel significantly deformed and remodeled collagen fibres imaged via confocal reflection microscopy and changed the gel stiffness quantified via optical tweezers. Taken from Han et al. (2018). **(F)** Cells that are derived directly from a patient are usually scarce. **(G)** The few isolated cells can be 3D-cultured in a biomimetic microfluidics device for drug discovery, personalized drug screening, or to investigate the impact of biomechanical/biochemical factors on cellular behaviour (taken from Whisler et al. (2023)). **(H)** Perfusable vascularized tumor spheroid-on-a-chip model incorporates patient's isolated cells as a personalized medicine approach (taken from Hu et al. (2022)).

tumor environment can be measured as a diagnostic tool (Plodinec et al., 2012). The mechanical properties of the tumor *per se*, as well as the micro-mechanical features of tumor environment have been characterized through a number of *in vivo*, *ex vivo*, and *in vitro* based assays at micro-nano- scale resolutions. As an alternative to conventional palpation methods, *in vivo* elastography measurements, such as ultrasonography (Wells and Liang, 2011), optical coherence tomography (Kennedy et al., 2015), and magnetic resonance imaging (Venkatesh et al., 2008), revealed significant stiffening of tumor tissues particularly in malignant tumors (Ramião et al., 2016; Ishihara and Haga, 2022). For example, pancreatic cancer tissue exhibits greater stiffness of ~6 kPa compared to the 1–3 kPa range observed in normal pancreatic tissue (Itoh et al., 2016). Lung solid tumors register stiffness levels of ~20–30 kPa, whereas normal lung parenchyma stiffness typically ranges from 0.5 to 5 kPa (Miyazawa et al., 2018). For mammary tissues, cancerous tissue displays a significantly higher stiffness of around 4 kPa, in stark contrast to the ~0.2 kPa stiffness found in normal mammary tissue (Paszek et al., 2005). Elastography-based ultrasound techniques offer a non-invasive and real-time approach to assessing tissue stiffness, enhancing the diagnostic accuracy, and providing valuable information for personalized cancer treatment (Figure 2B). Interestingly, Golatta et al. showed that adding combined shear wave elastography and strain elastography to routine B-mode breast ultrasound could help reduce the number of unnecessary biopsies in breast diagnostics by ~35% (Golatta et al., 2022). However, increased stiffness signature, that has been a well-known characteristic of solid tumors, alone has

a limited prognostic power. The prognostic potential enhances when examining other rheological properties of the tumor microenvironment through the application of *in vivo* multifrequency magnetic resonance elastography (MRE). Employing this technique, Sauer et al. (2023) outlined a roadmap for prognosis of a tumor's aggressiveness and metastatic potential based on stiffness, fluidity, spatial heterogeneity, and texture of the tumor (Figure 2C). They showed that cancer progression is accompanied by tissue fluidization, where portions of the tissue can change position across different length scales."

Alterations in cellular and extracellular composition/structures contribute to the increased tumor stiffness. For example, excessive proliferation of cancer cells and activation of stromal cells such as cancer associated fibroblasts (CAFs) (Calvo et al., 2013), induce ECM remodeling (Bertero et al., 2019); whereas tumor growth induces solid stress within the tumor itself (Nia et al., 2017; Nia et al., 2020). The presence of growth-induced solid stresses in tumors had been under suspicion for some time, as these stresses were largely estimated using mathematical models (Stylianopoulos et al., 2012). However, in the past decade various experimental techniques have emerged to directly measure such stresses. For instance, Campàs et al. (2014) introduced incompressible oil microdroplets into 3D cell aggregates and live embryonic tissue to assess the local anisotropic forces. Dolega et al. (2017) and Lee et al. (2019) employed compressible polyacrylamide microdroplets to quantify both radial and circumferential components of solid stress within spheroids. Additionally, L et al. (2017) showed that CAFs promote tumor invasion and metastasis through exerting mechanical forces on cancer cells which are mediated via adhesion proteins involving N-cadherin at the CAF membrane and E-cadherin at the cancer cell membrane. On the other hand, tumor vascularization leads to aberrant interactions between the blood flow that infiltrates and surrounds the tumor and the increased interstitial fluid pressure (Jain et al., 2014). To dissect the contribution of the different components of tumor microenvironment, high-resolution mechanical measurement techniques, such as AFM (atomic force microscopy), have been widely applied. AFM nanomechanical indentation tests on tumor slices showed a soft mechanical signature within the tumor core, where cancer cells are abundant, while the adjacent peripheral regions are stiffened mostly due to collagen alignment (Figure 2D) (Laklai et al., 2016; Stylianou and Stylianopoulos, 2016).

At the single cell level, several experimental methods such as magnetic twisting cytometry, magnetic and optical tweezers (Figure 2E) and AFM have been utilized to perturb small regions of the cell and characterize mechanical properties, such as stiffness, of isolated cancer cells. Furthermore, Kim et al. (2018) developed a multi-parametric single-cell-analysis method in which different cell lines were transported through a microfluidics channel to measure their mechanical properties. By defining a whole-cell deformability index, they showed that malignant and non-malignant cell lines have different mechanical signatures. Traction Force Microscopy has been widely utilized to observe force interaction of cells and measure cell-generated forces (Colin-York et al., 2019b; Javanmardi et al., 2021; Li et al., 2021). This force probing technique is based on imaging the cell-induced displacement of fiducial markers, embedded/targeted within extracellular environment, and use the computational procedure to back-calculate the cellular forces that generated the displacements. To streamline and simplify the computation procedures involved in TFM, Barrasa-Fano et al. (2021) developed TFMLAB, a MATLAB software package for 4D TFM. Interestingly, while highly metastatic cancer cells exhibited a softer phenotype (~0.5 kPa) compared to non-metastatic cells (~2 kPa), they generate stronger forces (Kraning-Rush et al., 2012; Kristal-Muscal et al., 2013) (~300 nN for MDA-MB231 vs ~150 nN for MCF10A) (Cross et al., 2007; Gal and Weihs, 2012)", allowing them to squeeze through 3D ECM and metastasize more readily (Coughlin et al., 2013). Also, in the cluster level, contractile forces generated by tumor spheroid have been measured and normalized in a scale-independent manner (Mark et al., 2020).

The mechanical behavior of ECM, cancer cells, and tissues are often assumed to be elastic solids for simplicity and their time-dependent mechanical responses are frequently overlooked. However, it has been demonstrated that ECM exhibits a more complex mechanical behavior, including viscoelasticity, mechanical plasticity, and nonlinear elasticity (Chaudhuri et al., 2020) and indeed, the viscoelasticity of ECM plays a fundamental role in the progression of cancer (Mierke, 2021). Additionally, cellular behavior is not affected by only the mechanics of solid compartment of the ECM; viscosity of the extracellular fluid has also been shown to facilitate tumor cell migration and dissemination on 2D surfaces and in 3D spheroids (Bera et al., 2022). In addition to ECM, cancer cells themselves typically show a lower levels of viscosity and membrane tension compared to healthy cells (Ren et al., 2023). Moreover, cytoplasm of the living cells also has been shown to behave as a poroelastic material (Moeendarbary et al., 2013) with an enhanced diffusion coefficient for cancer cells (Ren et al., 2023). At the tissue level, higher levels of viscos (loss) modulus in cancerous tissues (Deptuła et al., 2020) has improved the diagnostic accuracy and capabilities in ultrasound (Nabavizadeh et al., 2019) and MRE techniques (Reiter et al., 2022).

## Mechanobiology and challenges with translation

### Modulation of physical properties as a path of pharmacological intervention

It is now accepted that the ability of a cancer cell to successfully invade the surrounding ECM and cross endothelial barriers during metastasis requires a finely regulated set of mechanical properties. Thus, any alterations to either the surrounding physical environment or the cell cytoskeletal organization could potentially become a target of therapeutic intervention.

For example, neutralization of matrix degrading MMPs may increase steric hindrance and decrease the ability of tumor cells to cross ECM during the invasion phase. While some tumor cells appear to be resistant to these perturbations, being able to migrate in an amoeboid manner (without degradation), inhibition of the matrix-degradation may prove to be effective in other types of cancers. Nuclear deformation is also seen to be a rate-limiting factor in migration through narrow constrictions (Cao et al., 2016). Thus, overexpression of proteins such as lamins that maintain nuclear stiffness, could hinder large nuclear deformations and delay the rate at which tumor cells invade (Wirtz et al., 2011; Díaz de la Loza et al., 2017).

Once tumor cells have spread into the circulation, it might still be possible to intervene at the stage of intravascular adhesion and arrest. For instance, perturbation of tumor-endothelial adhesion molecules such as E-selectin, CD44, PODXL, VCAM1 or ICAM1 could decrease the rate of heterotypic interaction under shear flow, resulting in lower tumor cell retention rates in the circulation and limitation of metastatic seeding at the distant site (Rosette et al., 2005; Zen et al., 2008). Similarly, targeting tumor-interacting adhesion proteins on immune cells like platelets and leukocytes could yield comparable anti-metastatic effects. Care, however, must be taken in all cases to minimize the perturbation to the normal homeostatic functions of the non-cancer cells involved.

It is still a matter of debate whether the physical characteristics of cancer cells, such as deformability and stiffness, are conserved through generations, or whether these are developed in response to heterogeneous extracellular mechanical and biochemical cues, spread over time and space. Whether these physical properties are inherited or acquired throughout different stages of metastasis, it might be possible to alter them, either through pharmacological inhibition or through the activation of proteins affecting cell mechanics. Together, it may be possible to exogenously achieve a set of optimal mechanical microenvironmental conditions (i.e., cell stiffness, matrix density and pore size, interstitial fluid forces) such that the likelihood of proceeding through the metastatic cascade is lowered.

Lastly, applicability of targeting mechanics is a relatively new approach compared to genes or molecular biomarkers methods and therefore most of the clinical interventions leading to mechano-therapeutics are still in the trial phase. Jain et al. (2014), Huang et al. (2021), Jiang et al. (2022), and Di et al. (2023) compiled a list of such drugs; among which it is worth mentioning: Cilengitide, a selective αvβ3/αvβ5 integrin inhibitor that has been assessed in phase III clinical trial for treating glioblastoma or GB 2064 (formerly PAT-1251) and a LOXL2 inhibitor that lowers collagen accumulation and ECM stiffness and currently being evaluated in phase II clinical trial for treating Myelofibrosis. Additionally, pamrevlumab is being tested in phase III in patients with locally advanced, unresectable pancreatic cancer. Pamrevlumab is a monoclonal antibody that targets connective tissue growth factor, thereby reducing the fibrotic tissue and making unresectable tumors amenable to surgical excision (Sheridan, 2019).

## Mechanobiology in personalized medicine

It is well known that tumor cells can vary widely according to the oncogenic background. Often, further heterogeneity occurs within a metastatic tumor when different patients are considered. Lab-on-a-chip systems are particularly well poised to address such questions related to patient -specificity with key advantages such as the requirement of low sample and reagent inputs, which are often scarce when derived directly from a patient (Figure 2F). Further, the ability to multiplex and perform high-throughput experiments is particularly amenable in lab-on-a-chip assays, enabling clinical level drug screening to be done on a person-to-person basis. For instance, microfluidic assays that recapitulate the surrounding mechanical environment of tumor cells (matrix stiffness, composition, pore size) can be used to understand the migratory phenotype of individual tumor cells as a typical indicator of potential malignancy, and how different pharmacological perturbations modulate this behavior (Pathak and Kumar, 2012; Polacheck et al., 2013; Polacheck et al., 2014) (Figure 2G). More complex *in vitro* models that mirror not only the surrounding ECM but also other physical cues (such as vasculature and stromal cells and fluid flows (Achilli et al., 2012; Kim et al., 2015; Whelan et al., 2023) can be employed in a multiplexed and high throughput manner to understand how these variables influence tumor cell migration in a patient-specific manner. This is particularly important as the recent FDA modernization act aims to integrate complex *in vitro* models of different diseases into the drug development process. For instance, Prolyl hydroxylases (PHDs) inhibitors have been shown to improve drug distribution in mice tumors and increase the effectiveness of chemotherapy. To demonstrate such effects in human cell models, Hu et al. (2022) employed a perfusable vascularized spheroid-on-a-chip model to simulate tumor microenvironment *in vivo*. They showed that dimethylallyl glycine improves the efficacy of the anticancer drugs paclitaxel and cisplatin in human esophageal carcinoma (Eca-109) spheroids (Figure 2F). Additionally, this could allow further understanding of the effects of external physical features such as matrix composition, stiffness, pore size, tumor cell adhesion molecules, and MMPs, on tumor migratory abilities and potentially tumor type characterization.

In addition to personalized drug screening under relevant biomechanical condition, it may also be possible phenotyping tumor cells and assess for instance their degree of malignancy through mechanical measurements on patient derived single tumour cells. Stiffness values of tumor cells or even aggregates of cells like tumor spheroids can now be measured using various contact-based (e.g., AFM) and non-contact-based methods (e.g., Brillouin imaging (Scarcelli et al., 2015; Roberts et al., 2021)); correlations can be made between these stiffness values and the invasive properties of these cells, through parallel *in vitro* screening experiments, and even using clinical tumor phenotyping data. This could allow extrapolating the metastatic potential from a small number of patient-derived samples and would prove to be a useful predictor when used in conjunction with traditional diagnostic methods.

Lastly, a deep understanding of the physical and structural properties of the surrounding tumor matrix might be useful for optimizing drug delivery to tumor sites. As an example, second harmonic imaging is now widely used to quantify the structural composition of collagens in the tumor microenvironment (Condeelis and Weissleder, 2010), and allow the characterization of pore size and fiber thickness, which may have a large influence on the effectiveness of drug transport. Obtaining this data for patient-specific tumors and subsequent computational modelling of drug transport based on these parameters may aid in the construction of a more optimized drug delivery system in the clinic.

## Discussion

Accumulated evidence has demonstrated the fundamental role of mechanobiology in cancer research as the physical properties of both cells and their microenvironment play a crucial role in the development

and progression of cancer. In this short review we summarized the role of cellular biomechanical properties, e.g., stiffness, adhesion and motility, morphology, deformability, and contractility, as well as microenvironment properties such as ECM stiffness, tissue architecture, blood vessel permeability, and interstitial flow, in different steps of the tumor dissemination. Indeed, mechanobiological insight could benefit researchers and clinicians in various ways; For instance, mechanical quantification at the tissue level has been used as a diagnosis or prognosis tool for various types of cancer. Advancements in the *in vivo* non-invasive techniques such as MRE and ultrasound elastography as well as *ex vivo* techniques such as AFM have improved our diagnosis abilities in the past decade. Furthermore, at the cellular level, mechanobiology can contribute significantly to our comprehension of molecular and genetic alterations in cancer. The interplay between mechanical forces and cellular behaviors can influence how genes are expressed, proteins are synthesized, and signaling pathways are activated. Such insights are of crucial importance in the development of new therapeutic strategies, as many ongoing clinical trials target components of the extracellular matrix (Lampi and Reinhart-King, 2018; Huang et al., 2021) and proteins associated with mechanosignaling pathways (Jiang et al., 2022). Nonetheless, owing to the diversity in oncogenic backgrounds and the inherent variability within metastatic tumors, distinct therapeutic strategies are required for individual patients; In this regard, microfluidics technology holds substantial promise in advancing personalized medicine through its ability to create controlled environment for studying individualized patient samples and responses. Nevertheless, there are intriguing avenues for further research to enhance the translatability of mechanobiological knowledge derived from these platforms into clinical practice. This includes integration of the cancer mechanobiology insight with the data from genomics, transcriptomics, and proteomics approaches; this, in combination with single cell data analysis (obtained from limited number of tumor cells harvested from patient's blood or tissue) could augment our understanding of mechanotransducive pathways involved in cancer. Moreover, by introducing immune cells along with other supporting cell types into the 3D tumor-mimicking microenvironment established within microfluidic chips, we can investigate effects of mechanical signals on immune cell behavior, as well as their implications for immunotherapy responses and the emergence of resistance.

## Author contributions

AA and EM conceived the idea of the manuscript. MC, YJ, NS, BS, and EM performed the literature database and drafted the manuscript. YJ sketched and implemented figures. EM supervised the study. All authors contributed to the article and approved the submitted version.

## Funding

YJ and EM acknowledge financial support by Leverhulme Trust Research Project Grant (RPG-2018-443), the Cancer Research United Kingdom Multidisciplinary Award (C57744/A22057), and Biotechnology and Biological Sciences Research Council Grant (BB/V001418/1) supports.

## Acknowledgments

EM is grateful for Wellcome Trust-MIT Fellowship (WT103883).

## Conflict of interest

Authors BS and BD were employed by 199 Biotechnologies Ltd.

The remaining authors declare that the research was conducted in the absence of any commercial or financial relationships that could be construed as a potential conflict of interest.

## Publisher's note



## References

Aceto, N., Toner, M., Maheswaran, S., and Haber, D. A. (2015). En route to metastasis: circulating tumor cell clusters and epithelial-to-mesenchymal transition. *Trends Cancer* 1, 44–52. doi:10.1016/j.trecan.2015.07.006

Achilli, T.-M., Meyer, J., and Morgan, J. R. (2012). Advances in the formation, use and understanding of multi-cellular spheroids. *Expert Opin. Biol. Ther.* 12, 1347–1360. doi:10.1517/14712598.2012.707181

Agrawal, A., Shahreza, S., Javanmardi, Y., Szita, N., and Moeendarbary, E. (2022). The tumour microenvironment modulates cancer cell intravasation. *Organs-on-a-Chip* 4, 100024. doi:10.1016/j.ooc.2022.100024

Au, S. H., Storey, B. D., Moore, J. C., Tang, Q., Chen, Y.-L., Javaid, S., et al. (2016). Clusters of circulating tumor cells traverse capillary-sized vessels. *Proc. Natl. Acad. Sci.* 113, 4947–4952. doi:10.1073/pnas.1524448113

Barenholz-Cohen, T., Merkher, Y., Haj, J., Shechter, D., Kirchmeier, D., Shaked, Y., et al. (2020). Lung mechanics modifications facilitating metastasis are mediated in part by breast cancer-derived extracellular vesicles. *Int. J. Cancer* 147, 2924–2933. doi:10.1002/ijc.33229

Barrasa-Fano, J., Shapeti, A., Jorge-Peñas, Á., Barzegari, M., Sanz-Herrera, J. A., and Van Oosterwyck, H. (2021). TFMLAB: a MATLAB toolbox for 4D traction force microscopy. *SoftwareX* 15, 100723. doi:10.1016/j.softx.2021.100723

Bera, K., Kiepas, A., Godet, I., Li, Y., Mehta, P., Ifemembi, B., et al. (2022). Extracellular fluid viscosity enhances cell migration and cancer dissemination. *Nature* 611, 365–373. doi:10.1038/s41586-022-05394-6

Bertero, T., Oldham, W. M., Grasset, E. M., Bourget, I., Boulter, E., Pisano, S., et al. (2019). Tumor-stroma mechanics coordinate amino acid availability to sustain tumor growth and malignancy. *Cell Metab.* 29, 124–140. doi:10.1016/j.cmet.2018.09.012

Beyer, S., Blocki, A., Cheung, M. C. Y., Wan, Z. H. Y., Mehrjou, B., and Kamm, R. D. (2021). Lectin staining of microvascular Glycocalyx in microfluidic cancer cell extravasation assays. *Life* 11, 179. doi:10.3390/life11030179

Bocci, F., Gearhart-Serna, L., Boareto, M., Ribeiro, M., Ben-Jacob, E., Devi, G. R., et al. (2019). Toward understanding cancer stem cell heterogeneity in the tumor microenvironment. *Proc. Natl. Acad. Sci.* 116, 148–157. doi:10.1073/pnas.1815345116

Budden, T., Gaudy-Marqueste, C., Porter, A., Kay, E., Gurung, S., Earnshaw, C. H., et al. (2021). Ultraviolet light-induced collagen degradation inhibits melanoma invasion. *Nat. Commun.* 12, 2742. doi:10.1038/s41467-021-22953-z

Burdziak, C., Alonso-Curbelo, D., Walle, T., Reyes, J., Barriga, F. M., Haviv, D., et al. (2023). Epigenetic plasticity cooperates with cell-cell interactions to direct pancreatic tumorigenesis. *Sci. (80-)* 380, eadd5327. doi:10.1126/science.add5327

Calvo, F., Ege, N., Grande-Garcia, A., Hooper, S., Jenkins, R. P., Chaudhry, S. I., et al. (2013). Mechanotransduction and YAP-dependent matrix remodelling is required for the generation and maintenance of cancer-associated fibroblasts. *Nat. Cell Biol.* 15, 637–646. doi:10.1038/ncb2756

Campàs, O., Mammoto, T., Hasso, S., Sperling, R. A., O'Connell, D., Bischof, A. G., et al. (2014). Quantifying cell-generated mechanical forces within living embryonic tissues. *Nat. Methods* 11, 183–189. doi:10.1038/nmeth.2761

Cao, X., Moeendarbary, E., Isermann, P., Davidson, P. M., Wang, X., Chen, M. B., et al. (2016). A chemomechanical model for nuclear morphology and stresses during cell transendothelial migration. *Biophys. J.* 111, 1541–1552. doi:10.1016/J.BPJ.2016.08.011

Chaffer, C. L., and Weinberg, R. (2011). A perspective on cancer cell metastasis. *Science* 331, 1559–1564. doi:10.1126/science.1203543

Chaudhuri, O., Cooper-White, J., Janmey, P. A., Mooney, D. J., and Shenoy, V. B. (2020). Effects of extracellular matrix viscoelasticity on cellular behaviour. *Nature* 584, 535–546. doi:10.1038/s41586-020-2612-2

Chen, M. B., Whisler, J. A., Fröse, J., Yu, C., Shin, Y., and Kamm, R. D. (2017). On-chip human microvasculature assay for visualization and quantification of tumor cell extravasation dynamics. *Nat. Protoc.* 12, 865–880. doi:10.1038/nprot.2017.018

Chen, Y., Pan, C., Wang, X., Xu, D., Ma, Y., Hu, J., et al. (2021). Silencing of METTL3 effectively hinders invasion and metastasis of prostate cancer cells. *Theranostics* 11, 7640–7657. doi:10.7150/thno.61178

Colin-York, H., Javanmardi, Y., Barbieri, L., Li, D., Korobchevskaya, K., Guo, Y., et al. (2019a). Spatiotemporally super-resolved volumetric traction force microscopy. *Nano Lett.* 19, 4427–4434. doi:10.1021/acs.nanolett.9b01196

Colin-York, H., Javanmardi, Y., Skamrahl, M., Kumari, S., Chang, V. T., Khuon, S., et al. (2019b). Cytoskeletal control of antigen-dependent T cell activation. *Cell Rep.* 26, 3369–3379. doi:10.1016/j.celrep.2019.02.074

Condeelis, J., and Weissleder, R. (2010). *In vivo* imaging in cancer. *Cold Spring Harb. Perspect. Biol.* 2, a003848. doi:10.1101/cshperspect.a003848

Coughlin, M. F., Bielenberg, D. R., Lenormand, G., Marinkovic, M., Waghorne, C. G., Zetter, B. R., et al. (2013). Cytoskeletal stiffness, friction, and fluidity of cancer cell lines with different metastatic potential. *Clin. Exp. Metastasis* 30, 237–250. doi:10.1007/s10585-012-9531-z

Cox, T. R., and Erler, J. T. (2011). Remodeling and homeostasis of the extracellular matrix: implications for fibrotic diseases and cancer. *Dis. Model Mech.* 4, 165–178. doi:10.1242/dmm.004077

Craene, B. D, and Berx, G. (2013). Regulatory networks defining EMT during cancer initiation and progression. *Nat. Rev. Cancer* 13, 97–110. doi:10.1038/nrc3447

Cross, S. E., Jin, Y.-S., Rao, J., and Gimzewski, J. K. (2007). Nanomechanical analysis of cells from cancer patients. *Nat. Nanotechnol.* 2, 780–783. doi:10.1038/nnano.2007.388

Denais, C. M., Gilbert, R. M., Isermann, P., McGregor, A. L., te Lindert, M., Weigelin, B., et al. (2016). Nuclear envelope rupture and repair during cancer cell migration. *Sci. (80-)* 352, 353–358. doi:10.1126/science.aad7297

Deptuła, P., Łysik, D., Pogoda, K., Cieśluk, M., Namiot, A., Mystkowska, J., et al. (2020). Tissue rheology as a possible complementary procedure to advance histological diagnosis of Colon cancer. *ACS Biomater. Sci. Eng.* 6, 5620–5631. doi:10.1021/acsbiomaterials.0c00975

Deryugina, E. I., and Quigley, J. P. (2015). Tumor angiogenesis: MMP-mediated induction of intravasation- and metastasis-sustaining neovasculature. *Matrix Biol.* 44–46, 94–112. doi:10.1016/j.matbio.2015.04.004

Di, X., Gao, X., Peng, L., Ai, J., Jin, X., Qi, S., et al. (2023). Cellular mechanotransduction in health and diseases: from molecular mechanism to therapeutic targets. *Signal Transduct. Target Ther.* 8, 282. doi:10.1038/s41392-023-01501-9

Díaz de la Loza, M. C., Díaz-Torres, A., Zurita, F., Rosales-Nieves, A. E., Moeendarbary, E., Franze, K., et al. (2017). Laminin levels regulate tissue migration and anterior-posterior polarity during egg morphogenesis in Drosophila. *Cell Rep.* 20, 211–223. doi:10.1016/j.celrep.2017.06.031

Dolega, M. E., Delarue, M., Ingremeau, F., Prost, J., Delon, A., and Cappello, G. (2017). Cell-like pressure sensors reveal increase of mechanical stress towards the core of multicellular spheroids under compression. *Nat. Commun.* 8, 14056. doi:10.1038/ncomms14056

Dou, C., Zhou, Z., Xu, Q., Liu, Z., Zeng, Y., Wang, Y., et al. (2022). Correction: hypoxia-induced TUFT1 promotes the growth and metastasis of hepatocellular carcinoma by activating the Ca2+/PI3K/AKT pathway. *Oncogene* 41, 4330–4332. doi:10.1038/s41388-022-02421-8

Gal, N., and Weihs, D. (2012). Intracellular mechanics and activity of breast cancer cells correlate with metastatic potential. *Cell Biochem. Biophys.* 63, 199–209. doi:10.1007/s12013-012-9356-z

Galarza, S., Kim, H., Atay, N., Peyton, S. R., and Munson, J. M. (2020). 2D or 3D? How cell motility measurements are conserved across dimensions *in vitro* and translate *in vivo*. *Bioeng. Transl. Med.* 5, e10148. doi:10.1002/btm2.10148

Golatta, M., Pfob, A., Büsch, C., Bruckner, T., Alwafai, Z., Balleyguier, C., et al. (2022). The potential of combined shear wave and strain elastography to reduce unnecessary biopsies in breast cancer diagnostics – an international, multicentre trial. *Eur. J. Cancer* 161, 1–9. doi:10.1016/j.ejca.2021.11.005

Han, Y. L., Ronceray, P., Xu, G., Malandrino, A., Kamm, R. D., Lenz, M., et al. (2018). Cell contraction induces long-ranged stress stiffening in the extracellular matrix. *Proc. Natl. Acad. Sci. U. S. A.* 115, 4075–4080. doi:10.1073/pnas.1722619115

Hassanzadeh-Barforoushi, A., Warkiani, M. E., Gallego-Ortega, D., Liu, G., and Barber, T. (2020). Capillary-assisted microfluidic biosensing platform captures single cell secretion dynamics in nanoliter compartments. *Biosens. Bioelectron.* 155, 112113. doi:10.1016/j.bios.2020.112113

Herman, H., Fazakas, C., Haskó, J., Molnár, K., Mészáros, Á., Nyúl-Tóth, Á., et al. (2019). Paracellular and transcellular migration of metastatic cells through the cerebral endothelium. *J. Cell Mol. Med.* 23, 2619–2631. doi:10.1111/jcmm.14156

Hu, Z., Cao, Y., Galan, E. A., Hao, L., Zhao, H., Tang, J., et al. (2022). Vascularized tumor spheroid-on-a-chip model Verifies synergistic vasoprotective and chemotherapeutic effects. *ACS Biomater. Sci. Eng.* 8, 1215–1225. doi:10.1021/acsbiomaterials.1c01099

Huang, J., Zhang, L., Wan, D., Zhou, L., Zheng, S., Lin, S., et al. (2021). Extracellular matrix and its therapeutic potential for cancer treatment. *Signal Transduct. Target Ther.* 6, 153. doi:10.1038/s41392-021-00544-0

Huh, S. J., Liang, S., Sharma, A., Dong, C., and Robertson, G. P. (2010). Transiently entrapped circulating tumor cells interact with neutrophils to facilitate lung metastasis development. *Cancer Res.* 70, 6071–6082. doi:10.1158/0008-5472.CAN-09-4442

Ishihara, S., and Haga, H. (2022). Matrix stiffness contributes to cancer progression by regulating transcription factors. *Cancers (Basel)* 14, 1049. doi:10.3390/cancers14041049

Itoh, Y., Takehara, Y., Kawase, T., Terashima, K., Ohkawa, Y., Hirose, Y., et al. (2016). Feasibility of magnetic resonance elastography for the pancreas at 3T. *J. Magn. Reson Imaging* 43, 384–390. doi:10.1002/jmri.24995

Jain, R. K., Martin, J. D., and Stylianopoulos, T. (2014). The role of mechanical forces in tumor growth and therapy. *Annu. Rev. Biomed. Eng.* 16, 321–346. doi:10.1146/annurev-bioeng-071813-105259

Jain, R. K., Munn, L. L., and Fukumura, D. (2002). Dissecting tumour pathophysiology using intravital microscopy. *Nat. Rev. Cancer* 2, 266–276. doi:10.1038/nrc778

Javanmardi, Y., Agrawal, A., Malandrino, A., Lasli, S., Chen, M., Shahreza, S., et al. (2023). Endothelium and subendothelial matrix mechanics modulate cancer cell transendothelial migration. *Adv. Sci.* 10, e2206554. doi:10.1002/advs.202206554

Javanmardi, Y., Colin-York, H., Szita, N., Fritzsche, M., and Moeendarbary, E. (2021). Quantifying cell-generated forces: poisson's ratio matters. *Commun. Phys.* 41 (4), 237–310. doi:10.1038/s42005-021-00740-y

Jiang, Y., Zhang, H., Wang, J., Liu, Y., Luo, T., and Hua, H. (2022). Targeting extracellular matrix stiffness and mechanotransducers to improve cancer therapy. *J. Hematol. Oncol.* 15, 34. doi:10.1186/s13045-022-01252-0

Kalluri, R., and Weinberg, R. a. (2009). The basics of epithelial-mesenchymal transition. *J. Clin. Invest.* 119, 1420–1428. doi:10.1172/JCI39104

Kennedy, K. M., Chin, L., McLaughlin, R. A., Latham, B., Saunders, C. M., Sampson, D. D., et al. (2015). Quantitative micro-elastography: imaging of tissue elasticity using compression optical coherence elastography. *Sci. Rep.* 5, 15538. doi:10.1038/srep15538

Kim, J., Chung, M., Kim, S., Jo, D. H., Kim, J. H., and Jeon, N. L. (2015). Engineering of a biomimetic pericyte-covered 3D microvascular network. *PLoS One* 10, e0133880. doi:10.1371/journal.pone.0133880

Kim, J., Han, S., Lei, A., Miyano, M., Bloom, J., Srivastava, V., et al. (2018). Characterizing cellular mechanical phenotypes with mechano-node-pore sensing. *Microsystems Nanoeng.* 4, 17091. doi:10.1038/micronano.2017.91

Klein, E. A., Yin, L., Kothapalli, D., Castagnino, P., Byfield, F. J., Xu, T., et al. (2009). Cell-cycle control by physiological matrix elasticity and *in vivo* tissue stiffening. *Curr. Biol.* 19, 1511–1518. doi:10.1016/j.cub.2009.07.069

Koorman, T., Jansen, K. A., Khalil, A., Haughton, P. D., Visser, D., Rätze, M. A. K., et al. (2022). Spatial collagen stiffening promotes collective breast cancer cell invasion by reinforcing extracellular matrix alignment. *Oncogene* 41, 2458–2469. doi:10.1038/s41388-022-02258-1

Koumoutsakos, P., Pivkin, I., and Milde, F. (2013). The fluid mechanics of cancer and its therapy. *Annu. Rev. Fluid Mech.* 45, 325–355. doi:10.1146/annurev-fluid-120710-101102

Kraning-Rush, C. M., Califano, J. P., and Reinhart-King, C. A. (2012). Cellular traction stresses increase with increasing metastatic potential. *PLoS One* 7, e32572. doi:10.1371/journal.pone.0032572

Kristal-Muscal, R., Dvir, L., and Weihs, D. (2013). Metastatic cancer cells tenaciously indent impenetrable, soft substrates. *New J. Phys.* 15, 035022. doi:10.1088/1367-2630/15/3/035022

Kumar, S., and Weaver, V. M. (2009). Mechanics, malignancy, and metastasis: the force journey of a tumor cell. *Cancer Metastasis Rev.* 28, 113–127. doi:10.1007/s10555-008-9173-4

Labernadie, A., Kato, T., Brugués, A., Serra-Picamal, X., Derzsi, S., Arwert, E., et al. (2017). A mechanically active heterotypic E-cadherin/N-cadherin adhesion enables

fibroblasts to drive cancer cell invasion. *Nat. Cell Biol.* 19, 224–237. doi:10.1038/ncb3478

Labelle, M., Begum, S., and Hynes, R. O. (2011). Direct signaling between platelets and cancer cells induces an epithelial-mesenchymal-like transition and promotes metastasis. *Cancer Cell* 20, 576–590. doi:10.1016/j.ccr.2011.09.009

Laklai, H., Miroshnikova, Y. A., Pickup, M. W., Collisson, E. A., Kim, G. E., Barrett, A. S., et al. (2016). Genotype tunes pancreatic ductal adenocarcinoma tissue tension to induce matricellular fibrosis and tumor progression. *Nat. Med.* 22, 497–505. doi:10.1038/nm.4082

Lammerding, J. (2011). Mechanics of the nucleus. *Compr. Physiol.* 1, 783–807. doi:10.1002/cphy.c100038

Lampi, M. C., and Reinhart-King, C. A. (2018). Targeting extracellular matrix stiffness to attenuate disease: from molecular mechanisms to clinical trials. *Sci. Transl. Med.* 10, eaao0475. doi:10.1126/scitranslmed.aao0475

Laudani, S., La Cognata, V., Iemmolo, R., Bonaventura, G., Villaggio, G., Saccone, S., et al. (2020). Effect of a bone marrow-derived extracellular matrix on cell adhesion and neural induction of dental pulp stem cells. *Front. Cell Dev. Biol.* 8, 100. doi:10.3389/fcell.2020.00100

Lee, W., Kalashnikov, N., Mok, S., Halaoui, R., Kuzmin, E., Putnam, A. J., et al. (2019). Dispersible hydrogel force sensors reveal patterns of solid mechanical stress in multicellular spheroid cultures. *Nat. Commun.* 10, 144. doi:10.1038/s41467-018-07967-4

Leggett, S. E., Patel, M., Valentin, T. M., Gamboa, L., Khoo, A. S., Williams, E. K., et al. (2020). Mechanophenotyping of 3D multicellular clusters using displacement arrays of rendered tractions. *Proc. Natl. Acad. Sci.* 117, 5655–5663. doi:10.1073/pnas.1918296117

Leong, H. S., Robertson, A. E., Stoletov, K., Leith, S. J., Chin, C. A., Chien, A. E., et al. (2014). Invadopodia are required for cancer cell extravasation and are a therapeutic target for metastasis. *Cell Rep.* 8, 1558–1570. doi:10.1016/j.celrep.2014.07.050

Li, D., Colin-York, H., Barbieri, L., Javanmardi, Y., Guo, Y., Korobchevskaya, K., et al. (2021). Astigmatic traction force microscopy (aTFM). *Nat. Commun.* 12, 2168. doi:10.1038/s41467-021-22376-w

Liu, X., Ye, Y., Zhu, L., Xiao, X., Zhou, B., Gu, Y., et al. (2023). Niche stiffness sustains cancer stemness via TAZ and NANOG phase separation. *Nat. Commun.* 14, 238. doi:10.1038/s41467-023-35856-y

Lopez, J. I., Kang, I., You, W.-K., McDonald, D. M., and Weaver, V. M. (2011). *In situ* force mapping of mammary gland transformation. *Integr. Biol.* 3, 910–921. doi:10.1039/c1ib00043h

Lu, P., Weaver, V. M., and Werb, Z. (2012). The extracellular matrix: a dynamic niche in cancer progression. *J. Cell Biol.* 196, 395–406. doi:10.1083/jcb.201102147

Madsen, C. D., Pedersen, J. T., Venning, F. A., Singh, L. B., Moeendarbary, E., Charras, G., et al. (2015). Hypoxia and loss of PHD2 inactivate stromal fibroblasts to decrease tumour stiffness and metastasis. *EMBO Rep.* 16, 1394–1408. doi:10.15252/embr.201540107

Maity, G., Sen, T., and Chatterjee, A. (2011). Laminin induces matrix metalloproteinase-9 expression and activation in human cervical cancer cell line (SiHa). *J. Cancer Res. Clin. Oncol.* 137, 347–357. doi:10.1007/s00432-010-0892-x

Malandrino, A., Kamm, R. D., and Moeendarbary, E. (2018a). *In vitro* modeling of mechanics in cancer metastasis. *ACS Biomater. Sci. Eng.* 4, 294–301. doi:10.1021/acsbiomaterials.7b00041

Malandrino, A., Mak, M., Kamm, R. D., and Moeendarbary, E. (2018b). Complex mechanics of the heterogeneous extracellular matrix in cancer. *Extrem Mech. Lett.* 21, 25–34. doi:10.1016/j.eml.2018.02.003

Mark, C., Grundy, T. J., Strissel, P. L., Böhringer, D., Grummel, N., Gerum, R., et al. (2020). Collective forces of tumor spheroids in three-dimensional biopolymer networks. *Elife* 9, e51912. doi:10.7554/eLife.51912

Marrella, A., Fedi, A., Varani, G., Vaccari, I., Fato, M., Firpo, G., et al. (2021). High blood flow shear stress values are associated with circulating tumor cells cluster disaggregation in a multi-channel microfluidic device. *PLoS One* 16, e0245536. doi:10.1371/journal.pone.0245536

McEvoy, E., Sneh, T., Moeendarbary, E., Javanmardi, Y., Efimova, N., Yang, C., et al. (2022). Feedback between mechanosensitive signaling and active forces governs endothelial junction integrity. *Nat. Commun.* 13, 7089. doi:10.1038/s41467-022-34701-y

Micalet, A., Pape, J., Bakkalci, D., Javanmardi, Y., Hall, C., Cheema, U., et al. (2022). Evaluating the impact of a biomimetic mechanical environment on cancer invasion and matrix remodeling. *Adv. Healthc. Mater* 12, 2201749. doi:10.1002/adhm.202201749

Mierke, C. T. (2019). The matrix environmental and cell mechanical properties regulate cell migration and contribute to the invasive phenotype of cancer cells. *Rep. Prog. Phys.* 82, 064602. doi:10.1088/1361-6633/ab1628

Mierke, C. T. (2013). The role of focal adhesion kinase in the regulation of cellular mechanical properties. *Phys. Biol.* 10, 065005. doi:10.1088/1478-3975/10/6/065005

Mierke, C. T. (2021). Viscoelasticity acts as a marker for tumor extracellular matrix characteristics. *Front. Cell Dev. Biol.* 9, 785138. doi:10.3389/fcell.2021.785138

Minchinton, A. I., and Tannock, I. F. (2006). Drug penetration in solid tumours. *Nat. Rev. Cancer* 6, 583–592. doi:10.1038/nrc1893

Miyazawa, A., Ito, S., Asano, S., Tanaka, I., Sato, M., Kondo, M., et al. (2018). Regulation of PD-L1 expression by matrix stiffness in lung cancer cells. *Biochem. Biophys. Res. Commun.* 495, 2344–2349. doi:10.1016/j.bbrc.2017.12.115

MJMJJ, Paszek, Zahir, N., Johnson, K. R., Lakins, JNJN, Rozenberg, GIGI, Gefen, A., et al. (2005). Tensional homeostasis and the malignant phenotype. *Cancer Cell* 8, 241–254. doi:10.1016/j.ccr.2005.08.010

Moeendarbary, E., and Harris, A. R. (2014). Cell mechanics: principles, practices, and prospects. *Wiley Interdiscip. Rev. Syst. Biol. Med.* 6, 371–388. doi:10.1002/wsbm.1275

Moeendarbary, E., Valon, L., Fritzsche, M., Harris, A. R., Moulding, D. A., Thrasher, A. J., et al. (2013). The cytoplasm of living cells behaves as a poroelastic material. *Nat. Mater* 12, 253–261. doi:10.1038/nmat3517

Nabavizadeh, A., Bayat, M., Kumar, V., Gregory, A., Webb, J., Alizad, A., et al. (2019). Viscoelastic biomarker for differentiation of benign and malignant breast lesion in ultra-low frequency range. *Sci. Rep.* 9, 5737. doi:10.1038/s41598-019-41885-9

Nagrath, S., Sequist, L. V., Maheswaran, S., Bell, D. W., Irimia, D., Ulkus, L., et al. (2007). Isolation of rare circulating tumour cells in cancer patients by microchip technology. *Nature* 450, 1235–1239. doi:10.1038/nature06385

Nguyen, D. X., Bos, P. D., and Massagué, J. (2009). Metastasis: from dissemination to organ-specific colonization. *Nat. Rev. Cancer* 9, 274–284. doi:10.1038/nrc2622

Nia, H. T., Liu, H., Seano, G., Datta, M., Jones, D., Rahbari, N., et al. (2017). Solid stress and elastic energy as measures of tumour mechanopathology. *Nat. Biomed. Eng.* 1, 0004–0011. doi:10.1038/s41551-016-0004

Nia, H. T., Munn, L. L., and Jain, R. K. (2020). Physical traits of cancer. *Sci. (80-)* 370, eaaz0868. doi:10.1126/science.aaz0868

Pathak, A., and Kumar, S. (2012). Independent regulation of tumor cell migration by matrix stiffness and confinement. *Proc. Natl. Acad. Sci. U. S. A.* 109, 10334–10339. doi:10.1073/pnas.1118073109

Peng, H.-H., Liang, S., Henderson, A. J., and Dong, C. (2007). Regulation of interleukin-8 expression in melanoma-stimulated neutrophil inflammatory response. *Exp. Cell Res.* 313, 551–559. doi:10.1016/j.yexcr.2006.10.030

Pickup, M. W., Mouw, J. K., and Weaver, V. M. (2014). The extracellular matrix modulates the hallmarks of cancer. *EMBO Rep.* 15, 1243–1253. doi:10.15252/embr.201439246

Plodinec, M., Loparic, M., Monnier, C. A., Obermann, E. C., Zanetti-Dallenbach, R., Oertle, P., et al. (2012). The nanomechanical signature of breast cancer. *Nat. Nanotechnol.* 7, 757–765. doi:10.1038/nnano.2012.167

Polacheck, W. J., German, A. E., Mammoto, A., Ingber, D. E., and Kamm, R. D. (2014). Mechanotransduction of fluid stresses governs 3D cell migration. *Proc. Natl. Acad. Sci. U. S. A.* 111, 2447–2452. doi:10.1073/pnas.1316848111

Polacheck, W. J., Li, R., Uzel, S. G. M., and Kamm, R. D. (2013). Microfluidic platforms for mechanobiology. *Lab. Chip* 13, 2252–2267. doi:10.1039/c3lc41393d

Polyak, K., and Weinberg, R. A. (2009). Transitions between epithelial and mesenchymal states: acquisition of malignant and stem cell traits. *Nat. Rev. Cancer* 9, 265–273. doi:10.1038/nrc2620

Popova, N. V., and Jücker, M. (2022). The functional role of extracellular matrix proteins in cancer. *Cancers (Basel)* 14, 238. doi:10.3390/cancers14010238

Ramião, N. G., Martins, P. S., Rynkevic, R., Fernandes, A. A., Barroso, M., and Santos, D. C. (2016). Biomechanical properties of breast tissue, a state-of-the-art review. *Biomech. Model Mechanobiol.* 15, 1307–1323. doi:10.1007/s10237-016-0763-8

Reiter, R., Majumdar, S., Kearney, S., Kajdacsy-Balla, A., Macias, V., Crivellaro, S., et al. (2022). Investigating the heterogeneity of viscoelastic properties in prostate cancer using MR elastography at 9.4T in fresh prostatectomy specimens. *Magn. Reson Imaging* 87, 113–118. doi:10.1016/j.mri.2022.01.005

Ren, K., Feng, J., Bi, H., Sun, Q., Li, X., and Han, D. (2023). AFM-based Poroelastic@Membrane analysis of cells and its opportunities for translational medicine. *Small* 2023, e2303610. doi:10.1002/smll.202303610

Reuten, R., Zendehroud, S., Nicolau, M., Fleischhauer, L., Laitala, A., Kiderlen, S., et al. (2021). Basement membrane stiffness determines metastases formation. *Nat. Mater* 20, 892–903. doi:10.1038/s41563-020-00894-0

Reymond, N., d'Água, B. B., and Ridley, A. J. (2013). Crossing the endothelial barrier during metastasis. *Nat. Rev. Cancer* 13, 858–870. doi:10.1038/nrc3628

Rianna, C., Radmacher, M., and Kumar, S. (2020). Direct evidence that tumor cells soften when navigating confined spaces. *Mol. Biol. Cell* 31, 1726–1734. doi:10.1091/mbc.E19-10-0588

Rieger, H., and Welter, M. (2015). Integrative models of vascular remodeling during tumor growth. *Wiley Interdiscip. Rev. Syst. Biol. Med.* 7, 113–129. doi:10.1002/wsbm.1295

Roberts, A. B., Zhang, J., Raj Singh, V., Nikolić, M., Moeendarbary, E., Kamm, R. D., et al. (2021). Tumor cell nuclei soften during transendothelial migration. *J. Biomech.* 121, 110400. doi:10.1016/j.jbiomech.2021.110400

Rosette, C., Roth, R. B., Oeth, P., Braun, A., Kammerer, S., Ekblom, J., et al. (2005). Role of ICAM1 in invasion of human breast cancer cells. *Carcinogenesis* 26, 943–950. doi:10.1093/carcin/bgi070

Saha, K., Keung, A. J., Irwin, E. F., Li, Y., Little, L., Schaffer, D. V., et al. (2008). Substrate modulus directs neural stem cell behavior. *Biophys. J.* 95, 4426–4438. doi:10.1529/biophysj.108.132217

Samuel, T., Rapic, S., O'Brien, C., Edson, M., Zhong, Y., and DaCosta, R. S. (2023). Quantitative intravital imaging for real-time monitoring of pancreatic tumor cell hypoxia and stroma in an orthotopic mouse model. *Sci. Adv.* 9, eade8672. doi:10.1126/sciadv.ade8672

Sauer, F., Grosser, S., Shahryari, M., Hayn, A., Guo, J., Braun, J., et al. (2023). Changes in tissue fluidity Predict tumor aggressiveness *in vivo*. *Adv. Sci.* 10, e2303523. doi:10.1002/advs.202303523

Scarcelli, G., Polacheck, W. J., Nia, H. T., Patel, K., Grodzinsky, A. J., Kamm, R. D., et al. (2015). Noncontact three-dimensional mapping of intracellular hydromechanical properties by Brillouin microscopy. *Nat. Methods* 12, 1132–1134. doi:10.1038/nmeth.3616

Schumacher, D., Strilic, B., Sivaraj, K. K., Wettschureck, N., and Offermanns, S. (2013). Platelet-derived nucleotides promote tumor-cell transendothelial migration and metastasis via P2Y2 receptor. *Cancer Cell* 24, 130–137. doi:10.1016/j.ccr.2013.05.008

Sheridan, C. (2019). Pancreatic cancer provides testbed for first mechanotherapeutics. *Nat. Biotechnol.* 37, 829–831. doi:10.1038/d41587-019-00019-2

Shibue, T., and Weinberg, R. A. (2009). Integrin beta1-focal adhesion kinase signaling directs the proliferation of metastatic cancer cells disseminated in the lungs. *Proc. Natl. Acad. Sci.* 106, 10290–10295. doi:10.1073/pnas.0904227106

Sikic, L., Schulman, E., Kosklin, A., Saraswathibhatla, A., Chaudhuri, O., and Pokki, J. (2022). Nanoscale tracking combined with cell-scale Microrheology reveals stepwise increases in force generated by cancer cell protrusions. *Nano Lett.* 22, 7742–7750. doi:10.1021/acs.nanolett.2c01327

Soubéran, A., Brustlein, S., Gouarné, C., Chasson, L., Tchoghandjian, A., Malissen, M., et al. (2019). Effects of VEGF blockade on the dynamics of the inflammatory landscape in glioblastoma-bearing mice. *J. Neuroinflammation* 16, 191. doi:10.1186/s12974-019-1563-8

Sounni, N. E., Paye, A., Host, L., and Noël, A. (2011). MT-MMPS as regulators of vessel stability associated with angiogenesis. *Front. Pharmacol.* 2, 111. doi:10.3389/fphar.2011.00111

Spill, F., Reynolds, D. S., Kamm, R. D., and Zaman, M. H. (2016). Impact of the physical microenvironment on tumor progression and metastasis. *Curr. Opin. Biotechnol.* 40, 41–48. doi:10.1016/j.copbio.2016.02.007

Straehla, J. P., Hajal, C., Safford, H. C., Offeddu, G. S., Boehnke, N., Dacoba, T. G., et al. (2022). A predictive microfluidic model of human glioblastoma to assess trafficking of blood–brain barrier-penetrant nanoparticles. *Proc. Natl. Acad. Sci.* 119, e2118697119. doi:10.1073/pnas.2118697119

Stylianopoulos, T., Martin, J. D., Chauhan, V. P., Jain, S. R., Diop-Frimpong, B., Bardeesy, N., et al. (2012). Causes, consequences, and remedies for growth-induced solid stress in murine and human tumors. *Proc. Natl. Acad. Sci.* 109, 15101–15108. doi:10.1073/pnas.1213353109

Stylianou, A., and Stylianopoulos, T. (2016). Atomic force microscopy probing of cancer cells and tumor microenvironment components. *Bionanoscience* 6, 33–46. doi:10.1007/s12668-015-0187-4

Suresh, S. (2007). Biomechanics and biophysics of cancer cells. *Acta Mater* 55, 3989–4014. doi:10.1016/j.actamat.2007.04.022

Thiery, J. P., and Sleeman, J. P. (2006). Complex networks orchestrate epithelial-mesenchymal transitions. *Nat. Rev. Mol. Cell Biol.* 7, 131–142. doi:10.1038/nrm1835

Torrino, S., Grasset, E. M., Audebert, S., Belhadj, I., Lacoux, C., Haynes, M., et al. (2021). Mechano-induced cell metabolism promotes microtubule glutamylation to force metastasis. *Cell Metab.* 33, 1342–1357.e10. doi:10.1016/j.cmet.2021.05.009

Van Zijl, F., Krupitza, G., and Mikulits, W. (2011). Initial steps of metastasis: cell invasion and endothelial transmigration. *Mutat. Res. - Rev. Mutat. Res.* 728, 23–34. doi:10.1016/j.mrrev.2011.05.002

Venkatesh, S. K., Yin, M., Glockner, J. F., Takahashi, N., Araoz, P. A., Talwalkar, J. A., et al. (2008). MR elastography of liver tumors: preliminary results. *Am. J. Roentgenol.* 190, 1534–1540. doi:10.2214/AJR.07.3123

Voura, E. B., English, J. L., Yu, H.-Y. E., Ho, A. T., Subarsky, P., Hill, R. P., et al. (2013). Proteolysis during tumor cell extravasation *in vitro*: metalloproteinase involvement across tumor cell types. *PLoS One* 8, e78413. doi:10.1371/journal.pone.0078413

Wang, H. B., Dembo, M., and Wang, Y. L. (2000). Substrate flexibility regulates growth and apoptosis of normal but not transformed cells. *Am. J. Physiol. Cell Physiol.* 279, C1345–C1350. doi:10.1152/ajpcell.2000.279.5.C1345

Wang, N., Butler, J., and Ingber, D. (1993). Mechanotransduction across the cell surface and through the cytoskeleton. *Sci. (80-)* 260, 1124–1127. doi:10.1126/science.7684161

Wang, W. Y., Davidson, C. D., Lin, D., and Baker, B. M. (2019). Actomyosin contractility-dependent matrix stretch and recoil induces rapid cell migration. *Nat. Commun.* 10, 1186. doi:10.1038/s41467-019-09121-0

Warli, S. M., Putrantyo, II, and Laksmi, L. I. (2023). Correlation between tumor-associated collagen signature and fibroblast activation protein expression with prognosis of clear cell renal cell carcinoma patient. *World J. Oncol.* 14, 145–149. doi:10.14740/wjon1564

Watson, S. A., Javanmardi, Y., Zanieri, L., Shahreza, S., Ragazzini, R., Bonfanti, P., et al. (2022). Integrated role of human thymic stromal cells in hematopoietic stem cell extravasation. *Bioeng. Transl. Med.* 8, e10454. doi:10.1002/btm2.10454

Wei, S. C., Fattet, L., Tsai, J. H., Guo, Y., Pai, V. H., Majeski, H. E., et al. (2015). Matrix stiffness drives epithelial – mesenchymal transition and tumour metastasis through a TWIST1 – G3BP2 mechanotransduction pathway. *Nat. Cell Biol.* 17, 678–688. doi:10.1038/ncb3157

Weis, S., and Cheresh, D. (2011). Tumor angiogenesis: molecular pathways and therapeutic targets. *Nat. Med.* 17, 1359–1370. doi:10.1038/nm.2537

Wells, P. N. T., and Liang, H.-D. (2011). Medical ultrasound: imaging of soft tissue strain and elasticity. *J. R. Soc. Interface* 8, 1521–1549. doi:10.1098/rsif.2011.0054

Whelan, I. T., Burdis, R., Shahreza, S., Moeendarbary, E., Hoey, D. A., and Kelly, D. J. (2023). A microphysiological model of bone development and regeneration. *Biofabrication* 15, 034103. doi:10.1088/1758-5090/acd6be

Whisler, J., Shahreza, S., Schlegelmilch, K., Ege, N., Javanmardi, Y., Malandrino, A., et al. (2023). Emergent mechanical control of vascular morphogenesis. *Sci. Adv.* 9, eadg9781. doi:10.1126/sciadv.adg9781

Wirtz, D., Konstantopoulos, K., and Searson, P. C. (2011). The physics of cancer: the role of physical interactions and mechanical forces in metastasis. *Nat. Rev. Cancer* 11, 512–522. doi:10.1038/nrc3080

Wolf, K., and Friedl, P. (2009). Mapping proteolytic cancer cell-extracellular matrix interfaces. *Clin. Exp. Metastasis* 26, 289–298. doi:10.1007/s10585-008-9190-2

Wolf, K., Mazo, I., Leung, H., Engelke, K., von Andrian, U. H., Deryugina, E. I., et al. (2003). Compensation mechanism in tumor cell migration: mesenchymal-amoeboid transition after blocking of pericellular proteolysis. *J. Cell Biol.* 160, 267–277. doi:10.1083/jcb.200209006

Xu, W., Mezencev, R., Kim, B., Wang, L., Mcdonald, J., and Sulchek, T. (2012). Cell stiffness is a biomarker of the metastatic potential of ovarian cancer cells. *PLoS One* 7, e46609. doi:10.1371/journal.pone.0046609

Yang, H., Zhang, H., Yang, Y., Wang, X., Deng, T., Liu, R., et al. (2020). Hypoxia induced exosomal circRNA promotes metastasis of Colorectal Cancer via targeting GEF-H1/RhoA axis. *Theranostics* 10, 8211–8226. doi:10.7150/thno.44419

Zen, K., Liu, D.-Q., Guo, Y.-L., Wang, C., Shan, J., Fang, M., et al. (2008). CD44v4 is a major E-selectin ligand that mediates breast cancer cell transendothelial migration. *PLoS One* 3, e1826. doi:10.1371/journal.pone.0001826

Zervantonakis, I. K., Hughes-Alford, S. K., Charest, J. L., Condeelis, J. S., Gertler, F. B., and Kamm, R. D. (2012). Three-dimensional microfluidic model for tumor cell intravasation and endothelial barrier function. *Proc. Natl. Acad. Sci.* 109, 13515–13520. doi:10.1073/pnas.1210182109

Zhang, H., Lin, F., Huang, J., and Xiong, C. (2020). Anisotropic stiffness gradient-regulated mechanical guidance drives directional migration of cancer cells. *Acta Biomater.* 106, 181–192. doi:10.1016/j.actbio.2020.02.004

frontiers | Frontiers in Cell and Developmental Biology

TYPE Original Research
PUBLISHED 30 November 2023
DOI 10.3389/fcell.2023.1202193



OPEN ACCESS

EDITED BY
Yi Yao,
Renmin Hospital of Wuhan University, China

REVIEWED BY
Ashok Palaniappan,
SASTRA University, India
Qi Wang,
Jiangsu University, China

*CORRESPONDENCE
Wuguo Deng,
dengwg@sysucc.org.cn
Liren Li,
lilr@sysucc.org.cn

†These authors have contributed equally to this work

RECEIVED 07 April 2023
ACCEPTED 21 November 2023
PUBLISHED 30 November 2023

CITATION
Zhang L, Deng Y, Yang J, Deng W and Li L (2023), Neurotransmitter receptor-related gene signature as potential prognostic and therapeutic biomarkers in colorectal cancer.
*Front. Cell Dev. Biol.* 11:1202193.
doi: 10.3389/fcell.2023.1202193



# Neurotransmitter receptor-related gene signature as potential prognostic and therapeutic biomarkers in colorectal cancer

Linjie Zhang[1,2†], Yizhang Deng[1,2†], Jingbang Yang[1,2], Wuguo Deng[2*] and Liren Li[1,2*]

[1]Department of Colorectal Surgery, Sun Yat-sen University Cancer Center, Guangzhou, China, [2]State Key Laboratory of Oncology in South China, Collaborative Innovation Center for Cancer Medicine, Sun Yat-sen University Cancer Center, Guangzhou, Guangdong, China

**Background:** Colorectal cancer is one of the most common malignant tumors worldwide. A various of neurotransmitter receptors have been found to be expressed in tumor cells, and the activation of these receptors may promote tumor growth and metastasis. This study aimed to construct a novel neurotransmitter receptor-related genes signature to predict the survival, immune microenvironment, and treatment response of colorectal cancer patients.

**Methods:** RNA-seq and clinical data of colorectal cancer from The Cancer Genome Atlas database and Gene Expression Omnibus were downloaded. Neurotransmitter receptor-related gene were collected from publicly available data sources. The Weighted Gene Coexpression Network Analysis (WGCNA), Least Absolute Shrinkage and Selection Operator (LASSO) logistic regression, Support Vector Machine-Recursive Feature Elimination (SVM-RFE), and Random Forest (RF) algorithms were employed to construct the Neurotransmitter receptor-related gene prognostic signature. Further analyses, functional enrichment, CIBERSORTx, The Tumor Immune Single Cell Center (TISCH), survival analysis, and CellMiner, were performed to analyze immune status and treatment responses. Quantitative real-time polymerase chain reaction (qRT-PCR) assays were carried out to confirm the expression levels of prognostic genes.

**Results:** By combining machine learning algorithm and WGCNA, we identified CHRNA3, GABRD, GRIK3, and GRIK5 as Neurotransmitter receptor-related prognostic genes signature. Functional enrichment analyses showed that these genes were enriched with cellular metabolic-related pathways, such as organic acid, inorganic acid, and lipid metabolism. CIBERSORTx and Single cell analysis showed that the high expression of genes were positively correlated with immunosuppressive cells infiltration, and the genes were mainly expressed in cancer-associated fibroblasts and endothelial cells. A nomogram was further built to predict overall survival (OS). The expression of CHRNA3, GABRD, GRIK3, and GRIK5 in cancer cells significantly impacted their response to chemotherapy.

**Conclusion:** A neurotransmitter receptor-related prognostic gene signature was developed and validated in the current study, giving novel sights of neurotransmitter in predicting the prognostic and improving the treatment of CRC.

KEYWORDS

colorectal cancer, neurotransmitter receptor, TCGA, prognosis, biomarker, immune infiltration

# Introduction

Colorectal cancer (CRC), encompassing both colon and rectal malignancies, is prevalent cancer affecting the digestive system, ranking as a leading cause of cancer-associated mortality and morbidity globally (Siegel et al., 2020). Despite a stabilized or decreased incidence in recent decades, attributed to enhanced screening practices, such as colonoscopic polypectomy, and alterations in risk factors, including a reduction in smoking and increased aspirin consumption, the 5-year survival rate remains unsatisfactory (Edwards et al., 2014; Favoriti et al., 2016; Brenner and Chen, 2018; Keum and Giovannucci, 2019). The widely utilized tumor-node-metastasis (TNM) system plays a crucial role in clinical decision-making for risk assessment and treatment planning. However, owing to the high molecular heterogeneity of CRC, patients with seemingly identical clinicopathological features may exhibit considerable variation in the risk of recurrence and death (Lin et al., 2021). Thus, the identification of effective methods for early diagnosis has become a focal point of research endeavors.

Emerging evidence has highlighted the significance of the nervous system in the pathogenesis of malignancies, with nerves being identified as a critical component of the tumor microenvironment (Zahalka and Frenette, 2020). And as important neural signaling messengers, studies have suggested that neurotransmitters and their receptors play a crucial role in tumor proliferation, angiogenesis, and metastasis, contributing to cancer development. For example, activation of the β2-adrenoceptor has been shown to promote tumor growth and angiogenesis through increased expression of vascular endothelial growth factor, metalloproteases 2, and metalloproteases 9, which further enhance angiogenic and metastatic processes in ovarian, lung, and breast cancers (Thaker et al., 2006). Furthermore, neurotransmitter receptors are widely expressed on the surface of immune cells and are regulated by their corresponding neurotransmitters, thus affecting tumor immune responses (Jiang et al., 2020b; Cervantes-Villagrana et al., 2020).

The role of neurotransmitter receptors in CRC is also complex, as noted in the literature. Li et al. (Li et al., 2021) demonstrated that the overproduction of 5-hydroxytryptamine overproduction promotes colitis-associated CRC progression by enhancing NLRP3 inflammasome activation. In addition, another study found that atropine and muscarinic receptor 3 blockers reduced tumor weight, volume, and enhanced antitumor immune responses by increasing infiltration of $CD4^+$ and $CD8^+$ T cells and significantly reducing PD-L1 expression in a CRC mouse model (Kuol et al., 2022). Gamma-Aminobutyric Acid Type B Receptor (GABABR) also plays a pivotal role in CRC progression. GABABR1, a central component of GABABR, shows significantly lower expression in tumor tissues than in non-tumor normal tissues. It impairs the migration and invasion of CRC cells by inhibiting EMT and the Hippo/YAP1 pathway (Wang et al., 2021). However, studies focusing on subtype characterization and risk signatures based on neurotransmitter receptor-related genes in CRC remain limited.

Herein, we conducted Weighted Gene Co-Expression Network Analysis (WGCNA) and machine learning to establish a reliable signature rooted in neurotransmitter receptor-related genes (NRGs). And its prognostic utility was systematically evaluated in CRC patients. Additionally, we revealed the importance of these gene signatures in the immune microenvironment of CRC. The associations of antineoplastic drugs with MRS were also explored. Overall, this study provides a research basis for exploring the potential pathogenesis of CRC and offers new ideas for treating this disease.

# Material and methods

## Data collection

The workflow for this current study is presented in Figure 1. RNA sequencing and clinical data of 647 CRC cases were obtained from The Cancer Genome Atlas (TCGA) data portal, along with 51 normal tissue samples (https://portal.gdc.cancer. gov/). The microarray dataset GSE166555 and GSE74602 was downloaded from the Gene Expression Omnibus database (GEO, http://www.ncbi.nlm.nih. gov/geo/). Furthermore, the 114-NRGs list was obtained from the National Center for Biotechnology Information, United States National Library of Medicine (https://www.ncbi. nlm. nih.gov/gene/).

## Differentially expressed genes (DEGs) identification and survival Analysis

The TCGA sample was performed with DEGs analysis using the limma package (Ritchie et al., 2015). Survival analysis was conducted with the survivor R package, incorporating age to eliminate the impact of age on survival time. The results were visualized for COAD samples using the survminer R package. *p*-values were calculated using the Log-rank test.

## Weighted gene co-expression network analysis

The Weighted Gene Co-expression Network Analysis (WGCNA) method (Langfelder and Horvath, 2008; Li et al.,

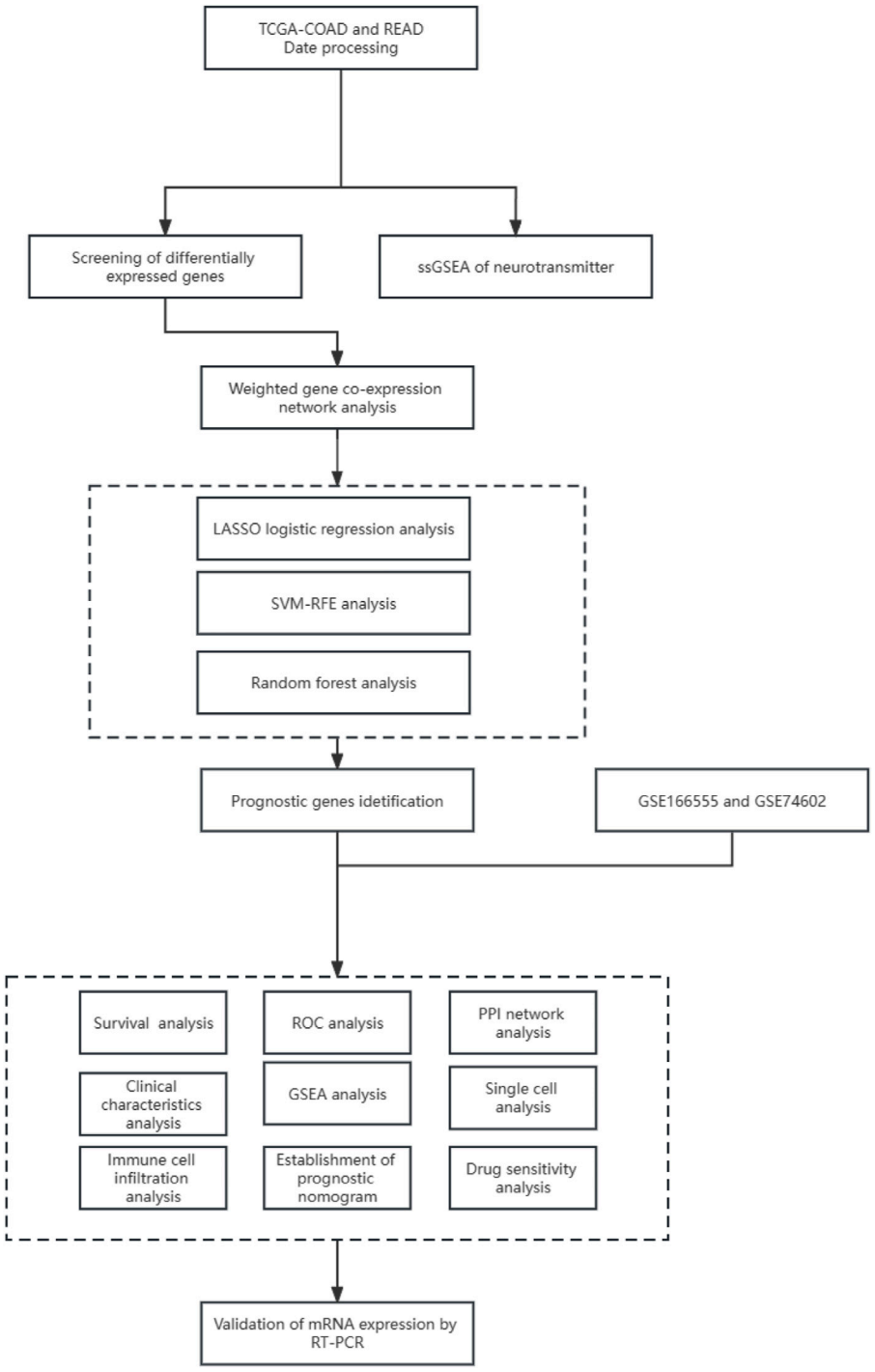


FIGURE 1
Schematic diagram of the workflow of the present study.

2023)was utilized to identify potential modules related to different subclusters of the DEGs expression matrix of TCGA. Abnormal samples were filtered out, and the Pearson correlation coefficient was calculated to construct the correlation adjacency matrix. Highly associated modules were selected for subsequent analysis. The intersection between the highly associated module and neurotransmitter receptor-related genes was estimated. Seven genes were present in both groups.

## Gene signature screening

Three machine learning algorithms were employed independently to screen diagnostic genes from the intersection, including Least Absolute Shrinkage and Selection Operator (LASSO) logistic regression (Zhao et al., 2020), Support Vector Machine-Recursive Feature Elimination (SVM-RFE) (Lin et al., 2012), and Random Forest (RF) (Guo et al., 2020). Genes

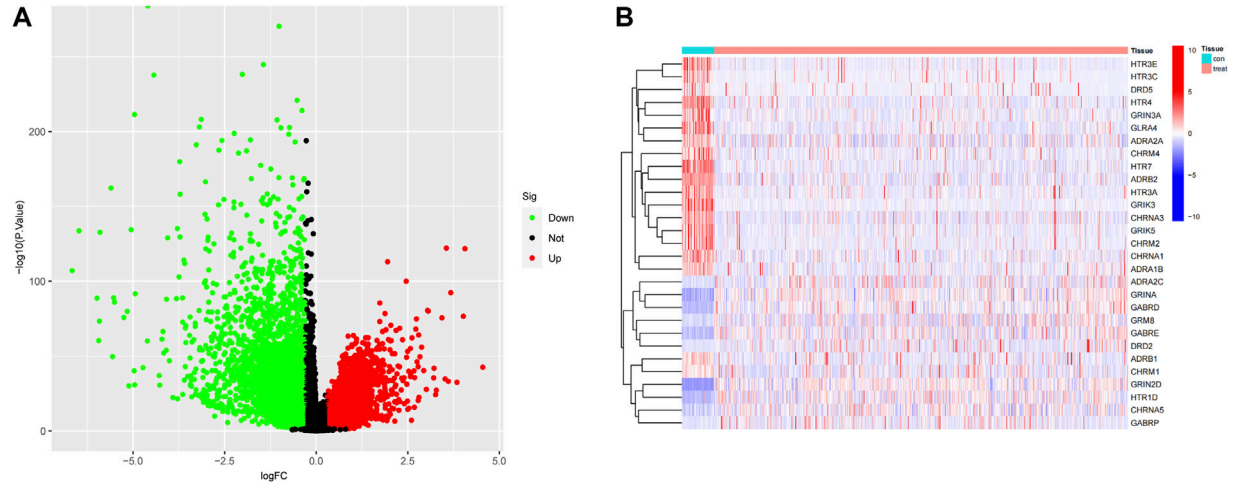


FIGURE 2
Identification of DEGs. **(A)** Differential Gene Expression Volcano Plot, where red indicates upregulation and green represents downregulation. **(B)** Neurotransmitter-related gene heatmap.

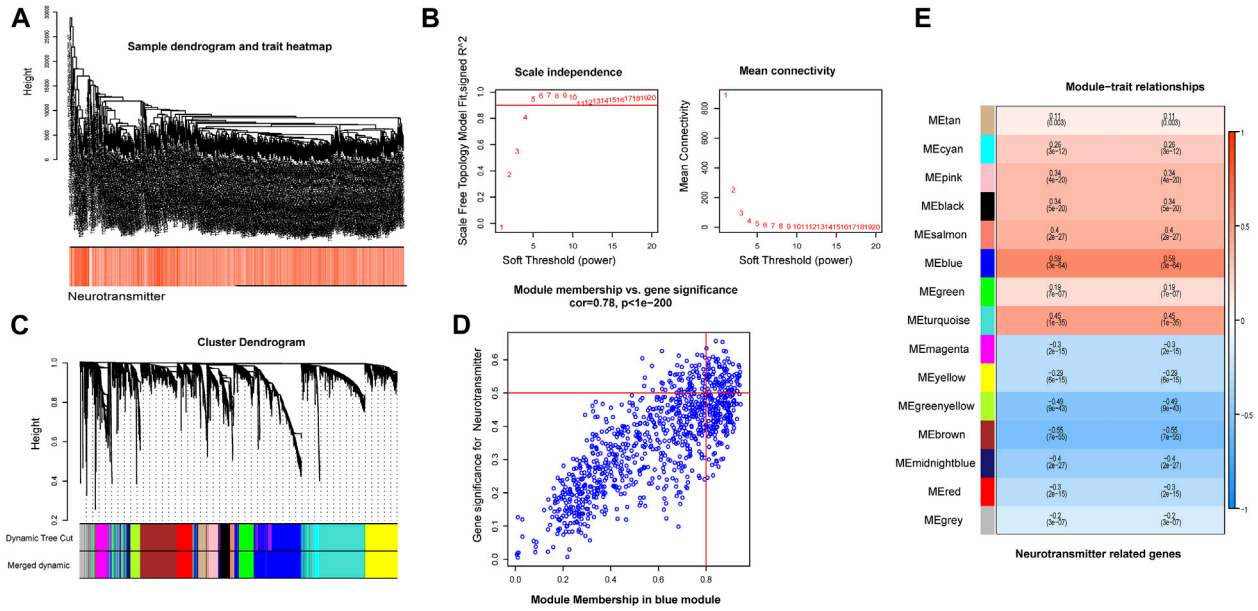


FIGURE 3
The co-expression modules analysis. **(A)** The samples were hierarchically clustered, and a clustering dendrogram was used to detect outliers. **(B)** Analysis of the scale-free fitting index (left) and average connectivity (right) used for selecting various soft-thresholding powers (β). **(C)** Clustering dendrogram of neurotransmitter-related genes; each color below represents a co-expressed gene module. **(D)** Scatter plot of key modules. Each point in the scatter plot represents a gene. **(E)** Heatmap describing the correlation between module and neurotransmitter score.

that overlapped among these algorithms were considered diagnostic biomarkers, and their predictive utility was estimated using ROC curve analysis and the calculation of AUC values with the pROC package. The reliability and differential expression of the identified biomarkers were further confirmed in external testing cohorts. To investigate the expression of these genes in different stages of CRC patients, the clinical correlation analysis was utilized between the expression levels of these genes and CRC clinical characteristics. And the diagnostic genes were also analyzed with the PPI network using the STRING database (Chin et al., 2014).

## Functional enrichment analyses

Functional enrichment was performed using the Kyoto Encyclopedia of Genes and Genomes (KEGG) and Gene Ontology

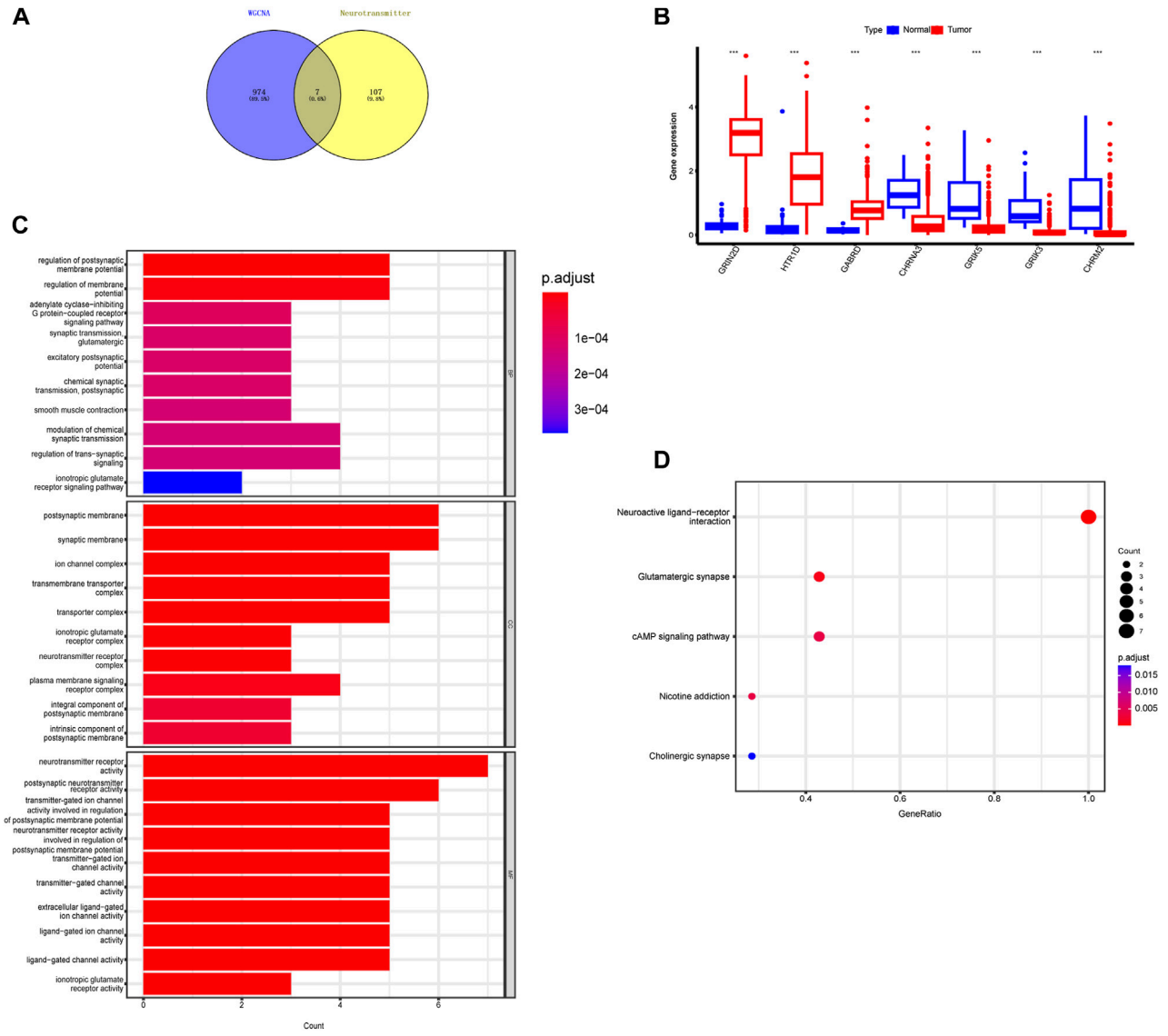


FIGURE 4
Identification of intersecting genes and functional enrichment analysis as well as expression of intersecting genes in CRC patients. **(A)** There are 7 intersecting genes between neurotransmitter-related genes and the blue gene module. **(B)** Expression of the 7 intersecting genes in colorectal cancer. **(C,D)** "GO enrichment analysis and KEGG enrichment analysis of the intersecting genes.

(GO) analyses with the ClusterProfiler and ggplot2 packages to interpret the biological effects of the intersection. Moreover, the prognosis genes was used to perform gene set enrichment analysis (GSEA) between subtypes through Java GSEA software and the results were visualized by the "enrich plot" R package.

## Analysis of immune cell infiltration

CIBERSORT was employed to calculate the immune cell content of each sample (Wang et al., 2023). We then used the Cor. test function to calculate the correlation coefficient between gene expression and immune cells. The correlation between gene expression and immune cells tested using Spearman's correlation. Visualization of the results was performed using the ggpubr R package.

## Single cell analysis

The Tumor Immune Single Cell Center (TISCH) (http://tisch.comp-genomics. org/) was used to study the expression of the CHRNA3, GABRD, GRIK3, and GRIK5 gene in the tumor microenvironment as a single cell subset. TISCH is a scRNA-seq database that provides detailed annotations of cell types within the TME, allowing for exploring the TME in different cancer types (Sun et al., 2021).

## Construction of the prognostic nomogram

A nomogram was constructed using independent prognostic factors. Calibration curves were used to evaluate the performance of

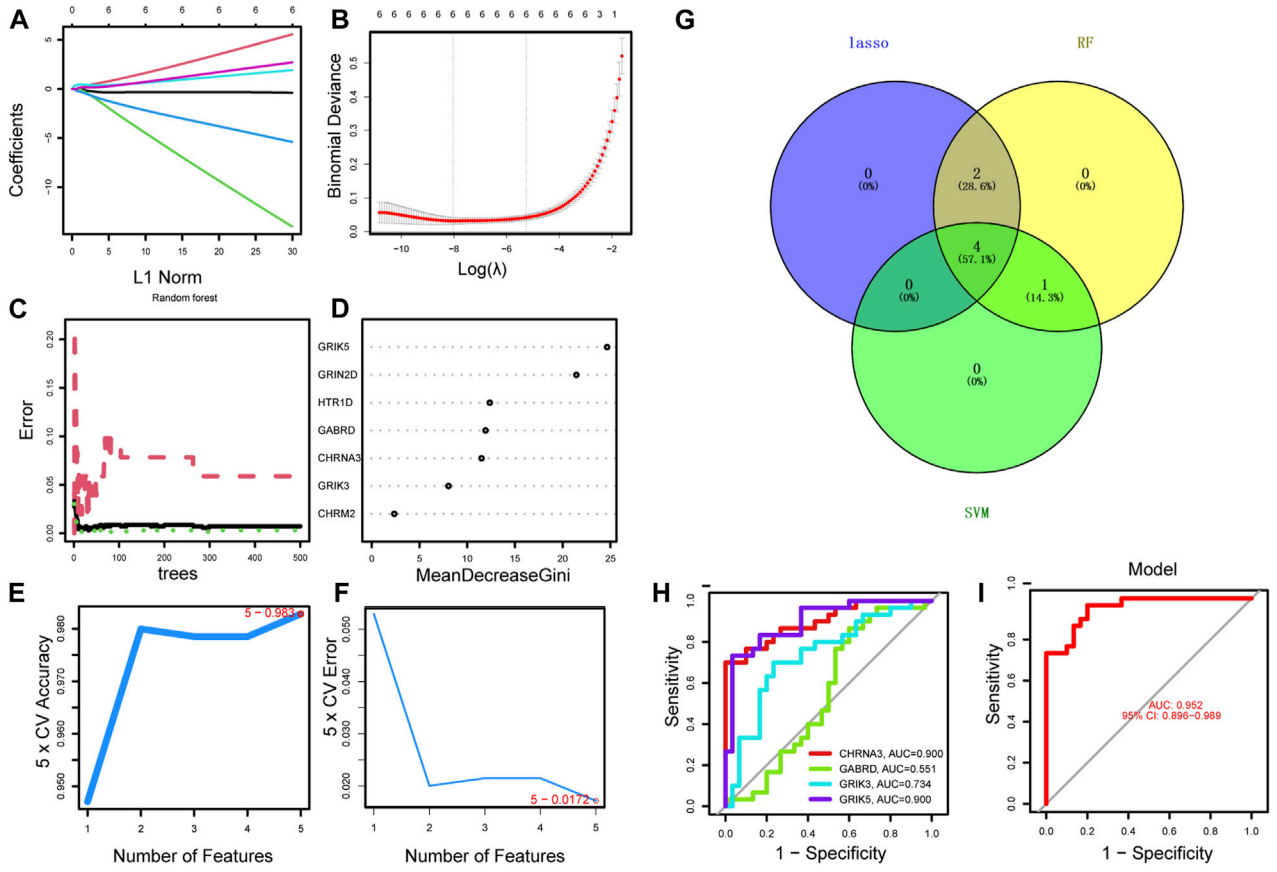


FIGURE 5
Identification of the diagnostic biomarkers from the intersecting genes. **(A)** Ten-fold cross-validation for tuning parameter selection in the LASSO model. Each curve corresponds to a gene. **(B)** LASSO coefficient analysis. The vertical solid line represents the standard error of the partial likelihood deviance. The vertical dotted line is drawn at the optimal λ. **(C)** Random forest for the relationship between the number of trees and the error rate. The minimum error was selected as the mtry node value, and the image value approaching stability was selected as the ntree value. **(D)** Ranking genes based on their relative importance. **(E–F)** SVM-RFE algorithm used for feature selection to narrow down the feature set and identify the most predictive feature genes. **(G)** The Venn diagram shows the intersection genes among LASSO, random forest, and SVM-RFE algorithms. **(H–I)** ROC curve to estimate the diagnostic performance of hub genes.

the nomogram. And decision curve analysis (DCA) was used to measure the net benefit of the nomogram.

## Drug sensitivity analysis

To investigate the relationship between prognosis genes expression and drug sensitivity, the study downloaded gene expression and drug sensitivity data from the CellMiner dataset. Drugs without clinical trials or FDA approval were removed. The correlation coefficient between the expression of prognosis genes and drug sensitivity was calculated using the cor. test function in R language, with correlation tests conducted. A *p*-value less than 0.05 was considered significant for the correlation between the target gene and drug sensitivity. A positive correlation between the expression of prognosis genes and drug sensitivity was indicated by a correlation coefficient greater than 0.

## RNA isolation and RT-qPCR assay

A total of 3 colorectal cancer specimens were obtained from the hospital specimen bank. And the Institutional Review Board of Sun Yat-Sen University Cancer Center approved this study (G2022-075-01). Total RNA was isolated using the RaPure Total RNA Micro Kit (R4012; Magen, Guangzhou, GD, China) followed by cDNA synthesis using the HiScript II Q RT SuperMix for qPCR kit (R223-01; Vazyme, Piscataway, NJ, United States). The qPCR assay was conducted using ChamQ SYBR qPCR Green Master Mix (Q311-02; Vazyme). The primers used were listed in Supplementary Table S2. Protein expression levels of GABRD were acquired from the HPA database through immunohistochemistry (IHC) staining and the utilization of downloaded IHC image data from the HPA database (Sjostedt et al., 2020).

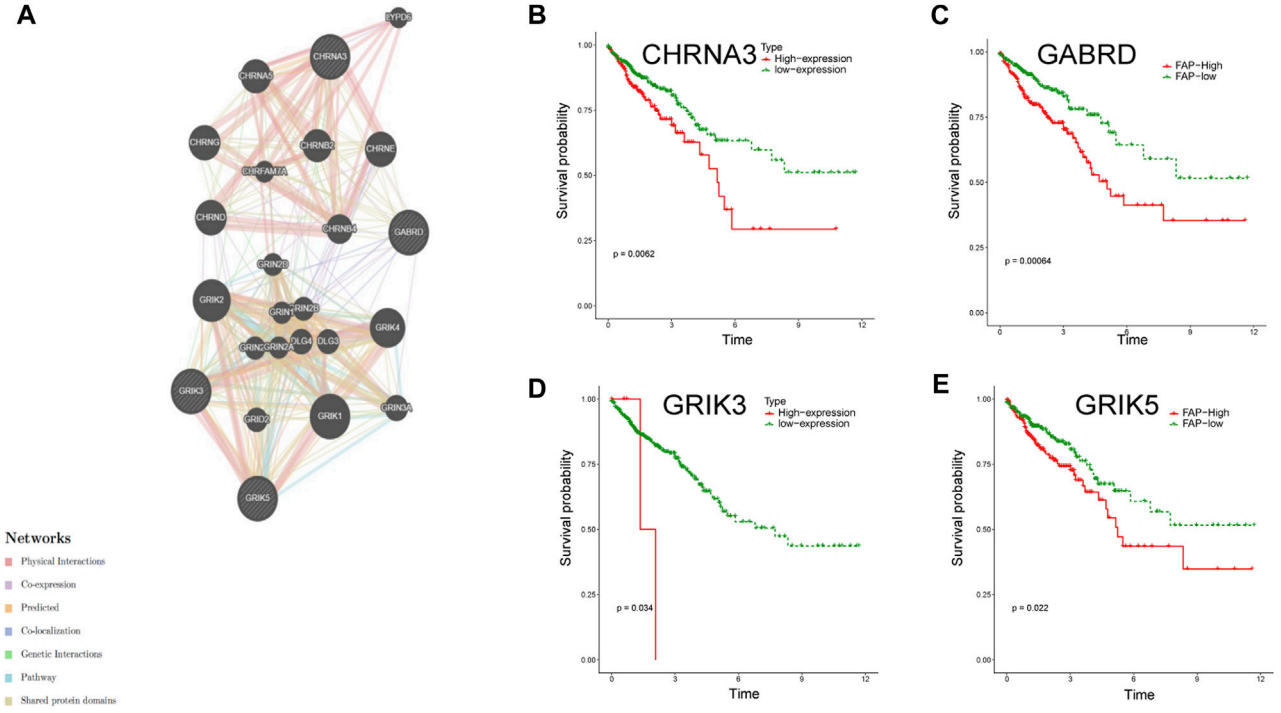


FIGURE 6
PPI and survival analysis of hub gene. **(A)** The GeneMANIA database performed PPI analysis on the diagnostic gene and its 6 interacting genes to predict correlations among co-localization, shared protein domains, co-expression, predicted and pathways. **(B–E)** Survival analysis of 4 hub genes.

## Statistical analysis

All data were analyzed and graphed using GraphPad Prism 6.0 and R software (version 4.0.5). The experimental data were presented as mean ± *s.d.* of three independent trials. The Wilcoxon signed-rank test was used to compare the differences between the two groups. A *p*-value less than 0.05 indicated statistical significance, and the significance levels were set at $^{*}p \leq 0.05$, $^{**}p \leq 0.01$, and $^{***}p \leq 0.001$.

# Results

## Differential analysis between normal and tumor colorectal tissues

The volcano maps for TCGA DEG analysis are shown in Figure 2A. There was 29 neurotransmitter receptor-related DEGs in CRC compared with normal tissues, including 10 upregulated and 19 downregulated genes (Figure 2B).

## Gene modules derived from WGCNA based on DEGs expression of TCGA

A co-expression network was constructed based on the DEGs expression matrix of TCGA (Figure 3A). We calculated a soft threshold and established a scale-free topology model with a data selection threshold of 5 (Figure 3B). After weight-based filtering, the cluster dendrogram was shown in Figure 3C. And the data were clustered into 17 modules. We then analyzed the correlation among the neurotransmitter scores of each module and found that the blue module had the strongest association with neurotransmitter scores (Figure 3E) (cor = 0.59 and P = 3e-64).

As a result, we selected the blue module as the crucial module for further analysis. A significant correlation existed between the blue modules' MM and gene significance (GS) (Figure 3D). The intersection between the blue module and neurotransmitter receptor-related genes was also estimated (Figure 4A). Seven genes were identified as the candidate genes in both groups, including CHRNA3, CHRM2, GABRD, GRIK3, GRIK5, GRIN2D, and HTR1D. Except for GRIN2D, HTR1D, GABRD other genes are less expressed in tumors than in normal tissues (Figure 4B). In addition, GO and KEGG pathway analyses were performed on the candidate genes and revealed that these genes are mainly involved in the neurotransmitter receptor activity pathway (Figures 4C, D).

## Hub gene identification and verification

Using the LASSO regression algorithm, six genes were identified as potential diagnostic biomarkers from the candidate genes (Figures 5A, B). RF identified five diagnostic genes (Figures 5C, D). All candidate genes were identified as potential biomarkers by the SVM-RFE algorithm (Figures 5E, F). Four genes (CHRNA3, GABRD, GRIK3 and GRIK5) were then overlapped via a Venn diagram, and served as robust diagnostic biomarkers (Figure 5G). The efficacy of these biomarkers was validated using the GSE74602 dataset, which showed high associated value with an AUC of 0.999 (Figures 5H, I). PPI

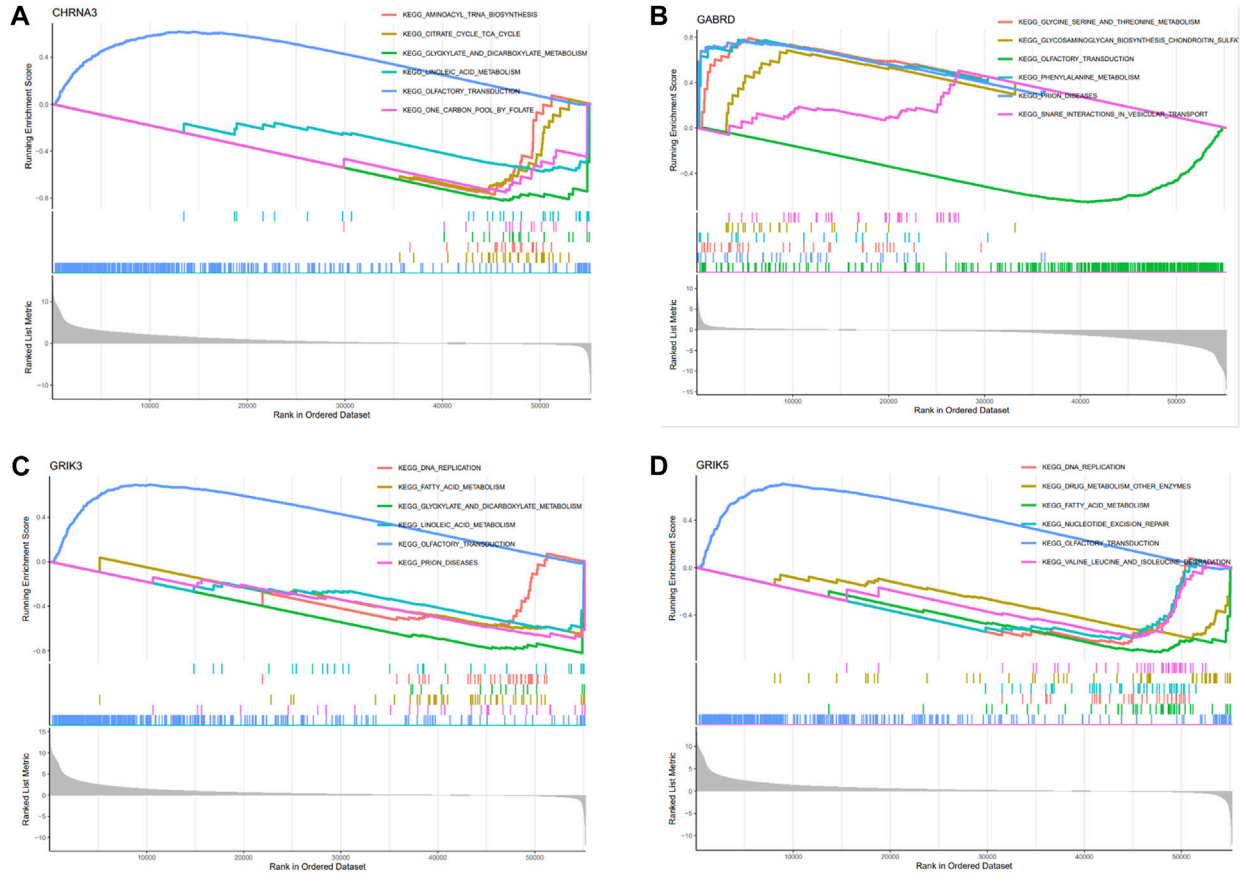


FIGURE 7
Enrichment analysis of hub genes. **(A–D)** Functional analysis of the 4 hub genes using GSEA.

analysis was also performed on the hub genes (Figure 6A). Finally, we explored the relationship between hub genes and clinical features and found that patients with advanced TNM stages had higher expression of the identified hub genes (Supplementary Figure S1). And high expression of CHRNA3, GABRD, and GRIK5 are significantly associated with poor prognosis (Figures 6B–E).

## GSEA analysis

We conducted GSEA analysis to investigate the signaling pathways associated with hub genes, and the top six pathways are presented in Figure 7. Our findings revealed that CHRNA3 was significantly linked to several pathways, including aminoacyl-tRNA biosynthesis, citric cycle/TCA cycle, glyoxylate and dicarboxylic acid metabolism, olfactory transduction, and one-carbon pool by folate (Figure 7A). The expression of GABRD was significantly associated with pathways related to glycine, serine, and threonine metabolism, glycosaminoglycan biosynthesis (chondroitin sulfate), olfactory transduction, phenylalanine metabolism, prion diseases, and SNARE interactions in vesicular transport (Figure 7B). The expression of GRIK3 was significantly correlated with pathways related to DNA replication, fatty acid metabolism, glyoxylate and dicarboxylic acid metabolism, linoleic acid metabolism, olfactory transduction, and prion diseases (Figure 7C). Lastly, the expression of GRIK5 was significantly linked to pathways related to DNA replication, drug metabolism (other enzymes), fatty acid metabolism, nucleotide excision, olfactory transduction, as well as valine, leucine, and isoleucine degradation (Figure 7D).

## Association of hub genes levels with tumor microenvironment

The Tumor Microenvironment (TME) consists of various components including endothelial cells, cancer-associated fibroblasts (CAFs), myofibroblasts, immune cells, and other factors (Ding et al., 2022). To investigate whether hub gene would be involved in TME, we observed the correlation of hub genes expression with stromal cell and immune cell infiltrations (Figure 8A, Supplementary Figure S2). The results showed that Tregs, naive B cells, and activated memory $CD4^+$ T cells were positively correlated with all hub genes, while activated memory $CD4^+$ T cells were negatively correlated. Macrophages M0 were found to be highly infiltrated in cases with high expression of CHRNA3, GABRD, and GRIK5. Only GRIK3 was positively correlated with the infiltration of resting memory $CD4^+$ T cells (Figure 8B). Moreover, we found that CHRNA3, GABRD, GRIK3, and GRIK5 were also expressed in both endothelial and stromal cell subpopulations (Figures 9A, B). Notably, CHRNA3,

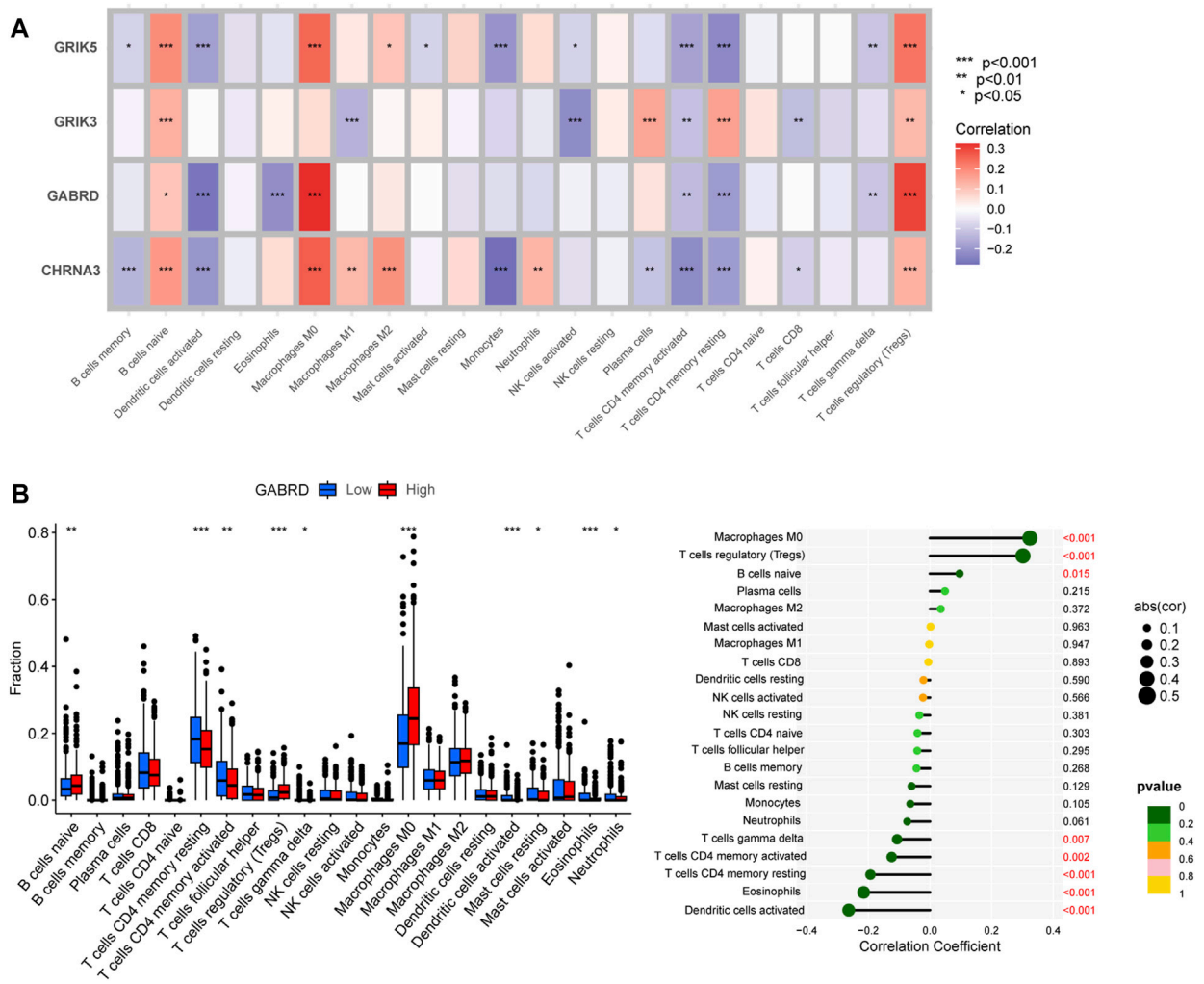


FIGURE 8
Association of hub genes with immune cell infiltration. **(A)** Correlation analysis between immune cells and hub genes. **(B)** Correlation analysis between GABRD and immune cells, as well as differences in immune cells between high and low gene expression groups.

GRIK3, and GRIK5 were highly expressed in fibroblasts compared to other cell subpopulations. And GABRD had high expression levels in endothelial cells, suggesting its role in angiogenesis within the TME (Figures 9C–F).

## Establishment of a prognostic nomogram for colorectal cancer

We developed a novel prognostic nomogram to offer a reliable and quantifiable method for predicting the progress of colorectal cancer based on the hub gene. In the nomogram, each hub gene is assigned a score, calculated by multiplying the gene's coefficient with its expression level. And the total score, determined by summing the scores of all the hub genes, corresponds to varying risk levels for patients (Figure 10A). In addition, calibration curves and Harrell's concordance index (C-index) showed the nomogram had good predictive power (Figures 10B, C). Subsequently, Decision curve analysis elicited that the nomogram provided a significant net benefit (Figure 10D). Overall, these results indicate that the nomogram possesses significant predictive value.

## Expression of genes with sensitivity of cancer cells to anti-tumor drugs

We obtained gene expression and drug sensitivity data from CellMiner and excluded drugs without clinical trials or FDA approval and calculated the correlation coefficient between hub genes expression and drug sensitivity (Figure 11). The CHRNA3, GABRD, GRIK3 and GRIK5 gene are associated with the sensitivity of certain anti-tumor drugs such as fluphenazine, pimozide, isotretinoin, and fludarabine. CHRNA3 was identified to increase the sensitivity of cancer cells to chemotherapeutic agents, such as chelerythrine, XK-469, and dexamethasone decad, while GABRD weakened the sensitivity of pimozide and rapamycin. These findings suggest that the expression levels of hub genes may serve as a predictor of drug sensitivity for a specific class of drugs.

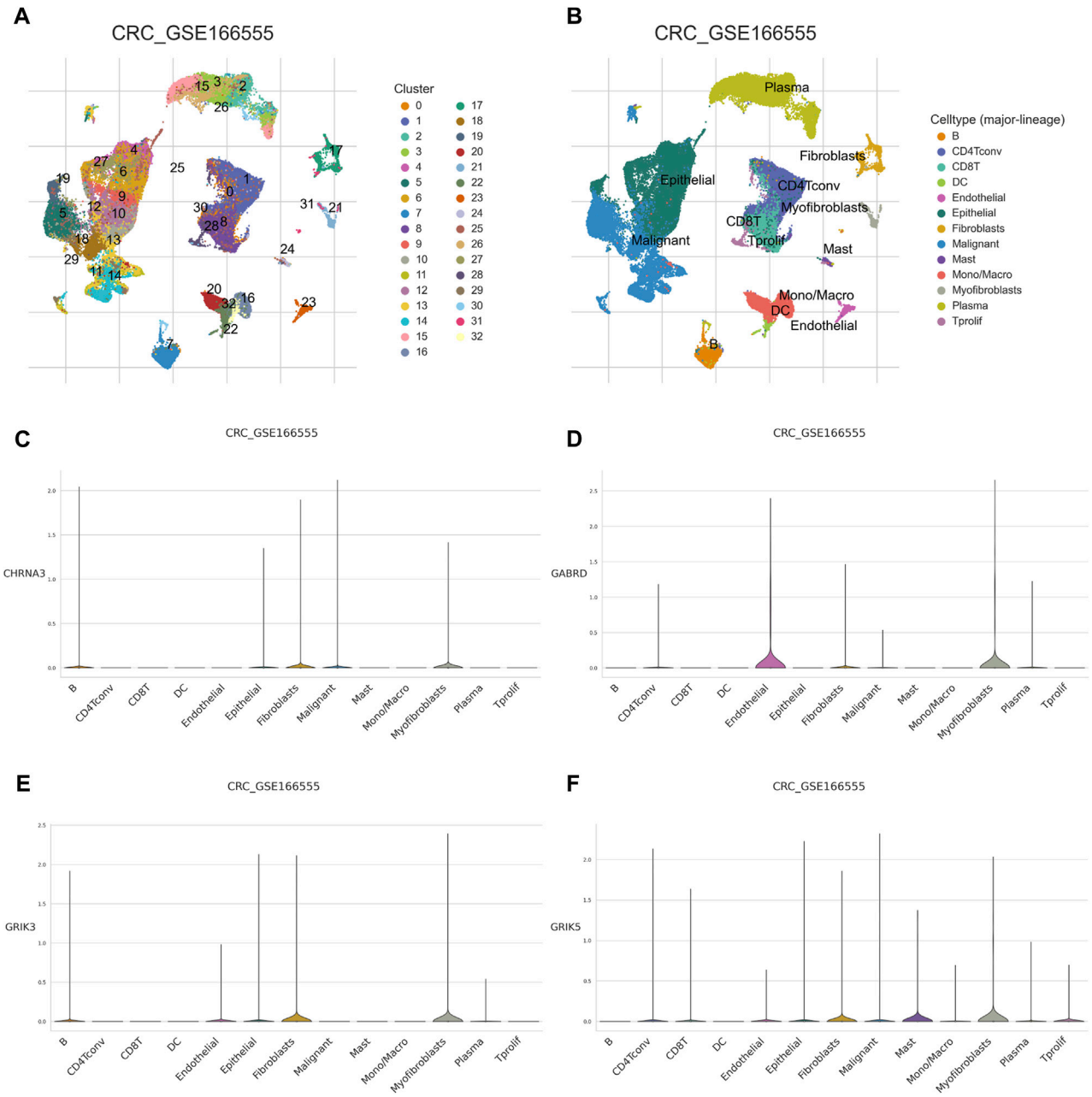


FIGURE 9
Single cell analysis of hub genes **(A)** Using the colorectal cancer GSE166555 dataset for study, dimensionality reduction and clustering analysis were performed. All cells were clustered into 32 clusters. **(B)** Cell annotation. A total of 13 cell types were identified. **(C–F)** expression of the 4 hub genes in single-cell data.

## Validation of mRNA expressions of prognostic NRGs

To confirm the significance of neurotransmitter receptor-related genes in CRC, we analyzed the differential mRNA levels of the four independent prognostic genes in the normal colorectal tissues and CRC tissues. Results revealed that, compared to normal tissues, the expression of CHRNA3, GRIK3, and GRIK5 is decreased in tumor tissues, while GABRD is highly expressed in tumor tissues, consistent with our bioinformatics analysis results (Figures 12A–C). Furthermore, we investigated the protein expression of GABRD through the HPA database. The outcomes revealed elevated protein levels of GABRD in CRC tissues (Figure 12D).

# Discussion

Neurotransmitters are traditionally known as nerve-secreted substances that modulate excitatory or inhibitory neuronal functions by binding to specific receptors. And our understanding of the regulatory role of the neurotransmitter system in tumor initiation and progression continues to advance.

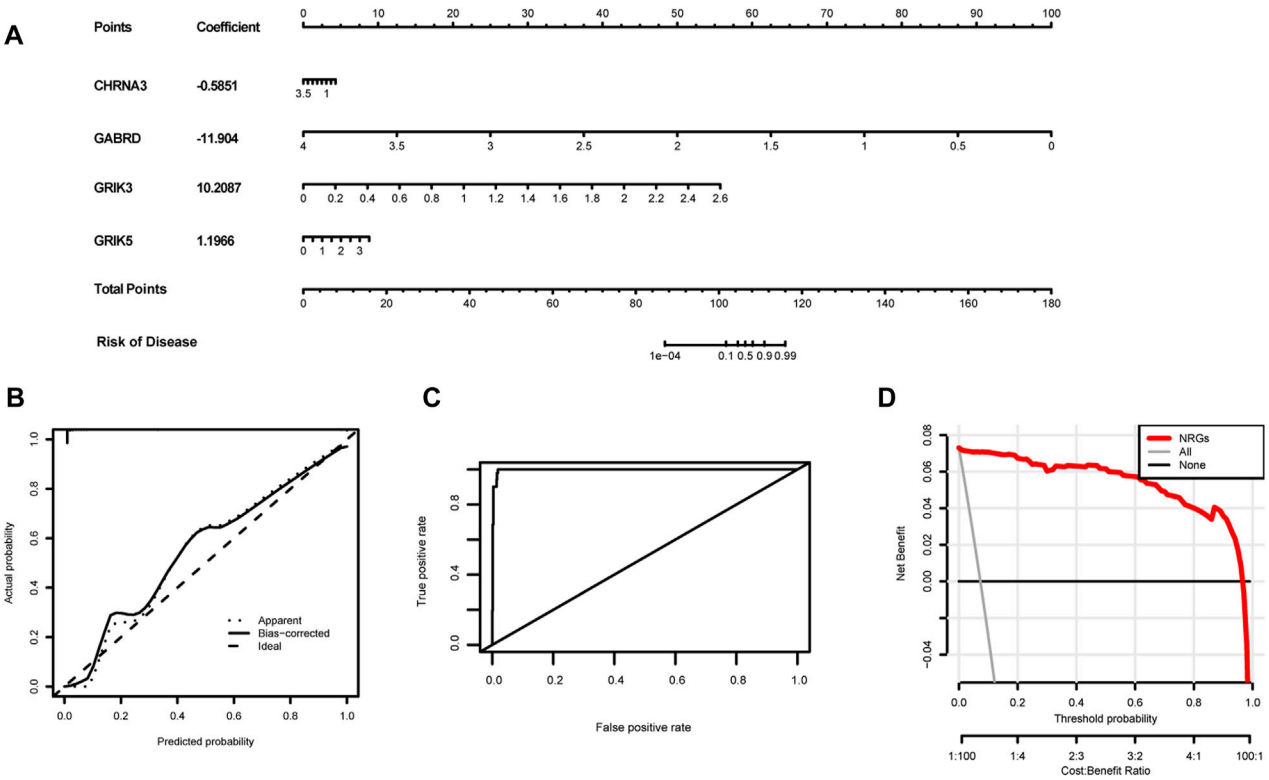


FIGURE 10
Establishment of the diagnostic nomogram. **(A)** Create a column chart of integrated hub genes, where each variable corresponds to a score that can be added together to calculate a total score, to predict the progression of colorectal cancer. **(B)** Calibration curves were used to estimate the predictive accuracy of the column chart. **(C)** Harrell's concordance index was used as performance metrics. **(D)**Decision curve analysis shows the clinical benefit of the nomogram for predicting the progression of colon cancer.

Neurotransmitters exhibit varying effects on the numerous functions of cancer cells, endothelial cells, and immune cells across various human cancer types. The aberrant expression of neurotransmitter signaling genes in colorectal cancer underscores the potential of neurotransmitters to enhance tumor growth and metastasis by stimulating processes such as cell proliferation, migration, invasion, and angiogenesis. In addition, neurotransmitters can influence immune cells and endothelial cells in the tumor microenvironment, fostering inflammation and contributing to the advancement of tumor growth (Battaglin et al., 2022). Nevertheless, the precise impact of various neurotransmitter receptors on colorectal cancer progression remains poorly understood. Therefore, we have identified a signature consisting of four genes associated with neurotransmitter receptors: CHRNA3, GABRD, GRIK3, and GRIK5 to predict prognosis and treatment response in CRC patients.

In our study, we employed WGCNA analysis and identified 17 modules to help explore the characteristic relationship between neurotransmitter scores and gene clusters. Additionally, we utilized machine learning algorithms to enhance the accuracy of biomarker screening. Three machine learning algorithms (LASSO logistic, SVM-RFE and RF) were primarily utilized to screen feature variables and establish the best classification model. As a result, we identified CHRNA3, GABRD, GRIK3, and GRIK5 as biomarkers by combining the machine learning algorithm and WGCNA. And these biomarkers were well-validated in the external validation cohorts.

CHRNA3 is a member of the nicotinic acetylcholine receptor (nAChRs) gene cluster, which serves as the "gateways" through which nicotine exerts its effects on the brain (Ware et al., 2012). PPI analysis reveals that CHRNA3 has a solid physical interaction with CHRNA5 and CHRNB4. Previous studies have reported that variations in CHRNA3-A5-B4 are independently and additively associated with increased cigarette consumption, nicotine dependence, and lung cancer risk (Chmielowiec et al., 2022). Despite the absence of evidence on the role of CHRNA3 in CRC progression, we have identified, for the first time, that high CHRNA3 expression is associated with poor prognosis in CRC patients. Gamma-aminobutyric acid (GABA) is the principal inhibitory neurotransmitter in the adult mammalian central nervous system. Its receptors, expressed in various tumor tissues, play a crucial role in regulating tumor cell proliferation and migration (Joseph et al., 2002; Kanbara et al., 2018; Jiang et al., 2020a; Zhang et al., 2023). The γ-aminobutyric acid type A receptor *d* subunit (GABRD), encoded in the human chromosome 1p36 region, has yet to be fully elucidated regarding its involvement in cancers (Zhang et al., 2019). Recently, Wu et al. conducted a study that found enhanced expression of GABRD to be predictive of poor prognosis in CRC patients (Yan et al., 2020), consistent with our results. And Huang et al. confirmed that GABRD receptors indicated by T cells directly inhibit $CD8^+$ T cells by participating in signal regulation (Huang et al., 2022). Glutamate ionotropic receptor kainate type subunit 3 (GRIK3) and

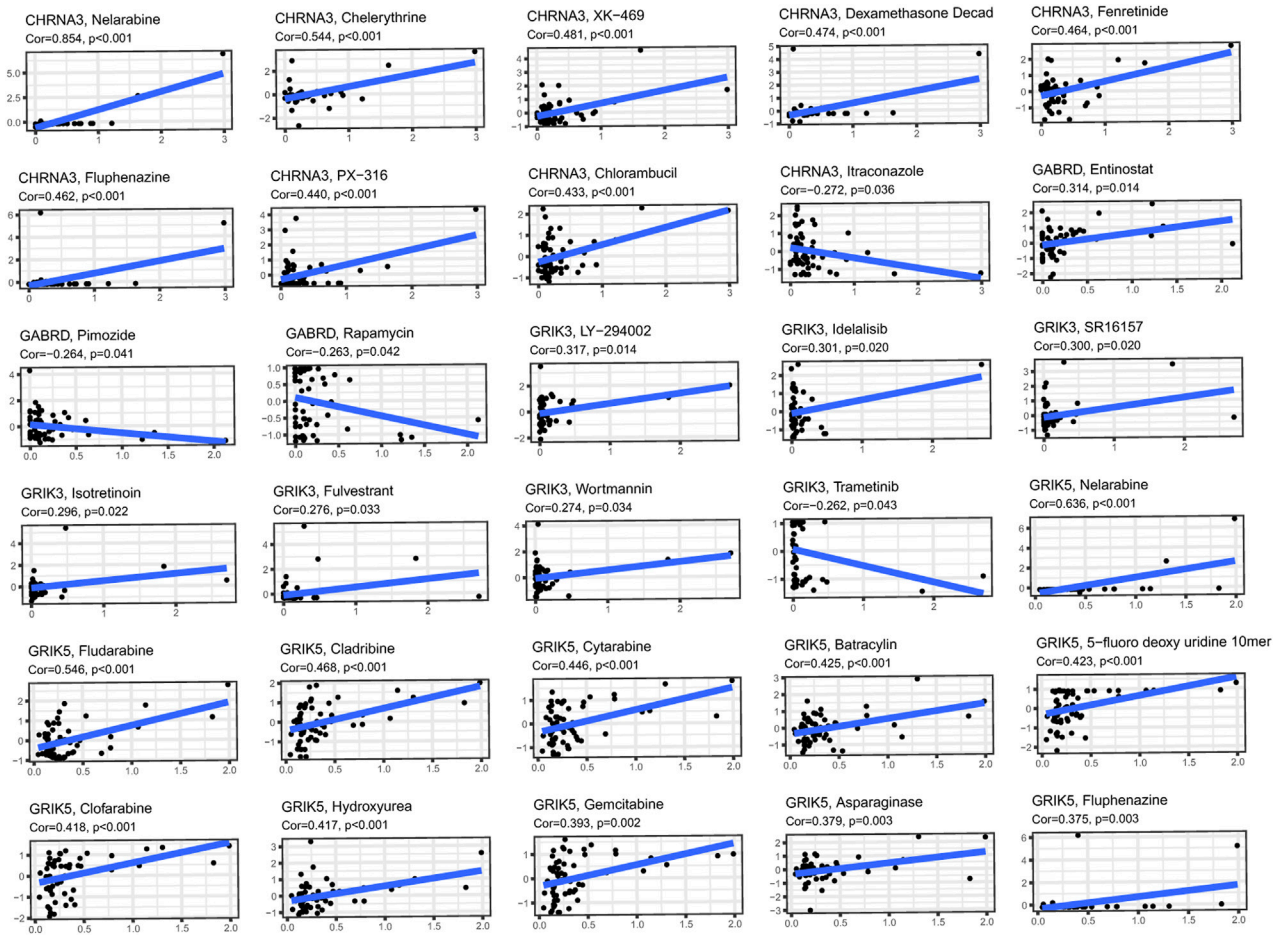


FIGURE 11
Investigating the correlation between 4 hub genes and common anti-cancer drugs using the Cellminer database.

glutamate receptor ionotropic kainate-5 (GRIK5) are members of the glutamate kainate receptor family and play crucial roles in the neuroactive ligand-receptor interaction pathway (Fang et al., 2021; Minoza et al., 2022). There is compelling evidence suggesting that GRIK3 participates in cancer progression. For example, GRIK3 was reported to mediate the function of CircRNA and promote the proliferation and metastasis of colon cancer cells (Fang et al., 2021). Xiao et al. found that GRIK3 promotes epithelial-mesenchymal transition in breast cancer cells by regulating SPDEF/CDH1 signaling (Xiao et al., 2019). Furthermore, GRIK5 has been identified as a potential biomarker for melanoma metastatic progression (Minoza et al., 2022). Although limited research exists on the relationship between GRIK5 expression and colorectal cancer (CRC), our study fills this gap by identifying a significant association between high GRIK5 expression and CRC progression.

Functional enrichments were performed to gain insights into the biological processes in which these hub genes may be involved. Our results suggest that these hub genes may play critical roles in cellular metabolic processes, particularly in organic acid, inorganic acid, and lipid metabolism. It is well-established that the hostile tumor microenvironment surrounding cancer cells drives metabolic changes that impact tumorigenesis and metastatic potential. Previous studies have validated the prominent status of lipid metabolism in cancer progression. Moreover, targeting dysfunctional lipid metabolism has shown promising results as an approach to impede tumor growth (Bian et al., 2021). Amino acids also represent a crucial aspect of the tumor microenvironment, which can significantly affect cancer cell metabolism and overall tumor development (Stepka et al., 2021). Our findings suggest that these biomarkers may contribute to the construction of a TME that favors tumor development. Thus, the current study investigated the correlation between tumor infiltrating cells and neurotransmitter receptor-related gene prognostic signatures. Using the CIBERSORT algorithm, we comprehensively evaluated the abundance and infiltration of twenty-two immune cells in COAD patients. The results showed that the high expression of gene signature groups exhibits elevated levels of immunosuppressive cells, such as Tregs and macrophages M0, and low infiltration of anti-tumor cells, including $CD4^+$ and dendritic cells. Previous studies have demonstrated that the significant infiltration of M0 macrophages in the tumor microenvironment may predict poor prognosis (Zheng et al., 2021), while Tregs can induce immune tolerance and facilitate immune escape and tumor metastasis (Bauer et al., 2014). These findings are consistent with our study, supporting that high expression of hub genes with increased immunosuppressive cell infiltration is associated with

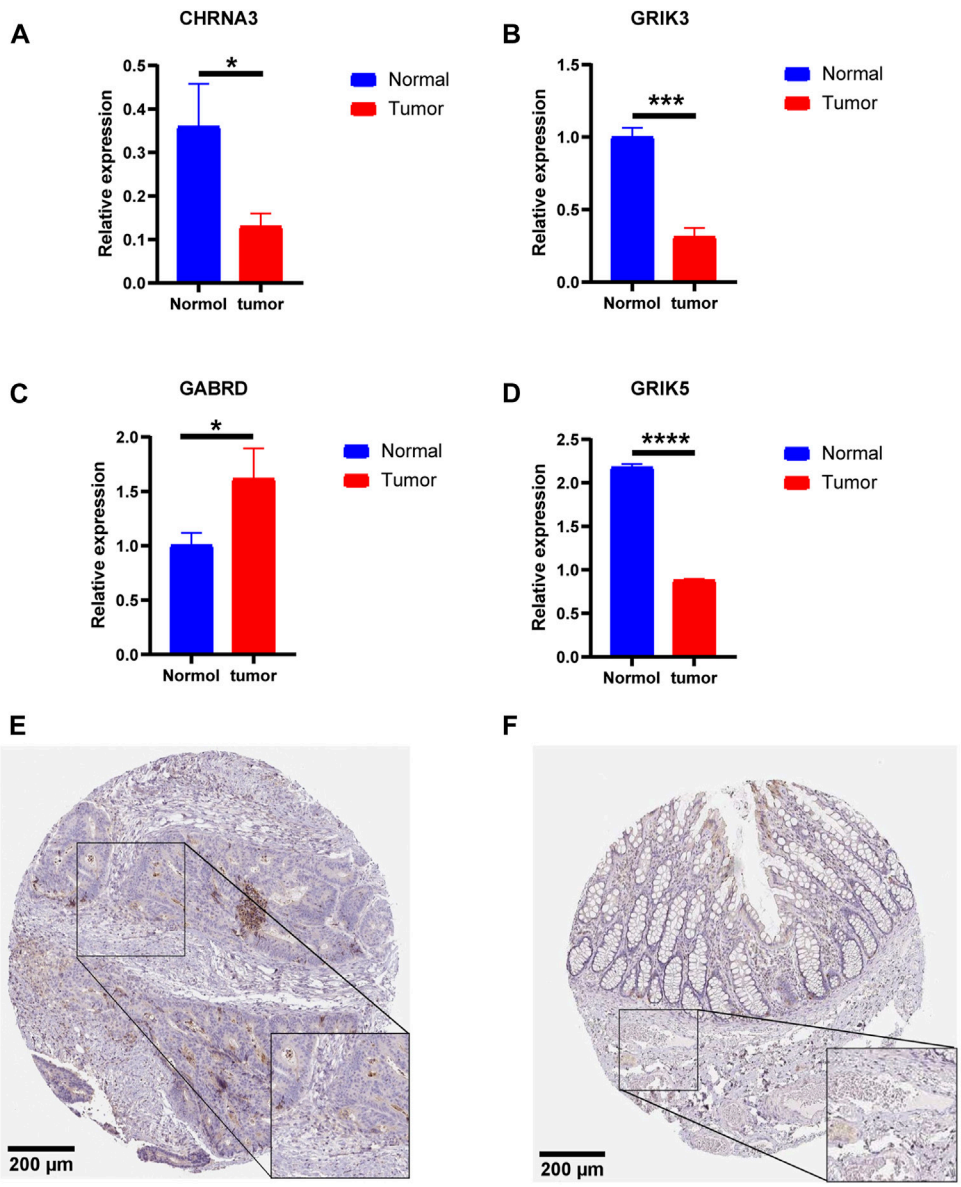


FIGURE 12
Validation of mRNA expressions of prognostic Neurotransmitter Receptor-Related Gene (NRGs). **(A–D)** The mRNA expressions of GABRD, CHRNA3, GRIK3, and GRIK5 in the normal colorectal and CRC tissues. **(E,F)** Immunohistochemistry of the GABRD in the normal and tumor groups from the HPA database. Data are shown as means ± SEM of three independent experiments. *$p < 0.05$, **$p < 0.01$, ***$p < 0.001$.

poor prognosis in COAD patients. The B cell populations in the TME exhibit significant heterogeneity in surface immunophenotype and function (Downs-Canner et al., 2022). Memory B cells are found in higher numbers in tumors than peripheral blood, accounting for 34% of B cells in tumors compared to 14% in peripheral blood, regardless of tumor grade. Interestingly, patients who respond to immune checkpoint inhibition therapy exhibit increased memory B cells, CXCR3+ cells, and germinal center-like B cells in the TME (Helmink et al., 2020). Here, we found a positive association between hub genes and naive B cells, indicating that the neurotransmitter receptor-related gene signature may serve as a predictive marker for the effectiveness of immunotherapy in CRC patients.

Stromal cells and endothelial cells are another important component of TME. Interestingly, in the current study, increased expression of CHRNA3, GRIK3, and GRIK5 was highly associated with stromal cells, especially CAFs. CAFs play a critical role in CRC progression and are instrumental in shaping the tumor-promoting immune microenvironment (Kobayashi et al., 2022). Additionally, endothelial cells have been identified as one of the primary sources of CAFs and play a vital role in promoting tumor metastasis (Yan et al., 2020). Notably, our results demonstrated that increased GABRD expression was highly associated with endothelial cells.

Based on the neurotransmitter receptor-related gene prognostic signatures, a prognostic nomogram was developed. And We have validated the accuracy of the nomogram through calibration plots and decision curve analysis, which supports its potential as a valuable instrument for personalized risk management. We also utilized the CellMiner database to examine the relationship between FDA-approved drugs and these four targets. Our analysis of drug sensitivity revealed that the expression of CHRNA3, GABRD, GRIK3, and GRIK5 in cancer cells significantly impacted their response to chemotherapy. Our discoveries could provide novel insights into the appropriate selection of drugs, offering guidance for forthcoming studies in oncology. Finally, we performed a simple validation of the expression of hub genes in CRC tissues and found that, compared to normal tissues, the mRNA levels of CHRNA3, GRIK3, and GRIK5 were decreased. CHRNA3, GRIK3, and GRIK5 are primarily expressed in connective tissue. Due to the predominance of tumor cells in tumor tissues, they are downregulated in tumor tissues compared to normal tissues. Both immunohistochemistry and RT-PCR confirmed the high expression of GABRD in tumor tissues. Interestingly, among these four hub genes, three of them exhibit relatively lower expression in colorectal cancer tissue compared to normal tissue. This observation indeed presents a complex and multifaceted biological phenomenon. We suggest that gene function can be independent of expression levels. The phenomenon of oncogene downregulation in tumor tissues contradicts common expectations, which generally predict higher expression levels of cancer genes. We delved into the literature and found similar instances where gene expression is influenced by various mechanisms, such as: The B-cell lymphoma 2 (BCL-2) family of proteins regulates apoptosis in normal cells. In various cancers, increased expression of BCL-2 protein is associated with enhanced drug resistance of tumor cells, although in some cases, its expression may be lower in tumor tissues compared to the surrounding normal tissues (Adams and Cory, 2007). And Hexokinase 2 (HK2) is involved in glucose metabolism in normal tissues, while in cancer cells, increased activity of HK2 is associated with cancer survival and growth, even if its expression levels are lower than in normal tissues, representing the role of metabolic reprogramming in tumors (Patra and Hay, 2014). Despite these genes being less commonly discussed, their existence and paradoxical behavior in cancer biology are well-documented. To address the question of why these three genes are expressed at lower levels in colorectal cancer tissue but are associated with a poorer prognosis in patients with high expression, further investigations in proteomics and epigenetics are required.

Though we have identified a significant gene signature in CRC based on the NRGs, there were some limitations. Firstly, our findings were based on public databases, and thus, it is crucial to validate these results in a prospective cohort from our hospital. Additionally, we need to investigate the functions of the hub genes implicated in CRC progression using cell lines and/or mouse models.

## Conclusion

In our study, we employed several bioinformatics approaches to identify a 4-gene signature related to neurotransmitter receptors to evaluate the prognosis of CRC patients. Our results indicated a significant association between the signature and the clinical features and immune system of colorectal cancer. Thus, the gene signature in our study could function as an independent prognostic indicator for CRC patients.

## Data availability statement

The original contributions presented in the study are included in the article/Supplementary Material, further inquiries can be directed to the corresponding authors.

## Ethics statement

The studies involving humans were approved by the Institutional Review Board of Sun Yat-Sen University Cancer Center (G2022-075-01). The studies were conducted in accordance with the local legislation and institutional requirements. The participants provided their written informed consent to participate in this study.

## Author contributions

LZ, WD, and LL conceptualized the study. LZ developed the methods and performed the investigations and data analyses. YD and JY wrote the original draft of the manuscript. LL acquired funding and supervised the study. All authors contributed to the article and approved the submitted version.

## Funding

This study was supported by grants from the National Natural Science Foundation of China 82172802.

## Conflict of interest

The authors declare that the research was conducted in the absence of any commercial or financial relationships that could be construed as a potential conflict of interest.

## Publisher's note



## Supplementary material

The Supplementary Material for this article can be found online at: https://www.frontiersin.org/articles/10.3389/fcell.2023.1202193/full#supplementary-material

# References


Adams, J. M., and Cory, S. (2007). The Bcl-2 apoptotic switch in cancer development and therapy. *Oncogene* 26, 1324–1337. doi:10.1038/sj.onc.1210220

Battaglin, F., Jayachandran, P., Strelez, C., Lenz, A., Algaze, S., Soni, S., et al. (2022). Neurotransmitter signaling: a new frontier in colorectal cancer biology and treatment. *Oncogene* 41, 4769–4778. doi:10.1038/s41388-022-02479-4

Bauer, C. A., Kim, E. Y., Marangoni, F., Carrizosa, E., Claudio, N. M., and Mempel, T. R. (2014). Dynamic Treg interactions with intratumoral APCs promote local CTL dysfunction. *J. Clin. Invest.* 124, 2425–2440. doi:10.1172/JCI66375

Bian, X., Liu, R., Meng, Y., Xing, D., Xu, D., and Lu, Z. (2021). Lipid metabolism and cancer. *J. Exp. Med.* 218, e20201606. doi:10.1084/jem.20201606

Brenner, H., and Chen, C. (2018). The colorectal cancer epidemic: challenges and opportunities for primary, secondary and tertiary prevention. *Br. J. Cancer* 119, 785–792. doi:10.1038/s41416-018-0264-x

Cervantes-Villagrana, R. D., Albores-Garcia, D., Cervantes-Villagrana, A. R., and Garcia-Acevez, S. J. (2020). Tumor-induced neurogenesis and immune evasion as targets of innovative anti-cancer therapies. *Signal Transduct. Target Ther.* 5, 99. doi:10.1038/s41392-020-0205-z

Chin, C. H., Chen, S. H., Wu, H. H., Ho, C. W., Ko, M. T., and Lin, C. Y. (2014). cytoHubba: identifying hub objects and sub-networks from complex interactome. *BMC Syst. Biol.* 8 (4), S11. doi:10.1186/1752-0509-8-S4-S11

Chmielowiec, K., Chmielowiec, J., Stronska-Pluta, A., Trybek, G., Smiarowska, M., Suchanecka, A., et al. (2022). Association of polymorphism CHRNA5 and CHRNA3 gene in people addicted to nicotine. *Int. J. Environ. Res. Public Health* 19, 10478. doi:10.3390/ijerph191710478

Ding, X., Liu, H., Yuan, Y., Zhong, Q., and Zhong, X. (2022). Roles of GFPT2 expression levels on the prognosis and tumor microenvironment of colon cancer. *Front. Oncol.* 12, 811559. doi:10.3389/fonc.2022.811559

Downs-Canner, S. M., Meier, J., Vincent, B. G., and Serody, J. S. (2022). B cell function in the tumor microenvironment. *Annu. Rev. Immunol.* 40, 169–193. doi:10.1146/annurev-immunol-101220-015603

Edwards, B. K., Noone, A. M., Mariotto, A. B., Simard, E. P., Boscoe, F. P., Henley, S. J., et al. (2014). Annual Report to the Nation on the status of cancer, 1975-2010, featuring prevalence of comorbidity and impact on survival among persons with lung, colorectal, breast, or prostate cancer. *Cancer* 120, 1290–1314. doi:10.1002/cncr.28509

Fang, G., Wu, Y., and Zhang, X. (2021). CircASXL1 knockdown represses the progression of colorectal cancer by downregulating GRIK3 expression by sponging miR-1205. *World J. Surg. Oncol.* 19, 176. doi:10.1186/s12957-021-02275-6

Favoriti, P., Carbone, G., Greco, M., Pirozzi, F., Pirozzi, R. E., and Corcione, F. (2016). Worldwide burden of colorectal cancer: a review. *Updat. Surg.* 68, 7–11. doi:10.1007/s13304-016-0359-y

Guo, L., Wang, Z., DU, Y., Mao, J., Zhang, J., Yu, Z., et al. (2020). Random-forest algorithm based biomarkers in predicting prognosis in the patients with hepatocellular carcinoma. *Cancer Cell Int.* 20, 251. doi:10.1186/s12935-020-01274-z

Helmink, B. A., Reddy, S. M., Gao, J., Zhang, S., Basar, R., Thakur, R., et al. (2020). B cells and tertiary lymphoid structures promote immunotherapy response. *Nature* 577, 549–555. doi:10.1038/s41586-019-1922-8

Huang, D., Wang, Y., Thompson, J. W., Yin, T., Alexander, P. B., Qin, D., et al. (2022). Cancer-cell-derived GABA promotes beta-catenin-mediated tumour growth and immunosuppression. *Nat. Cell Biol.* 24, 230–241. doi:10.1038/s41556-021-00820-9

Jiang, S. H., Hu, L. P., Wang, X., Li, J., and Zhang, Z. G. (2020a). Neurotransmitters: emerging targets in cancer. *Oncogene* 39, 503–515. doi:10.1038/s41388-019-1006-0

Jiang, S. H., Zhang, X. X., Hu, L. P., Wang, X., Li, Q., Zhang, X. L., et al. (2020b). Systemic regulation of cancer development by neuro-endocrine-immune signaling network at multiple levels. *Front. Cell Dev. Biol.* 8, 586757. doi:10.3389/fcell.2020.586757

Joseph, J., Niggemann, B., Zaenker, K. S., and Entschladen, F. (2002). The neurotransmitter gamma-aminobutyric acid is an inhibitory regulator for the migration of SW 480 colon carcinoma cells. *Cancer Res.* 62, 6467–6469.

Kanbara, K., Otsuki, Y., Watanabe, M., Yokoe, S., Mori, Y., Asahi, M., et al. (2018). GABA(B) receptor regulates proliferation in the high-grade chondrosarcoma cell line OUMS-27 via apoptotic pathways. *BMC Cancer* 18, 263. doi:10.1186/s12885-018-4149-4

Keum, N., and Giovannucci, E. (2019). Global burden of colorectal cancer: emerging trends, risk factors and prevention strategies. *Nat. Rev. Gastroenterol. Hepatol.* 16, 713–732. doi:10.1038/s41575-019-0189-8

Kobayashi, H., Gieniec, K. A., Lannagan, T. R. M., Wang, T., Asai, N., Mizutani, Y., et al. (2022). The origin and contribution of cancer-associated fibroblasts in colorectal carcinogenesis. *Gastroenterology* 162, 890–906. doi:10.1053/j.gastro.2021.11.037

Kuol, N., Davidson, M., Karakkat, J., Filippone, R. T., Veale, M., Luwor, R., et al. (2022). Blocking muscarinic receptor 3 attenuates tumor growth and decreases immunosuppressive and cholinergic markers in an orthotopic mouse model of colorectal cancer. *Int. J. Mol. Sci.* 24, 596. doi:10.3390/ijms24010596

Langfelder, P., and Horvath, S. (2008). WGCNA: an R package for weighted correlation network analysis. *BMC Bioinforma.* 9, 559. doi:10.1186/1471-2105-9-559

Lin, D., Fan, W., Zhang, R., Zhao, E., Li, P., Zhou, W., et al. (2021). Molecular subtype identification and prognosis stratification by a metabolism-related gene expression signature in colorectal cancer. *J. Transl. Med.* 19, 279. doi:10.1186/s12967-021-02952-w

Lin, X., Yang, F., Zhou, L., Yin, P., Kong, H., Xing, W., et al. (2012). A support vector machine-recursive feature elimination feature selection method based on artificial contrast variables and mutual information. *J. Chromatogr. B Anal. Technol. Biomed. Life Sci.* 910, 149–155. doi:10.1016/j.jchromb.2012.05.020

Li, T., Fu, B., Zhang, X., Zhou, Y., Yang, M., Cao, M., et al. (2021). Overproduction of gastrointestinal 5-HT promotes colitis-associated colorectal cancer progression via enhancing NLRP3 inflammasome activation. *Cancer Immunol. Res.* 9, 1008–1023. doi:10.1158/2326-6066.CIR-20-1043

Li, Z., Wang, Q., Huang, X., Yang, M., Zhou, S., Li, Z., et al. (2023). Lactate in the tumor microenvironment: a rising star for targeted tumor therapy. *Front. Nutr.* 10, 1113739. doi:10.3389/fnut.2023.1113739

Minoza, J. M. A., Rico, J. A., Zamora, P. R. F., Bacolod, M., Laubenbacher, R., Dumancas, G. G., et al. (2022). Biomarker discovery for meta-classification of melanoma metastatic progression using transfer learning. *Genes (Basel)* 13, 2303. doi:10.3390/genes13122303

Patra, K. C., and Hay, N. (2014). The pentose phosphate pathway and cancer. *Trends Biochem. Sci.* 39, 347–354. doi:10.1016/j.tibs.2014.06.005

Ritchie, M. E., Phipson, B., Wu, D., Hu, Y., Law, C. W., Shi, W., et al. (2015). Limma powers differential expression analyses for RNA-sequencing and microarray studies. *Nucleic Acids Res.* 43, e47. doi:10.1093/nar/gkv007

Siegel, R. L., Miller, K. D., Goding Sauer, A., Fedewa, S. A., Butterly, L. F., Anderson, J. C., et al. (2020). Colorectal cancer statistics, 2020. *CA Cancer J. Clin.* 70, 145–164. doi:10.3322/caac.21601

Sjostedt, E., Zhong, W., Fagerberg, L., Karlsson, M., Mitsios, N., Adori, C., et al. (2020). An atlas of the protein-coding genes in the human, pig, and mouse brain. *Science* 367, eaay5947. doi:10.1126/science.aay5947

Stepka, P., Vsiansky, V., Raudenska, M., Gumulec, J., Adam, V., and Masarik, M. (2021). Metabolic and amino acid alterations of the tumor microenvironment. *Curr. Med. Chem.* 28, 1270–1289. doi:10.2174/0929867327666200207114658

Sun, D., Wang, J., Han, Y., Dong, X., Ge, J., Zheng, R., et al. (2021). TISCH: a comprehensive web resource enabling interactive single-cell transcriptome visualization of tumor microenvironment. *Nucleic Acids Res.* 49, D1420–D1430. doi:10.1093/nar/gkaa1020

Thaker, P. H., Han, L. Y., Kamat, A. A., Arevalo, J. M., Takahashi, R., Lu, C., et al. (2006). Chronic stress promotes tumor growth and angiogenesis in a mouse model of ovarian carcinoma. *Nat. Med.* 12, 939–944. doi:10.1038/nm1447

Wang, H., Zhang, H., Sun, Z., Chen, W., and Miao, C. (2021). GABAB receptor inhibits tumor progression and epithelial-mesenchymal transition via the regulation of Hippo/YAP1 pathway in colorectal cancer. *Int. J. Biol. Sci.* 17, 1953–1962. doi:10.7150/ijbs.58135

Wang, Q., Liu, Y., Li, Z., Tang, Y., Long, W., Xin, H., et al. (2023). Establishment of a novel lysosomal signature for the diagnosis of gastric cancer with *in-vitro* and *in-situ* validation. *Front. Immunol.* 14, 1182277. doi:10.3389/fimmu.2023.1182277

Ware, J. J., VAN Den Bree, M., and Munafo, M. R. (2012). From men to mice: CHRNA5/CHRNA3, smoking behavior and disease. *Nicotine Tob. Res.* 14, 1291–1299. doi:10.1093/ntr/nts106

Xiao, B., Kuang, Z., Zhang, W., Hang, J., Chen, L., Lei, T., et al. (2019). Glutamate Ionotropic Receptor Kainate Type Subunit 3 (GRIK3) promotes epithelial-mesenchymal transition in breast cancer cells by regulating SPDEF/CDH1 signaling. *Mol. Carcinog.* 58, 1314–1323. doi:10.1002/mc.23014

Yan, L., Gong, Y. Z., Shao, M. N., Ruan, G. T., Xie, H. L., Liao, X. W., et al. (2020). Distinct diagnostic and prognostic values of gamma-aminobutyric acid type A receptor family genes in patients with colon adenocarcinoma. *Oncol. Lett.* 20, 275–291. doi:10.3892/ol.2020.11573

Zahalka, A. H., and Frenette, P. S. (2020). Nerves in cancer. *Nat. Rev. Cancer* 20, 143–157. doi:10.1038/s41568-019-0237-2

Zhang, H., Zhang, L., Tang, Y., Wang, C., Chen, Y., Shu, J., et al. (2019). Systemic screening identifies GABRD, a subunit gene of GABAA receptor as a prognostic marker in adult IDH wild-type diffuse low-grade glioma. *Biomed. Pharmacother.* 118, 109215. doi:10.1016/j.biopha.2019.109215

Zhang, P., Pei, S., Wu, L., Xia, Z., Wang, Q., Huang, X., et al. (2023). Integrating multiple machine learning methods to construct glutamine metabolism-related signatures in lung adenocarcinoma. *Front. Endocrinol. (Lausanne)* 14, 1196372. doi:10.3389/fendo.2023.1196372

Zhao, E., Xie, H., and Zhang, Y. (2020). Predicting diagnostic gene biomarkers associated with immune infiltration in patients with acute myocardial infarction. *Front. Cardiovasc Med.* 7, 586871. doi:10.3389/fcvm.2020.586871

Zheng, Y., Tian, H., Zhou, Z., Xiao, C., Liu, H., Liu, Y., et al. (2021). A novel immune-related prognostic model for response to immunotherapy and survival in patients with lung adenocarcinoma. *Front. Cell Dev. Biol.* 9, 651406. doi:10.3389/fcell.2021.651406

frontiers | Frontiers in Cell and Developmental Biology

TYPE Original Research
PUBLISHED 22 December 2023
DOI 10.3389/fcell.2023.1310397



OPEN ACCESS

EDITED BY
Yi Yao,
Renmin Hospital of Wuhan University, China

REVIEWED BY
Yan-Ruide Li,
University of California, Los Angeles, United States
Ana Salomé Pires,
University of Coimbra, Portugal

*CORRESPONDENCE
Pedro V. Baptista,
pmvb@fct.unl.pt
Alexandra R. Fernandes,
ma.fernandes@fct.unl.pt

†These authors have contributed equally to this work

RECEIVED 09 October 2023
ACCEPTED 27 November 2023
PUBLISHED 22 December 2023

CITATION
Valente R, Cordeiro S, Luz A, Melo MC, Rodrigues CR, Baptista PV and Fernandes AR (2023), Doxorubicin-sensitive and -resistant colorectal cancer spheroid models: assessing tumor microenvironment features for therapeutic modulation.
*Front. Cell Dev. Biol.* 11:1310397.
doi: 10.3389/fcell.2023.1310397



# Doxorubicin-sensitive and -resistant colorectal cancer spheroid models: assessing tumor microenvironment features for therapeutic modulation

Ruben Valente[1,2†], Sandra Cordeiro[1,2†], André Luz[1,2†], Maria C. Melo[1,2], Catarina Roma Rodrigues[1,2], Pedro V. Baptista[1,2*] and Alexandra R. Fernandes[1,2*]

[1]Associate Laboratory i4HB–Institute for Health and Bioeconomy, NOVA School of Science and Technology, NOVA University Lisbon, Caparica, Portugal, [2]UCIBIO–Applied Molecular Biosciences Unit, Department of Life Sciences, NOVA School of Science and Technology, NOVA University Lisbon, Caparica, Portugal

**Introduction:** The research on tumor microenvironment (TME) has recently been gaining attention due to its important role in tumor growth, progression, and response to therapy. Because of this, the development of three-dimensional cancer models that mimic the interactions in the TME and the tumor structure and complexity is of great relevance to cancer research and drug development.

**Methods:** This study aimed to characterize colorectal cancer spheroids overtime and assess how the susceptibility or resistance to doxorubicin (Dox) or the inclusion of fibroblasts in heterotypic spheroids influence and modulate their secretory activity, namely the release of extracellular vesicles (EVs), and the response to Dox-mediated chemotherapy. Different characteristics were assessed over time, namely spheroid growth, viability, presence of hypoxia, expression of hypoxia and inflammation-associated genes and proteins. Due to the importance of EVs in biomarker discovery with impact on early diagnostics, prognostics and response to treatment, proteomic profiling of the EVs released by the different 3D spheroid models was also assessed. Response to treatment was also monitored by assessing Dox internalization and its effects on the different 3D spheroid structures and on the cell viability.

**Results and Discussion:** The results show that distinct features are affected by both Dox resistance and the presence of fibroblasts. Fibroblasts can stabilize spheroid models, through the modulation of their growth, viability, hypoxia and inflammation levels, as well as the expressions of its associated transcripts/proteins, and promotes alterations in the protein profile exhibit by EVs. Summarily, fibroblasts can increase cell-cell and cell-extracellular matrix interactions, making the heterotypic spheroids a great model to study TME and understand TME role in chemotherapies resistance. Dox resistance induction is shown to influence the internalization of Dox, especially in homotypic spheroids, and it is also shown to influence cell viability and consequently the chemoresistance of those spheroids when exposed to Dox. Taken together

these results highlight the importance of finding and characterizing different 3D models resembling more closely the *in vivo* interactions of tumors with their microenvironment as well as modulating drug resistance.

KEYWORDS

**colorectal cancer, tumor microenvironment, heterotypic spheroid models, extracellular vesicles, chemoresistance, doxorubicin**

## 1 Introduction

Colorectal cancer (CRC) is one of the most prevalent and high-mortality cancers worldwide, being strongly linked to lifestyle (Keum and Giovannucci, 2019; Sawicki et al., 2021; Sung et al., 2021). Cancer cells establish crosstalk with different cellular and non-cellular components, such as stromal and immune cells, extracellular matrix (ECM), and extracellular vesicles (EVs), that together constitute the tumor microenvironment (TME) (Roma-Rodrigues et al., 2021). From all these components, cancer-associated fibroblasts (CAFs) are the most abundant cells and present a high level of heterogeneity and different functions, such as synthesis and remodeling of ECM, immunomodulation, production of growth factors, promoting angiogenesis and epithelial to mesenchymal transition (EMT) (Balkwill et al., 2012; Kalluri, 2016; Belli et al., 2018; Sahai et al., 2020; Maia and Wiemann, 2021; Mendes et al., 2021).

Cancer cells induce stromal cell migration, ECM remodeling, and expansion of the vasculature, whereas TME modulates tumor growth, invasion and metastasis, immune evasion, and response to therapy (Balkwill et al., 2012; Chen et al., 2015; Labani-Motlagh et al., 2020). During tumor growth, some tumor regions exhibit low supply of oxygen and nutrients, characterized by a hypoxic and acidic environment (Petrova et al., 2018; Sormendi and Wielockx, 2018; Aguilar-Cazares et al., 2019; Mendes et al., 2021). In these areas, tumor hypoxia and inflammation mechanisms are interconnected, being highly regulated by hypoxia-inducible factors (HIFs) and nuclear factor kappa B (NF-κB), which are responsible for activating genes associated with the promotion of tumor growth and progression and activation of cells within the TME (D'Ignazio et al., 2017; Belli et al., 2018; Petrova et al., 2018; Sormendi and Wielockx, 2018; Aguilar-Cazares et al., 2019; Roma-Rodrigues et al., 2019; Watts and Walmsley, 2019). Indeed, HIF-1 is a transcription factor composed of two subunits (HIF-1α and HIF-1β) that are constitutively expressed, but HIF-1α is only stabilized under hypoxic conditions (Petrova et al., 2018; Sormendi and Wielockx, 2018; Watts and Walmsley, 2019). HIF-1α/HIF-1β dimer activates the transcription of several target genes, which are involved in adaptive responses to hypoxia, including angiogenesis (such as *VEGFA*), glycolysis and erythropoiesis, ECM remodeling (such as *CTSD* and *MMP2*), cell survival, proliferation, apoptosis, and immune responses. (Sethi et al., 2008; Kumari et al., 2016). On the other hand, NF-κB plays an important role in several pathways, regulating downstream the expression of various genes/proteins involved in inflammation (like the pro-inflammatory cytokines IL-6 and TNF-α), immune responses, angiogenesis (such as vascular endothelial growth factor A, *VEGFA*), ECM remodeling (MMPs)

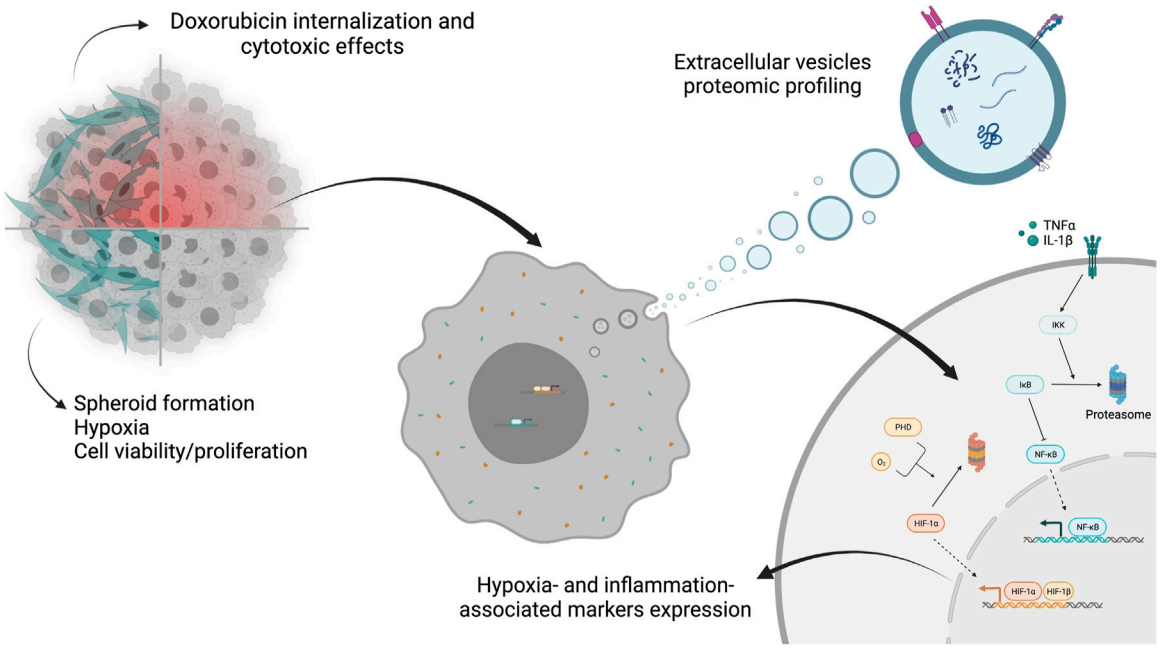


GRAPHICAL ABSTRACT

and cell survival (like *HIF1A* gene) (Hoesel and Schmid, 2013; Biddlestone et al., 2015; D'Ignazio et al., 2017; Giridharan and Srinivasan, 2018).

EVs are key elements in TME since they can serve as dynamic carriers of bioactive molecules (e.g., proteins, nucleic acids and lipids), and play a crucial role in intercellular communications between cancer cells and other components of the TME. Ultimately, by promoting the autocrine and paracrine communication between several TME components, EVs can transfer oncogenic molecules (Cocucci and Meldolesi, 2015; Tkach and Théry, 2016). These can influence TME progression and metastasis formation by promoting tumor cell proliferation, angiogenesis, invasion, and evasion from the immune system, ultimately contributing to the establishment of a pro-inflammatory and immunosuppressive microenvironment (Peinado et al., 2011; Zhang and Grizzle, 2011; Becker et al., 2016; Cavallari et al., 2020; Robado de Lope et al., 2023).

Considering the above, the development and characterization of cancer models that mimic tumors and TME *in vivo* are key to characterize the events leading to cancer progression and for the development of more efficient therapeutic strategies (Figure 1) (Hoarau-Véchot et al., 2018; Jensen and Teng, 2020; Zanoni et al., 2020). Despite having many limitations (e.g. inability to replicate the complexity of tumors and TME, which can lead to an inaccurate response of cells to therapy), two-dimensional (2D) cell cultures have been widely used because of their reproducibility, low cost, and easy manipulation (Hoarau-Véchot et al., 2018; Xin et al., 2019; Jensen and Teng, 2020; Zanoni et al., 2020). In contrast, animal models allow a systemic study of cancer mechanisms and therapy response, but are expensive, time-consuming, and raise ethical problems (Jensen and Teng, 2020; Zanoni et al., 2020).

In three-dimensional (3D) cell cultures, such as multicellular tumor spheroids and organoids, the formation of cell-to-cell and cell-matrix interactions allows a better replication of the complex *in vivo* tumor environment and constitutes a pivotal bridge between 2D cultures and animal models (Hoarau-Véchot et al., 2018; Xin et al., 2019; Jensen and Teng, 2020; Zanoni et al., 2020). In these models, cells are organized into three layers with different functions and metabolic activity: an external proliferative layer, an intermediate layer with quiescent and senescent cells, and a hypoxic and necrotic core (Hoarau-Véchot et al., 2018; Zanoni et al., 2020). Spheroids mimic tumor organization and some mechanisms, such as hypoxia and acidosis, due to the formation of gradients of nutrients, oxygen, metabolism products, and pH (Hoarau-Véchot et al., 2018; Roma-Rodrigues et al., 2019). Combination of different cell types allow further mimicking of TME (Hoarau-Véchot et al., 2018; Xin et al., 2019; Zanoni et al., 2020).

Herein, we assessed how the susceptibility or resistance to doxorubicin (Dox) of cancer cells is modulated by the presence of fibroblasts (important TME players) and impact in the response to Dox chemotherapy. We generated Dox sensitive and resistant 3D-spheroids, in homotypic or heterotypic with fibroblasts and characterized chemotherapy response via spheroid progression over time in term of size, cell number, viability, triggering of hypoxia and inflammatory response and the proteomic composition of secreted EVs.

# 2 Methods

## 2.1 Cell lines and cell culture maintenance

HCT116 colorectal carcinoma cell line (CCL-247) and Primary Dermal neonatal Fibroblasts (PCS-201-010) were obtained from American Type Culture Collection (ATCC®, United States). HCT116 doxorubicin-resistant cell line (HCT116-DoxR) was previously generated by culturing doxorubicin-sensitive HCT116 cells with increasing concentrations of doxorubicin (Dox, Sigma-Aldrich, United States), up to a maximum of 3.6 μM, as previously described (Pedrosa et al., 2018). Moreover, Pedrosa et al. (2018) were able to demonstrate, using Western blot, that the mechanism of resistance was due to the overexpression of P-glicoprotein (P-gP). Cells were cultured and maintained in Dulbecco's Modified Eagle Medium (DMEM, Gibco™ by Life Technologies, United States), supplemented with 10% heat-inactivated fetal bovine serum (FBS; Gibco™ by Life Technologies, United States) or exosome-depleted heat-inactivated FBS for EVs isolation, 100 U/mL penicillin and 0.1 mg/mL streptomycin, and incubated at 37 °C, with 99% humidity and 5% (v/v) $CO_2$. Fibroblast's culture medium was additionally supplemented with 5 ng/mL fibroblast growth factor (FGF, Sigma-Aldrich, United States). For maintaining Dox selective pressure, HCT116-DoxR cells were cultivated in the presence of 3.6 μM of Dox, unless otherwise stated.

## 2.2 Spheroids formation and monitoring

Spheroids were produced using commercially available ultra-low attachment plates (BIOFLOAT™ 96-well plates, faCellitate, Germany), as described by Roma-Rodrigues et al., 2020. HCT116/HCT116-DoxR homotypic and HCT116/HCT116-DoxR-Fibroblasts heterotypic spheroids were produced, keeping initial cell seeding at $5 \times 10^3$ cells per spheroid. Fibroblast seeding was made 72 h after initial cell seeding, at a HCT116/HCT116-DoxR: Fibroblasts cell ratio of 1:4, and culture medium was supplemented with 5 ng/mL of FGF.

Spheroids were monitored with CytoSMART™ Lux2 Live Cell Imager (Axion biosystems, United States) and Ti-U Eclipse Inverted microscope (Nikon Instruments, Japan).

## 2.3 Fibroblasts monitoring and cell count in 3D heterotypic spheroids

To track fibroblasts in heterotypic spheroids, fibroblasts were labeled with Cell Tracking Red Dye Kit (Abcam, United Kingdom), following manufacturer's instructions. Labeled fibroblasts were resuspended in phenol red-free culture medium and added to each well on the third day of growth of heterotypic spheroids. Fluorescence microscopy images were taken between the 3rd and 10th days of spheroid growth using CytoSMART™ Lux3 FL (Axion biosystems, United States).

## 2.4. Spheroids dissociation and cell count

To determine the cell number, spheroids were dissociated through a 30 min incubation with TrypLE™ Express (Gibco™ by

Life Technologies, United States), followed by a centrifugation at 500 x g for 5 min. Viable cells were counted via Trypan Blue exclusion method.

The ratio of fibroblasts/HCT116 cells was assessed by flow cytometry. Fibroblasts were labeled as described in Section 2.3 and added to the heterotypic spheroids at the 3rd day of growth. Spheroids were then disassembled as referred above, and cell populations were analyzed by Attune® Acoustic Focusing Flow Cytometer (Life Technologies, Carlsbad, United States) using BL2 channel (488 nm excitation and 574/26 nm emission) (HCT116 cells = Total cells–Red fluorescent Fibroblasts) and results were processed with Attune® Cytometric software. To validate total cell events, cells were also counted using trypan blue exclusion method.

## 2.5 Cell viability

Cell viability was assessed using CellTox™ Green Cytotoxicity Assay (Promega Corporation, United States), according to the manufacturer's recommendations. CellTox™ Green dye enters cells with compromised plasma membrane, binding to their DNA, which enhances its emitted fluorescence. Considering this, an increase in the green fluorescence correlates with a decrease of cell viability. Briefly, phenol red-free culture medium supplemented with CellTox™ Green dye 1x, for 24 h. As control, spheroids were fixed with 4% paraformaldehyde (positive control). Fluorescence images were acquired with Ti-U Eclipse inverted microscope (Nikon Instruments, Japan), with a FITC filter (excitation at 465–495 nm and emission at 515–555 nm).

## 2.6 Transmission Electron Microscopy

To analyze spheroids' internal structure and cell morphology, Transmission Electron Microscopy (TEM) was performed. TEM was provided as a service by Instituto Gulbenkian de Ciência, Portugal. Homotypic and heterotypic spheroids with 8 days of growth were fixed, dehydrated, and incubated with resin to form blocks. For each type of spheroid, sections were made at approximately one-half of the spheroids and subsequently analyzed by TEM.

## 2.7 Hypoxia detection

To evaluate hypoxia in spheroids, Image-iT™ Red Hypoxia Reagent (Invitrogen, United States) was used. Briefly, spheroids were incubated with phenol red-free DMEM with 5 µM Image-iT™ Red Hypoxia Reagent and 7.5 µg/mL Hoechst 33258, for 24 h at 37°C in a $CO_2$ incubator. As a negative control, spheroids were incubated with 0.1% (v/v) DMSO, under the same conditions. Fluorescence images were acquired with Ti-U Eclipse inverted microscope (Nikon Instruments, Japan). Images of the nucleus were obtained using a DAPI filter (excitation at 340–380 nm and emission at 435–485 nm), and images of hypoxia with a G-2A filter (excitation at 510–560 nm and emission >590 nm).

## 2.8 Inflammation and hypoxia markers expression

### 2.8.1 At gene level

Inflammation and hypoxia markers *HIF1A*, *RELA*, *VEGFA*, *MMP2*, *CTSD*, *IL6*, and *TNFA* genes expression was assessed by reverse transcription quantitative polymerase chain reaction (RT-qPCR). First, total RNA was extracted from 10 spheroids of each condition using SV Total RNA Isolation System (Promega Corporation, United States). Then, complementary DNA (cDNA) synthesis was achieved using NZY M-MulV First-Strand cDNA Synthesis Kit (nzytech, Portugal), following the manufacturer's recommendations. cDNA amplification was performed using Rotor-Gene (Qiagen, Germany), using NZYSupreme qPCR Green Master Mix (2x) (nzytech, Portugal). The primers sequences and qPCR cycling programs used to evaluate each gene expression are described in the (Supplementary Tables S1, S2).

The RT-qPCR was used as endogenous control. Relative levels of gene expression were quantified based on the $2^{-\Delta\Delta CT}$ method (Schmittgen and Livak, 2008), using the 18S ribosomal RNA (18S) gene as endogenous control (Schmittgen and Zakrajsek, 2000).

### 2.8.2 At protein level

Levels of hypoxia- and inflammation-associated proteins were assessed by Western blot. For protein extraction, 20 spheroids from each condition were collected, protein was extracted and quantified as previously described (Sequeira et al., 2021). 20 µg of protein were separated by an 8% (for HIF-1α, Cathepsin D, and MMP2) or 12.5% (for TNF-α, IL-6, VEGFA, and NF-κB p65) acrylamide-bisacrylamide gel (SDS-PAGE) and then transferred to PVDF membranes (GE Healthcare, United States) using a semi-dry system transfer (Bio-Rad, United States).

Membranes were blocked with a 5% (w/v) non-fat milk solution in TBST (50 mM Tris-HCl, 150 mM NaCl, pH 7.5% and 0.1% (v/v) Tween 20) during 2 h, at 4°C with agitation. Then membranes were blotted with anti-HIF-1α mouse antibody (1:300); anti-Cathepsin D rabbit antibody (1:1000); anti-MMP2 mouse antibody (1:750); anti-TNF-α mouse antibody (1:1000); anti-IL-6 rabbit antibody (1:1000), anti-VEGFA rabbit antibody (1:1000), and anti-NF-κB p65 rabbit antibody (1:500), with overnight incubation at 4°C, with agitation. All primary antibodies were purchased from abcam, United Kingdom. Afterwards, membranes were washed 3x with TBST for 5 min, and incubated with the respective secondary antibody conjugated with horseradish peroxidase (HRP) (anti-mouse IgG HRP-linked, 1:3000, or anti-rabbit IgG HRP-linked antibody, 1:2000, Cell Signaling, United States) for 1 h at RT, with agitation. Signal acquisition was achieved using WesternBright™ ECL substrate (Advansta, United States) and Hyperflm ECL (GE Healthcare, United States). Images of the films were obtained with Gel Doc™ EZ Imager (Bio-Rad, United States), and proteins were quantified by densitometry using ImageJ software. β-actin expression was used as a control to normalize the results, as previously described (Choroba et al., 2023).

## 2.9 Challenging with doxorubicin

### 2.9.1 Internalization of doxorubicin

Dox internalization was analyzed by fluorescence microscopy (Shah et al., 2017). Dox-sensitive spheroids were incubated with DMEM (without phenol red) supplemented with 8 µM Dox, and Dox-resistant

spheroids were incubated with 8 μM or 120 μM Dox, for 24 and 48 h, as described by Roma-Rodrigues et al., 2020. As a control, spheroids were incubated with 0.1% (v/v) DMSO (Sigma-Aldrich, United States), under the same conditions. Fluorescence images were acquired with Ti-U Eclipse inverted microscope (Nikon Instruments, Japan), with a G-2A filter.

### 2.9.2 Evaluation of doxorubicin cytotoxic effect

For 2D cell cultures, fibroblasts and HCT116 Dox-R cells were seeded at a density of 0.75 × $10^5$ cells/mL into 96 well-plates and incubated at 37°C and 5% (v/v) $CO_2$ for 24 h. After the 24 h of incubation, culture medium was replaced by fresh medium supplemented with Dox. As negative control, 0.1% (v/v) DMSO was used. Following a 24 h or 48 h incubation, cell viability was indirectly assessed with CellTiter 96® Aqueous One Solution Cell Proliferation Assay kit (Promega, Madison, United States) (Niles et al., 2008; Das et al., 2018). In metabolically active cells, mitochondrial dehydrogenases reduce 3-(4,5- dimethylthiazol-2-yl)-5-(3-carboxymethoxyphenyl)-2-(4-sulfophenyl)-2H-tetrazolium, inner salt (MTS) to formazan, whose absorbance can be measured at 490 nm in a microplate reader, Tecan Infinite M200 (Tecan, Mannedorf, Switzerland). Thus, formazan's absorbance is directly proportional to the number of viable cells. Using Prism 8 (GraphPad software), it is possible to determine the $IC_{50}$ (concentration that induces a 50% reduction in cell viability) of Dox for each cell line (Niles et al., 2008; Das et al., 2018).

For 3D cultures, spheroids from each culture were used on days 2, 5 and 7 of growth. At those days culture media was replaced by medium with 8 μM and 120 μM of Dox. Spheroids were then incubated for 24 h or 48 h in a humidified atmosphere at 37°C and 5% (v/v) $CO_2$ and, then medium was replaced by a mixture containing the MTS reagent and DMEM medium (20:100). Spheroids were incubated for another 6 h period and transferred into a 96-well plate with flat bottom to be analysed in the microplate reader Tecan Infinite M200 (Tecan, Mannedorf, Switzerland) (Choroba et al., 2023).

## 2.10 Image analysis

The ImageJ software was used to estimate Feret's diameter (Al-Thyabat and Miles, 2006), for fluorescence quantification and image processing, and for densitometry analysis of Western blot films, to quantify protein bands.

For fluorescence quantification, Corrected Total Cell Fluorescence (CTCF) was determined using Eq. 1. To normalize fluorescence by spheroids' size, the CTCF values were divided by the area of the spheroids.

Eq. 1. Corrected Total Cell Fluorescence (CTCF) calculation (Rueden et al., 2017).

$$\text{CTCF} = \text{integrated density of spheroid} - (\text{area of spheroid} \times \text{background mean fluorescence}) \quad (1)$$

## 2.11 Extracellular vesicles isolation and protein content analysis

EVs were isolated between the 8th and 10th days after spheroids formation using the Exoquick-TC™ kit (System Biosciences, United States), following manufacturer's instructions. Isolated EVs were characterized via TEM, provided as a service by Instituto Gulbenkian de Ciência, Portugal and Nanoparticle Tracking Analysis (NTA).

Protein content was measured using Pierce 660™ method (Thermofisher, United States) (Antharavally et al., 2009). Subsequently, RIPA solution (25 mM Tris-HCl, 150 mM NaCl, 1% NP40, 1% Sodium deoxycholate, 0.1% SDS) was added to 100 μg of EVs/protein and incubated for 5 min at 95 °C to allow EVs lysis. The protein content of EVs was analyzed by Liquid Chromatography Mass Spectrometry (LC-MS/MS), performed as a service by LAQV, FCT-NOVA.

### 2.11.1 Protein correlation analysis

The software STRING: functional protein association networks version 11.5 (available at https://string-db.org/) was used for protein correlation analysis, using the default settings to detect the most representative biological processes. Only biological processes with q-value <0.05 and the highest number of represented proteins were considered.

## 2.12 Statistical analysis

Statistical analysis was performed using the GraphPad Prism program (version 8.0.1). The Dunnett non-parametric two-way ANOVA test with multiple comparisons was used to compare different days in the same type of spheroid and the same day between different types of spheroids, by estimating the $p$-value. Results were considered statistically significant for $p < 0.05$.

Tukey's Honest Significant Difference test (with an FDR of 0.05) was performed in order to compare the expression of proteins detected in EVs from the different models of spheroids studied and the respective controls of 2D models.

# 3 Results and discussion

## 3.1 Tumor spheroid formation

The formation of tumor spheroids involves an initial step of tumor cell aggregation, followed by spheroids' condensation (Cui et al., 2017; Han et al., 2021), which may be easily monitored over time by brightfield microscopy (Figures 2A, B; Supplementary Videos S1, S2). Dox-sensitive (HCT116) and Dox-resistant (HCT116-DoxR) spheroids follow a similar global pattern of condensation regardless of the presence (heterotypic spheroids) or absence of fibroblasts (homotypic spheroids) (Figures 2B). There are some small differences: HCT116 spheroids condense as a whole (Figures 2B; Supplementary Video S1), showing a small contraction of their volume from 15 to 2.5 × $10^8$ $\mu m^3$, as previously demonstrated by Tartagni et al., 2023, whereas, HCT116-DoxR spheroids form several small cell aggregates close to each other, that overtime condense with less variation of their total volume (approximately from 12 to 5.8 × $10^8$ $\mu m^3$) (Supplementary Video S2).

Also, for the first couple of days, HCT116 homotypic spheroids grow at an approximate rate of 1.8 × $10^3$ cells/day, increasing to 5.8 × $10^3$ cells/day between the 2nd and the 10th day (Figures 2C).

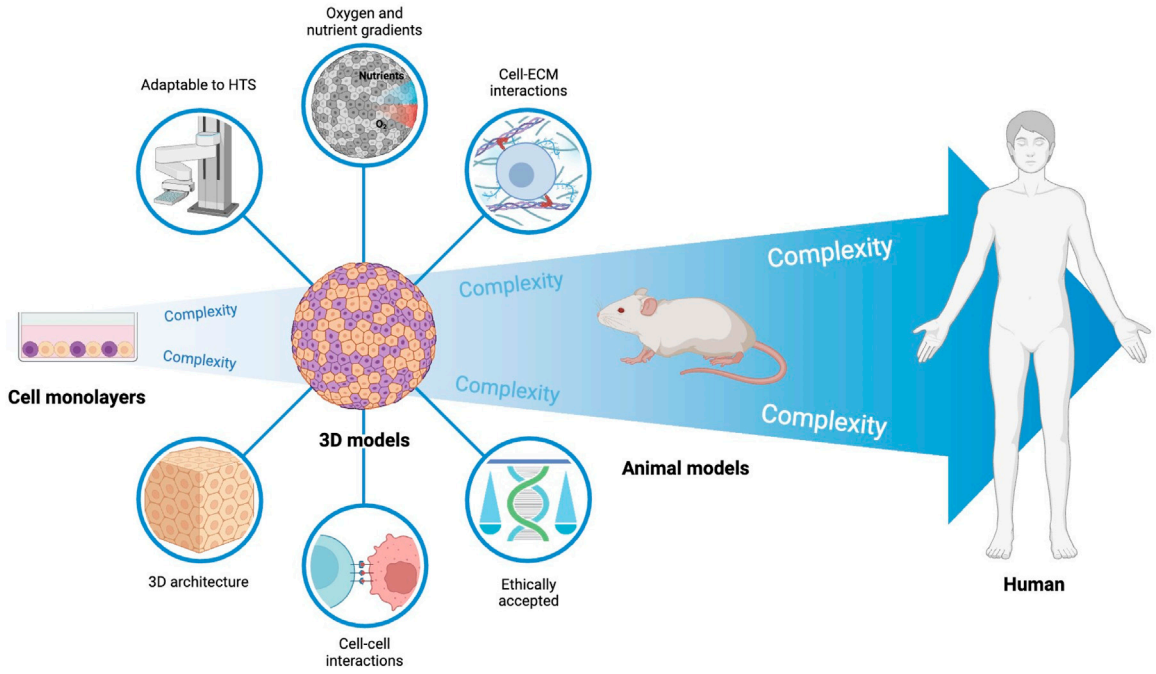


FIGURE 1
Cancer models used in preclinical research. Preclinical research in cancer heavily relies on cells cultured as monolayers. Despite being suitable for high throughput screening, these models can only mimic the *in vivo* tumor complexity to a low extent. On the opposite side, animal models have increased mimicking of the *in vivo* context, but are associated with high ethical issues, do not fully represent human context, and are not adapted to high-throughput screening. 3D human cell models and, particularly, heterotypic 3D models (tumor cells and fibroblasts used in this work) may recapitulate the *in vivo* human solid tumor phenomena to considerable levels, while being adapted to high-throughput screening necessary in pre-clinical research.

Conversely, In HCT116-DoxR homotypic spheroids, a consistent linear increase of cell density is observed (approximately $5.2 \times 10^3$ cells/day). These values support the longer lag phase for the first 2 days for HCT116 homotypic spheroids (Figures 2C). Around day 9, both types of spheroids reach a 10-fold increase of cells compared to the initial seeding (Figure 2). Similar condensation patterns are observed for heterotypic spheroids, where initial cell seeding is lower, which seems to demonstrate that its growth behavior is not dependent on cell number (Figures 2C). Altogether, these data hint at the involvement of critical and specific interactions between cells and cell types during spheroid progression.

## 3.2 Fibroblast tracking

In heterotypic spheroids, the interaction between fibroblasts and the already formed HCT116 or HCT116-DoxR spheroids becomes a critical point to understand the interplay between cell players. For this purpose, fibroblasts were previously stained with a cell tracker and spheroids formation monitored by fluorescence microscopy (Figure 3; Supplementary Videos S3, 4) (Massignani et al., 2010). Noteworthy, fibroblasts are not evenly distributed within HCT116 and HCT116-DoxR spheroids, but rather in clusters in a small area of the spheroid (Figures 3A). Moreover, flow cytometry data show that the ratio of fibroblasts/CRC cells is relatively stable overtime both in Dox-sensitive (Figures 3B) and resistant spheroids (Figures 3C), which highlights that the architecture of these spheroids is considerably stable.

In both heterotypic spheroids the proportion of fibroblasts show a slight increase in the first days of culture (from 17% to 36% in HCT116-DoxR and from 11% to 31% in HCT116), followed by an apparent stabilization of their proportion in different 3D cultures. As healthy cells, fibroblasts usually have a considerably low division rate when compared with HCT116 cancer cell line (Schäuble et al., 2012). Fibroblasts display doubling time of approximately 33 h (Supplementary Figure S1), whereas HCT116 and HCT116-DoxR cell lines duplicate their number in approximately 15 h and 18 h, respectively (Supplementary Figure S2, S3).

In the heterotypic spheroids under study, a different scenario is observed. The considerable differences in cell proliferation profiles of cancer and healthy cells decrease and fibroblasts' proportions stabilize after the 5th or 7th day in HCT116 and HCT116-DoxR heterotypic spheroids, respectively (Figures 3B, C). This indicate that, after the adaptation phase, HCT116/HCT116-DoxR cells and fibroblasts possess comparable growth kinetics, which might be associated with a modulation of fibroblasts behavior by tumor cells, as previously described for the *in vivo* cancerous growth (transition into cancer-associated fibroblasts, CAFs) (Fang et al., 2023).

## 3.3 Spheroids viability

Spheroids are important models to study cancer since their organization and structure more closely resemble *in vivo* tumors. In

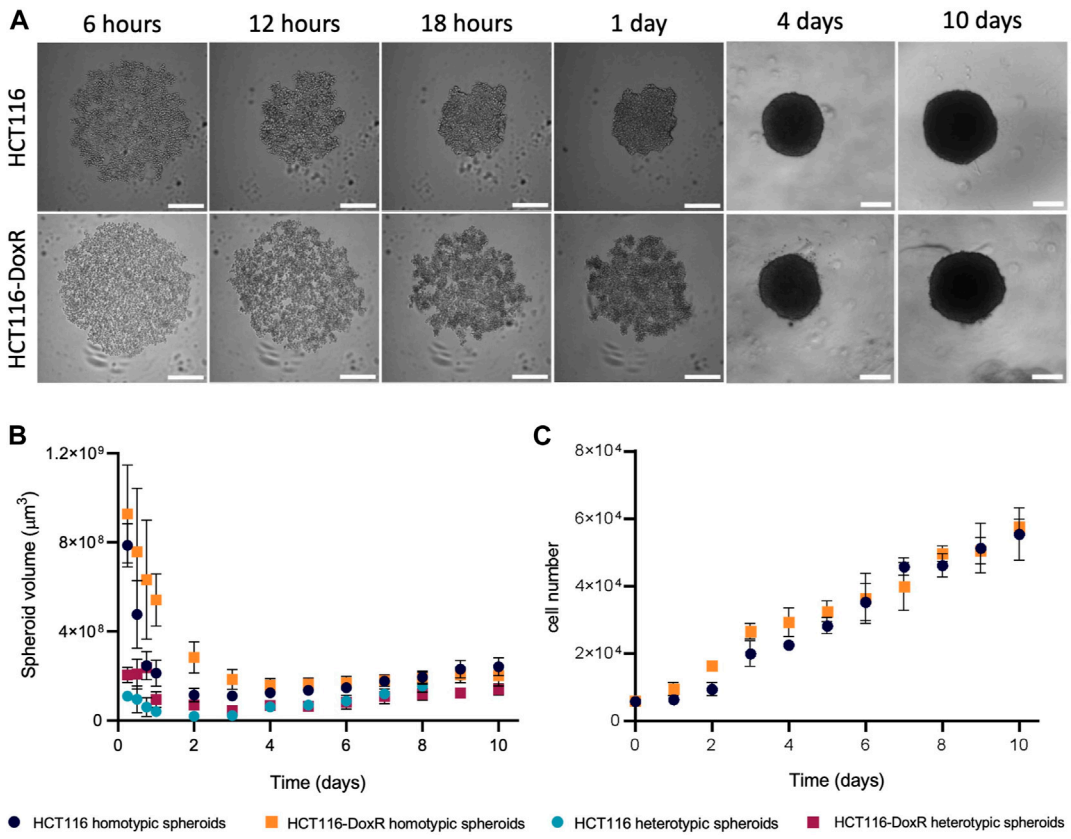


FIGURE 2
HCT116/HCT116-DoxR spheroids formation and growth over 10 days of culture. **(A)** Brightfield microscopy images of HCT116 and HCT116-DoxR homotypic spheroids; **(B)** evolution of HCT116 or HCT116-DoxR spheroids volume over 10 days of culture; and **(C)** evolution of HCT116 or HCT116-DoxR cell number over 10 days of culture. Scale bar corresponds to 300 μm. Data expressed as the mean ± SD of at least two independent assays.

spheroids with more than 500 μm in diameter, it is expected the formation of three cell layers: a highly proliferative external layer, a quiescent intermediate layer, and an internal necrotic core (Zanoni et al., 2020). While homotypic spheroids presented a diameter greater than 500 μm during the 10 days studied, the heterotypic spheroids diameter only exceeds 500 μm on the 5$^{th}$ day (as spheroids' condensation was observed only after day 2 or 3 for HCT116 and HCT116-DoxR heterotypic spheroids, respectively) (Figures 2B). Simultaneously, the viability of the cells involved the formation of the different layers of spheroids (external, middle layer and internal necrotic core) was accessed. For homotypic spheroids, cell viability was analyzed between the 2$^{nd}$ and 10th days of growth, while in heterotypic spheroids, cell viability was monitored from the 5$^{th}$ day onward (diameter >500 μm).

In HCT116 homotypic spheroids (Figures 4C, D; Supplementary Figure S4), cell death increases over time, but most significantly from day 9 to day 10 (Figures 4C). Between days 2 and 9, approximately 5%–10% of the cells within the spheroid show some degree of impairment and/or are nonviable (Figures 4D). This percentage almost doubles on day 10, being approximately 19%. Furthermore, fluorescence images reveal an accumulation of green (membrane compromised) cells at the center of spheroids, from day 6 onwards, corresponding to the formation of a necrotic core (Figures 4A).

In HCT116-DoxR homotypic spheroids, CTCF/area values are slightly higher on day 2 and 3 than on day 4 (Figure 4C). These variations may be associated to cell death concomitant to spheroid condensation, which may be related to the increase in cell number between the day 2 and 3 (Figures 2C) since CellTox probe is added to cells 24 h prior to analysis. From day 4 onwards, fluorescence increases over time, particularly from day 8 to day 9 (Figures 4C). In HCT116-DoxR spheroids, the percentage of cell death at day 10 is lower than the corresponding values in their HCT116 counterparts (Figures 4D). This observation may be correlated to the showed accumulation of dead cells at the core of HCT116 homotypic spheroids from the sixth day onwards (Supplementary Figure S5).

Homotypic spheroids, both Dox-sensitive or resistant have similar progressions of cell death levels (Figures 4C, D). It should be noted that the corrected fluorescence values are rather similar between both cultures (Figures 4C), but cell death levels exhibit a distinct progression (Figures 4D). Globally, cell death is more marked for the HCT116 homotypic spheroids than in HCT116-DoxR homotypic spheroids, especially on the 10th day of growth.

In heterotypic spheroids, between days 5 and 7, no considerable accumulation of dead cells at the core of the spheroids is observed, but some clusters can be seen in more peripheral areas (Supplementary Figures S6, S7). As shown in Figures 3A, upon

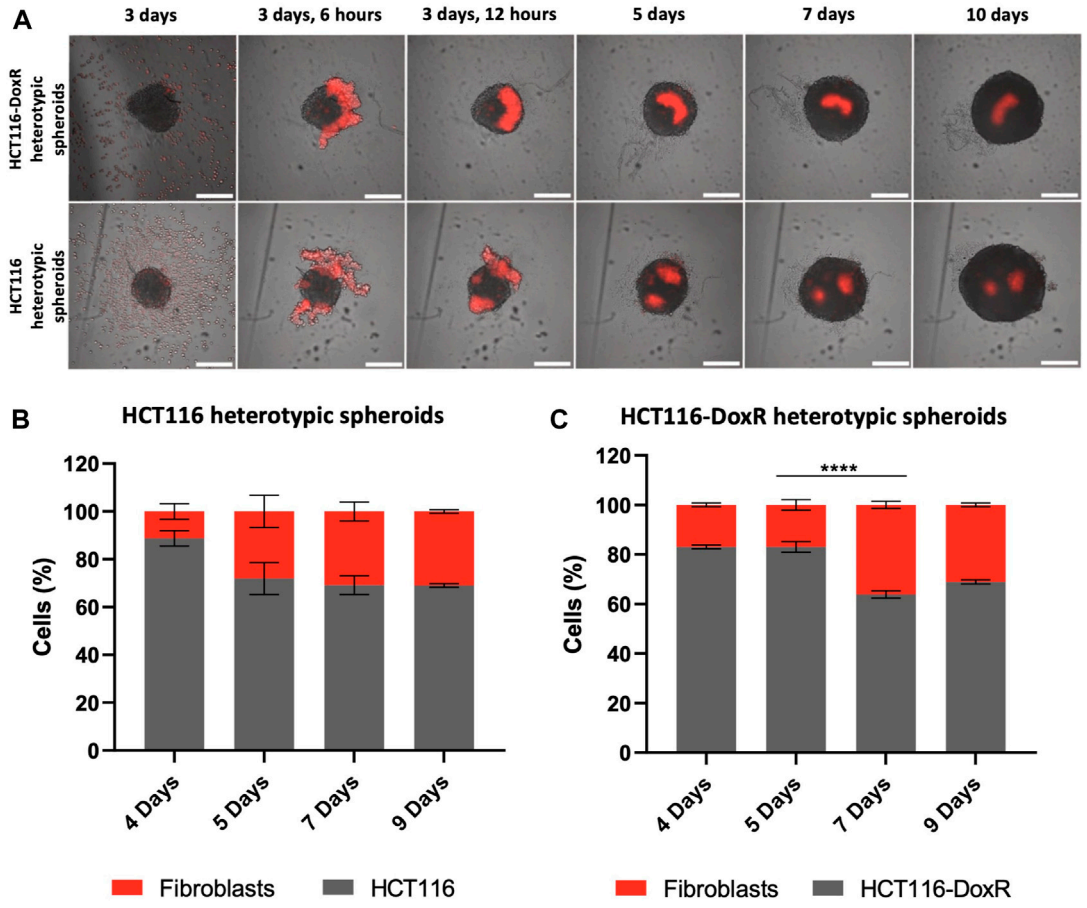


FIGURE 3
Cell tracking of fibroblasts in heterotypic spheroids. **(A)**–Fluorescence images of HCT116 and HCT116-DoxR heterotypic spheroids between days 3 and 10; Percentages of Dox-sensitive **(B)** or -resistant **(C)** cells and Fibroblasts in heterotypic spheroids at days 4, 5, 7, and 9. Fibroblasts were labeled with Cell Tracking Red Dye Kit - Longer cell staining, DMSO-free. Scale bars represent 300 μm. Data expressed as the mean ± SEM of at least two independent assays (**** $p < 0.0001$). Statistical analysis was performed by two-way ANOVA method.

addition to the pre-formed spheroids, fibroblasts tend to form clusters, that could be related to those masses of non-viable cells. Thus, the higher intensity of fluorescence between these days might correspond to fibroblasts that did not adapt to the spheroid structure and became non-viable. Fluorescence then decreases on day 8, when the previously observed fluorescence clusters disappear and an accumulation of dead cells at the center of spheroids occurs, originating the necrotic core (Figures 4B; Supplementary Figures S7A). From day 8 onwards, there is an increase in cell death (Figures 4F).

Cell death in HCT116 heterotypic spheroids (Figures 4F) is significantly higher on day 6–7 (approximately 20%), followed by a minimum value of 11% on day 8 and later an increase up to day 10. In HCT116-DoxR heterotypic spheroids (Figures 4F), the percentage of cell death is lower than in HCT116 heterotypic spheroids, as also observed for HCT116 and HCT116-DoxR homotypic spheroids. As for HCT116 heterotypic spheroids, cell death levels are higher on days 6 and 7 (approximately 17%), then decrease on day 8 to approximately 13%, and a second increase is observed until day 10. In heterotypic spheroids (Figures 4E, F), it is also possible to note similar profiles along time for HCT116 and HCT116-DoxR, regarding corrected fluorescence intensity values as well as for percentage of cell death. By comparing homotypic with heterotypic spheroids (Figures 4G–I), large differences in CTCF/area values and in the percentage of cell death are observed. In Dox-sensitive spheroids (Figures 4G, H), these differences are more significant between days 5 and 7, with higher levels of cell death for HCT116 heterotypic spheroids. Regarding Dox-resistant spheroids (Figures 4I, J), HCT116-DoxR heterotypic spheroids present higher levels of fluorescence and cell death, on all the days studied, except on day 10, where corrected fluorescence levels are higher in homotypic spheroids.

Altogether, these data agree with what is referred in literature, that in all types of spheroids a necrotic core is formed (Hari et al., 2019; Zanoni et al., 2020). Furthermore, Dox susceptibility or resistance does not seem to have a strong influence in the formation of this necrotic core. However, the presence of fibroblasts in heterotypic spheroids appears to result in an overall cell viability decrease. Indeed, when fibroblasts are inserted into a new environment - pre-formed HCT116/HCT116-DoxR spheroids, an adaptation phase is needed and some of them will adapt to the new environment, others will not and will die. Moreover, tumor cells have high demands of nutrients

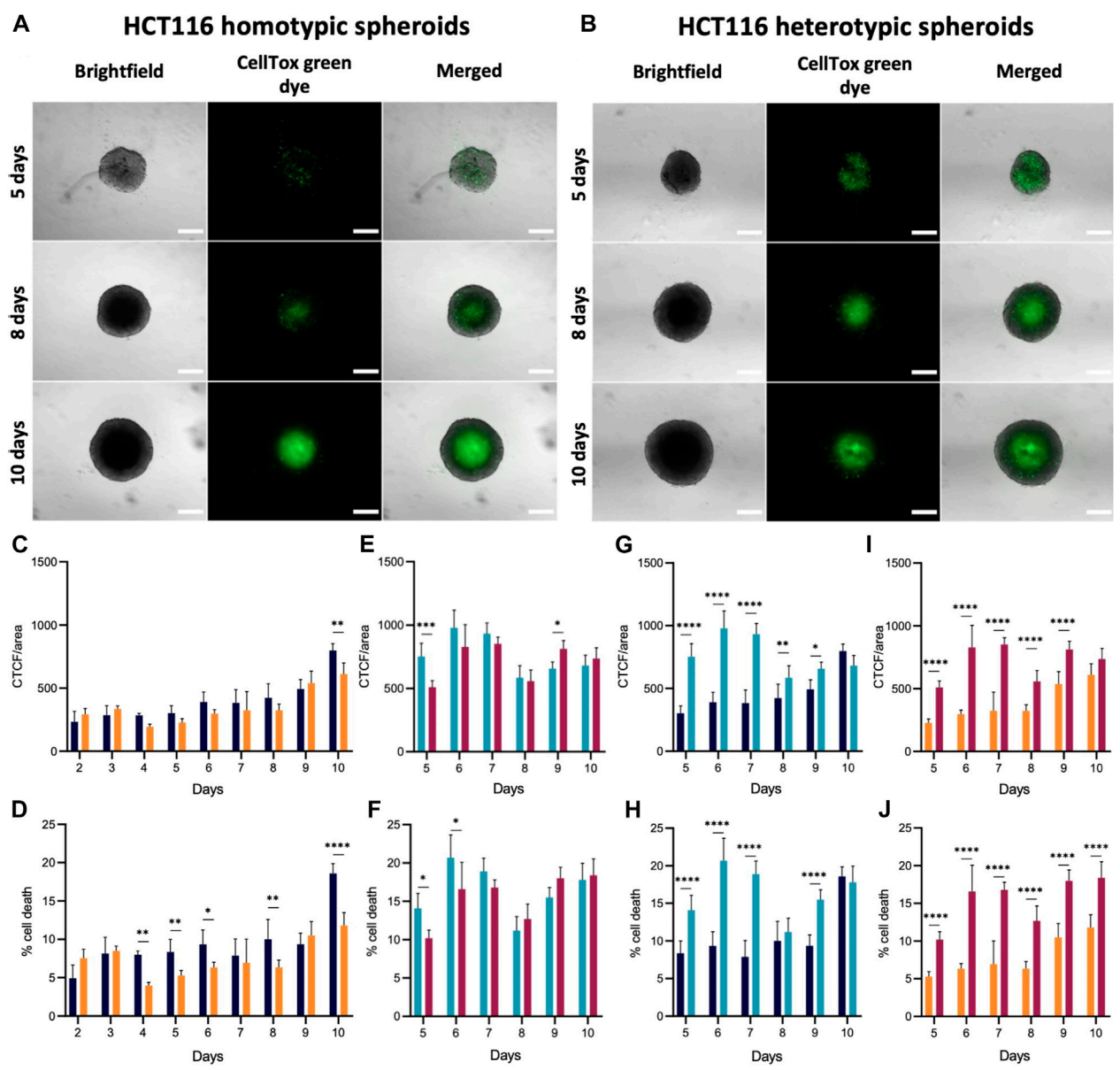


FIGURE 4
Cell viability in HCT116/HCT116-DoxR homotypic and heterotypic spheroids. **(A)** Fluorescence and brightfield microscopy images of HCT116 homotypic spheroids with 2, 6 and 10 days of growth. **(B)** Fluorescence and brightfield microscopy images of HCT116 heterotypic spheroids with 5, 8 and 10 days of growth. **(C–J)** CTCF/area values and percentage of cell death for HCT116/HCT116-DoxR homotypic and heterotypic spheroids between 2 and 10 days or between 5 and 10 days of growth, respectively. Spheroids were incubated with CellTox™ Green dye 1x for 24 h. Scale bars correspond to 300 μm. Data expressed as the mean ± SD of at least two independent assays. Statistical analysis was performed by two-way ANOVA method (*$p < 0.1$, **$p < 0.01$, ***$p < 0.001$, ****$p < 0.0001$).

and oxygen, due to the sustained activation of proliferation pathways (e.g. c-MYC) fostering the competition with fibroblasts for those requirements. The sustained activation of different cellular pathways in tumor cells also promote their metabolic adaptation, inhibition of cell death mechanisms, leading to an increased competitive behavior which trigger the elimination of rival non-adapted populations–in this case fibroblasts - via induction of apoptosis or other cell death mechanisms (Di Giacomo et al., 2017). These crosstalk between tumoral cells and fibroblasts that can adapt (usually referred to as cancer-associated fibroblasts (CAFs), allow them to activate ECM synthesis and microenvironmental remodeling, leading to stromal desmoplasia (Yang et al., 2023). CAFs have been described as having higher proliferative capabilities (Fang et al., 2023), as we also shown in our 3D models (Figure 3) where fibroblasts demonstrated proliferation rates like the ones observed for tumoral cells. This competition phenomenon that occurs between tumoral cells and fibroblasts and the adaptation of the latter to the new system, may explain the reduction of cell viability between the days 5 and 7 (corresponding to 2$^{nd}$ and 4$^{th}$ days after the addition of fibroblasts to the system). During this period, most fibroblasts will die and the ones that survive acquire a more aggressive phenotype, corresponding to CAFs.

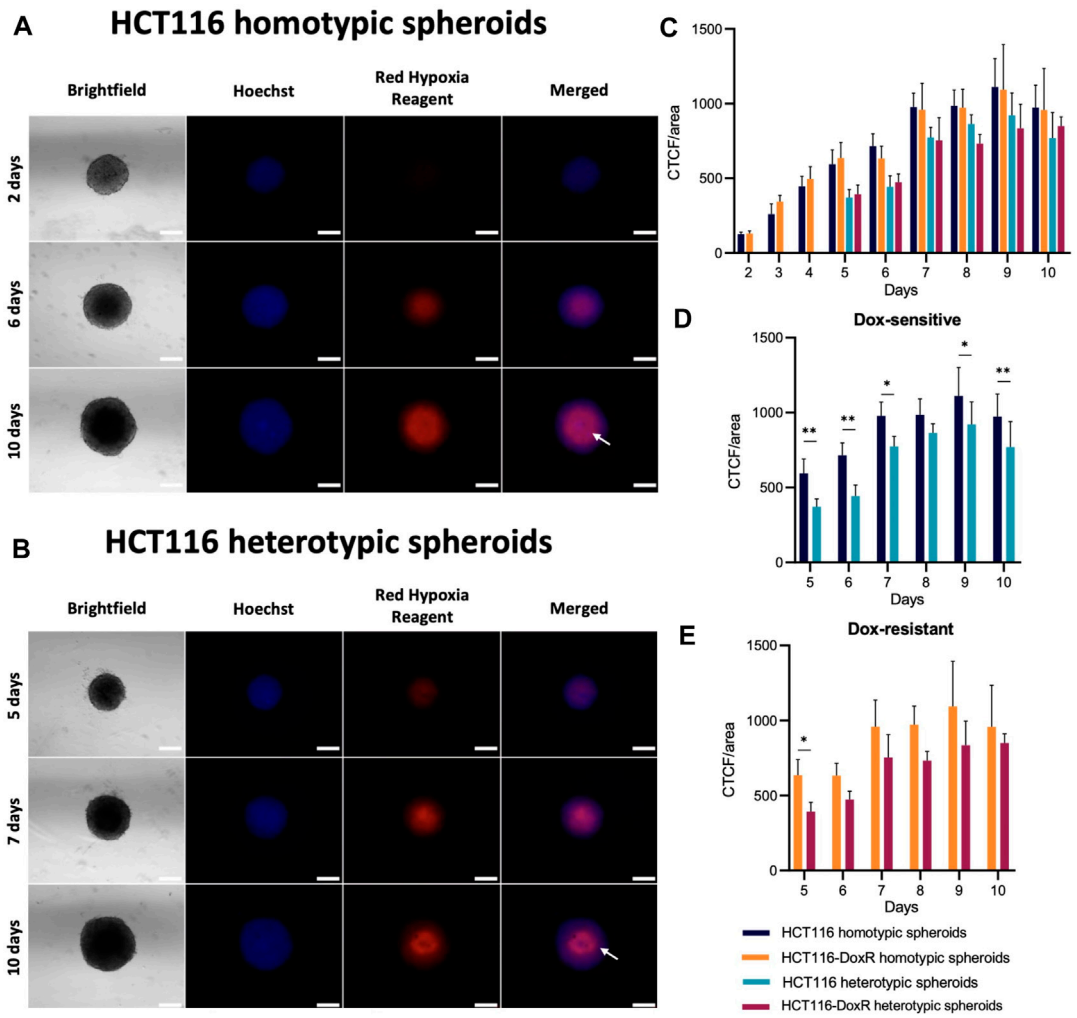


FIGURE 5
Presence of hypoxia in HCT116/HCT116-DoxR homotypic and heterotypic spheroids. **(A)** Fluorescence microscopy images of HCT116 homotypic spheroids with 2, 6, and 10 days of growth incubated with Hoechst 33258 and Image-iT™ Red Hypoxia Reagent for 24 h; **(B)** Fluorescence microscopy images of HCT116 heterotypic spheroids with 2, 6, and 10 days of growth incubated with Hoechst 33258 and Image-iT™ Red Hypoxia Reagent for 24 h; **(C)** CTCF/area values for hypoxia between 2 and 10 days of growth; **(D,E)** comparisons of the CTCF/area values for Dox-sensitive and -resistant spheroids, respectively. The white arrow on the 10th day indicates the reduction of hypoxia detected exactly in the center of the spheroid. Scale bar corresponds to 300 μm. Data expressed as the mean ± SD of at least two independent assays. Statistical analysis was performed by two-way ANOVA method (**$p < 0.01$).

## 3.4 Hypoxia

The analysis of spheroids' viability revealed an accumulation of dead cells in the center of all the studied cultures, that most probably correspond to a necrotic and hypoxic core. To better understand this phenomenon, spatial occurrence of hypoxia was assessed using Image-iT™ Red Hypoxia Reagent, a fluorogenic compound that enables the visualization of hypoxic regions (for $O_2$ concentrations below 5%) (Zhang et al., 2010). In fact, *in vivo* TME is characterized by oxygen levels between 0.3% and 4.2% (McKeown, 2014), so hypoxia regions detected using this probe might be correlated to *in vivo* data.

In all types of spheroids (Figure 5), hypoxia levels increase steadily until the sixth day of growth, as expected since spheroid' diameter increases in this period, surpassing the hypoxia threshold of approximately 400–500 μm (Riffle and Hegde, 2017; Zanoni et al., 2020). A significant rise in hypoxia levels is observed for day 6–7 (Supplementary Figure S8) that tends to steady up to the 10th day of growth. Interestingly, hypoxia at the core of homotypic spheroids occurs from 4$^{th}$ day onwards, while the accumulation of death cells occurs from the 6$^{th}$ day onward (Supplementary Figures S9, 10). This supports the idea that a necrotic core is formed as spheroids grow, due to the decrease of oxygen saturation and nutrient deficiency. In heterotypic spheroids, a similar pattern is observed. The development of a hypoxic core takes place on day 6, whereas the accumulation of dead cells in this region can be observed 2 days later, on the eighth day of growth (Supplementary Figure S11, S12). The hypoxia levels seem to have a similar trend over time for homotypic and heterotypic spheroids (Figures 5C). However, when comparing both types of spheroids (Figures 5C, D), higher levels of hypoxia are observed for homotypic spheroids on most days, although the differences are not as significant as those observed in cell viability (Figures 4G–J).

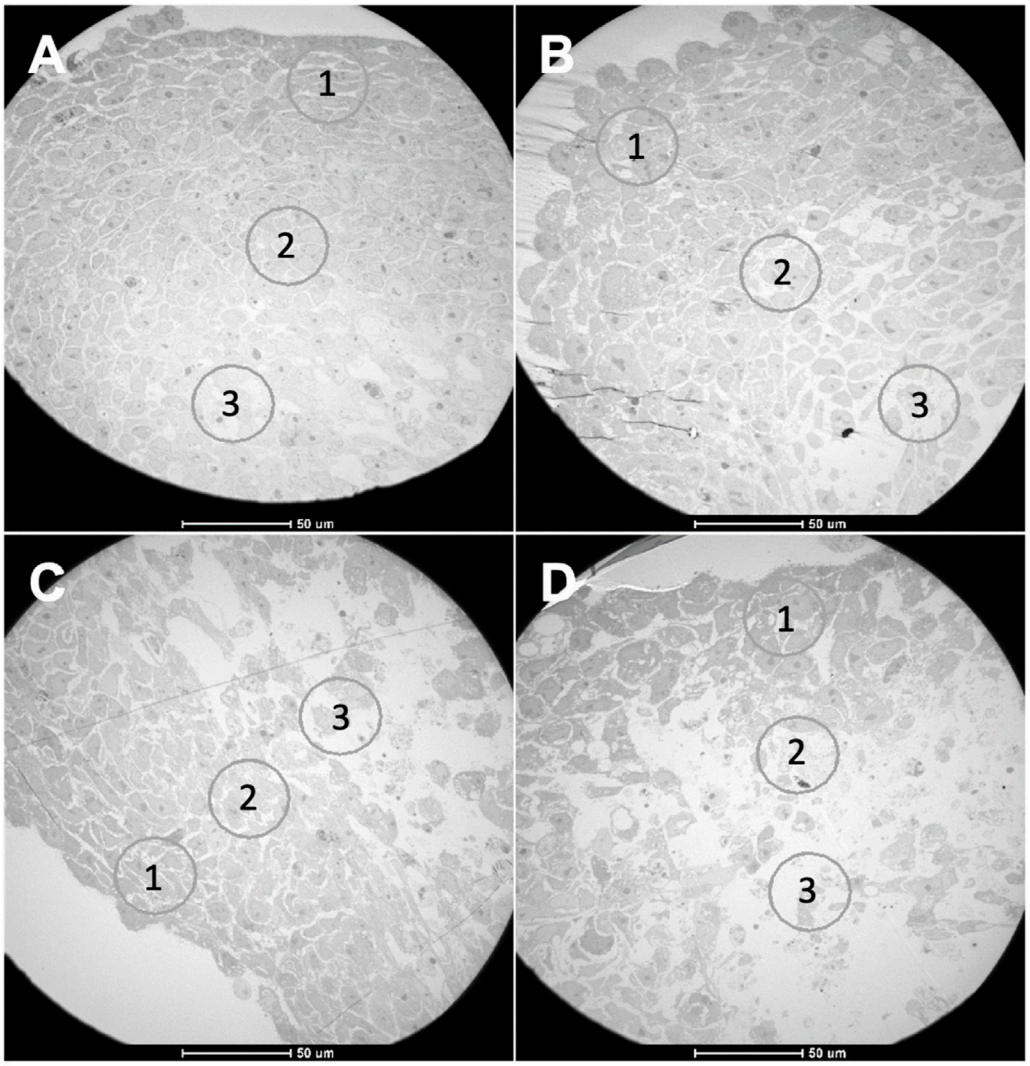


FIGURE 6
TEM images from spheroids with 8 days of growth. **(A)** HCT116 homotypic, **(B)** HCT116 heterotypic, **(C)** HCT116-DoxR homotypic, and **(D)** HCT116-DoxR heterotypic spheroids. Circles 1, 2, and 3 in each image correspond to areas from different cell layers: (1) outer layer, (2) intermediate layer, (3) core. Scale bars correspond to 50 μm.

Interestingly, in Dox-sensitive spheroids with 10 days of growth (Figures 5A, B), it is possible to observe a reduction in hypoxia levels at the spheroids' core. As Image-iT™ Red Hypoxia Reagent enables the detection of hypoxia in live cells, this may indicate that those regions are hollow, or only composed of dead/dying cells, thus not yielding fluorescence under hypoxia.

These results show that, although cell viability is lower in heterotypic spheroids, the levels of hypoxia tend to be higher in homotypic spheroids.

## 3.5 Transmission Electron Microscopy

During tumor progression, cancer cells are exposed to various types of stress, whether it be oxidative, metabolic, or mechanical, due to lack of nutrients, hypoxia, amongst others (Chen and Xie, 2018). To adapt and survive in this environment, maintaining high proliferation levels, cancer cells change their metabolism from oxidative phosphorylation to glycolysis (Warburg effect), even in the presence of oxygen (Petrova et al., 2018; Sormendi and Wielockx, 2018; Mendes et al., 2021). As such, during spheroid growth, it is expected that cells become organized in different layers due to oxygen, nutrients, and pH gradients (Hoarau-Véchot et al., 2018; Zanoni et al., 2020). Considering that all spheroids presented a necrotic and hypoxic core from day 8, we proceeded to assess the cell structure of these 3D models via TEM. Equatorial sectioning should allow to visualize any difference in strata of the spheroids.

Through the analysis of TEM images, it was possible to differentiate the three expected zones in all types of spheroids: a more external layer, an intermediate layer, and a necrotic core (Figure 6).

For each type of spheroid, images from the outer layer and the core were compared (Figure 7). In all types of spheroids, it was observed that the outer layer presented higher cell density, with a

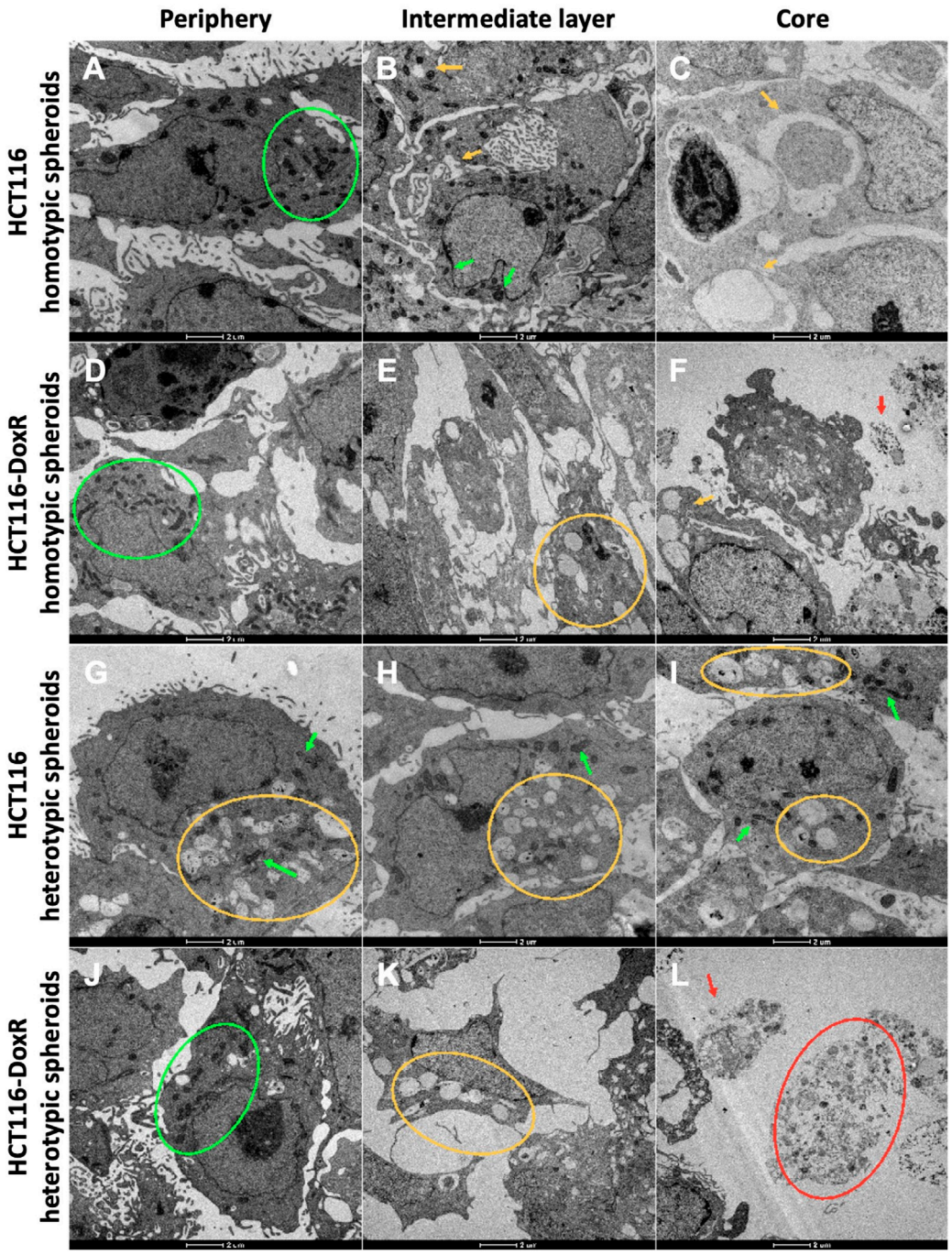


FIGURE 7
TEM images from the three cell layers of HCT116 homotypic **(A–C)**, HCT116-DoxR homotypic **(D–F)**, HCT116 heterotypic **(G–I)**, and HCT116-DoxR heterotypic **(J–L)** spheroids. For all spheroids, it was possible to identify three cell layers: **(A,D,G,J)** an outer layer, **(B,E,H,K)** an intermediate layer, and **(C,F,I,L)** a core. Green arrows and circles indicate the presence of mitochondria. Yellow arrows and circles point out vesicles. Red arrows and circles denote dead cells and cell debris. Scale bars correspond to 2 μm.

high number of mitochondria per cell. Mitochondria are essential organelles involved in ATP production and regulation of cell signaling, cell death, and oxidative stress, being important in the adaptation of cells to the environment (Vyas et al., 2016).

As expected, cells in the inner layer presented higher levels of stress with a lower cell density and showing numerous vesicles. These vesicular bodies may correspond to autophagic vesicles. A growing number of cellular debris is also observed that should correspond to a necrotic core.

However, in HCT116 heterotypic spheroids (Supplementary Figure S13), though cell density was higher in the outer layer for the other types of spheroids, cells in this layer already present several vesicles, and in the inner layer it was also possible to observe a high number of mitochondria per cell. Since CAFs play an important role

in tumor progression and cell survival (Kalluri, 2016; Sahai et al., 2020; Maia and Wiemann, 2021), fibroblasts in HCT116 heterotypic spheroids might be improving cell survival in the inner layers. However, the same is not observed for HCT116-DoxR heterotypic spheroids (Supplementary Figure S14).

TEM images from the outer layer, intermediate layer, and core were also compared for the four types of spheroids (Figure 7). Although no significant differences were observed in cell count between Dox-sensitive and resistant homotypic spheroids at day 8 (Figures 2C), TEM micrographs demonstrated that Dox-resistant spheroids (Figures 7D–F; Supplementary Figure S15) presented lower cell density and more cell debris in the inner layers compared to their sensitive counterparts (Supplementary Figure S16). This could imply that the acquired resistance in Dox-resistant spheroids somehow affects the ability of cells to better adapt to stress, such as the observed in the inner layers of the spheroids, where hypoxia levels are higher.

The lower number of mitochondria in cells at the core could be a consequence of mitophagy - a process responsible for the degradation of mitochondria when they are damaged or dysfunctional or when cells are under stress conditions, such as hypoxia or nutrient deficiency (Vara-Perez et al., 2019; Song et al., 2022). Under hypoxic conditions, the transcription factor HIF1 activates the expression of several genes involved in the mitophagy pathway, coding for glucose transporters and glycolytic enzymes (Petrova et al., 2018; Vara-Perez et al., 2019; Watts and Walmsley, 2019). Abnormal mitophagy in cancer is associated with tumor growth and cancer metabolic reprogramming (Vara-Perez et al., 2019; Song et al., 2022).

## 3.6 Gene expression and protein levels of hypoxia and inflammation effectors

Within the TME, hypoxia and inflammation are usually associated (D'Ignazio et al., 2017). Hypoxia can promote inflammation through the activation of TME cells and induction of pro-inflammatory agents release (Biddlestone et al., 2015). On the other hand, inflammation can elevate the hypoxia levels by impairing oxygen diffusion within tumor tissue (Biddlestone et al., 2015).

Therefore, we assessed the expression of genes and respective proteins involved in hypoxia and inflammation in tumor spheroids, namely the main regulator of hypoxia–HIF-1, and the main regulator of inflammation and cell survival–NF-κB, and their target genes (Figure 8).

Normalized expression (Figures 8B; Supplementary Figure S17) shows a downregulation of *CTSD*, *IL6*, and *MMP2* genes in homotypic spheroids, while in heterotypic spheroids there is an overexpression of *IL6* (between the 5th and 7th days of growth) and *MMP2* (at all the analyzed time points), which may occur due to the increased complexity of the 3D cultures after the addition of fibroblasts. Indeed, fibroblasts within TME are important modulators of cytokines and metalloproteinases release during tumor progression (Liu et al., 2019). Nevertheless, in HCT116 homotypic spheroids it is possible to observe that the remaining genes under study (*VEGFA*, *RELA*, *HIF1A and TNFA)* are overexpressed (Figures 8B; Supplementary Figure S17). The expression of the *HIF1A* gene in this type of spheroids demonstrates a first peak at the 4$^{th}$ day of growth (corroborating what is depicted in Figure 4, that shows an increase in hypoxia). Regarding HCT116-DoxR homotypic spheroids, an overexpression of the *HIF1A* gene was detected for all time points and for *TNFA* gene the overexpression was observed after 5, 6, 7 and 10 days of growth.

*RELA*, *VEGFA* and *HIF1A* genes show similar patterns of expression in HCT116 heterotypic as in its homotypic spheroids' counterparts, with *HIF1A* expression being slightly higher in heterotypic spheroids than in homotypic spheroids. *HIF1A* expression shows a peak at day 5 and its effect is observed at day 6, where hypoxia levels increase (Figure 5, Figures 8B).

*TNFA* gene is mostly downregulated in heterotypic spheroids. These observations may indicate that the gene that is triggering both inflammation and hypoxia signaling pathways is the *HIF1A* gene, which is able to influence the expression of NF-κB subunits and associated molecules (Biddlestone et al., 2015). On the other hand, in HCT116-DoxR heterotypic spheroids an overexpression of the *TNFA* and *HIF1A* genes occurs, but a low expression of *RELA* and *VEGFA* genes is observed. In this case, *HIF1A* gene may be negatively influencing the expression of *RELA*, preventing its expression and activation of the signaling pathway, as previously demonstrated by (Szatkowski et al., 2020). *HIF1A* exhibits a peak of expression at day 6, when hypoxia was first detected (Figures 8B; Supplementary Figure S11, S12).

The expression of the correlated proteins (as effectors of the gene expression) was also assessed through WB (Figures 8C; Supplementary Figure S18). Although hypoxia was detected in all types of spheroids by fluorescence microscopy (Figure 5; Supplementary Figures S9–S12), HIF-1α and TNF-α proteins were only detected in a few time points, which might be due to the short half-life of these proteins (Simó et al., 2012; Masoud and Li, 2015). For the other proteins, bands with the expected size were obtained (Supplementary Table S3). However, in heterotypic spheroids, only the light chain of Cathepsin D was detected.

Regarding HIF-1α and TNF-α expression, when detected, HIF-1α expression is lower than its basal expression, which may be due to its short half-life, as mentioned before. On the other hand, TNF-α only presents higher values than the basal expression in HCT116 homotypic spheroids at days 4 and 7, and a downregulation was observed at the remaining time points.

In HCT116 homotypic spheroids, two peaks of TNF-α expression levels were detected, as mentioned before, which are consistent with the progression of the NF-κB expression levels. After day 4, it is possible to observe that NF-κB expression starts to increase, as well as for VEGFA expression. This may indicate that VEGFA is one of the main target genes of NF-κB (Hu et al., 2016), since it is the first to respond to its increase. After the peak of NF-κB expression at day 7, it decreases to values near to the basal levels. On day 9, it is possible to observe an increase of VEGFA, IL-6, MMP2 and Cathepsin D levels. All these proteins play a role in the NF-κB signaling pathway (Hoesel and Schmid, 2013; D'Ignazio et al., 2017; Giridharan and Srinivasan, 2018), therefore it may be hypothesized that this increase of expression is a delayed response to the peak of NF-κB at day 7. The gene expression pattern exhibited by HCT116 homotypic spheroids shows the induction of the NF-κB signaling pathway through *TNFA*, with *VEGFA* also being expressed, which is mirrored at the protein level.

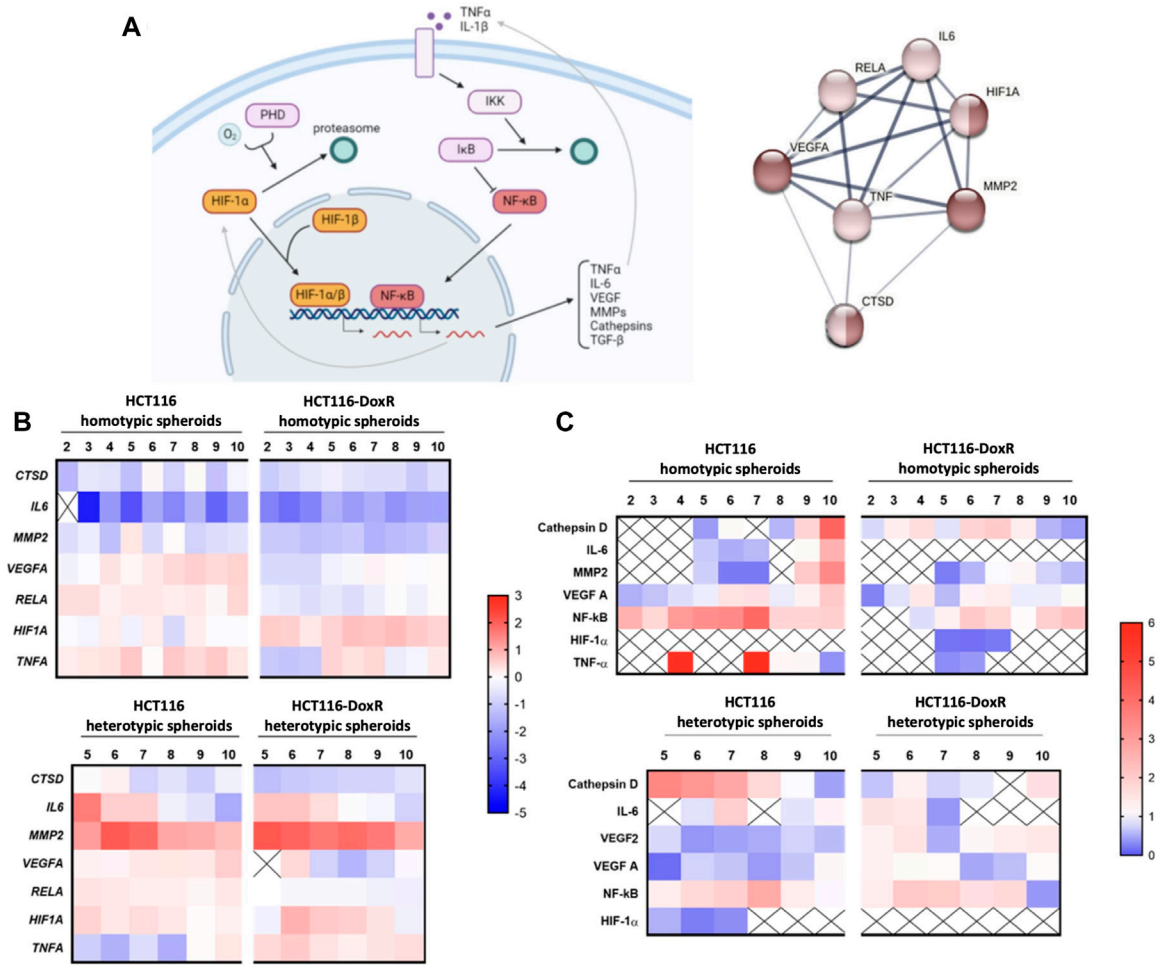


FIGURE 8
**(A)** HIF-1 and NF-κB signaling pathways of hypoxia and inflammation processes, respectively, in cancer. Dark brown nodes represent proteins involved in hypoxia response and light brown nodes identify the proteins related to inflammatory response. Image created with BioRender.com and STRING software. **(B)** Gene expression of *HIF1A*, *RELA*, *VEGFA*, *MMP2*, *CTSD*, *IL6* and *TNFA* in different types of spheroids, HCT116 homotypic and heterotypic spheroids and HCT116-DoxR homotypic and heterotypic spheroids, for 2–10 days of growth, in the case of the homotypic spheroids, and 5–10 days of growth, in the case of heterotypic spheroids. Gene expression was analyzed via the $2^{-\Delta\Delta CT}$ method, and all data was normalized to the gene expression of its correspondent 2D culture (HCTT116 or HCT116-DoxR cell lines). The value 0 is considered as basal expression and the red color represents overexpression and the blue color under expression of the genes. Data is expressed as the means of at least two independent biological assays with three technical replicates each. **(C)** Protein levels of HIF-1α, TNF-α, NF-κB p65, IL-6, VEGFA, MMP2 and Cathepsin D in different types of spheroids, HCT116 homotypic and heterotypic spheroids and HCT116-DoxR homotypic and heterotypic spheroids, for 2–10 days of growth, in the case of the homotypic spheroids, and 5–10 days of growth, in the case of heterotypic spheroids. All data was normalized to the protein expression of its correspondent 2D culture (HCTT116 or HCT116-DoxR cell lines). Value 1 is considered as basal expression, and the red color represents overexpression and the blue color under expression of the proteins. Data is expressed as the means of at least two independent biological assays with three technical replicates each.

When analyzing HCT116-DoxR homotypic spheroids protein expression, TNF-α was detected at day 5 and 7, i.e. the same days for gene expression peaks. HIF-1α was detected between days 5 and 7, which also corresponds to gene expression peak. Following TNF-α and HIF-1α peaking, NF-κB and VEGFA proteins also show an increase of expression levels, confirming the interplay between these proteins. In this protein profile it is also possible to observe that Cathepsin D shows higher levels of expression at days 4, 6 and 7 of growth. Cathepsin D is associated with one of most known programmed cell death processes, apoptosis, and is also known to be an anti-angiogenic protein (Yoshida et al., 2005; Sheikh et al., 2010). *HIF1A* gene overexpression corroborates the fact that these spheroids are under hypoxia conditions (see Supplementary Figure S10, where hypoxia levels increase after 4 days of growth). Under hypoxia, Cathepsin D overexpression can be associated with the inhibition of VEGFA (Yoshida et al., 2005), which is expected to be highly overexpressed after activation of the NF-κB signaling pathway. Cathepsin D can be an inducer or inhibitor of the apoptotic process. It has been reported that, under hypoxic conditions, it mostly works as an apoptotic inducer (Sheikh et al., 2010). This may explain the accumulation of dead cells and cell debris at the core of HCT116-DoxR homotypic spheroids as of day 6 (Figures 4C, D), when the peak of Cathepsin D occurred.

In HCT116 heterotypic spheroids, Cathepsin D is the first to show a definite increase in its expression, with a peak at day 5, which then decreases to basal levels at day 9. Once again, it is possible that

Cathepsin D is inhibiting the VEGFA protein, since *VEGFA* transcript is being synthesized and VEGFA protein has low levels of expression. It is also possible that Cathepsin D is promoting cell death mechanisms, as explained before, since an increase of cell death was observed (Figures 4A) 3 days after its peak and 2 days after hypoxia levels had been detected (Supplementary Figure S11). HIF-1α is detected in the time points correspondent to its gene expression peaks, after which an increase of NF-κB is noted until it reaches its peak at day 8. Interestingly, a peak of IL-6 occurs at day 7, one day before the peak of NF-κB and 2 days after its gene expression peak. These results seem to indicate that HIF-1α is the responsible for the induction of NF-κB and IL-6, and the latter being also capable of promoting the increase of NF-κB expression (Chung et al., 2017).

In HCT116-DoxR heterotypic spheroids, NF-κB is slightly overexpressed, reaching its peak between days 6–7. The same was not observed for *RELA* expression, which is always near to basal levels. It can also be observed that IL-6 and VEGFA exhibit a decreasing trend, with their peak at day 5, 1 day before the peak of NF-κB. IL-6 might be one of the main triggers of NF-κB increased expression (Chung et al., 2017), even though *HIF1A* and *TNFA* genes demonstrated to be overexpressed. MMP2 presents a peak on day 6 and another on day 10, while Cathepsin D remains close to basal levels. As Cathepsin D, MMP2 can also be associated with induction of apoptosis (Ben-Yosef et al., 2005; Seo et al., 2009). In fact, all these cultures exhibited an increase of cell death at day 8, i.e., 2 days after the peak of MMP2, which supports the influence of this protein in cell death in these spheroids.

Globally, we verified that NF-κB seemed to trigger VEGFA expression and that heterotypic spheroids express more MMP2 and IL-6 than homotypic spheroids. Concerning MMP2, it is not possible to draw many conclusions regarding protein levels, but for IL-6 protein levels in HCT116 spheroids, it was also verified that its levels decrease over time and are initially higher in heterotypic spheroids. Since stromal cells, namely fibroblasts, are the major contributors to high IL-6 and MMP2 synthesis (Liu et al., 2019), these results demonstrate that the presence of fibroblasts in the heterotypic spheroids influence protein expression. MMP2 and Cathepsin D in the different types of spheroids can promote cell death under hypoxic conditions.

It was also verified that HCT116 spheroids exhibit higher levels of expression of the effector protein related to hypoxia and inflammation. On the other hand, HCT116-DoxR spheroids show higher expression of precursor proteins. These observations suggest that when comparing the HCT116 and HCT116-DoxR spheroids the HCT116-DoxR spheroids have activated the hypoxia and inflammation pathways prior to the HCT116 spheroids.

Together, these results demonstrate the enormous potential of 3D models to recapitulate *in vivo* processes, such as hypoxia and inflammation, paramount in the TME context (D'Ignazio et al., 2017). Therefore, spheroids are great models to better understand drug resistance within tumors and the active pathways for tumor growth and development.

## 3.7 EVs protein content analysis

So far, a very good correlation has been obtained between gene and protein expression of hypoxia and inflammation biomarkers in these tumor spheroids, making them highly attractive as simplified models of the TME. Still, there are several other relevant indicators involved in cell modulation that ought to be analyzed. For example, EVs have emerged as pivotal players in intercellular communication and the regulation of diverse biological processes, influencing cellular behavior and modulating the TME (Roma-Rodrigues et al., 2014; Tao and Guo, 2020).

Prior to proteomic analysis of EVs content, EVs released by HCT116 and HCT116-DoxR both homotypic and heterotypic spheroids, as well as by 2D cultures of HCT116, HCT116-DoxR and Fibroblasts, were firstly characterized via TEM and NTA (Supplementary Figure S19, S20 and Supplementary Videos S5, S6).

Proteomic analysis of the EVs content has identified 24 relevant proteins (Figures 9A). EVs isolated from fibroblasts monolayers show a prevalence of proteins associated with the ECM such as fibronectin (FN1) and thrombospondin 1 (THBS1), whereas HCT116-DoxR 3D culture-derived EVs have a predominance of proteins linked to the cytoskeleton, such as various cytokeratins like KRT1, KRT9, and KRT10.

A comparison between EVs isolated from 2D and 3D models (Figures 9B, C; Supplementary Table S4) revealed significant changes to protein levels, namely for proteins associated with ECM organization and cell structure, whose levels were elevated in homotypic spheroids. This might be attributed to the way cells grow - in 2D culture, cells grow on flat surfaces, which do not fully recapitulate the complex three-dimensional environment found *in vivo*. As result, certain cell structure functions, including ECM remodeling and cytoskeletal dynamics, might be altered diverge from the 3D spatial organization, with more relevant cell-cell and cell-ECM interactions. These cell-matrix and cell-cell interactions in 3D models might trigger differential expression of proteins involved in cell structure, allowing adaptation to the surrounding environment (Duval et al., 2017; Kapałczyńska et al., 2018).

A higher expression of proteins associated with cell death was observed in EVs isolated from HCT116-DoxR homotypic spheroids compared to those isolated from 2D models. This can be associated to the mechanical stress during growth in a 3D confining matrix where oxygen and nutrient gradients may lead to a suppression of cell proliferation and induction of cell death, namely by necrosis in cells located at the center of the 3D structure–necrotic core (Cheng et al., 2009; Costa et al., 2016). Also, levels of caspase recruitment domain-containing protein 8 (CARD8) appear to be reduced in EVs derived from the 3D models, which may indicate a cumulative effect on programmed cell death, since CARD8 participates in a mechanism that negatively regulates the activation of the NF-κB signaling pathway commonly involved in cell proliferation and inhibition of apoptosis (Razmara et al., 2002; Escárcega et al., 2007).

A comparison between the proteomic profiles of the EVs isolated from heterotypic and homotypic spheroids revealed altered expression of proteins associated with cell structure, either in cytoskeleton or in ECM (Figures 9D, E; Supplementary Table S5). It can be observed that a group of those structural proteins may also be involved with modulation of the PI3K-AKT pathway, a signaling cascade involved in cell growth regulation, survival, metabolism and migration, which is aberrantly activated in cancer (Fruman et al., 2017; Molinaro et al., 2019; Hopkins et al., 2020). The increased expression of proteins like THSB1 and FN1 in EVs from heterotypic spheroids could have potential indirect implications in PI3K-AKT

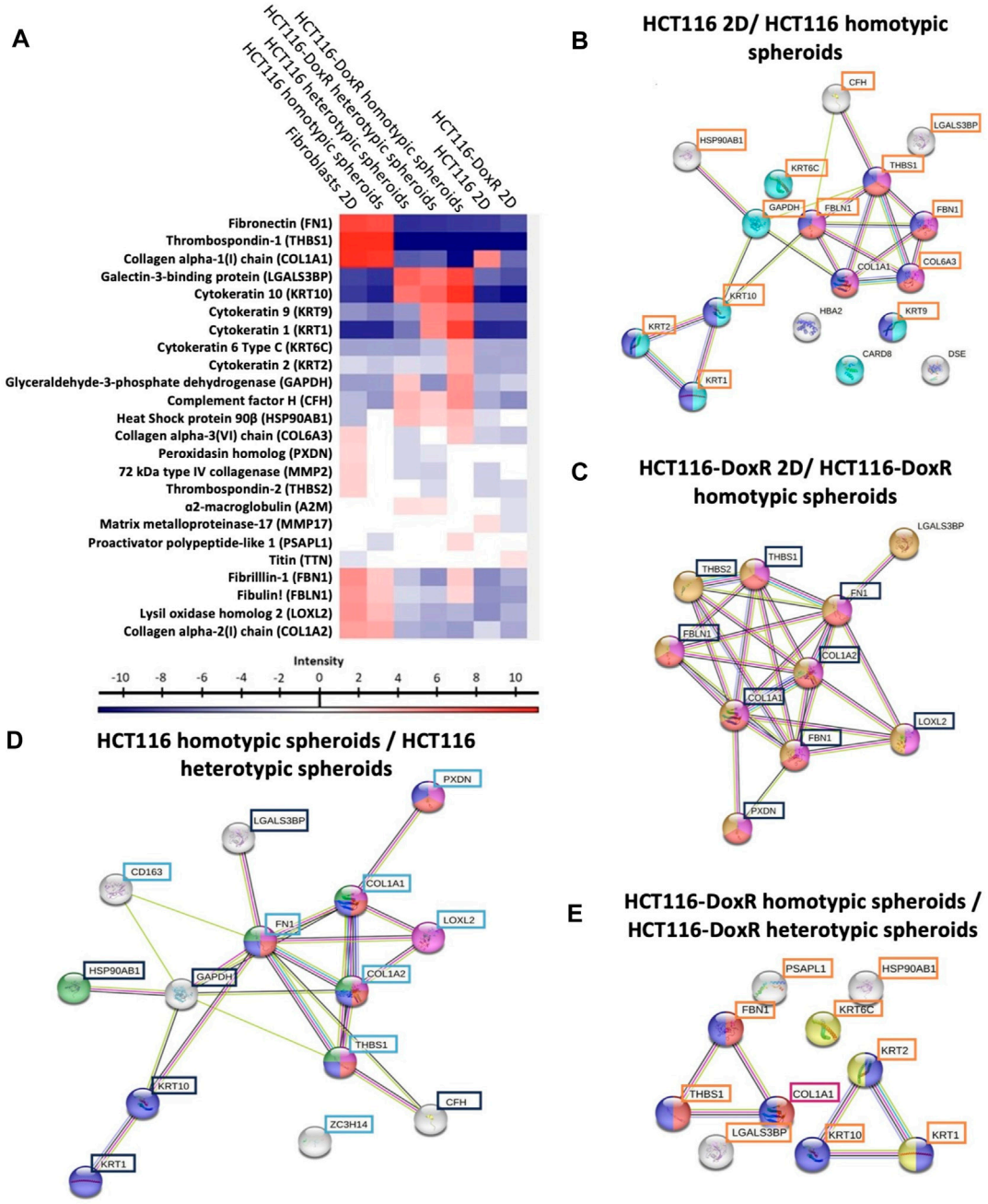


FIGURE 9
Proteomic profiling of extracellular vesicles isolated from the different culture models. **(A)** Hierarchical cluster of 24 significant proteins (multiple sample ANOVA test, based FDR 0.05) from *Homo sapiens* detected in EVs. Proteins with altered expression in EVs isolated from: **(B)** HCT116-doxR 2D culture and HCT116-DoxR homotypic spheroids; **(C)** HCT116 2D culture and HCT116 homotypic spheroids; **(D)** HCT116-DoxR heterotypic and homotypic spheroids; **(E)** and HCT116 heterotypic and homotypic spheroids. Tukey's Honest Significant Difference test, based FDR 0.05. Nodes represent proteins and the lines connecting them indicate direct or indirect interactions. Blue nodes indicate a structural molecule activity (Molecular function–GO:0005198); red nodes indicate ECM structural constituents (Molecular function–GO:0005201); purple nodes indicate proteins with a role in ECM organization (Biological process - GO:0030198); cyan nodes indicate proteins involved in programmed cell death (Biological process–GO: 0012501); orange nodes indicate collagen-containing ECM components (cellular component–GO:0062023); yellow nodes indicate keratin filament components (Cellular component–O:0045095); green nodes indicate proteins involved in PI3K-Akt signaling pathway (KEGG Pathways); and white nodes indicate proteins without a biological process associated. Proteins highlighted by blue, orange, cyan or purple boxes displayed increased levels in EVs extracted from HCT116 homotypic, HCT116-DoxR homotypic, HCT116 heterotypic or HCT116-DoxR heterotypic spheroids, respectively.

pathway. THSB1 and FN1's increased expression may enhance cell adhesion by integrin engagement and ECM remodeling, that can lead to an activation of PI3K and initiate downstream AKT signaling (Engelman, 2009; Horton et al., 2015; Aksorn and Chanvorachote, 2019). In contrast, a higher expression of heat shock protein HSP 90β (HSP90AB1) in EVs from homotypic spheroids suggests a

potential direct modulation of the PI3K-AKT pathway in recipient cells upon EV uptake (Solit et al., 2003; Workman, 2004; Whitesell and Lindquist, 2005). This indicates that the presence of fibroblasts in 3D models, and consequent interaction with tumor cells, results in secretion of EVs that modulate the structure of the spheroid by ECM modulation and induction of cell proliferation (Supplementary Figure S21; Supplementary Table S6).

Regarding proteins present in ECM or involved in its remodeling (e.g., DSE, COL1A1, COL1A2, COL6A3, FBLN1, FBN1, FN1, PXDN, LOXL2, A2M and MMP2), these are mostly observed in heterotypic spheroids, following the order 2D homotypic cultures < homotypic spheroids < heterotypic spheroids.

Integrating these data with that from gene and protein expression, highlights *MMP2* gene with increased expression in heterotypic spheroids, strengthened by higher protein expression in HCT116-DoxR heterotypic spheroids. This may be related to high presence of fibroblasts–key players in ECM proteins secretion and ECM remodeling, namely by the secretion of MMP2 (Liu et al., 2019). Same conclusions can be taken by analyzing the Cathepsin D protein expression, which has the same cleavage role of ECM components as MMP2 (Corcoran et al., 1996). Even though the *CTSD* gene expression has been demonstrated to be low in heterotypic spheroids, CSTD protein levels are considerably elevated in HCT116 heterotypic spheroids between the 5$^{th}$ and the 8$^{th}$ days of growth.

A2M is a multifunctional protein that acts as a protease inhibitor (Vandooren and Itoh, 2021) and can bind to MMP2 inhibiting its function (Lindner et al., 2010; Kim et al., 2018). Its presence in EVs derived from heterotypic spheroids may be helpful to understand the considerably low MMP2 protein levels detected in HCT116 heterotypic spheroids, despite its transcript overexpression.

Although the expression levels of THBS1 and TBHS2, both angiogenesis-associated proteins (Zhang et al., 2009), were consistently higher in 3D cultures, different patterns of expression were observed. In Dox-resistant 3D models, heterotypic spheroids were associated with increased THBS1 and THBS2 levels, whereas the opposite was observed in Dox-sensitive 3D spheroids. It was also observed that these proteins always have higher levels in fibroblasts when comparing with the heterotypic spheroids. THBS1 has been reported to have an anti-angiogenic role by modulating the uptake of VEGF and antagonize its function by inhibiting the activation of the MMP9, and consequently inhibiting the mobilization of VEGF through the ECM (Zhang et al., 2009; Matuszewska et al., 2022). The regulation between those two proteins is demonstrated by the downregulation of the VEGFA protein, although *VEGFA* gene appears to be overexpressed in HCT116 heterotypic spheroids.

CD163, an immune response related protein, is highly present in HCT116 heterotypic spheroids when compared with the homotypic spheroids. CD163 is considered an inflammatory biomarker and can be found in its free form or bound to macrophages' membrane. IL-6 is more expressed (at gene and protein levels) in HCT116 heterotypic than in HCT116 homotypic spheroids. IL-6 has been reported to increase the CD163 protein expression (Buechler et al., 2000; Calu et al., 2021).

When analyzing the proteins released by EVs in HCT116 and HCT116-DoxR spheroids, HCT116 spheroids, especially heterotypic spheroids, it is observed an increased presence of inflammation related proteins (i.e. CD163), leading to higher inflammation levels on these types of spheroids and consequently to higher expression of proteins related to this process, such as IL-6 (Figures 8C). On the other hand, HCT116-DoxR spheroids demonstrated a higher presence of anti-angiogenic proteins (such as THBS1 and THBS2). These observations are very interesting for the study of the mechanisms that may be involved in tumor chemoresistance, enabling us to understand some of the signaling pathways that may be activated in cells with acquired drug resistance.

Altogether, our data demonstrate the great potential of 3D models to recapitulate the *in vivo* tumor context and that EVs released by these models, have an important role in intercellular communication and consequent tumor progression, enabling a better understanding of the complexity of tumors and revealing new biomarkers for targeted therapy.

## 3.8 Challenging with doxorubicin

Dox inhibits topoisomerase II and intercalates with DNA base pairs, triggering apoptosis (Tacar et al., 2013). Due to its intrinsic fluorescence (Shah et al., 2017), it may be easily tracked during internalization into spheroids over time. Dox internalization was analyzed after 24 or 48 h of incubation and the effect on spheroids size was evaluated. Cell viability was determined for the 3D homotypic and heterotypic spheroids under study (Supplementary Figure S22), and the $IC_{50}$ for 24 h or 48 h incubation of the different types of 2D cultures are shown in Table 1.

All spheroids were incubated with 8 μM Dox, which corresponds to ~20x the $IC_{50}$ concentration in HCT116 2D cultures, after 48 h of incubation (Roma-Rodrigues et al., 2020). Dox-resistant spheroids were additionally incubated with 120 μM of Dox, which corresponds to ~20 × 6 μM, that resulted in a reduction of less than 50% in HCT116-DoxR 2D cultures, after 48 h of exposure. The resistance of HCT116-DoxR cells is associated to an overexpression of ABC efflux pumps (Pedrosa et al., 2018). As such, higher intracellular levels of Dox are expected for Dox-sensitive spheroids.

In all types of spheroids incubated with 8 μM Dox (Figures 10AD), the detected fluorescence intensity was higher after 48 h than after 24 h of incubation. However, in HCT116-DoxR spheroids incubated with 120 μM Dox (Figures 10E and **-F**), these differences were less pronounced. This may indicate that, at higher concentrations, the rate of Dox uptake overtakes the rate of efflux by pumps at the cell membrane, leading to higher intracellular accumulation of the drug. In addition, all spheroids incubated with 120 μM Dox showed the formation of a round body (Supplementary Figure S25), which disappeared upon media renewal before fluorescence acquisition. This seems to indicate increased death after incubation at this higher concentration of Dox.

Comparing homotypic spheroids (Figures 11A, B), fluorescence levels were consistently higher in HCT116 homotypic spheroids, both after 24 and 48 h of incubation, i.e. Dox internalization was higher as expected. Fluorescence levels did not suffer a considerable variation between 24 h and 48 h incubation, which indicates that the uptake of this drug is faster in the first 24 h.

**TABLE 1 Relative $IC_{50}$ of Dox after 24 h and 48 h incubation with monolayer cultures. Data expressed as mean ± SEM.**

| Culture type | Hours | $IC_{50}$ (μM) | References |
|---|---|---|---|
| Fibroblasts 2D | 24 | >120 | Supplementary Figure S23 |
| | 48 | 12.1 ± 0.2 | Choroba et al. (2023) |
| HCT116 2D | 24 | 0.38 | Pedrosa et al. (2018) |
| | 48 | 0.5 ± 0.1 | Choroba et al. (2023) |
| HCT116-DoxR 2D | 24 | >120 | Supplementary Figure S24 |
| | 48 | >6 | Pedrosa et al. (2018) |

As observed in homotypic spheroids, Dox internalization levels in heterotypic spheroids (Figures 11C, D) are higher after 48 h than after 24 h, but different internalization patterns are observed. While internalization values are similar between HCT116 and HCT116-DoxR heterotypic spheroids, after 48 h those levels are significantly higher in Dox-resistant spheroids. As HCT116-DoxR cells have an overexpression of P-gP and accumulate lower amounts of Dox (Pedrosa et al., 2018; Roma-Rodrigues et al., 2020), this may lead to an increased uptake of Dox by fibroblasts, leading to an overall increased accumulation of Dox in Dox-resistant heterotypic spheroids.

A comparison between heterotypic and homotypic spheroids demonstrates that the addition of fibroblasts leads to significant changes in the accumulation of Dox, particularly in Dox-resistant spheroids (Figure 11; Supplementary Figure S26). Internalization levels were comparable in Dox-sensitive homotypic and heterotypic spheroids, whereas in Dox-resistant spheroids internalization levels suffered considerable increases upon the addition of fibroblasts to the 3D cultures, after incubation with 8 μM and 120 μM of Dox (Supplementary Figure S26).

Knowing that Dox induces cell death (Tacar et al., 2013), the variation in the total spheroid volume upon incubation with Dox was evaluated (Figure 12; Supplementary Figure S27). The reduction in volume was expected to be more pronounced after 48 h of incubation and, in the case of Dox-resistant spheroids, also higher after incubation with 120 μM Dox. Since elevated levels of Dox internalization were detected in HCT116-DoxR heterotypic spheroids, a higher variation in size was also expected, similar to Dox-sensitive spheroids. Regarding Dox-sensitive spheroids (Figures 12A, B), it was observed a decrease in volume after 24 h

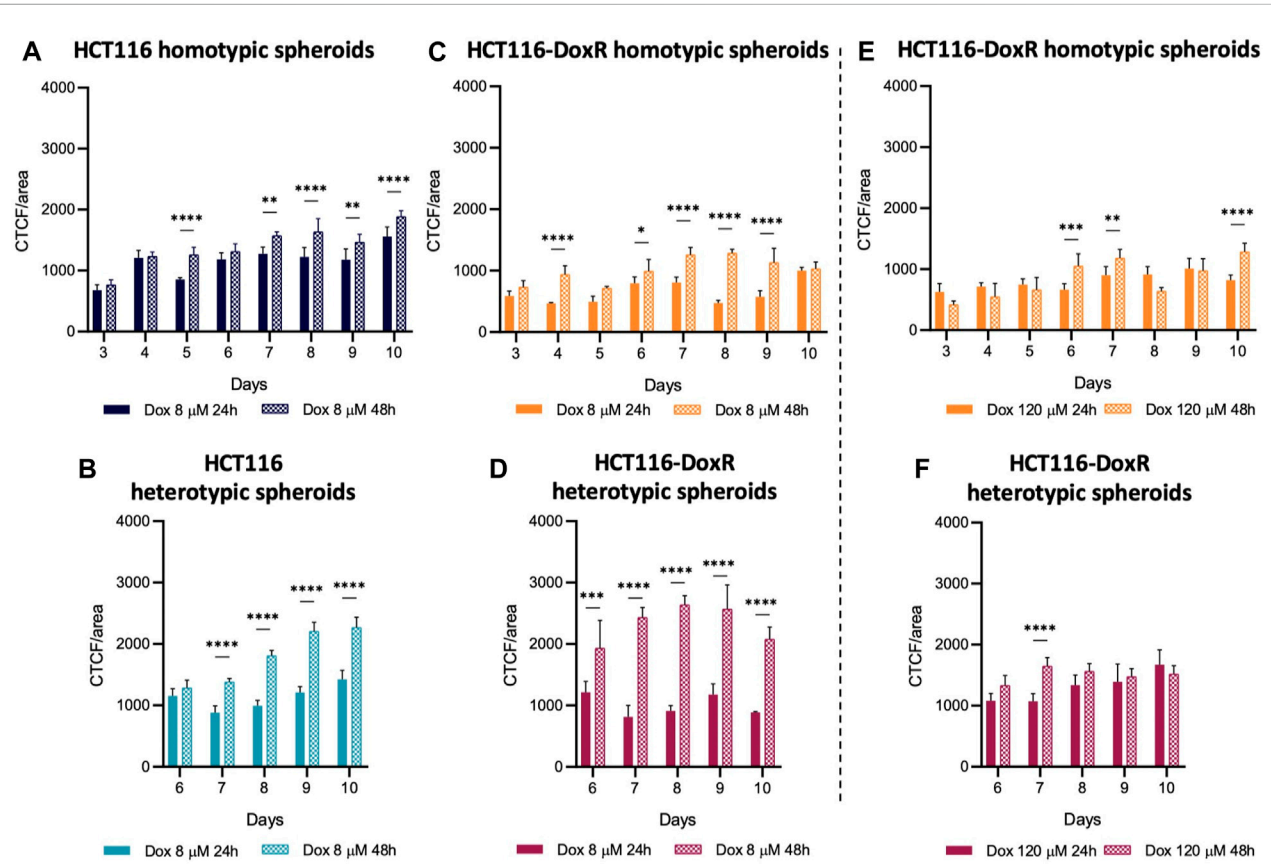


FIGURE 10
Doxorubicin internalization in spheroids. Internalization values after 24 h or 48 h in **(A)** HCT116 homotypic, **(B)** HCT116 heterotypic, **(C)** HCT116-DoxR homotypic and **(D)** HCT116-DoxR heterotypic spheroids incubated with 8 μM of Dox; and **(E)** HCT116-DoxR homotypic and **(F)** HCT116-DoxR heterotypic spheroids incubated with 120 μM of Dox. Data expressed as the mean ± SD of at least two independent assays. Statistical analysis was performed by two-way ANOVA method (*$p < 0.1$, **$p < 0.01$, ***$p < 0.001$, ****$p < 0.0001$). Data in **(E,F)** must not be directly compared with those in the other graphs, as fluorescence acquisition parameters were changed for those conditions.

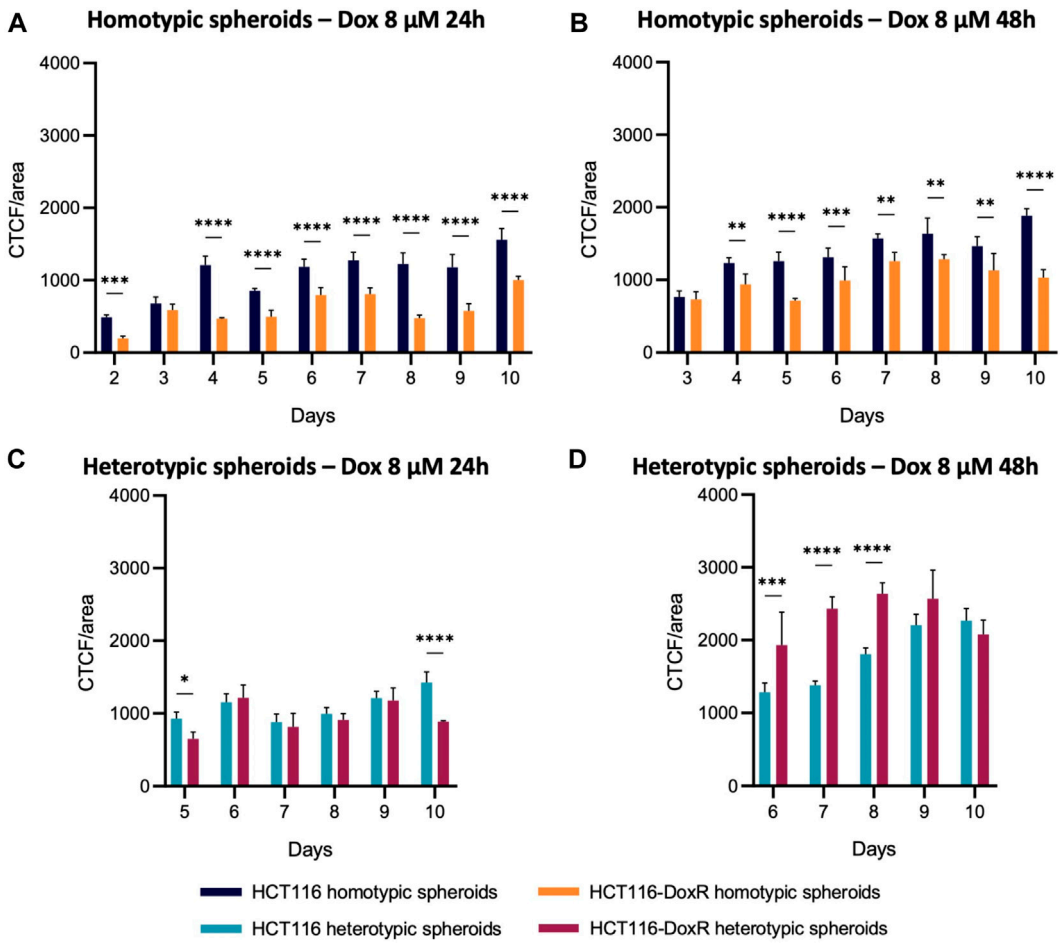


FIGURE 11
Comparison of Dox internalization between homotypic and heterotypic spheroids. CTCF/area values were compared between **(A,B)** homotypic or **(C,D)** heterotypic spheroids after 24 h or 48 h incubation with 8 µM Dox. Data expressed as the mean ± SD of at least two independent assays. Statistical analysis was performed by two-way ANOVA method (*$p$ < 0.1, **$p$ < 0.01, ***$p$ < 0.001, ****$p$ < 0.0001).

incubation with Dox, and this decrease was more evident after 48 h. In HCT116-DoxR homotypic spheroids (Figures 12C, D), the variation in volume was larger after incubation with 120 µM Dox, comparing with 8 µM Dox incubation, and no differences were observed between 24 or 48 h of incubation.

In HCT116-DoxR heterotypic spheroids (Figures 12E, F), although these showed higher fluorescence overall and thus higher Dox internalization, there was only a small decrease in volume after incubation with 8 or 120 µM Dox, contrary to what was expected. Fluorescence images of HCT116-DoxR heterotypic spheroids (Supplementary Figure S22) exhibit saturation of the fluorescence signal, that is neither uniform nor concentrated in the center, but rather in a few regions, which may correspond to the clusters of fibroblasts.

These results show that, as expected, Dox-sensitive spheroids are more susceptible to Dox action. Contrary to what was expected, they do not internalize more Dox. On the other hand, HCT116-DoxR heterotypic spheroids have a faster internalization of Dox, although they do not appear to be susceptible to Dox action, as seen by the small variation in volume (Figure 12). When fibroblasts are cultured in 2D, they are less sensitive to the cytotoxic action of doxorubicin (higher $IC_{50}$ at 48 h of 12.1 µM; Table 1) compared to HCT116 2D or even HCT116-DoxR 2D cells ($IC_{50}$ at 48 h of 0.5 µM or >6 µM, respectively). However, heterotypic spheroids with fibroblasts and tumor cells, particularly in the presence of HCT116-DoxR cells [with an overexpression of P-gP and lower accumulation of Dox (Pedrosa et al., 2018)], might have a higher internalization of Dox by fibroblasts leading to high fluorescence levels (Figures 10, 11). This also agrees with the higher growth rate of fibroblasts in heterotypic spheroids (see Table 1), resembling CAFs (Fang et al., 2023). Nevertheless, their lower sensitivity to Dox might explain the small variation in volume observed (Figure 12). However, we may not discard that when exposed to 8 µM or particularly 120 µM of Dox, HCT116-DoxR cells might trigger additional resistance mechanisms (efflux independent) that might allow higher accumulation of Dox without cytotoxicity (Wang et al., 2022).

Seemingly, the presence of fibroblasts does not affect Dox internalization in Dox-sensitive spheroids, but in Dox-resistant spheroids significantly increases Dox internalization, but without affecting Dox resistance.

To better understand the dynamic of the different types of cells within the spheroids upon incubation with Dox, viability of the cells

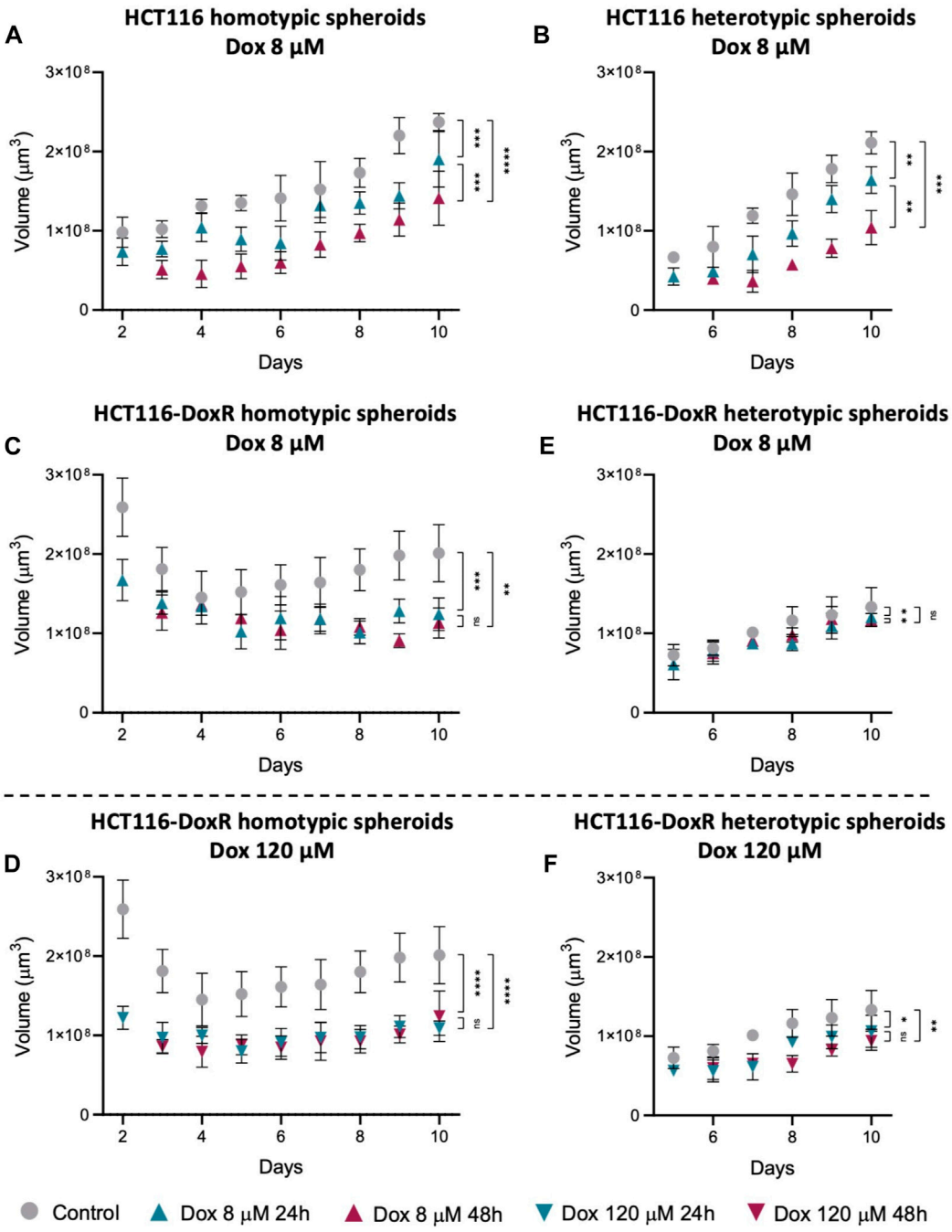


FIGURE 12
Spheroids volume after incubation with Dox. Variation in: **(A)** HCT116 homotypic spheroids incubated with 8 µM Dox; **(B)** HCT116 heterotypic spheroids incubated with 8 µM Dox; HCT116-DoxR homotypic spheroids incubated with 8 µM **(C)** or **(D)** 120 µM Dox; and HCT116-DoxR heterotypic spheroids incubated with 8 µM **(E)** or 120 µM **(F)** Dox. Data expressed as the mean ± SD of at least two independent assays. Statistical analysis was performed by ratio paired *t*-test (ns: not significant, *$p < 0.1$, **$p < 0.01$, ***$p < 0.001$, ****$p < 0.0001$).

in the 3D models was assessed by MTS method (Figure 13) (Choroba et al., 2023).

In HCT116 homotypic spheroids incubated with 8 µM of Dox (Figures 13A), a higher loss of cell viability is observed, attaining a minimum of approximately 70% after 48 h of incubation at the 5$^{th}$ day of growth. Interestingly, these viability values are considerable higher than those for its 2D counterpart, reinforcing the relevance of 3D models in pre-clinical research. These results agree with the data obtained for the analysis of spheroids' volume, where the change in their volume was more pronounced after 24 h incubation with Dox (Figures 12A).

On the other hand, HCT116-DoxR homotypic spheroids (Figures 13B, E), show an increased loss of cell viability after 24 h incubation, especially for 120 µM of Dox, but after 48 h of incubation, cell viability values are close to 100% indicating a cell recovery.

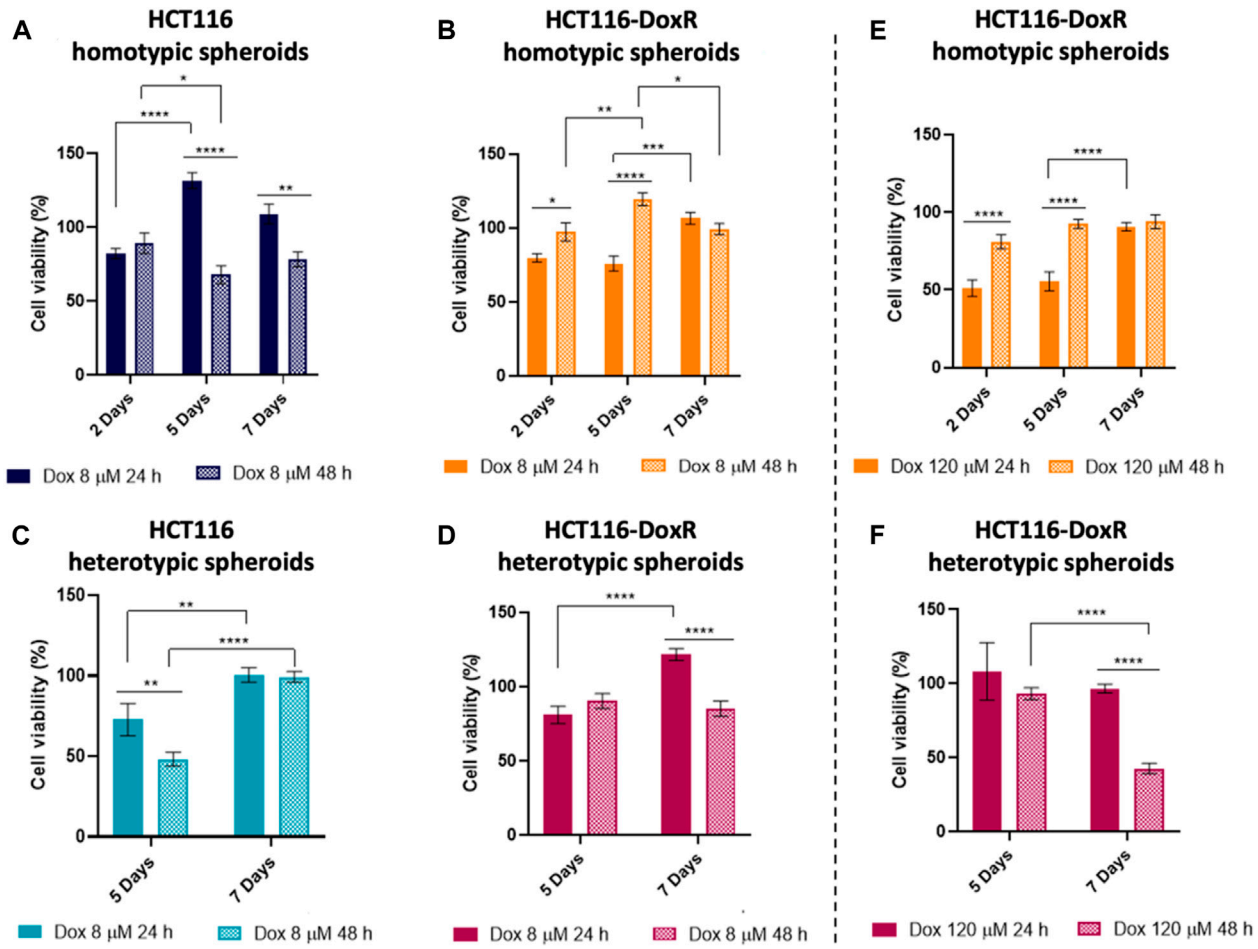


FIGURE 13
Percentage of cell viability assessed by the MTS assay of different types of spheroids after exposure to Dox for 24 h or 48 h **(A)** HCT116 homotypic, **(B)** HCT116-DoxR homotypic, **(C)** HCT116 heterotypic and **(D)** HCT116-DoxR heterotypic spheroids incubated with 8 μM of Dox; and **(E)** HCT116-DoxR homotypic and **(F)** HCT116-DoxR heterotypic spheroids incubated with 120 μM of Dox. 0.1% (v/v) DMSO was used as the vehicle control. Data are expressed as mean ± SEM of two independent assays. Statistical analysis was performed by two-way ANOVA method (* $p < 0.1$, ** $p < 0.01$, *** $p < 0.001$, **** $p < 0.0001$).

Comparing both homotypic spheroids, it is possible to state that HCT116 spheroids are more susceptible to Dox action than HCT116-DoxR spheroids, especially after 48 h incubation since these last ones seem to overcome Dox action and possibly trigger additional resistance mechanisms, as mentioned above (Wang et al., 2022).

Heterotypic HCT116-DoxR spheroids (Figures 13D, F) show higher viability values upon incubation with 8 μM of Dox, compared to HCT116 heterotypic spheroids (Figures 13C). The increase of Dox concentration to 120 μM resulted in a significant reduction of cell viability, especially after 48 h incubation on the 7$^{th}$ day (40% cell viability).

Comparing homotypic and heterotypic spheroids, in HCT116 models, the addition of fibroblasts resulted in a less noticeable difference in cell viability between the different incubation times, both at the 5th and 7th days of growth. In HCT116-DoxR spheroids, cell viability values are consistently lower in heterotypic models after 48 h incubation with 8 μM and 120 μM of Dox, being more pronounced upon incubation with 120 μM of Dox (approx. 80% at 5th day and 40% at the 7th day). Correlating these results with the variation of the spheroids' volume and fluorescence images of Dox internalization (Figure 12; Supplementary Figure S27), the cell viability loss that is observed after 48 h incubation with 120 μM in HCT116-DoxR heterotypic spheroids at the 7th day may be due to the higher accumulation of Dox within fibroblasts, which may affect total viability but will not significantly reduce the volume of the spheroids since the periphery of the spheroids is mainly occupied by HCT116-DoxR cells, present in higher proportions compared to fibroblasts in those heterotypic spheroids.

## 4 Conclusion

The development of models that better recapitulate the TME to mimic tumor growth and progression, are critical for the

characterization of the interplay between cells in this complex milieu and to evaluate the effects of TME on the response of cancer cells to therapeutic challenges. The use of 3D spheroids models enables a closer approximation to the TME and tumor organization. Herein, we characterized homotypic and heterotypic spheroids, sensitive or resistant to Dox, namely in what concerns their growth, cell viability, presence of hypoxia and inflammation, Dox internalization and extracellular vesicles content, to provide a basis for more effective translation of existing 2D culture data to the more complex models. Overall, this study reports the development of novel CRC heterotypic 3D models used as a strategy to better recapitulate the physiologic context and structure verified *in vivo*. These models allow to open new perspectives and strategies in the heterotypic 3D models context, which may be adapted to different tumor contexts. Different TME components (such as tumor-associated macrophages, tumor-infiltrating lymphocytes and myeloid-derived suppressor cells) can also be inserted to maximize the mimicking degree of the *in vivo* reality.

All types of spheroids have a similar growth progression and the susceptibility or resistance to Dox in homotypic spheroids does not affect the cell number within the spheroid. Moreover, a necrotic and hypoxic core was identified in all types of spheroids, resulting from the differential diffusion of nutrients, oxygen, and metabolic products to and from the center of these cell masses. TEM imaging further supported the presence of different strata in these spheroids, with a clear reduction of cell density towards the core with increasing amounts of cell debris, compatible with the formation of the necrotic core. Besides, the detection of low oxygen levels at the center of spheroids reinforces the idea that the formation of a necrotic core in spheroids occurs because of hypoxia. Still, there were differences between the types of spheroids in terms of hypoxia and cell viability: while homotypic spheroids tend to exhibit higher levels of hypoxia, Dox-resistance spheroids present lower levels of cell death. It is possible to claim that difference in Dox susceptibility in the CRC cell lines tested, does not influence spheroid formation and development, namely for terms of cell death and hypoxia. Also, fibroblasts in heterotypic spheroids seem to stabilize these cultures, even though with a small increase of cell death levels.

Analysis of transcript and protein levels of different hypoxia and inflammation-associated genes, indicates that the presence of fibroblasts modulates expression of some key genes/proteins, namely MMP2 and IL-6. It was also possible to verify the presence of proteins, such as MMP2 and Cathepsin D in the different types of spheroids, which may be the promotors of cell death under the observed hypoxic conditions. A deeper characterization of the secreted proteins by each cell type in heterotypic models would give greater insights about which pathways are more activated in each cell type and would enable a further understanding of the role of each cell type in tumor progression and invasion.

The overall cell to cell modulation seems to be conveyed by the protein content within EVs. In fact, several key effectors were identified pointing out to a cell-cell and cell-ECM interaction due to increase complexity of the studied spheroid models. Such observation shows that these 3D spheroid models are getting one step closer to better recapitulate the TME observed *in vivo*. Interestingly, these proteins within EVs suggests that interactions occur not only in a direct way (cell expression) but also in an indirect way, where EVs act as vehicles, carrying bioactive molecules and proteins that facilitate the crosstalk among cells, in an autocrine and paracrine way. On the other hand, this EV-mediated communication appears to have a role in other cellular processes, such as programmed cell death and modulation of signaling pathways like the PI3K-AKT pathway.

Finally, possible differences in the internalization of chemotherapeutics and cell viability after exposure to Dox were also evaluated via assessment of internalization and toxicity. As expected, the amount of drug internalization is higher for longer periods of incubation (48 h vs. 24 h), and Dox-sensitive spheroids were more susceptible to Dox action. However, contrary to what was expected, HCT116-DoxR heterotypic spheroids internalized more Dox than the other spheroids, and a small variation of the overall spheroid size (volume) is observed. Although, exposure to 120 μM Dox for 48 h induced a significant decrease of spheroids' cell viability, an exposure for 48h to 8 μM Dox did not show any effect. This may suggest that the presence of fibroblasts is somehow affecting Dox internalization, but without affecting the ability of these spheroids to resist Dox toxicity. Such observations seem to indicate that both the presence or absence of fibroblasts and the resistance or susceptibility to Dox can affect spheroid viability, hypoxia, and Dox internalization.

## Data availability statement

The datasets presented in this study can be found in online repositories. The names of the repository/repositories and accession number(s) can be found in the article/Supplementary Material.

## Ethics statement

Ethical approval was not required for the studies on animals in accordance with the local legislation and institutional requirements because only commercially available established cell lines were used.

## Author contributions

RV: Formal Analysis, Investigation, Methodology, Validation, Writing–original draft, Writing–review and editing. SC: Formal Analysis, Investigation, Methodology, Validation, Writing–original draft, Writing–review and editing. AL: Formal Analysis, Investigation, Methodology, Validation, Writing–original draft, Writing–review and editing. MM: Formal Analysis, Investigation, Methodology, Validation, Writing–original draft, Writing–review and editing. CR: Formal Analysis, Investigation, Methodology, Validation, Writing–review and editing. PB: Conceptualization, Funding acquisition, Project administration, Supervision, Validation, Writing–review and editing. AF: Conceptualization, Funding acquisition, Project administration, Supervision, Validation, Writing–review and editing.

## Funding

The author(s) declare financial support was received for the research, authorship, and/or publication of this article. This work was financed by national funds from FCT–Fundação para a Ciência e a Tecnologia, I.P./MCTES through the projects PTDC/QUIQIN/0146/2020, PTDC/QUI-QOR/1304/2020, and 2022.04315. PTDC–NANOHEAT and also in the scope of the project UIDP/04378/2020 and UIDB/04378/2020 of the Research Unit on Applied Molecular Biosciences–UCIBIO and the project LA/P/0140/2020 of the Associate Laboratory Institute for Health and Bioeconomy–i4HB. CR, AL, RV, and SC were funded by FCT/MCTES, grant numbers SFRH/BPD/124612/2016, 2022.12161.BD, 2022.09845.BD, and 2021.08629.BD, respectively.

## Conflict of interests

The authors declare that the research was conducted in the absence of any commercial or financial relationships that could be construed as a potential conflict of interest.

The author(s) declared that they were an editorial board member of Frontiers, at the time of submission. This had no impact on the peer review process and the final decision

## Publisher's note

All claims expressed in this article are solely those of the authors and do not necessarily represent those of their affiliated organizations, or those of the publisher, the editors and the reviewers. Any product that may be evaluated in this article, or claim that may be made by its manufacturer, is not guaranteed or endorsed by the publisher.

## Supplementary material

The Supplementary Material for this article can be found online at: https://www.frontiersin.org/articles/10.3389/fcell.2023.1310397/full#supplementary-material

## References

Aguilar-Cazares, D., Chavez-Dominguez, R., Carlos-Reyes, A., Lopez-Camarillo, C., Hernadez de la Cruz, O. N., and Lopez-Gonzalez, J. S. (2019). Contribution of angiogenesis to inflammation and cancer. *Front. Oncol.* 9, 1399. doi:10.3389/fonc.2019.01399

Aksorn, N., and Chanvorachote, P. (2019). Integrin as a molecular target for anti-cancer approaches in lung cancer. *Anticancer Res.* 39, 541–548. doi:10.21873/anticanres.13146

Al-Thyabat, S., and Miles, N. J. (2006). An improved estimation of size distribution from particle profile measurements. *Powder Technol.* 166, 152–160. doi:10.1016/j.powtec.2006.05.008

Antharavally, B. S., Mallia, K. A., Rangaraj, P., Haney, P., and Bell, P. A. (2009). Quantitation of proteins using a dye–metal-based colorimetric protein assay. *Anal. Biochem.* 385, 342–345. doi:10.1016/j.ab.2008.11.024

Balkwill, F. R., Capasso, M., and Hagemann, T. (2012). The tumor microenvironment at a glance. *J. Cell. Sci.* 125, 5591–5596. doi:10.1242/jcs.116392

Becker, A., Thakur, B. K., Weiss, J. M., Kim, H. S., Peinado, H., and Lyden, D. (2016). Extracellular vesicles in cancer: cell-to-cell mediators of metastasis. *Cancer Cell.* 30, 836–848. doi:10.1016/j.ccell.2016.10.009

Belli, C., Trapani, D., Viale, G., D'Amico, P., Duso, B. A., Della Vigna, P., et al. (2018). Targeting the microenvironment in solid tumors. *Cancer Treat. Rev.* 65, 22–32. doi:10.1016/j.ctrv.2018.02.004

Ben-Yosef, Y., Miller, A., Shapiro, S., and Lahat, N. (2005). Hypoxia of endothelial cells leads to MMP-2-dependent survival and death. *Am. J. Physiology-Cell Physiology* 289, C1321–C1331. doi:10.1152/ajpcell.00079.2005

Biddlestone, J., Bandarra, D., and Rocha, S. (2015). The role of hypoxia in inflammatory disease (review). *Int. J. Mol. Med.* 35, 859–869. doi:10.3892/ijmm.2015.2079

Buechler, C., Ritter, M., Orsó, E., Langmann, T., Klucken, J., and Schmitz, G. (2000). Regulation of scavenger receptor CD163 expression in human monocytes and macrophages by pro- and antiinflammatory stimuli. *J. Leukoc. Biol.* 67, 97–103. doi:10.1002/jlb.67.1.97

Calu, V., Ionescu, A., Stanca, L., Geicu, O. I., Iordache, F., Pisoschi, A. M., et al. (2021). Key biomarkers within the colorectal cancer related inflammatory microenvironment. *Sci. Rep.* 11, 7940. doi:10.1038/s41598-021-86941-5

Cavallari, C., Camussi, G., and Brizzi, M. F. (2020). Extracellular vesicles in the tumour microenvironment: eclectic supervisors. *Int. J. Mol. Sci.* 21, 6768. doi:10.3390/ijms21186768

Chen, F., Zhuang, X., Lin, L., Yu, P., Wang, Y., Shi, Y., et al. (2015). New horizons in tumor microenvironment biology: challenges and opportunities. *BMC Med.* 13, 45. doi:10.1186/s12916-015-0278-7

Chen, M., and Xie, S. (2018). Therapeutic targeting of cellular stress responses in cancer. *Thorac. Cancer* 9, 1575–1582. doi:10.1111/1759-7714.12890

Cheng, G., Tse, J., Jain, R. K., and Munn, L. L. (2009). Micro-environmental mechanical stress controls tumor spheroid size and morphology by suppressing proliferation and inducing apoptosis in cancer cells. *PLoS One* 4, e4632. doi:10.1371/journal.pone.0004632

Choroba, K., Filipe, B., Świtlicka, A., Penkala, M., Machura, B., Bieńko, A., et al. (2023). *In vitro* and *in vivo* biological activities of dipicolinate oxovanadium(IV) complexes. *J. Med. Chem.* 66, 8580–8599. doi:10.1021/acs.jmedchem.3c00255

Chung, S. S., Wu, Y., Okobi, Q., Adekoya, D., Atefi, M., Clarke, O., et al. (2017). Proinflammatory cytokines IL-6 and TNF-α increased telomerase activity through NF-κB/STAT1/STAT3 activation, and withaferin A inhibited the signaling in colorectal cancer cells. *Mediat. Inflamm.* 2017, 5958429. doi:10.1155/2017/5958429

Cocucci, E., and Meldolesi, J. (2015). Ectosomes and exosomes: shedding the confusion between extracellular vesicles. *Trends Cell. Biol.* 25, 364–372. doi:10.1016/j.tcb.2015.01.004

Corcoran, M. L., Hewitt, R. E., Kleiner, D. E., Jr, and Stetler-Stevenson, W. G. (1996). MMP-2: expression, activation and inhibition. *Enzyme Protein* 49, 7–19. doi:10.1159/000468613

Costa, E. C., Moreira, A. F., de Melo-Diogo, D., Gaspar, V. M., Carvalho, M. P., and Correia, I. J. (2016). 3D tumor spheroids: an overview on the tools and techniques used for their analysis. *Biotechnol. Adv.* 34, 1427–1441. doi:10.1016/j.biotechadv.2016.11.002

Cui, X., Hartanto, Y., and Zhang, H. (2017). Advances in multicellular spheroids formation. *J. R. Soc. Interface* 14, 20160877. doi:10.1098/rsif.2016.0877

Das, K., Beyene, B. B., Datta, A., Garribba, E., Roma-Rodrigues, C., Silva, A., et al. (2018). EPR and electrochemical interpretation of bispyrazolylacetate anchored Ni(ii) and Mn(ii) complexes: cytotoxicity and anti-proliferative activity towards human cancer cell lines. *New J. Chem.* 42, 9126–9139. doi:10.1039/C8NJ01033A

Di Giacomo, S., Sollazzo, M., de Biase, D., Ragazzi, M., Bellosta, P., Pession, A., et al. (2017). Human cancer cells signal their competitive fitness through MYC activity. *Sci. Rep.* 7, 12568. doi:10.1038/s41598-017-13002-1

D'Ignazio, L., Batie, M., and Rocha, S. (2017). Hypoxia and inflammation in cancer, focus on HIF and NF-κB. *Biomedicines* 5, 21. doi:10.3390/biomedicines5020021

Duval, K., Grover, H., Han, L.-H., Mou, Y., Pegoraro, A. F., Fredberg, J., et al. (2017). Modeling physiological events in 2D vs. 3D cell culture. *Physiology* 32, 266–277. doi:10.1152/physiol.00036.2016

Engelman, J. A. (2009). Targeting PI3K signalling in cancer: opportunities, challenges and limitations. *Nat. Rev. Cancer* 9, 550–562. doi:10.1038/nrc2664

Escárcega, R. O., Fuentes-Alexandro, S., García-Carrasco, M., Gatica, A., and Zamora, A. (2007). The transcription factor nuclear factor-kappa B and cancer. *Clin. Oncol.* 19, 154–161. doi:10.1016/j.clon.2006.11.013

Fang, Z., Meng, Q., Xu, J., Wang, W., Zhang, B., Liu, J., et al. (2023). Signaling pathways in cancer-associated fibroblasts: recent advances and future perspectives. *Cancer Commun.* 43, 3–41. doi:10.1002/cac2.12392

Fruman, D. A., Chiu, H., Hopkins, B. D., Bagrodia, S., Cantley, L. C., and Abraham, R. T. (2017). The PI3K pathway in human disease. *Cell.* 170, 605–635. doi:10.1016/j.cell.2017.07.029

Giridharan, S., and Srinivasan, M. (2018). Mechanisms of NF-κB p65 and strategies for therapeutic manipulation. *J. Inflamm. Res.* 11, 407–419. doi:10.2147/JIR.S140188

Han, S. J., Kwon, S., and Kim, K. S. (2021). Challenges of applying multicellular tumor spheroids in preclinical phase. *Cancer Cell. Int.* 21, 152. doi:10.1186/s12935-021-01853-8

Hari, N., Patel, P., Ross, J., Hicks, K., and Vanholsbeeck, F. (2019). Optical coherence tomography complements confocal microscopy for investigation of multicellular tumour spheroids. *Sci. Rep.* 9, 10601. doi:10.1038/s41598-019-47000-2

Hoarau-Véchot, J., Rafii, A., Touboul, C., and Pasquier, J. (2018). Halfway between 2D and animal models: are 3D cultures the ideal tool to study cancer-microenvironment interactions? *Int. J. Mol. Sci.* 19, 181. doi:10.3390/ijms19010181

Hoesel, B., and Schmid, J. A. (2013). The complexity of NF-κB signaling in inflammation and cancer. *Mol. Cancer* 12, 86. doi:10.1186/1476-4598-12-86

Hopkins, B. D., Goncalves, M. D., and Cantley, L. C. (2020). Insulin–PI3K signalling: an evolutionarily insulated metabolic driver of cancer. *Nat. Rev. Endocrinol.* 16, 276–283. doi:10.1038/s41574-020-0329-9

Horton, E. R., Byron, A., Askari, J. A., Ng, D. H. J., Millon-Frémillon, A., Robertson, J., et al. (2015). Definition of a consensus integrin adhesome and its dynamics during adhesion complex assembly and disassembly. *Nat. Cell. Biol.* 17, 1577–1587. doi:10.1038/ncb3257

Hu, L., Zang, M., Wang, H., Li, J., Su, L., Yan, M., et al. (2016). Biglycan stimulates VEGF expression in endothelial cells by activating the TLR signaling pathway. *Mol. Oncol.* 10, 1473–1484. doi:10.1016/j.molonc.2016.08.002

Jensen, C., and Teng, Y. (2020). Is it time to start transitioning from 2D to 3D cell culture? *Front. Mol. Biosci.* 7, 33. doi:10.3389/fmolb.2020.00033

Kalluri, R. (2016). The biology and function of fibroblasts in cancer. *Nat. Rev. Cancer* 16, 582–598. doi:10.1038/nrc.2016.73

Kapałczyńska, M., Kolenda, T., Przybyła, W., Zajączkowska, M., Teresiak, A., Filas, V., et al. (2018). 2D and 3D cell cultures – a comparison of different types of cancer cell cultures. *Archives Med. Sci.* 14, 910–919. doi:10.5114/aoms.2016.63743

Keum, N., and Giovannucci, E. (2019). Global burden of colorectal cancer: emerging trends, risk factors and prevention strategies. *Nat. Rev. Gastroenterol. Hepatol.* 16, 713–732. doi:10.1038/s41575-019-0189-8

Kim, K. M., Chung, K. W., Jeong, H. O., Lee, B., Kim, D. H., Park, J. W., et al. (2018). MMP2-A2M interaction increases ECM accumulation in aged rat kidney and its modulation by calorie restriction. *Oncotarget* 9, 5588–5599. doi:10.18632/oncotarget.23652

Kumari, N., Dwarakanath, B. S., Das, A., and Bhatt, A. N. (2016). Role of interleukin-6 in cancer progression and therapeutic resistance. *Tumor Biol.* 37, 11553–11572. doi:10.1007/s13277-016-5098-7

Labani-Motlagh, A., Ashja-Mahdavi, M., and Loskog, A. (2020). The tumor microenvironment: a milieu hindering and obstructing antitumor immune responses. *Front. Immunol.* 11, 940. doi:10.3389/fimmu.2020.00940

Lindner, I., Hemdan, N. Y. A., Buchold, M., Huse, K., Bigl, M., Oerlecke, I., et al. (2010). Alpha2-macroglobulin inhibits the malignant properties of astrocytoma cells by impeding beta-catenin signaling. *Cancer Res.* 70, 277–287. doi:10.1158/0008-5472.CAN-09-1462

Liu, T., Han, C., Wang, S., Fang, P., Ma, Z., Xu, L., et al. (2019). Cancer-associated fibroblasts: an emerging target of anti-cancer immunotherapy. *J. Hematol. Oncol.* 12, 86. doi:10.1186/s13045-019-0770-1

Maia, A., and Wiemann, S. (2021). Cancer-associated fibroblasts: implications for cancer therapy. *Cancers (Basel)* 13, 3526. doi:10.3390/cancers13143526

Masoud, G. N., and Li, W. (2015). HIF-1α pathway: role, regulation and intervention for cancer therapy. *Acta Pharm. Sin. B* 5, 378–389. doi:10.1016/j.apsb.2015.05.007

Massignani, M., Canton, I., Sun, T., Hearnden, V., MacNeil, S., Blanazs, A., et al. (2010). Enhanced fluorescence imaging of live cells by effective cytosolic delivery of probes. *PLoS One* 5, e10459. doi:10.1371/journal.pone.0010459

Matuszewska, K., ten Kortenaar, S., Pereira, M., Santry, L. A., Petrik, D., Lo, K.-M., et al. (2022). Addition of an Fc-IgG induces receptor clustering and increases the *in vitro* efficacy and *in vivo* anti-tumor properties of the thrombospondin-1 type I repeats (3TSR) in a mouse model of advanced stage ovarian cancer. *Gynecol. Oncol.* 164, 154–169. doi:10.1016/j.ygyno.2021.11.006

McKeown, S. R. (2014). Defining normoxia, physoxia and hypoxia in tumours—implications for treatment response. *Br. J. Radiol.* 87, 20130676. doi:10.1259/bjr.20130676

Mendes, B. B., Sousa, D. P., Conniot, J., and Conde, J. (2021). Nanomedicine-based strategies to target and modulate the tumor microenvironment. *Trends Cancer* 7, 847–862. doi:10.1016/j.trecan.2021.05.001

Molinaro, A., Becattini, B., Mazzoli, A., Bleve, A., Radici, L., Maxvall, I., et al. (2019). Insulin-driven PI3K-AKT signaling in the hepatocyte is mediated by redundant PI3Kα and PI3Kβ activities and is promoted by RAS. *Cell. Metab.* 29, 1400–1409.e5. doi:10.1016/j.cmet.2019.03.010

Niles, A. L., Moravec, R. A., and Riss, T. L. (2008). Update on *in vitro* cytotoxicity assays for drug development. *Expert Opin. Drug Discov.* 3, 655–669. doi:10.1517/17460441.3.6.655

Pedrosa, P., Mendes, R., Cabral, R., Martins, L. M. D. R. S., Baptista, P. V., and Fernandes, A. R. (2018). Combination of chemotherapy and Au-nanoparticle photothermy in the visible light to tackle doxorubicin resistance in cancer cells. *Sci. Rep.* 8, 11429. doi:10.1038/s41598-018-29870-0

Peinado, H., Lavotshkin, S., and Lyden, D. (2011). The secreted factors responsible for pre-metastatic niche formation: old sayings and new thoughts. *Semin. Cancer Biol.* 21, 139–146. doi:10.1016/j.semcancer.2011.01.002

Petrova, V., Annicchiarico-Petruzzelli, M., Melino, G., and Amelio, I. (2018). The hypoxic tumour microenvironment. *Oncogenesis* 7, 10. doi:10.1038/s41389-017-0011-9

Razmara, M., Srinivasula, S. M., Wang, L., Poyet, J.-L., Geddes, B. J., DiStefano, P. S., et al. (2002). CARD-8 protein, a new CARD family member that regulates caspase-1 activation and apoptosis. *J. Biol. Chem.* 277, 13952–13958. doi:10.1074/jbc.M107811200

Riffle, S., and Hegde, R. S. (2017). Modeling tumor cell adaptations to hypoxia in multicellular tumor spheroids. *J. Exp. Clin. Cancer Res.* 36, 102. doi:10.1186/s13046-017-0570-9

Robado de Lope, L., Sánchez-Herrero, E., Serna-Blasco, R., Provencio, M., and Romero, A. (2023). Cancer as an infective disease: the role of EVs in tumorigenesis. *Mol. Oncol.* 17, 390–406. doi:10.1002/1878-0261.13316

Roma-Rodrigues, C., Fernandes, A. R., and Baptista, P. V. (2014). Exosome in tumour microenvironment: overview of the crosstalk between normal and cancer cells. *Biomed. Res. Int.* 2014, 179486. doi:10.1155/2014/179486

Roma-Rodrigues, C., Mendes, R., Baptista, P. V., and Fernandes, A. R. (2019). Targeting tumor microenvironment for cancer therapy. *Int. J. Mol. Sci.* 20, 840. doi:10.3390/ijms20040840

Roma-Rodrigues, C., Pombo, I., Fernandes, A. R., and Baptista, P. V. (2020). Hyperthermia induced by gold nanoparticles and visible light photothermy combined with chemotherapy to tackle doxorubicin sensitive and resistant colorectal tumor 3D spheroids. *Int. J. Mol. Sci.* 21, 8017. doi:10.3390/ijms21218017

Roma-Rodrigues, C., Raposo, L. R., Valente, R., Fernandes, A. R., and Baptista, P. V. (2021). Combined cancer therapeutics—tackling the complexity of the tumor microenvironment. *WIREs Nanomedicine Nanobiotechnology* 13, e1704. doi:10.1002/wnan.1704

Rueden, C. T., Schindelin, J., Hiner, M. C., DeZonia, B. E., Walter, A. E., Arena, E. T., et al. (2017). ImageJ2: ImageJ for the next generation of scientific image data. *BMC Bioinforma.* 18, 529. doi:10.1186/s12859-017-1934-z

Sahai, E., Astsaturov, I., Cukierman, E., DeNardo, D. G., Egeblad, M., Evans, R. M., et al. (2020). A framework for advancing our understanding of cancer-associated fibroblasts. *Nat. Rev. Cancer* 20, 174–186. doi:10.1038/s41568-019-0238-1

Sawicki, T., Ruszkowska, M., Danielewicz, A., Niedźwiedzka, E., Arłukowicz, T., and Przybyłowicz, K. E. (2021). A review of colorectal cancer in terms of epidemiology, risk factors, development, symptoms and diagnosis. *Cancers (Basel)* 13, 2025. doi:10.3390/cancers13092025

Schäuble, S., Klement, K., Marthandan, S., Münch, S., Heiland, I., Schuster, S., et al. (2012). Quantitative model of cell cycle arrest and cellular senescence in primary human fibroblasts. *PLoS One* 7, e42150. doi:10.1371/journal.pone.0042150

Schmittgen, T. D., and Livak, K. J. (2008). Analyzing real-time PCR data by the comparative CT method. *Nat. Protoc.* 3, 1101–1108. doi:10.1038/nprot.2008.73

Schmittgen, T. D., and Zakrajsek, B. A. (2000). Effect of experimental treatment on housekeeping gene expression: validation by real-time, quantitative RT-PCR. *J. Biochem. Biophys. Methods* 46, 69–81. doi:10.1016/S0165-022X(00)00129-9

Seo, E., Kim, S., and Jho, E. (2009). Induction of cancer cell-specific death via MMP2 promoter-dependent Bax expression. *BMB Rep.* 42, 217–222. doi:10.5483/bmbrep.2009.42.4.217

Sequeira, D., Baptista, P. V., Valente, R., Piedade, M. F. M., Garcia, M. H., Morais, T. S., et al. (2021). Cu(i) complexes as new antiproliferative agents against sensitive and doxorubicin resistant colorectal cancer cells: synthesis, characterization, and mechanisms of action. *Dalton Trans.* 50, 1845–1865. doi:10.1039/D0DT03566A

Sethi, G., Sung, B., and Aggarwal, B. B. (2008). TNF: a master switch for inflammation to cancer. *Front. Bioscience-Landmark* 13, 5094–5107. doi:10.2741/3066

Shah, S., Chandra, A., Kaur, A., Sabnis, N., Lacko, A., Gryczynski, Z., et al. (2017). Fluorescence properties of doxorubicin in PBS buffer and PVA films. *J. Photochem Photobiol. B* 170, 65–69. doi:10.1016/j.jphotobiol.2017.03.024

Sheikh, A. M., Li, X., Wen, G., Tauqeer, Z., Brown, W. T., and Malik, M. (2010). Cathepsin D and apoptosis related proteins are elevated in the brain of autistic subjects. *Neuroscience* 165, 363–370. doi:10.1016/j.neuroscience.2009.10.035

Simó, R., Barbosa-Desongles, A., Lecube, A., Hernandez, C., and Selva, D. M. (2012). Potential role of tumor necrosis factor-α in downregulating sex hormone-binding globulin. *Diabetes* 61, 372–382. doi:10.2337/db11-0727

Solit, D. B., Basso, A. D., Olshen, A. B., Scher, H. I., and Rosen, N. (2003). Inhibition of heat shock protein 90 function down-regulates Akt kinase and sensitizes tumors to Taxol. *Cancer Res.* 63, 2139–2144.

Song, C., Pan, S., Zhang, J., Li, N., and Geng, Q. (2022). Mitophagy: a novel perspective for insighting into cancer and cancer treatment. *Cell. Prolif.* 55, e13327. doi:10.1111/cpr.13327

Sormendi, S., and Wielockx, B. (2018). Hypoxia pathway proteins as central mediators of metabolism in the tumor cells and their microenvironment. *Front. Immunol.* 9, 40. doi:10.3389/fimmu.2018.00040

Sung, H., Ferlay, J., Siegel, R. L., Laversanne, M., Soerjomataram, I., Jemal, A., et al. (2021). Global cancer statistics 2020: GLOBOCAN estimates of incidence and mortality worldwide for 36 cancers in 185 countries. *CA Cancer J. Clin.* 71, 209–249. doi:10.3322/caac.21660

Szatkowski, P., Krzysciak, W., Mach, T., Owczarek, D., Brzozowski, B., and Szczeklik, K. (2020). Nuclear factor-κB - importance, induction of inflammation, and effects of pharmacological modulators in Crohn's disease. *J. Physiol. Pharmacol.* 71. doi:10.26402/jpp.2020.4.01

Tacar, O., Sriamornsak, P., and Dass, C. R. (2013). Doxorubicin: an update on anticancer molecular action, toxicity and novel drug delivery systems. *J. Pharm. Pharmacol.* 65, 157–170. doi:10.1111/j.2042-7158.2012.01567.x

Tao, S.-C., and Guo, S.-C. (2020). Role of extracellular vesicles in tumour microenvironment. *Cell. Commun. Signal.* 18, 163. doi:10.1186/s12964-020-00643-5

Tartagni, O., Borók, A., Mensà, E., Bonyár, A., Monti, B., Hofkens, J., et al. (2023). Microstructured soft devices for the growth and analysis of populations of homogenous multicellular tumor spheroids. *Cell. Mol. Life Sci.* 80, 93. doi:10.1007/s00018-023-04748-1

Tkach, M., and Théry, C. (2016). Communication by extracellular vesicles: where we are and where we need to go. *Cell.* 164, 1226–1232. doi:10.1016/j.cell.2016.01.043

Vandooren, J., and Itoh, Y. (2021). Alpha-2-Macroglobulin in inflammation, immunity and infections. *Front. Immunol.* 12, 803244. doi:10.3389/fimmu.2021.803244

Vara-Perez, M., Felipe-Abrio, B., and Agostinis, P. (2019). Mitophagy in cancer: a tale of adaptation. *Cells* 8. doi:10.3390/cells8050493

Vyas, S., Zaganjor, E., and Haigis, M. C. (2016). *Mitochondria and Cancer*. doi:10.1038/nrc3365

Wang, Q., Shen, X., Chen, G., and Du, J. (2022). Drug resistance in colorectal cancer: from mechanism to clinic. *Cancers (Basel)* 14, 2928. doi:10.3390/cancers14122928

Watts, E. R., and Walmsley, S. R. (2019). Inflammation and hypoxia: HIF and PHD isoform selectivity. *Trends Mol. Med.* 25, 33–46. doi:10.1016/j.molmed.2018.10.006

Whitesell, L., and Lindquist, S. L. (2005). HSP90 and the chaperoning of cancer. *Nat. Rev. Cancer* 5, 761–772. doi:10.1038/nrc1716

Workman, P. (2004). Combinatorial attack on multistep oncogenesis by inhibiting the Hsp90 molecular chaperone. *Cancer Lett.* 206, 149–157. doi:10.1016/j.canlet.2003.08.032

Xin, X., Yang, H., Zhang, F., and Yang, S.-T. (2019). 3D cell coculture tumor model: a promising approach for future cancer drug discovery. *Process Biochem.* 78, 148–160. doi:10.1016/j.procbio.2018.12.028

Yang, D., Liu, J., Qian, H., and Zhuang, Q. (2023). Cancer-associated fibroblasts: from basic science to anticancer therapy. *Exp. Mol. Med.* 55, 1322–1332. doi:10.1038/s12276-023-01013-0

Yoshida, D., Kim, K., Yamazaki, M., and Teramoto, A. (2005). Expression of hypoxia-inducible factor 1alpha and cathepsin D in pituitary adenomas. *Endocr. Pathol.* 16, 123–131. doi:10.1385/EP:16:2:123

Zanoni, M., Cortesi, M., Zamagni, A., Arienti, C., Pignatta, S., and Tesei, A. (2020). Modeling neoplastic disease with spheroids and organoids. *J. Hematol. Oncol.* 13, 97. doi:10.1186/s13045-020-00931-0

Zhang, H.-G., and Grizzle, W. E. (2011). Exosomes and cancer: a newly described pathway of immune suppression. *Clin. Cancer Res.* 17, 959–964. doi:10.1158/1078-0432.CCR-10-1489

Zhang, S., Hosaka, M., Yoshihara, T., Negishi, K., Iida, Y., Tobita, S., et al. (2010). Phosphorescent light–emitting iridium complexes serve as a hypoxia-sensing probe for tumor imaging in living animals. *Cancer Res.* 70, 4490–4498. doi:10.1158/0008-5472.CAN-09-3948

Zhang, X., Kazerounian, S., Duquette, M., Perruzzi, C., Nagy, J. A., Dvorak, H. F., et al. (2009). Thrombospondin-1 modulates vascular endothelial growth factor activity at the receptor level. *FASEB J.* 23, 3368–3376. doi:10.1096/fj.09-131649

frontiers | Frontiers in Cell and Developmental Biology

TYPE Review
PUBLISHED 08 February 2024
DOI 10.3389/fcell.2024.1302490



OPEN ACCESS

EDITED BY
Xiangsheng Zuo,
University of Texas MD Anderson Cancer Center, United States

REVIEWED BY
Eswari Dodagatta-Marri,
University of California, San Francisco, United States
Hongbin Wang,
California Northstate University, United States

*CORRESPONDENCE
Ruchi Saxena,
ruchi.saxena@duke.edu

RECEIVED 26 September 2023
ACCEPTED 08 January 2024
PUBLISHED 08 February 2024

CITATION
Saxena R, Gottlin EB, Campa MJ, Bushey RT, Guo J, Patz EF Jr. and He Y-W (2024), Complement factor H: a novel innate immune checkpoint in cancer immunotherapy. *Front. Cell Dev. Biol.* 12:1302490. doi: 10.3389/fcell.2024.1302490



# Complement factor H: a novel innate immune checkpoint in cancer immunotherapy

Ruchi Saxena[1]*, Elizabeth B. Gottlin[2], Michael J. Campa[2], Ryan T. Bushey[2], Jian Guo[1], Edward F. Patz Jr.[2,3] and You-Wen He[1]

[1]Department of Integrative Immunobiology, Duke University School of Medicine, Durham, NC, United States, [2]Department of Radiology, Duke University School of Medicine, Durham, NC, United States, [3]Department of Pharmacology and Cancer Biology, Duke University School of Medicine, Durham, NC, United States

The elimination of cancer cells critically depends on the immune system. However, cancers have evolved a variety of defense mechanisms to evade immune monitoring, leading to tumor progression. Complement factor H (CFH), predominately known for its function in inhibiting the alternative pathway of the complement system, has recently been identified as an important innate immunological checkpoint in cancer. CFH-mediated immunosuppression enhances tumor cells' ability to avoid immune recognition and produce an immunosuppressive tumor microenvironment. This review explores the molecular underpinnings, interactions with immune cells, clinical consequences, and therapeutic possibilities of CFH as an innate immune checkpoint in cancer control. The difficulties and opportunities of using CFH as a target in cancer immunotherapy are also explored.

KEYWORDS

**complement, complement factor H, immunosuppression, tumor micro-environment, immune checkpoint, immunotherapy**

## 1 Introduction

The immune system is crucial in identifying and eradicating cancer cells (Fridman, 2012; Fridman et al., 2017). Tumors, however, have developed a variety of ways to elude immune surveillance, create an immunosuppressive microenvironment, and often coopt the immune system to promote tumor growth (Vinay et al., 2015; Abbott and Ustoyev, 2019). The concept of immunological checkpoints, which has emerged as a ground-breaking field, has highlighted the relevance of immune mechanisms that inhibit the host response (He and Xu, 2020; Pisibon et al., 2021; Guo et al., 2023). While immune checkpoints like PD-1/PD-L1, and CTLA4 have attracted a lot of attention, more recent data suggests that fundamental innate immune mechanisms including the complement system are also involved in immune escape mechanism in cancer (Parente et al., 2017; Moore et al., 2021).

The complement system constitutes an essential component of the innate immunity comprising of over 32 different proteins, including membrane proteins, serum proteins, and serosal proteins. Three distinct mechanisms can activate the complement system: the alternative pathway (AP), the classical pathway (CP), and the lectin pathway (LP) (Ricklin and Pouw, 2021; Kemper et al., 2023). While the CP and LP are initiated by antibody- and carbohydrate-mediated recognition processes, respectively, the AP is activated by

hydrolysis of C3 and is constitutively active. Though the three pathways differ in the initiation of the complement cascade, they converge at the formation of C3 convertase (C4bC2b in CP and LP and C3bBb in AP) resulting in cleavage of C3 to C3a and C3b. Furthermore, by binding C3b, C3 convertases forms C5 convertases (i.e., C4bC2aC3b in CP and LP and C3bBbC3b in the AP), resulting in the assembly of cell lytic, membrane-attack complex (MAC, C5b-9). Membrane bound C3b also act as opsonin and triggers ingestion by phagocytosis. Furthermore, the anaphylatoxins C3a and C5a, formed as split products of C3 and C5 cleavage, associate with the cells of the innate and adaptive immune system to induce chemotactic and inflammatory responses (Ling and Murali, 2019; Kemper et al., 2023).

Complement factor H (CFH) is the most important inhibitory regulator of AP activation. It is a serum protein that plays a crucial function in suppressing complement activation on cells and in the extracellular matrix of host tissues (Ferreira et al., 2010) by binding to cell surfaces via glycosaminoglycans (Blaum et al., 2015; Langford-Smith et al., 2015). While liver is the predominant source of CFH (Schwaeble et al., 1987), it is also produced by other cell types (Brooimans et al., 1990; Chen et al., 2007; Licht et al., 2009; Ferreira et al., 2010; Sakaue et al., 2010; Tu et al., 2010). In addition, a truncated form of CFH, known as factor H-like protein 1 (FHL-1), produced by alternative splicing of the *cfh* gene (Ripoche et al., 1988), can be found locally, such as in retinal pigment epithelial cells and the liver (Clark et al., 2014). CFH competes with factor B for binding to C3b and has three complement-regulating functions: 1) prevents the formation of C3 convertase (C3bBb) via the AP; 2) accelerates the dissociation of already formed C3bBb; 3) serves as a cofactor for the serine protease complement factor I (CFI) making C3b susceptible to cleavage leading to the formation of iC3b (Makou et al., 2013). When bound to cell surface, the iC3b fragment undergoes further hydrolysis by CFI and membrane-bound cofactors like CR1, resulting in the release of C3dg and C3d. While C3b deposition initiates series of reactions culminating in the formation of MAC, its proteolytic degradation products, iC3b, C3dg, and C3d lead to lymphocyte activation and maturation by interacting with their receptor, complement receptor 2 (CR2) on immune cells like B cells and DCs (Kalli et al., 1991; Nagar et al., 1998; Carroll, 2004; Lyubchenko et al., 2005; Carroll and Isenman, 2012; Merle et al., 2015). Thus, by preventing the production and amplification of C3 convertases and encouraging the decay of already produced convertases, CFH plays a crucial part in controlling amplification of the complement system (Jozsi et al., 2019). By interacting with a different complement protein, including C3b and C3d, as well as cell surface glycosaminoglycans (GAGs) and complement receptor 3 (CR3), CFH prevents complement activation. However, dysregulation of CFH expression and function in the context of cancer has also been linked to immune evasion, fostering tumor development and metastasis (Jozsi and Uzonyi, 2021).

## 2 Dysregulation of CFH in cancer and impact on clinical outcomes

CFH is overexpressed on many different types of cancer cells and is usually associated with poor prognosis. The first report of the association of CFH with cancer was published in 1998 where it was demonstrated that the presence of CFH on lung cancer cells makes them resistant to complement mediated lysis (Varsano et al., 1998). Since then, several reports have confirmed the role of CFH in various solid tumors including glioblastoma (Junnikkala et al., 2000), bone cancer (Fedarko et al., 2000), ovarian cancer (Junnikkala et al., 2002), colon cancer (Wilczek et al., 2008), cutaneous squamous cell carcinoma (Riihila et al., 2014) and breast cancer (Smolag et al., 2020). In contrast, a few reports have shown the anti-tumoral effect of CFH. Bonavita et al. demonstrate that in a mouse model of sarcoma, CFH exerts antitumoral effect by inhibiting the production of anaphylatoxins thus creating an immunosuppressive environment (Bonavita et al., 2015). Another study reports spontaneous hepatic tumor formation in aged mice with CFH deficiency (Laskowski et al., 2020). This was presumably due to life-long inflammation or potentially due to non-canonical effects of CHF; it is not clear if this finding would be relevant to humans undergoing treatment with an anti-CFH antibody. Thus, CFH has become a therapeutic target of interest, although the exact way to target CFH without off-target effects has been challenging.

CFH is also produced by cells other than the liver, including cancer cells. In renal cell carcinoma, intracellular CFH has been reported to drive tumor growth independent of the complement cascade (Daugan et al., 2021). It has been shown that CFH is upregulated in lung cancer, and that this overexpression is associated with larger tumors, lymph node metastases, and worse overall survival (Ajona et al., 2004; Cui et al., 2011). Increased CFH expression is also linked to larger tumor size, metastasis, and late stage tumors in breast cancer (Smolag et al., 2020). Further, CFH levels are elevated in cutaneous squamous cell carcinoma and overexpression is linked to immunosuppression (Johnson et al., 2022). Increased CFH expression has also been detected in tumor tissues relative to neighboring normal tissues in this disease. CFH dysregulation in cancer has significant implications for clinical outcomes. Increased CFH level in the tumors of lung adenocarcinoma patients is linked to poorer overall and disease-free survival and serves as a prognostic marker (Cui et al., 2011). Additionally, CFH may function as a prognostic biomarker in other malignancies including cutaneous squamous cell carcinoma (Johnson et al., 2022). Furthermore, it has been linked to the invasion and spread of cancer cells. Small extracellular vesicles, called exosomes, secreted by cancer cells can promote metastasis by delivering protein and mRNA cargo to other cancer cells and to non-cancer cells at distant sites, helping to prepare "premetastatic niches" where cancer cells can seed. Mao et al. have shown that CFH on tumor extracellular vesicles stimulates tumorigenesis and metastasis (Mao et al., 2020). Another study by Bushey et al. confirms that CFH-containing exosomes, secreted from tumors that express CFH, may be shielded from complement-dependent destruction by their CFH and a higher level of these exosomes has been linked to higher metastatic potential of cancer cell lines (Bushey et al., 2021).

Interestingly, early-stage non-small cell lung cancer patients who do not develop metastasis or recurrence after surgical resection had autoantibodies against CFH. These anti-CFH autoantibodies were found to recognize a conformationally unique CFH epitope hypothesized to be presented on the surface of tumor cells (Amornsiripanitch et al., 2010; Campa et al., 2015). The autoantibodies inhibited CFH binding to lung cancer cells,

increased C3b deposition, and induced complement mediated lysis of tumor cells (Campa et al., 2015) and also served as prognostic marker for stage I NSCLC (Gottlin et al., 2022).

# 3 CFH functions as innate immune checkpoint

CFH is a key component in the process of cancer immune evasion (Ricklin et al., 2010). Multiple studies have established that cancer cells use CFH to undermine complement-mediated immune responses and enhance tumor growth and progression (Afshar-Kharghan, 2017; Revel et al., 2020). The importance of CFH in age-related macular degeneration and its connection to cancer are highlighted by Riihilä et al. (Riihila et al., 2014) who discuss how CFH overexpression may help cancer cells evade the immune system. CFH has been shown to create immunosuppressive effects by preventing complement activation, impairing antigen presentation, and encouraging regulatory T cell development (Parente et al., 2017). It also impacts immune cell trafficking, cytokine production, and tumor-associated macrophage polarization, contributing to an immunosuppressive tumor microenvironment (TME) (Wang et al., 2016; Parente et al., 2017; Bushey et al., 2023). The following five mechanisms have been proposed to explain how CFH helps cancer cells to evade complement-mediated toxicity or immune responses and advance tumor growth.

## 3.1 CFH causes complement evasion

As discussed previously, the activation of the complement pathway through CP, LP and AP results in the production of complement components that participate in various effector functions. These include opsonization, inflammation, and direct lysis of target cells. In the context of cancer, the complement system's role extends beyond its traditional function, as it has been implicated in cancer immune evasion and tumor progression (Ajona et al., 2019b; Senent et al., 2022). Studies have demonstrated the involvement of complement in cancer immune surveillance. For instance, Reis et al. provide an extensive review on the role of complement in cancer immunotherapy, highlighting its importance in tumor recognition, inflammation, and clearance (Reis et al., 2018). Zhang et al. discuss the implications of the complement system in tumor development, prevention, and therapy, emphasizing the role in immunosurveillance and the potential for targeting complement components in cancer treatment (Zhang et al., 2019). These studies collectively underscore the critical role of the complement system in cancer immune surveillance and its potential as a target for cancer immunotherapy.

CFH gives cancer cells the ability to sabotage complement-mediated immune responses and advance tumor growth as discussed above. The formation of the membrane attack complex (MAC) and consequent cell lysis are both prevented by CFH's ability to attach to the surfaces of cancer cells and suppress complement activation (Parente et al., 2017). Additionally, CFH can obstruct opsonization, which is necessary for phagocytic cells to recognize and destroy cancer cells. CFH binds to C3b and thus prevents C3b from adhering to cancer cells and inhibiting phagocytosis. Further, by modulating the complement cascade, CFH can limit the production of pro-inflammatory complement fragments C3a and C5a and suppress immune cell-mediated tumor destruction. In addition, CFH prevents the cleavage of C3b and thus the formation of cleavage products displaying the C3d moiety that serves as a ligand for CR2 receptors on B cells and DCs. The binding of C3d to CR2 receptor on immune cells is important for activation and affinity maturation of lymphocytes (Alcorlo et al., 2015; De Groot et al., 2015). Due to these evasion tactics, cancer cells are better able to survive and proliferate by evading immune surveillance.

## 3.2 CFH impairs antigen presentation, T cell expansion, and B cell functions

CFH has been found to interfere with antigen presentation, a critical step at the beginning of adaptive immune responses against cancer cells. Dendritic cells (DCs) can bind CFH and lose their capacity to effectively deliver tumor antigens to T cells. This reduced antigen presentation restricts the activation and growth of tumor-specific T cells, suppressing the adaptive anti-tumor immune response and fostering immunological tolerance (Olivar et al., 2016; Dixon et al., 2017). CFH also enhances the differentiation of anti-inflammatory and tolerogenic monocyte derived DCs. These immature DCs show lower expression of maturation markers and costimulatory molecules, decreased production of pro-inflammatory Th1-cytokines like IL-6, IL8, IL-12, TNF, IFN-γ, and favored immunomodulatory cytokines production including TGF-β and IL-10. These DCs do not cause activation of allo-stimulated T cells and increased the production of regulatory T cells (Tregs) (Olivar et al., 2016).

In addition, CFH directly engages with T cells and inhibits their activation, proliferation, and effector activities (Wang et al., 2016). CFH inhibits intratumoral effector T cell function through direct binding to its receptor CR3 or indirectly through inhibiting production of complement activation products C3a and C5a. It has been shown that CR3 is expressed on activated $CD4^+$ and $CD8^+$ T cells (Gray and Horwitz, 1988; Savary and Lotzova, 1992; Hamann et al., 1997; Wagner et al., 2001) and a majority of $CD8^+$ TILs from melanoma (Hersey and Jamal, 1990) and pancreatic cancer (Ademmer et al., 1998). The upregulated CR3 delivers a negative signal to effector T cells because not only is CR3 expression associated with dysfunctional ($CD28^-$, CD4low, CD8low, or $CD57^+$) T cells in different diseases (Dianzani et al., 1994; Mollet et al., 1998) but also direct engagement of CR3 on T cells by C3bi-coated zymosan was shown to inhibit T cell proliferation (Wagner et al., 2001). Recent reports strongly support the premise that tumor-associated/derived CFH binds to CR3 on $CD4^+$ and $CD8^+$ TILs and directly inhibits their expansion. Further, it is known that locally produced C3a/C5a signaling through Ca3R/Ca5R on T cells is required for CD28 upregulation and T cell activation (Lalli et al., 2008; Strainic et al., 2008). Since CFH inhibits the production of these anaphylatoxins (Ajona et al., 2004) further T cell activation is impeded. However, the role of C3a/C5a in T cell function tumor immunity is still controversial (Reis et al., 2018; Ajona et al., 2019a; Wang et al., 2019).

Merle et al. discovered that CFH also inhibits B cell activation and function. (Merle et al., 2015). The C3 split product, C3d when conjugated with antigen interacts with its receptor CR2 on B cells and follicular DC to induce both B cell activation and follicular DCs mediated B cell affinity maturation thus presenting these antigens in germinal centers to incite effector and memory B cell responses (Carroll and Isenman, 2012; Merle et al., 2015). CFH interferes with the production of complement split product C3d and thus inhibits B cell responses. Further, uninhibited systemic complement activation is induced by loss of CFH resulting in increased production of C3 fragments with concomitant elevated surface levels of CR2 on mature B cells associated with increased BCR signaling (Kiss et al., 2019).

## 3.3 CFH promotes regulatory T cell expansion

Though the direct interaction of CFH with Tregs has not been established, the proliferation and activation of Tregs in the TME have been linked to CFH overexpression. It has been shown that tumor cell-expressed indoleamine 2,3-dioxygenase 1 increased CFH and FHL-1 expression independent of tryptophan metabolism resulting in Treg proliferation and activation. Further, increased expression levels of CFH and FHL-1 levels were associated with poorer survival in glioblastoma patients (Zhai et al., 2021). One possible explanation for the effect of CFH on Tregs is that CFH inhibits production of C3d. C3d binds to CR2 on intratumoral Tregs (itTregs) and cause suppression of Id2 expression which in turn triggers apoptosis and loss in function of itTregs. Amplified CFH expression or activity creates an environment that is more immunosuppressive and favorable to Treg accumulation and function. Platt et al., have shown that C3d in the tumor augments anti-tumor immunity via eliminating itTregs by binding and signaling through its cognate receptor CR2 on itTregs (Platt et al., 2017). Furthermore, increased CFH expression is associated with increased prevalence of Tregs and an immunosuppressive TME in cutaneous squamous cell carcinoma (Johnson et al., 2022).

## 3.4 CFH modulates immune cell trafficking and function

CFH has the capacity to control cytokine production and immune cell trafficking in the TME. It can influence the recruitment and activation of other immune cells, such as neutrophils and macrophages (Ricklin and Pouw, 2021). CFH binds to CR3 receptors (CD11b/CD18) on neutrophils via its SCR7 and SCR19-20 domains (Avery and Gordon, 1993; DiScipio et al., 1998), to modulate cell activation and function (Losse et al., 2010). It is known that complement pathways and neutrophils serve to activate each other and the AP acts as a positive feedback amplification of neutrophil activation (Camous et al., 2011; Halbgebauer et al., 2018). Studies have shown that neutrophils with immunosuppressive properties expand in the TME and are associated with poor prognosis. The neutrophils in the TME secrete proteases, chemokines and cytokines attracting other tumor promoting immune cells or immunosuppressive T cells along with ROS generation and formation of neutrophil extracellular traps (NETs) facilitating cancer progression. These neutrophils can serve as biomarkers for progression and therapy response in cancer patients and may be used as targets to augment the efficacy of anti-cancer therapy (Masucci et al., 2019; Wu et al., 2020). Further, Zhao et al. have shown that a higher ratio of neutrophil-to-lymphocyte is associated with adverse overall outcome in many solid tumors (Wu et al., 2020; Zhao et al., 2020). Interestingly, there are reports to show that CFH not only facilitates neutrophil recruitment, but it also has an anti-inflammatory effect induced by the formation of neutrophil extracellular traps (NETs) (Schneider et al., 2016; Chen et al., 2018). In addition, CFH treatment of neutrophils induces reactive oxygen species (ROS) production and degranulation in neutrophils activated by PMA, fibronectin plus b-glucan, or anti-neutrophil cytoplasmic autoantibody, thus inhibiting neutrophil apoptosis (Kasahara et al., 1997).

Further, there is evidence to show that neutrophils and monocytes also engage CFH through membrane bound molecules such as integrins (e.g., αIIbβ3) and L-selectin (Lambris et al., 1980; Malhotra et al., 1999; Kang et al., 2012), that are known CFH receptors. In addition, CFH possibly binds to CR4 receptors on macrophages and DCs and exhibits similar cellular effects as binding to CR3 receptors on neutrophils (Parente et al., 2017). These additional interactions mediate the control of cell adhesion and migration, and cytokine production confirming that CFH has a direct anti-inflammatory and tolerogenic effect on intra-tumoral leukocytes.

CFH can also enhance Myeloid- derived suppressor cells (MDSC) accumulation, expansion, and immunosuppressive functions within the TME, contributing to immune evasion, probably via direct interaction with CR3 receptors (Sun et al., 2012; Parente et al., 2017) as discussed below. The role of MDSC accumulation in the TME in cancer progression has been confirmed by several studies (Pillay et al., 2013; Wu et al., 2020), and the importance of targeting these cells for cancer immunotherapy has also been demonstrated (Law et al., 2020; Li K. et al., 2021; Li X. et al., 2021). Dysregulation of CFH can lead to immunological escape from tumors by impairing immune cell homeostasis and changing the ratio of pro-inflammatory to anti-inflammatory cytokines (Jozsi et al., 2019; Smolag et al., 2020).

## 3.5 CFH promotes tumor-associated macrophage polarization

CFH can promote tumor-associated macrophages (TAMs) polarization towards an immunosuppressive M2-like phenotype, characterized by the release of immunosuppressive and anti-inflammatory cytokines. It favors differentiation of $CD14^{+}$ monocyte into IL-10 producing (HLA-DRlowPD-L1hi) macrophages with immunosuppressive properties. CFH binds to unidentified receptor(s) on monocytes surface through it SCR19-20 region that leads to its internalization triggering downstream intracellular events to transform the transcriptome into an immunosuppressive signature. (Smolag et al., 2020). This polarization also favors tumor growth and creates an immunosuppressive TME.

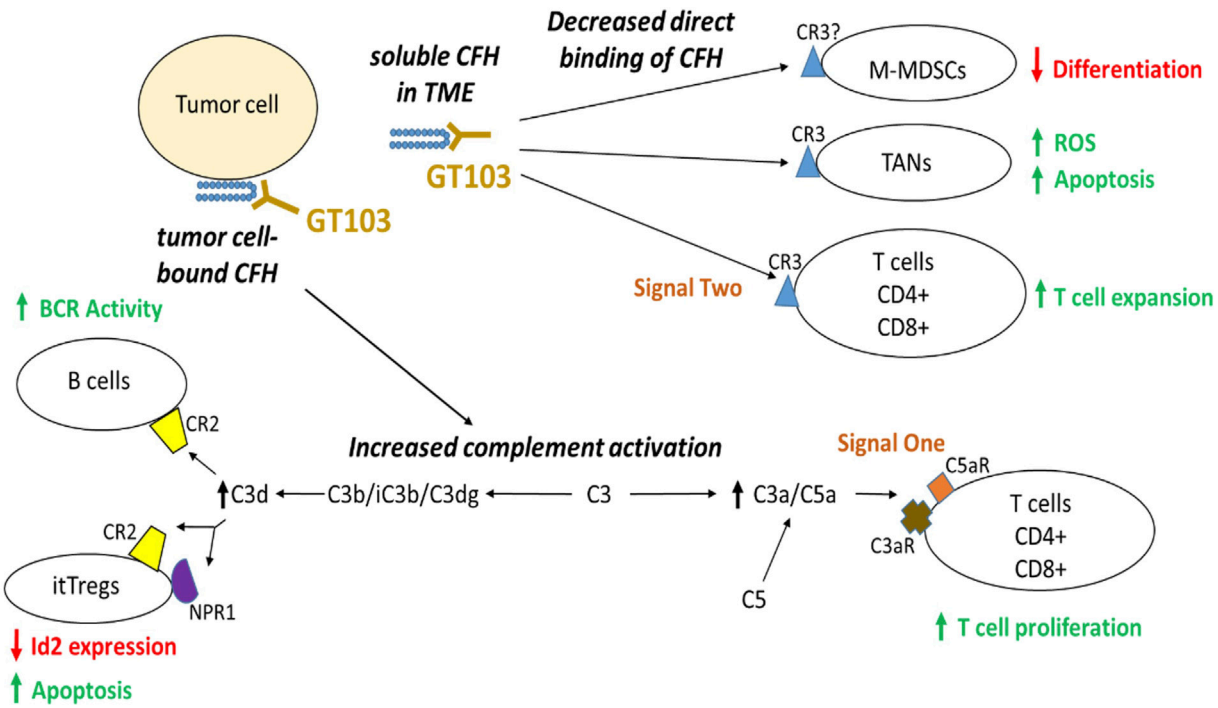


FIGURE 1
Anti-tumor mechanism of GT103. CFH in the TME inhibits antitumor immunity by two major modes of actions: direct binding to its receptor CR3 on TANs and activated T cells as well as possibly M-MDSCs, and indirectly through suppressing complement activation. GT103 blockade of CFH actions in the TME results in reduced M-MDSC differentiation, increased apoptosis of itTregs and TANs, as well as enhanced expansion of effector $CD4^+/CD8^+$ T cells and activated B cells.

In summary, CFH mediates immune evasion by cancer cells through a variety of cellular and molecular pathways. Because of its overexpression, inhibition of opsonization, and support for an immunosuppressive TME, CFH helps cancer cells resist complement-mediated and complement-independent immune responses. Understanding these pathways lays the groundwork for the creation of innovative therapeutic approaches that target CFH to boost antitumor immune responses and enhance cancer treatment results.

## 4 Targeting CFH as an immune checkpoint for cancer immunotherapy

Targeting CFH and its related molecular pathways is a novel therapeutic approach to modify the TME, improve anticancer immune responses, and decrease tumor growth and spread. Multiple strategies could be used for targeting CFH for anti-cancer therapies. Use of monoclonal antibodies (mAbs) designed to specifically target CFH could neutralize its immunosuppressive effects and inhibit cancer progression. These mAbs can potentially block CFH's interactions with complement components, permit complement activation of tumor cells, while driving anti-tumor immune program. Campa et al. have shown that CFH autoantibodies isolated from early stage lung cancer patients can activate the complement system and cause cytotoxicity of tumor cells *in vitro* (Campa et al., 2015). Based on this study and the correlation of anti-CFH autoantibodies with early stage NSCLC, better outcome, and longer time to recurrence (Amornsiripanitch et al., 2010; Gottlin et al., 2022), a monoclonal anti-CFH antibody was cloned from a single peripheral B cell of a NSCLC patient. This therapeutic antibody, GT103 identifies a conformationally distinct epitope of CFH located in SCR 19 domain (Bushey et al., 2016). It exhibits growth inhibitory activity *in vivo* in several different cancer models (Bushey et al., 2016; Bushey et al., 2021; Bushey et al., 2023; Saxena et al., 2023). Further, it enhances CDC of rituximab-resistant malignant B cells (Winkler et al., 2017). GT103 has shown potential as a therapeutic agent in cancer (Clarke et al., 2022).

Studies on the mechanism of action of GT103 show that it overcomes CFH-mediated complement evasion in the TME. In summary, GT103 modulates the TME and limits tumor growth via the following processes (summarized in Figure 1). 1. GT103 causes complement activation through the CP and induces CDC of cancer cells both *invitro* and *invivo* (Bushey et al., 2016; Bushey et al., 2021; Bushey et al., 2023). 2. GT103 enhances antigen presentation and T cell expansion. GT103 treatment increases antigen specific $CD4^+$ and $CD8^+$ T cells in the TME in a syngeneic model of lung cancer (Saxena et al., 2023). Further, it increases the influx of effector T and B cells along with DCs and also leads to increased activation of B cell receptor pathways, mechanisms crucial for antigen presentation (Bushey et al., 2023; Saxena et al., 2023). 3. GT103 inhibits Treg activation and expansion. GT103 treatment decreases itTregs in the TME possibly by inhibiting their activation and inducing their apoptosis (Saxena et al., 2023). 4. It creates a favorable TME by modulating immune cell trafficking and cytokine production,

counteracting the effect of CFH. GT103 reduces the influx of immunosuppressive tumor associated neutrophils, MDSCs, and itTregs. It further reduces serum levels of pro-inflammatory and pro-tumorigenic cytokines (Saxena et al., 2023). 5. GT103 inhibits tumor-associated macrophage polarization to an immunosuppressive phenotype as evidenced by decreased M2-type macrophages in the TME (Saxena et al., 2023). 6. Further, it inhibits hepatocellular carcinoma (HCC) tumorigenesis and metastasis driven by tumor extracellular vesicles overexpressing CFH (Mao et al., 2020). GT103 can also target CFH-expressing tumor-derived exosomes for destruction via innate immune mechanisms via Fc interactions with C1q or, presumably Fc gamma receptors on macrophages (Bushey et al., 2021). Thus, by promoting complement activation and immune cell recruitment to the TME, the anti-CFH antibody GT103 has demonstrated efficacy in suppressing tumor growth in preclinical models. The antibody is currently being evaluated as monotherapy in a phase Ib clinical trial (Clarke et al., 2022) and in combination with Keytruda in phase II for advanced, refractory/relapsed NSCLC patients.

In addition to using monoclonal antibodies to target CFH, small molecule inhibitors that can disrupt CFH's interaction with tumor cells and immune cells can be created as therapeutic agents and utilized as single agents or in combination with other therapies to improve their efficacy. Furthermore, CFH-based vaccines can be designed to encourage the immune system to recognize and destroy CFH-overexpressing tumor cells. CFH peptides or fusion proteins can be used as antigens in these vaccines to elicit specific immune responses against CFH-expressing tumor cells. To improve immunogenicity, CFH-based vaccines can be coupled with adjuvants or immune-stimulatory drugs. Adoptive cell therapy with CFH-specific immune cells such T cells or natural killer (NK) cells can also be utilized to target and eradicate CFH-expressing tumor cells. To improve specificity and cytotoxicity against tumor cells, these immune cells can be modified to express CFH-specific receptors such as T cell receptors (TCRs) or chimeric antigen receptors (CARs). Furthermore, gene editing techniques, such as CRISPR-Cas9, can be used to alter CFH expression in tumor cells and could potentially be used as anti-cancer therapy. These immunotherapeutic approaches have the potential to increase immune surveillance and promote anti-tumor immune responses and need to be explored as anti-CFH therapy for cancer. In addition, treatment outcomes for cancer could be greatly enhanced by combining CFH-targeted treatments with other therapeutic techniques. Multiple facets of tumor growth and immune evasion can be addressed by combinations with immunotherapies, chemotherapy, and targeted treatments. By releasing the inhibitory effects of CFH and further activating anti-tumor immune responses, immune checkpoint inhibitors, such as anti-PD-1/PD-L1 or anti-CTLA-4 antibodies, can be used in conjunction with CFH-targeted therapies to increase the effectiveness of immune checkpoint blockade (Ajona et al., 2019b; Ricklin et al., 2019; Saxena et al., 2023). CDC of rituximab resistant malignant B cells from CLL patients can be augmented by GT103 (Winkler et al., 2017) and CDC of human lung tumor cell lines by the anti-PD-L1 drug avelumab can be augmented by GT103 (Saxena et al., 2023). Further, chemotherapeutic drugs can be used in conjunction with CFH-targeted therapies to take advantage of the immunomodulatory effects of CFH inhibition while also specifically targeting tumor cells. In addition to promoting immune-mediated tumor clearance, this combined approach can synergistically increase the cytotoxic effects on tumor cells.

## 5 Future perspectives and challenges

A thorough knowledge of the molecular pathways underpinning CFH-mediated immune evasion is essential to take full advantage of the therapeutic potential of CFH and requires further investigation. Targeted therapy development will benefit from understanding the intricate interactions between CFH, complement proteins, immune cells, and the TME. While anti-CFH therapy has shown promise in preclinical and early clinical trials, there are significant obstacles to its use in cancer treatment. Targeting a major component of the immune system, such as CFH, might have unintended consequences, such as upsetting immunological balance, which can lead to autoimmune reactions and increased susceptibility to infections. The development of atypical hemolytic uremic syndrome (aHUS) is a major concern, as evidenced by a finding that shows autoantibodies against the CFH SCR 19-20 domains are correlated with aHUS (Blanc et al., 2012; Durey et al., 2016). As a result, the challenge is to develop anti-CFH agents that specifically target cancer cells while protecting healthy cells that express CFH. Furthermore, the duration and dosage of anti-CFH medication can influence the likelihood of autoimmune responses. Prolonged or high-dosage treatment may increase the risk of immune system dysregulation; thus, the dose must be carefully regulated.

Furthermore, the effectiveness of anti-CFH therapy might also depend on the type of cancer and individual patient characteristics. Some tumors may not respond as well to this sort of treatment, as the targeting epitope may be absent. Identifying the patients who would gain the most from anti-CFH therapy is still a challenge. Patient selection based on biomarkers, the patient immune status, or genetic profile is crucial, although it is still in its early stages. Furthermore, patients with pre-existing autoimmune disorders could experience progressive or new symptoms when exposed to anti-CFH therapy and may not be suitable candidates.

In addition, cancer cells may develop resistance to anti-CFH treatment over time as is seen with other targeted medicines. This has the potential to result in therapy failure and disease progression. To achieve the most favorable results, anti-CFH therapy may need to be combined with other treatment modalities such as chemotherapy, immunotherapy, or radiation therapy. The successful implementation of CFH-targeted medicines depends on selecting the right patient populations, tailoring treatment plans, and addressing potential off-target consequences.

## 6 Conclusion

The complement system is a complex but important part of innate immunity. Through its control of the complement system, interactions with immune cells, and effects on the TME, complement factor H contributes significantly to immune evasion in cancer. Developing efficient strategies to combat immunological evasion while driving an effective adaptive immune response in

cancer requires an understanding of the intricate interactions between CFH and numerous immune system elements. As a therapeutic strategy to boost anti-tumor immune responses and better patient outcomes, targeting CFH shows promise. To fully investigate the therapeutic potential of CFH as a therapeutic target in cancer immunotherapy, additional study and clinical trials are required.

## Author contributions

RS: Writing–original draft, Writing–review and editing. EG: Writing–review and editing. MC: Writing–review and editing. RB: Writing–review and editing. JG: Writing–review and editing. EP: Funding acquisition, Writing–review and editing. Y-WH: Conceptualization, Funding acquisition, Writing–review and editing.

## Funding

The author(s) declare financial support was received for the research, authorship, and/or publication of this article. The study was supported by the Department of Defense through Lung Cancer Research Program Translational Research Partnership Award No. W81XWH-19-1-0342 to EP and Y-WH, and by an award from the Sunny Li Family Fund to Y-WH.

## Conflict of interest

EFP is a Founder, CEO and Board Member of Grid Therapeutics, LLC. MJC and EBG are Founders and Board Members of Grid Therapeutics, LLC. RS, RTB, JG and YWH have no potential conflicts of interest.

The remaining authors declare that the research was conducted in the absence of any commercial or financial relationships that could be construed as a potential conflict of interest.

The author(s) declared that they were an editorial board member of Frontiers, at the time of submission. This had no impact on the peer review process and the final decision.

## Publisher's note



## References

Abbott, M., and Ustoyev, Y. (2019). Cancer and the immune system: the history and background of immunotherapy. *Semin. Oncol. Nurs.* 35 (5), 150923. doi:10.1016/j.soncn.2019.08.002

Ademmer, K., Ebert, M., Muller-Ostermeyer, F., Friess, H., Buchler, M. W., Schubert, W., et al. (1998). Effector T lymphocyte subsets in human pancreatic cancer: detection of CD8+CD18+ cells and CD8+CD103+ cells by multi-epitope imaging. *Clin. Exp. Immunol.* 112 (1), 21–26. doi:10.1046/j.1365-2249.1998.00546.x

Afshar-Kharghan, V. (2017). The role of the complement system in cancer. *J. Clin. Invest.* 127 (3), 780–789. doi:10.1172/JCI90962

Ajona, D., Castano, Z., Garayoa, M., Zudaire, E., Pajares, M. J., Martinez, A., et al. (2004). Expression of complement factor H by lung cancer cells: effects on the activation of the alternative pathway of complement. *Cancer Res.* 64 (17), 6310–6318. doi:10.1158/0008-5472.CAN-03-2328

Ajona, D., Ortiz-Espinosa, S., and Pio, R. (2019a). Complement anaphylatoxins C3a and C5a: emerging roles in cancer progression and treatment. *Semin. Cell Dev. Biol.* 85, 153–163. doi:10.1016/j.semcdb.2017.11.023

Ajona, D., Ortiz-Espinosa, S., Pio, R., and Lecanda, F. (2019b). Complement in metastasis: a comp in the camp. *Front. Immunol.* 10, 669. doi:10.3389/fimmu.2019.00669

Alcorlo, M., Lopez-Perrote, A., Delgado, S., Yebenes, H., Subias, M., Rodriguez-Gallego, C., et al. (2015). Structural insights on complement activation. *FEBS J.* 282 (20), 3883–3891. doi:10.1111/febs.13399

Amornsiripanitch, N., Hong, S., Campa, M. J., Frank, M. M., Gottlin, E. B., and Patz, E. F., Jr. (2010). Complement factor H autoantibodies are associated with early stage NSCLC. *Clin. Cancer Res.* 16 (12), 3226–3231. doi:10.1158/1078-0432.CCR-10-0321

Avery, V. M., and Gordon, D. L. (1993). Characterization of factor H binding to human polymorphonuclear leukocytes. *J. Immunol.* 151 (10), 5545–5553. doi:10.4049/jimmunol.151.10.5545

Blanc, C., Roumenina, L. T., Ashraf, Y., Hyvarinen, S., Sethi, S. K., Ranchin, B., et al. (2012). Overall neutralization of complement factor H by autoantibodies in the acute phase of the autoimmune form of atypical hemolytic uremic syndrome. *J. Immunol.* 189 (7), 3528–3537. doi:10.4049/jimmunol.1200679

Blaum, B. S., Hannan, J. P., Herbert, A. P., Kavanagh, D., Uhrin, D., and Stehle, T. (2015). Structural basis for sialic acid-mediated self-recognition by complement factor H. *Nat. Chem. Biol.* 11 (1), 77–82. doi:10.1038/nchembio.1696

Bonavita, E., Gentile, S., Rubino, M., Maina, V., Papait, R., Kunderfranco, P., et al. (2015). PTX3 is an extrinsic oncosuppressor regulating complement-dependent inflammation in cancer. *Cell* 160 (4), 700–714. doi:10.1016/j.cell.2015.01.004

Brooimans, R. A., van der Ark, A. A., Buurman, W. A., van Es, L. A., and Daha, M. R. (1990). Differential regulation of complement factor H and C3 production in human umbilical vein endothelial cells by IFN-gamma and IL-1. *J. Immunol.* 144 (10), 3835–3840. doi:10.4049/jimmunol.144.10.3835

Bushey, R. T., Gottlin, E. B., Campa, M. J., and Patz, E. F., Jr. (2021). Complement factor H protects tumor cell-derived exosomes from complement-dependent lysis and phagocytosis. *PLoS One* 16 (6), e0252577. doi:10.1371/journal.pone.0252577

Bushey, R. T., Moody, M. A., Nicely, N. L., Haynes, B. F., Alam, S. M., Keir, S. T., et al. (2016). A therapeutic antibody for cancer, derived from single human B cells. *Cell Rep.* 15 (7), 1505–1513. doi:10.1016/j.celrep.2016.04.038

Bushey, R. T., Saxena, R., Campa, M. J., Gottlin, E. B., He, Y. W., and Patz, E. F. (2023). Antitumor immune mechanisms of the anti-complement factor H antibody GT103. *Mol. Cancer Ther.* 22, 778–789. doi:10.1158/1535-7163.MCT-22-0723

Camous, L., Roumenina, L., Bigot, S., Brachemi, S., Fremeaux-Bacchi, V., Lesavre, P., et al. (2011). Complement alternative pathway acts as a positive feedback amplification of neutrophil activation. *Blood* 117 (4), 1340–1349. doi:10.1182/blood-2010-05-283564

Campa, M. J., Gottlin, E. B., Bushey, R. T., and Patz, E. F., Jr. (2015). Complement factor H antibodies from lung cancer patients induce complement-dependent lysis of tumor cells, suggesting a novel immunotherapeutic strategy. *Cancer Immunol. Res.* 3 (12), 1325–1332. doi:10.1158/2326-6066.CIR-15-0122

Carroll, M. C. (2004). The complement system in regulation of adaptive immunity. *Nat. Immunol.* 5 (10), 981–986. doi:10.1038/ni1113

Carroll, M. C., and Isenman, D. E. (2012). Regulation of humoral immunity by complement. *Immunity* 37 (2), 199–207. doi:10.1016/j.immuni.2012.08.002

Chen, M., Forrester, J. V., and Xu, H. (2007). Synthesis of complement factor H by retinal pigment epithelial cells is down-regulated by oxidized photoreceptor outer segments. *Exp. Eye Res.* 84 (4), 635–645. doi:10.1016/j.exer.2006.11.015

Chen, S. F., Wang, F. M., Li, Z. Y., Yu, F., Chen, M., and Zhao, M. H. (2018). Complement factor H inhibits anti-neutrophil cytoplasmic autoantibody-induced neutrophil activation by interacting with neutrophils. *Front. Immunol.* 9, 559. doi:10.3389/fimmu.2018.00559

Clark, S. J., Schmidt, C. Q., White, A. M., Hakobyan, S., Morgan, B. P., and Bishop, P. N. (2014). Identification of factor H-like protein 1 as the predominant complement regulator in Bruch's membrane: implications for age-related macular degeneration. *J. Immunol.* 193 (10), 4962–4970. doi:10.4049/jimmunol.1401613

Clarke, J., Stinchcombe, T., Crawford, J., Mamdani, H., Gu, L., Ready, N., et al. (2022). 699 Interim results from a phase IB, first-in-human study of a novel complement factor

h inhibitor (GT103) in patients with refractory non-small cell lung cancer (NSCLC). *J. Immunother. Cancer* 10 (2), A730. doi:10.1136/jitc-2022-SITC2022.0699

Cui, T., Chen, Y., Knosel, T., Yang, L., Zoller, K., Galler, K., et al. (2011). Human complement factor H is a novel diagnostic marker for lung adenocarcinoma. *Int. J. Oncol.* 39 (1), 161–168. doi:10.3892/ijo.2011.1010

Daugan, M. V., Revel, M., Thouenon, R., Dragon-Durey, M. A., Robe-Rybkine, T., Torset, C., et al. (2021). Intracellular factor H drives tumor progression independently of the complement cascade. *Cancer Immunol. Res.* 9 (8), 909–925. doi:10.1158/2326-6066.Cir-20-0787

De Groot, A. S., Ross, T. M., Levitz, L., Messitt, T. J., Tassone, R., Boyle, C. M., et al. (2015). C3d adjuvant effects are mediated through the activation of C3d-specific autoreactive T cells. *Immunol. Cell Biol.* 93 (2), 189–197. doi:10.1038/icb.2014.89

Dianzani, U., Omede, P., Marmont, F., DiFranco, D., Fusaro, A., Bragardo, M., et al. (1994). Expansion of T cells expressing low CD4 or CD8 levels in B-cell chronic lymphocytic leukemia: correlation with disease status and neoplastic phenotype. *Blood* 83 (8), 2198–2205. doi:10.1182/blood.v83.8.2198.bloodjournal8382198

DiScipio, R. G., Daffern, P. J., Schraufstatter, I. U., and Sriramarao, P. (1998). Human polymorphonuclear leukocytes adhere to complement factor H through an interaction that involves αMβ2 (CD11b/CD18). *J. Immunol.* 160 (8), 4057–4066. doi:10.4049/jimmunol.160.8.4057

Dixon, K. O., O'Flynn, J., Klar-Mohamad, N., Daha, M. R., and van Kooten, C. (2017). Properdin and factor H production by human dendritic cells modulates their T-cell stimulatory capacity and is regulated by IFN-γ. *Eur. J. Immunol.* 47 (3), 470–480. doi:10.1002/eji.201646703

Durey, M. A., Sinha, A., Togarsimalemath, S. K., and Bagga, A. (2016). Anti-complement-factor H-associated glomerulopathies. *Nat. Rev. Nephrol.* 12 (9), 563–578. doi:10.1038/nrneph.2016.99

Fedarko, N. S., Fohr, B., Robey, P. G., Young, M. F., and Fisher, L. W. (2000). Factor H binding to bone sialoprotein and osteopontin enables tumor cell evasion of complement-mediated attack. *J. Biol. Chem.* 275 (22), 16666–16672. doi:10.1074/jbc.M001123200

Ferreira, V. P., Pangburn, M. K., and Cortes, C. (2010). Complement control protein factor H: the good, the bad, and the inadequate. *Mol. Immunol.* 47 (13), 2187–2197. doi:10.1016/j.molimm.2010.05.007

Fridman, W. H. (2012). The immune microenvironment as a guide for cancer therapies. *Oncoimmunology* 1 (3), 261–262. doi:10.4161/onci.19651

Fridman, W. H., Zitvogel, L., Sautes-Fridman, C., and Kroemer, G. (2017). The immune contexture in cancer prognosis and treatment. *Nat. Rev. Clin. Oncol.* 14 (12), 717–734. doi:10.1038/nrclinonc.2017.101

Gottlin, E. B., Campa, M. J., Gandhi, R., Bushey, R. T., Herndon, J. E., and Patz, E. F. (2022). Prognostic significance of a complement factor H autoantibody in early stage NSCLC. *Cancer Biomark.* 34, 385–392. doi:10.3233/CBM-210355

Gray, J. D., and Horwitz, D. A. (1988). Lymphocytes expressing type 3 complement receptors proliferate in response to interleukin 2 and are the precursors of lymphokine-activated killer cells. *J. Clin. Invest.* 81 (4), 1247–1254. doi:10.1172/JCI113442

Guo, R., Li, X., Hao, M., Liang, Y., Wang, L., and Yang, Z. (2023). Advances in predictive biomarkers associated with immune checkpoint inhibitors for tumor therapy. *Sheng Wu Gong Cheng Xue Bao* 39 (4), 1403–1424. doi:10.13345/j.cjb.220650

Halbgebauer, R., Schmidt, C. Q., Karsten, C. M., Ignatius, A., and Huber-Lang, M. (2018). Janus face of complement-driven neutrophil activation during sepsis. *Semin. Immunol.* 37, 12–20. doi:10.1016/j.smim.2018.02.004

Hamann, D., Baars, P. A., Rep, M. H., Hooibrink, B., Kerkhof-Garde, S. R., Klein, M. R., et al. (1997). Phenotypic and functional separation of memory and effector human CD8+ T cells. *J. Exp. Med.* 186 (9), 1407–1418. doi:10.1084/jem.186.9.1407

He, X., and Xu, C. (2020). Immune checkpoint signaling and cancer immunotherapy. *Cell Res.* 30 (8), 660–669. doi:10.1038/s41422-020-0343-4

Hersey, P., and Jamal, O. (1990). Immunohistological relation between DR antigen expression on melanoma cells and infiltration by $CD8^+$ T cells. *Pathology* 22 (3), 133–139. doi:10.3109/00313029009063551

Johnson, E. M., Uppalapati, C. K., Pascual, A. S., Estrada, S. I., Averitte, R. L., Leyva, K. J., et al. (2022). Complement factor H in cSCC: evidence of a link between sun exposure and immunosuppression in skin cancer progression. *Front. Oncol.* 12, 819580. doi:10.3389/fonc.2022.819580

Jozsi, M., Schneider, A. E., Karpati, E., and Sandor, N. (2019). Complement factor H family proteins in their non-canonical role as modulators of cellular functions. *Semin. Cell Dev. Biol.* 85, 122–131. doi:10.1016/j.semcdb.2017.12.018

Jozsi, M., and Uzonyi, B. (2021). Detection of complement factor B autoantibodies by ELISA. *Methods Mol. Biol.* 2227, 141–145. doi:10.1007/978-1-0716-1016-9_14

Junnikkala, S., Hakulinen, J., Jarva, H., Manuelian, T., Bjorge, L., Butzow, R., et al. (2002). Secretion of soluble complement inhibitors factor H and factor H-like protein (FHL-1) by ovarian tumour cells. *Br. J. Cancer* 87 (10), 1119–1127. doi:10.1038/sj.bjc.6600614

Junnikkala, S., Jokiranta, T. S., Friese, M. A., Jarva, H., Zipfel, P. F., and Meri, S. (2000). Exceptional resistance of human H2 glioblastoma cells to complement-mediated killing by expression and utilization of factor H and factor H-like protein 1. *J. Immunol.* 164 (11), 6075–6081. doi:10.4049/jimmunol.164.11.6075

Kalli, K. R., Hsu, P. H., Bartow, T. J., Ahearn, J. M., Matsumoto, A. K., Klickstein, L. B., et al. (1991). Mapping of the C3b-binding site of CR1 and construction of a (CR1)2-F(ab')2 chimeric complement inhibitor. *J. Exp. Med.* 174 (6), 1451–1460. doi:10.1084/jem.174.6.1451

Kang, Y. H., Urban, B. C., Sim, R. B., and Kishore, U. (2012). Human complement Factor H modulates C1q-mediated phagocytosis of apoptotic cells. *Immunobiology* 217 (4), 455–464. doi:10.1016/j.imbio.2011.10.008

Kasahara, Y., Iwai, K., Yachie, A., Ohta, K., Konno, A., Seki, H., et al. (1997). Involvement of reactive oxygen intermediates in spontaneous and CD95 (Fas/APO-1)-mediated apoptosis of neutrophils. *Blood* 89 (5), 1748–1753. doi:10.1182/blood.v89.5.1748

Kemper, C., Ferreira, V. P., Paz, J. T., Holers, V. M., Lionakis, M. S., and Alexander, J. J. (2023). Complement: the road less traveled. *J. Immunol.* 210 (2), 119–125. doi:10.4049/jimmunol.2200540

Kiss, M. G., Ozsvar-Kozma, M., Porsch, F., Goderle, L., Papac-Milicevic, N., Bartolini-Gritti, B., et al. (2019). Complement factor H modulates splenic B cell development and limits autoantibody production. *Front. Immunol.* 10, 1607. doi:10.3389/fimmu.2019.01607

Lalli, P. N., Strainic, M. G., Yang, M., Lin, F., Medof, M. E., and Heeger, P. S. (2008). Locally produced C5a binds to T cell-expressed C5aR to enhance effector T-cell expansion by limiting antigen-induced apoptosis. *Blood* 112 (5), 1759–1766. doi:10.1182/blood-2008-04-151068

Lambris, J. D., Dobson, N. J., and Ross, G. D. (1980). Release of endogenous C3b inactivator from lymphocytes in response to triggering membrane receptors for beta 1H globulin. *J. Exp. Med.* 152 (6), 1625–1644. doi:10.1084/jem.152.6.1625

Langford-Smith, A., Day, A. J., Bishop, P. N., and Clark, S. J. (2015). Complementing the sugar code: role of GAGs and sialic acid in complement regulation. *Front. Immunol.* 6, 25. doi:10.3389/fimmu.2015.00025

Laskowski, J., Renner, B., Pickering, M. C., Serkova, N. J., Smith-Jones, P. M., Clambey, E. T., et al. (2020). Complement factor H-deficient mice develop spontaneous hepatic tumors. *J. Clin. Invest.* 130 (8), 4039–4054. doi:10.1172/JCI135105

Law, A. M. K., Valdes-Mora, F., and Gallego-Ortega, D. (2020). Myeloid-derived suppressor cells as a therapeutic target for cancer. *Cells* 9 (3), 561. doi:10.3390/cells9030561

Li, K., Shi, H., Zhang, B., Ou, X., Ma, Q., Chen, Y., et al. (2021a). Myeloid-derived suppressor cells as immunosuppressive regulators and therapeutic targets in cancer. *Signal Transduct. Target Ther.* 6 (1), 362. doi:10.1038/s41392-021-00670-9

Li, X., Zhong, J., Deng, X., Guo, X., Lu, Y., Lin, J., et al. (2021b). Targeting myeloid-derived suppressor cells to enhance the antitumor efficacy of immune checkpoint blockade therapy. *Front. Immunol.* 12, 754196. doi:10.3389/fimmu.2021.754196

Licht, C., Pluthero, F. G., Li, L., Christensen, H., Habbig, S., Hoppe, B., et al. (2009). Platelet-associated complement factor H in healthy persons and patients with atypical HUS. *Blood* 114 (20), 4538–4545. doi:10.1182/blood-2009-03-205096

Ling, M., and Murali, M. (2019). Analysis of the complement system in the clinical immunology laboratory. *Clin. Lab. Med.* 39 (4), 579–590. doi:10.1016/j.cll.2019.07.006

Losse, J., Zipfel, P. F., and Jozsi, M. (2010). Factor H and factor H-related protein 1 bind to human neutrophils via complement receptor 3, mediate attachment to Candida albicans, and enhance neutrophil antimicrobial activity. *J. Immunol.* 184 (2), 912–921. doi:10.4049/jimmunol.0901702

Lyubchenko, T., dal Porto, J., Cambier, J. C., and Holers, V. M. (2005). Coligation of the B cell receptor with complement receptor type 2 (CR2/CD21) using its natural ligand C3dg: activation without engagement of an inhibitory signaling pathway. *J. Immunol.* 174 (6), 3264–3272. doi:10.4049/jimmunol.174.6.3264

Makou, E., Herbert, A. P., and Barlow, P. N. (2013). Functional anatomy of complement factor H. *Biochemistry* 52 (23), 3949–3962. doi:10.1021/bi4003452

Malhotra, R., Ward, M., Sim, R. B., and Bird, M. I. (1999). Identification of human complement Factor H as a ligand for L-selectin. *Biochem. J.* 341 (1), 61–69. doi:10.1042/bj3410061

Mao, X., Zhou, L., Tey, S. K., Ma, A. P. Y., Yeung, C. L. S., Ng, T. H., et al. (2020). Tumour extracellular vesicle-derived Complement Factor H promotes tumorigenesis and metastasis by inhibiting complement-dependent cytotoxicity of tumour cells. *J. Extracell. Vesicles* 10, e12031. doi:10.1002/jev2.12031

Masucci, M. T., Minopoli, M., and Carriero, M. V. (2019). Tumor associated neutrophils. Their role in tumorigenesis, metastasis, prognosis and therapy. *Front. Oncol.* 9, 1146. doi:10.3389/fonc.2019.01146

Merle, N. S., Noe, R., Halbwachs-Mecarelli, L., Fremeaux-Bacchi, V., and Roumenina, L. T. (2015). Complement system Part II: role in immunity. *Front. Immunol.* 6, 257. doi:10.3389/fimmu.2015.00257

Mollet, L., Sadat-Sowti, B., Duntze, J., Leblond, V., Bergeron, F., Calvez, V., et al. (1998). CD8hi+CD57+ T lymphocytes are enriched in antigen-specific T cells capable of

down-modulating cytotoxic activity. *Int. Immunol.* 10 (3), 311–323. doi:10.1093/intimm/10.3.311

Moore, S. R., Menon, S. S., Cortes, C., and Ferreira, V. P. (2021). Hijacking factor H for complement immune evasion. *Front. Immunol.* 12, 602277. doi:10.3389/fimmu.2021.602277

Nagar, B., Jones, R. G., Diefenbach, R. J., Isenman, D. E., and Rini, J. M. (1998). X-ray crystal structure of C3d: a C3 fragment and ligand for complement receptor 2. *Science* 280 (5367), 1277–1281. doi:10.1126/science.280.5367.1277

Olivar, R., Luque, A., Cardenas-Brito, S., Naranjo-Gomez, M., Blom, A. M., Borras, F. E., et al. (2016). The complement inhibitor factor H generates an anti-inflammatory and tolerogenic state in monocyte-derived dendritic cells. *J. Immunol.* 196 (10), 4274–4290. doi:10.4049/jimmunol.1500455

Parente, R., Clark, S. J., Inforzato, A., and Day, A. J. (2017). Complement factor H in host defense and immune evasion. *Cell Mol. Life Sci.* 74 (9), 1605–1624. doi:10.1007/s00018-016-2418-4

Pillay, J., Tak, T., Kamp, V. M., and Koenderman, L. (2013). Immune suppression by neutrophils and granulocytic myeloid-derived suppressor cells: similarities and differences. *Cell Mol. Life Sci.* 70 (20), 3813–3827. doi:10.1007/s00018-013-1286-4

Pisibon, C., Ouertani, A., Bertolotto, C., Ballotti, R., and Cheli, Y. (2021). Immune checkpoints in cancers: from signaling to the clinic. *Cancers (Basel)* 13 (18), 4573. doi:10.3390/cancers13184573

Platt, J. L., Silva, I., Balin, S. J., Lefferts, A. R., Farkash, E., Ross, T. M., et al. (2017). C3d regulates immune checkpoint blockade and enhances antitumor immunity. *JCI Insight* 2 (9), e90201. doi:10.1172/jci.insight.90201

Reis, E. S., Mastellos, D. C., Ricklin, D., Mantovani, A., and Lambris, J. D. (2018). Complement in cancer: untangling an intricate relationship. *Nat. Rev. Immunol.* 18 (1), 5–18. doi:10.1038/nri.2017.97

Revel, M., Daugan, M. V., Sautes-Fridman, C., Fridman, W. H., and Roumenina, L. T. (2020). Complement system: promoter or suppressor of cancer progression? *Antibodies (Basel)* 9 (4), 57. doi:10.3390/antib9040057

Ricklin, D., Hajishengallis, G., Yang, K., and Lambris, J. D. (2010). Complement: a key system for immune surveillance and homeostasis. *Nat. Immunol.* 11 (9), 785–797. doi:10.1038/ni.1923

Ricklin, D., Mastellos, D. C., and Lambris, J. D. (2019). Therapeutic targeting of the complement system. *Nat. Rev. Drug Discov.* doi:10.1038/s41573-019-0055-y

Ricklin, D., and Pouw, R. B. (2021). Complement and disease: out of the shadow into the spotlight. *Semin. Immunopathol.* 43 (6), 755–756. doi:10.1007/s00281-021-00897-2

Riihila, P. M., Nissinen, L. M., Ala-Aho, R., Kallajoki, M., Grenman, R., Meri, S., et al. (2014). Complement factor H: a biomarker for progression of cutaneous squamous cell carcinoma. *J. Invest. Dermatol* 134 (2), 498–506. doi:10.1038/jid.2013.346

Ripoche, J., Erdei, A., Gilbert, D., Al Salihi, A., Sim, R. B., and Fontaine, M. (1988). Two populations of complement factor H differ in their ability to bind to cell surfaces. *Biochem. J.* 253 (2), 475–480. doi:10.1042/bj2530475

Sakaue, T., Takeuchi, K., Maeda, T., Yamamoto, Y., Nishi, K., and Ohkubo, I. (2010). Factor H in porcine seminal plasma protects sperm against complement attack in genital tracts. *J. Biol. Chem.* 285 (3), 2184–2192. doi:10.1074/jbc.M109.063495

Savary, C. A., and Lotzova, E. (1992). Adhesion molecules on MHC-nonrestricted lymphocytes: high density expression and role in oncolysis. *Lymphokine Cytokine Res.* 11 (3), 149–156.

Saxena, R., Bushey, R., Campa, M., Gottlin, E., Guo, J., Patz, E., et al. (2023). *Creation of a favorable antitumor microenvironment by the anti-complement factor H antibody mGT103*. Durham: Research Square.

Schneider, A. E., Sandor, N., Karpati, E., and Jozsi, M. (2016). Complement factor H modulates the activation of human neutrophil granulocytes and the generation of neutrophil extracellular traps. *Mol. Immunol.* 72, 37–48. doi:10.1016/j.molimm.2016.02.011

Schwaeble, W., Zwirner, J., Schulz, T. F., Linke, R. P., Dierich, M. P., and Weiss, E. H. (1987). Human complement factor H: expression of an additional truncated gene product of 43 kDa in human liver. *Eur. J. Immunol.* 17 (10), 1485–1489. doi:10.1002/eji.1830171015

Senent, Y., Tavira, B., Pio, R., and Ajona, D. (2022). The complement system as a regulator of tumor-promoting activities mediated by myeloid-derived suppressor cells. *Cancer Lett.* 549, 215900. doi:10.1016/j.canlet.2022.215900

Smolag, K. I., Mueni, C. M., Leandersson, K., Jirstrom, K., Hagerling, C., Morgelin, M., et al. (2020). Complement inhibitor factor H expressed by breast cancer cells differentiates CD14(+) human monocytes into immunosuppressive macrophages. *Oncoimmunology* 9 (1), 1731135. doi:10.1080/2162402X.2020.1731135

Strainic, M. G., Liu, J., Huang, D., An, F., Lalli, P. N., Muqim, N., et al. (2008). Locally produced complement fragments C5a and C3a provide both costimulatory and survival signals to naive CD4+ T cells. *Immunity* 28 (3), 425–435. doi:10.1016/j.immuni.2008.02.001

Sun, H. L., Zhou, X., Xue, Y. F., Wang, K., Shen, Y. F., Mao, J. J., et al. (2012). Increased frequency and clinical significance of myeloid-derived suppressor cells in human colorectal carcinoma. *World J. Gastroenterol.* 18 (25), 3303–3309. doi:10.3748/wjg.v18.i25.3303

Tu, Z., Li, Q., Bu, H., and Lin, F. (2010). Mesenchymal stem cells inhibit complement activation by secreting factor H. *Stem Cells Dev.* 19 (11), 1803–1809. doi:10.1089/scd.2009.0418

Varsano, S., Rashkovsky, L., Shapiro, H., Ophir, D., and Mark-Bentankur, T. (1998). Human lung cancer cell lines express cell membrane complement inhibitory proteins and are extremely resistant to complement-mediated lysis; a comparison with normal human respiratory epithelium *in vitro*, and an insight into mechanism(s) of resistance. *Clin. Exp. Immunol.* 113 (2), 173–182. doi:10.1046/j.1365-2249.1998.00581.x

Vinay, D. S., Ryan, E. P., Pawelec, G., Talib, W. H., Stagg, J., Elkord, E., et al. (2015). Immune evasion in cancer: mechanistic basis and therapeutic strategies. *Semin. Cancer Biol.* 35, S185–S198. doi:10.1016/j.semcancer.2015.03.004

Wagner, C., Hansch, G. M., Stegmaier, S., Denefleh, B., Hug, F., and Schoels, M. (2001). The complement receptor 3, CR3 (CD11b/CD18), on T lymphocytes: activation-dependent up-regulation and regulatory function. *Eur. J. Immunol.* 31, 1173–1180. doi:10.1002/1521-4141(200104)31:4<1173::AID-IMMU1173>3.0.CO;2-9

Wang, Y., Sun, S. N., Liu, Q., Yu, Y. Y., Guo, J., Wang, K., et al. (2016). Autocrine complement inhibits IL10-dependent T-cell-mediated antitumor immunity to promote tumor progression. *Cancer Discov.* 6, 1022–1035. doi:10.1158/2159-8290.CD-15-1412

Wang, Y., Zhang, H., and He, Y. W. (2019). The complement receptors C3aR and C5aR are a new class of immune checkpoint receptor in cancer immunotherapy. *Front. Immunol.* 10, 1574. doi:10.3389/fimmu.2019.01574

Wilczek, E., Rzepko, R., Nowis, D., Legat, M., Golab, J., Glab, M., et al. (2008). The possible role of factor H in colon cancer resistance to complement attack. *Int. J. Cancer* 122 (9), 2030–2037. doi:10.1002/ijc.23238

Winkler, M. T., Bushey, R. T., Gottlin, E. B., Campa, M. J., Guadalupe, E. S., Volkheimer, A. D., et al. (2017). Enhanced CDC of B cell chronic lymphocytic leukemia cells mediated by rituximab combined with a novel anti-complement factor H antibody. *PLoS One* 12 (6), e0179841. doi:10.1371/journal.pone.0179841

Wu, L., Saxena, S., and Singh, R. K. (2020). Neutrophils in the tumor microenvironment. *Adv. Exp. Med. Biol.* 1224, 1–20. doi:10.1007/978-3-030-35723-8_1

Zhai, Y., Celis-Gutierrez, J., Voisinne, G., Mori, D., Girard, L., Burlet-Schiltz, O., et al. (2021). Opposing regulatory functions of the TIM3 (HAVCR2) signalosome in primary effector T cells as revealed by quantitative interactomics. *Cell Mol. Immunol.* 18 (6), 1581–1583. doi:10.1038/s41423-020-00575-7

Zhang, R., Liu, Q., Li, T., Liao, Q., and Zhao, Y. (2019). Role of the complement system in the tumor microenvironment. *Cancer Cell Int.* 19, 300. doi:10.1186/s12935-019-1027-3

Zhao, Y., Rahmy, S., Liu, Z., Zhang, C., and Lu, X. (2020). Rational targeting of immunosuppressive neutrophils in cancer. *Pharmacol. Ther.* 212, 107556. doi:10.1016/j.pharmthera.2020.107556

# Frontiers in
# Cell and Developmental Biology

**Explores the fundamental biological processes of life, covering intracellular and extracellular dynamics.**

The world's most cited developmental biology journal, advancing our understanding of the fundamental processes of life. It explores a wide spectrum of cell and developmental biology, covering intracellular and extracellular dynamics.

---

## Discover the latest Research Topics

See more →


**Frontiers**

Avenue du Tribunal-Fédéral 34
1005 Lausanne, Switzerland
frontiersin.org

**Contact us**

+41 (0)21 510 17 00
frontiersin.org/about/contact